ÉCOLE DOCTORALE DES SCIENCES DE LA VIE ET DE LA SANTÉ

CNRS UPR3212 – Institut des Neurosciences Cellulaires et Intégratives

THÈSE présentée par :

Angel BAUDON

soutenue le : **20 juin 2023**

pour obtenir le grade de : **Docteur de l'université de Strasbourg**

Discipline/ Spécialité : Neurosciences

Étude de l'effet de l'ocytocine sur le circuit astro-neuronal de l'amygdale centrale

Study of the oxytocin effect on the central amygdala astro-neuronal network

THÈSE dirigée par :
  M. CHARLET Alexandre   DR, Université de Strasbourg, France.

RAPPORTEURS :
  Mme. PANATIER Aude   DR, Neurocentre Magendie, Université de Bordeaux, France.
  Mme. ESCARTIN Carole   DR, Laboratoire des maladies neurodégénératives, France

AUTRES MEMBRES DU JURY :
  M. DESAINTJAN Didier   CR, Université de Strasbourg, France.

« La thèse c'est comme la grimpe, un bon frühstück,
un bloc-bloc quand on est coincé
et à la fin c'est que de la rési. »

Quentin Leboulleux

Remerciements

Salutations distinguées messires et gentes dames, *révérence*

Avant de tourner les pages du présent grimoire, je dois vous avertir. Vous allez trouver ici des illustrations d'une fabrique exceptionelle. Essayez donc de ne point tourner de l'oeil devant tant de beauté. Ces chefs-d'oeuvres ont été réalisés par les quidams qui méritent toute ma gratitude. Cette missive s'adresse donc tout d'abord à vous, estimé jury, pour vous transmettre mes sincères remerciements pour le temps que vous allez passer sur l'évaluation de mon ouvrage et de sa défense.

Pour le reste du contenu de ce manuscrit, c'est à vous qu'il incombe d'en juger la qualité. Sachez néamoins que les experiences alchimiques qui y sont archivées n'auraient jamais vu le jour sans Mestre Charlet. Attentif et à l'écoute, il m'a permis de parer mon âme des atours de la science. La relation que nous avons est chère a mon cœur car tu as su me considérer comme un collègue. Je te suis reconaissant des belles années que j'ai passées avec toi. Au cours de ce périple, j'ai eu la chance d'avoir à mes côtés l'indéfectible soutien d'Étienne. Compagnon de route et de voie, nous nous sommes formés côte à côte sur la rocailleuse route de la science. Je t'adresse donc un énorme schmoutz et t'offre toute ma gratitude. A mon arrivée au temple des neurociences, j'ai aussi rencontré deux joyeux lurons, Damien et Louis. Ces collègues sont devenus des camarades aguéris, et je les en remercie grandement. Enfin, merci à toi Tatin baby boy pour ton humeur au beau fixe et ta compagnie chaleureuse. Bon courage pour les révisions, allez ciao héhé !

Des turbo poutous pour pour Jarion, Théo, Jamille et Tonchie babe. Dès le début on a formé une chouette équipe et on s'est portés jusqu'au bout. Je pense qu'une grande part de mon intéret pour la science est née de l'émulsion formée par notre groupe, et ça, c'est cooooool. Spéciale dédicace à toi petite Jahionr, merci de partager ma vie et de me soutenir en toutes situations. Tornades de bisous.

Puisse l'univers bénir Philippe, car dans les heures sombres, il a su ramener la lumière de la passion. Tendres pensées à Yannick et Pascal, à leur mine joviale, leur crâne étincelant et leur compagnie bienveillante. J'aimerais aussi rendre hommage aux diverses personnes de l'INCI qui m'ont soutenu telles que Marie-Pierre, Sophie et Dom, Stéphane et Julie. Je vous ai fait pas mal tourner en bourrique, merci de votre patience !

Mais qui serais-je si j'oubliais tous les amis qui ont illuminé mes journées au quotidien ? Moultes bisous à tout le gang de l'INCI, Sarah, Quentin, Louise, Valod, Flo, Zélie, Théo, Lucien, Robin, Karim, Alice et tutti quanti. Et même Ludo. Non quand même pas Ludo.

Au cours de ma dernière année j'ai aussi intégré une coloc du feu de dieu. Non en vrai c'est le feu. Ils m'ont donné une bonne dose d'énergie, gros merci aux BK gang.

Et forcément, on n'oublie pas les bases. Un méga merci à ma famille et à tous mes amis de longue date, sauf les gogols de la rue Breteuil qui m'ont pas fait de dessin.

Pour les figures participatives, vous trouverez le détail des artistes ci-dessous. Les autres sont remerciés dans les légendes.

Figure 1 : Tatin, Marie, Sarah, Quentin, Tiénou, Maodow, Jahionr, Chloé, Laureline, Joussial, Clo, Marty et Jamille

Figure 24 : Suzy, Toto, Clemence, Robin, Chulele, Lunishka, Valod, Kai-Yi, NMC, Loulou, Tonchie babe, Karim et Luigi bbq.

Enfin, merci à l'ASCPA pour son acceuil chaleureux ainsi qu'à l'école doctorale et à la fondation pour la recherche médicale pour avoir financé ma thèse.

Bonne lecture,
Angel

Contents

Abbreviations:

A

AChE: acetylcholinesterase

AM: amplitude modulation

AN: accessory nuclei

AStr: Amygdalostriatal area

AVP: arginine vasopressin

B

BA: basal amygdala

BLA: basolateral amygdala

C

$[Ca^{2+}]_{IC}$: intracellular Ca^{2+} concentration

CA1/2/3: Cornu Ammonis 1/2/3

CeA: central amygdala

CeL/C: laterocapsular part of the CeA

CeM: medial part of the CeA

CoA: cortical amygdala

CRH: corticotropin-releasing hormone

CS: conditioned stimulus

D

DAG: diacylglycerol

DVC: dorsal vagal complex, PAG: periaqueducal grey

E

ECS: extracellular space

(m)EPSCs: (miniature) excitatory postsynaptic currents

ER/SR: endo/sarcoplasmic reticulum

ERE: estrogen regulatory element

ERK1/2: extracellular signal-regulated kinases 1/2

F

FM: frequency modulation

FWER: family-wise error range

G

GABA: gamma-aminobutyric acid

GDP: guanosine diphosphate

GEF: guanine nucleotide exchange factor

GECI: genetically encoded Ca^{2+}

GFP: green fluorescence protein

GFAP: glial fibrillary acidic protein indicator

GHK: Goldman-Hodgkin-Katz

GIRK: G protein-coupled inwardly rectifying potassium channel

GPCR: G-protein coupled receptors

GRK: GPCR kinases

GTP: guanosine triphosphate

I

ICM: intercalated cell mass

IP3: inositol trisphosphate

IP3R: inositol trisphosphate receptor

IPAC: interstitial nucleus of the posterior limb of the anterior commissure

K

$[K^+]_{EC}$: extracellular K^+ concentration

K_{ir}: inward rectifier K^+ channels

L
LDCV: large dense core vesicles
LTP: long-term potentiation
M
MAPK: mitogen-activated protein kinase
MCU: mitochondrial Ca^{2+} uniporter
MeA: medial amygdala
mPTP: mitochondrial permeability transition pore
MSN: medium spiny neurons
N
(m)NCX: (mitochondrial) Na^+/Ca^{2+} exchanger
NMDA: N-methyl-D-aspartate
O
OGB1: Oregon BAPTA green 1
OT: oxytocin
OTR: oxytocin receptors
P
PAPs: perisynaptic astrocyte processes
PAG: periaqueducal gray
PI3K: phosphoinositide 3-kinase
PIP$_2$: phosphatidylinositol 4,5-bisphosphate
PKA/B/C: protein kinase A/B/C
PLC: phospholipase C
PMCA: plasma membrane Ca2+ ATPase
PON: preoptic nucleus of the hypothalamus

Ppp1r1b: protein phosphatase 1 regulatory inhibitor subunit 1B
PVN: paraventricular nucleus of the hypothalamus
R
R/G: receptor/G-protein
Rhod2: rhodamine 2
ROS: reactive oxygen species
Rspo2: R-Spondin 2
RyR: ryanodine receptor
S
SERCA: sarco/endoplasmic reticulum Ca^{2+} ATPase
SIC: slow inward current
SNARE: SNAp REceptor
SOM: somatostatin
SON: supraoptic nucleus of the hypothalamus
SR101: surlforhodamine 101
STED: stimulated emission depletion
T
TCA: tricarboxylic acid
TGOT: [Thr$_4$,Gly$_7$]-oxytocin
TRPV1: transient receptor potential cation channel subfamily V member 1
U
US: unconditioned stimulus
V
VGCC: voltage-gated Ca^{2+} channels
Vm: membrane voltage
V1/2: AVP receptors type 1/2
Others
3V: third ventricle

1. The oxytocin system

1.1. OT system during evolution

The tale of oxytocin began more than 600 million years ago (Gwee et al., 2009). At this time, this neuropeptide and its twin, vasopressin (AVP), was probably one unique peptide: vasotocin. The function of this ancestral peptide was to regulate osmolarity, one of the most crucial parameters of homeostasis. Then, time went on and the vasotocin gene duplicated to follow two evolutionary lineages with distinct physiological functions. The first one stayed true to himself and gave rise to vasopressin, a neuropeptide highly involved in water homeostasis, whereas the second one diverged from its initial functions and gave rise to isotocin, mesotocin or oxytocin, according to the evolutionary path (Gimpl and Fahrenholz, 2001; Jurek and Neumann, 2018, Figure 1). This last family of peptides is involved in many physiological functions such as the control of reproduction, alimentation, emotion control, *etc.*

OT homologs are found in a wide range of species in the animal kingdom. In basal vertebrates (Anamnia: fish and amphibians), OT and AVP homologs can be found in magnocellular neurons of the preoptic nucleus (PON) that lie near the 3V (Knobloch and Grinevich, 2014, Figure 2). However, in advanced vertebrates (Amniota: reptiles, birds, and mammals), there are three main OT nuclei: the paraventricular (PVN), the supraoptic (SON), and the accessory (AN) nuclei (Figure 2). This mono-to-polycentric transition of the OT system is not fully understood but it seems that it could be due to the migration of OT-producing cells of the ventral PON ventrolaterally to form the SON (Herget et al., 2014). During this migration, some cells may have stopped their migration in the way, forming the AN. For instance, in platypus, most OT-producing cells form a stream that lies between the PVN and the retrochiasmatic part of the SON (Ashwell et al., 2006). Another argument to strengthen this theory comes from brain development. According to Haeckel's law, mechanisms
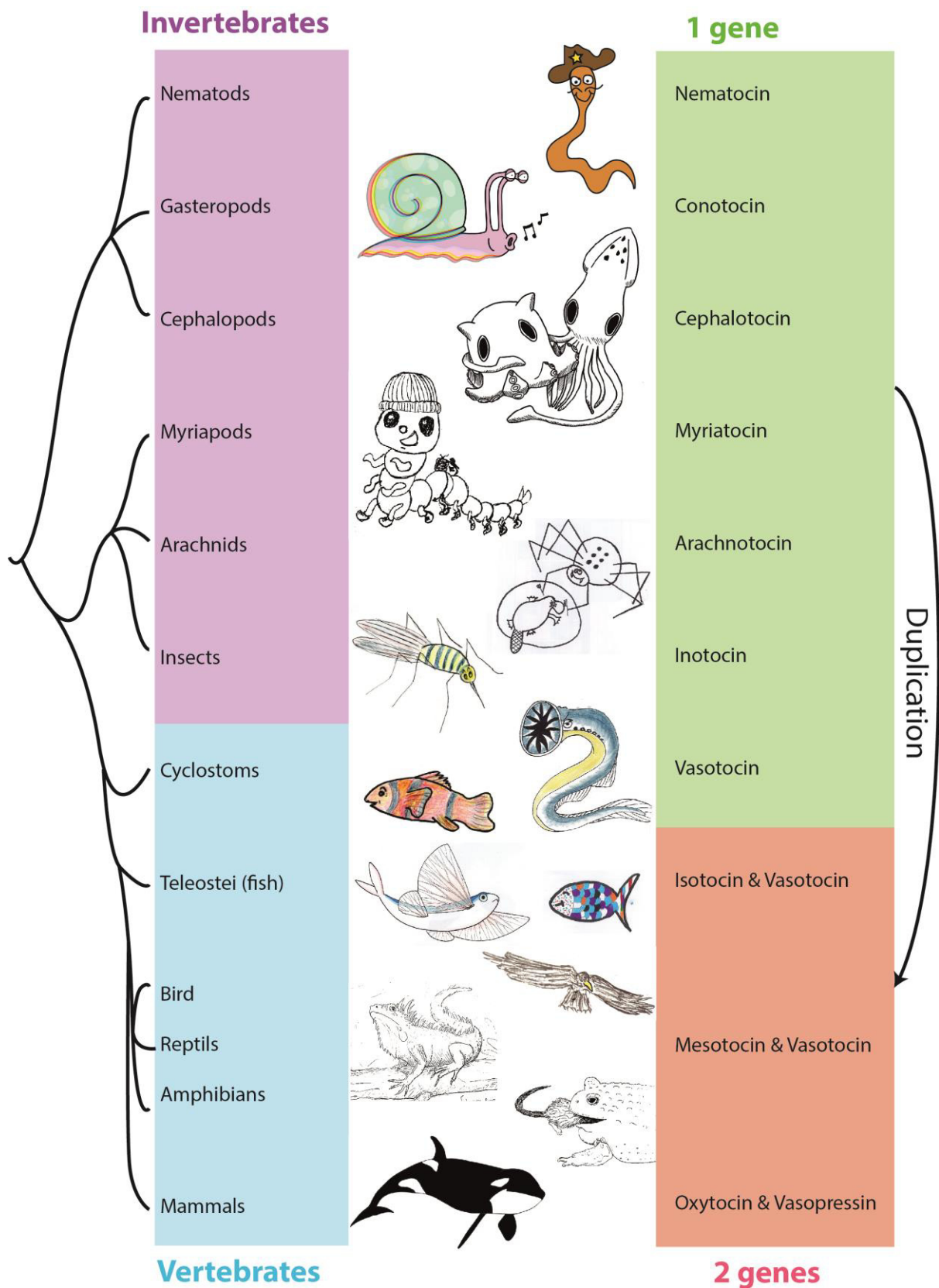
Figure 1: Evolution of the Oxytocin/Vasopressin system in animals. Adapted from (Jurek and Neumann, 2018). Artists are listed in the "Remerciement" section.

observed during embryogenesis resemble those observed during phylogenesis, and indeed, magnocellular OT cells migrate ventrolaterally along radial glia from the 3rd ventricle during the embryogenesis of amniota (Knobloch and Grinevich, 2014).
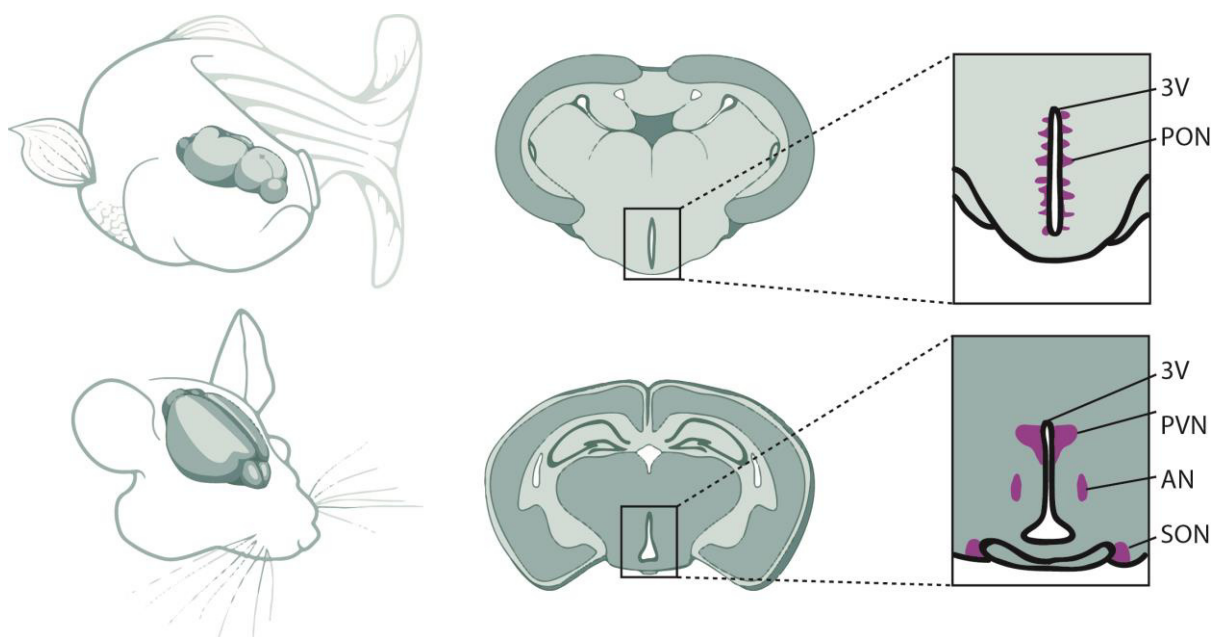
Figure 2: Localisation of Isotocin/OT-producing neurons in fish and mice. Upper panel: fish isotocin-producing neurons (in purple) are clustered in the preoptic nucleus (PON) that lay along the wall of the 3rd ventricle (3V). Lower panel: mice have three hypothalamic nuclei that produce oxytocin: the supraoptic nucleus (SON), the paraventricular nucleus (PVN), and the accessory nuclei (AN). Adapted from (Knobloch and Grinevich, 2014).

1.2. OT system in mammals

1.2.1. From OT synthesis to its release

Synthesis

OT is synthesized in several regions of the body such as the hypothalamus, the uterus, the testis, and the heart. In the brain, this synthesis takes place in neurons located in 3 nuclei of the hypothalamus (the paraventricular, supraoptic, and accessory nuclei), in the medial preoptic area of the hypothalamus, the lateral amygdala, and the bed nucleus of the stria terminalis (Lee et al., 2009; Otero-García et al., 2016; Young and Gainer, 2003).

The recipe of the OT peptide is archived in a gene named *Oxt* located in chromosome 3 for rats and mice and chromosome 4 for humans. This gene contains three exons and is head-to-tail with the gene encoding the AVP, wisely named *Avp*. OT is encoded in the first exon, alongside a signal peptide (Figure 3), whereas the two other exons encode another peptide named Neurophysin 1 (Gimpl and Fahrenholz, 2001).

The expression of OT is controlled by several regulatory sequences, among which we can find an Estrogen Regulatory Element (ERE) that allows the transcription of OT to be stimulated by estradiol (Lee et al., 2009). This regulation of OT expression is of particular importance since the level of estradiol varies a lot during the estrous cycle in females, influencing OT peptide transcription, and eventually OT-regulated behaviors (Acevedo-Rodriguez et al., 2015). Once transcribed, the *Oxt* mRNA is then translated by the ribosomes at the surface of the rough endoplasmic reticulum. The product of this translation is a preprohormone named preprooxyphysin (Figure 3) which is then cleaved to give rise to the OT peptide and the Neurophysin 1 protein (Jurek and Neumann, 2018). OT is a small nine-amino acid peptide whereas Neurophysin 1 is much bigger, reaching 90 to 97 amino acids. The exact function of Neurophysin 1 is still unclear but it is thought to be a carrier protein important for the correct targeting, packaging, and storage of OT in vesicles (Jurek and Neumann, 2018).
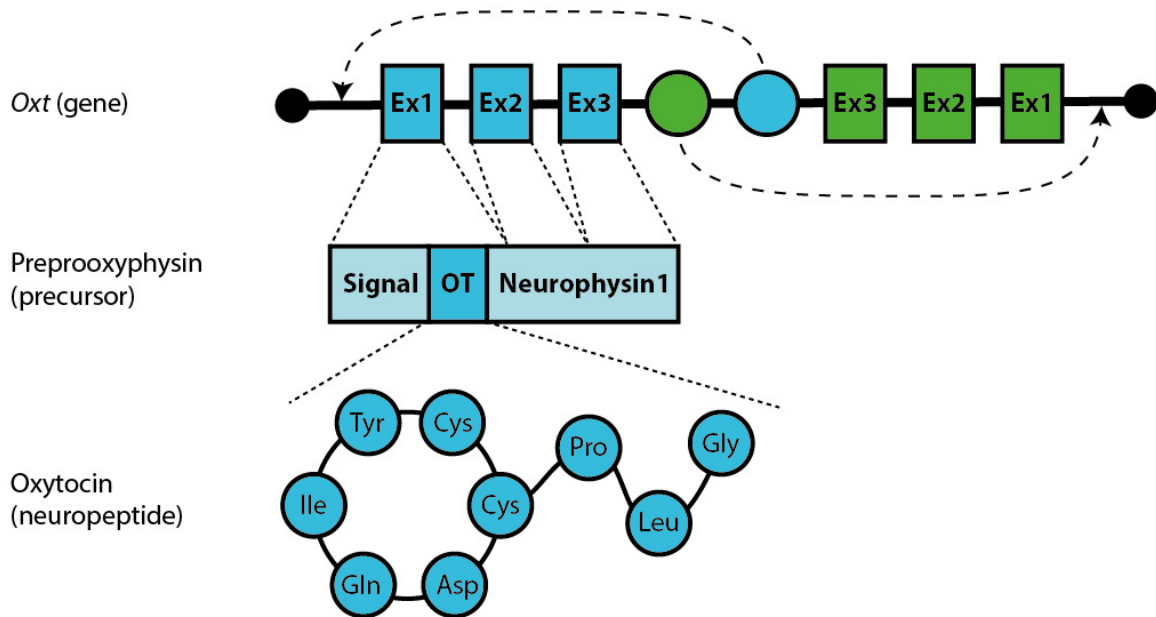
Figure 3: The synthesis of oxytocin. Upper panel: the Oxt gene (in blue) contains three exons and is head-to-tail with the AVP gene (in green). The sequence between the exons of the two genes comprises regulatory elements. Middle panel: The precursor of OT is a prepropeptide that contains a signal sequence and the coding sequences of OT and Neurophysin 1. Lower panel: OT is a nine amino acids peptide that comprises a disulfide bond between cysteines at positions 1 and 6. Adapted from (Gimpl and Fahrenholz, 2001).

Storage

OT is stored in large dense core vesicles (LDCVs, ~100nm diameter, Del-Bel and De-Miguel, 2018). It has been estimated that each vesicle contains approximately 85,000 OT molecules (Leng and Ludwig, 2008). These vesicles can be found at different sites in OT neurons including the soma, the dendrites, axonal varicosities, and synaptic buttons (Leng and Ludwig, 2008, Figure 4A).

LDCVs rest at a distance from the plasma membrane, so a single action potential cannot trigger large exocytosis (Del-Bel and De-Miguel, 2018). Indeed, only trains of action potentials (or a sustained depolarization) that can generate giant Ca^{2+} waves (aka Ca^{2+} tsunamis) can evoke important events of exocytosis that can last several hundreds of seconds (Del-Bel and De-Miguel, 2018). Although we have no exact values for the OT system in particular, it has been estimated that several

hundreds of spikes are necessary to trigger the release of one single LDCV at a given release site (Leng and Ludwig, 2008). The huge Ca^{2+} signaling arising therefrom is necessary to move LDCVs across the actin cortex, which can represent a journey of 0.6 to 6 μm in serotoninergic neurons. Knowing that LDCVs travel at a speed of 15 to 90 nm/s, these vesicles can take 6 seconds to 1 minute to reach the cell membrane (Del-Bel and De-Miguel, 2018).

Release

There are two types of OT neurons: magnocellular and parvocellular cells. First, magnocellular neurons are large cells (20-35μm soma diameter) found in the three hypothalamic nuclei and projecting to the neurohypophysis to release OT in the blood flow (Jurek and Neumann, 2018). These neurons also have collaterals that reach forebrain regions including the piriform and the auditory cortices, the amygdala, and the striatum (Zhang et al., 2021). The other OT synthesizing neurons are called parvocellular because of their tiny size (12-15μm soma diameter). These neurons do not project in the neurohypophysis but rather project to midbrain structures, the brainstem, and the spinal cord (Knobloch et al., 2012; Zhang et al., 2021).

Once OT neurons are activated, they can release OT in several ways (Grinevich and Ludwig, 2021; Leng and Ludwig, 2008):

1) Action potential generated at the Hill segment can backpropagate and provoke the fusion of somatic and dendritic LDCV to the plasma membrane, a mechanism called "somatodendritic release" (Figure 4B).

2) After their generation, action potentials also propagate anterogradely and travel along the axon to meet some swellings (*ie.* varicosities) that contain LDCV. The action potential triggers LDCV fusion to the plasma membrane but then continues its journey along the axon (Figure 4B).

3) Finally reaching the axon terminal, the action potential can trigger a classic synaptic transmission (Figure 4B).

Even if we know that these three releasing modes exist, it is still unclear which one takes place in which condition. Indeed, classical asymmetric synapses have been only shown in the central amygdala (Grinevich and Ludwig, 2021; Knobloch et al., 2012), while varicosity-containing axons have been shown in the central amygdala (Hasan et al., 2019; Knobloch et al., 2012) and the spinal cord (Oti et al., 2021).

A.

Dendrites (2-4 per cell)
~15 000 vesicles per soma-dendrites

Hypophysis

Nerve swellings (436 per cell)
~2 240 vesicles per swelling

Nerve endings (1840 per cell)
~258 vesicles per endings

B.

OT neuron

OT releasing sites

OT vesicles

Terminal bouton
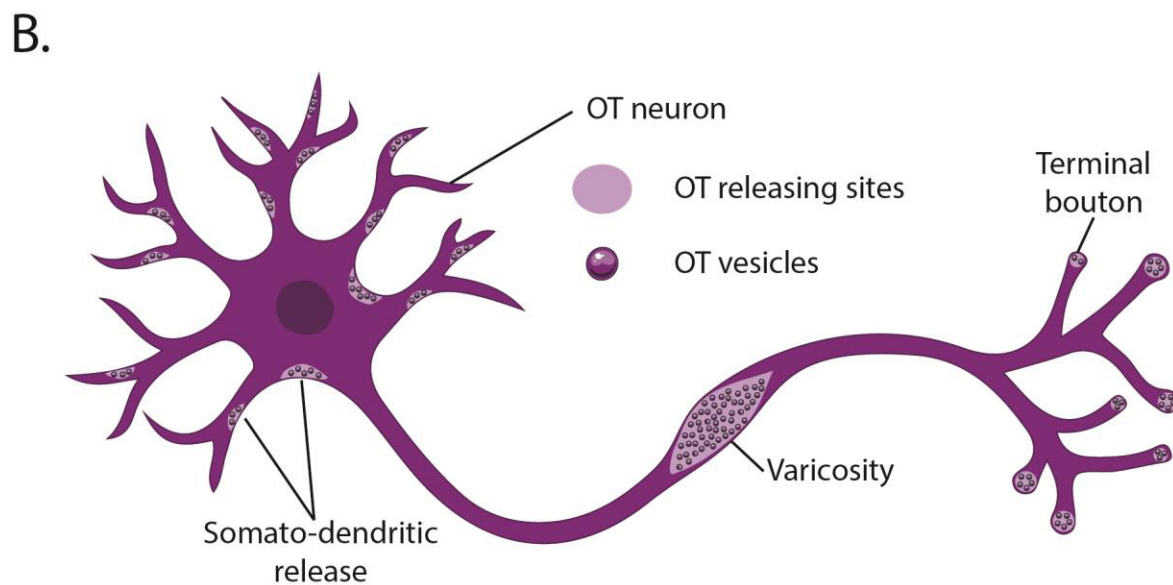
Varicosity

Somato-dendritic release
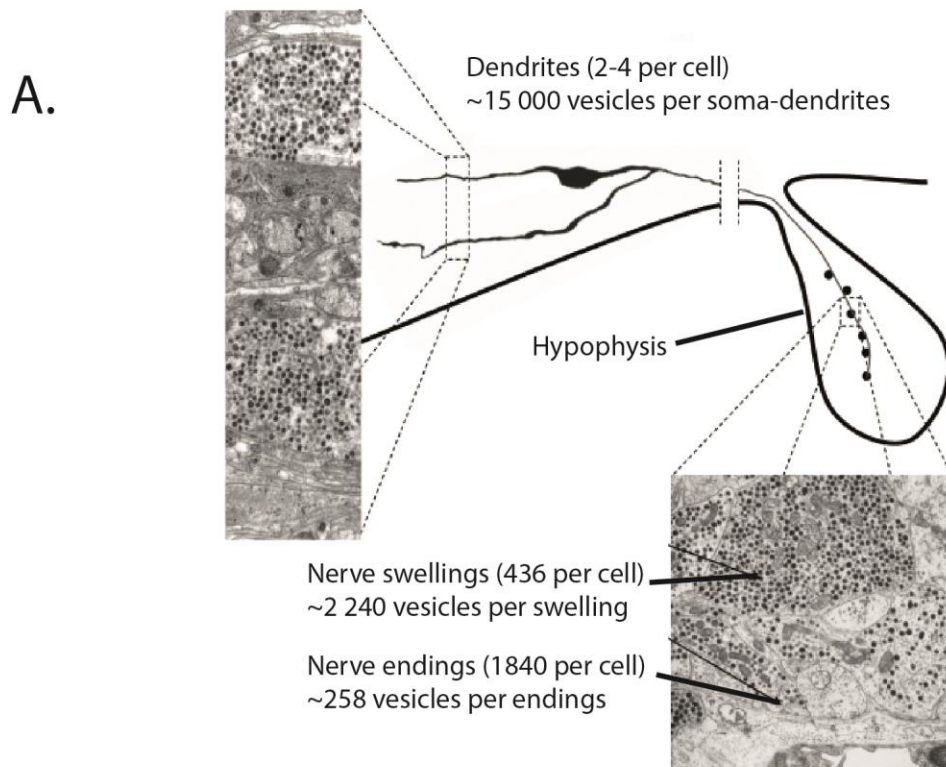
Figure 4: OT release from hypothalamic neurons. A. Repartition of OT-containing molecules in OT-producing magnocellular neurons. From (Leng and Ludwig, 2008). B. OT releasing sites in hypothalamic neurons.

Is OT a neuromodulator or a neurotransmitter?

As with many other neuropeptides, OT is thought to act as a neuromodulator rather than a neurotransmitter. Primarily defined by their action on neurons, neuromodulators have also other characteristics that separate them from classic neurotransmitters (Lentz, 2023). For instance, neuromodulator signaling is often more diffuse in space and time than classical synaptic transmission (Leng and Ludwig, 2008). Although this model is NOT demonstrated, it is strengthened by several clues.

1) The major mode of OT release is thought to be volumic, meaning that it does not involve juxtaposed postsynaptic elements but rather floods the extracellular milieu with OT. In stark contrast with classical synapses, this open communication channel is not spatially restricted and gains its specificity only by acting on cells that express the oxytocin receptor (OTR). These elements had recently been highlighted (Grinevich and Ludwig, 2021) and it is supposed that OT signaling is mainly mediated in a volumic fashion, making synapses found in the CeA an exception rather than the rule. However, in this analysis, they do not take into account that, to our knowledge, only one has investigated this issue using electron microscopy (Knobloch et al., 2012). Moreover, they assume that varicosity-forming axons are a sign of volume transmission but these varicosities can perfectly be the presynaptic site of classical synapses (Shepherd and Raastad, 2003). The other way around, volume transmission can also take place in axon terminals at classical synapses by the spillover of neurotransmitters.

2) Due to the lack of an efficient anti-OTR antibody, we do not know precisely where OTR is expressed in cells, so we cannot assume that this receptor is present at postsynaptic elements (Grinevich and Ludwig, 2021; Jurek and Neumann, 2018). The action site of OT neuromodulatory effects is still under debate since some studies point toward presynaptic effects whereas others suggest postsynaptic ones (Bakos et al., 2018). The general trend seems to indicate that OT may act presynaptically, particularly on inhibitory GABAergic synapses (Crane et al., 2020; Dölen et al., 2013; McKay and Counts, 2020 but see Bakos et al., 2018 for a complete review of pre and postsynaptic effects on excitatory and inhibitory synapses).

3) Upon neuron excitation, LDCV fuses to the plasma membrane and provokes the release of tens of thousands of molecules. It has been estimated that OT could activate OTR present as far as 55µm away (Chini et al., 2017, Figure 5). Note that I found no study on OT diffusion in the brain, making this model approximate.
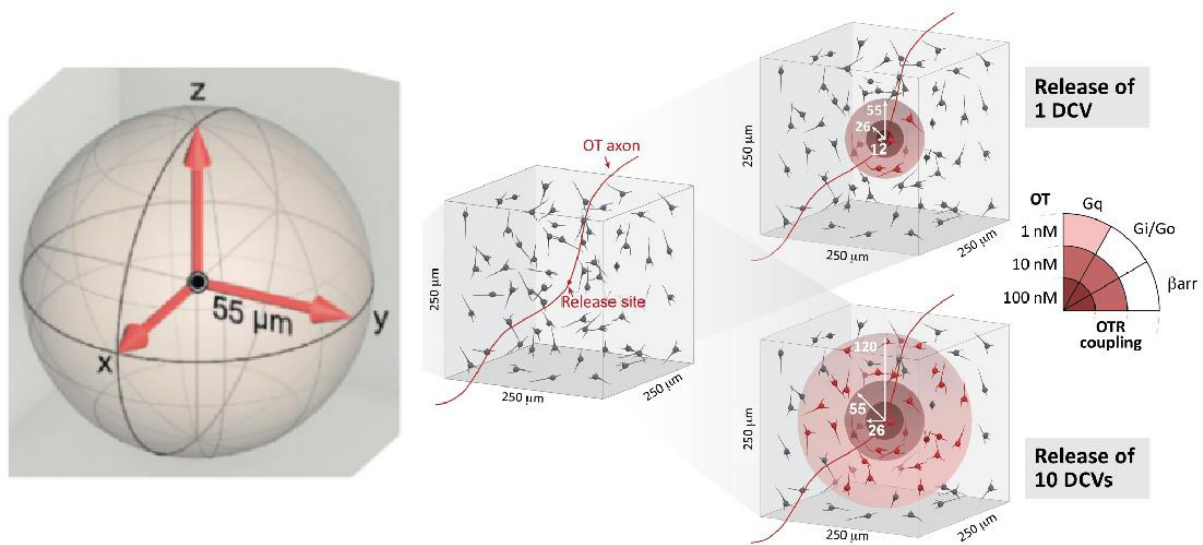
Figure 5: The action radius of Oxytocin. Left: it has been estimated that the fusion of one OT-containing large dense core vesicle (LDCV) can activate OTR as far as 55 µm away. Right: Estimated concentration gradient of OT produced by the releasing of 1 (top) or 10 (down) OT-containing vesicles. The quarter circle on the right shows the activation of the various intracellular pathways activated downstream of OTR activation in function of extracellular OT concentration. Reproduced from (Chini et al., 2017).

Degradation

We have previously seen that OT probably diffuses away from its releasing site to activate distant targets. The length of its trip depends on the quantity of OT-degrading enzymes in the extracellular space. These so-called "oxycotinases" are part of the M1 family of aminopeptidases, and degrade several kinds of peptides, thereby reducing their action radius (Tsujimoto and Hattori, 2005). These enzymes are found throughout the brain (Fernando et al., 2005), and are mainly located in the somata and dendrites of neurons (Tobin et al., 2014). Given the relative sparseness of these enzymes in the brain, OT has a half-life of 20 to 30 min in the central nervous system, against 1 to 2 min in the blood (Mens et al., 1983, reviewed in Gimpl and Fahrenholz, 2001).

1.2.2. OT detection via OTR and downstream effects

The oxytocin receptor (OTR)

Before they are degraded, the lucky OT molecules can find a mate: the oxytocin receptor (OTR). This 7 transmembrane domain receptor contains 388 amino acids and belongs to the class A (Rhodopsin-like) GPCR (Busnelli and Chini, 2018; Inoue et al., 1994, Figure 6). There is only one OTR, encoded by a single gene (*Oxtr*) present in chromosome 6 for mice, 4 for rats, and 3 for humans. Once more, the transcription of this gene is under the control of estrogens, since an ERE element can be found in the promoter of the *Oxtr* gene. The transcript of this gene can have two sizes as shown in the breast where the OTR mRNA is 3.6 kb long and in the ovary where it reaches 4.4 kb (Gimpl and Fahrenholz, 2001). However, no data exists to our knowledge that point toward the existence of different types of OTR proteins, whether structurally or functionally. Yet, many OTR variants have been found in the human population and some of them showed functional differences in OT-triggered Ca^{2+} transients, β-arrestin recruitment, OTR activation and desensitization, *etc.* (Malik et al., 2021).
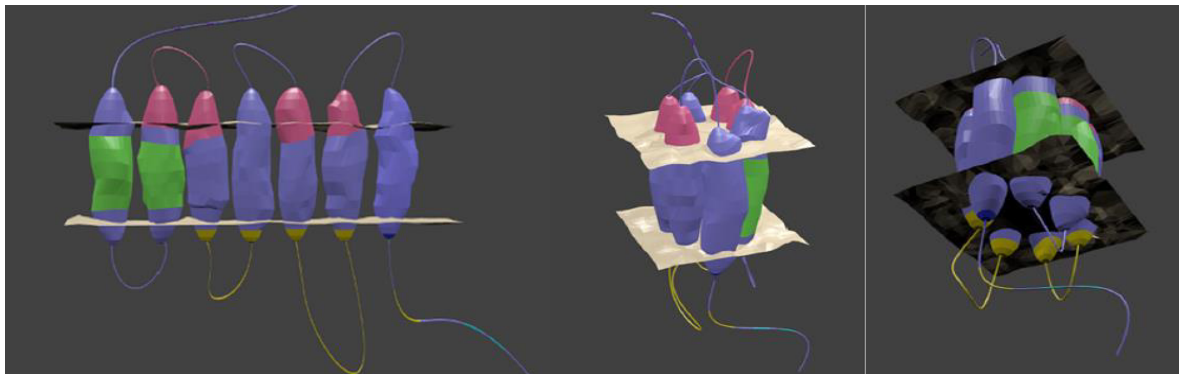
Figure 6: Structure of the OTR. Pink: OT recognition sites, green: probable dimerization site, yellow: G protein binding site, light blue: β-Arrestin binding site. Reproduced from (McKay and Counts, 2020).

Transduction pathways triggered by OTR activation

Once it binds to the OTR, OT can trigger a conformational change that triggers wide and complex intracellular signaling cascades.

Heterotrimeric G proteins. When OT settles his nest in the binding pocket of the OTR, the latter changes its tridimensional conformation and enters an "active" state. During this step, it binds to its substrate, the heterotrimeric G proteins that are composed of three subunits called α, β, and γ. The α subunit (G_α) is bound to a Guanosine diphosphate (GDP), preventing its activity and favoring its sequestration by the β and the γ subunits ($G_{\beta\gamma}$). The activation of the GPCR triggers its guanine exchange factor (GEF) activity: the OTR binds to G proteins and activates them by replacing their GDP bound to the G_α subunit with a GTP molecule. This has the dual effect of activating the G_α enzymatic activity and triggering the release of the $G_{\beta\gamma}$ complex, resulting in its activation (Sutkeviciute and Vilardaga, 2020).

G_α proteins. There is a wide variety of G_α subunits, which can be classified into four families based on their sequence homology and cellular functions: $G\alpha_s$ ($G\alpha_s$ and $G\alpha_{olf}$), $G\alpha_i$ ($G\alpha_i$, $G\alpha_o$, $G\alpha_z$, and $G\alpha_t$), $G\alpha_q$ ($G\alpha_q$, $G\alpha_{11}$, and $G\alpha_{14-15}$), and $G\alpha_{12}$ ($G\alpha_{12}$ and $G\alpha_{13}$). All these proteins have distinct targets and different cellular effects. The OTR has the astonishing particularity to couple both $G\alpha_i$- and $G\alpha_q$-containing G proteins (Busnelli et al., 2012; Phaneuf et al., 1993; Strakova and Soloff, 1997 reviewed in Grinevich et al., 2016, Figure 7). Interestingly, it is not the only receptor in this case. The parathyroid hormone receptor 1 and the Corticotropin-releasing hormone receptor 1 are also known to couple both $G\alpha_q$- and $G\alpha_s$-containing proteins (Sutkeviciute and Vilardaga, 2020; Taché and Bonaz, 2007), the α2- and β2-adrenergic receptors bind $G\alpha_s$ and $G\alpha_i$ proteins, and the melanin-concentrating hormone receptor 1 couple $G\alpha_i$ and $G\alpha_q$ proteins (Kim et al., 2020). Recent evidence has initiated a shift in our understanding of GPCR interaction with G proteins, with some of them specific to a G proteins subfamily and others that have common contacts across many types of G proteins (Sandhu et al., 2022).

Given that $G\alpha_i$ and $G\alpha_q$ have antagonistic effects on many aspects of cellular functions, we can wonder about the usefulness of such a coupling. Interestingly, it seems that this dual coupling can be modulated by the location of the OTR on the cell:

when OTR is activated in lipid rafts, it triggers a mitogenic effect through the $G\alpha_q$ pathway but inhibits cell growth in a $G\alpha_i$-dependent manner when activated outside of these rafts (Guzzi et al., 2002). This may allow subregion-specific signaling in the same cell, increasing the complexity and signaling possibilities of the receptor. To date, we do not know if this dual coupling is ubiquitous or restricted to specific cell types or tissues. Molecularly, it has been shown that the coupling depends on specific intracellular regions of the OTR; more precisely, the C-terminal region of the receptor is necessary to recruit the $G\alpha_q$ pathway but not the $G\alpha_i$ one (Hoare et al., 1999).

Gα proteins downstream targets. Because the intracellular cascades triggered by G proteins are wide and complex, I am going to restrict this overview to the elements needed for the comprehension of the present manuscript. For an exhaustive overview, please see Chatterjee et al., 2016. The OTR was initially described to couple $G\alpha_q$-containing G proteins which activation triggers the activation of the phospholipase C (PLC) and thereby breaks down the membrane phospholipid phosphatidylinositol diphosphate (PIP_2) into inositol triphosphate (IP_3) and diacylglycerol (DAG, Figure 7). The former reaches IP_3 receptors on the endoplasmic reticulum and triggers a Ca^{2+} release from the intracellular store, which helps DAG to activate the protein kinase C (Hu et al., 2021). Apart from this classical $G\alpha_q$-PLC-IP_3-Ca^{2+} pathway, the activation of $G_{\alpha q}$-containing G proteins also activates the protein kinase B pathway (aka. PI_3K/Akt), the $ERK_{1/2}$ pathway (Busnelli and Chini, 2018), and modulates the activity of small Rho GTPases (McKay and Counts, 2020, Figure 7). On the other hand, activation of the $G\alpha_i$-dependent signalization decreases adenylyl cyclase activity, thereby reducing the activity of the protein kinase A (PKA), increases p38 MAPK activation, and triggers hyperpolarization of the plasma membrane, probably through interacting with Ca^{2+}-dependent K^+ channels and K^+ leak channels (Chatterjee et al., 2016; McKay and Counts, 2020, Figure 7). Note that since $G\alpha_i$ action downstream the activation of the OTR is less studied than the effect of $G\alpha_q$ proteins, our knowledge of this pathway is still sparse.
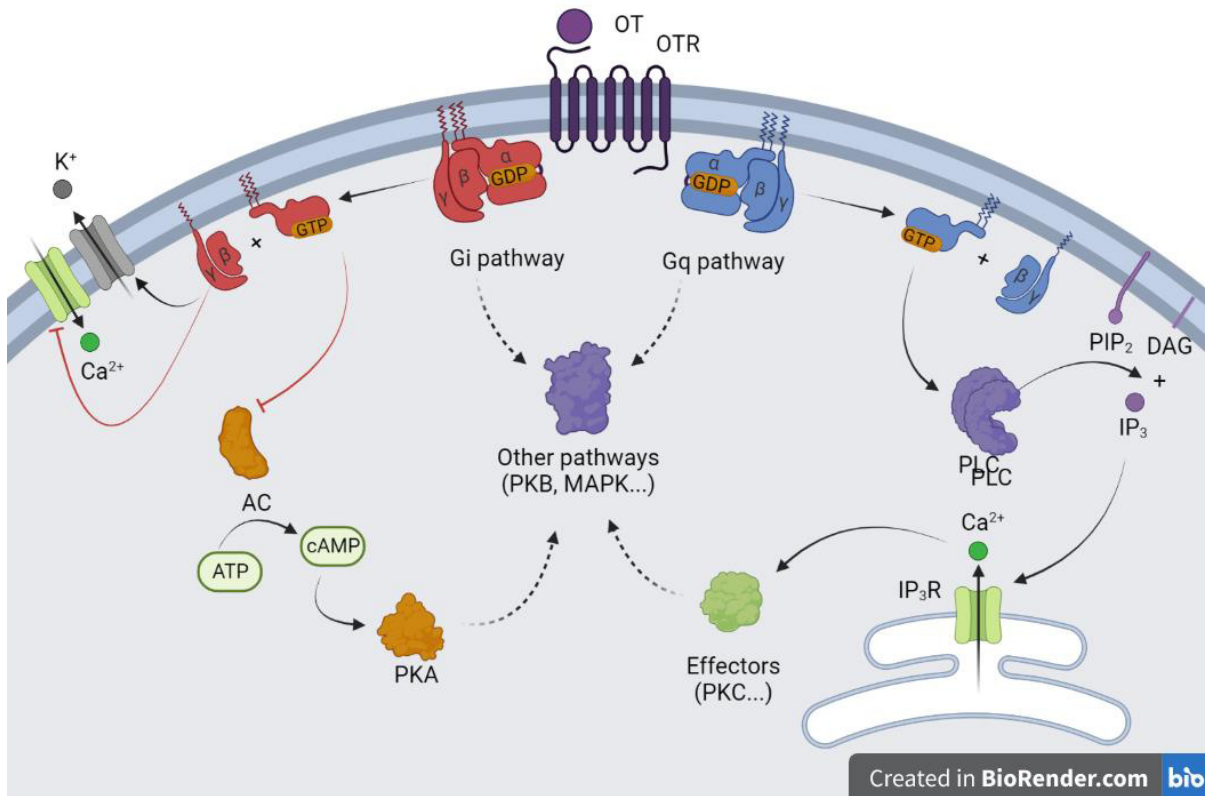
Figure 7: Transduction pathway activated by OTR. Black and red arrows represent activation and inhibition, respectively. The dashed arrows show indirect activations. GTP: guanosine triphosphate, GDP: guanosine diphosphate, PIP$_2$: Phosphatidylinositol bisphosphate, DAG: diacylglycerol, IP$_3$: inositol trisphosphate, PLC: phospholipase C, IP$_3$R: IP$_3$ receptor, PKA/B/C: protein kinases A/B/C, AC: adenylyl cyclase, ATP: adenosine triphosphate, cAMP: cyclic adenosine monophosphate, MAPK: mitogen-activated protein kinase.

Biased agonists. To activate one pathway or the other, Chini's lab identified special ligands called "biased agonists". These molecules bind the OTR and trigger a specific intracellular pathway. For instance, when atosiban binds to the OTR, it produces a conformational change of the receptor that favors its coupling to the $G\alpha_i$ pathway. On the other hand, carbetocin binding triggers the activation of the $G\alpha_q$ pathway (Busnelli and Chini, 2018, Figure 8). Interestingly, OTR stimulation with carbetocin or OT results in receptor internalization whereas atosiban application
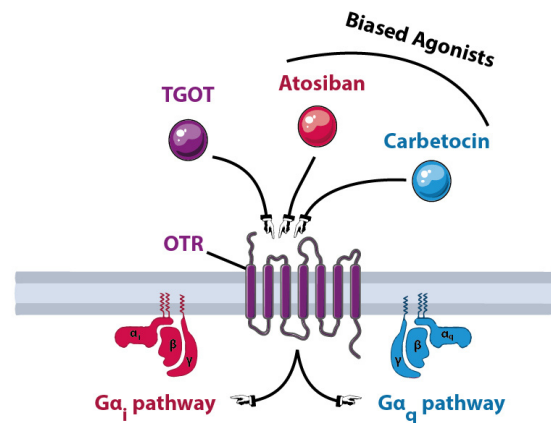
Figure 8: OTR agonists. The full agonist TGOT activates both $G\alpha_i$ and $G\alpha_q$ protein. Atosiban and carbetocin are biased agonist that they activates only the $G\alpha_i$ or the $G\alpha_q$ pathway, respectively.

does not produce OTR internalization (Busnelli and Chini, 2018). From now on, I am going to refer to these two agonists as "biased agonist", in contrast with the TGOT which recruit both intracellular pathways (Busnelli et al., 2012) and is considered a "full agonist".

It is still unknown whether some OTR are coupled to $G\alpha_q$ and others are coupled to $G\alpha_i$, or if the binding of the agonist decides which intracellular pathway must be activated. In the first scenario, OTR may be predetermined to couple a G protein depending on the receptor localization, or the cell type in which it is expressed. For instance, the OTR may couple $G\alpha_q$ protein in neurons and $G\alpha_i$ proteins in astrocytes. In the other model, all couplings are possible and depend on scaffolding proteins, allosteric modulators, cholesterol composition of the plasma membrane, *etc*. Unfortunately, no data exists for the OTR specifically but we can wonder in a more general way whether GPCRs are pre-coupled to G proteins before ligand binding or if the binding triggers receptor-G proteins (R/G) interaction. The literature is divided on this matter. In this debate, the first front is composed of the defenders of the "pre-coupling model" which argues that the R/G interaction precedes ligand binding (Navarro et al., 2018; Vilardaga et al., 2009). On the other side of the battlefield, we can find the guardians of the "collision coupling model" for which G-proteins freely

diffuse in the cytosol and interact with GPCRs when they are in their activated conformation (*ie.* bonded with a ligand, Berlin et al., 2020; Vilardaga et al., 2009).

OT was at first described to trigger the contraction of uterine muscle (Dale, 1906) by triggering a Ca^{2+} surge in smooth muscle (Gimpl and Fahrenholz, 2001). For this reason, the activation of the $G\alpha_q$ pathways was under intense scrutiny, leaving apart a potential activation of other $G\alpha$ proteins. Thereby, most of the literature assumes that OTR is only coupled to $G\alpha_q$, leading to serious interpretation problems. One of these is the use of the $G\alpha_i$-biased agonist atosiban as an antagonist (Barrett et al., 2021; Roy et al., 2018; Ryan et al., 2017). When looking at some effects of OT, atosiban is indeed an antagonist: in obstetric studies, atosiban has a tocolytic activity, reducing uterus contractions and thereby antagonizing OT effects; in neurosciences, OT increases the spiking activity of neurons and this effect is blocked in the presence of atosiban. In these conditions, the antagonizing effect of atosiban on muscle contraction and neuronal activity is true but one can miss an entire panel of the OTR signaling.

Gβγ complex. After its binding to GTP, the Gα subunit dissociates from the Gβ and Gγ proteins, which stay bound together and form a functional complex. According to their structure and functions, we can identify 6 subtypes of Gβ and 12 subtypes of Gγ, allowing 72 possible combinations (Clapham and Neer, 1997). The composition of the Gβγ complex confers the target specificity of the Gβγ complex among the wide range of possible downstream effectors. Among the possible targets of the Gβγ complex, we can find the G protein-coupled inwardly-rectifying potassium channel (GIRK), GPCR kinases (GRK), voltage-gated Ca^{2+} channels (VGCC), phospholipases, adenylyl cyclase (with types II & IV being activated and types I, III, V, VI, VII being inhibited), PI_3K, small G proteins (Ras, Raf), and tyrosine kinases receptors. (Clapham and Neer, 1997).

In neurons, the activity of the Gβγ complex decreases the firing activity by several mechanisms. For instance, it increases the activity of GIRK channels, allowing K^+ to leak from the cell, thereby triggering an outward current that hyperpolarizes the plasma membrane, bringing it closer to the K^+ equilibrium potential (around -98mV, Verkhratsky and Nedergaard, 2018). Moreover, the Gβγ complex inhibits VGCC,

reducing their opening upon cell membrane depolarization. All these mechanisms make the neuron hyperpolarized and less excitable, preventing it from firing action potentials (Sladek and Song, 2012).

However, in glial cells such as astrocytes, it has been shown that the activation of the Gβγ complex can trigger Ca^{2+} transients, another form of excitation (Durkee et al., 2019; Nagai et al., 2019). Interestingly, such effects have been shown after OTR activation in CHO cells and the rat myometrium (Hoare et al., 1999).

Atypical OT signaling. Like most class A GPCRs, the OTR can homo- or heteromerize to form a new functional unit. Studies using bivalent ligands have shown that homomerized OTR had a 1,000-higher sensitivity to divalent ligands compared to monomeric OTRs. Moreover, heteromerization has been shown between the OTR and the type 2 dopamine receptors (László et al., 2020; Romero-Fernandez et al., 2013; Stoop, 2012) and with the vasopressin receptors V1a and V2 (Cottet et al., 2010; Devost and Zingg, 2003; Terrillon et al., 2003). Knowing this, we can wonder what can be the functional output of such a new functional unit, particularly in the case where the OTR associates with a receptor with a completely different coupling such as the $Gα_s$-coupled V2 vasopressin receptor.

Beyond its effect on OTR, OT can also modulate the activity of other receptors. First, OT has been shown to directly bind and activate to transient receptor cation channel vanilloid type 1 (TRPV1, Nersesyan et al., 2017). Such activation has been found in subicular neurons where the application of the OTR-selective agonist TGOT excites the neurons in a TRPV1-dependent manner (Hu et al., 2021). However, no direct binding has been demonstrated in this study, leaving that TRPV1 activation may be secondary to OTR activation. Moreover, OT seems to be a positive allosteric modulator of the $Gα_i$-coupled μ and κ-opioid receptors (Meguro et al., 2018; Miyano et al., 2021).

Internalization and recycling of the OTR

After its activation, the OTR is phosphorylated by the GRK2 (Willets et al., 2009) or 6 (Hasbi et al., 2004) initiating a strong interaction with the β-arrestin (Jurek and Neumann, 2018; McKay and Counts, 2020, Figure 9). The binding of OTR with β-arrestin 1 & 2 show astonishing different kinetics (half-times = 107s & 18s, Busnelli et

al., 2012), and these interactions were triggered with different sensitivity to OT; β-arrestin 1 is recruited at high dose (EC_{50} = 229 nM) whereas β-arrestin 2 is recruited at lower doses (EC_{50} = 1.85 nM, Busnelli et al., 2012). These interactions trigger the internalization of the receptor to eventually induce a β-arrestin dependent signaling (Jean-Charles et al., 2017 note that it has not been shown for the OTR).

This internalization began 5 minutes after OTR activation and lasted at least 10 minutes (Conti et al., 2009; Rimoldi et al., 2003; Smith et al., 2006; Willets et al., 2009 reviewed in Busnelli and Chini, 2018). Once internalized, the OTR is recycled back to the plasma membrane, a process called resensitization (Conti et al., 2009, Figure 9). The dynamics of these mechanisms are variable (tens of minutes to hours), depending on the duration and the amount of ligand in the milieu (McKay and Counts, 2020). Interestingly, OTR desensitization is different according to the brain region, with rapid and long-lasting desensitization observed in the central nucleus of the amygdala and the bed nucleus of the stria terminalis compared to what is observed in the medial amygdala (Terenzi and Ingram, 2005; Wilson et al., 2005).

Figure 9: Internalisation and recycling of OTR. P: phosphate, GRK2/6: G protein-coupled receptor kinase 2/6.

1.2.3. OT functions

OT as a peripheral hormone.

Reproductive system. Initially discovered for its uterotonic activity (Dale, 1906), it is now well-known that OT triggers smooth muscle contraction during labor (Gimpl and Fahrenholz, 2001; Lee et al., 2009; Sheldrick and Flint, 1985). Apart from labor *per se*, OT is also involved in many aspects of the functioning of the reproductive system. For instance, OT can stimulate the release of the luteinizing hormone (Rettori et al., 1997), triggering ovulation and the development of the corpus luteum (Gimpl

and Fahrenholz, 2001). In males, OT functions are not left apart. In addition to its spermination-enhancing effect, OT increases the contractility of seminiferous tubules to promote the transport of the spermatozoa to the epididymis. Moreover, OT has a critical function in the prostate where it triggers its contractile activity to expel prostatic secretions during ejaculation (Gimpl and Fahrenholz, 2001). Finally, if the offspring needs to be nurtured and fed, such as in mammals, OT plays a pivotal role in milk ejection from the breast. Indeed, in this case, the tactile sensory stimulation of the nipple triggers synchronized bursts of action potentials in OT neurons which then release OT in the blood. The hormone then travels through the blood circulation to reach the mammary glands where it triggers the contraction of myoepithelial cells of the lactiferous duct, eventually resulting in milk ejection from the mammary gland (Froemke and Carcea, 2017). Interestingly, there is evidence of OT synthesis in many structures of the reproductive system, providing local OT to exert its functions (Gimpl and Fahrenholz, 2001).

Control of water and ion balance. One of the most crucial functions of OT is also the regulation of osmolarity in the blood. OT and AVP neurons are sensitive to variations in blood pressure or osmolarity. For instance, in hyperosmotic conditions, OT has a natriuretic effect in the kidney, reducing tubular reabsorption of Na^+ to recreate a balance in the osmotic homeostasis. In the cardiovascular system, OT can also decrease arterial pressure and reduce heart rate (Gimpl and Fahrenholz, 2001).

OT as a neuropeptide.

OTR expression in the brain. The OTR is widely expressed throughout the brain, particularly in the olfactory bulb, the neocortex, the hippocampus, the amygdala, the bed nucleus of the stria terminalis, the nucleus accumbens, and the ventromedial hypothalamus (Veinante and Freund-Mercier, 1997). The distribution of this receptor shows a strong sexual dimorphism in some regions, and OTR expression is usually higher in females (Carter, 2007). However, some regions do not show any significant differences in the expression of this receptor between genders, including the PVN, the SON, or the central amygdala (Uhl-Bronner et al., 2005). Recently, Kim's lab mapped the whole brain of $Oxtr^{venus}$ mice to produce a map at a cellular level (available at http://kimlab.io/brain-map/OTR/) that includes different time points, from P7 to P56. Interestingly, they did observe an important variation in OTR expression, with a peak

during early postnatal periods (Newmaster et al., 2020). These results are in accordance with a previously shown difference in the quantity of OTR expression and neuromodulatory effect during the development (Mitre et al., 2016), engaging to be careful with the age of used animals.

The neuromodulatory action of OT has been identified in so many brain regions that it will be presumptuous to list them all. Here I am going to present only a few examples of behaviors in which OT are involved that are going to be useful for the understanding of the present thesis. For a complete overview of OT effects in the brain, please refer to (Gimpl and Fahrenholz, 2001; Jurek and Neumann, 2018; Lee et al., 2009).

Social behavior. OT is involved in almost all social behaviors, ranging from pair bonding to postpartum maternal aggressiveness. First, OT is involved in social memory and preference by modulating neurons in the mice's olfactory bulb, hypothalamus, and amygdala (Lee et al., 2009). Then, OT is crucial in the central amygdala to recognize the emotions of conspecific individuals (Ferretti et al., 2019). Maternal behavior is also dependent on OT release in the paraventricular thalamus (Lefevre et al., 2021), bed nucleus of the stria terminalis, medial preoptic area, and lateral septum (Lee et al., 2009). Finally, OT released in the central nucleus of the amygdala increases aggressive behavior toward intruders observed in females during the postpartum period (Lee et al., 2009).

Analgesia. One other powerful function of OT is to decrease pain sensation through its antinociceptive effects and by modulating the integration of the nociceptive information in the brain. This effect is mediated by many actors throughout the whole pain matrix in the brain and in the peripheral nervous system. Starting at the detection site of the nociceptive stimulus, OT can modulate the electrical activity of nociceptors (Juif and Poisbeau, 2013). One step further, OT can modify the integration of this message in the dorsal horn of the spinal cord by reducing the activity of wide dynamic range neurons, the first relay of the nociceptive message in the central nervous system. This inhibition can be both direct (Eliava et al., 2016) or indirect (Breton et al., 2008; Iwasaki et al., 2023). All the way up, the nociceptive message reaches the supraspinal centers where the nociceptive information is integrated, eventually leading

to a pain sensation. This last step requires the cooperation of many cerebral structures that analyze the different parts of the message. Thus, the somatosensory cortices examine the precise nature and location of the stimulus, the amygdala generates the emotional value of the event, and the frontal cortices investigate the cognitive meaning of the nociceptive information. Among these structures, the amygdala shows a high OTR expression, and infusing OT in it has an analgesic effect (Han and Yu, 2009).

Stress and anxiety-like behaviors. OT can be released during various stressful events, such as osmotic stress, physiological challenges, and socio-emotional stress. For instance, the release of OT is increased in the PVN, SON, central amygdala, and the bloodstream during a forced swim test (Jurek and Neumann, 2018; Olivera-Pasilio and Dabrowska, 2020). During social defeat, where a rat is exposed to a larger and aggressive conspecific, OT level is increased in several brain regions (Jurek and Neumann, 2018). Once released OT has an anti-stress and anxiolytic activity (Gimpl and Fahrenholz, 2001; Jurek and Neumann, 2018; Lee et al., 2009; Olivera-Pasilio and Dabrowska, 2020). Indeed, intracerebroventricular administration of OT decreases the release of corticosterone induced by stress and reduces anxiety-like behaviors (Windle et al., 1997). More precisely, OT infusion directly in the amygdala triggers anxiolytic effects in rodents (Bale et al., 2001; Wahis et al., 2021). Interestingly, OT may also induce stress, anxiety-like behaviors, and social fear/avoidance in some conditions (Duque-Wilckens et al., 2020; Luo et al., 2022; Maroun and Wagner, 2016). These reports are in contrast with the anxiolytic and trust-enhancing effects previously described, suggesting a region and state-specific action of OT in the brain.

Memory and learning. To survive, living beings must record and recognize the world that surrounds them. OT is involved in several aspects of this function, particularly in social and emotional memory. Rodent recognition of other individuals is mainly mediated through olfactory cues that are analyzed by the olfactory bulb, the medial amygdala, and the olfactory cortices. Interestingly, OT is crucial in these two last regions to mediate social recognition (Maroun and Wagner, 2016; Oettl et al., 2016). During this process, it is also crucial to remember the emotional value previously given to the stimulus. OT is also involved in this panel of the memory, controlling the attribution of the emotional value to the stimulus and its storage. To this

end, OT acts on the prefrontal cortex, the amygdala, and the hippocampus, three regions involved in the memory of emotionally meaningful events (Bazaz et al., 2022; Ehrlich et al., 2009; Hasan et al., 2019; Jurek and Neumann, 2018; Knobloch et al., 2012; Lee et al., 2009; Maroun and Wagner, 2016; Viviani et al., 2011). In the amygdala and the hippocampus, for instance, endogenous OT release reduces fear expression (*ie*. freezing) in rats. For a complete review of the effect of OT on fear memory and expression, please refer to (Baldi et al., 2021).

In a larger scope, OT is thought to modulate the salience and the valence of sensory stimuli in the brain (Lefevre et al., 2021). The salience is the importance given to a stimulus when analyzing it. To control this aspect of information integration, OT modulates the excitation/inhibition balance of sensory circuits to increase the weight of socially relevant stimuli (Lefevre et al., 2021). At the same time, OT controls the attribution of the emotional value given to stimuli. This effect is mainly mediated by its effect on the amygdala, which is a central hub for the evaluation of the pleasantness (or unpleasantness) of sensory information (Lefevre et al., 2021). This last point explains why although OT functions are very wide in the brain, it often involves at least one of the nuclei of the amygdala complex.

Box: on the incongruent effect of OTR activation in neurons

In neuroscience, and particularly through the electrophysiological prism, we often consider that $G\alpha_q$ and $G\alpha_i$-dependent signaling are antagonists, leading to an increase or a decrease in neuronal activity, respectively. This vision is hard to conciliate with the dual coupling of the OTR. Indeed, if both pathways are activated simultaneously, they must cancel each other out, resulting in no change in neuronal activity. What can be the point of such a strange coupling? Here I formulate five hypotheses that can shed light on this mystery.

1) The coupling of the OTR is specific to the cell type or its location.

Neuronal OTRs may only be coupled to the $G\alpha_q$ pathway. Indeed, lots of reports have shown that OTR agonists increase neuronal activity in many brain regions including the amygdala (Knobloch et al., 2012; Wahis et al., 2021), the hippocampus (Bazaz et al., 2022; Tirko et al., 2018), the parabrachial nucleus (Ryan et al., 2017), the ventral tegmental area (Tang et al., 2014), the striatum (Xiao et al., 2017), *etc.* Some of these studies have investigated the intracellular pathway involved in such activation and found the involvement of the $G\alpha_q$ pathway (Hu et al., 2021; Tang et al., 2014; Tirko et al., 2018).

However, none of these studies have investigated the potential role of the $G\alpha_i$ pathway (except for Tirko et al., 2018 but they removed all mention of the potential involvement of a $G\alpha_i$-dependent mechanism during the process of submission). Only a few studies have shown the recruitment of $G\alpha_i$ proteins in neurons. The first demonstration was made using the $G\alpha_i$-biased agonist atosiban on the wide dynamic range neurons of the spinal cord and show that recruitment of OTR-$G\alpha_i$ triggers a shift in neuronal firing type, from repetitive to phasic (Eliava et al., 2016). Unfortunately, they did not investigate the potential of the $G\alpha_q$ pathway, possibly omitting the activation of this signaling cascade after OTR activation by OT. Moreover, OTR is coupled to both pathways in immature olfactory neurons, producing an antagonistic effect on GIRK channel activity (Gravati et al., 2010). OT can also depolarize vagal neurons through two distinct mechanisms, among which, one is cAMP-dependent, suggesting an involvement of the $G\alpha_i$ pathway (Alberi et al., 1997). Finally, the anti-nociceptive effect of OT is sensitive to pertussis toxin, pointing toward the involvement of the $G\alpha_i$ pathway (Espinosa de Los Monteros-Zúñiga et al., 2021). These elements

tend to show that neuronal OTR can be coupled to the $G\alpha_i$ pathway. However, the coupling can be different among neurons, or between different brain regions, but no evidence exists to strengthen this hypothesis.

2) Cellular processes are not restricted to electrophysiological properties.

As with any GPCR, OTR can activate a myriad of intracellular pathways. These pathways trigger changes in cellular functions that are not necessarily visible when performing short electrophysiological recordings. For instance, it can modify gene expression to eventually change the cellular plasticity profile, morphology, energy consumption, *etc*. The $G\alpha_i$ and the $G\alpha_q$ pathways can even cooperate and have synergistic functions. For instance, the $G\beta\gamma$ complex that dissociates from activated $G\alpha_i$ proteins can interact with the PLC to relieve its auto-inhibition, favoring subsequent PLC-dependent Ca^{2+} transients (Pfeil et al., 2020).

3) The $G\alpha_i$ and $G\alpha_q$ pathways are recruited at different doses of OT.

One possible utility of this dual coupling could also be the recruitment of one pathway or the other depending on OT concentration. Indeed, it has been shown that the $G\alpha_q$ pathway is recruited at lower doses (EC_{50} = 2nM) than the $G\alpha_i$ pathway (EC_{50} = 10 to 100nM, depending on the $G\alpha_i$ protein) (Busnelli et al., 2012, Figure 10).
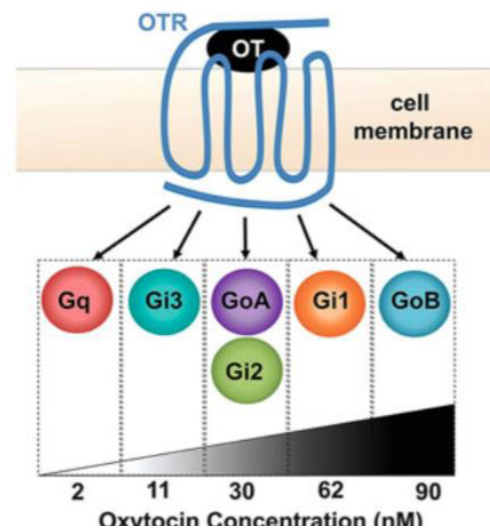
Figure 10: Affinity of OTR for G proteins depend on the concentration of OT.

5) The $G\beta\gamma$ complex may be more important than the $G\alpha$ subunit.

Initially considered as a mere $G\alpha$ inhibitor, it is now known that the $G\beta\gamma$ complex also has an activity of its own. This is no exception for the OT system, where the bursting effect of OT on SON neurons depends on the signaling triggered by the $G\beta\gamma$ complex of a $G\alpha_q$ protein (Wang and Hatton, 2007a). Another mechanism involving the $G\beta\gamma$ complex can be the activation of Tyrosine Kinases that eventually triggers cytosolic Ca^{2+} increases observed after OTR activation (Hoare et al., 1999).

2. The Amygdala

2.1. Structure and functions

The amygdala (or *corpus amygdaloideum*) is a complex of nuclei that lies in the intern part of the temporal lobe of the brain (Figure 11). The function of this structure is to attribute and store the emotional value of external stimuli (Veinante et al., 2013). To do so, the amygdala receives information from many brain regions. Among them, we can find sensory inputs arising from the thalamus, internal feelings carried by hypothalamic fibers, and highly integrated information such as traces from the past that come from the hippocampus and the cortex (LeDoux, 2000; Veinante et al., 2013). For instance, the view of a pesto pasta dish (visual information from the visual cortex) will have a positive value if internal information arising from the hypothalamus informs of a hunger sensation. All this information is analyzed to create a more or less pleasant feeling toward something. This so-called emotional valence is then integrated with other information, to create a general feeling called emotion.
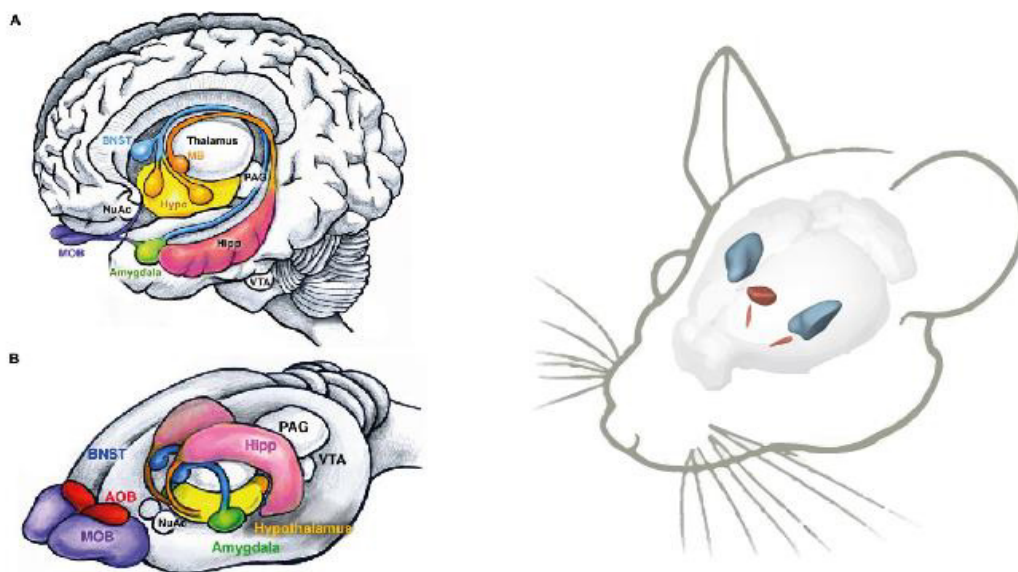
Figure 11: Location of the amygdala in the brain. Left: drawing of a human (A) and a rodent (B) brain with the principal internal structures shown in color. The amygdala is shown in green and the hypothalamus in yellow. Right: Simplified drawing of a mouse brain that illustrates the position of the amygdala (blue) and the hypothalamic OT nuclei (red).

2.1.1. Anatomy

To accomplish this difficult task, the amygdala contains around twelve nuclei that can be classified into four groups based on their location: the cortical (CoA), the basolateral (BLA), the medial (MeA), and the central (CeA) amygdala (Veinante et al., 2013, Figure 12). Based on the structure of these nuclei, we can find two different groups. The first one is composed of the CoA and the BLA that shared cortical features. They contain a majority of excitatory pyramidal neurons and few inhibitory neurons (Beyeler and Dabrowska, 2020; Fu et al., 2020). Pyramidal neurons project toward other structures, carrying the functional output of the nuclei while inhibitory cells make local, modulatory connections. The second group encompasses the CeA and the MeA, which share striatopallidal features. These nuclei are composed of medium spiny neurons that synthesize the GABA inhibitory neurotransmitter (Veinante et al., 2013 but see Keshavarzi et al., 2014).
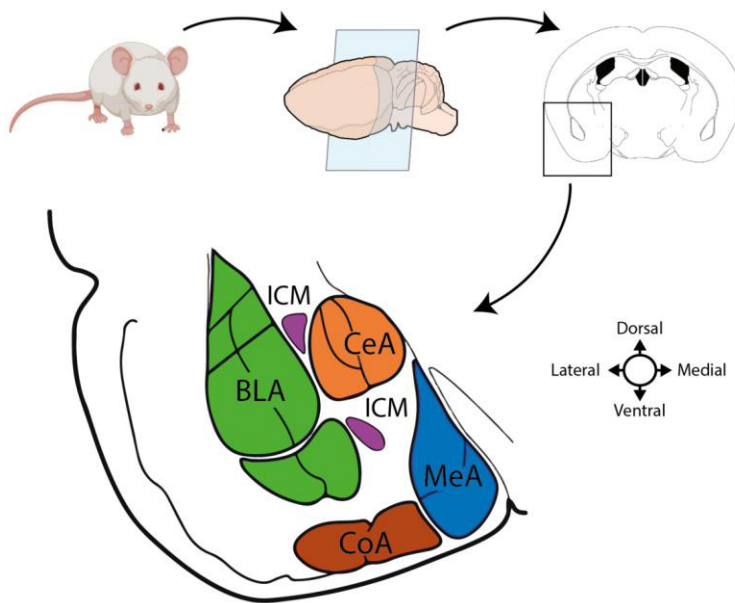
Figure 12: Organisation of the amygdala. Upper panel: coronal slice of the brain. Lower panel: position of the different amygdala nuclei. Green: basolateral amygdala (BLA), orange: central cmygdala (CeA), purple: intercalated cell mass (ICM), blue: medial amygdala, brown: cortical amygdala (CoA).

Based on their connectivity and the type of information they convey, we can observe two parallel (yet interacting) circuits. The first one is composed of the CoA and the MeA (thus called the cortico-medial group) and is highly involved in the processing of olfactory information. After the identification of an odor by the olfactory bulbs and the piriform cortex, olfactory information arrived on the cortico-medial

amygdala circuit and an emotional valence is attributed to the stimulus (Keshavarzi et al., 2014; Root et al., 2014). The second circuit regroups the basolateral (BLA) and the central (CeA) nuclei of the amygdala and receives many types of inputs from different cortices, the thalamus, *etc.* Because this latter circuit is highly involved in pain, stress, and anxiety (LeDoux, 2000; Veinante et al., 2013), I decided to focus on this second circuit in the present manuscript.

2.1.2. The Basolateral complex of the amygdala

The basolateral complex of the amygdala (BLA) can be divided into two subnuclei: the lateral amygdala (LA) and the basal amygdala (BA) (Figure 13). The LA is the major input nuclei of the amygdala and conveys information to BA and other amygdala nuclei. These nuclei are composed of ~80% of spiny pyramidal neurons called principal cells and ~20% of inhibitory interneurons (Duvarci and Pare, 2014).

Pyramidal neurons are divided into two groups. The first one is composed of parvocellular neurons expressing *Ppp1r1b* and promote appetitive behaviors. The second group is composed of magnocellular pyramidal neurons, which express *Rspo2* and inhibit appetitive behaviors (Kim et al., 2017). As in other cortical areas, the BLA contains many different types of inhibitory interneurons that modulate the activity of pyramidal neurons. The output message of the BLA complex is carried by pyramidal cells whose main target are CeA neurons (Duvarci and Pare, 2014).

There are two ways to access the CeA from the BLA. The first one is a direct path, where glutamatergic axons directly make synapses on CeA neurons, whereas the second path makes a stopover in the intercalated cell masses (ICM) to connect GABAergic neurons that project to the CeA. Thanks to this relay, the excitatory glutamatergic message arising from pyramidal BLA neurons can be transformed into a GABAergic message, inhibiting CeL neurons (Duvarci and Pare, 2014, Figure 13).
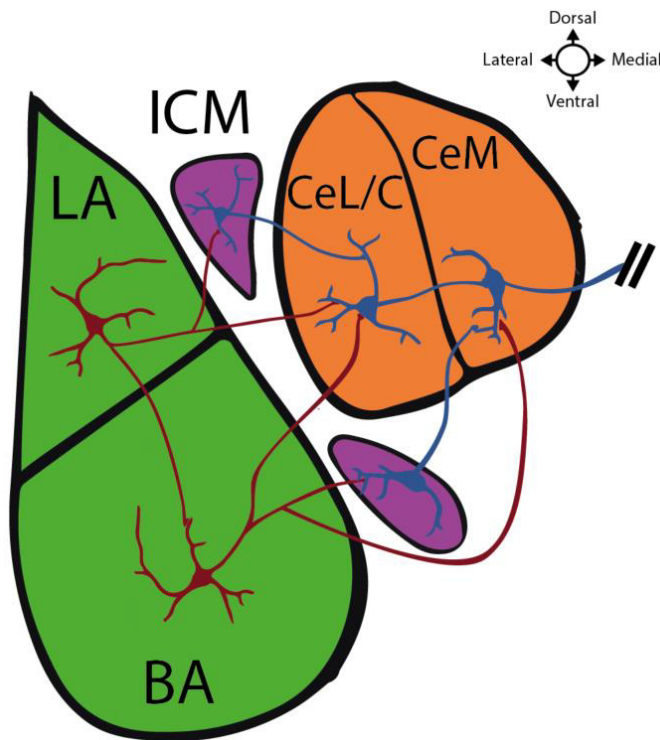
Figure 13: BLA-to-CeA connectivity. The lateral and the basal nucleus of the amygdala (LA and BA) contains pyramidal neurons that project to the ICM and to the laterocapsular and the medial part of the central amygdala (CeL/C and CeM). Excitatory neurons are shown in red and inhibitory ones in blue.

2.1.3. The Central nucleus of the amygdala

The central amygdala (CeA) is also composed of two subnuclei: a laterocapsular part (CeL/C) and a medial part (CeM) (Figure 13). Both subnuclei are composed of GABAergic medium spiny neurons (MSN), but they have several different features. CeL/C neurons have small somata, many primary dendrites that make many ramifications, and are covered with dendritic spines. CeM neuron dendrites on the other hand make fewer ramifications and exhibit a lower density of dendritic spines (Duvarci and Pare, 2014).

CeL/C neurons can be divided into 3 groups according to their transcriptional profile: PKCδ, SOM, and CRH-expressing neurons (Fadok et al., 2017; Hartley et al., 2019; Haubensak et al., 2010; Kim et al., 2017; McCullough et al., 2018). The first population is distinct from the other two with only 2% of neurons co-expressing PKCδ/SOM and 8% that co-express PKCδ/CRH. On the contrary, the SOM and CRH-expressing neurons overlap significantly, with as much as 50% of SOM neurons co-expressing CRH (Kim et al., 2017) and 4 to 70% of CRH^{+} neurons expressing SOM, depending on the location on the anteroposterior axis (McCullough et al., 2018). In

terms of connectivity, PKCδ$^+$ and PKCδ$^-$ neurons mutually inhibit each other (Haubensak et al., 2010), and the same has been shown for SOM$^+$ and SOM$^-$ neurons (Li et al., 2013). Unfortunately, this simple view of two populations that make a reciprocal inhibitory connection is challenged by a recent study which shows that neurons belonging to a type preferentially project to neurons of the same type; thus the more frequent connexions found in the CeL/C are PKCδ$^+$ to PKCδ$^+$ and SOM$^+$ to SOM$^+$ synapses (Hunt et al., 2017). It is noteworthy that these results are not contradictory; the two first studies have stimulated PKCδ$^+$ or SOM$^+$ neurons and recorded PKCδ$^-$ or SOM$^-$ neurons, limiting their description to a portion of possible connections.

One of the most important features of neurons is their reaction to sustain stimulation. In the CeL/C, some cells will fire action potentials only at the beginning of depolarization and then adapt to the new voltage membrane, detecting changes in their environment (Adaptive, Figure 14). Other neurons can emit action potentials with a regular frequency that depends on the intensity of the stimulation (Regular Spiking, Figure 14). These neurons may encode the intensity of a stimulus, indicating the amplitude of the change that occurs. Finally, late spiking neurons do not spike at the beginning of the stimulation but fire action potentials after a delay, probably informing that the stimulation is sustained and lasts in time (Late spiking, Figure 14). Depending on the studies, there is either a third of each population in the CeL/C (Lopez de Armentia and Sah, 2004), a majority of adaptive cells (Chieng et al., 2006; Martina et al., 1999), or a majority of regular spiking with only a few late spiking neurons (Adke et al., 2021; Dumont et al., 2002). Interestingly, some of these studies have been conducted in rats (Chieng et al., 2006; Dumont et al., 2002; Lopez de Armentia and Sah, 2004), mice (Adke et al., 2021), guinea pigs (Dumont et al., 2002; Martina et al., 1999), and cats (Dumont et al., 2002), indicating that the repartition of neuron' firing type may vary depending on the species used. Concerning other electrophysiological parameters, the resting membrane voltage of late spiking neurons is more hyperpolarized than the other types but no other difference can be observed in other passive membrane properties (Chieng et al., 2006; Dumont et al., 2002; Lopez de Armentia and Sah, 2004; Martina et al., 1999).
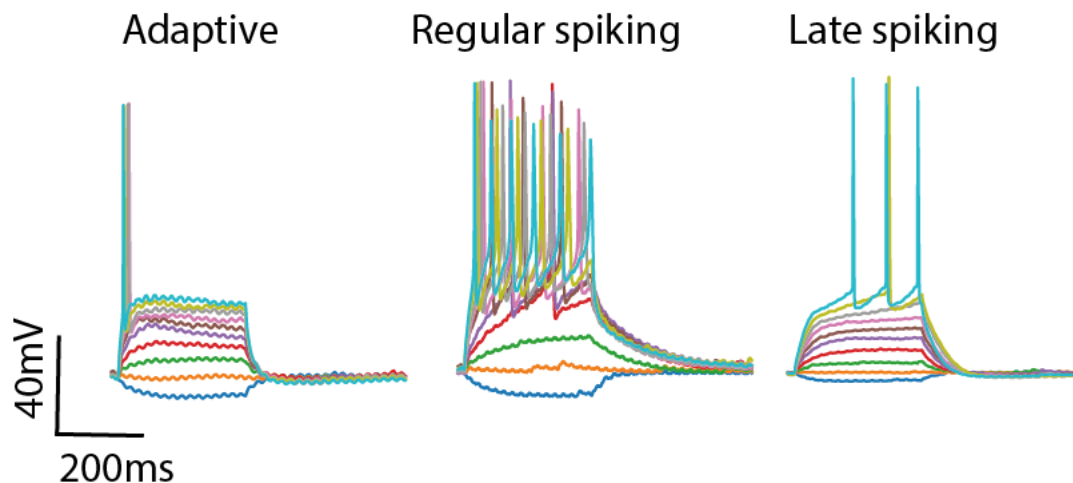
Figure 14: Firing type in the laterocapsular nucleus of the central amygdala (CeL/C). Example traces of CeL/C neuron's membrane voltage in response to a current steps protocol. From left to right are shown traces from adaptive neurons, regular spiking neurons, and late spiking neurons. The different colors of the line show different sweeps.

At this point, the million-dollar question is 'Does the transcriptional identification of CeL/C neurons match their electrophysiological classification?' Let's not maintain the suspense: the answer is no, since all electrophysiological types have been found both in PKCδ and in SOM-expressing neurons (Adke et al., 2021; Hunt et al., 2017; Wilson et al., 2019 but see Haubensak et al., 2010). However, SOM neurons are more excitable than PKCδ ones and did not show accommodation of the interspike interval during a repetitive firing episode, indicating that these two parameters may separate the different cell types (Adke et al., 2021).

In the CeM, neurons can also express different transcriptomic markers such as SOM, neurotensin, and tachykinin 2 (Kim et al., 2017). However, since the activation of these three cell types promotes the same kind of appetitive behavior, no clear difference in their function has been identified (Kim et al., 2017).

In terms of hodology, the CeL/C is the landing place of information that comes from the BLA or the ICMs. Within the CeL/C, another step of processing is made thanks to the reciprocal connectivity of different types of inhibitory neurons (Figure 15). Once the different information is confronted and mixed, CeL/C neurons contact CeM projection neurons, which are the main functional output of the BLA-to-CeA amygdala pathway (Figure 15). Note that this scheme is simplified since BLA neurons (especially *Ppp1r1b+* neurons) can directly project on CeM neurons (Duvarci and Pare, 2014; Kim et al., 2017; Ye and Veinante, 2019).
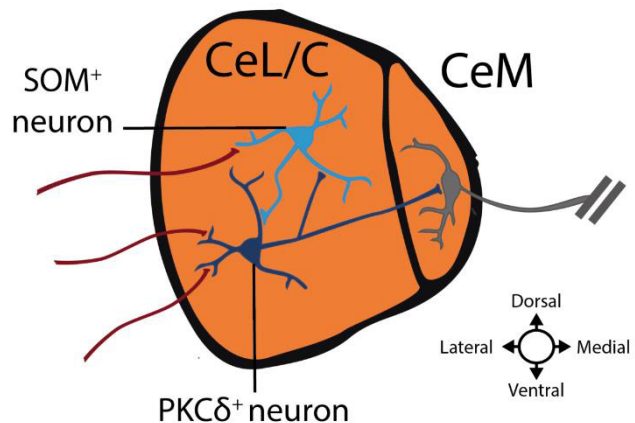
Figure 15: Connectivity in the CeL/C nucleus of the amygdala. Red axons represent excitatory inputs.

2.1.4. Integrating amygdala circuitry

The organization of the amygdala can be conceptualized in a larger scope according to the theory of the basal forebrain anatomo-functional macrosystem (Zahm, 2006). In this view, the amygdala and neighboring interconnected regions form the "extended amygdala". This macrosystem is arranged like other telencephalic systems, with a layered organization between different brain structures (Ye and Veinante, 2019, Figure 16). First, inputs of the system arrive at the level of a cortex-like structure containing glutamatergic pyramidal neurons under the control of local inhibitory interneurons. The information then flows to MSN-containing striatum-like structures where all neurons are inhibitory and interconnected. These neurons then connect a pallidum-like structure containing inhibitory projection neurons that connect the thalamus and brainstem nuclei (Zahm, 2006, Figure 16).

This organization contains two paths, one direct and the other indirect. In the cortico-striato-pallidal pathway, for instance, the direct path promotes the initiation of movement and the indirect path prevents it. Analogous to this organization, the direct BLA-CeA pathway promotes appetitive behavior and suppresses defensive ones,

whereas the indirect BLA-ICM-CeA pathway exerts the opposite function on appetitive and defensive behaviors (Kim et al., 2017). The astonishing similarity between forebrain macrocircuits can be explained by the duplication and specialization of the structures, thereby creating specialized circuits (Kim et al., 2017).

In that kind of macrocircuit, the upper layers are under the control of neuromodulators, influencing the way information is integrated into the system. One clear example can be seen in the cortico-striato-pallidal macrosystem that controls locomotion. In this circuit, dopamine controls the activity balance between two populations of inter-inhibiting neurons in the striatum. A loss of such neuromodulation triggers the bradykinesia observed in Parkinson's disease (Bologna et al., 2020). A similar mechanism has been observed in the extended amygdala macrosystem that controls emotions. In this circuit, the CeL/C also contains MSN neurons that inhibit each other and the release of several neuromodulators can modify emotional processes such as fear and anxiety (Pomrenze et al., 2019), nociceptive reactions and associated physiological adaptations (Neugebauer et al., 2020; Veinante et al., 2013). Despite the BLA, the CeA also receives projections from other structures. For instance, the hypothalamus sends oxytocinergic projections directly to the CeA.
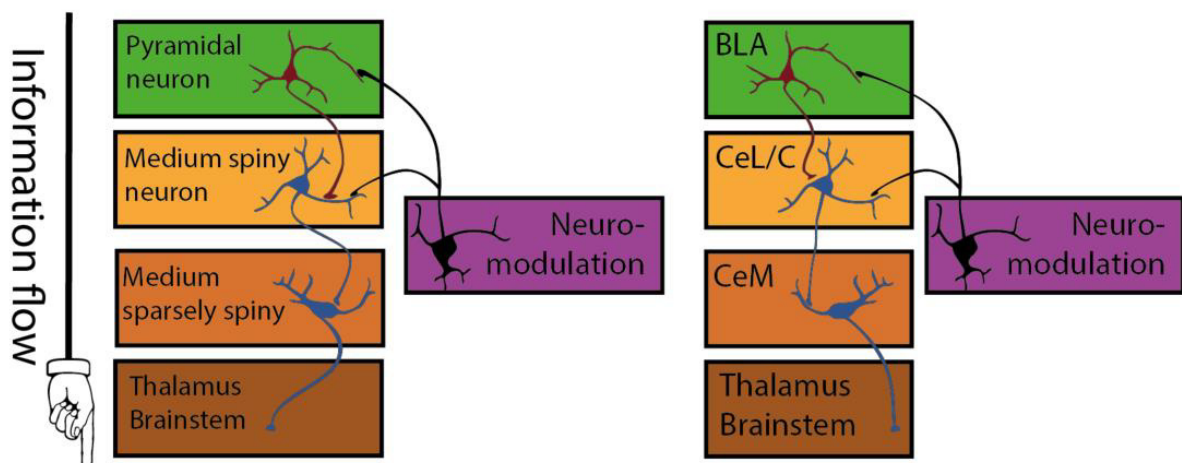
Figure 16: Telencephalic macrosystem theory. Left: general organization shared by several macrosystems in the forebrain. Left: organization of the BLA-CeA circuit.

2.2. Oxytocinergic control of the amygdala

Early investigations have shown that OT infusion in the CeA reduces the immobility response triggered by conditioned stress (Roozendaal et al., 1992), suggesting the involvement of OT in the regulation of emotions. This result was then strengthened by anatomical studies of OT binding sites in the brain, revealing a high presence of OTR in the CeL/C (Veinante and Freund-Mercier, 1997, Figure 17), and innervation of the CeL/C by OT fibers (Knobloch et al., 2012; Otero-García et al., 2016). Starting from this point, the involvement of OT in amygdala-related behaviors comes under intense scrutiny, and the two last decades have seen many studies investigating the effect of OT on fear, stress, anxiety, pain, and other emotions (Campbell-Smith et al., 2015; Duque-Wilckens et al., 2020; Ferretti et al., 2019; Gunduz-Cinar et al., 2020; Harper et al., 2019; Lahoud and Maroun, 2013; Oliveira et al., 2022; Rickenbacher et al., 2017; Terburg et al., 2018; Tunstall et al., 2019). For documentation on the effect of OT on other parts of the amygdala, particularly the BLA, see Baldi et al., 2021.
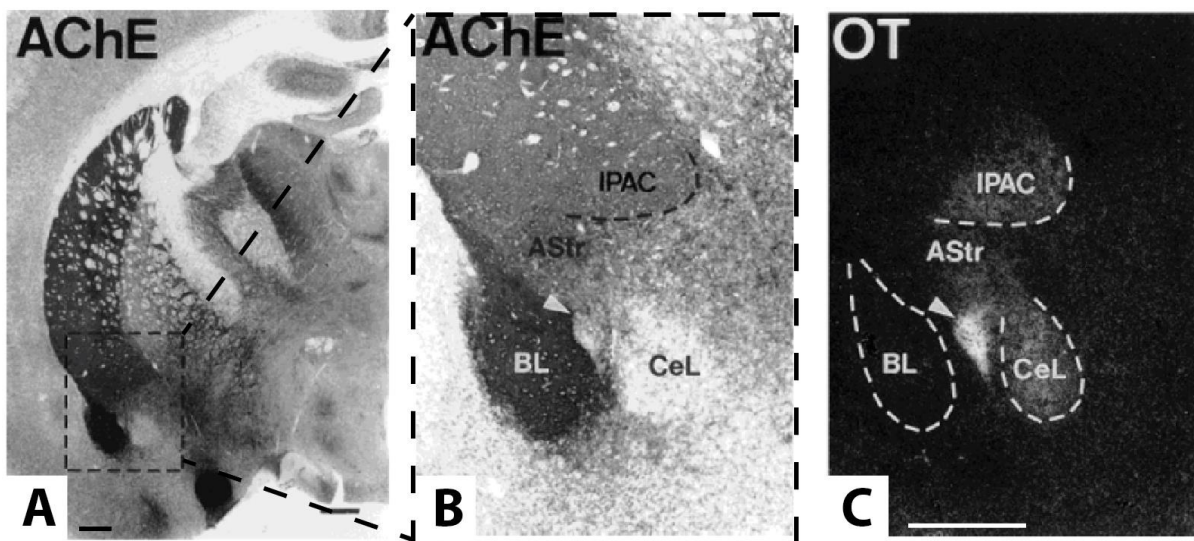
Figure 17: OT binding sites in a mouse brain coronal section. A. Coronal section stained for acetylcholinesterase (AChE). This staining allows to locate precisely the BLA and the CeL. B. Zoom in on the inset framed with the dashed line in (A). C. Histoautoradiograph showing OT binding. AChE: acetylcholinesterase, IPAC: interstitial nucleus of the posterior limb of the anterior commissure, AStr: Amygdalostriatal area, BL: Basolateral amygdala, CeL: lateral nucleus of the central amygdala. Scales bar = 500µm. Adapted from (Veinante and Freund-Mercier, 1997).

2.2.1. Fear behavior

Fear is the feeling of immediate danger accompanied by behavioral (vigilance, startle, freezing) and physiological (cardiovascular, respiratory) responses that aim to favor survival (Moscarello and Penzo, 2022; Olivera-Pasilio and Dabrowska, 2020). Early investigators observed a lack of fear in rhesus monkeys after a lesion of the amygdala (Lanska, 2018). Interestingly, related symptoms can be observed in humans with amygdala damage (Adolphs et al., 1994; Terburg et al., 2018).

Fear responses are wide and diverse, but can be organized according to a threat-imminence continuum, a scale ranging from "safety" to "imminent danger" (Moscarello and Penzo, 2022, Figure 18). The first rung of this scale is *safety*, where no fear mechanisms can be observed. As a potential threat arrives, the *pre-encounter* mode is set off and the animal explores its environment to gather information to assess potential risks. At a behavioral level, rodents sniff, rear, and explore cautiously their environment in a stretch posture to avoid detection by predators. When the predator (or the threat in general) is observed in the surroundings, the *post-encounter* mode is reached and a whole set of innate defensive reactions are triggered to avoid detection and to prepare a fight-or-flight reaction. In rodents, these mechanisms include freezing behavior, increased muscle tone to prepare a potential flight, and strong analgesia that prevents pain to interfere with a potential intense endeavor against death or injury. When suddenly the predator attacks, the circa-strike mode is triggered in the form of a fight-or-flight reaction. At this point, the animal immediately judges if it can fight back or dodge the attack (Moscarello and Penzo, 2022, Figure 18).
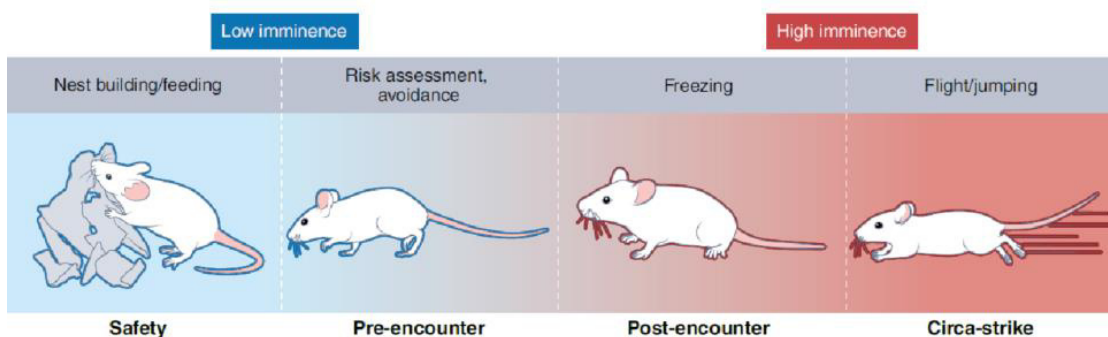
Figure 18: Threat-imminence continuum and its neural basis. Different stages of fear from safety to circa-strike reactions. From (Moscarello and Penzo, 2022).

Although critical for survival, fear reactions can become pathologic and cause post-traumatic stress disorders and/or chronic anxiety (Zoellner et al., 2011). For this reason, we decided to investigate the mechanisms that underlie the learning of fear and its extinction. However, since fear is an emotion, it is difficult to study it in animal models that cannot describe such feelings. Because we cannot quantify the fear itself, we have to measure fear-related behavior such as the freezing reaction in rodents. To generate this fear-triggered immobility, we used a fear-conditioning test, which consists of 3 phases (Figure 19):

- The **habituation** phase where the subject is acclimated to environment A.

- In the **conditioning** phase, the subject receives a conditioned stimulus (CS, usually a sound) and an unconditioned stimulus (US, usually a brief electric shock). During this phase, the emotionally neutral CS becomes aversive due to the CS-US association. Importantly, this phase takes place in an environment B, to dissociate the context from the US-CS association.

- During the **re-exposition** phase(s), the subjects are re-exposed to the CS without the US in the first environment (A). This step aims to evaluate the strength of the memorized association between the US and the CS, indicating the robustness of the memory. Since the CS is no longer presented with the US, the subject learns to disassociate the US from the CS, a process called "extinction". Importantly, this process is not a simple forgetting of the association but rather a new active learning process during which the subject creates a new memory where the two stimuli are dissociated (Ehrlich et al., 2009).

The strength of the CS-US association primarily resides in the emotional valence of the US. Indeed, if the US is neutral, the subject will not pay particular attention to the US and US-related events. As mentioned before, this emotional valence is computed in the CeA, and when OT is injected before the conditioning phase in adult rats, it decreases fear expression, measured by a reduction in freezing behavior during the re-exposition (Campbell-Smith et al., 2015; Kritman et al., 2017; Lahoud and Maroun, 2013). OT had a similar effect when injected/released before the retention test (*i.e.* first re-exposition) (Knobloch et al., 2012; Viviani et al., 2011 but see Campbell-Smith et al., 2015).

A.

B.

| Habituation | Fear Conditionning | Reexposition 1 | Reexposition 2 |
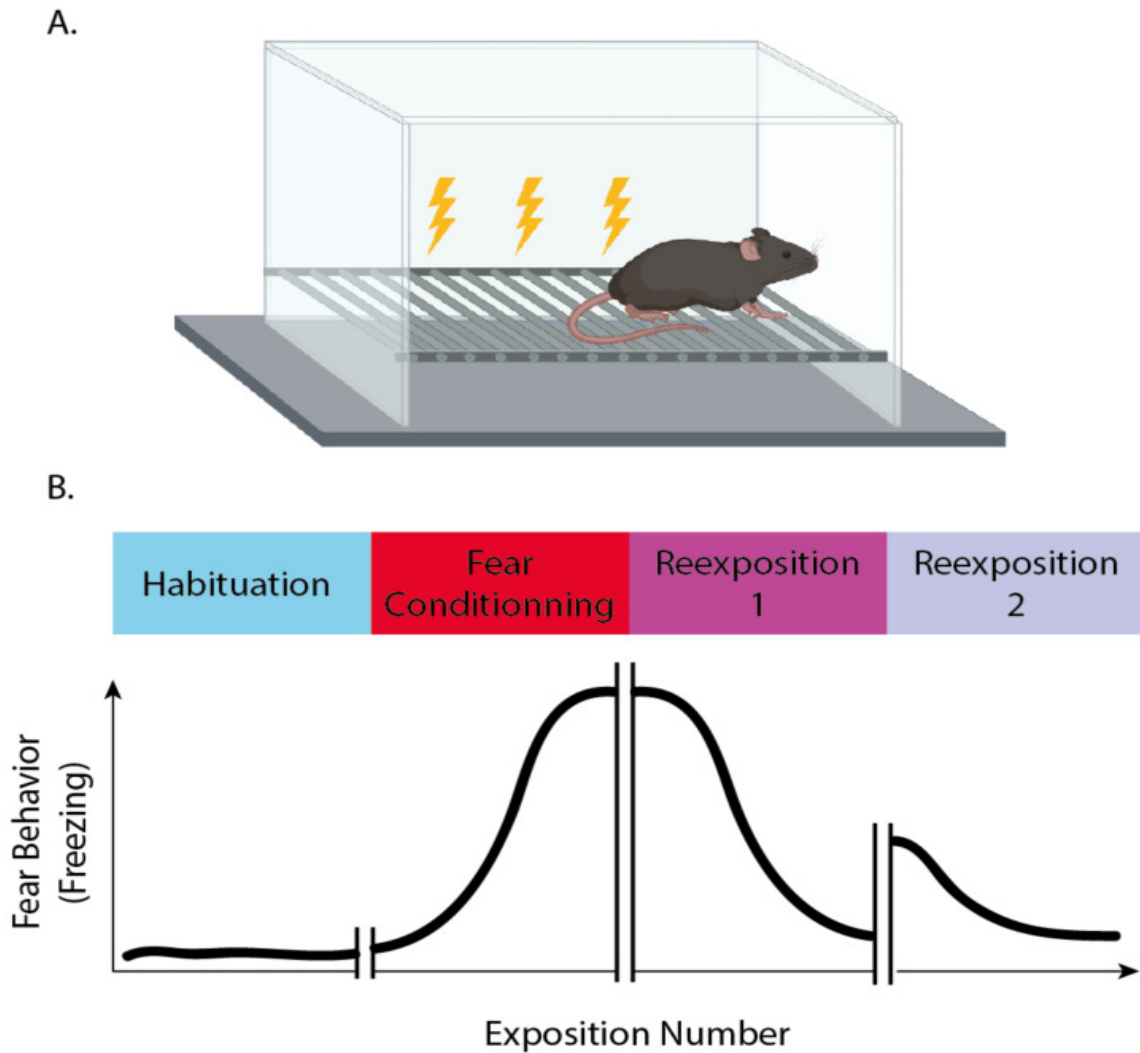
Figure 19: Fear-conditioning protocol. A. Mice are placed in a fear-conditioning box that contained a grid floor through which electrical choc can be applied. B. Different phases of the fear conditioning protocol and expected fear behavior observed.

These observations suggest two things: 1) OT may act in the CeA to reduce the unpleasantness of the US, thereby reducing its emotional salience and the association CS-US, and 2) OT may modify the memory of US unpleasantness, thus both events are robustly associated but the reaction elicited by a clue indicating the arrival of the US did not produce a strong reaction.

Thus, amygdala OT reduces fear reactions at a behavioral level. However, we do not know how this peptide modulates how the CeA computes the emotional valence associated with fear at the cellular level.

It is known that OT excites a population of CeL/C neurons that projects to CeM (Huber et al., 2005; Viviani et al., 2011). Given the GABAergic nature of these neurons, this activation results in an inhibition of CeM output neurons (Huber et al., 2005). Interestingly, only PAG-projecting neurons are inhibited by OT-sensitive CeL/C neurons, while the activity of neurons projecting to the dorsal vagal complex (DVC) is not modified after OT application. This is of particular importance given that the behavioral response to fear (*i.e.* freezing) is generated in the PAG and one of its physiological counterparts (heart rate increase) is mediated by the DVC (Viviani et al., 2011, Figure 20). Thus, OT can activate a CeL/C→CeM circuit that reduces freezing behavior without affecting the variation of heart rate triggered by the fear sensation. This suggests that fear behavior and physiological adaptations are computed by parallel circuits in the CeA, and more precisely, by different neuronal populations in the CeL/C. Interestingly, 81% of OTR-expressing neurons in the CeL also express PKCδ (Haubensak et al., 2010), suggesting that these neurons may be responsible for the unfreezing action of oxytocin.
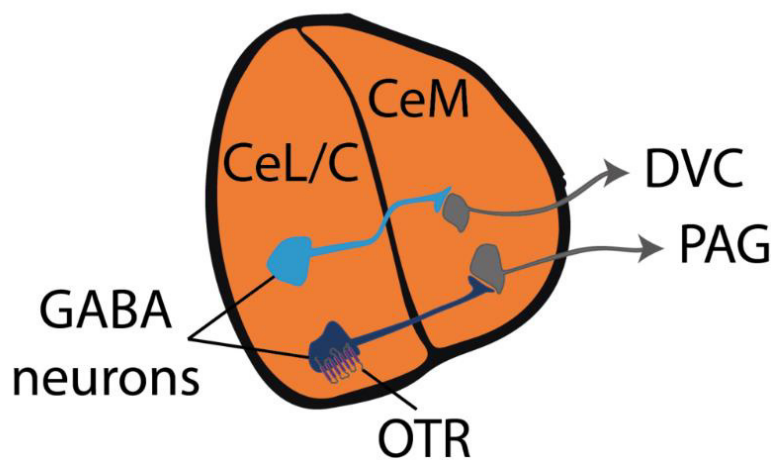
Figure 20: Schematic connectivity of OTR$^+$ and OTR$^-$ CeL/C neurons in the CeA. DVC: dorsal vagal complex, PAG: periaqueducal grey. Adapted from (Viviani et al., 2011).

Fearful stimuli increase the activity of a population of neurons representing ~30% of the CeL/C (called CeL$_{ON}$) while decreasing the firing of ~25% of CeL/C neurons (CeL$_{OFF}$, Ciocchi 2010). The first population probably contains neurons that express SOM and CRH because their activation increases freezing and flight, respectively whereas their inhibition prevents it (Fadok et al., 2017). CeL$_{OFF}$ neurons have been more formally identified to be part of PKCδ$^+$ neurons (Haubensak et al., 2010). These three types of neurons are thought to inhibit each other, forming a Mexican standoff (Figure 21) in which the winner takes all. Thus, CeL$_{OFF}$ neurons can inhibit CeL$_{ON}$ to prevent *post-encounter* reactions while the activity of CeL$_{ON}$ triggers

such reactions. If CeL$_{ON}$ neurons win, the choice of the adapted behavior to adopt is then decided by a balance between the activity of SOM and CRH neurons, the first ones promoting passive defensive behaviors (*eg.* freezing), whereas the second ones favor active response such as flight (Fadok et al., 2017; Yu et al., 2016).
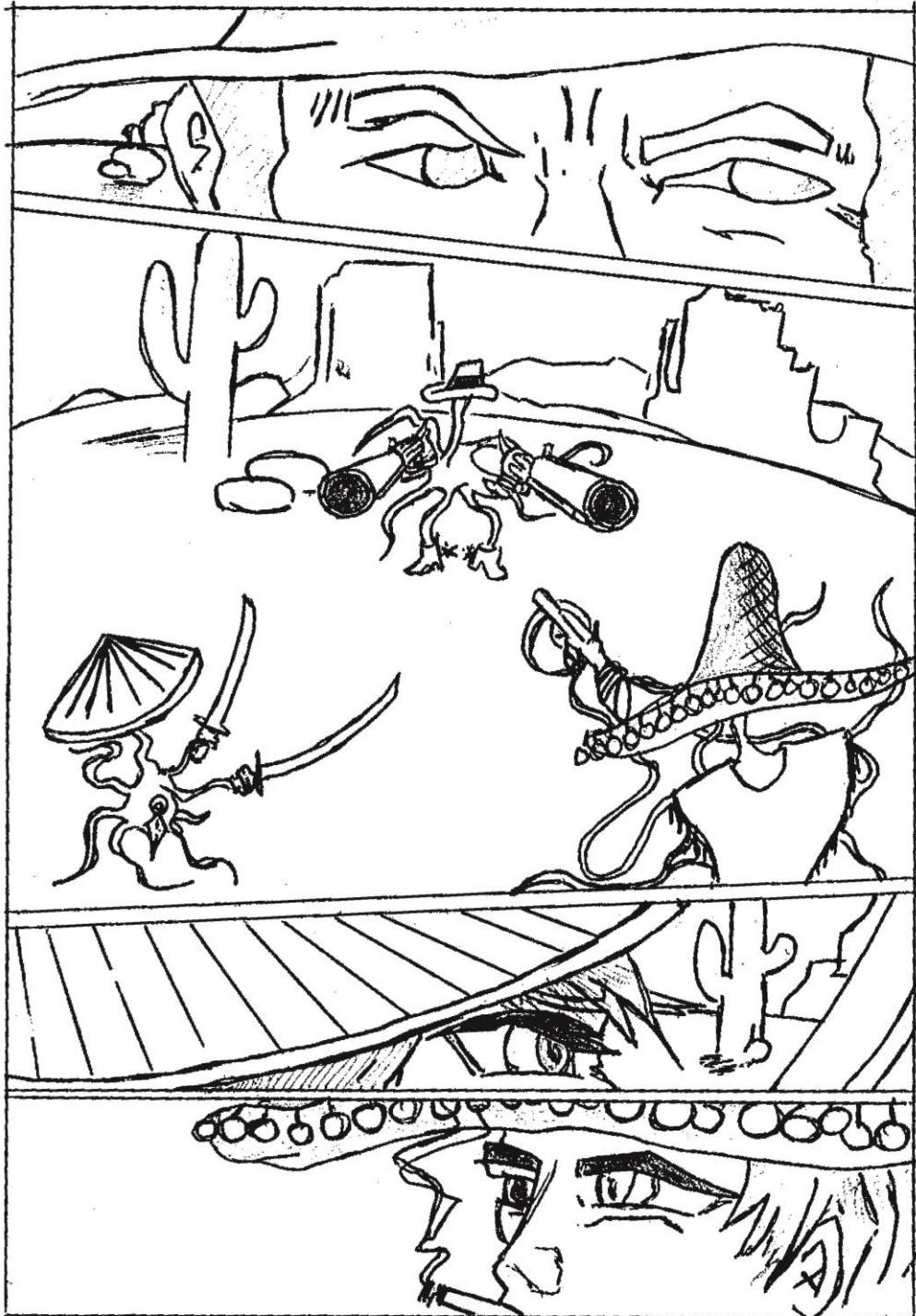
Figure 21: Reciprocal inhibition of CeL/C neurons forming a Mexican standoff.

Interestingly, OT seems to modulate this intricate circuit throughout the threat-imminence continuum (Moscarello and Penzo, 2022), probably by favoring the salience of meaningful stimuli, thereby increasing the relative importance of relevant threat-signaling cues (Olivera-Pasilio and Dabrowska, 2020). To exert such a difficult task, OT could modulate the activity of PKCδ$^+$ neurons that express the OTR, thereby explaining the anti-freezing effect of OT in the CeA (Knobloch et al., 2012; Viviani et al., 2011). Moreover, OT seems also implicated in the CRH/SOM balance since this neuropeptide can switch the defensive mechanism from passive to active (*i.e.* from freezing to flight, Terburg et al., 2018).

At this point, I invite the reader to note the absence of a section on the effect of OT on stress. This decision is motivated by an integrated vision of this mechanism. Indeed, stress is "the physiological or psychological response to internal or external stressors" (American Psychological Association), and for that reason, is assessed by measuring physiological parameters (Amico et al., 2004; Neumann et al., 2000; Windle et al., 1997) but never behavioral outputs. On the other hand, fear is an "intense emotion aroused by the detection of imminent threat, involving an immediate alarm reaction that mobilizes the organism by triggering a set of physiological changes" (American Psychological Association) and is evaluated based on behavioral outputs. Given that fear reaction triggers the same physiological parameters as a stressor did, we can wonder whether they are not two sides of the same coin. In this scope, stress is the physiological change induced by a fear sensation, and fear is the integrated sensation triggered by a stressor. Thus, I will use the term fear to describe the sensation of danger elicited by a potential death or injury, including thereby not only fear evoked by predators but also by the fear of injuries due to potential fighting elicited by social stress, and the fear of dying during hydric restriction.

2.2.2. Anxiety-like behaviors

Anxiety is an emotion characterized by feelings of tension, worried thoughts, and physiological changes (American Psychological Association). Importantly, anxiety differs from fear since it is a "generalized response to an *unknown* threat or internal conflict, whereas fear is focused on *known* external danger" (Steimer, 2002). Unlike fear reactions, anxiety involves other structures belonging to the extended amygdala,

such as the bed nucleus of the stria terminalis (Duque-Wilckens et al., 2020; Luo et al., 2022). Interestingly, the feeling of immediate concrete danger (*ie.* fear) is primarily computed in the CeA whereas the apprehension of unpredictable diffuse threat may rely on integration in the bed nucleus of the stria terminalis (Olivera-Pasilio and Dabrowska, 2020). However, a decrease in anxiety-like behaviors has been observed after CeA injection of OT (de la Mora et al., 2016; László et al., 2020; McCarthy et al., 1996). Little is known about the precise mechanisms involved in this anxiolytic effect but it seems that it may involve a functional coupling with the dopaminergic system since the co-infusion of dopamine receptors antagonists prevents the reduction of anxiety-like behavior observed after OT infusion in the CeA (de la Mora et al., 2016).

We can also suggest that, as for fear, several subcircuits may exist in the amygdala that can trigger or prevent anxiety. Indeed, activation of CeL/C SOM neurons triggers anxiety-like behaviors in mice (Ahrens et al., 2018; Chen et al., 2022; Sun et al., 2020), however activation of PKC-expressing neurons did not modify anxiety levels in mice (Chen et al., 2022).

2.2.3. Pain and Nociception

Pain can be described as the emotion that arouses from the integration of several aspects of nociceptive stimuli, ranging from a strict somatosensorial aspect (location, strength, nature of the event), to its emotional valence. OT modulates this last parameter since in patients with amygdalectomia, the subject does not perceive high-intensity thermal stimuli as painful but can perfectly describe the stimulus (Thompson and Neugebauer, 2017).

When injected in rat CeA, OT triggers mechanical and thermal hypoalgesia, and the subsequent application of atosiban reduces the effect of OT, suggesting that the hypoalgesia may be mediated by an OTR-Gα_q pathway (Han and Yu, 2009). Moreover, blocking OTR signaling in the CeA by infusing an OTR antagonist increases the vocalizations evoked by a noxious stimulus but did not change the hindlimb withdrawal threshold for spinal reflexes, suggesting that OT may play a role in the central integration of the nociceptive message in the CeA (Cragg et al., 2016). Interestingly, no other studies have investigated the role of OT in the CeA during pain processing.

Moreover, it has been recently suggested that equivalently to CeL_{ON} and CeL_{OFF} cells observed in fear protocols, the CeL might also contain cells that are sensitized and others that are inhibited by chronic pain. The activation of the first triggers pain-related responses whereas the stimulation of the latter drives anti-nociception in mice. Interestingly, pain-activated cells express the PKCδ marker whereas SOM-expressing neurons prevent pain-related behaviors (Chen et al., 2022; Wilson et al., 2019). Thus, if SOM neurons are activated, the animal may feel fear, thereby increasing its nociceptive threshold. On the other hand, if the animal feels safe, PKCδ neurons may increase pain sensitivity, thereby favoring the conservation of the body's integrity. However, PKCδ neurons express the OTR, suggesting that OT could activate these neurons to trigger a higher sensibility to pain, a suggestion highly incongruent with the literature. We can imagine that several subpopulations of neurons coexist in the CeL/C and are involved in different functions. For instance, it has been proposed that two population may coexist in CeL SOM neuron and differentially regulates pain, fear, and anxiety (Lin et al., 2022). Based on this example, we can imagine that PKCδ neurons may contain several subpopulations of neurons.

2.2.4. Other behaviors

Among the wide range of OT-modulated behaviors, the emotion discrimination of conspecifics is under the control of OT since inhibiting OTergic PVN-to-CeA projecting neurons prevents emotion discrimination in mice (Ferretti et al., 2019). OT can also prevent the synaptic changes triggered by alcohol consumption and thereby, prevent alcohol-seeking motivation in rats (Tunstall et al., 2019). Another side of OT action in the CeA can be observed after an aggressive encounter, where OT infusion enhances the aggression of female rats toward an intruder. Interestingly, this effect may last since the intrusion and aggression trigger an increased binding of OTR in the CeA, suggesting plasticity at this level (Oliveira et al., 2022). Intriguingly, the function of OT in the CeA during positive events is left aside, leaving an entire area of possible OT action in this structure.

Although the quasi-omnipresence of OT control in emotions can be surprising, we can rationalize this by integrating the function of OT within amygdala circuits. Given the primary function of the amygdala is to attribute emotional valence to external

stimuli, OT may influence the way this valence is computed, thereby modifying virtually all amygdala-related behaviors.

When looking closer on the effect of OT in the CeA, we can observe that this effect is relatively slow and long. At an electrophysiological level, the bursts of inhibitory postsynaptic currents evoked by OT-mediated CeL neurons activation are observed several tens of seconds, sometimes a minute after OT application (*Unquantified observations*). A similar latency is also observed at a behavioral level, where the evoked endogenous OT release decreases freezing behavior after 30 to 60s (Knobloch et al., 2012). This delayed effect is too long to be explained by classic neurotransmission, which usually ranges for milliseconds, suggesting the involvement of another actor in the circuit that slowed the signal.

3. Astrocytes as neuron's playmate

3.1. Astrocyte at a glance

3.1.1. Appetizer

In the dawn of metazoan life, some cells specialized and unlock the electrical signaling. These rudimentary neurons have probably adapted the electrical signaling observed in motile single cells to create a rapid form of intercellular communication (Lentz, 2023). The ability of neurons to produce such rapid electrical influxes comes from the high expression and localized presence of voltage-gated ion channels, particularly those permeable to sodium (Na^+) and potassium (K^+). Indeed, these two types of channels closely collaborate since the opening of the former triggers the influx of Na^+, thereby depolarizing the plasma membrane, which opens the latter, allowing K^+ to leak out of the cell, thereby repolarizing the cell (Barnett and Larkman, 2007). This stereotyped millisecond-range depolarization of the plasma membrane called "action potential" allows neurons to encode information in a binary way. For that reason, neuroscientists have put many hopes in deciphering this digital code to understand brain functions.

However, when paying close attention to the brain's histological composition, we can observe that this organ is not only made of neurons but also contains cells that lie between them (Figure 22). These so-called "glial" cells were initially thought to be a mere glue, a physical support for neurons. This dichotomy comes from the fact that, unlike neurons, glial cells cannot fire action potentials. The absence of such electrical signaling has resulted in the conceptual separation of brain cells into two casts: the neuronal guild that treats information and makes long-range projections throughout the body, and the glial alliance that supports neurons in this task by feeding them, cleaning their environment, *etc*. However, the past decades have seen the rise of glial cells as active players in information processing in brain circuits. Among these glial cells, astrocytes are particularly involved in the brain's computational power since they control a wide range of neuronal features (Verkhratsky and Nedergaard, 2018).
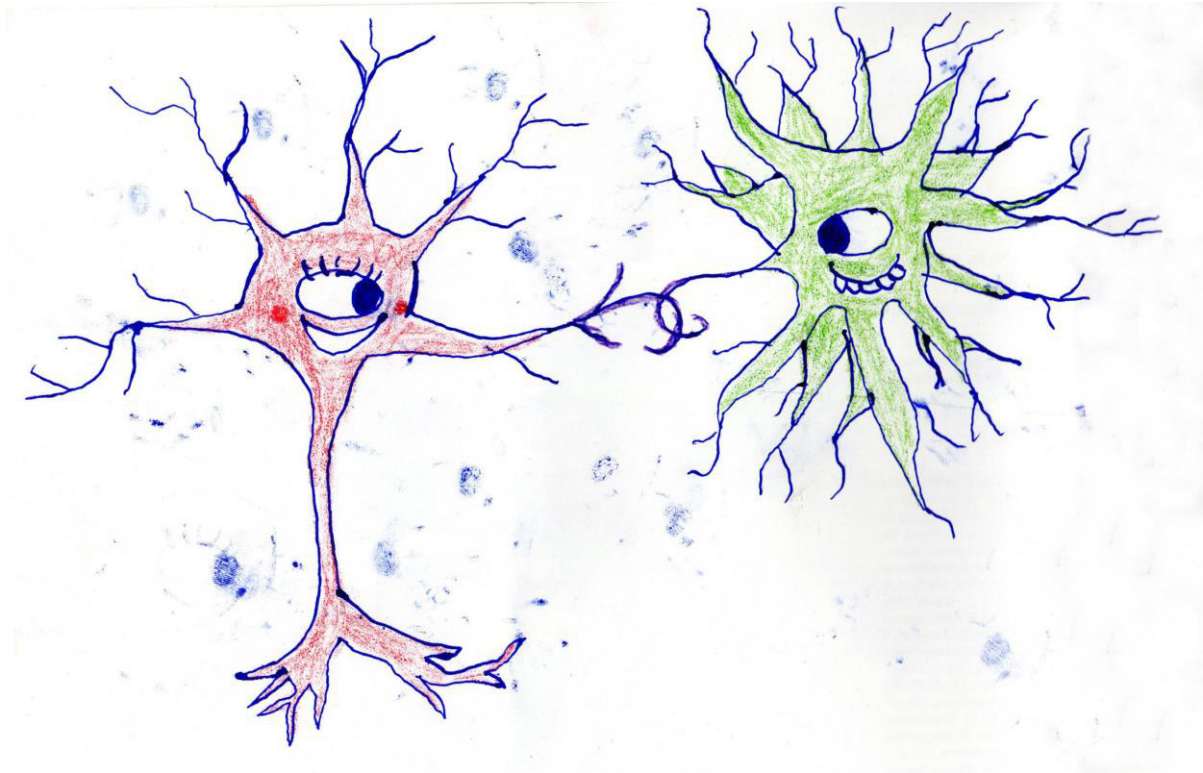
Figure 22: Astrocytes as neuron's playmate. Drawing by Aurore Baudon.

Originally named *Nervenkitt*, which means "nerve glue", these glial cells were renamed astrocytes in 1893 (Nagai et al., 2021). Composed of the Greek words "*Astron*" which means "star" and "*kytos*" which signifies "cell", this name highlights one of the most important features of astrocytes: their stellate morphology.

3.1.2. Where did you come from little star?

Astrocytes are thought to emerge when neurons began to cluster together, during the transition from diffuse to centralized nervous system. Given the high specialization of neurons, these cells are not able to manage all the aspects of cell life and particularly homeostatic functions. To overcome this problem, some cells have co-evolved with neurons to assure the homoeostatic support neurons need (Verkhratsky and Nedergaard, 2018). And Evolution said, "Let there be glial cells", and there were glial cells (Figure 23).
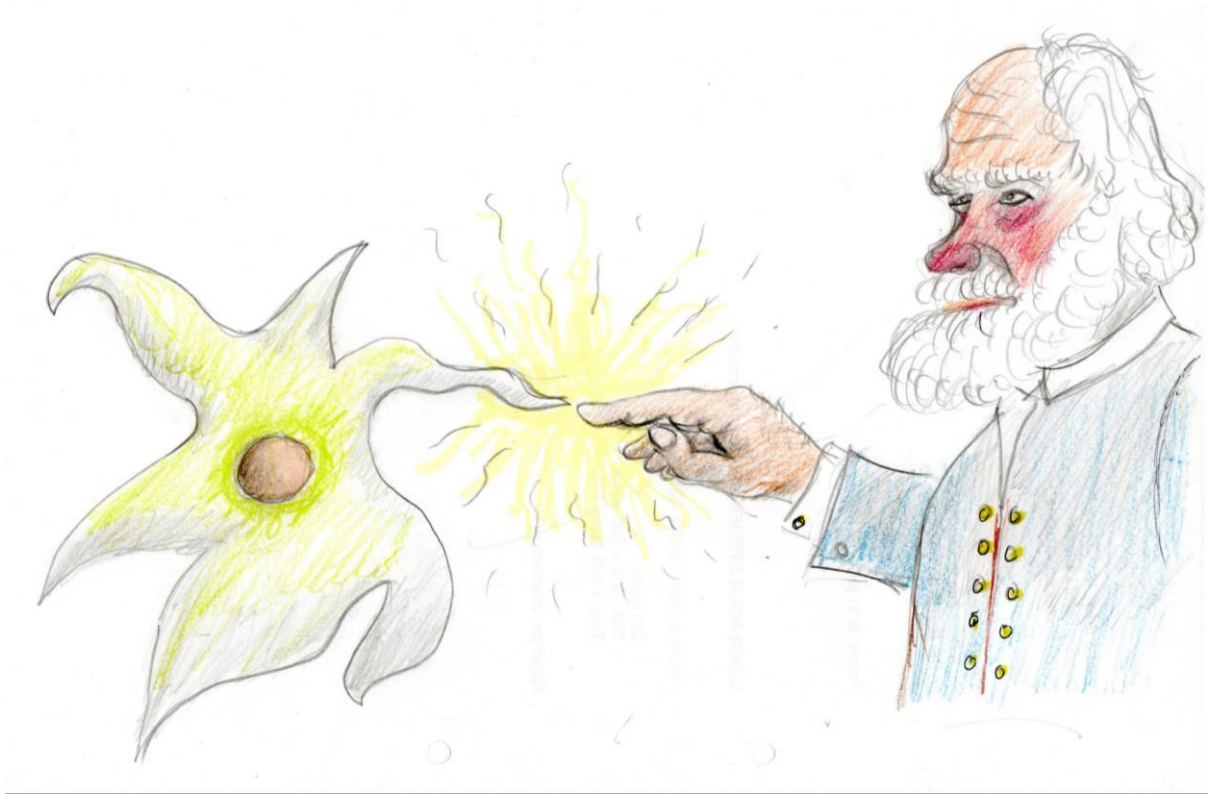
Figure 23: Evolution creating astrocytes. Drawing by Jean-Claude Baudon.

Like most neural cells, astrocytes came from the neuroectoderm. Although early developmental stages are dedicated to neuron generation through asymmetric radial glial cell division, the neurogenic period ends during the gliogenic switch that begins at embryonic days 12 to 18 in mice and peaks after birth. During the postnatal period, astrocytes divide asymmetrically throughout the brain, thereby generating ~50% of all astrocytes. In adulthood, astrocytes still proliferate but at low rates that vary depending on the brain region (Verkhratsky and Nedergaard, 2018).

According to the moment and the place of their birth, astrocytes can have different features (Figure 24). Therefore, we can classify many types of astrocytes according to their morphology, functions, transcriptomic, *etc.* (Endo et al., 2022; Khakh and Deneen, 2019).
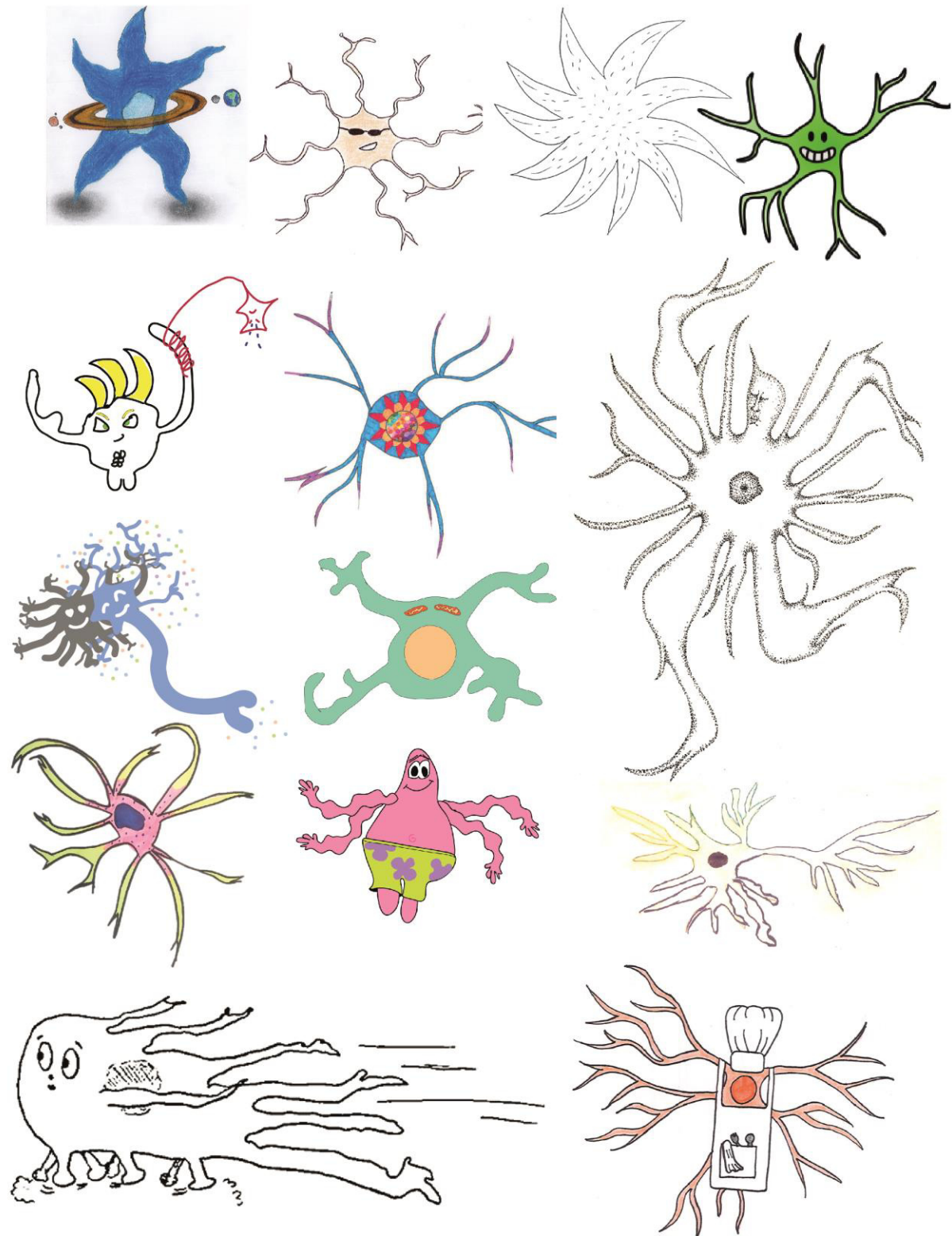
Figure 24: Astrocytes are heterogeneous cells.

3.1.3. Properties

Morphology.

First described by their morphology, astrocytes are complex cells that exhibit a highly branched "bushy" morphology. As mentioned earlier, there are many different astrocyte morphologies, but the most frequent in the gray matter is the protoplasmic one since ~10-30,000 protoplasmic astrocytes can be found in 1 mm^3 of gray matter (Verkhratsky and Nedergaard, 2018). Protoplasmic astrocytes are composed of a small soma (~10 μm diameter) from which emerge 4-10 primary processes called "branches" that are a few tens of micrometers long (Figure 25). These branches bear second-order short processes (~2-10 μm) called branchlets and ultrathin processes (~100 nm) baptized leaflets (Khakh and Deneen, 2019; Verkhratsky and Nedergaard, 2018) (Figure 25). This highly branched morphology gives astrocytes a spongiform shape where the vast majority (~90%) of the astrocyte is composed of processes (Chai et al., 2017). This extensive plasma membrane surface gives astrocytes a huge interface with their environment, allowing the cell to sense localized modification. For instance, perisynaptic astrocytic processes (PAPs) represent 80% of the total astrocyte surface but only stand for 4 to 10% of the cell volume (Augusto-Oliveira et al., 2020), illustrating how astrocytes enwrap the synapses to sense and react synaptic transmission. This so-called "astroglial cradle" (Augusto-Oliveira et al., 2020) hosts the synapses and together, by the power of friendship, form the tripartite synapse (Araque et al., 1999).

Unfortunately, it is quite difficult to evaluate the precise morphology of astrocytes because of several hurdles:

1) No protein marker allows the immunolabeling of the entire astrocyte. Several markers have been used to evaluate astrocyte morphology including the intermediate filament protein glial fibrillary acidic protein (GFAP). Unfortunately, only ~15% of processes, including the big primary processes and a few secondary processes can be observed using this approach (Khakh and Sofroniew, 2015). To overcome this issue, some authors have induced the expression of the green fluorescent protein (GFP) in astrocytes or directly loaded fluorophores using a patch clamp to reach a high concentration of fluorophore in the cytoplasm. This strategy leads to increased accuracy of the morphology estimation, allowing the visualization of branches and branchlets but the leaflets remain out of range for light microscopy.
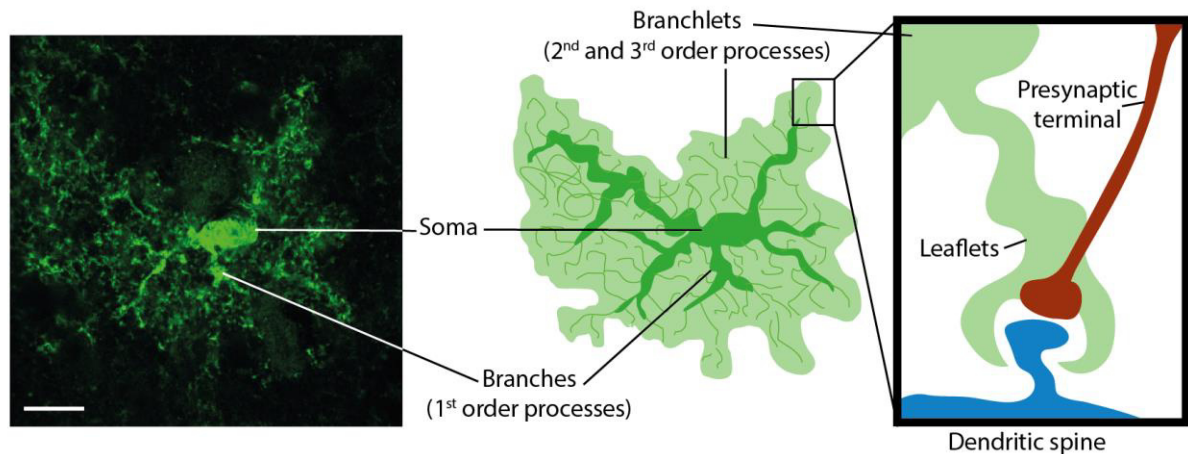
Figure 25: Astrocyte morphology. Left: picture of a GFP-filled astrocyte. Center: scheme of its morphology. Right: astrocyte leaflet that ensheathes a synapse. The presynaptic element is shown in brown and the postsynaptic in blue. Scale = 10µm.

2) Ultrathin processes are often too small to be observed with optic microscopes. Indeed, confocal microscopes cannot discriminate between two points closer than the wavelengths of the light used to observe them, a problem called the diffraction limit of optical microscopes. This is due to the impossibility to illuminate a point smaller than the wavelength used since the light diffuses around and stimulates nearby points, which blurs the image. To break the diffraction limit, some have used super-resolution techniques such as stimulated emission depletion (STED) microscopy that deplete fluorescence around the center of the excitation spot, thereby reducing image blurring. Using this approach, authors were able to reconstruct astrocytes' complex spongiform morphology and they observed a "reticular meshwork of nodes and shafts that often formed loops-like structures". Interestingly, these authors show that astrocytic processes can be branched at the level of nodes and can form circular structures named "rings" (Arizono et al., 2020, Figure 26A). Recently, another study revealed the structure of ultrathin astrocytic processes using electron microscopy, which can reach a resolution of 0.1 nm. Here again, authors observed these O-ring structures that ensheath dendrites and axons bundles. Interestingly, they show that these structures are formed by processes that are not fused to the process they originate (Aten et al., 2022, Figure 26B). This observation is of tremendous importance given that it may change the way electrical or ionic signals can propagate within the PAPs rings and back to their initial process.
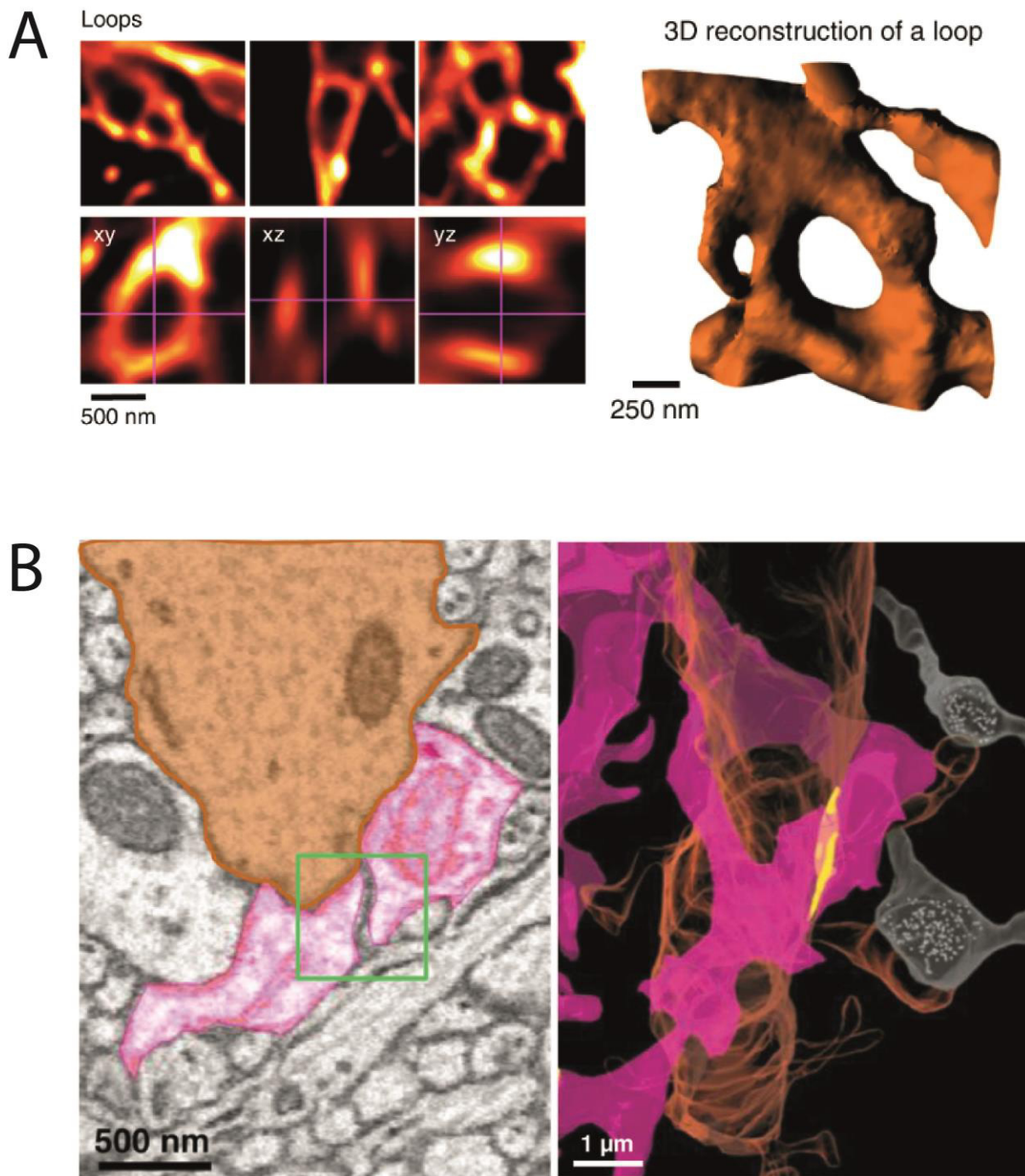
Figure 26: Structure of ultrathin astrocytic processes ensheathing dendrites and synapses. A. Rings structures observed with STED microscopy. From Arizono et al., 2020. B. Left: reflexive astrocytic processes observed with electron microscopy. Right: 3D reconstruction of the dendrite and the astrocytic process. The yellow part is the zone of contact between the primary astrocyte branch and the reflexive process. From Aten et al., 2022.

Electrophysiological properties.

As mentioned above, astrocytes cannot fire action potentials. This is due to their low expression of voltage-dependent channels and their low membrane resistance (< 5 MOhms). This latter feature is mostly due to a high expression of potassium channels, which make the cell very permeable to K^+ ions and set their membrane voltage close to the K^+ equilibrium potential (usually around -98 mV, Khakh and Deneen, 2019). Although it is really difficult to clamp astrocyte membrane voltage due to this high permeability, many studies showed that an increase in extracellular potassium concentration ($[K^+]_{EC}$) caused by neuronal activity triggers inward currents in astrocytes due to the uptake of K^+ ions through inwardly rectifier K^+ channels (K_{ir}). This uptake is crucial for the ion homeostasis of the extracellular medium during synaptic activity since a high $[K^+]_{EC}$ increases the membrane voltage of nearby neurons, making them more excitable (Kofuji and Newman, 2004).

Interestingly, these K^+-evoked currents propagate throughout several astrocytes that are connected by gap junctions, thereby forming functional syncytia. It has been observed that one astrocyte is generally connected to more than one hundred other astrocytes in the striatum and hippocampus (Chai et al., 2017). This ability of astrocytes allows the network to equilibrate the membrane voltage among a functional syncytium, thereby creating an isopotential network. This feature is crucial given that transporters and channel functions depend on the driving forces of ions, which are ruled by the membrane voltage and the local concentration of the ion. In astrocytes networks, ions can cross gap junctions to diffuse in the entire network, allowing cells to buffer local increases of K^+, without creating an overload in one astrocyte (Kofuji and Newman, 2004; Pannasch and Rouach, 2013; Stephan et al., 2021).

3.1.4. Functions

K⁺ homeostasis.

One of the most important functions of astrocytes is to regulate the ion composition of the extracellular medium, thereby maintaining ion homeostasis. Among those ions, K^+ varies a lot in the extracellular space due to its massive outflux from neurons during the repolarization phase of action potentials. This results in an increase in $[K^+]_{EC}$ which reduces the electrochemical gradient of K^+, and thereby reduces its relative importance in the setting of the membrane voltage of neurons, ultimately depolarizing the cell.

Figure 27: Astrocyte buffering potassium at the synaptic level. Drawing by Ondine Baudon.

To avoid this side effect of K^+ extrusion from neurons, astrocytes uptake this ion to maintain a constant $[K^+]_{EC}$ (Figure 27). This K^+ buffering is mainly done by inwardly rectifier K^+ channels (K_{ir}). These channels are open at the resting membrane potential of astrocytes and lipids and G proteins control their opening. As mentioned above, this load of K^+ then diffuses within the astrocytic network allowing a high buffering capacity (Figure 28) (Kofuji and Newman, 2004; McNeill et al., 2021).

Figure 28: Astrocytes buffering potassium. When neurons (in black) undergo intense activity, they release potassium in the extracellular space. Astrocytes uptake this potassium, which diffuses throughout the astrocyte syncytium and is released in locations where extracellular potassium levels are low.

Energy supply.

Although the brain stands for only 2% of the body weight, it consumes around 20% of the body's glucose. This high energy demand is caused by neuronal activity since those cells utilize 80 to 95% of the glucose whereas glial cells use the remaining 5 to 20% (Mergenthaler et al., 2013). Even if neurons metabolize glucose, these cells preferentially use lactate as an energy substrate during the phases of intense neuronal activity (Karagiannis et al., 2021). Intriguingly, this lactate comes in major part from astrocytes that take up glucose in the blood through transporters and metabolize it into lactate which is then transferred to neurons (Karagiannis et al., 2021) (Figure 29). Once in the neuronal cytoplasm, lactate is reconverted into pyruvate that can enter the Krebs cycle to produce energy for neurons. This so-called "lactate shuttle" allows neurons to use glucose without performing glycolysis (Verhoog et al., 2020; Verkhratsky and Nedergaard, 2018).
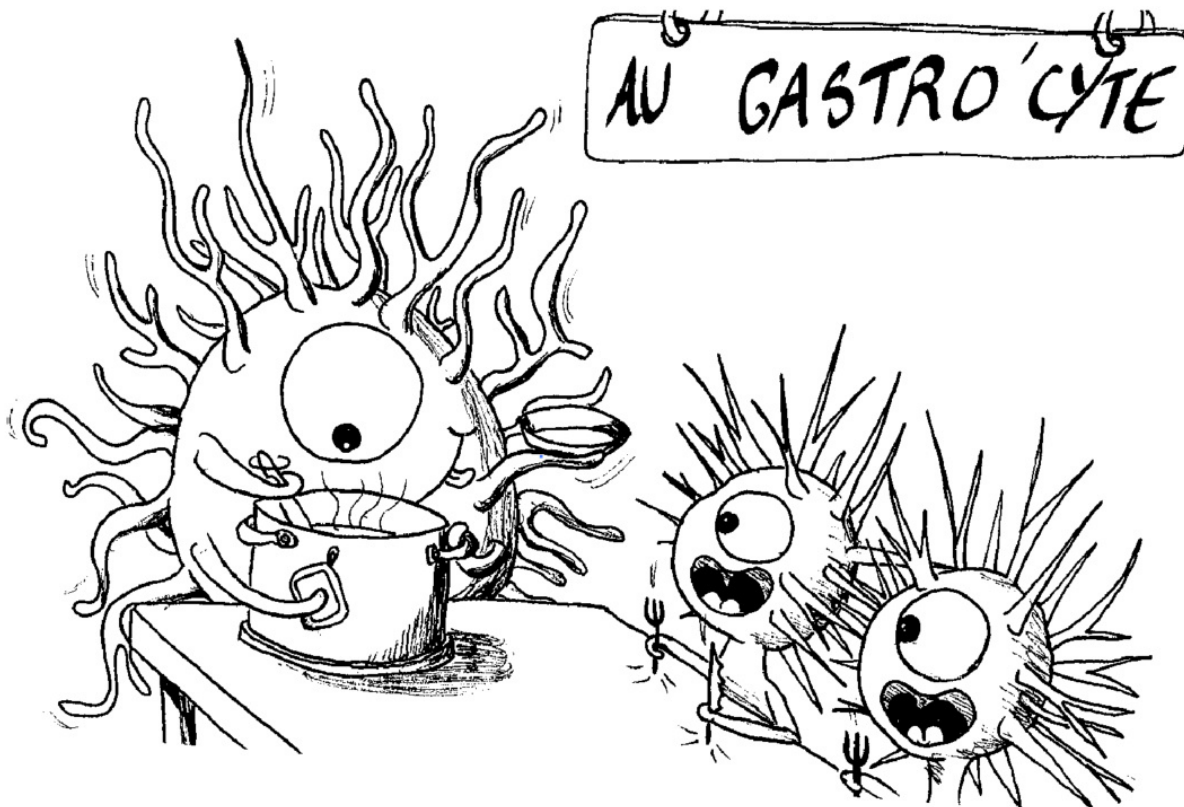
Figure 29: Astrocytes feeding neurons with lactate soup. Drawing by Clara Bottlaender.

Gliotransmission.

Upon stimulation, astrocytes can release neuroactive substances through different mechanisms (channels, vesicular release, secretory lysosome, *etc.*) (Araque et al., 2014; Savtchouk and Volterra, 2018; Verkhratsky and Nedergaard, 2018) (Figure 30). Due to its slow kinetics and lack of a precise target, this so-called "gliotransmission" (see criteria in (Zorec et al., 2012)) was thought not to be involved in information processing in the brain (Savtchouk and Volterra, 2018). However, the better this type of communication is understood, the more its involvement in brain computational power seems obvious. In stark contrast to neurons, astrocytes seem to be able to release gliotransmitter through several mechanisms including vesicular release, channel- or hemichannel-mediated release, inversion of neurotransmitter uptake pumps, *etc*. The story of gliotransmission begins in the '90s when Parpura observed that Bradykinin application on astrocytes culture makes them release glutamate (Parpura et al., 1994). Later, Araque and colleagues showed that glutamate released by astrocytes can regulate synaptic transmission (Araque et al., 1998). Since then, many studies have described similar releases of gliotransmitters including ATP/Adenosine, d-Serine, GABA, *etc.* (Perea et al., 2009; Santello et al., 2019). Interestingly, it seems that the same astrocytes can release different gliotransmitter depending on the strength of the stimulation (Mederos et al., 2021). This suggests that it may exist different releasing sites with transporters or vesicles filled with those transmitters but to date, no evidence showed that gliotransmission may be spatially restricted (Parpura et al., 2011).

Neurotransmitter uptake.

Another function of astrocytes is to recycle neurotransmitters released by neurons. Indeed, during synaptic transmission, only a small proportion of neurotransmitters are directly reuptake by the presynaptic neurons, while perisynaptic astrocytes processes (PAPs) buffer the major part of these molecules. For instance, the glutamate and GABA are reuptake by PAPs where the glutamine synthetase enzyme converts them into glutamine (Figure 31). Glutamine is then transferred back to neurons to recreate glutamate and eventually GABA for gabaergic neurons (Figure 31). This glutamate-glutamine cycle is crucial for the refilling of glutamine in neurons and thereby supports sustained activation of neurons (Andersen et al., 2021; Augusto-Oliveira et al., 2020; Schousboe et al., 2014).
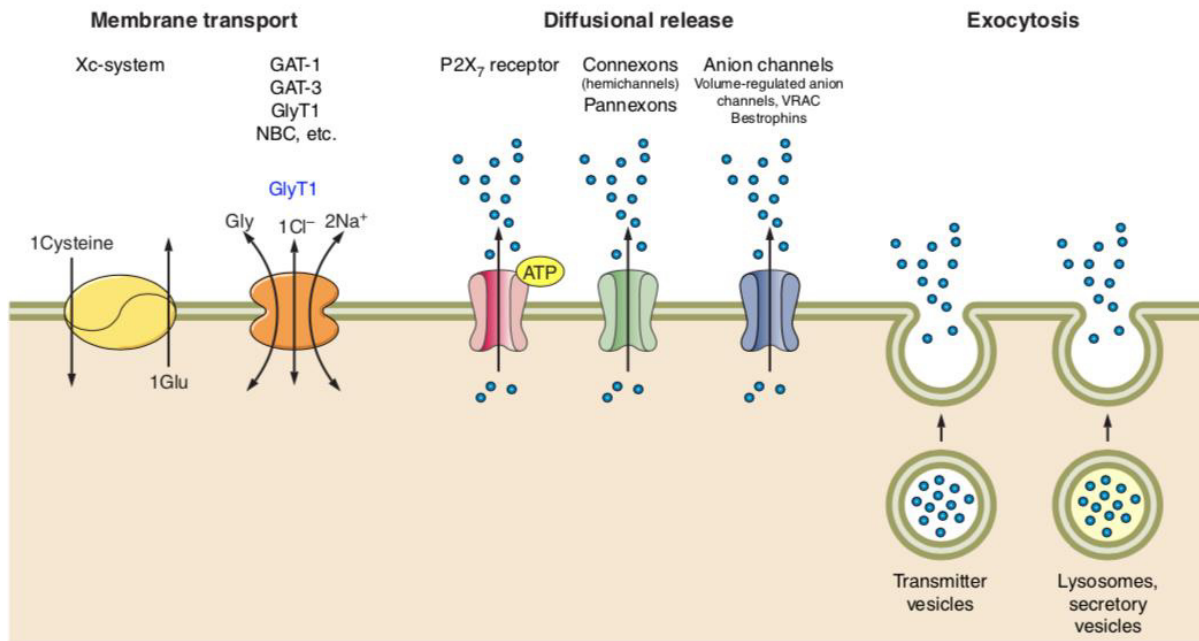
Figure 30: Astrocytes secretory strategies. Left: astrocytes can use membrane transporters to secrete energy molecules or gliotransmitters. Center: signaling molecules can cross the astroglial plasma membrane to reach their targets in the extracellular space. Right: vesicles can fuse to the plasma membrane to release various signaling molecules. From (Verkhratsky and Nedergaard, 2018).
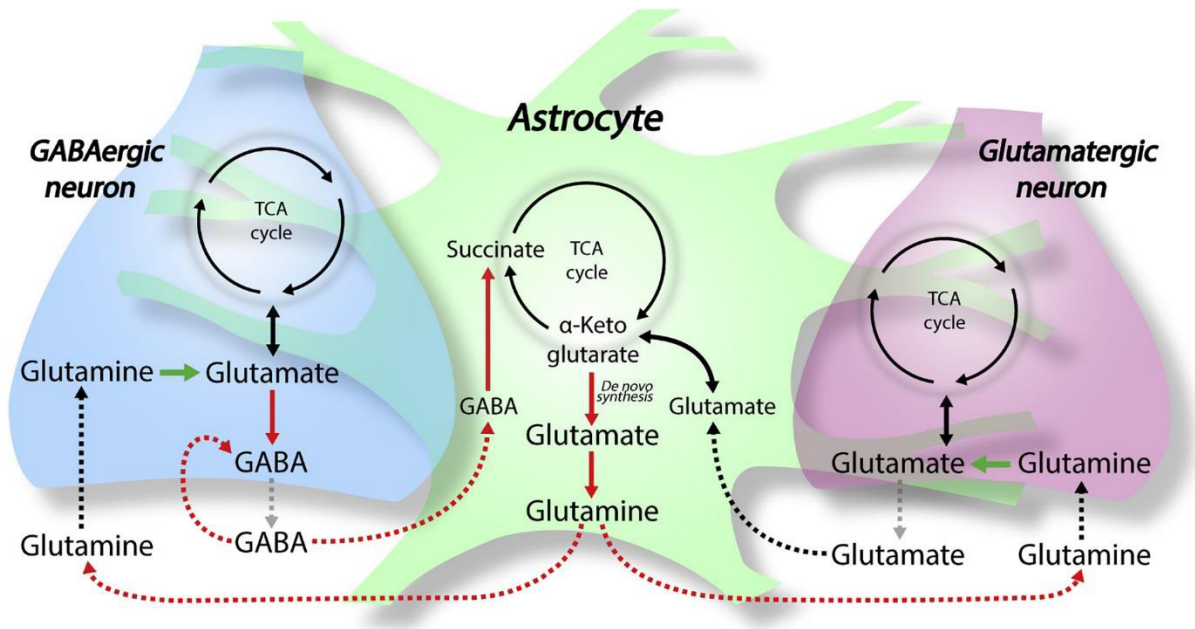
Figure 31: The glutamate/glutamine cycle. After the release of glutamate or GABA in the extracellular space, astrocytes uptake those neurotransmitters to recycle them into glutamine which is eventually transferred back to neighboring neurons. TCA: tricarboxylic acid. From Andersen et al., 2021.

Other functions.

Astrocytes have plenty of other functions, such as the control of water balance and the regulation of extracellular space (ECS) volume, the control of ECS pH, the ionic homeostasis of Cl^-, Na^+, and Ca^{2+}, the regulation of synaptogenesis, and even the control of the circulation of the ECS within the brain (Nagai et al., 2019; Theparambil et al., 2020; Verhoog et al., 2020; Verkhratsky and Nedergaard, 2018). However, I did not focus on these aspects during my thesis so I will not develop them in the present manuscript.

3.1.5. Sense and adapt: from activity to reactivity

Astrocytes are equipped to sense almost all the parameters of their environment, making them ideally suited to react not only to neuronal activity but also to all information outside the neuronal world. We can distinguish two ways astrocytes adapt to environmental changes: activity and reactivity (Escartin et al., 2021, 2019).

Astrocyte activity. Astrocytes can be activated during small physiological changes in their environment such as the ones caused by neurotransmission or acidification of the ECS (Bazargani and Attwell, 2016). This physiological response is described as rapid and reversible (Escartin et al., 2019). Often characterized by the increased probability of observing Ca^{2+} transients in the cell, astrocytes activation can lead to different outputs such as gliotransmission (Perea et al., 2009; Santello et al., 2019), modification of K^+ buffering (Sibille et al., 2014), or PAPs rearrangement (Lawal et al., 2022; Santello et al., 2019). This astrocyte activation is part of the physiological functions of astrocytes and is crucial for normal brain functions.

Astrocyte reactivity. In pathological situations, astrocytes can undergo another type of response called astrocyte reactivity (Escartin et al., 2021). In this abnormal brain state, astrocytes undergo a metamorphosis that modifies almost all aspects of their structure and functions (Figure 32). First, the transcriptional profile of reactive astrocytes is completely changed, leading to molecular changes such as upregulation of the GFAP and the vimentin proteins and downregulation of genes involved in normal astrocytes functions such as potassium buffering, or the glutamate-glutamine cycle

(Escartin et al., 2019). Reactive astrocytes also have a modified morphology, with hypertrophy of the soma and the main processes (Wilhelmsson et al., 2006). Finally, these cells can migrate and proliferate (Wang et al., 2018). This reactive state is a total modification of astrocytes' physiology but if the situation is eventually resolved, reactive astrocytes can go back to their initial state and their original functions (Escartin et al., 2019).
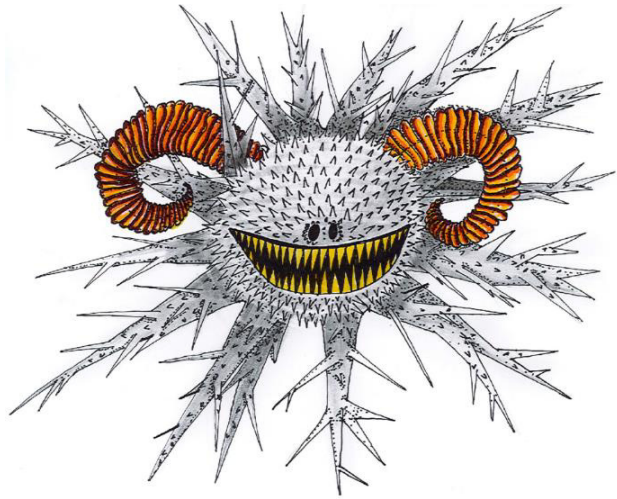
Figure 32: Reactive astrocyte. Drawing by Pola Tuduri

3.2. Astrocyte as active players in information processing

3.2.1. Excitability : Ca^{2+} as a landmark

The major secondary messenger in eukaryotic cellular biology is calcium and glia are no exception to this rule. Indeed, it is well known that glial cells, and mostly astrocytes, can respond to external stimuli by modifying their intracellular calcium concentration ($[Ca^{2+}]_{IC}$). However, Ca^{2+} signaling is used in almost every cell mechanism, including apoptosis (Berridge et al., 2003), so how can a specific stimulus trigger a precise reaction in the cell?

This point of crucial importance has been widely studied in many cell models and the curtain begins to rise; for instance, we know that apoptosis is triggered by a strong and sustained $[Ca^{2+}]_{IC}$ increase but the release of vesicles is activated by rapid and localized $[Ca^{2+}]_{IC}$ transient. However, despite the huge amount of studies that have investigated glial involvement in neuronal processing, the calcium coding strategies in glial cells are still an enigma.

3.2.2. Astrocytes are sensitive cells.

Astrocytes sense neuronal activity.

The first feature of interest in astrocyte physiology is that astroglial cells respond to a wide range of substances. Particularly, astrocytes display calcium transients following exposure to neuroactive molecules such as neurotransmitters, neuromodulators, or neuropeptides. The detection of such stimuli is allowed by the expression of a great diversity of membrane receptors: ligand-gated ion channels, GPCR, receptor tyrosine kinase, *etc.* Nevertheless, GPCR seems to be preferred in the astroglial arsenal, maybe because the high affinity of these receptors for their ligands allows them to detect small amounts of substances (Kofuji and Araque, 2021).

Astrocytes respond to their environment.

Following detection, the signal is transduced (*i.e.* encoded in a cell-readable format) by recruiting an intracellular signaling cascade. Following this observation, astrocytes have traveled from non-excitable cells to active cells, finally reaching the status of sensitive cells. We now suspect an infinite complexity in astrocytes activity that can involve a large number of signaling pathways. However, the common landmark of astrocyte activity is their Ca^{2+} signaling (Charles et al., 1991), even if Na^+ signaling seems to be promising to understand other aspects of astrocyte physiology (see the work of Rose's lab, reviewed in Verkhratsky et al., 2020).

3.2.3. Encoding extracellular stimuli with Ca^{2+} signals.

Intrapeak coding.

Calcium signals can have many shapes thanks to the "Ca^{2+} toolkit" (Berridge et al., 1998), which gathers numerous actors that can take part in the beginning and the shutdown of Ca^{2+} signals (ON and OFF mechanisms).

The building blocks of Ca^{2+} signaling rely on tiny, rapid, and localized $[Ca^{2+}]_{IC}$ increases caused by Ca^{2+} influx from the extracellular space (Shigetomi et al., 2010) or intracellular organelles such as the endoplasmic reticulum (Okubo, 2020), or the mitochondria (Agarwal et al., 2017). Once started, Ca^{2+} signals regulate themselves thereby sculpting the final shape of the signal (Figure 33). A good example of this is the Ca^{2+} dependence of endoplasmic reticulum (ER) Ca^{2+} channels; inositol

trisphosphate receptor (IP3R) and ryanodine receptor (RyR) have indeed a strong bell-shaped Ca^{2+} sensitivity, where the $[Ca^{2+}]_{IC}$ can be stimulatory at low concentrations or inhibitory at high concentrations (>300 nM) (Berridge et al., 2003).
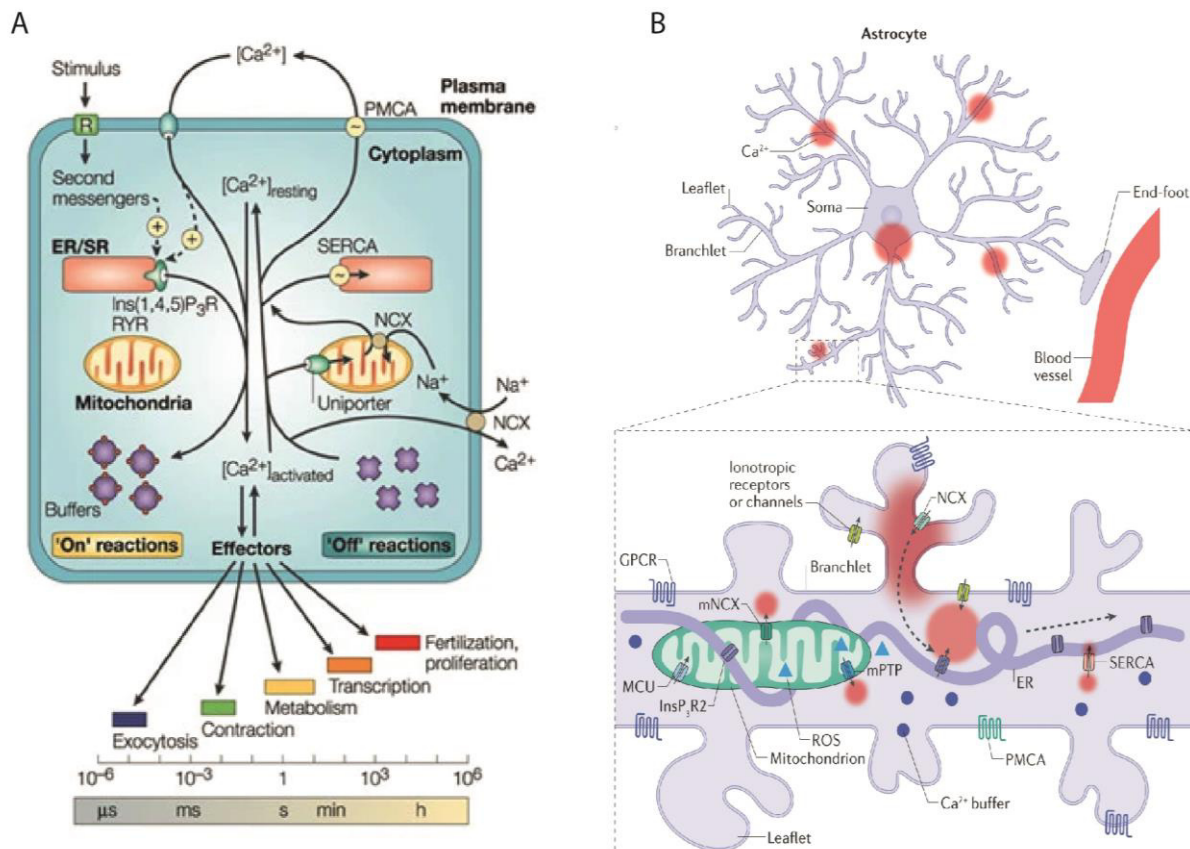
Figure 33: The calcium toolbox. A. General mechanisms that drive ON and OFF reactions and a few examples of output mechanisms. From Berridge et al., 2003. B. Actors involved in the Ca^{2+} homeostasis in astrocytes. From Semyanov et al., 2020. ER/SR: endo/sarcoplasmic reticulum, RyR: ryanodine receptor, PMCA: plasma membrane Ca^{2+} ATPase, SERCA: sarco/endoplasmic reticulum calcium ATPase, (m)NCX: (mitochondrial) Na^+/Ca^{2+} exchanger, mPTP: mitochondrial permeability transition pore, ROS: reactive oxygen species, MCU: mitochondrial calcium uniporter.

Cells express specific variants of the Ca^{2+} toolkit components, allowing them to correctly encode Ca^{2+} signals according to the desired output. For instance, IP_3R2 is the major type of IP_3R in astrocytes and is involved in the spatial spread of Ca^{2+} signals, particularly contrasting with other IP_3R whose opening produces tiny, localized $[Ca^{2+}]_{IC}$ increases (Shigetomi et al., 2019). Because the knockout of IP_3R2 dramatically reduced the number of Ca^{2+} transients in astrocytes somata (Petravicz et al., 2008), it was thought that astrocytes Ca^{2+} signaling was mainly based on Ca^{2+} release from the ER through IP_3R2, putting this channel under intense scrutiny. Many studies have investigated its role in astrocyte physiology and have found contradictory results, feeding an intense debate, even questioning the utility of Ca^{2+} signaling in astrocytes (Bazargani and Attwell, 2016; Petravicz et al., 2008; Volterra et al., 2014). This point have been resolved several years later: it seems that Ca^{2+} transients recorded at the level of the soma rely on ER Ca^{2+} in an IP_3R2-dependent fashion, whereas Ca^{2+} peaks observed in gliopil are supposed to be produced by Ca^{2+} influx from the extracellular space (Bazargani and Attwell, 2016; Shigetomi et al., 2016). Considering that the huge majority of Ca^{2+} transients are observed in processes and not in the soma, it explains why even if IP_3R2 is deleted in astrocytes, no substantial changes are observed *in* and *ex vivo* (Shigetomi et al., 2016 but see Bazargani and Attwell, 2016). The IP_3R2 case perfectly illustrates how our ignorance of the astrocytic Ca^{2+} toolkit can lead to misinterpretation in the study of Ca^{2+} astroglial physiology.

Many other mechanisms can be involved in the ON and OFF mechanisms (molecular buffers, organelles, intercellular coupling by gap junction, pumps, *etc.*) and eventually, the combination of these mechanisms shapes the Ca^{2+} signals.

Interpeak coding.

Another way to approach astrocyte Ca^{2+} coding is by integrating the occurrence of multiple Ca^{2+} transients over time. A wide range of temporal patterns of response has been observed in astrocytes and a few have been correlated to specific responses. Just as for the tripartite synapse, the story starts in the periphery to reach the central nervous system. At first, Robitaille's lab showed that a single calcium peak is observed in perisynaptic Schwann cells after a continuous stimulation of the motor neuron, and this trigger a post-tetanic potentiation of the neuromuscular junction. On the other hand, a bursting pattern of the motor neuron induces Ca^{2+} oscillations in

these glial cells, conducting to post-tetanic depression (Todd et al., 2010). Therefore, it seems plausible that in the central nervous system, distinct patterns of synaptic activity can be differentially encoded at the level of Ca^{2+} signaling (Corkrum et al., 2020; Perea et al., 2009) to eventually respond appropriately.

We can thus suggest that Ca^{2+} coding may rely on the amplitude modulation (AM coding) or the frequency modulation (FM coding) of the calcium signal (Figure 34). However, little evidence exists to strengthen this hypothesis (but see Pasti et al., 2001 for FM coding), probably due to the random-like pattern of Ca^{2+} signaling in astrocytes. This irregular pattern may come from the huge number of parameters involved in the generation of Ca^{2+} signals, giving the impression that these events occur randomly. However, if we take a deep look at spontaneous Ca^{2+} transients, we can observe that it depends on several parameters. For instance, the stimulation of a single synapse produces spontaneous-like Ca^{2+} peaks (Nett et al.,

Figure 34: Potential Ca^{2+} interpeak coding strategies in astrocytes. From De Pittà et al., 2012.

2002; Panatier et al., 2011; Perea and Araque, 2005; Santello et al., 2011; Wang et al., 2006 but see Bazargani and Attwell, 2016). Besides, Ca^{2+} from the ER seems a crucial element since the overloading of the ER by the overexpression of transient receptor potential channel 4 observed in Rett syndrome is correlated with a very high frequency of spontaneous Ca^{2+} transient (Shigetomi et al., 2019).

Thus, from this extreme astrocyte Ca^{2+} signaling sensibility to external and internal parameters arise a complex, random-like Ca^{2+} activity. Based on this pseudo-random Ca^{2+} activity in astrocytes, a probabilistic way of coding has been proposed

(Thurley et al., 2014). According to this view, Ca^{2+} transients appear spontaneously with a large stochastic component but the Ca^{2+} peak probability increases following astrocyte stimulation (Croft et al., 2016). In line with this hypothesis, each agonist has a defined probability to trigger a Ca^{2+} transient and this probability varies with agonist concentration (Croft et al., 2016). This probability modulation can be seen as an adaptation of the FM coding for cells with an irregular, non-oscillatory pattern of Ca^{2+} peak.

Spatial coding.

As previously mentioned, the neuro-glial communication interfaces are mostly found at the level of leaflets (Bushong et al., 2002; Grosche et al., 1999; Panatier et al., 2011) but the organizations of the functional astrocyte output sites are largely unknown. It seems that astrocytes can secrete neuroactive substances without spatial restrictions (Bezzi et al., 2004; Parpura et al., 2011), making Ca^{2+} signals spatial study of crucial importance.

Ca^{2+} signals are thought to be hierarchically structured: it starts with tiny, localized $[Ca^{2+}]_{IC}$ increases (elementary events), amplified into local transients, and finally, spread in the cell in a wave-like fashion (Berridge et al., 2000). In astrocytes, this hierarchy has not been established but the correspondence of different scale events has been observed (Figure 35):

1) micrometer-scale focal events (Bindocci et al., 2017; Di Castro et al., 2011; Grosche et al., 1999; Shigetomi et al., 2016),

2) intermedial events of ~10 μm (Di Castro et al., 2011; Volterra et al., 2014),

3) events that encompass the entire cell (Khakh and Deneen, 2019; Lim et al., 2021).

At a few nanometers of the focal points of Ca^{2+} entry, its concentration can reach tens of μM but the numerous buffers rapidly sequester it, preventing its spatial diffusion and so, its long-range signaling (Parekh, 2011). To overcome this issue, Ca^{2+} signals are regenerative and propagate proximally in a saltatory fashion (Berridge et al., 2003). In astrocytes, Ca^{2+} waves are indeed not uniform but are more like the spreading of sparkling $[Ca^{2+}]_{IC}$ elevations starting at multiple loci in astrocyte processes (Bindocci et al., 2017). When looking at this, one can suggest that calcium events sum up and are amplified to create big events observed in the soma. Some

studies indeed suggest that somatic Ca^{2+} events are due to the propagation of Ca^{2+} events that initiate in the processes (Bindocci et al., 2017; Gaidin et al., 2020 but see Beierlein and Regehr, 2006).

Thus, the Ca^{2+} event shape, its localization, and its integration over time can create a wide diversity of signals, probably allowing the differential encoding of distinct stimuli. The next step is then to evaluate whether these Ca^{2+} patterns can elicit different responses according to these stimuli.
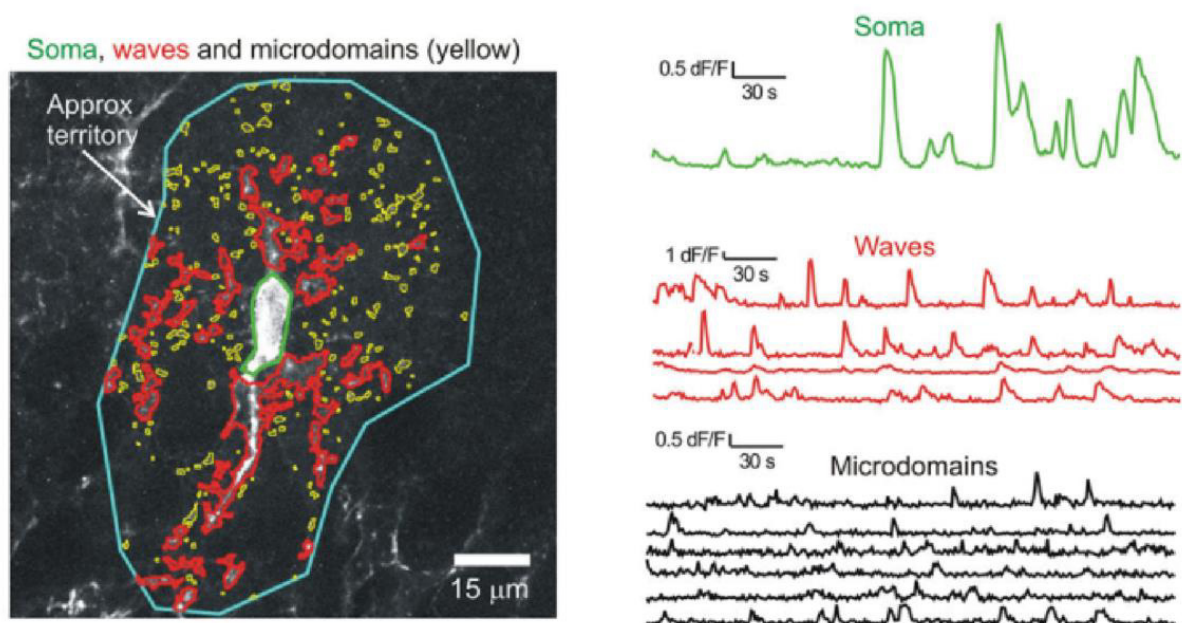
Figure 35: Spatial heterogeneity of astrocyte calcium signaling. Left: picture of an astrocyte expressing a genetically encoded Ca^{2+} indicator. Right: Example traces of somatic Ca^{2+} events, "waves" events in the processes (red), and microdomain events (yellow outline but black traces). From Srinivasan et al., 2015.

3.2.4. Decoding calcium events

Given the numerous functions of astrocytes in the brain, we can imagine a vast field of possible mechanisms ruled by astrocytes' Ca^{2+} signaling. Here I am going to focus on two cellular effects of Ca^{2+} signaling in astrocytes: the spatial remodeling of astrocyte processes and the release of gliotransmitters from these cells.

Spatial remodeling.

One of the most important features in intercellular communication is the distance between actors. Some studies have shown that astrocyte morphology can be dynamically modified, thereby changing the distance between synapses and PAPs or between neuronal somata and astrocyte processes. This structural reorganization controls the distance between cells and thereby, strengthens or weakens astrocytes' control of nearby cells (K^+ uptake, neurotransmitter reuptake, cluttering of the ECS, *etc.*) (Augusto-Oliveira et al., 2020; Haber et al., 2006; Henneberger et al., 2020; Khakh and Sofroniew, 2015; Lawal et al., 2022; Perea et al., 2009; Theodosis et al., 2008). In the hippocampus, for instance, neuronal activity can induce Ca^{2+} signaling in CA1 astrocytes, thereby triggering a dynamic remodeling of synapse coverage. In this case, a PAP displacement of around ~125 nm starts 5 minutes after the stimulation and reaches maximum mobility ~20 minutes later, with a majority of those processes moving away from the synapse (Perez-Alvarez et al., 2014). Similar results were found after the induction of long-term potentiation at the CA3-to-CA1 synapse (Henneberger et al., 2020, Figure 36A), or in unstimulated conditions (Haber et al., 2006, Figure 36B). In the lateral amygdala, astrocytes enwrap fewer synapses after fear conditioning, suggesting that the activation of this structure may result in the retraction of astrocyte processes from synapses (Ostroff et al., 2014).
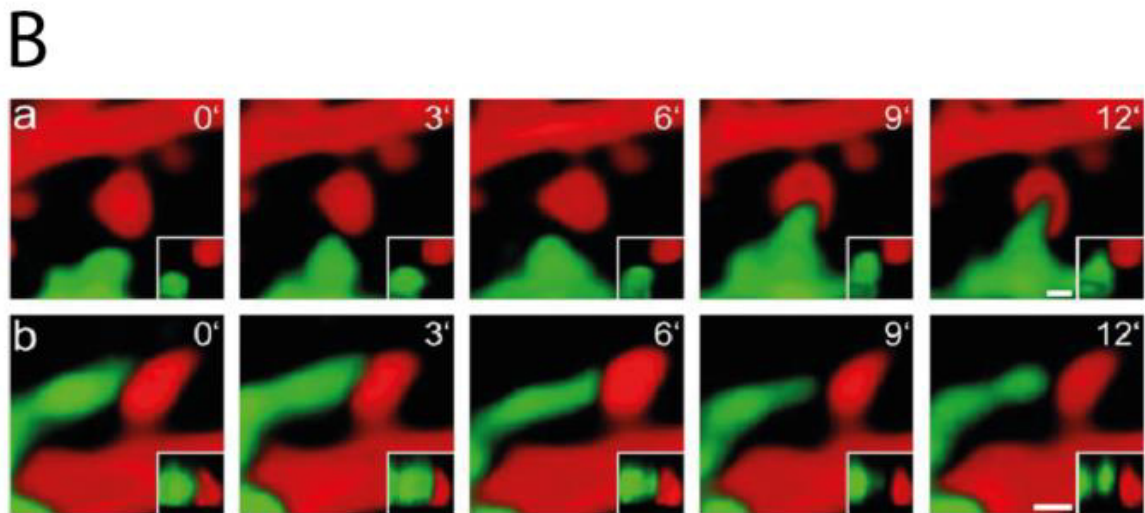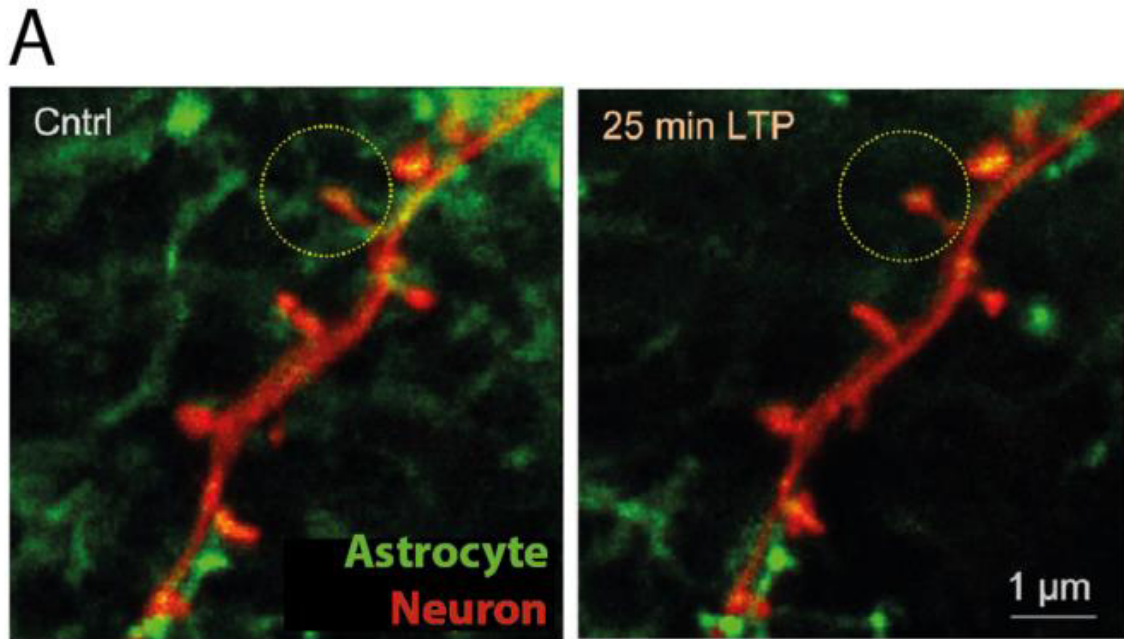
Figure 36: Spatial remodeling of astrocyte structure. A. Pictures of an astrocyte (green) and a pyramidal neuron (red). The pictures have been taken before (left) and after (right) the induction of long-term potentiation (LTP). Adapted from (Henneberger et al., 2020). B. Tracking of the morphology of perisynaptic astrocytes processes (green) and dendritic spine (red) over time. The upper row illustrates an example of an astrocyte process extending toward the spine whereas the lower row shows an example of a process retracting away from the spine. The numbers in the upper right corner of the picture represent the time in minutes. Scale bar = 1µm. From (Haber et al., 2006).

Gliotransmitter release.

Even if we know that the release of gliotransmitters can be Ca^{2+}-dependent (Fellin, 2009), the precise link between Ca^{2+} dynamics and gliotransmitter release patterns are far from being understood. However, studies have helped to gain more insights into the mechanisms underlying gliotransmitter release. For instance, Ca^{2+} plateaus (> 1 minute) observed after $G\alpha_q$ activation of exogenous receptors do not lead to glutamate release whereas IP_3 uncaging-mediated fast Ca^{2+} peaks (10-20 seconds) trigger glutamate release and neuronal excitation (Fellin, 2009; Fiacco et al., 2007).

Vesicular release. Because the neuron's major output mechanism is the Ca^{2+}-dependent vesicular release of neurotransmitter, the existence of such a mechanism in astrocytes have been widely studied (Savtchouk and Volterra, 2018). First, synaptic-like microvesicles have been identified in astrocytes (Jourdain et al., 2007; Oliet and Mothet, 2009; Sahlender et al., 2014) even if their presence is very sparse (Aten et al., 2022). Moreover, specific isoforms of exocytotic proteins (SNARE) and Ca^{2+} sensors, which are required for vesicular release, have been identified in astrocytes (Bazargani and Attwell, 2016; Chai et al., 2017; Parpura et al., 2011; Savtchouk and Volterra, 2018). At the functional level, it has been shown that uncaging of Ca^{2+} in CA1 astrocytes triggers a SNARE-dependent glutamate release (Perea and Araque, 2007). Finally, the stimulation of GPCRs can trigger a rapid Ca^{2+}- and SNARE-dependent gliotransmitter release (Bezzi et al., 2004; Jourdain et al., 2007; Pangršič et al., 2007; Papouin et al., 2017). Interestingly, gliotransmitters seem to be released during the rising phase of Ca^{2+} peaks (Perea and Araque, 2005), suggesting that astrocytes may be more sensitive to a variation of Ca^{2+} concentration than to the Ca^{2+} concentration by itself.

Channel-mediated gliotransmitter release. Gliotransmitters can also be released through plasmalemmal channels (Volterra and Meldolesi, 2005). For instance, ATP and Glutamate can cross the plasma membrane following the opening of hemichannels of connexins. The opening probability of these channels is increased by increases in $[Ca^{2+}]_{IC}$ (Meunier et al., 2017), and once open, this hemichannel allows the crossing of d-Serine across the plasma membrane, thereby increasing N-methyl-D-aspartate (NMDA)-mediated excitatory postsynaptic currents (Meunier et al., 2017).

4. Ph.D. Objectives

After these tens of pages to convince you that oxytocin can modify amygdala activity and that astrocytes are crucial in the regulation of neurons' activity, I hope you now have burning questions in mind. I did. This is why I investigated the involvement of astrocytes in oxytocin-mediated neuromodulation of the central amygdala during my Ph.D. thesis. More precisely, I tried to answer two questions: 1) Does the neuromodulatory effect of oxytocin in the central amygdala involve the activation of astrocytes?, and 2) Is the effect of oxytocin on amygdala astrocyte needed for behavioral adaptations induced by emotional challenges?

To address the first interrogation, we used calcium imaging to observe astrocyte activity, patch-clamp approaches to evaluate the neuromodulatory effect of oxytocin, and behavioral tests to assess the final output of this neuromodulation. In this first study, we focused on the rapid effect of oxytocin on the activity of neuronal networks.

In the second part of my Ph.D. work, I evaluate the involvement of astrocytes in emotion-driven plasticity in the central amygdala. As a model, I choose a fear-conditioning approach to elicit a strong emotion and its memorization. To study the function of astrocytes in this memorization, we evaluated astrocytes' morphology and function after the fear-conditioniçng protocol. Finally, we tried to link astrocytes' functions with neurons' activity in the central amygdala.

5. Scientific results

5.1. Article 1: Astrocytes mediate the effect of oxytocin in the central amygdala on neuronal activity and affective states in rodents.

5.1.1. Introduction

Oxytocin is a hypothalamic neuropeptide with a large range of functions. From its crucial role in delivery to its implication in maternal behavior, the functions of oxytocin have been widely studied for decades. Many studies have recently highlighted its implication in complex behaviors, such as conspecifics recognition and preference, pain control, or anxiety modulation (Gimpl and Fahrenholz, 2001; Lee et al., 2009). All these functions are thought to be mediated by a direct effect of oxytocin on neurons but some evidence shows that glial cells, and especially astrocytes, can express the oxytocin receptor (Di Scala-Guenot and Strosser, 1992).

5.1.2. Results

To test whether astrocytes of the central amygdala (CeA) express the oxytocin receptor (OTR), we combined immunohistochemical staining and *in situ* hybridization and observed that a population of astrocytes in the laterocapsular part of the CeA (CeL/C) of the amygdala transcribes the OTR. Interestingly, these astrocytes are different from their neighbors, with a more ramified morphology and a bigger surface territory.

Since the activation of OTR leads to calcium elevation in astrocytes (Di Scala-Guenot et al., 1994), we then used calcium imaging to test whether astrocytic OTR was functional in the CeL/C. To activate the OTR we either applied a selective OTR agonist or triggered the endogenous release of OT and we observed that these stimulations led to calcium signaling in CeL/C astrocytes of both rats and mice. To

understand the purpose of this OT-induced astrocyte activity, we then measured the activity of the neighboring neuronal network.

To do so, we performed patch-clamp experiments to measure:

1) the excitatory inputs of CeL/C neurons given by miniature excitatory currents,

2) the activity of CeL/C neurons given by their action potential firing,

3) the output message of this circuit is measured as the frequency of inhibitory post-synaptic currents in CeM neurons.

These three approaches allowed us to show that astrocyte stimulation by oxytocin can increase excitatory inputs in CeL/C neurons, thereby increasing their activity. This neuromodulation results in an increased inhibitory tone at the level of the CeM, reducing the activity of the main output nucleus of the central amygdala. Crucially, this oxytocin-driven neuromodulation was prevented by removing OTR from CeL/C astrocytes, indicating a crucial role of these cells in the oxytocin control of the amygdala.

Curious to see if this astrocyte-dependent oxytocin neuromodulatory effect also affects animal behavior, we evaluated the involvement of astrocytic OTR in behaviors known to be under the control of the amygdala. We observed that removing astrocytic OTR prevented the rewarding effect of oxytocin and its anxiolytic effects, indicating an active function of astrocytic OTR in the control of these behaviors.

By unveiling this astro-neuronal circuit, this work aims to highlight that neuropeptides, like other neurotransmitters, can modulate astrocyte calcium activity, eventually controlling neuronal networks' activity and their related behaviors.

5.1.3. Personal contribution

This study was the fruit of the contribution of many people throughout many years. For my part, I performed calcium imaging and patch-clamp experiments alongside Damien Kerspern and Jérôme Wahis. I also performed calcium-imaging experiments and I automatized their analysis pipeline using Python programs.

Astrocytes mediate the effect of oxytocin in the central amygdala on neuronal activity and affective states in rodents

Jérôme Wahis[1,16,19], Angel Baudon[1,19], Ferdinand Althammer[2,19], Damien Kerspern[1,19], Stéphanie Goyon[1], Daisuke Hagiwara[3], Arthur Lefevre[1,3], Lara Barteczko[3], Benjamin Boury-Jamot[4], Benjamin Bellanger[1], Marios Abatis[4], Miriam Da Silva Gouveia[5], Diego Benusiglio[3], Marina Eliava[3], Andrei Rozov[6], Ivan Weinsanto[1], Hanna Sophie Knobloch-Bollmann[7,17], Matthew K. Kirchner[2], Ranjan K. Roy[2], Hong Wang[8,18], Marie Pertin[9], Perrine Inquimbert[1], Claudia Pitzer[10], Jan Siemens[8], Yannick Goumon[1], Benjamin Boutrel[4], Christophe Maurice Lamy[11], Isabelle Decosterd[9,12], Jean-Yves Chatton[9], Nathalie Rouach[13], W. Scott Young[14], Javier E. Stern[2], Pierrick Poisbeau[1], Ron Stoop[4], Pascal Darbon[1], Valery Grinevich[3,20✉] and Alexandre Charlet[1,15,20✉]

Oxytocin (OT) orchestrates social and emotional behaviors through modulation of neural circuits. In the central amygdala, the release of OT modulates inhibitory circuits and, thereby, suppresses fear responses and decreases anxiety levels. Using astrocyte-specific gain and loss of function and pharmacological approaches, we demonstrate that a morphologically distinct subpopulation of astrocytes expresses OT receptors and mediates anxiolytic and positive reinforcement effects of OT in the central amygdala of mice and rats. The involvement of astrocytes in OT signaling challenges the long-held dogma that OT acts exclusively on neurons and highlights astrocytes as essential components for modulation of emotional states under normal and chronic pain conditions.

O T is a neuropeptide that acts as both a peripheral neurohormone and a central neuromodulator to modulate key physiological functions, from ion homeostasis to complex social behaviors[1]. OT is produced in hypothalamic magnocellular neurons that project further to virtually all forebrain regions. When activated, OTergic axons release OT both synaptically and extra-synaptically in the extra-cellular fluid[2,3]. This last mode of OT release has the potential to activate virtually every cell type expressing OT receptors (OTRs) located in close proximity to the sites of axonal OT release[3].

A few studies using immunohistochemistry on central nervous system (CNS) sections or a knock-in mice model found that not only neurons but also astrocytes express OTRs in various brain regions[4,5]. Early studies indicated that locally released OT induces morphological and functional changes in both the astroglial and neuronal networks of the hypothalamic nuclei producing the neuropeptide[6]. Astrocytes are part of the tripartite synapse and capable to modulate neuronal activity as well as to sense the release of neuromodulators into the neuropil[7]. Astrocytes express receptors for various neuromodulators, and accumulating evidence demonstrates that they actually mediate part of their neurophysiological effects[7], but such evidence is lacking for OT. Mapping of OTR expression in the rodent brain found that it was expressed at high levels in several

brain regions[4] and, of interest in this study, particularly in the lateral and capsular part (CeL) of the CeA[8], albeit the types of cells expressing the OTR in this brain region were never elucidated.

Functionally, the release of OT in the CeL leads to increased firing of GABA-expressing interneurons[2,8]. These interneurons inhibit projection neurons in the medial CeA (CeM), which serve as CeA output. OT action in this circuit affects amygdala-related functions, including activity of the autonomous nervous system, fear expression and anxious behaviors[2,9,10]. Furthermore, the CeA is involved in the pathophysiology of several neurological diseases, including neuropathic pain and anxiety[11,12], in which both astrocytes[13] and the OT system[14] are thought to play an important role. Therefore, it is crucial to understand how the OT system controls pain and its emotional comorbidities and if astrocytes are involved in these mechanisms.

Indeed, a role for astrocytes in the regulation of CeA circuits has already been proven in the CeM[15], where astrocyte activity can reduce fear expression in a fear-conditioning paradigm—a role that is surprisingly similar to the effect of OTR signaling in the CeL[2]. We, therefore, sought to investigate if CeL astrocytes could also play a role in the OT-mediated regulation of CeA circuits and some of their behavioral correlates.

Our study shows the expression of OTRs in CeL astrocytes and demonstrates that OT directly acts on CeL astrocytes to gate CeL neuron excitability through N-methyl-D-aspartate receptor (NMDAR) (co)activation. Furthermore, we found that the astrocyte-mediated OTR signaling underlies the anxiolytic and positive reinforcement effects of OT in the CeA. We, thus, provide the first evidence that OT drives astrocyte activity and that this effect is an essential part of the OTergic modulation of amygdala neuronal circuits and the behaviors they regulate.

Results

CeL astrocytes express functional OTRs in rats and mice. To investigate whether CeA astrocytes express OTRs, we performed fluorescence in situ hybridization (FISH) combined with immunohistochemistry on rat CeA sections and found some overlap between OTR messenger RNA (mRNA) signal and an astrocyte marker, glutamine synthase (GS) (Fig. 1a,b and Extended Data Fig. 1a). Within the rat CeL, $18.6 \pm 1.8\%$ of astrocytes and $67.8 \pm 3.1\%$ of neurons expressed OTR mRNA (Fig. 1c), with similar results in mice (Extended Data Fig. 1b). We confirmed these results using other astrocyte markers, namely ALDH1L1 and GFAP (Extended Data Fig. 1c,d). Next, we employed immunohistochemistry-based three-dimensional (3D) reconstruction using the Imaris technique and a semi-automated pipeline[16] by combining immunohistochemical staining for GS and GFAP with FISH for OTR mRNA in the rat CeL (Fig. 1d,e). This analysis confirmed the presence of OTR mRNA in astrocytes and revealed that OTR+ astrocytes have, on average, a significantly larger cell volume and surface area and a higher number and an increased length of processes compared to OTR− astrocytes (Fig. 1e). Subsequent Sholl analysis revealed that OTR+ astrocytes bear more complex morphological features than OTR− astrocytes (Fig. 1f), suggesting that OTR+ astrocytes represent a distinct subpopulation of astrocytes within the CeL.

To test whether CeL astrocytes respond to endogenous OT release, we expressed the ChR1/VChR1 chimera channel rhodopsin variant[17] (referred to here as C1V1) in OTergic neurons to optogenetically control CeA-innervating OT axons (POT-C1V1-mCherry; referred to as OxytOpto). To this end, we employed a previously characterized adeno-associated viral (AAV) vector equipped with the OT promoter[2], which was injected into the paraventricular (PVN), supraoptic and accessory nuclei of rat hypothalamus (Fig. 2a and Extended Data Fig. 2a,b). We then identified CeL astrocytes through sulforhodamine 101 (SR101) labeling and measured the relative changes in cytosolic calcium using the small organic dye Oregon Green 488 BAPTA-1 (OGB1) (Fig. 2b and Extended Data Fig. 2c–e). We found that $61.9 \pm 8.7\%$ of recorded astrocytes responded to the optogenetic OT axon stimulation (Fig. 2c,d). To avoid the possibility that astrocyte activity was increased due to the increased spiking of CeL interneurons caused by optogenetically evoked OT release, tetrodotoxin (TTX) was added to the bath before the stimulation (Fig. 2c,d). Further calcium imaging experiments described below use TTX incubation (unless stated otherwise) for the same reason. We analyzed the area under the curve (AUC) and Ca^{2+} transient frequency normalized to the baseline of astrocyte responses (Method in Extended Data Fig. 2f) and found both parameters to be increased after stimulation of OT axons (Fig. 2d). Taken together, these results indicate that optogenetically evoked OT release from axons present in the CeL elicits an increase in activity of CeL astrocytes.

To ensure that the observed responses are exclusively due to OTR activation, we applied the selective agonist of OTR ([Thr⁴Gly⁷]-oxytocin, TGOT), which increased calcium transients in $60.1 \pm 9.2\%$ of the recorded astrocytes, a result unchanged when replicated with slices pre-incubated with TTX (Fig. 2e,f). Similar pre-incubation of the slices with the OTR antagonist [d(CH₂)⁵,Tyr(Me)²,Orn⁸]-vasotocin (dOVT) reduced the proportion, AUC and Ca^{2+} transient frequency of TGOT-evoked calcium responses in astrocytes (Fig. 2e,f), confirming that the activation of astrocytes by TGOT is indeed mediated by OTR.

To test whether these effects involve the direct stimulation of astrocytic OTR, we employed a transgenic mouse line with *LoxP* sites flanking the OTR gene[18] (OTR conditional knockout (cKO) mice). To specifically delete OTRs in astrocytes, we injected AAV PGFAP-Cre in the CeL of OTR cKO mice (Fig. 2g). This led to expression of Cre in $56.0 \pm 4.9\%$ of astrocytes within the injection site, with a specificity reaching $96.2 \pm 1.05\%$ (Extended Data Fig. 2g). PGFAP-Cre AAV injection in OTR cKO mice resulted in a drastic decrease in OTR mRNA signal in astrocytes (Fig. 2h) but not in neurons (Extended Data Fig. 2h). TGOT application in TTX-treated acute slices of the CeL from control mice led to responses in $43.9 \pm 7.2\%$ of astrocytes (Fig. 2i), whereas these responses were largely reduced in CeL astrocytes from PGFAP-Cre AAV-injected OTR cKO mice (GFAP OTR KO; Fig. 2i). These results confirm that astrocyte response to TGOT is a direct consequence of astrocytic OTR activation and not secondary to neuronal activity.

Activation of OTR+ astrocytes propagates through the astrocyte network. Because astrocytes are known to form extensive intercellular networks, we next studied the spatial connectivity of OTR+ astrocytes in the CeL. (Fig. 3a and Extended Data Fig. 3a). We found that the distance between OTR+ astrocyte pairs ($96.0 \pm 4.0\,\mu m$) was larger than the distance between OTR–astrocyte pairs ($37.4 \pm 0.9\,\mu m$; Fig. 3a). In addition, we found that OTR+ astrocytes had significantly more contacts with OTR− astrocytes than with OTR+ astrocytes (Fig. 3a), whereas OTR− astrocytes regularly contact other OTR− astrocytes.

These anatomical results suggest a specific distribution pattern of OTR+ astrocytes within the CeL, where OTR+ astrocytes are found distant from one another and exhibit many connections with their OTR− counterparts. Interestingly, the proportion of rats and mice astrocytes responsive to OTR activation always exceeded 40% of recorded cells (Fig. 2) despite our FISH/Imaris results indicating that fewer than 20% of astrocytes expressed OTR mRNA (Fig. 1). This apparent discrepancy led us to test whether the sole activation of OTR+ astrocytes could drive the activity of the overall astrocyte network, including that of OTR− astrocytes.

There are two common signaling pathways typical for astrocytes that could facilitate the spread of activation from OTR+ to OTR− astrocytes. This could occur via 1) paracrine purinergic communication (for example, ATP release) or 2) spread of Ca^{2+}
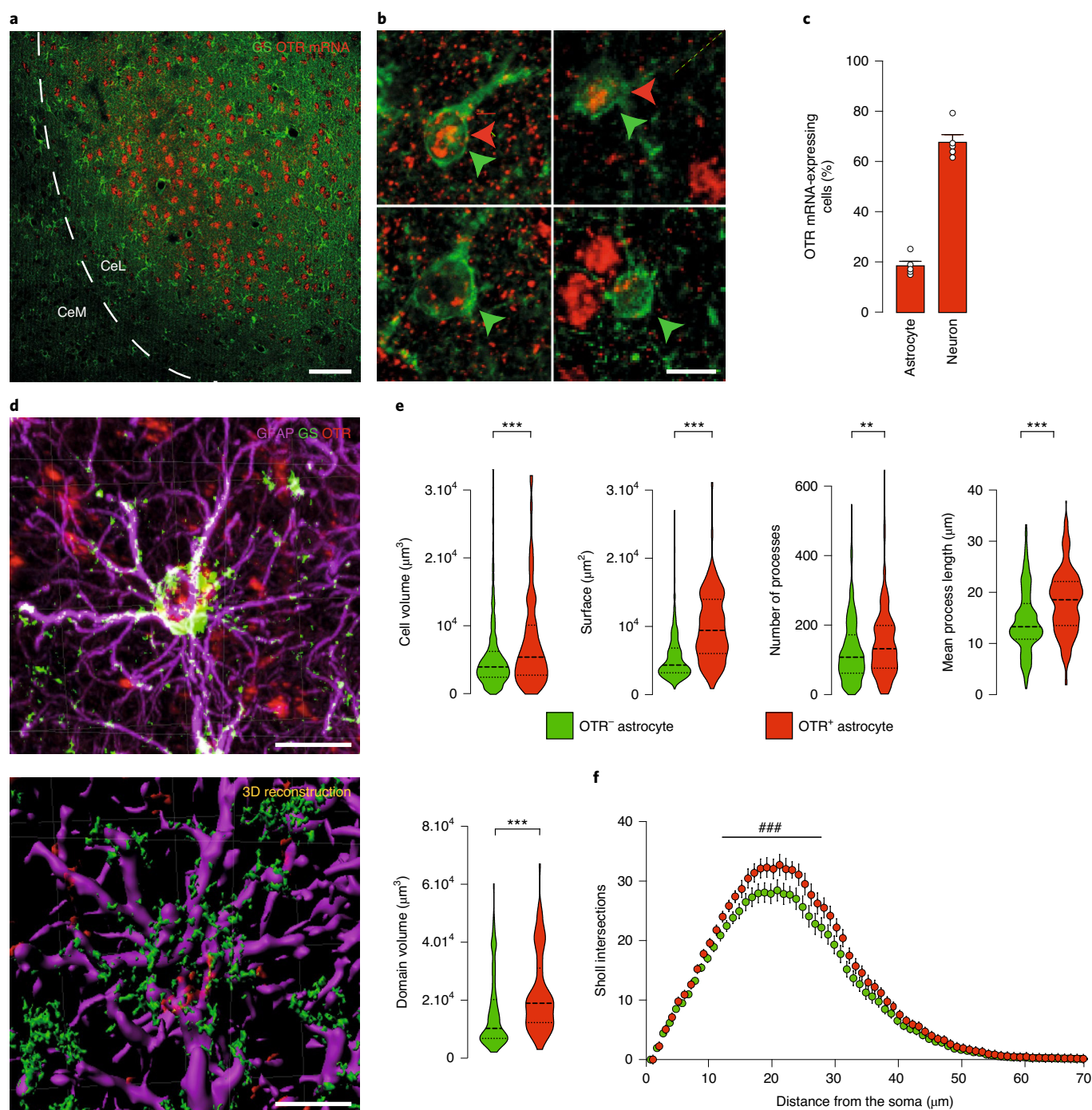
Fig. 1 | Specific CeL astrocytes express OTRs. a, Overview of CeA FISH of OTR mRNA (red) and GS immunostaining (green). **b**, High-magnification images of cells positive for OTR mRNA and/or GS (double arrows); green arrows point to GS-positive cells; red arrows point to OTR mRNA-positive cells. Scale bars, 100 μm (**a**) and 10 μm (**b**). **c**, Proportion of CeL astrocytes (GS-positive cells, left) and neurons (NeuN-positive cells, right) positive for OTR mRNA (red) ($n_{rats} = 5$, $n_{slices} = 20$, $n_{astrocytes} = 1,354$, $n_{neurons} = 1,254$). **d**, Cells were reconstructed in 3D using Imaris, and morphological parameters were evaluated. Scale bar, 20 μm. **e**, OTR-expressing astrocytes are bigger and more complex, as indicated by several morphological parameters (cell volume, surface, number of processes, process length and domain volume, OTR-negative: $n_{mice} = 5$, $n_{slices} = 20$, $n_{astrocytes} = 1,142$; OTR-positive: $n_{mice} = 5$, $n_{slice} = 20$, $n_{astrocytes} = 212$). **f**, OTR-expressing astrocytes display a more complex morphology, as revealed by Sholl analysis (OTR-negative: $n_{mice} = 5$, $n_{slices} = 20$, $n_{astrocytes} = 1,142$; OTR-positive: $n_{mice} = 5$, $n_{slice} = 20$, $n_{astrocytes} = 212$). All data are expressed as mean ± s.e.m., except in violin plots where the hatched line represents the median and the dot lines are the first and third quartiles. $^{***}P < 0.001$, $^{**}P < 0.01$, two-sided unpaired Student's t-test; $^{###}P < 0.001$, two-way ANOVA followed by Tukey post hoc test. Statistics are presented in Supplementary Table 1.

activity through a connexin gap junction network. To decipher the underlying mechanism, we first blocked purinergic receptors using pyridoxalphosphate-6-azophenyl-2',4'-disulfonic acid (PPADS)

and found that this blocker did not significantly affect the average proportion of astrocytes activated by TGOT (Fig. 3b) nor the properties of these responses (Fig. 3b), a result replicated using a set
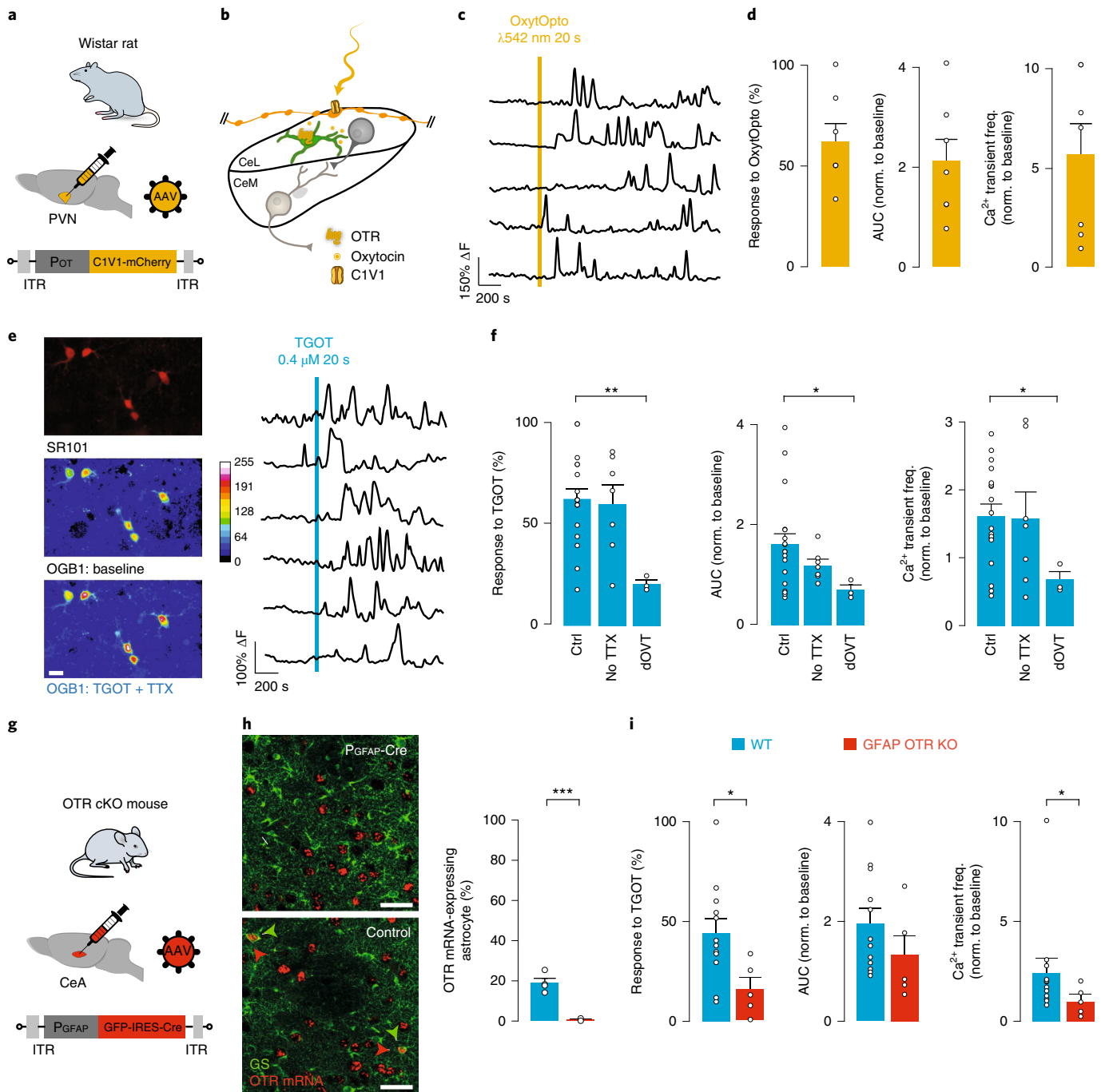
Fig. 2 | Astrocytic OTR activation evokes calcium transients in CeL astrocytes of rats and mice. a, Experimental strategy to express the ChR1/VChR1 chimera channel rhodopsin variant C1V1 in OTergic neurons (OxytOpto). **b**, Experimental scheme of the horizontal CeA slice preparation used, showing C1V1-expressing OT axons (yellow) arising from the PVN and projecting to the CeL. **c**, Typical traces of relative changes in intracellular calcium in astrocytes (ΔF) induced by the activation of C1V1 in OT axons located in the CeL through λ542-nm light pulses (10-ms width, 30 Hz, duration 20 s). **d**, Proportion of responding astrocytes (left), AUC of ΔF traces (middle), and Ca^{2+} transient frequency (right) normalized to baseline values after C1V1 activation in CeL OT axons, n_{slice} (n_s) = 7, $n_{astrocytes}$ (n_a) = 36. **e**, Left: images of CeL astrocytes identified through SR101 (red, top) and corresponding pseudocolor images of OGB1 fluorescence during baseline and after drug application (middle, bottom, stacks of 50 images over 25 s of recording; $n = 18$). Scale bar, 10 μm. Right: typical ΔF traces after TGOT + TTX (Ctrl) application. **f**, Proportion of responding astrocytes (left), AUC of ΔF traces (middle), and Ca^{2+} transient frequency (right), normalized to baseline values after application of TGOT (0.4 μM) with TTX (1 μM) (Ctrl, $n_s = 18$, $n_a = 136$), without TTX (No TTX, $n_s = 7$, $n_a = 43$) and with an OTR antagonist (dOVT, 1 μM; $n_s = 3$, $n_a = 24$). Data are expressed as means across slices plus s.e.m. **g**, Experimental strategy for the specific deletion of OTRs in mice CeL astrocytes. **h**, Left: example pictures of OTR mRNA (red) and GS (green) labeling in mice injected with PGFAP-GFP-IRES-Cre (top) or PGFAP-GFP rAAV vector (bottom); right: proportion of CeL astrocytes (GS-positive cells) also positive for OTR mRNA (left, blue, PGFAP-GFP: $n_{astrocytes} = 897$, $n_{mice} = 4$; right, red, PGFAP-GFP-IRES-Cre: $n_{astrocytes} = 940$, $n_{mice} = 4$). Scale bar, 50 μm. **i**, Proportion of responding astrocytes (left), AUC of ΔF traces (middle), and Ca^{2+} transient frequency (right), normalized to baseline values after application of TGOT + TTX in control (blue, $n_s = 12$, $n_a = 237$) or GFAP OTR KO mice (red, $n_s = 5$, $n_a = 47$; red) acute brain slices. Calcium imaging data are expressed as means across slices plus s.e.m., and white circles indicate averages across astrocytes per slice. *$P < 0.05$, **$P < 0.01$, ***$P < 0.001$, two-sided unpaired t-test or Mann–Whitney U test. Statistics are presented in Supplementary Table 2. ITR, inverted terminal repeat; WT, wild type.
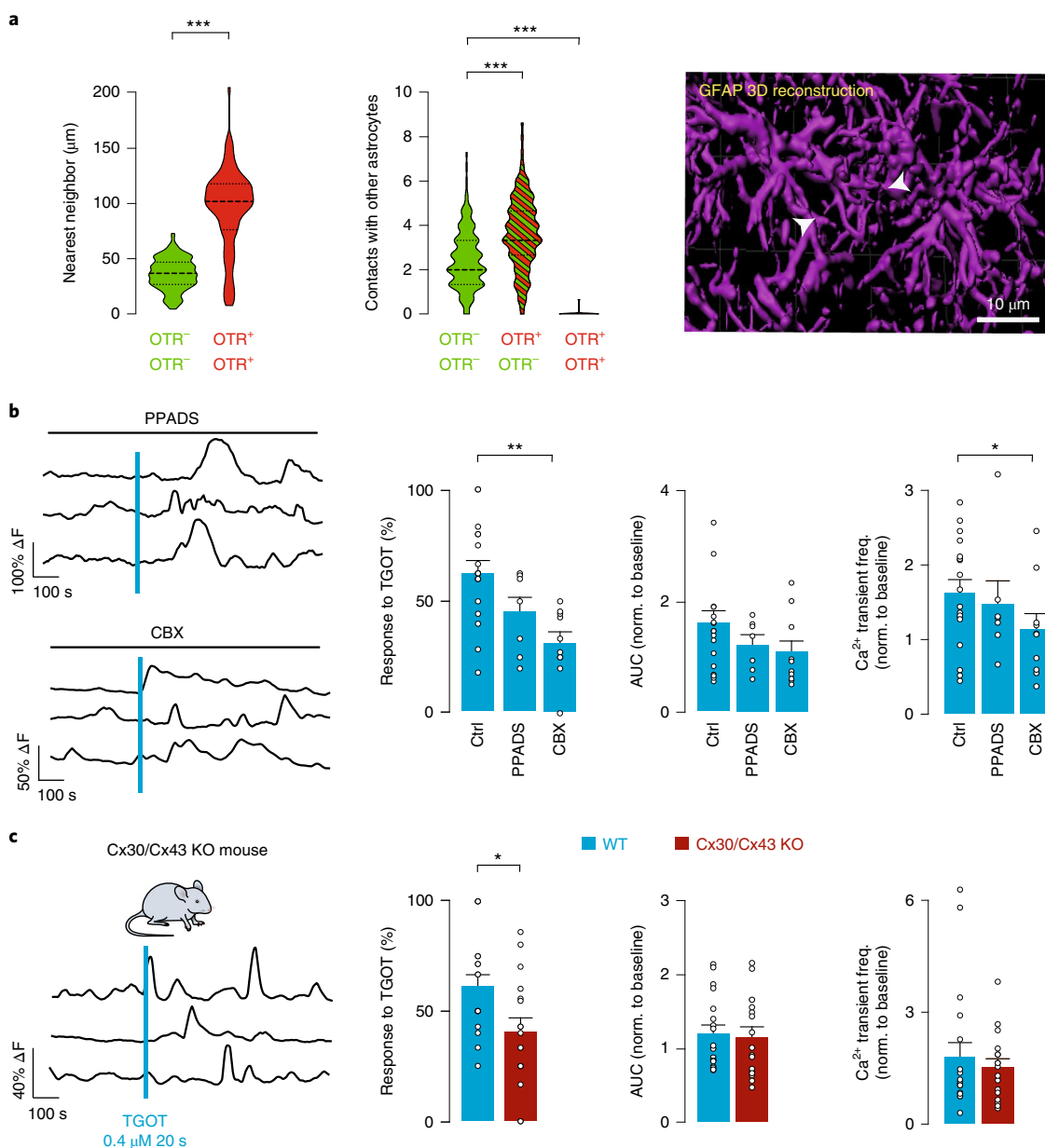
Fig. 3 | OTR-expressing CeL astrocytes are positioned to recruit a CeL astrocyte network through gap junction. a, Left: the distance between two OTR⁺ astrocytes is larger than the distance between two OTR⁻ astrocytes. Right: OTR⁺ astrocytes predominantly form contacts with OTR⁻ astrocytes ($n_{astrocytes}$ = 1,354; OTR⁺ $n_{astrocytes}$ = 212; n_{rats} = 4). Contacts are defined by a proximity of less than 1 μm between GFAP-positive fibers/endfeet from two different astrocytes. **b**, Left: typical ΔF traces after TGOT + TTX application in the presence of CBX (100 μM, top) or PPADS (50 μM, bottom). Right: proportion of responding astrocytes, AUC of ΔF traces and Ca²⁺ transient frequency normalized to baseline values after application of TGOT + TTX (0.4 μM) in the presence of CBX (n_s = 9, n_a = 75) or PPADS (n_s = 7, n_a = 53). **c**, Left: typical ΔF traces after TGOT + TTX application in Cx30/Cx43 KO mice brain slices. Right: proportion of responding astrocytes, AUC of ΔF traces and Ca²⁺ transient frequency, normalized to baseline values after TGOT + TTX application in wild-type mice (n_s = 19, n_a = 78) and in Cx30/Cx43 KO mice acute brain slices (n_s = 17, n_a = 100). Calcium imaging data are expressed as means across slices plus s.e.m., and white circles indicate averages across astrocytes per slice. *P < 0.05, **P < 0.01, ***P < 0.001, two-sided unpaired t-test or Mann–Whitney U test. Statistics are presented in Supplementary Table 3. WT, wild type.

of purinergic receptor antagonists blocking most known puriner-gic receptors (Extended Data Fig. 3b,c). However, the incubation with the gap junction blocker carbenoxolone (CBX) significantly reduced the number of astrocytes responsive to TGOT + TTX application (Fig. 3b). Given that astrocyte gap junctions are primar-ily composed of connexins 30 and 43, we assessed astrocyte Ca²⁺ activity in CeL slices obtained from Cx30/Cx43 double-KO mice[19] and found that the number of astrocytes activated by TGOT was significantly reduced in these mice (Fig. 3c). These results indicate

that gap junctions play a role in the propagation of responses after OTR activation in the CeL astrocytes network, possibly from OTR⁺ to OTR⁻ astrocytes.

CeL astrocyte activity increases CeL neuron excitability. We next wanted to test if this direct astrocyte network response to OTR activation could be relevant to the known effect of OTR signaling on CeA neuronal networks[2,8,9]. To manipulate astro-cytic activity, we expressed the opsin C1V1 under the control of

the GFAP promoter using recombinant AAV (rAAV) injections (PGFAP-C1V1-mCherry, referred to as AstrOpto; Fig. 4a). After confirmation of vector expression in $62.5 \pm 3.1\%$ of CeL astrocytes, with a specificity reaching $98.8 \pm 0.7\%$ (Extended Data Fig. 4a), we evaluated the effect of C1V1 stimulation on astrocyte calcium activity (Fig. 4b). We observed responses in $60.8 \pm 9.0\%$ of astrocytes (Fig. 4c), a proportion similar to what we observed after OTR stimulation by TGOT + TTX (AstrOpto versus TGOT + TTX; $P = 0.8265$, unpaired two-sided t-test). The removal of extracellular calcium prevented the C1V1-driven astrocyte activity (Extended Data Fig. 4b). This indicates that influx of extracellular calcium through the plasma membrane is required to generate calcium transient activity in astrocytes after C1V1 activation (Extended Data Fig. 4b).

Next, we measured the effect of evoked astrocyte activity, using AstrOpto or direct OTR stimulation through TGOT application, on CeL neuron inputs. Optical stimulation of C1V1 in astrocytes increased the frequency of miniature excitatory post-synaptic currents (mEPSCs) in CeL neurons (Fig. 4d), and bath-applied TGOT had a similar effect (Fig. 4f). To block the increase in calcium transients evoked by TGOT, we infused BAPTA specifically in astrocytes and found that this was sufficient to block TGOT effect on CeL neuron mEPSCs (Fig. 4e,f). This indicates that OTR activation and the ensuing increase in calcium transients in astrocytes is driving up excitatory inputs to CeL neurons.

To identify the intercellular communication pathway involved in astrocyte–neuron communication after OTR activation of astrocytes, we studied whether NMDA receptor (NMDAR), a well-known neuronal receptor that can be activated by astrocytic gliotransmitter D-serine[20–22] and whose activation in the CeA relies on astrocytes[23], was involved. Thus, we applied an NMDAR antagonist (2R)-amino-5-phosphonovaleric acid (AP5) before TGOT application and found that it inhibited TGOT effect on mEPSC frequency (Fig. 4f). Notably, AP5 had no effect on astrocyte responses to TGOT (Extended Data Fig. 3d). Finally, we repeated the mEPSC measurements in control and GFAP OTR KO mice. TGOT application increased mEPSC frequency in control mice but not in GFAP OTR KO mice (Fig. 4g,h), confirming the role of astrocytic OTR in mediating the effects of OTR signaling on synaptic inputs in CeL neurons.

To investigate whether the increase in mEPSC frequency in CeL neurons after OTR activation was able to increase their firing frequency, we applied the same stimulation protocols as before and subsequently recorded spontaneous action potential (AP) firing (Fig. 5a,b). First, AstrOpto increased firing of CeL neurons, an effect that was blocked by previous infusion of BAPTA in the astroglial network, hence indicating that AstrOpto effect on neurons depends on astrocyte calcium signaling (Fig. 5c). Similarly, and in agreement with its effect on CeL neuron mEPSCs, TGOT also increased neuronal spiking activity (Fig. 5d), an effect that was abolished by BAPTA infusion in the astroglial network or pre-incubation of AP5 in the

recording bath and, crucially, in mice lacking OTR in astrocytes (Fig. 5d–f).

These results unequivocally demonstrate that OTR signaling in the CeL requires the activation of astrocytic OTR, astrocytic calcium activity and downstream NMDAR activation to increase excitability of CeL interneurons.

CeL astrocyte activity increases inhibitory inputs onto CeM projection neurons. Previous work showed that the activation of CeL OTRs leads to increased activity of GABAergic CeL neurons (replicated here (Fig. 5)), resulting in an increased frequency of $GABA_A$-mediated inhibitory post-synaptic currents (IPSCs) in CeM projection neurons[2,8,9]. In agreement with these findings, we found that optogenetic activation of CeL astrocytes (through AstrOpto) evoked an increase in IPSC frequency in rat CeM neurons (Fig. 6a–c). This effect was also dependent on CeL astrocytic calcium signaling, as BAPTA infusion in CeL astrocytes abolished it (Fig. 6c). Furthermore, the effect of AstrOpto on CeM IPSC frequency was suppressed by application of AP5 in agreement with AP5 effects on CeL neurons (Fig. 4f). An important element of NMDAR activation is the binding of a co-agonist on the glycine site. D-serine can bind the glycine site in the CeA[23] and is a known gliotransmitter whose levels are increased after astrocytic GPCR activation[21]. We incubated CeA slices in D-amino acid oxidase[23] (DAAO) before measuring IPSCs and found that it also suppressed effects of AstrOpto (Extended Data Fig. 5a). Altogether, these results indicate that the effect of AstrOpto on IPSCs in CeM neurons is dependent on the activation of NMDARs in CeL neurons. TGOT application produced a similar effect on CeM neurons, also dependent on CeL astrocytic calcium signaling (Fig. 6d) and on NMDARs (Fig. 6d and Extended Data Fig. 5b) but not on AMPA receptors (Extended Data Fig. 5b). Initial incubation with DAAO similarly blocked the effect of TGOT on IPSC frequency (Extended Data Fig. 5c). Crucially, D-serine supplementation in the DAAO-treated slices after the first, effectless TGOT application rescued the effect of a second TGOT application on IPSC frequency (Extended Data Fig. 5c–e). This confirms the involvement of neuronal NMDARs and their co-agonist D-serine in OTR-mediated modulation of the CeA neuronal network. Another known mode of astrocyte-to-neuron communication relies on purinergic signaling, notably in the CeM[15]. To test if purinergic signaling was also involved here, we pre-incubated slices with the purinergic receptor antagonists PPADS, CPT or SCH 58261 and found that they had no effects (Extended Data Fig. 5f). This confirms that the primary mode of astrocyte-to-neuron communication engaged after OTR signaling in CeA involves NMDARs, but not purinergic signaling in neurons, and is mediated by an increase in D-serine levels.

TGOT application also led to an increased IPSC frequency in CeM neurons in brain slices from control mice but not in slices

Fig. 4 | CeL astrocyte activity promotes excitatory transmission into CeL neurons. a, Experimental strategy for the specific expression of C1V1 in mice CeL astrocytes (AstrOpto). **b**, Experimental scheme of the horizontal CeA slice preparation used, showing a C1V1 expressing astrocytes and a patched CeL neuron, recorded in whole-cell voltage-clamp configuration with bath-applied TTX and bicuculline to isolate mEPSCs. **c**, Left: proportion of responding astrocytes, AUC of ΔF traces and Ca^{2+} transient frequency after AstrOpto activation ($n_s = 12$, $n_a = 49$); right: typical ΔF traces after AstrOpto activation. **d**, Frequency of mEPSCs in CeL neurons before (basal), during (AstrOpto) and after (Wash) AstrOpto activation (λ542 nm, 3 min long, 1-s width pulse at 0.5 Hz; $n = 17$). **e**, Example of an astrocyte in CeL patched with a BAPTA–biocytin-filled capillary (white arrow). Biocytin can be seen diffusing in neighboring astrocytes ($n = 3$). Scale bars, 400 μm (top) and 50 μm (bottom). **f**, Frequency of mEPSCs in CeL neurons before (basal), during (TGOT, 0.4 μM) and after (Wash) TGOT application (left, $n = 16$). This effect can be blocked by loading BAPTA in the CeL astrocyte network (middle, BAPTAstro, $n = 11$) and by prior incubation of an NMDAR antagonist (right, AP5, 50 μM, $n = 9$). **g**, Experimental strategy for the specific deletion of OTRs in mice CeL astrocytes. **h**, Frequency of mEPSCs in CeL neurons before (basal), during (TGOT, 0.4 μM) and after (Wash) TGOT application in acute brain slices from wild-type mice (left, blue, $n = 10$) and from GFAP OTR KO mice (right, red, $n = 8$). Calcium imaging data are expressed as means across slices plus s.e.m., and white circles indicate averages across astrocytes per slice. Patch-clamp data are expressed as average frequency plus s.e.m. across cells; linked white circles indicate individual cell values; example traces of the various conditions are displayed on the right. #$P < 0.05$, ###$P < 0.001$, one-way repeated-measures ANOVA and Holm–Sidak multiple comparisons or Friedman and Dunn multiple comparisons; *$P < 0.05$, **$P < 0.01$, Mann–Whitney U test. Statistics are presented in Supplementary Table 4. ITR, inverted terminal repeat; WT, wild type.

from GFAP OTR KO mice (Fig. 6e,f). These ex vivo results indicate that direct, OTR-mediated CeL astrocyte activation leads to an NMDAR-dependent increase in CeL neuron excitability, which further increases inhibitory inputs into CeM projection neurons.

Our data so far demonstrate that, when OTR signaling is engaged in astrocytes, these cells increase the excitability of CeL neurons, directly leading to an increase in inhibitory inputs into CeM

projection neurons. Altogether, these results demonstrate that the effect of OT on neuronal activity is abolished when astrocyte function is compromised, establishing, for the first time, that OT signaling in CeA circuitry is locally transduced by astrocytes.

OTR signaling effects on CeA behavioral correlates rely on astrocytes. The CeA is a key nucleus for the processing of emotional
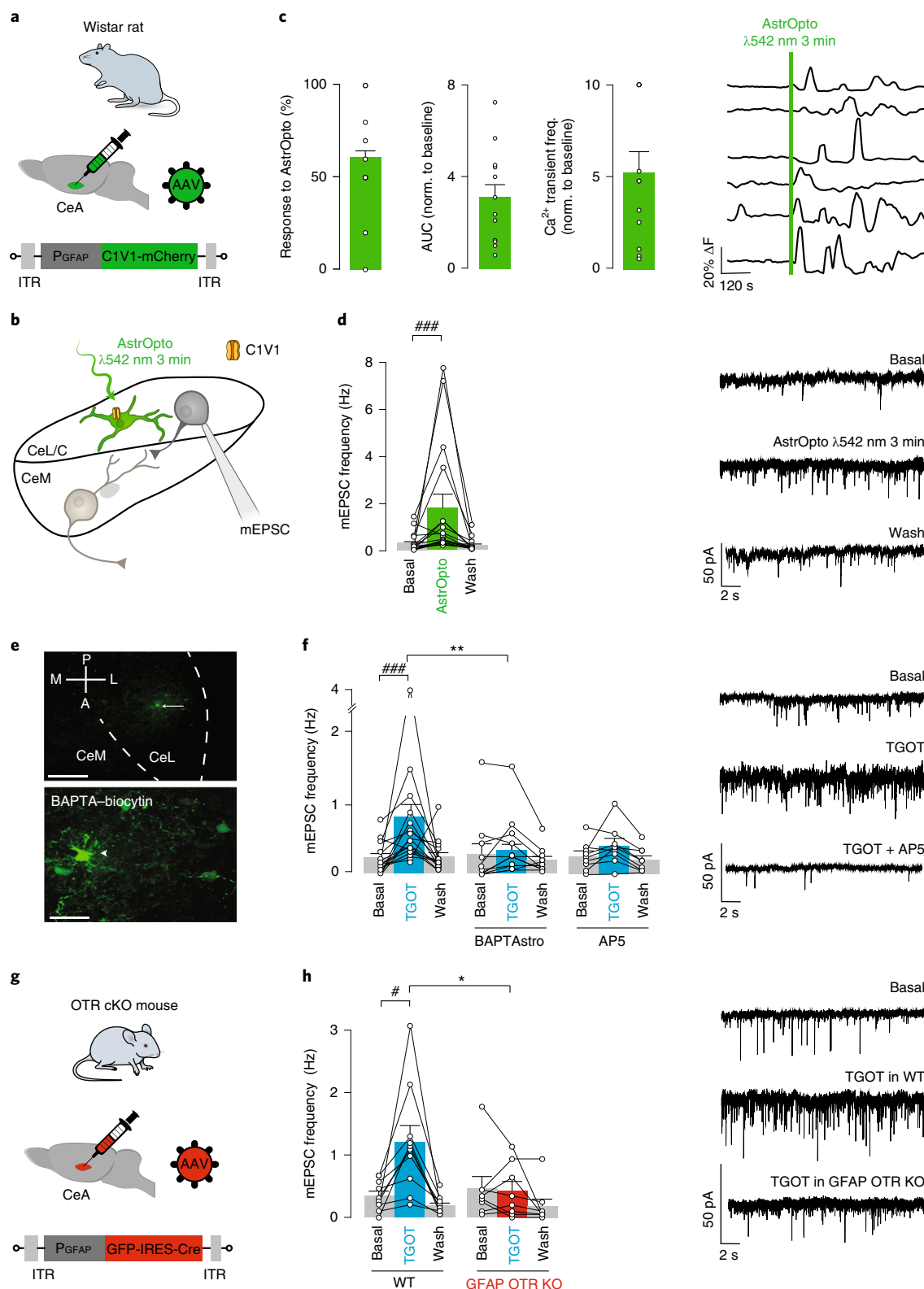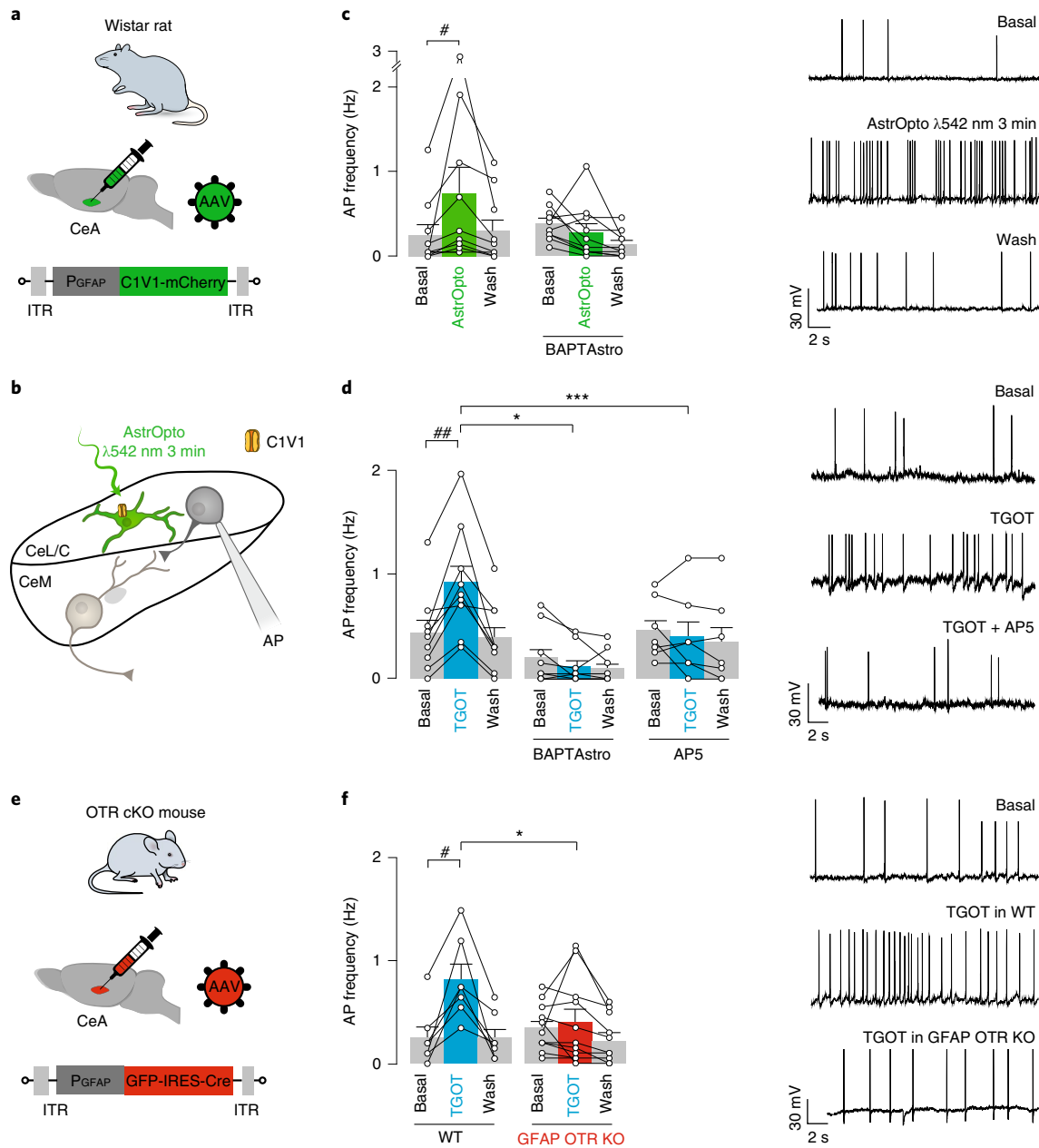
Fig. 5 | CeL astrocyte activity promotes CeL neuron firing. a, Experimental strategy for the specific expression of C1V1 in mice CeL astrocytes (AstrOpto). **b**, Experimental scheme of the horizontal CeA slice preparation used, showing a C1V1 expressing astrocytes and a patched CeL neuron, recorded in whole-cell current-clamp configuration to record APs. **c**, Frequency of APs in CeL neurons before (basal), during (AstrOpto) and after (Wash) AstrOpto activation (λ542 nm, 3 min long, 1-s width pulse at 0.5 Hz) in control condition (left, $n = 10$) or after BAPTA loading in the CeL astrocyte network (right, BAPTAstro, $n = 12$). **d**, Frequency of APs in CeL neurons before (basal), during (TGOT, 0.4 µM) and after (Wash) TGOT application (left, $n = 9$). This effect can be blocked by loading BAPTA in the CeL astrocyte network (middle, BAPTAstro, $n = 9$) and by prior incubation of the NMDAR antagonist AP5 (right, AP5, 50 µM, $n = 7$). **e**, Experimental strategy for the specific deletion of OTRs in mice CeL astrocytes (GFAP OTR KO). **f**, Frequency of APs in CeL neurons before (basal), during (TGOT, 0.4 µM) and after (Wash) TGOT application in acute brain slices from wild-type mice (left, blue, $n = 7$) and GFAP OTR KO mice (right, red, $n = 11$). Example traces of the various conditions are displayed on the right. Patch-clamp data are expressed as average frequency plus s.e.m. across cells; linked white circles indicate individual cell values. $^{\#}P < 0.05$, $^{\#\#}P < 0.01$, one-way repeated-measures ANOVA and Holm–Sidak multiple comparisons or Friedman and Dunn multiple comparisons; $^{*}P < 0.05$, $^{***}P < 0.001$, two-sided unpaired t-test or Mann–Whitney U test. Statistics are presented in Supplementary Table 5. ITR, inverted terminal repeat; WT, wild type.

information and, notably, plays an important role in pain-associated disorders[11], in which OT is a crucial regulator[14]. We, therefore, sought to test the involvement of astrocyte-mediated OTR signaling in modulating mechanical pain hypersensitivity, levels of anxiety and reinforcement behavior in rats and mice in conditions of

neuropathic pain after a spared nerve injury (SNI) surgery[24] (Extended Data Fig. 6a).

We found that SNI animals displayed a decreased mechanical threshold, but bilateral micro-injections of TGOT in the CeA had no clear effect on it, with a mild anti-nociceptive effect only in rats
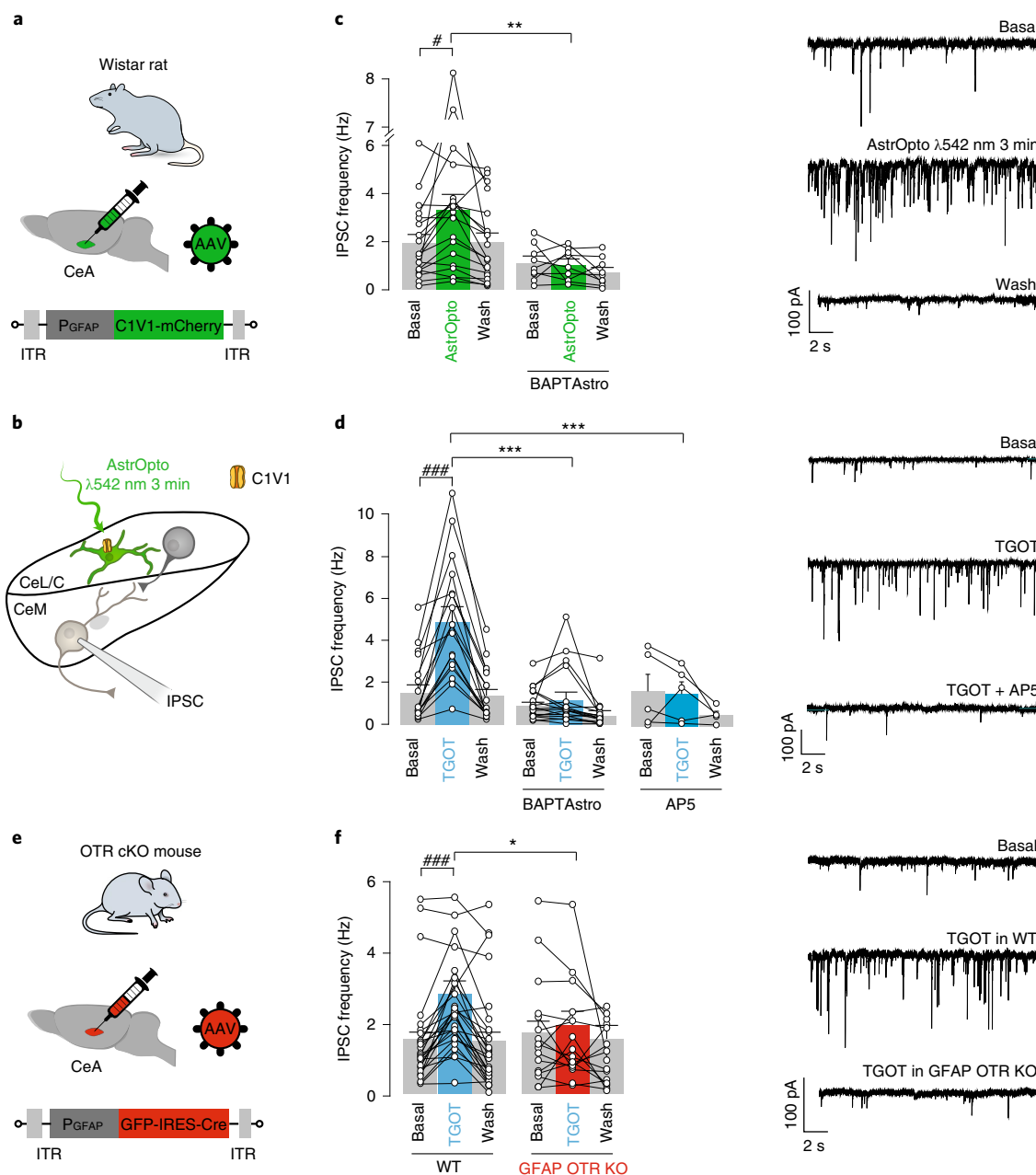
Fig. 6 | Astrocyte-driven CeL neuron activity modifies amygdala output. a, Experimental strategy for the specific expression of C1V1 in mice CeL astrocytes (AstrOpto). **b**, Experimental scheme of the horizontal CeA slice preparation used, showing a C1V1 expressing astrocytes and a patched CeM neuron, recorded in whole-cell voltage-clamp configuration to record IPSCs. **c**, Frequency of IPSCs in CeL neurons before (basal), during (AstrOpto) and after (Wash) AstrOpto activation (λ542 nm, 3 min long, 1-s width pulse at 0.5 Hz) in control condition (left, $n = 19$) or after BAPTA loading in the CeL astrocyte network (right, BAPTAstro, $n = 9$). **d**, Frequency of IPSCs in CeL neurons before (basal), during (TGOT, 0.4 μM) and after (Wash) TGOT application (left, $n = 17$). This effect can be blocked by loading BAPTA in the CeL astrocyte network (middle, BAPTAstro, $n = 17$) and by prior incubation of the NMDAR antagonist AP5 (right, AP5, 50 μM, $n = 5$). **e**, Experimental strategy for the specific deletion of OTRs in mice CeL astrocytes (GFAP OTR KO). **f**, Frequency of APs in CeL neurons before (basal), during (TGOT, 0.4 μM) and after (Wash) TGOT application in acute brain slices from wild-type mice (left, blue, $n = 27$) and GFAP OTR KO mice (right, red, $n = 15$). Example traces of the various conditions are displayed on the right. Patch-clamp data are expressed as averaged frequency plus s.e.m. across cells; linked white circles indicate individual cell values. $^{\#}P < 0.05$, $^{\#\#\#}P < 0.001$, one-way repeated-measures ANOVA and Holm–Sidak multiple comparisons or Friedman and Dunn multiple comparisons; $^{*}P < 0.05$, $^{**}P < 0.01$, $^{***}P < 0.001$, Mann–Whitney U test. Statistics are presented in Supplementary Table 6. ITR, inverted terminal repeat; WT, wild type.

(Fig. 7b,f). Moreover, neither the bilateral optogenetic stimulation of rat CeL astrocytes (AstrOpto; Fig. 7a) nor the removal of OTR from mice astrocytes (Fig. 7e) had a noticeable effect on mechanical threshold (Fig. 7b,f and Extended Data Fig. 7b,f). Given that there is a proven link between chronic pain etiology and synaptic changes

in the CeA[25], we tested whether the effect of TGOT on astrocyte calcium signaling and CeM neuron IPSC frequency was altered in SNI rats, but we did not find any differences compared to sham-operated animals (Extended Data Fig. 6b–d). These last results indicate that the absence of powerful OTR-induced anti-nociceptive action in

neuropathic animals is not the consequence of an altered OTR signaling in the CeA, at least at the level of the circuit studied here.

To assess the effect of the neuropathic pain state on anxiety behavior, we used the elevated plus maze and found that SNI animals spent significantly more time in the closed arm compared to sham-operated ones, indicating that the SNI procedure induced a state of elevated anxiety (Fig. 7c,g), as expected[26]. When TGOT was injected in the CeA, time spent in the closed arm was significantly reduced to levels similar to those observed in sham animals, indicating an anxiolytic effect of OTR signaling in both rats and mice (Fig. 7c,g), in line with an earlier report[27]. Crucially, AstrOpto in rats had a similar effect (Fig. 7c), whereas the deletion of OTR from CeL astrocytes in mice abolished the anxiolytic effects of TGOT (Fig. 7g). Interestingly, sham mice lacking OTR in CeL astrocytes displayed an anxiety-like behavior (Fig. 7g). Together, these data indicate that astrocyte-mediated OT signaling in the CeA is central to the regulation of anxiety-like behavior in pain-free conditions and to the beneficial effect of OT signaling on neuropathic pain-induced increased anxiety[28]. Furthermore, in a conditioned place preference (CPP) assay, both SNI and sham animals exhibited a preference for the chamber paired with intra-CeA TGOT infusion, in line with an earlier report[27]. Strikingly, this effect was lost by the deletion of OTR in astrocytes but recapitulated by bilateral optogenetic stimulation of CeL astrocytes (Fig. 7d,h). These experiments highlight the central role of astrocyte-mediated OT signaling in the regulation of emotional states under normal and chronic pain conditions. Notably, neither the treatments nor the SNI procedure significantly affected the motor activity of animals in elevated plus maze or CPP tests (Extended Data Fig. 7).

Collectively, our findings demonstrate, from the local circuit to the behavioral levels, that OTR signaling through CeL astrocytes is a novel and important mechanism involved in emotional state regulation, under both normal and chronic pain conditions (Fig. 7i).

Discussion

We demonstrate here that OTR signaling through astrocytes is crucial for the oxytocin-ergic modulation of the local CeA microcircuit and its behavioral correlates. We further propose that this effect relies on a morphologically defined subpopulation of OTR[+] astrocytes (Figs. 1 and 2) that convey their activation by OT to other astrocytes through gap junctional communication (Fig. 3), leading to an increase in activity in the overall CeL astrocyte network (Figs. 2 and 3). In turn, astrocytes increase the excitability of CeL interneurons by gating the activation of NMDARs (Figs. 4 and 5), likely through the release of D-serine, leading to an increase in GABAergic

inhibitory inputs into CeM neurons (Fig. 6). At the behavioral level, this OTR-mediated modulation of CeA astro-neuronal network promotes a positive emotional state, measured as clear anxiolytic and positive reinforcement effects (Fig. 7).

Mechanistically, our results reinforce previous demonstrations of a role of astrocytes in transforming neuromodulator signaling into a change on the gain of neuronal circuits, notably by (co)activating neuronal NMDAR[20–22]. Despite the high proportion of OTR^{+} neurons (up to 70%) compared to the limited number of OTR[+] astrocytes (~18%) in the CeL, the activation of OTRs in astrocytes was required to gate CeL neuron responses to OTR activation by allowing a sustained (co)activation of NMDARs. Other mechanisms are probably at play: OTR activation in CeL neurons might inhibit K^{+} leak current, as has been shown in olfactory neuronal cells[29] and in spinal cord[30]. These mechanisms might act in synergy to induce an elevation in firing rates of CeL neurons by increasing the gain of excitatory inputs in these cells. Furthermore, similar mechanisms of astrocyte-to-neuron communication through neuronal NMDAR (co)activation have been proposed by other studies to favor a synchronous increase in excitability across an ensemble of neurons[31,32]. This would allow a synchronized and long-lasting switch in the gain of the CeA neuronal circuits, thereby amplifying the effect of OT on CeA outputs in both the spatial and temporal domains. In light of the predominantly non-synaptic mode of OT release from axons en passant, which could lead to CeL-restricted micro-volume transmission of the neuropeptide[3], it seems, then, plausible that astrocytes are required to relay and amplify OT signaling to CeL neurons. Another mechanism that was repeatedly found to be involved in neuromodulator signaling through astrocytes is the activation of purinergic signaling in neurons[33,34]. However, in the case of OT signaling within the CeA, purinergic signaling was not involved (Extended Data Fig. 5). It would, then, be interesting to test if astrocytes are important to OT signaling in other brain regions, and, if they are, if the same mechanisms of astrocyte-to-neuron communication are at stake.

We found that CeA astrocytes can be divided into two defined populations: OTR[+] and OTR[−] astrocytes. OTR[+] astrocytes are morphologically more complex and have more close contacts with neighboring OTR[−] astrocytes while being quite distant from their OTR[+] counterparts, with which they have almost no contacts (Figs. 1 and 2). Thus, we hypothesize that these morphological peculiarities allow the propagation of OTR-evoked calcium transients (Fig. 2) to a much larger number of OTR[−] astrocytes through, at least partially, gap junctions (Fig. 3b,c). Therefore, only a few strategically positioned OTR[+] astrocytes are sufficient to result in a network-wide effect of OT release in the CeL, despite the relatively moderate

Fig. 7 | CeL astrocytes modulate CeA behavioral correlates of comfort and are required for their OTR-mediated modulation. a,e, Experimental strategy for the specific expression of C1V1 in mice CeL astrocytes (**a**, AstrOpto) or the specific deletion of OTRs in mice CeL astrocytes (**e**, GFAP OTR KO). The treatments applied are color coded, as the legend key indicates. Control indicates a vehicle injection. **b,f,** Four weeks after the SNI surgery, mechanical pain threshold was assessed on the neuropathic paw before (Ctrl) and at different time points after either TGOT injection or C1V1 activation of CeL astrocytes (gray arrow) for sham (top) and SNI (bottom, gray box) animals. Rats (n): sham control n=12, TGOT n=11, C1V1 n=6, SNI control n=12, TGOT n=10, C1V1 n=10. Mice (n): sham WT n=6, OTR cKO n=8; SNI WT n=5, OTR cKO n=13. **c,g,** Anxiety levels were assessed through measurements of the time spent in the closed arms of the elevated plus maze after TGOT injections or C1V1 light-driven activation of CeL astrocytes for sham (top) and SNI (bottom, gray box). Rats (n): sham Veh n=10, TGOT n=8, C1V1 n=9, SNI Veh n=20, TGOT n=9, C1V1 n=7. Mice (n): sham WT Veh n=7, WT TGOT n=6, sham OTR cKO Veh n=5, OTR cKO TGOT n=7, SNI WT Veh n=7, WT TGOT n=8, SNI OTR cKO Veh n=5, OTR cKO TGOT n=7. **d,h,** CPP was assessed through measurements of the Δ time spent in the paired chamber before and after pairing. Pairing was realized through TGOT injections or C1V1 light-driven activation of CeL astrocytes for sham (top) and SNI (bottom, gray box). Rats (n): sham Veh n=13, TGOT n=6, C1V1 n=5, SNI Veh n=10, TGOT n=8, C1V1 n=8. Mice (n): sham WT Veh n=5, WT TGOT n=8, sham OTR cKO Veh n=5, OTR cKO TGOT n=4, SNI WT Veh n=5, WT TGOT n=5, SNI OTR cKO Veh n=4, OTR cKO TGOT n=6. Data are expressed as averages across rats or mice plus s.e.m. (details and statistics in Supplementary Table 7). #P < 0.001, ##P < 0.01, Wilcoxon signed-rank test; *P < 0.05, **P < 0.01, ***P < 0.001, ANOVA or mixed-design ANOVA followed by post hoc Bonferroni test. Statistics are presented in Supplementary Table 7. **i,** OT-dependent cellular interactions in the CeA. We hypothesize that OT released from axons of PVN neurons within the CeL activates OTR[+] astrocytes (red), which, consequently, spread their activation to neighboring OTR[−] astrocytes (green) through, at least partly, gap junctions. Subsequently, the CeL astrocytes release D-serine, which gates the activation of NMDAR on CeL interneurons, ultimately increasing their firing rate. This, in turn, inhibits CeM output projection neurons, resulting in anxiolysis and the promotion of a positive emotional state. ITR, inverted terminal repeat; WT, wild type.

number of OT fibers found in this nucleus[2]. By describing a new population of astrocytes, our work adds to the recent advances in describing molecular, morphological and functional heterogeneity in astrocyte populations[35,36] and opens up new perspectives into understanding how astrocyte subpopulations are functionally organized and communicate inside CNS circuits.
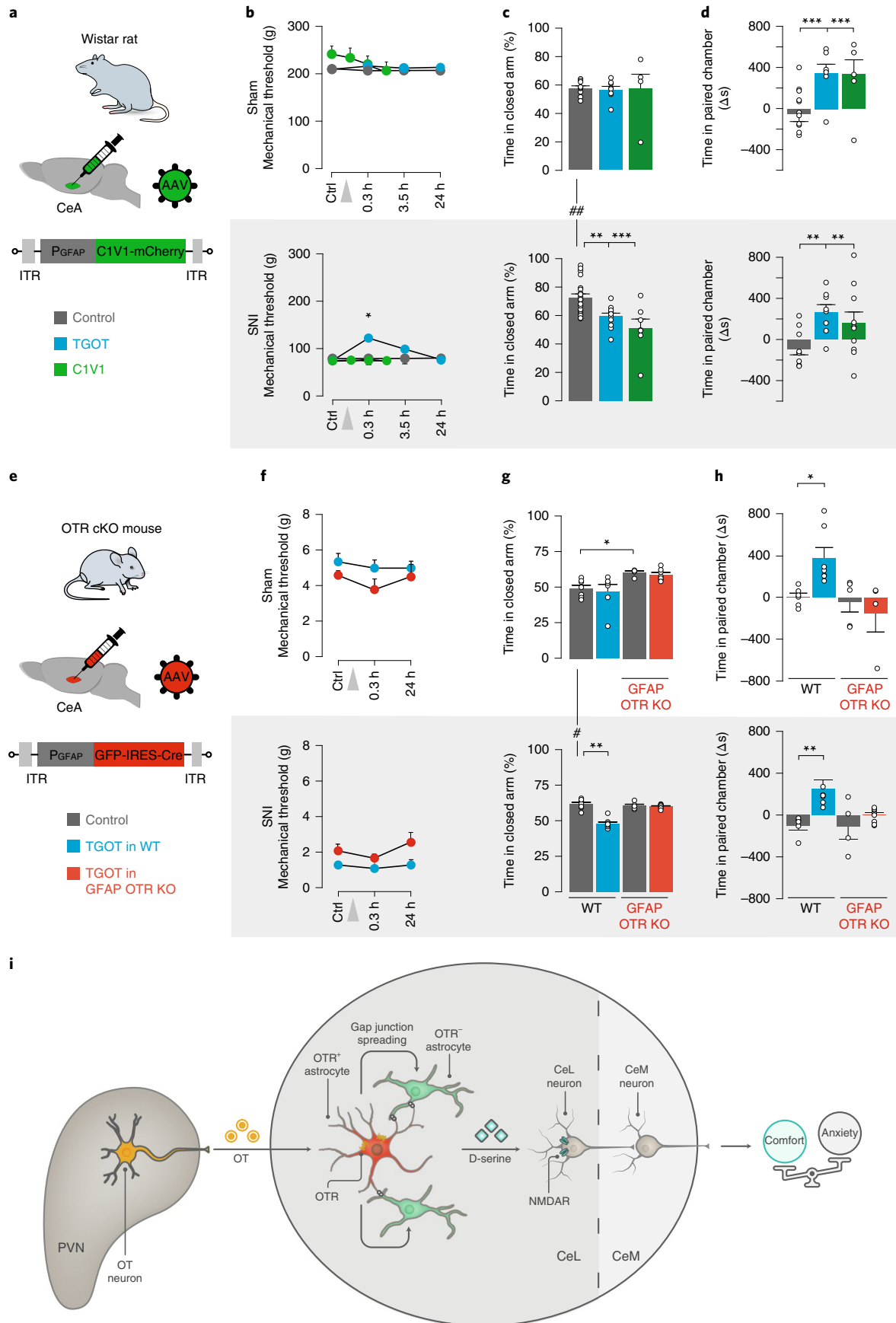
OT and its effects on brain circuits, and ultimately behavior, are under intense scrutiny, from fundamental research in animal models to behavioral and physiological studies in humans[37,38]. Among other roles, OT is considered a powerful anxiolytic peptide through its action in the human amygdala[39]. However, so far, it has been widely assumed that OT acts directly on neurons, despite the controversies regarding the cellular substrates of blood oxygenation level-dependent functional magnetic resonance imaging signals often used in human studies, with some results arguing for a major contribution of astrocyte activity to these signals[40,41]. Furthermore, many studies demonstrated that astrocytes or their invertebrate counterparts are key, if not primary, targets of neuromodulators[20–22,33,34,42] and that astrocytes might be the causal elements behind shifts in brain state transitions[42–44], a function usually attributed mainly to neuromodulator direct action on neurons. Neuromodulators are the targets of many, already available, treatments of psychiatric diseases using either small-molecule drugs or electrical stimulation protocols, such as deep brain[45] or transcranial stimulations[46], for which astrocytes also seem particularly involved[45,46]. Taken together, this indicates a need for a more global and systematic consideration of astrocyte roles in brain circuits, notably regarding the effect of neuromodulators and, in particular, OT. We think that this is especially relevant for the development of better therapeutics in the field of chronic pain, which imposes a massive burden to society, affecting ~20% of the global population[47].

Indeed, considering that general anxiety and depression are frequent comorbidities of chronic pain[48], our finding that the activation of OT signaling in CeL astrocytes promotes a form of emotional comfort by alleviating anxious behavior and has positive reinforcement properties is promising: it demonstrates that activation of a particular astrocyte-mediated OTR pathway affects one of the most important aspects of the chronic pain sphere—the emotional one. This further highlights astrocytes as important cellular substrates of emotional regulation, in line with other studies (see ref. [49] and the references therein). In this context, targeting the OT system and/or astrocytes specifically, in the amygdala or other CNS regions, might lead to the development of new therapeutic avenues to improve patient well-being.

Online content

Any methods, additional references, Nature Research reporting summaries, source data, extended data, supplementary information, acknowledgements, peer review information; details of author contributions and competing interests; and statements of data and code availability are available at https://doi.org/10.1038/s41593-021-00800-0.

References

1. Lee, H.-J., Macbeth, A. H., Pagani, J. H. & Young, W. S. Oxytocin: the great facilitator of life. *Prog. Neurobiol.* **88**, 127–151 (2009).
2. Knobloch, H. S. et al. Evoked axonal oxytocin release in the central amygdala attenuates fear response. *Neuron* **73**, 553–566 (2012).
3. Chini, B., Verhage, M. & Grinevich, V. The action radius of oxytocin release in the mammalian CNS: from single vesicles to behavior. *Trends Pharmacol. Sci.* **38**, 982–991 (2017).
4. Mitre, M. et al. A distributed network for social cognition enriched for oxytocin receptors. *J. Neurosci.* **36**, 2517–2535 (2016).
5. Yoshida, M. et al. Evidence that oxytocin exerts anxiolytic effects via oxytocin receptor expressed in serotonergic neurons in mice. *J. Neurosci.* **29**, 2259–2271 (2009).
6. Theodosis, D. T. Oxytocin-secreting neurons: a physiological model of morphological neuronal and glial plasticity in the adult hypothalamus. *Front. Neuroendocrinol.* **23**, 101–135 (2002).
7. Pacholko, A. G., Wotton, C. A. & Bekar, L. K. Astrocytes—the ultimate effectors of long-range neuromodulatory networks? *Front. Cell. Neurosci.* **14**, 1–12 (2020).
8. Huber, D., Veinante, P. & Stoop, R. Vasopressin and oxytocin excite distinct neuronal populations in the central amygdala. *Science* **308**, 245–248 (2005).
9. Viviani, D. et al. Oxytocin selectively gates fear responses through distinct outputs from the central amygdala. *Science* **333**, 104–107 (2011).
10. Han, R. T. et al. Long-term isolation elicits depression and anxiety-related behaviors by reducing oxytocin-induced GABAergic transmission in central amygdala. *Front. Mol. Neurosci.* **11**, 246 (2018).
11. Neugebauer, V., Li, W., Bird, G. C. & Han, J. S. The amygdala and persistent pain. *Neuroscientist* **10**, 221–234 (2004).
12. Tye, K. M. et al. Amygdala circuitry mediating reversible and bidirectional control of anxiety. *Nature* **471**, 358–362 (2011).
13. Ji, R.-R., Donnelly, C. R. & Nedergaard, M. Astrocytes in chronic pain and itch. *Nat. Rev. Neurosci.* **20**, 667–685 (2019).
14. Poisbeau, P., Grinevich, V. & Charlet, A. Oxytocin signaling in pain: cellular, circuit, system, and behavioral levels. *Curr. Top. Behav. Neurosci.* **35**, 193–211 (2018).
15. Martin-Fernandez, M. et al. Synapse-specific astrocyte gating of amygdala-related behavior. *Nat. Neurosci.* **20**, 1540–1548 (2017).
16. Althammer, F. et al. Three-dimensional morphometric analysis reveals time-dependent structural changes in microglia and astrocytes in the central amygdala and hypothalamic paraventricular nucleus of heart failure rats. *J. Neuroinflammation* **17**, 221 (2020).
17. Yizhar, O. et al. Neocortical excitation/inhibition balance in information processing and social dysfunction. *Nature* **477**, 171–178 (2011).
18. Lee, H. J., Caldwell, H. K., Macbeth, A. H., Tolu, S. G. & Young, W. S. A conditional knockout mouse line of the oxytocin receptor. *Endocrinology* **149**, 3256–3263 (2008).
19. Wallraff, A. et al. The impact of astrocytic gap junctional coupling on potassium buffering in the hippocampus. *J. Neurosci.* **26**, 5438–5447 (2006).
20. Papouin, T., Dunphy, J. M., Tolman, M., Dineley, K. T. & Haydon, P. G. Septal cholinergic neuromodulation tunes the astrocyte-dependent gating of hippocampal NMDA receptors to wakefulness. *Neuron* **94**, 840–854 (2017).
21. Robin, L. M. et al. Astroglial CB1 receptors determine synaptic D-serine availability to enable recognition memory. *Neuron* **98**, 935–944 (2018).
22. Corkrum, M., Rothwell, P. E., Thomas, M. J., Kofuji, P. & Araque, A. Opioid-mediated astrocyte-neuron signaling in the nucleus accumbens. *Cells* **8**, 586 (2019).
23. Li, Y. et al. Identity of endogenous NMDAR glycine site agonist in amygdala is determined by synaptic activity level. *Nat. Commun.* **4**, 1760 (2013).
24. Decosterd, I. & Woolf, C. J. Spared nerve injury: an animal model of persistent peripheral neuropathic pain. *Pain* **87**, 149–158 (2000).
25. Thompson, J. M. & Neugebauer, V. Amygdala plasticity and pain. *Pain Res. Manag.* **2017**, 8296501 (2017).
26. Sieberg, C. B. et al. Neuropathic pain drives anxiety behavior in mice, results consistent with anxiety levels in diabetic neuropathy patients. *Pain Rep.* **3**, e651 (2018).
27. László, K. et al. Positive reinforcing effect of oxytocin microinjection in the rat central nucleus of amygdala. *Behav. Brain Res.* **296**, 279–285 (2016).
28. Goodin, B. R., Ness, T. J. & Robbins, M. T. Oxytocin - a multifunctional analgesic for chronic deep tissue pain. *Curr. Pharm. Des.* **21**, 906–913 (2015).
29. Gravati, M. et al. Dual modulation of inward rectifier potassium currents in olfactory neuronal cells by promiscuous G protein coupling of the oxytocin receptor. *J. Neurochem.* **114**, 1424–1435 (2010).
30. Breton, J.-D. et al. Oxytocin-induced antinociception in the spinal cord is mediated by a subpopulation of glutamatergic neurons in lamina I–II which amplify GABAergic inhibition. *Mol. Pain* **4**, 19 (2008).
31. Angulo, M. C., Kozlov, A. S., Charpak, S. & Audinat, E. Glutamate released from glial cells synchronizes neuronal activity in the hippocampus. *J. Neurosci.* **24**, 6920–6927 (2004).
32. Fellin, T. et al. Neuronal synchrony mediated by astrocytic glutamate through activation of extrasynaptic NMDA receptors. *Neuron* **43**, 729–743 (2004).
33. Corkrum, M. et al. Dopamine-evoked synaptic regulation in the nucleus accumbens requires astrocyte activity. *Neuron* **105**, 1036–1047.e5 (2020).
34. Ma, Z., Stork, T., Bergles, D. E. & Freeman, M. R. Neuromodulators signal through astrocytes to alter neural circuit activity and behaviour. *Nature* **539**, 428–432 (2016).
35. Pestana, F., Edwards-Faret, G., Belgard, T. G., Martirosyan, A. & Holt, M. G. No longer underappreciated: the emerging concept of astrocyte heterogeneity in neuroscience. *Brain Sci.* **10**, 1–21 (2020).
36. Khakh, B. S. & Deneen, B. The emerging nature of astrocyte diversity. *Annu. Rev. Neurosci.* **42**, 187–207 (2019).
37. Grinevich, V. & Neumann, I. D. Brain oxytocin: how puzzle stones from animal studies translate into psychiatry. *Mol. Psychiatry* **26**, 265–279 (2021).
38. Quintana, D. S. et al. Advances in the field of intranasal oxytocin research: lessons learned and future directions for clinical research. *Mol. Psychiatry* **26**, 80–91 (2021).

39. Kirsch, P. et al. Oxytocin modulates neural circuitry for social cognition and fear in humans. *J. Neurosci.* **25**, 11489–11493 (2005).

40. Takata, N. et al. Optogenetic astrocyte activation evokes BOLD fMRI response with oxygen consumption without neuronal activity modulation. *Glia* **66**, 2013–2023 (2018).

41. Figley, C. R. & Stroman, P. W. The role(s) of astrocytes and astrocyte activity in neurometabolism, neurovascular coupling, and the production of functional neuroimaging signals. *Eur. J. Neurosci.* **33**, 577–588 (2011).

42. Kastanenka, K. V. et al. A roadmap to integrate astrocytes into systems neuroscience. *Glia* **68**, 5–26 (2019).

43. Poskanzer, K. E. & Yuste, R. Astrocytes regulate cortical state switching in vivo. *Proc. Natl Acad. Sci. USA* **2016**, 1–10 (2016).

44. Kjaerby, C., Rasmussen, R., Andersen, M. & Nedergaard, M. Does global astrocytic calcium signaling participate in awake brain state transitions and neuronal circuit function? *Neurochem. Res.* **42**, 1810–1822 (2017).

45. Fenoy, A. J., Goetz, L., Chabardès, S. & Xia, Y. Deep brain stimulation: are astrocytes a key driver behind the scene? *CNS Neurosci. Ther.* **20**, 191–201 (2014).

46. Monai, H. & Hirase, H. Astrocytes as a target of transcranial direct current stimulation (tDCS) to treat depression. *Neurosci. Res.* **126**, 15–21 (2018).

47. Mills, S. E. E., Nicolson, K. P. & Smith, B. H. Chronic pain: a review of its epidemiology and associated factors in population-based studies. *Br. J. Anaesth.* **123**, e273–e283 (2019).

48. Woo, A. K. Depression and anxiety in pain. *Rev. Pain* **4**, 8–12 (2010).

49. Oliveira, J. F., Sardinha, V. M., Guerra-Gomes, S., Araque, A. & Sousa, N. Do stars govern our actions? Astrocyte involvement in rodent behavior. *Trends Neurosci.* **38**, 535–549 (2015).

Methods

Animals. Animals were housed under standard conditions with food and water available ad libitum and maintained on a 12-h light/dark cycle, and all experiments were conducted in accordance with European Union rules and approbation from the French Ministry of Research (01597.05). For ex vivo and in vivo experiments, male and female Wistar rats or C5BL/6 mice were used. Ex vivo experiments used animals between 18 and 25 d old, except in experiments where rAAVs were injected, in which case animals were between 2 and 6 months old at the time of sacrifice. In in vivo experiments, animals that were 2 months old at the time of the first surgery were used. In total, 398 rats and mice were used in this study.

Specific deletion of OTRs in CeL astrocytes. To specifically ablate OTRs in CeA astrocytes, transgenic cKO mice, in which *loxP* sites flank the OTR coding sequence[18], received bilateral injections (280 nl) of rAAV-GFAP-GFP-IRES-Cre. After 4 weeks of expression of the viral proteins, mice were intracardially perfused with 1× PBS and 4% paraformaldehyde (PFA). Brain sections were used for FISH (OTR mRNA) and immunohistochemistry (GS) to verify the validity of the approach. Representative images and quantifications are provided in Fig. 2h and Extended Data Fig. 2g,h.

Specific deletion of Cx30 and Cx43 in astrocytes. To specifically impair gap junction coupling, we used Cx30$^{-/-}$Cx43$^{fl/fl}$:hGFAP-Cre mice (Cx30/Cx43 double KO), which were previously characterized[19,50,51], with conditional deletion of Cx43 in astrocytes[52] and additional deletion of Cx30 (ref. [53]).

Cloning and production of rAAV vectors. The generation of rAAVs allowing for the specific expression of the protein of interest in OT cells was described in our previous work[2]. Briefly, the conserved promoter region of 2.6 kb was chosen using the software BLAT from UCSC (http://genome.ucsc.edu/cgi-bin/hgBlat), was amplified from BAC clone RP24-388N9 (RPCI-24 Mouse, BACPAC Resources, CHORI) and was subcloned into an rAAV2 backbone carrying an ampicillin resistance.

To construct the OTp-C1V1(t/t)-TS-mCherry AAV vector, we used previously cloned OTp-DIO-GFP-WRE plasmid[2] equipped with the characterized 2.6-kb OT promoter[2]. In this plasmid, the DIO-GFP sequence was replaced by C1V1 (t/t)-TS-mCherry from the rAAV CaMKIIa-C1V1(t/t)-TS-mCherry (Addgene, plasmid no. 35500).

To generate GFAP-C1V1(t/t)-TS-mCherry AAV vector, we replaced the CamKIIa promoter from the rAAV CaMKIIa-C1V1(t/t)-TS-mCherry by the Gfa promoter from the pZac2.1 gfaABC1D-tdTomato (Addgene, plasmid no. 44332). The cell type specificity of the rAAV carrying the Gfa promoter was confirmed[54]. In analogy, the generation of the GFAP-GFP-IRES-Cre vector was achieved using pZac2.1 gfaABC1D-tdTomato (Addgene, plasmid no. 44332). First, the promoter was cloned into an rAAV2 backbone, and sticky ends were blunted with EcoR1 and Basrg1. Next, pAAV-CamKIIa-C1V1(t/t)-TS-mCherry was blunted using BamHI and BsrGI. Finally, the pBS-ires cre construct was used, and IRES-Cre was inserted into the GFAP-driven vector, resulting in the GFAP-GFP-IRES-Cre construct.

Production of chimeric virions (rAAV 1 and rAAV2) was described in ref. [2]. Briefly, human embryonic kidney cells 293 (HEK293; Agilent no. 240073) were calcium phosphate transfected with the recombinant AAV2 plasmid and a three-helper system. rAAV genomic titers were determined with QuickTiter AAV Quantitation Kit (Cell Biolabs) and are ~10^{13} genomic copies per ml for all rAAV vectors used in this study.

Surgeries. *Neuropathic pain model: SNI procedure.* Animals were randomly separated in two groups to undergo either posterior left hindpaw SNI or sham procedure, with the right hindpaw untouched. Animals were anaesthetized using isoflurane at 1.5–2.5%. Incision was made at mid-thigh level using the femur as a landmark, and a section was made through the biceps femoris. The three peripheral branches (sural, common peroneal and tibial nerves) of the sciatic nerve were exposed. Both tibial and common peroneal nerves were ligated using a 5.0 silk suture and transected. The sural nerve was carefully preserved by avoiding any nerve stretch or nerve contact[24]. For animals undergoing sham surgery, the same procedure was performed, but nerves remained untouched. Animals were routinely observed daily for 7 d after surgery and daily tested by the experimenter (Extended Data Fig. 6a). Besides observing weight and social and individual behavior, the operated hindpaw was examined for signs of injury or autotomy. In case of autotomy or suffering, the animal was euthanized in respect of the ethical recommendations of the European Union. No analgesia was provided after the surgery to avoid interference with chronic pain mechanisms, and this is in accordance with our veterinary authorization. Suffering was minimized by careful handling and increased bedding.

Stereotaxic surgery: injection of rAAV vectors. Stereotaxic surgery was performed under deep ketamine–xylazine anesthesia, using the KOPF (model 955) stereotaxic instrument. For specific control of rat CeA astroglial cells, 200 nl of rAAV serotype 1/2 (GFAPp-C1V1(t/t)-mCherry, cloned from plasmid nos. 35500 and 44332, Addgene), was injected bilaterally at the coordinates corresponding to CeL: rostro-caudal: −2.7 mm, medio-lateral: 4.2 mm, dorso-ventral: −8.0 mm

(from Paxinos and Watson Atlas). For specific control of OT neurons, 200 nl of rAAV serotype 1/2 (OTp-C1V1(t/t)-mCherry or OTp-ChR2-mCherry) was injected bilaterally at the coordinates corresponding to each hypothalamic OT nuclei. PVN: rostro-caudal: −1.8 mm; medio-lateral: ±0.4 mm; dorso-ventral: −8.0 mm; SON: rostro-caudal: −1.4 mm; medio-lateral: ±1.6 mm; dorso-ventral: −9.0 mm; AN: rostro-caudal: −2 mm; medio-lateral: ±1.2 mm; dorso-ventral: −8.5 mm (from Paxinos and Watson Atlas). For specific deletion of OTR in mice CeL astrocytes, 280 nl of rAAV serotype 1/2 (GFAPp-GFP-IRES-Cre) was injected bilaterally at the coordinates corresponding to CeL: rostro-caudal: −1.4 mm, medio-lateral: ±2.6 mm, dorso-ventral: −4.3 mm (from Paxinos and Watson Atlas) in OTR cKO mice.

Stereotaxic surgery: intra-CeL cannulae. <u>Cannulae implantation.</u> Animals were bilaterally implanted with guide cannulae for direct intra-CeL infusions. As guide cannulae, we used C313G/Spc guide metallic cannulae (Plastics One) cut 5.8 mm below the pedestal. For this purpose, animals were deeply anesthetized with 4% isoflurane, and their heads were fixed in a stereotaxic frame. The skull was exposed, and two holes were drilled according to coordinates that were adapted from brain atlas (rats: 2.3 mm rostro-caudal, 4 mm lateral, 7.5 mm dorso-ventral relative to bregma; mice: 1.4 mm rostro-caudal, 2.6 mm lateral, 4.3 mm dorso-ventral relative to bregma) by comparing the typical bregma–lambda distance with the one measured in the experimental animal. Two screws were fixed to the caudal part of the skull to have an anchor point for the dental cement. Acrylic dental cement was finally used to fix the cannulae, and the skin was sutured. In case of long-lasting experiments (neuropathy-induced anxiety) with a cannula implantation at distance of the behavioral assay (>4 weeks), cannulae were sometimes lost or cloaked, and animals of concern were, therefore, excluded from testing.

Drug infusions. We used bilateral injections of 0.5 µl containing either vehicle (NaCl 0.9%) or OTR agonist TGOT (1 µM) dissolved in NaCl 0.9%. For this procedure, two injectors (cut to fit 5.8-mm guide cannulae protruding 2–2.5 mm beyond the lower end of the cannula in older animals and 1.8 mm in 3–4-week-old rats) were bilaterally lowered into the guide cannula and connected via polythene tubing to two Hamilton syringes that were placed in an infusion pump, and 0.5 µl of liquid was injected in each hemisphere over a 2-min period. After the injection procedure, the injectors were kept in place for an additional minute to allow a complete diffusion of liquid throughout the tissue. Rats were subsequently left in the home cage for 15 min to recover from the stress of the injection and then handled for mechanical pain threshold or anxiety assessment. Animals that received TGOT injections for the first experiment (mechanical sensitivity assessment) were switched to the vehicle-injected groups for the elevated plus maze experiment.

Stereotaxic surgery: intra-CeL optical fiber. <u>Optical fiber implantation.</u> Sham and rAAV-injected animals both underwent a single surgical procedure in which, after vector injection or no injection for sham, optical fibers designed to target the CeL were implanted and firmly maintained on the skull using dental cement. See 'Cannulae implantation' for the surgical procedure. Implantable optical fibers were homemade using optical fiber cut at appropriate length (FT200EMT, Thorlabs) and inserted and glued using epoxy-based glue in ferrules (CFLC230-10, Thorlabs).

Horizontal and coronal slices. *Slice preparations.* In all cases, animals were anaesthetized using ketamine (Imalgene 90 mg kg^{-1}) and xylazine (Rompun, 10 mg kg^{-1}) administered intraperitoneally. Intracardiac perfusion was then performed using one of the following artificial cerebrospinal fluid (aCSF) dissection solutions. For animals between 18 and 25 d old, an ice-cold sucrose-based dissection aCSF was used containing (in mM): sucrose (170), KCl (2.5), NaH$_2$PO$_4$ (1.25), NaHCO$_3$ (15), MgSO$_4$ (10), CaCl$_2$ (0.5), HEPES (20), D-glucose (20), L-ascorbic acid (5), thiourea (2), sodium pyruvate (3), N-acetyl-L-cysteine (5) and kynurenic acid (2). For animals between 2 and 6 months old, an ice-cold NMDG-based aCSF was used containing (in mM): NMDG (93), KCl (2.5), NaH$_2$PO$_4$ (1.25), NaHCO$_3$ (30), MgSO$_4$ (10), CaCl$_2$ (0.5), HEPES (20), D-glucose (25), L-ascorbic acid (5), thiourea (2), sodium pyruvate (3), N-acetyl-L-cysteine (10) and kynurenic acid (2). In both cases, pH was adjusted to 7.4 using either NaOH or HCl, this after bubbling in 95% O$_2$/5% CO$_2$ gas, bubbling which was maintained throughout the duration of use of the various aCSFs. Those aCSF formulae were based on the work in ref. [55]. After decapitation, brain was swiftly removed in the same ice-cold dissection aCSFs as for intracardiac perfusion, and 350-µm-thick horizontal slices containing the CeA was obtained using a Leica VT1000S vibratome. For experiments in Extended Data Fig. 2a,b, coronal slices of the same thickness containing the PVN were used. Upon slicing, brain slices were hemisected and placed, for 1 h minimum before any experiments were conducted, in a holding chamber at room temperature containing normal aCSFs. For 2–6-month-old animals, slices were first let for 10 min in 35 °C NMDG aCSF before placing them in the holding chamber at room temperature. Normal aCSF, also used during all ex vivo experiments, is composed of (in mM): NaCl (124), KCl (2.5), NaH$_2$PO$_4$ (1.25), NaHCO$_3$ (26), MgSO$_4$ (2), CaCl$_2$ (2), D-glucose (15), adjusted for pH values of 7.4 with HCL or NaOH and continuously bubbled in 95%

O_2/5% CO_2 gas. All aCSFs were checked for osmolality and kept for values between 305 and 310 mOsm L^{-1}. In electrophysiology or calcium imaging experiments, slices were transferred from the holding chamber to an immersion recording chamber and superfused at a rate of 2 ml min^{-1} with normal aCSFs, unless indicated otherwise.

Drug application. OTR agonists were bath applied through a 20-s-long pumping of agonist solution, corresponding to several times the volume of the recording chamber. Other drugs (antagonists and TTX) were applied for at least 20 min in the bath before performing any experiments. BAPTA (or BAPTA-free solution for controls) loading of CeL astrocytes was realized following[56] protocol. Two distant CeL astrocytes per slice (label with SR101, 1 µM) were patched in whole-cell configuration, and voltage steps were applied (2 Hz, Δ40 mV) to help loading the BAPTA contained in the patch pipette (in mM): MgCl$_2$ (1), NaCl (8), ATP Na$_2$ (2) GTP Na$_2$ (0.4) HEPES (10) and BAPTA (40), and osmolality was checked to be between 275 and 285 mOsm L^{-1}. The whole-cell configuration was maintained during 45 min to allow BAPTA diffusion into the astrocyte network[57].

Calcium imaging and identification of astrocytes. To identify astrocytes, SR101 (1 µM) was added to aCSF in a culture well, and slices were incubated for 20 min at 35 °C. The specificity of SR101 labeling to astrocytes of the CeL was verified through patch-clamp experiments, the results of which can be found in Extended Data Fig. 2c,d. The synthetic calcium indicator OGB1 or Rhod-2 was bulk loaded following an adapted version of the method described previously[58], reaching final concentrations of 0.0025% (~20 µM) for calcium indicators, 0.002% for Cremophor EL, 0.01% for Pluronic F-127 and 0.5% for DMSO in aCSF and incubated for 45–60 min at 38 °C. Upon incubation time, slices were washed in aCSF for at least 1 h before any recording was performed. Astrocytes recorded for this study were those co-labeled in rats for SR101 and OGB1 and in mice for GFP and Rhod2. The spinning disk confocal microscope used to perform astrocyte calcium imaging was composed of a Zeiss Axio examiner microscope with a ×40 water immersion objective (numerical aperture of 1.0), mounted with a X-Light Confocal Unit–CRESTOPT spinning disk. Images were acquired at 2 Hz with either a Rolera em-c² emCCD or an optiMOS sCMOS camera (Qimaging). Cells within a confocal plane were illuminated for 100–150 ms for each wavelength (SR101 and Rhod-2: 575 nm, OGB1 and GFP: 475 nm) using a Spectra 7 LUMENCOR. The different hardware elements were synchronized through the MetaFluor 7.8.8.0 software (Molecular Devices). Astrocytic calcium levels were measured in hand-drawn regions of interest (ROIs) comprising the cell body plus, when visible, proximal processes. In all recordings, the Fiji rolling ball algorithm was used to increase the signal-to-noise ratio. Further offline data analysis was performed using a custom-written Python-based script available on editorial website. Intracellular calcium variation was estimated as changes in fluorescence signals. To take into account micro-movements of the specimen on long-duration recordings, the fluorescence values were also calculated for SR101 (or GFP) and subsequently subtracted to the ones of OGB1 (or Rhod2), except in the case of Fig. 2a–d, where astrocytes were identified through SR101 fluorescence after the recordings, to avoid unwanted stimulation of the C1V1 opsin. On this last case, recordings in which movements and drifts were visible were discarded. Then, a linear regression and a median filter were applied to each trace. Calcium transients were detected using the find_peaks function of the SciPy library. More precisely, fluorescence variation was identified as a calcium peak if its prominence exceeds the s.d. (or two times the s.d. for recordings acquired with the sCMOS camera) and if the maximum peak value surpasses 50 fluorescence units (or 3 units for sCMOS recordings). ROIs with zero calcium variations were excluded from the analysis. The remaining ROIs were considered as living astrocytes, and the number of peaks was quantified before and after the drug application. All data were normalized according to the duration of the recording, and astrocytes were labeled as 'responsive' when their AUC or their calcium transient frequency was increased by at least 20% after drug application. Because the time after stimulation is longer than the baseline (10 min versus 5 min), the probability of observing a spontaneous calcium peak is stronger after stimulation. To avoid this bias, astrocytes with only one calcium peak during the whole recording were not considered as responsive. Finally, all data were averaged across astrocytes per slice, and this result was used as the statistical unit. All data were expressed as ratio (baseline/drug effect)—a ratio of 1 meaning neither an increase nor a decrease of the measured parameter. For inter-ratio comparison, parametric or non-parametric (depending on data distribution) unpaired statistical tests were used. Fiji software was also used on SR101/OGB1 pictures to produce illustrative pictures. All calcium imaging experiments were conducted at controlled room temperature (26 °C), and cells with an unstable baseline were discarded.

Electrophysiology. Whole-cell patch-clamp recordings of CeL neurons, CeL astrocytes and CeM neurons were visually guided by infrared oblique light visualization of neurons and completed by SR101 fluorescence observation for astrocytes. Patch-clamp recordings were obtained with an Axon MultiClamp 700B Amplifier coupled to a Digidata 1440A Digitizer (Molecular Devices). Borosilicate glass electrodes (R = 3.5–7 MΩ) with inner filament (OD 1.5 mm, ID 0.86 mm; Sutter Instrument) were pulled using a horizontal flaming/brown micropipette puller (P97; Sutter Instrument). Recordings were filtered at 2 kHz, digitized at 40 kHz and stored with the pClamp 10 software suite (Molecular Devices). Analysis

of patch-clamp data was performed using Clampfit 10.7 (Molecular Devices) and Mini Analysis 6 software (Synaptosoft) in a semi-automated fashion (automatic detection of events with chosen parameters followed by a visual validation). Cells with an unstable baseline were discarded.

Whole-cell recording of CeL neurons. Recording pipettes were filled with an intracellular solution containing (in mM): KMeSO$_4$ (125), CaCL$_2$ (2), EGTA (1), HEPES (10), ATP Na$_2$ (2) and GTP Na$_2$ (0.3). The pH was adjusted to 7.3 with KOH, and osmolality was checked to be between 290 and 295 mOsm L^{-1}, adjusted with sucrose if needed. For mEPSC recordings, neurons were recorded in voltage-clamp configuration and held at a membrane potential of −65 mV. For AP recordings, neurons were recorded in current-clamp configuration and held at $I = 0$. Series capacitances and resistances were compensated electronically throughout the experiments using the main amplifier. For mEPSC measurements in CeL neurons (Fig. 4), whole-cell recordings were conducted in an Mg^{2+}-free aCSF, also containing biccuculin (10 µM) and TTX (1 µM) as in ref. [59]. Average event frequencies per cell were calculated on 20-s windows, chosen for TGOT or photostimulation during maximal effect, as determined by the visually identified maximal slope of the cumulative plot of the number of events. CeL neurons were classified as TGOT responsive when the average event frequency was increased by at least 20% during 20 s after TGOT application when compared to baseline average frequency. Baseline and recovery frequencies were measured, respectively, at the beginning and end of each recording. All patch-clamp experiments were conducted at room temperature.

Biocytin filling of CeL astrocytes. In the lateral part of the CeA slices visualized with infrared differential contrast optics, astrocytes were identified by their morphological appearance revealed by SR101 and the absence of APs in response to depolarizing current injections. Cells were patched with pipettes filled with (in mM) 110 K-gluconate, 30 KCl, 4 ATP Na$_2$, 10 phosphocreatine, 0.3 GTP Na$_2$, 10 HEPES and 5 biocytin (pH 7.3; 310 mOsm). After obtaining whole-cell configuration, astrocytes were held at −80 mV, and typical filling time was 45 min. Then, the pipettes were carefully retracted, and slices were incubated for additional 20 min in the oxygenated aCSF before fixation. Only one cell was filled per slice. Slices with filled cells were immersion fixed at 4 °C for 5 d in 4% PFA-PBS solution. Next, the slices were flat embedded in 6% agar-PBS, and areas of interest were cut out of and re-embedded onto the agar block and vibratome cut into 80-µm-thick free-floating sections. Then, the sections were incubated with avidin conjugated to Alexa Fluor 488 (1:1,000) (Thermo Fisher Scientific) in 1% Triton-PBS at 4 °C, washed in PBS, mounted and cover slipped. The tissue was analyzed, and images were taken with a Leica TCS SP5 confocal microscope.

Whole-cell recording of CeM neurons. Pipettes were filled with an intracellular solution containing (in mM): KCl (150), HEPES (10), MgCl$_2$ (4), CaCl$_2$ (0.1), BAPTA (0.1), ATP Na$_2$ (2) and GTP Na$_2$ (0.3). pH was adjusted to 7.3 with KOH, and osmolality was checked to be between 290 and 295 mOsm L^{-1}, adjusted with sucrose if needed. All cells were held at a membrane potential of −70 mV. Series capacitances and resistances were compensated electronically throughout the experiments using the main amplifier. Average event frequencies per cell were calculated on 20-s windows, chosen for TGOT or photostimulation during maximal effect, as determined by the visually identified maximal slope of the cumulative plot of the number of events. CeM neurons were classified as TGOT responsive when the average IPSC frequency was increased by at least 20% during 20 s after TGOT application when compared to baseline average frequency. Baseline and recovery frequencies were measured, respectively, at the beginning and end of each recording. All patch-clamp experiments were conducted at room temperature.

Immunohistochemistry and in situ hybridization. *In situ hybridization for OTR mRNA in rat CeL.* The probe for OTR mRNA was in vitro transcribed from a 902-bp fragment containing 133–1,034 bases of the rat OTR complementary DNA (cDNA) (NCBI Reference Sequence: NM_012871.3) subcloned into pSP73 Vector (Promega). The digoxigenin (DIG)-labeled anti-sense and sense RNA probe from the linearized *oxtr* cDNA template was synthesized using DIG RNA Labeling Kit (SP6/T7) (Roche Diagnostics). Sections containing two consecutive sections of the CeL (corresponding to bregma: 2.5) were processed for FISH. Rats were transcardially perfused with PBS, followed by 4% PFA. Brains were dissected out and post-fixed overnight in 4% PFA at 4 °C with gentle agitation. Then, 50-µm vibratome sections were cut, collected and fixed in 4% PFA at 4 °C overnight. The free-floating sections were washed in RNase-free PBS, immersed in 0.75% glycine in PBS, treated with 0.5 µg ml^{-1} of proteinase K for 30 min at 37 °C, acetylated with 0.25% acetic anhydride in 0.1 M triethanolamine and then hybridized with DIG-labeled RNA probe overnight at 65 °C. After RNase treatment and after intensive wash, the hybridized DIG-labeled probe was detected by incubation with Anti-Digoxigenin-POD (1:200, 11207733910, Roche Diagnostics) for 3 d at 4 °C. Signals were developed with the tyramid signal amplification method. Rhodamine-conjugated tyramide was synthesized by coupling NHS-Rhodamine (Pierce Biotechnology, Thermo Fisher Scientific) to Tyramine HCl (Sigma-Aldrich) in dimethylformamide with triethylamine. For the quantification of OTR

mRNA-positive astrocytes, all confocal images were obtained using the same laser intensities and processed with the same brightness/contrast settings in Adobe Photoshop. Because the in situ signal for the OTR mRNA in astrocytes was weak, we first calculated the average intensity (signal intensity of all pixels divided by the total number of pixels) of the rhodamine-stained OTR mRNA signal for each individual section containing the CeL. Next, we calculated the s.d. for each individual confocal image based on the intensity of all pixels comprising the image. We defined the threshold for OTR mRNA-positive astrocytes: if more than 1/4 of all pixels comprising an astrocyte soma displayed a signal intensity exceeding the average background intensity by more than four times the s.d., the astrocytes were considered OTR mRNA positive.

Astrocyte markers. The aldehyde dehydrogenase 1 antibody is a commonly used marker for glial cells, including astrocytes. Therefore, we used the ALDH1L1 for immunohistochemistry in our initial experimental studies (Extended Data Figs. 1c and 4a). However, owing to inconsistencies in staining quality as a result of batch-dependent antibody properties, especially in combination with the OTR mRNA FISH, we decided to employ GS (Fig. 1). GS is a commonly used glial marker[60] that stains astrocyte cell bodies, faint processes and even astrocytes not expressing GFAP. Using GS, we achieved consistent results in combination with our OTR mRNA FISH.

GS and ALDH1L1 co-localization with OTR mRNA in rat CeL. After development and washing steps, the sections were stained with antibodies against GS (mouse monoclonal, 1:500, ref: MAB302, Merck Milipore) and ALDH1L1 (rabbit polyclonal, 1:500, ref: ab87117, Abcam) in PBS and kept at 4 °C on a shaker in a dark room overnight. After intensive washing with PBS, sections were stained with the respective secondary antibodies, Alexa Fluor488 (goat anti-mouse, 1:1,000, ref: A11001, Life Technologies) and Alexa Fluor 680 (goat anti-mouse, 1:1,000, ref: A27042, Thermo Fisher Scientific) for 2 h at room temperature. After intensive washing with PBS, sections were mounted using Mowiol.

Double in situ hybridizations for OTR mRNA and GFAP mRNA in mice CeL. FISH in Extended Data Fig. 1d was performed on 25-μm cryostat-cut coronal sections prepared from fresh-frozen mouse brain (male C57BL/6J, P22). After extraction, brains were immediately frozen in Tissue-Tek O.C.T. compound and stored at −80 °C. FISH was performed according to the manufacturer's instructions (Advanced Cell Diagnostics) for Fresh Frozen RNAscope Multiplex Fluorescent Assay. Treatment of amygdala-containing sections were adjusted with the three-plex negative control, and then co-expression of OTR and GS was examined using ACD-designed target probes as well as the nuclear stain DAPI. Single-plan images were collected with an upright laser scanning microscope (LSM-710, Carl Zeiss) using a ×40 objective, keeping acquisition parameters constant between control and probe-treated sections.

AAV-GFAP-C1V1(t/t)-mCherry specificity. After 3 weeks of vector expression in the brain, rats were transcardially perfused with 4% PFA solution. Tissue blocks containing CeA were dissected from the fixed brain and vibratome cut into 50-μm-thick free-floating sections. After several rinse steps, sampled sections were blocked with 5% NGS in PBS and incubated for 48 h at 4 °C with polyclonal rabbit anti-ALDH1L1 antibody (1:500, Abcam) in 1% Triton-PBS buffer, containing 0.1% NGS. Appropriate secondary antibody (Alexa Fluor 488-conjugated goat anti-rabbit (1:1,000, Life Technologies) was used for further antigen detection. Intrinsic mCherry fluorescence of vector-expressing cells was strong enough to detect them in the tissue without any additional antibody enhancement. The immunolabeled sections were mounted onto Superfrost slides, cover slipped with Mowiol, analyzed and documented using a Leica SP5 confocal microscope.

3D assessment of astrocyte complexity and interaction analysis using Imaris. For the 3D reconstruction of astrocytes, we took Z-stack images (50-μm depth, 1-μm steps, ×40 magnification) of CeL using a Zeiss LSM 780 confocal microscope (1,024×1,024 pixels, 16-bit depth, pixel size 0.63 microns, zoom 0.7). Raw CZI files were used for further analysis using Imaris software (version 9.31, Oxford Instruments). First, Imaris was used to reconstruct the astrocyte surface using the following custom settings: surfaces Detail 0.700 μm (smooth); thresholding Background subtraction (Local Contrast), diameter of largest Sphere, which fits into the object: 2.00; Color: base, diffusion transparency: 65%. After surface reconstruction, we used the filter function to remove unspecific background signals: Filter: Volume max − 400 μm³. It is important to note that these settings have to be adjusted for every new batch/immunohistochemistry staining to guarantee a reliable reconstruction. All astrocytes with incomplete somata (cut by the *x*, *y* or *z* plane) were manually removed and not included in further analysis. Fused astrocytes that were falsely recognized as one entity by the software were manually separated using the cut function or entirely removed from the sample if a separation was not feasible. The 'filter/area function' was used to remove small astrocytic segments that occurred during manual deletion. After deletion of all background signals, the 'mask all' function was used to create the final surface reconstruction. Next, the surface reconstruction was used as the template for the filament reconstruction using the following custom settings: detect new starting

points: largest Diameter 7.00 μm, seed points 0.300 μm; remove seed points around starting points: diameter of sphere regions: 15 μm. Seed points were corrected for (either placed in or removed from the center of the somata) manually if the Imaris algorithm placed them incorrectly. All surface and filament parameters were exported into separate Excel files and used for data analysis. All images used for analysis were taken with the same confocal settings (pinhole, laser intensity, digital gain and digital offset). Sholl analysis was performed using Imaris in the filament reconstruction mode, and individual datasets were exported into separate Excel files for further analysis (each individual sphere) per individual astrocyte. For the nearest neighbor and interaction analysis, we used the 'Native Distance Measurements' function as depicted in this video: https://imaris.oxinst.com/learning/view/article/imaris-9-5-native-distance-measurements. In brief, we reconstructed astrocytic surfaces based on the GFAP fluorescence and OTR mRNA signal. Next, we manually labeled OTR⁺ and OTR⁻ astrocytes and performed the native distance measurement, allowing us to assess the shortest distance between GFAP-positive processes of different astrocytes. We defined 'astrocytic interaction' when GFAP-positive processes of two different astrocytes were no further than 1 μm apart. It is important to note that this method does not allow the discrimination of different astrocytic entities so that several close contacts (contacts being defined as a distance of less than 1 μm between GFAP-positive processes or endfeets from two different astrocytes) originating from the same astrocyte result in a higher number of total interactions. For the nearest neighbor analysis, we calculated the distance from the center of the soma to the nearest astrocyte neighbor using GS fluorescence and an artificially created sphere that was placed within the soma and measured the distance accordingly. Distribution plots and correlations, as well as all statistics, were performed using GraphPad Prism version 8.0.0 (GraphPad Software).

Optogenetics. *Ex vivo.* We opted for a ChR1/VChR1 chimera channel rhodopsin displaying a red-shifted absorption spectrum, referred to here as C1V1 (ref. [17]). This choice was made over a classical channelrhodopsin-2 to avoid unwanted stimulation of OT axons while imaging our 488-nm light-sensitive calcium indicator (OGB1). Optogenetic green light stimulation of C1V1 in ex vivo experiments was performed using either the Spectra 7 LUMENCOR (λ542 nm) or light source X-Cite 110LED from Excelitas Technologies through a Cy3 filter, controlled via MetaFluor or Clampex-driven TTL pulses, respectively.

In vivo. Animals were habituated to the fixation of an optical fiber on the ferrule without light stimulation for 1 week before the experiment. In all cases, optical fibers were attached to the ferrules using an adapter (ADAF2, Thorlabs), and animals were let free to move in a typical home cage for the duration of the stimulation. Implanted optical fibers were connected to two lasers (LRS-0532-GFM-00100-03 LaserGlow 532-nm DPSS Laser System), and the output power was adjusted to correspond to 20–30 mW measured at the tip of 200-μm diameter fibers similar to the one implanted. Stimulation of 500-ms duration at a frequency of 0.5 Hz was given for 3 min.

Behavior. *Mechanical sensitivity assessment.* In experiments with rats, we used a calibrated forceps (Bioseb) previously developed in our laboratory to test the animal mechanical sensitivity[61]. Briefly, the habituated rat was loosely restrained with a towel masking the eyes to limit stress by environmental stimulations. The tips of the forceps were placed at each side of the paw and a graduate force applied. The pressure producing a withdrawal of the paw or, in some rare cases, vocalization was considered as the nociceptive threshold value. This manipulation was performed three times for each hindpaw, and the values were averaged as being the final nociceptive threshold value. In experiments with mice, we used von Frey filament tests. Mechanical allodynia (a symptom of neuropathic pain) was tested using von Frey hairs, and results were expressed in grams. Tests were performed during the morning starting at least 2 h after lights on. Mice were placed in clear Plexiglas boxes (7 cm × 9 cm × 7 cm) on an elevated mesh floor. Calibrated von Frey filaments (Bioseb) were applied to the plantar surface of each hindpaw until they just bent in a series of ascending forces to the mechanical threshold. Filaments were tested five times per paw, and the paw withdrawal threshold was defined as the lower of two consecutive filaments for which three or more withdrawals out of the five trials were observed. Animals with cannulae/optic fiber issues were removed from the analysis.

Elevated plus maze. Following protocol from ref. [62], the arena is composed of four arms, two open (without walls) and two closed (with walls; rats 30 cm high; mice 15 cm high). Arms are 10 cm wide, 50 cm long and elevated 50 cm off the ground for rats and 5 cm wide, 30 cm long and elevated 40 cm off the ground for mice. Two lamps with intensity adjustable up to 50 W were positioned on the top of the maze, uniformly illuminating it. Animals were video tracked using a video-tracking system (Ethovision Pro 3.16, Noldus, and Anymaze, Stoelting). After each trial, the maze was cleaned with 70% ethanol and dried with a paper towel. Twenty minutes after intracerebral injections or directly after optical stimulation, the animal was let free at the center of the plus maze, facing the open arm opposite to where the experimenter is, and was able to freely explore the entire apparatus for 6 min. Total time and time spent in closed and open arms were recorded in seconds, and the percentage of time spent in closed arms was calculated as a measure of anxiety-like

behavior. As internal control, the total distance travelled during the test period was quantified and compared among all different groups (Extended Data Fig. 7). Animals falling from the apparatus during the test, freezing more than 50% of the total time or with cannulae/optic fiber issues were removed from the analysis.

CPP. The device is composed of two opaque conditioning boxes (rats: 30×32 cm; mice: 22×22 cm) and one clear neutral box (30×20 cm) Animals were video tracked using a video-tracking system (Anymaze, Stoelting). After each trial, the device was cleaned with a disinfectant (Surfa'Safe, Anios Laboratory). Based on ref. [63], all animals underwent a 3-d habituation period during which they were able to freely explore the entire apparatus for 30 min. On day 3, behavior was recorded for 15 min to verify the absence of pre-conditioning chamber preference. The time spent in the different compartments was measured, and the paired compartment was chosen as the compartment in which rat spent less time during the third day of habituation. On day 4, animals were placed in the morning in one compartment for 15 min with no stimulation (unpaired box). Four hours later, the animals were placed for 15 min in the opposite box (paired box), and CeL astrocyte-expressing C1V1 vector was optogenetically stimulated (3 min–1 s light pulse at 0.5 Hz–λ542 nm) or TGOT micro-infused through intracerebral cannulae. On day 5, the animals were placed in the CPP box and allowed to freely explore the entire apparatus for 15 min. As internal control, the total distance travelled during the test period was quantified and compared among all different groups (Extended Data Fig. 7). Animals spending more than 80% of the total time in a single chamber before the conditioning, or with cannulae/optic fiber issues, were removed from the analysis.

Quantification and statistical analysis. *Randomization and blinding.* Randomization was used to assign cells and animals to experimental groups. All measurements were made using a machine and are not subject to operator bias. Data collection and analysis were not performed blinded to the conditions of the experiments.

Statistical analysis. No statistical methods were used to pre-determine sample sizes, but our sample sizes are similar to those reported in previous publications. All parametrical statistical tests presented in figure captions or the manuscript were performed following correct verification of the assumptions on the distribution of data, and, if not, non-parametric tests were used. Tests were performed using either GraphPad Prism software (version 8.0.0 for Windows) or the SciPy Python-based library[64]. All values, group compositions and statistical tests for each experiment and figure panel are detailed in Supplementary Tables 1–7.

Technical limitations. We acknowledge several technical limitations in our study, which are discussed in detail below.

mRNA detection. It is surprising to find that the loss of OTR expression in astrocytes results in a loss of function of OTR signaling in the CeA–CeM projection, especially considering the high proportion of OTR+ neurons (up to 70%) compared to the lower fraction of OTR+ astrocytes (18%) in the CeL. One methodological limitation here is that we remained limited to measuring mRNA levels through FISH and could not measure OTR expression at the protein level, notably due to the poor availability of reliable OTR antibodies. It is also possible that a comparison between the OTR mRNA content of astrocytes and neurons is biased; indeed, astrocytes have a lower total mRNA content than neurons, as publicly available databases of single-cell RNA sequencing indicate[65,66]. Interestingly, a similar discrepancy exists between low receptor levels observed in astrocytes compared to neurons, and, yet, a crucial functional relevance of the receptors of astrocytes in neuromodulation is also observed for another GPCR: the CB1 receptor (ref. [67] and references therein).

C1V1 red-shifted opsin to activate astrocytes. It has been recently demonstrated that the activation of such depolarizing channel rhodopsins in astrocytes or neurons can lead to a significant leak of potassium ions in the extracellular space, resulting in increased neuronal excitability[68]. However, we provide results in which we buffered the astrocytes' intracellular calcium using BAPTA infusion before activating astrocytic C1V1 and found that it abolished its effects on CeA neurons (Figs. 4–6). Furthermore, we demonstrate that the AstrOpto effect on CeA neuronal circuit is dependent on NMDARs (Extended Data Fig. 5a). This indicates that the consequences of astrocytic C1V1 activation are dependent on the evoked astrocyte calcium signaling rather than on potassium leakage.

Bulk loading of organic calcium indicator dyes. It should also be noted that we used bulk loading of organic calcium indicator dyes. This means that we could not precisely measure cytosolic calcium changes in fine astrocyte processes[69], which might have revealed more complex activities of astrocytes. We note that it has been proven that endogenous or exogenous (designer receptor exclusively activated by designer drug (DREADD) receptors) GPCR signaling in astrocytes produces a global increase in calcium in both the cell body and processes (ref. [67] and references therein).

Reporting Summary. Further information on research design is available in the Nature Research Reporting Summary linked to this article.

Data and code availability
Python code (used for ex vivo calcium imaging data analysis) can be found in Supplementary Software. All data that support the findings of this study are available from the corresponding authors upon reasonable request.

References
50. Rouach, N., Koulakoff, A., Abudara, V., Willecke, K. & Giaume, C. Astroglial metabolic networks sustain hippocampal synaptic transmission. *Science* **322**, 1551–1555 (2008).
51. Pannasch, U. et al. Astroglial networks scale synaptic activity and plasticity. *Proc. Natl Acad. Sci. USA* **108**, 8467–8472 (2011).
52. Theis, M. et al. Accelerated hippocampal spreading depression and enhanced locomotory activity in mice with astrocyte-directed inactivation of connexin43. *J. Neurosci.* **23**, 766–776 (2003).
53. Teubner, B. et al. Connexin30 (Gjb6)-deficiency causes severe hearing impairment and lack of endocochlear potential. *Hum. Mol. Genet.* **12**, 13–21 (2003).
54. Shigetomi, E. et al. Imaging calcium microdomains within entire astrocyte territories and endfeet with GCaMPs expressed using adeno-associated viruses. *J. Gen. Physiol.* **141**, 633–647 (2013).
55. Ting, J. T. et al. Preparation of acute brain slices using an optimized N-methyl-D-glucamine protective recovery method. *J. Vis. Exp.* (132), 53825 (2018).
56. Serrano, A., Haddjeri, N., Lacaille, J., Robitaille, R. & Centre-ville, S. GABAergic network activation of glial cells underlies hippocampal heterosynaptic depression. *J. Neurosci.* **26**, 5370–5382 (2006).
57. Jourdain, P. et al. Glutamate exocytosis from astrocytes controls synaptic strength. *Nat. Neurosci.* **10**, 331–339 (2007).
58. Ikegaya, Y., Le Bon-Jego, M. & Yuste, R. Large-scale imaging of cortical network activity with calcium indicators. *Neurosci. Res.* **52**, 132–138 (2005).
59. Shigetomi, E., Bowser, D. N., Sofroniew, M. V. & Khakh, B. S. Two forms of astrocyte calcium excitability have distinct effects on NMDA receptor-mediated slow inward currents in pyramidal neurons. *J. Neurosci.* **28**, 6659–6663 (2008).
60. Anlauf, E. & Derouiche, A. Glutamine synthetase as an astrocytic marker: its cell type and vesicle localization. *Front. Endocrinol.* **4**, 144 (2013).
61. Luis-Delgado, O. E. et al. Calibrated forceps: a sensitive and reliable tool for pain and analgesia studies. *J. Pain* **7**, 32–39 (2006).
62. Walf, A. A. & Frye, C. A. The use of the elevated plus maze as an assay of anxiety-related behavior in rodents. *Nat. Protoc.* **2**, 322–328 (2007).
63. King, T. et al. Unmasking the tonic-aversive state in neuropathic pain. *Nat. Neurosci.* **12**, 1364–1366 (2009).
64. Virtanen, P. et al. SciPy 1.0: fundamental algorithms for scientific computing in Python. *Nat. Methods* **17**, 261–272 (2020).
65. Zeisel, A. et al. Cell types in the mouse cortex and hippocampus revealed by single-cell RNA-seq. *Science* **347**, 1138–1142 (2015).
66. Batiuk, M. Y. et al. Identification of region-specific astrocyte subtypes at single cell resolution. *Nat. Commun.* **11**, 1220 (2020).
67. Kofuji, P. & Araque, A. G-protein-coupled receptors in astrocyte–neuron communication. *Neuroscience* https://doi.org/10.1016/j.neuroscience.2020.03.025 (2020).
68. Octeau, J. C. et al. Transient, consequential increases in extracellular potassium ions accompany channelrhodopsin2 excitation. *Cell Rep.* **27**, 2249–2261 (2019).
69. Reeves, A. M. B., Shigetomi, E. & Khakh, B. S. Bulk loading of calcium indicator dyes to study astrocyte physiology: key limitations and improvements using morphological maps. *J. Neurosci.* **31**, 9353–9358 (2011).

Author contributions

Conceptualization: A.C.; Methodology: A.C., B.Boutrel, C.M.L., C.P., D.K., F.A., I.D., J.E.S., J.W., J.Y.C., N.R., P.D., P.P., R.S., V.G., W.S.Y. and YG; Analysis: A.C., B.Bellanger, B.B.J., C.M.L., D.K., F.A., H.S.K.B., J.W. and S.G.; In situ hybridization: D.H., F.A., H.S.K.B., H.W., J.S. and M.E.; Immunohistochemistry: A.L., D.H., F.A., J.W., M.E. and M.D.S.G.; Imaris analysis: F.A., M.K.K. and R.K.R.; Ex vivo patch-clamp electrophysiology: A.B., A.C., J.W., S.G., D.K., I.W., B.Bellanger and M.A.; Ex vivo calcium imaging: A.B., C.M.L., D.K. and J.W.; Astrocyte characterization: A.B., A.R., B.Bellanger, D.K., I.W., M.E. and S.G.; Behavior: A.C., B.B.J., D.K. and J.W.; Mice line validation: W.S.Y.; Viral vectors validation: D.B., L.B., M.D.S.G., M.E. and V.G.; Spared nerve injuries: P.I. and M.P.; Writing: A.B., A.C., D.K., F.A., J.W. and V.G.; Funding acquisition: A.C. and V.G.; Supervision: A.C. and V.G.; Project administration: A.C.

Competing interests

The authors declare no competing interests.

Additional information

Extended data is available for this paper at https://doi.org/10.1038/s41593-021-00800-0.

Supplementary information The online version contains supplementary material available at https://doi.org/10.1038/s41593-021-00800-0.

Correspondence and requests for materials should be addressed to V.G. or A.C.

Peer review information *Nature Neuroscience* thanks Thomas Papouin, Gertrudis Perea, and the other, anonymous, reviewer(s) for their contribution to the peer review of this work.

Reprints and permissions information is available at www.nature.com/reprints.
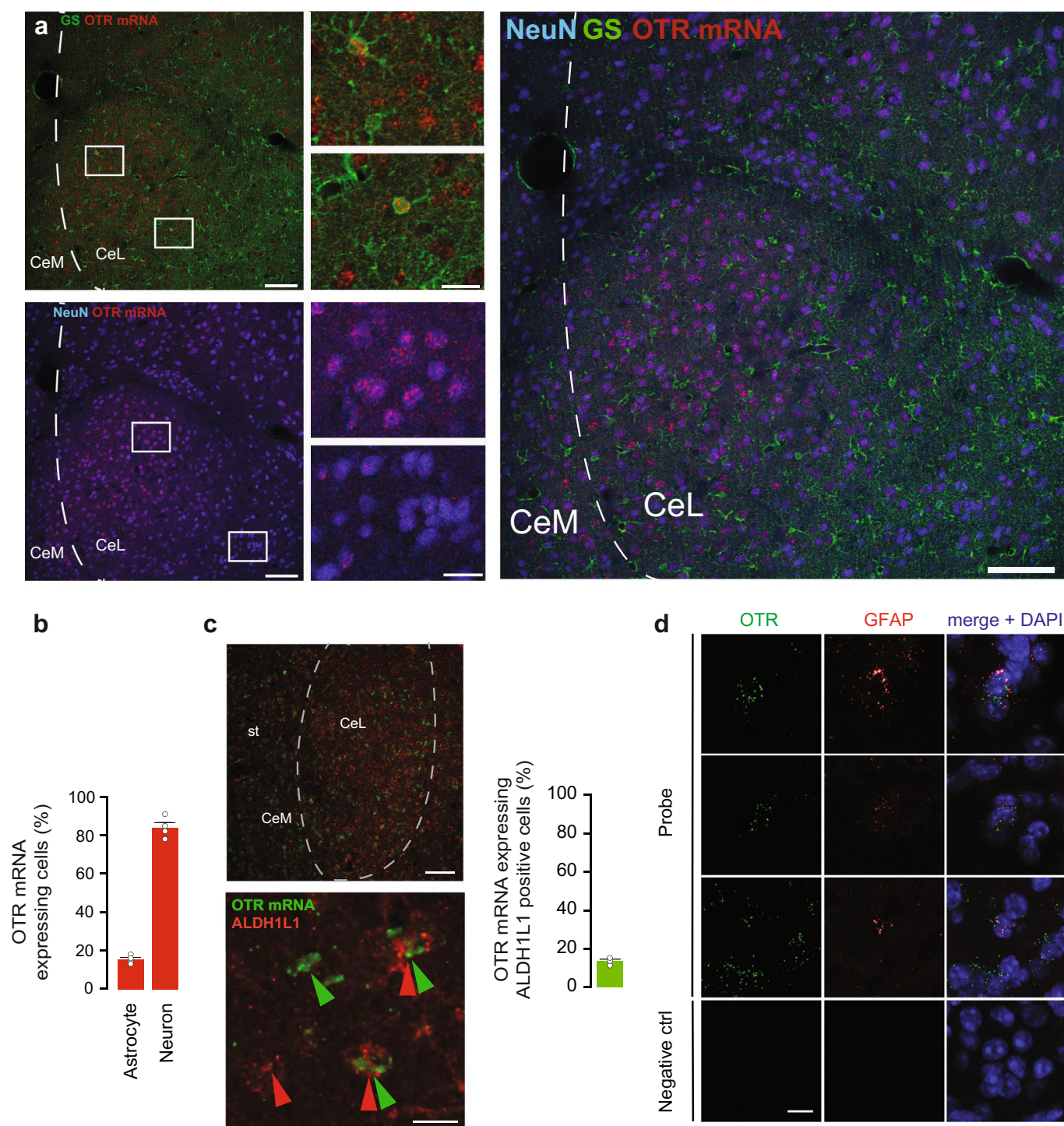
Extended Data Fig. 1 | Validation of OTR expression in CeL astrocytes using several astrocytic markers. a, Combination of FISH and IHC showing co-localization of GS (top left), NeuN (bottom left) and both markers (right) with OTR mRNA in rats. Scale bars are 100µm and 10µm. (n_{rats} = 5, n_{slices} = 20, $n_{astrocytes}$ = 1354, $n_{neurons}$ = 1254). **b**, proportion of OTR positive astrocytes and neurons in mice. $n_{astrocytes}$ = 897; $n_{neurons}$ = 688; n_{rats} = 4 **c**, (top left) FISH overview for OTR mRNA (green), counterstained with polyclonal anti-ALDH1L1 antibody (red) in CeA. (bottom left) High magnification image of cells positive for both OTR mRNA and ALDH1L1 (double arrows); green arrows point OTR mRNA-positive cells; red arrows point ALDH1L1-positive cells. Scale bars: 400 (Top) and 50µm (Bottom). (Right) Quantification of ALDH1L1-positive cells positive for OTR mRNA. $n_{astrocytes}$ = 450; n_{rats} = 4. **d**, RNAscope *in situ* hybridization showing GFAP (red) and OTR (green) expressing cells in mice CeA. Merged images include DAPI stain (blue); n = 3. (Bottom) Negative control probe targeting the bacterial gene DapB; n = 3. Scale bar is 10µm. st: stria terminalis. Data are expressed as mean across slices plus SEM and white circles represent individual cell data. (Statistics and numbers in Supplementary Table 1).

a mCherry

PVN

rAAV-OTp-C1V1(t/t)-mCherry
(OxytOpto)

b

500 pA
500 ms

20 mV
500 ms

c SR101 OGB1

d Astrocytes

Neurons

Cm (pF) ***

Rm (Mohm) ***

Ra (Mohm)

Resting potential (mV) ***

e avidinALEXA488
NeuN

f OxytOpto
λ542nm 20s

Calcium Transient

AUC

20% ΔF
100s

Baseline   Post stimulation

Values averaged
across cells per slice

$\overline{X}_{slice}$

AUC

2.10^3

1.10^3

Baseline   post stim

Ratio = $\dfrac{\overline{X}_{slice}\ post\ stim}{\overline{X}_{slice}\ baseline}$

AUC (norm. to baseline)

g GS
GFAPp-Cre-GFP
Cre

CeL   CeM

Efficiency (%)

Specificity (%)

h NeuN
OTR mRNA   Control

+ P_GFAP-Cre

OTR mRNA
expressing neurons (%)

Control   +P_GFAP-Cre

Extended Data Fig. 2 | See next page for caption.

Extended Data Fig. 2 | Validation of astrocyte-specific approaches. a, (left) C1V1-mCherry (OxyOpto) expressing oxytocin neuron of the PVN. Scale bar is 20μm; n = 11. (right) Schematic representation of the whole cell patch clamp of the OxytOpto-expressing cells of the PVN. **b**, (left) λ542nm light exposure (yellow line) induce a depolarizing current, (right) enabling precise spiking of OxytOpto-expressing cells. **c**, Typical confocal image of CeL astrocytes co-labeled with SR101 and OGB1; n = 46. Scale bar 20μm. **d**, (left) Pseudo-color pictures of an SR101 positive cell identified as an astrocyte compared to neurons identified under oblique infrared light, Scale bar 10μm. (Middle) Electrophysiological properties of patched SR101+ (red, n = 82) and SR101- cells (grey, n = 20). Medians, quartiles and whiskers can be found in Supplementary Table 2. (Right) Typical responses to 20pA current steps of a SR101+ (red) and a SR101- cells (black). **e**, CeL SR101 positive cell filled with biocytin through whole cell patch-clamp (green) lacks NeuN signal (Blue); n = 3. Scale bar 50 μm. **f**, Illustration of calcium imaging data analysis method. (left) Fluorescence traces were splited into a "baseline" and a "post-stimulation" trace. Calcium transients were detected according to a prominence threshold and their frequency was quantified before and after the drug application. All data were averaged across astrocytes per slice, and this results was used as statistical unit. All data were compared (before *vs.* after drug application) and the results were expressed in ratio (baseline/drug effect), a ratio of 1 meaning neither an increase nor a decrease of the measured parameter. $n_s = 7$, $n_a = 36$. **g**, (top left) Immunohistochemical staining for glutamine synthase (GS; blue), Cre-GFP (green) and Cre recombinase (red). (bottom left) Overview of the CeA, displaying correct viral targeting of the CeL subdivision. (right) Quantification of efficiency and specificity of the transduction. Efficiency: Over 1001 GS positive cells, 561 were also GFP positive, indicating an efficiency of 56±4.9%. Specificity: we counted a total of n = 977 GFP-positive cells, 940 of which were positive for GS (96.2±2.1%). None of the GFP or Cre signals were detected in NeuN positive cells (0 out of n = 850, 4 mice, not shown). Finally, 99.82 ± 0.2% of GS-positive astrocytes containing GFP signal were Cre-positive (n = 1001). $n_{mice} = 4$. Scale bars: 400 (Bottom) and 20μm (Top). **h**, Immunohistochemical analysis of OTR expression in NeuN-positive cells of the CeL revealed no difference in OTR levels between control and GFAP-Cre injected animals; 85.0 ± 1.6% (n = 688, n = 4 mice) and 86.7 ± 1.6% (n = 660, n = 4 mice) respectively. Scale bars: 20μm. Data in f-h are expressed as mean across slices plus SEM and white circles represent individual cell data. ***p < 0.001, two-sided Mann-Whitney U test. (Statistics and numbers in Supplementary Table 2).

$$\text{Number of contacts} = \sum_{i=1}^{n} X_i$$
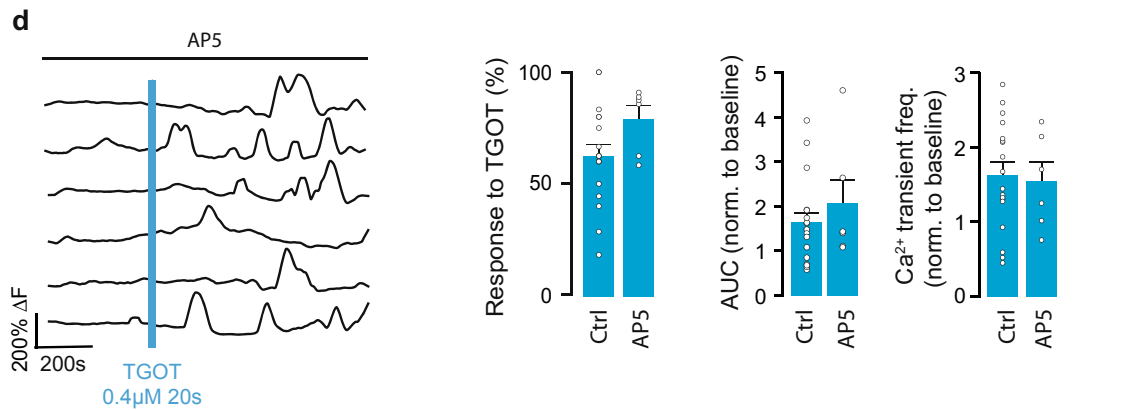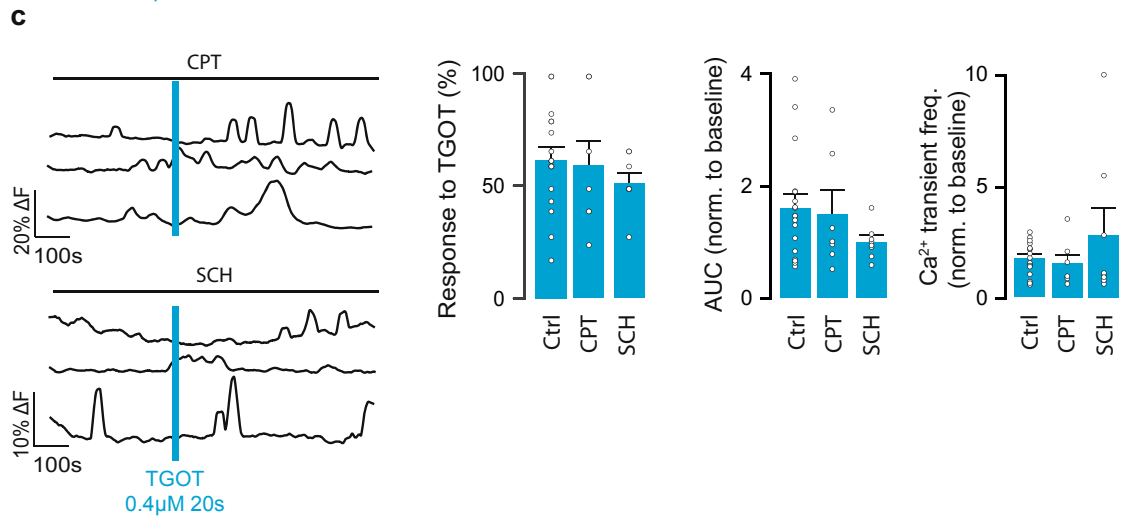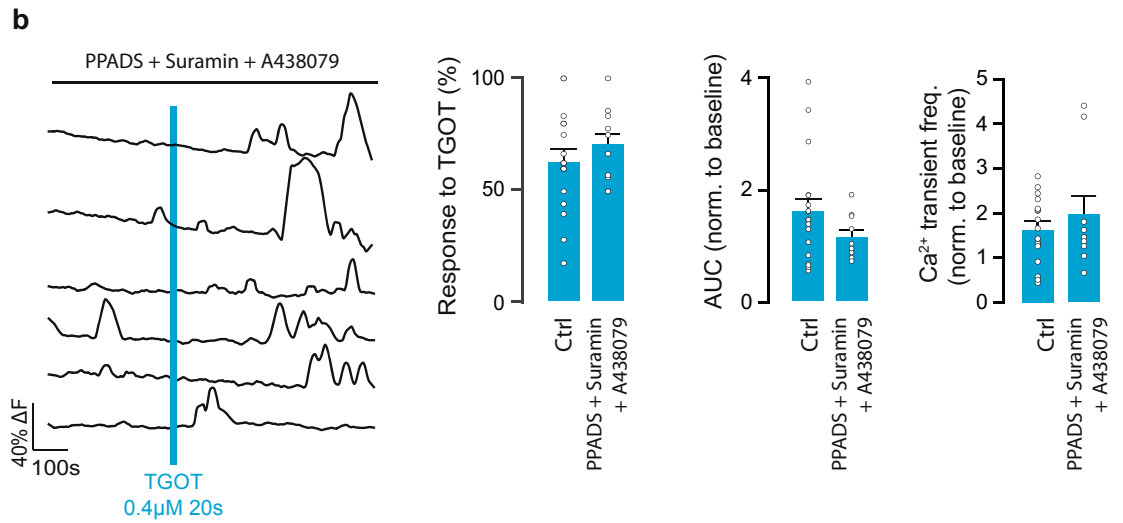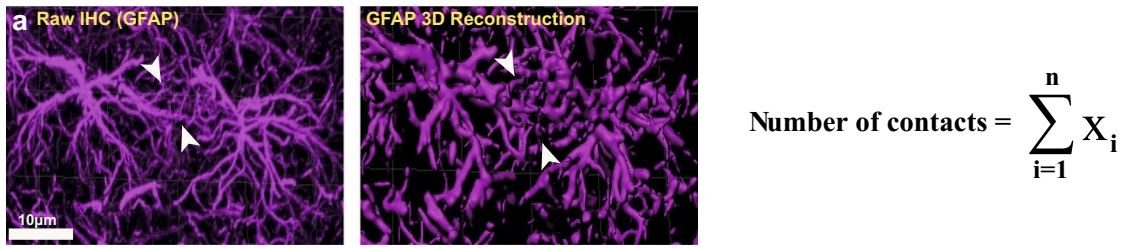
Extended Data Fig. 3 | See next page for caption.

Extended Data Fig. 3 | Astro-astrocytic communication in the CeL do not depends on purinergic nor NMDAR-dependent signalling. a, Illustration of the 3D reconstruction and the quantification of the number of contact between astrocytes. (left) Pictures of the raw fluorescence obtained after anti-GFAP immunohistochemistry, (middle) based on this staining, we performed a 3D reconstruction of astrocytes and (right) evaluate the number of astrocyte-astrocyte contact using the given formula. With n = upper limit of summation, i = index of summation, x_i = typical element (*that is* astrocytic contacts with 1µm or less proximity). With this approach, we quantified all astrocyte contacts without discrimination between individual astrocyte entities. **b**, (left) Typical ΔF traces following TGOT+TTX application in presence of PPADS (50 µM) + Suramin (75 µM) + A438079 (1 µM). (right) Proportion of responding astrocytes, AUC of ΔF traces and Ca2+ transients frequency normalized to baseline values following application of TGOT+TTX (0.4 µM) in presence of PPADS (50 µM) + Suramin (75 µM) + A438079 (1 µM) (n_s = 10, n_a = 112). **c**, (left) Typical ΔF traces following TGOT+TTX application in presence of CPT (5 µM) or SCH 58261 (100 nM). (right) Proportion of responding astrocytes, AUC of ΔF traces and Ca2+ transients frequency normalized to baseline values following application of TGOT+TTX (0.4 µM) in presence of CPT (n_s = 7, n_a = 22) or SCH (n_s = 8, n_a = 32). **d**, (left) Typical ΔF traces following TGOT+TTX application in presence of AP5 (50 µM). (right) Proportion of responding astrocytes, AUC of ΔF traces and Ca2+ transients frequency normalized to baseline values following application of TGOT+TTX (0.4 µM) in presence of AP5 (n_s = 6, n_a = 55). Data are expressed as mean across slices plus SEM and white circles represent individual cell data. White circles indicate average across astrocytes per slice. (Statistics and numbers in Supplementary Table 3).
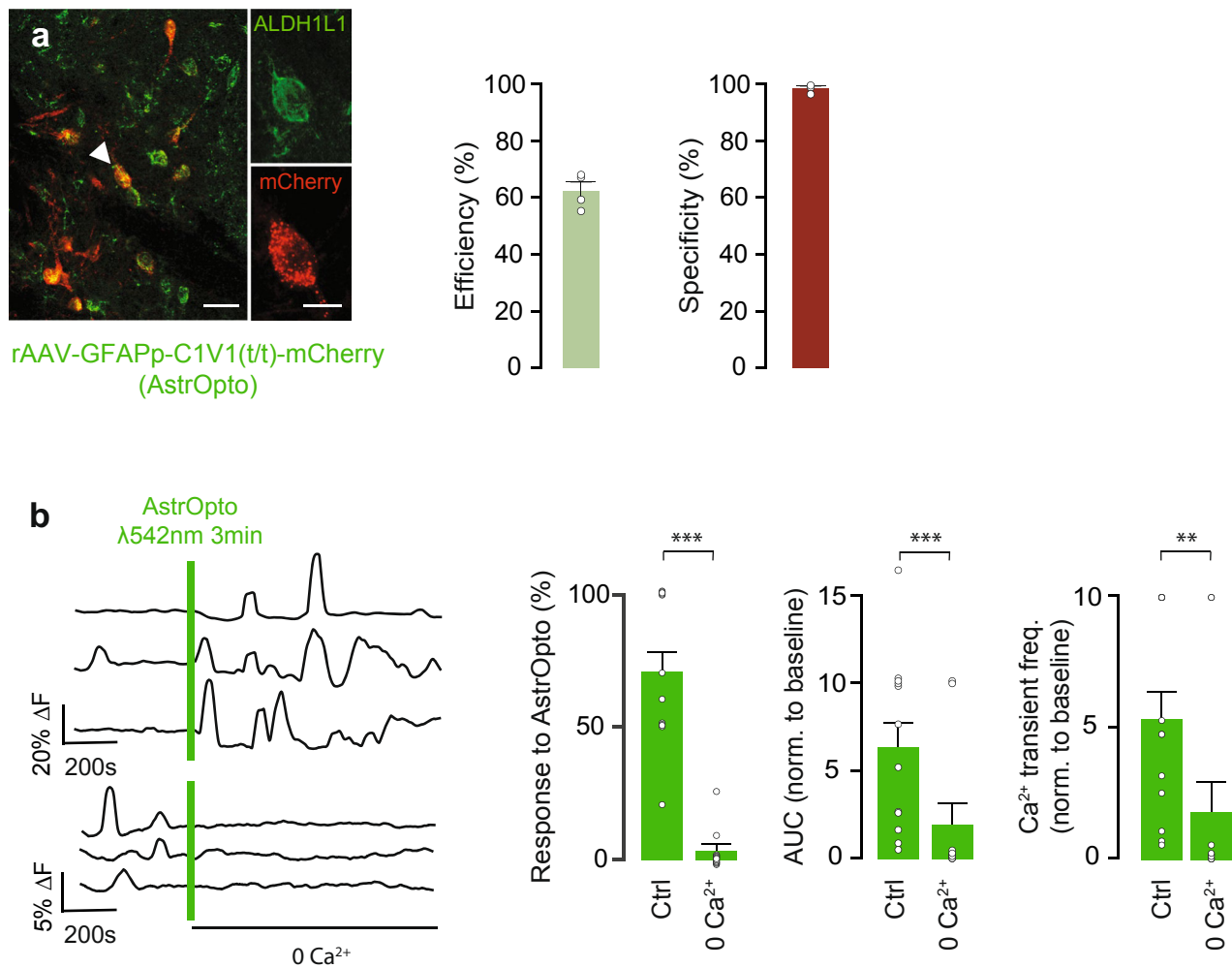
Extended Data Fig. 4 | Specific optogenetic stimulation of CeL astrocytes elicit calcium transients in a Ca2+-dependent manner. a, (left) Immunohistochemistry image shows CeL cells transfected with rAAV-Gfap-C1V1(t/t)-mCherry (AstrOpto) with co-labeling for ALDH1L1. White arrow shows one cell expanded in insets. Scale bars are 25 and 10 μm (insets). (right) Quantification of the efficiency and specificity of transduction of C1V1 in CeL astrocytes. PGFAP- C1V1-mCherry rAAV vector was injected into rat CeA (bilaterally, 200nl). Specificity: Over 1090 mCherry-positive cells, $98.8 \pm 0.7\%$ were positive for ALDH1L1. None of the analyzed cells were positive for NeuN. Efficiency: Over 1090 ALDH1L1 positive cells, $62.3 \pm 3.5\%$ were also mCherry positive. n = 4 rats. **b**, (left) Typical ΔF traces following AstrOpto activation. $\lambda 542nm$ (1s @ 0.5Hz during 3 minutes) with (top 3 traces) or without (bottom 3 traces) extracellular calcium. (right) Proportion of responding astrocytes, AUC of ΔF traces and Ca2+ transients frequency normalized to baseline values following AstrOpto stimulation with ($n_s = 12$, $n_a = 49$) or without Ca^{2+} in the ACSF ($n_s = 12$, $n_a = 53$). Data are expressed as mean across slices plus SEM. White circles indicate average across astrocytes per slice. $**p<0.01$, $***p<0.001$, two-sided Mann-Whitney U test. (Statistics and numbers in Supplementary Table 4).
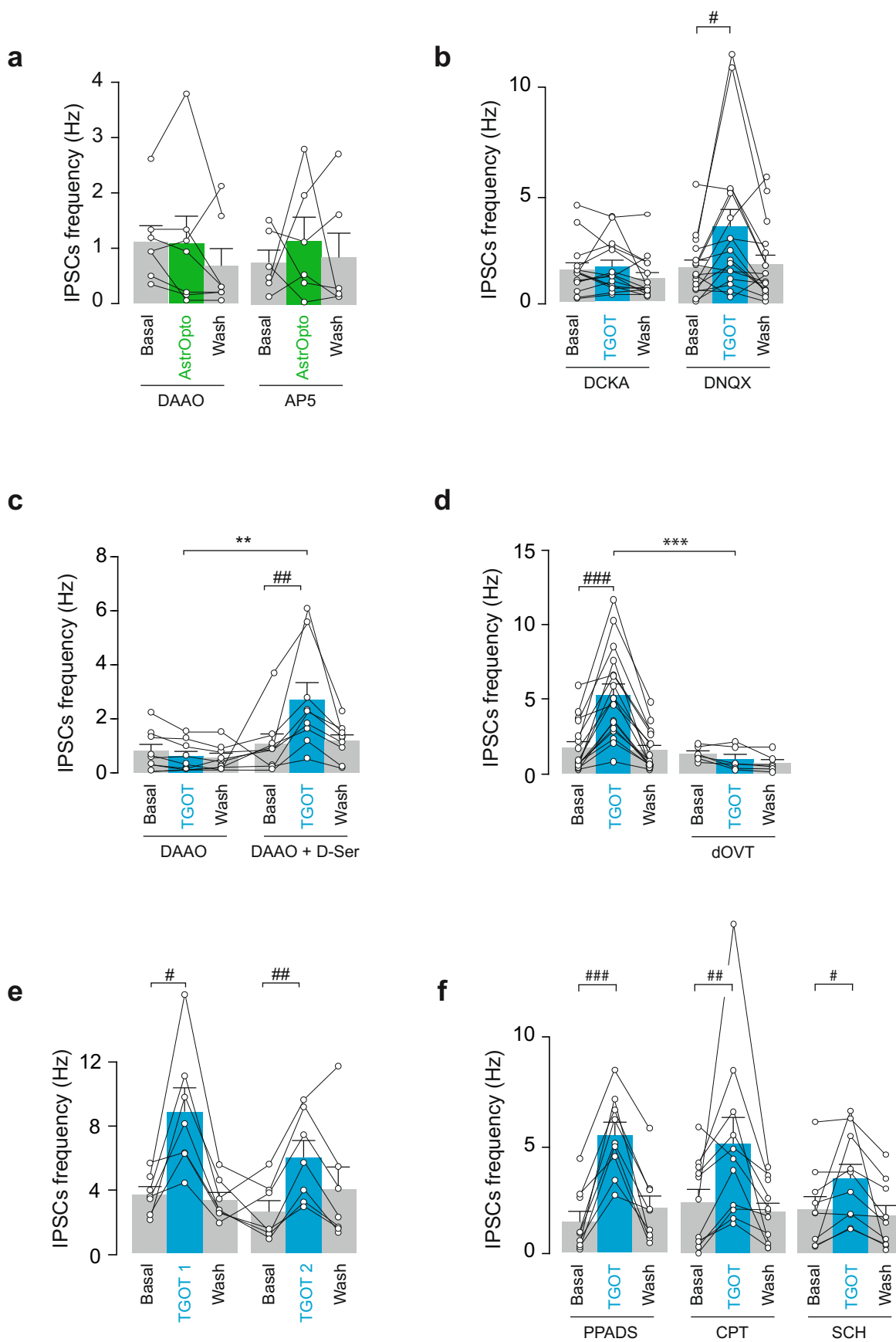
Extended Data Fig. 5 | See next page for caption.

Extended Data Fig. 5 | Astro-neuronal communication depends on NMDAR but not purinergic transmission. Figure 5. **a**, DAAO (0.15 IU/ml, incubation time > 1h30; n = 7) and AP5 (50 μM; n = 6) prevent the effect of photoactivation of astrocytes (AstrOpto) on IPSC frequency in CeM neurons. **b**, Two consecutive TGOT application effects on IPSCs frequencies in CeM neurons after DAAO (0.15 U/ml, incubation time > 1h30) followed by D-Serine (20 min, 100 μM) incubation of the same cells (n = 7). **c**, dOVT (1 μM; n = 6) prevents the effect of TGOT on IPSCs frequencies in CeM neurons. **d**, Effect of double (20 min apart) application of TGOT on IPSCs frequencies in CeM (0.4 μM n = 7). **e**, Effect of DCKA (10 μM, n = 15) and DNQX (25 μM; n = 10) on TGOT-induced increase in IPSC frequency in CeM neurons. **f**, Purinergic antagonists do not prevent TGOT effect on IPSC frequency in CeM neurons. PPADS (50 μM; n = 9), CPT (5 μM; n = 11), SCH (100 nM; n = 10). Data are expressed as averages plus SEM and white circles represent individual cell data. $^{\#}p < 0.05$, $^{\#\#}p < 0.01$, $^{\#\#\#}p < 0.001$, Friedman and Dunn's Multiple comparisons, $^{**}p < 0.01$, $^{***}p < 0.001$, two-sided unpaired t-test or Mann-Whitney U test. (Statistics and numbers in Supplementary Table 5).
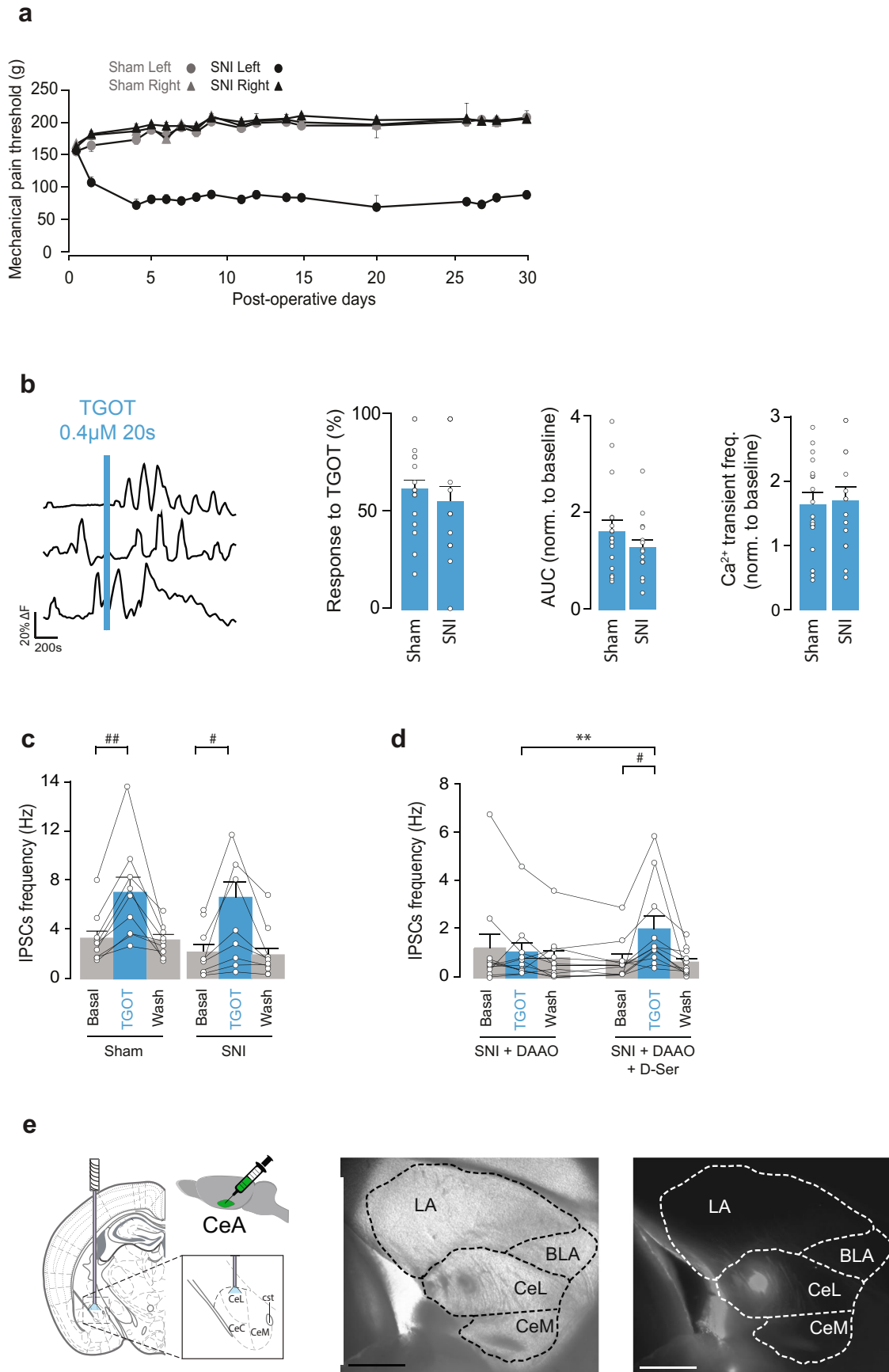
Extended Data Fig. 6 | See next page for caption.

Extended Data Fig. 6 | SNI procedure does not modify the effect of OTR activation on CeL microcircuit activity. a, 30 days post surgeries time course of mechanical pain threshold evolution across sham (n = 23) and SNI (n = 22) rats. Data are expressed as mean across animals plus SEM. **b**, (left) Typical ΔF traces following TGOT+TTX application in SNI rats. (right) Proportion of responding astrocytes, AUC of ΔF traces and Ca2+ transients frequency normalized to baseline values following application of TGOT+TTX (0.4 μM) in sham (n_s = 16, n_a = 74) or SNI (n_s = 18 et n_a = 136) rats. Data are expressed as mean across slices plus SEM. White circles indicate average across astrocytes per slice. **c**, TGOT effect on CeM neurons IPSCs frequencies is unchanged between Sham (n = 9) or SNI (n = 9) rats. Data are expressed as average plus SEM and white circles represent individual cell data. **d**, Two consecutive TGOT application effects on IPSCs frequencies in CeM neurons after DAAO (0.15 U/ml, incubation time > 1h30) followed by D-Serine (20 min, 100 μM) incubation of the same cells from acute brain slices of SNI animals (n = 11). Data are expressed as averages plus SEM and white circles represent individual cell data. **e**, Verification of cannulae implantation sites. (left) Schematic representation of the stereotaxic injection viewed in a coronal slice; n_{rats} = 67, n_{mice} = 52. (middle, right) Infrared and fluorescence microscopy picture showing the injection site of fluorescent latex beads in the CeL on horizontal slices. Scale is 1mm. ** p<0.01, *** P<0.001, two-sided paired t-test or Wilcoxon test, #p<0.05 Friedman test followed by Dunn's multiple comparison. (Statistics and numbers in Supplementary Table 6).
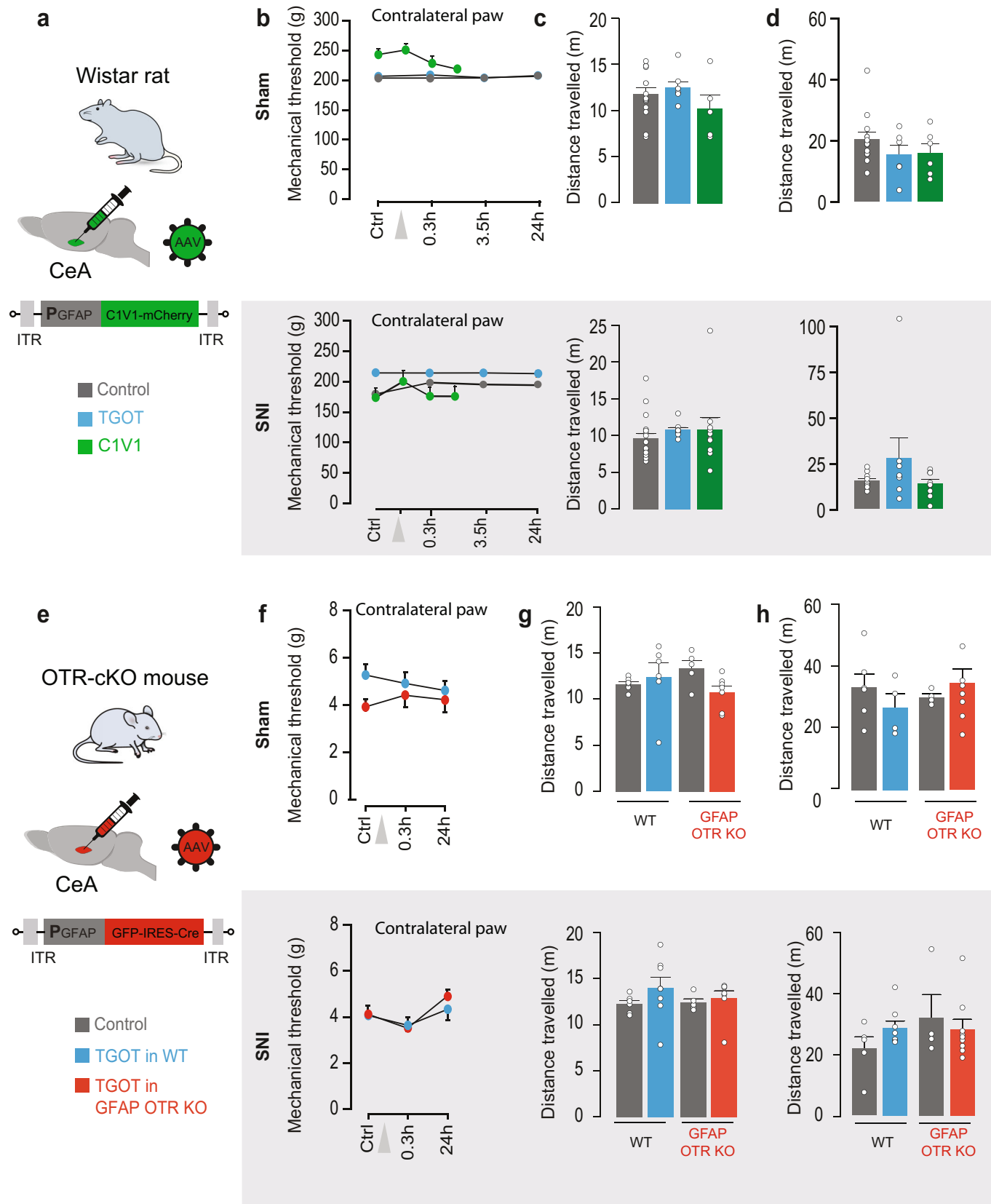
Extended Data Fig. 7 | See next page for caption.

Extended Data Fig. 7 | Effects of CeL astrocytes and OTR activities manipulations on locomotion and contralateral hindpaw sensitivity. a,e,
Experimental strategy for the specific expression of C1V1 in mice CeL astrocytes (**a**, AstrOpto) or the specific deletion of OTRs in mice CeL astrocytes (**e**, GFAP OTR KO). The treatments applied are color coded as the legend key indicate. Control indicate a vehicle injection. **b,f,** Mechanical pain threshold was assessed on the non-injured paw of SNI (bottom, gray box) and its equivalent in Sham (top) groups. TGOT or its vehicle, or astrocytes light-evoked activation of C1V1, were administered in the CeL and mechanical pain threshold assessed again at different time points. Rats (n): Sham control n = 12, TGOT n = 10, C1V1 n = 6; SNI control n = 12, TGOT n = 10, C1V1, n = 9. Mice (n): Sham WT n = 6, OTR cKO n = 8; SNI WT n = 5, OTR cKO n = 13. **c,g,** Locomotion was assessed through measurement of the distance travelled during the length of the elevated plus maze experiment, after administration of the different treatments. Rats (n): Sham control n = 10, TGOT n = 8, C1V1 n = 9; SNI control n = 20, TGOT n = 9, C1V1, n = 7. Mice (n): Sham WT Veh n = 7, WT TGOT n = 6; Sham OTR cKO Veh n = 5, OTR cKO TGOT n = 7; SNI WT Veh n = 7, WT TGOT n = 8; SNI OTR cKO Veh n = 5, OTR cKO TGOT n = 7. **d,h,** Locomotion was assessed through measurement of the distance travelled during the time of the conditioned place preference experiment, after administration of the different treatments. Rats (n): Sham control n = 13, TGOT n = 6, C1V1 n = 5; SNI control n = 10, TGOT n = 8, C1V1, n = 8. Mice (n): Sham WT Veh n = 5, WT TGOT n = 8; Sham OTR cKO Veh n = 5, OTR cKO TGOT n = 4; SNI WT Veh n = 5, WT TGOT n = 5; SNI OTR cKO Veh n = 4, OTR cKO TGOT n = 6. Data are expressed as mean across animals plus SEM. (Animals number and Statistics in Supplementary Table 7).

TABLE 1: Numerical values and statistical analysis of data presented in Fig.1 and Extended Data Fig.1

Fig	Statistical unit	Groups tested	Paired ?	N (animals, slices, cells)	Unit	Mean	SEM
1c	Proportion of OTR+ cells	Astrocytes (GS+)	\	5, 30, 1354	%	1,86E+01	1,79E+00
		Neurons (NeuN+)	\	5, 30, 1254	%	6,78E+01	3,07E+00

Fig	Statistical unit	Groups tested	Paired ?	N	Unit	Mean	SEM	Median	Quartiles (25/75)	Test	Statistic	p-value
1e	Cell volume	OTR+ astrocytes	No	5, 20, 212	μm^3	7,80E+03	5,61E+02	5,60E+03	2992; 10300	2-tailed t-test	3,58E+00	4,00E-04
		OTR- astrocytes	No	5, 20, 1142	μm^3	5705	3,05E+02	4,19E+03	26712; 6437			
	Surface	OTR+ astrocytes	No	5, 20, 212	μm^2	9,92E+03	4,69E+02	9,45E+03	60522; 14028	2-tailed t-test	9,12E+00	<0,0001
		OTR- astrocytes	No	5, 20, 1142	μm^2	5626	2,34E+02	4,34E+03	32282; 6839			
	Number of processes	OTR+ astrocytes	No	5, 20, 212	\	1,51E+02	6,410	1,34E+02	77,632; 202	2-tailed t-test	2,97E+00	3,10E-03
		OTR- astrocytes	No	5, 20, 1142	\	127,3	4,941	1,09E+02	62,812; 175,3			
	Process length	OTR+ astrocytes	No	5, 20, 212	μm	1,82E+01	0,3750	1,33E+01	10,89; 17,86	2-tailed t-test	4,90E+00	1,00E-04
		OTR- astrocytes	No	5, 20, 1142	μm	14,41	0,2965	1,86E+01	13,54; 22,16			
	Domain volume	OTR+ astrocytes	No	5, 20, 85	μm^3	22319	1467	18976	12289; 31111	2-tailed t-test	3,41E+00	8,00E-04
		OTR- astrocytes	No	5, 20, 97	μm^3	15709	1281	10313	6827; 20240			

Fig	Statistical unit	Groups tested	Paired ?	N	Unit	Test	Statistic	p-value
1f	Sholl intersections	OTR+ astrocytes	No	5, 20, 212	\	2-way ANOVA	9,61E+01	1,00E-04
		OTR- astrocytes	No	5, 20, 1142				

Fig	Statistical unit	Groups tested	Paired ?	N	Unit	Mean	SEM
E.D.1b	% of OTR positive cells in mice	Astrocytes (GS+)	\	4, 16, 897	%	1,55E+01	1,05E+00
		Neurons (NeuN+)		4, 16, 688		8,42E+01	2,73E+00
E.D.1c	% of OTR+ cells	Astrocytes (Aldh1l1+)	\	4, 8, 450	%	1,35E+01	8,77E-01

TABLE 2: Numerical values and statistical analysis of data presented in Fig,2 and Extended Data Fig,2

Figure	Statistical unit	Groups tested	Paired?	N (Animals, Slices, Cells)	Unit	Mean	SEM	Test	Statistic	p-value
	Response %	TGOT+TTX	No	12,18,136	%	6,30E-01	5,16E-02	2-tailed t-test	1,09E-01	9,14E-01
		OxytOpto		3,7,36		6,19E-01	8,69E-02			
2d	AUC ratio	TGOT+TTX	No	12,18,136	ratio	1,62E+00	2,22E-01	Mann-Whitney	4,80E+01	1,90E-01
		OxytOpto		3,7,36		2,10E+00	4,39E-01			
	Hz ratio	TGOT+TTX	No	12,18,136	ratio	1,63E+00	1,71E-01	Mann-Whitney	2,90E+01	2,13E-02
		OxytOpto		3,7,36		5,59E+00	1,50E+00			
	Response %	TGOT	No	4,7,43	%	6,01E-01	9,23E-02	2-tailed t-test	2,87E-01	7,77E-01
		TGOT+TTX		12,18,136		6,30E-01	5,16E-02			
		TGOT+TTX+dOVT	No	2,3,24	%	2,11E-01	2,04E-02	2-tailed t-test	3,24E+00	4,30E-03
		TGOT+TTX		12,18,136		6,30E-01	5,16E-02			
2f	AUC ratio	TGOT	No	4,7,43	ratio	1,19E+00	1,14E-01	Mann-Whitney	4,60E+01	1,59E-01
		TGOT+TTX		12,18,136		1,62E+00	2,22E-01			
		TGOT+TTX+dOVT	No	2,3,24	ratio	7,18E-01	1,04E-01	Mann-Whitney	8,00E+00	3,15E-02
		TGOT+TTX		12,18,136		1,62E+00	2,22E-01			
	Hz ratio	TGOT	No	4,7,43	ratio	1,59E+00	3,94E-01	Mann-Whitney	9,78E-02	9,23E-01
		TGOT+TTX		12,18,136		1,63E+00	1,71E-01			
		TGOT+TTX+dOVT	No	2,3,24	ratio	6,78E-01	1,22E-01	Mann-Whitney	2,21E+00	3,96E-02
		TGOT+TTX		12,18,136		1,63E+00	1,71E-01			
2h	% of mice OTR positive astrocytes	OTR cKO + rAAV-GFAP-GFP	\	4, 18, 897	%	1,87E+01	2,35E+00	2-tailed t-test	7,64E+00	0.0003
		OTR cKO + rAAV-GFAP-Cre-GFP	\	4, 16, 940	%	5,75E-01	3,33E-01			
	Response %	TGOT+TTX in GFAP OTR KO	No	2,5,47	%	1,56E-01	6,03E-02	2-tailed t-test	-2,36E+00	3,21E-02
		TGOT+TTX in control		3,12,237		4,39E-01	7,21E-02			
2i	AUC ratio	TGOT+TTX in GFAP OTR KO	No	2,5,47	ratio	1,30E+00	4,07E-01	2-tailed t-test	-1,21E+00	2,45E-01
		TGOT+TTX in control		3,12,237		1,94E+00	2,92E-01			
	Hz ratio	TGOT+TTX in GFAP OTR KO	No	2,5,47	ratio	9,80E-01	3,19E-01	Mann-Whitney	1,25E+01	3,65E-02
		TGOT+TTX in control		3,12,237		2,41E+00	7,18E-01			

Figure	Statistical unit	Groups tested	Paired	N	Unit	Mean	SEM	Min	Max	Median	1st quartile	3rd quartile	Test	Statistic	p-value
	Cells capacitance	Astrocytes	No	4, 24, 82	pF	1,08E+02	9,92E+00	1,21E+01	5,31E+02	8,99E+01	5,03E+01	1,41E+02	Mann-Whitney	3,89E+02	2,00E-04
		Neurons		4, 24, 20		4,74E+01	5,72E+00	8,09E+00	9,35E+01	5,10E+01	2,78E+01	6,56E+01	Mann-Whitney		
E.D.2d	Cells membrane resistance	Astrocytes	No	4, 24, 82	Mohm	2,23E+01	2,39E+00	4,30E+00	1,78E+02	1,68E+01	1,09E+01	2,71E+01	Mann-Whitney	1,12E+02	<0,0001
		Neurons		4, 24, 20		2,11E+02	4,32E+01	5,20E+00	9,04E+02	1,53E+02	1,28E+02	2,68E+02	Mann-Whitney		
	Cells acess resistance	Astrocytes	No	4, 24, 82	Mohm	1,02E+01	7,92E-01	1,50E+00	3,27E+01	7,75E+00	4,88E+00	1,43E+01	Mann-Whitney	4,61E+02	4,38E-01
		Neurons		4, 24, 13		8,96E+00	1,94E+00	2,40E+00	2,54E+01	6,20E+00	3,80E+00	1,37E+01	Mann-Whitney		
	Cells resting potential	Astrocytes	No	4, 24, 20	mV	-8,53E+01	1,13E+00	-9,14E+01	-7,40E+01	-8,75E+01	-8,98E+01	-8,03E+01	Mann-Whitney	0,00E+00	<0,0001
		Neurons		4, 24, 12		-6,03E+01	1,42E+00	-6,80E+01	-4,80E+01	-6,00E+01	-6,18E+01	-5,93E+01	Mann-Whitney		

Figure	Statistical unit	Groups tested	Paired	N	Unit	Mean	SEM	Test	Statistic	p-value
E.D.2g	Efficiency	Glutamibe Synthase + rAAV-GFAPp-Cre-GFP	\	4, 16, 1001	%	5,60E+01	4,92E+00			
	Specificity	rAAV-GFAPp-Cre-GFP + Glutamine Synthase	\	4, 16, 977	%	9,62E+01	1,05E+00			
E.D.2h	Proportion of OTR positive neurons	OTR cKO + rAAV-GFAP-GFP	No	4, 16, 688	%	8,50E+01	1,66E+00	2-tailed t-test	7,39E-01	7,63E-01
		OTR cKO + rAAV-GFAP-Cre-GFP		4, 16, 660		8,67E+01	1,64E+00			

TABLE 3: Numerical values and statistical analysis of data presented in Fig,3 and Extended Data Fig,3

Fig	Statistical unit	Groups tested	Paired ?	N (Animals, Slices, Cells)	Unit	Mean	SEM	Median	Quartiles	Test	Stat	p-value
3a	Nearest Neighbor	OTR+ astrocytes	No	4, 24, 212	\	95,98	3,99E+00	1,03E+02	77,25; 118,5	2-tailed t-test	21,73	<0,0001
		OTR- astrocytes	No	4, 24, 1142	\	37,39	8,58E-01	3,80E+01	28; 48			
	Contacts	OTR-/OTR-	No	4, 24, 1049	\	3,708	1,18E-01	3,00E+00	2; 5	2-tailed t-test	9,62	<0,0001
		OTR+/OTR-	No	4, 24, 1509	\	5,507	1,47E-01	5,00E+00	4; 7			
		OTR+/OTR+	No	4, 24, 5	\	0,04808	2,11E-02	0,00E+00	0; 0		18,42	<0,0001

Fig	Statistical unit	Groups tested	Paired ?	N	Unit	Mean	SEM	Test	Statistic	p-value
3b	Response %	TGOT+TTX TGOT+TTX+CBX	No	12,18,136 5,9,75	%	6,30E-01 3,43E-01	5,16E-02 3,86E-02	2-tailed t-test	3.6636	1,20E-03
		TGOT+TTX TGOT+TTX+PPADS	No	12,18,136 2,7,53	%	6,30E-01 4,46E-01	5,16E-02 6,88E-02	2-tailed t-test	1.9628	6,19E-02
	AUC ratio	TGOT+TTX TGOT+TTX+CBX	No	12,18,136 5,9,75	ratio	1,62E+00 1,16E+00	2,22E-01 2,18E-01	Mann-Whitney	5,90E+01	1,34E-01
		TGOT+TTX TGOT+TTX+PPADS	No	12,18,136 2,7,53	ratio	1,62E+00 1,24E+00	2,22E-01 1,70E-01	Mann-Whitney	5,00E+01	2,25E-01
	Hz ratio	TGOT+TTX TGOT+TTX+CBX	No	12,18,136 5,9,75	ratio	1,63E+00 1,04E+00	1,71E-01 2,05E-01	2-tailed t-test	2.0863	4,73E-02
		TGOT+TTX TGOT+TTX+PPADS	No	12,18,136 2,7,53	ratio	1,63E+00 1,48E+00	1,71E-01 3,08E-01	Mann-Whitney	4,90E+01	2,07E-01
3c	Response %	TGOT+TTX in mice TGOT+TTX Cx30/Cx43 mice	No	2,19,78 2,17,100	%	6,14E-01 4,06E-01	5,07E-02 6,05E-02	2-tailed t-test	-2,66E+00	0.0118
	AUC ratio	TGOT+TTX in mice TGOT+TTX Cx30/Cx43 mice	No	2,19,78 2,17,100	ratio	1,21E+00 1,18E+00	1,11E-01 1,31E-01	Mann-Whitney	1,47E+02	0.3287
	Hz ratio	TGOT+TTX in mice TGOT+TTX Cx30/Cx43 mice	No	2,19,78 2,17,100	ratio	1,82E+00 1,46E+00	3,94E-01 2,21E-01	Mann-Whitney	1,57E+02	0.4496
E.D. 3b	Response %	TGOT+TTX TGOT+TTX+PPADS+Suramin+A438079	No	12,18,136 3,10,112	%	6,30E-01 7,02E-01	5,16E-02 5,35E-02	2-tailed t-test	8,70E+01	3,77E-01
	AUC ratio	TGOT+TTX TGOT+TTX+PPADS+Suramin+A438079	No	12,18,136 3,10,112	ratio	1,62E+00 1,17E+00	2,22E-01 1,25E-01	Mann-Whitney	7,00E+01	1,75E-01
	Hz ratio	TGOT+TTX TGOT+TTX+PPADS+Suramin+A438079	No	12,18,136 3,10,112	ratio	1,63E+00 1,94E+00	1,71E-01 4,06E-01	Mann-Whitney	-8,99E-01	4,52E-01
E.D. 3c	Response %	TGOT+TTX TGOT+TTX+CPT	No	12,18,136 2,7,22	%	6,30E-01 6,02E-01	5,16E-02 1,13E-01	2-tailed t-test	2,54E-01	8,02E-01
		TGOT+TTX TGOT+TTX+SCH	No	12,18,136 2,8,32	%	6,30E-01 5,27E-01	5,16E-02 4,34E-02	2-tailed t-test	2,30E+03	2,30E-01
	AUC ratio	TGOT+TTX TGOT+TTX+CPT	No	12,18,136 2,7,22	ratio	1,62E+00 1,50E+00	2,22E-01 3,99E-01	Mann-Whitney	5,10E+01	2,43E-01
		TGOT+TTX TGOT+TTX+SCH	No	12,18,136 2,8,32	ratio	1,62E+00 1,01E+00	2,22E-01 1,07E-01	Mann-Whitney	4,20E+01	5,06E-02
	Hz ratio	TGOT+TTX TGOT+TTX+CPT	No	12,18,136 2,7,22	ratio	1,63E+00 1,39E+00	1,71E-01 3,92E-01	2-tailed t-test	6,36E-01	5,31E-01
		TGOT+TTX TGOT+TTX+SCH	No	12,18,136 2,8,32	ratio	1,63E+00 2,74E+00	1,71E-01 1,19E+00	Mann-Whitney	6,70E+01	4,01E-01
E.D. 3d	Response %	TGOT+TTX TGOT+TTX+AP5	No	12,18,136 2,6,55	%	6,30E-01 7,90E-01	5,16E-02 5,93E-02	Mann-Whitney	2,95E+01	5,42E-02
	AUC ratio	TGOT+TTX TGOT+TTX+AP5	No	12,18,136 2,6,55	ratio	1,62E+00 2,04E+00	2,22E-01 5,62E-01	Mann-Whitney	4,80E+01	3,57E-01
	Hz ratio	TGOT+TTX TGOT+TTX+AP5	No	12,18,136 2,6,55	ratio	1,63E+00 1,54E+00	1,71E-01 2,59E-01	2-tailed t-test	2,68E-01	7,91E-01

TABLE 4: Numerical values and statistical analysis of data presented in Fig,4 and Extended Data Fig,4

Fig	Statistical unit	Groups tested	Paired?	N (animals, slices, cells)	Unit	Mean	SEM	Test	Statistic	p-value
4c	Response %	TGOT+TTX	No	12,18,136	%	6,30E-01	5,16E-02	2-tailed t-test	2,21E-01	8,27E-01
		AstrOpto		3,12,49		6,08E-01	9,08E-02			
	AUC ratio	TGOT+TTX	No	12,18,136	ratio	6,30E-01	5,16E-02	Mann-Whitney	6,20E+01	2,70E-02
		AstrOpto		3,12,49		3,13E+00	6,01E-01			
	Hz ratio	TGOT+TTX	No	12,18,136	ratio	1,62E+00	2,22E-01	Mann-Whitney	4,70E+01	5,20E-03
		AstrOpto		3,12,49		5,23E+00	1,11E+00			
E.D.4 b	Response %	AstrOpto	No	3,12,49	%	6,08E-01	9,08E-02	Mann-Whitney	1,00E+01	1,00E-04
		AstrOpto in 0 Ca2+		3,12,53		6,25E-02	2,92E-02			
	AUC ratio	AstrOpto	No	3,12,49	ratio	3,13E+00	6,01E-01	Mann-Whitney	1,60E+01	7,00E-04
		AstrOpto in 0 Ca2+		3,12,53		9,68E-01	3,80E-01			
	Hz ratio	AstrOpto	No	3,12,49	ratio	5,23E+00	1,11E+00	Mann-Whitney	2,00E+01	1,30E-03
		AstrOpto in 0 Ca2+		3,12,53		1,78E+00	1,11E+00			

Fig	Statistical unit	Groups tested	Paired?	N	Unit	Mean	SEM	Test	Statistic	p-value	Post hoc	Comparison	p-value	Inter Group Comparison: Groups	Paired?	Test	Statistic	p-value
4d	mESPCs frequency in CeL neurons	AstrOpto	Yes	4,17,17	Hz	3,18E-01	9,89E-02	Friedman	2,33E+01	<0,0001	Dunn's MC	Basal/Stim	1,00E-04			/		
						1,75E+00	5,80E-01					Basal/Wash	>0,9999					
						1,88E-01	6,40E-02					Stim/Wash	1,00E-04					
4f	mESPCs frequency in CeL neurons	TGOT	Yes	6,16,16	Hz	2,22E-01	5,36E-02	Friedman	1,87E+01	< 0,0001	Dunn's MC	Basal/TGOT	9,00E-04	TGOT in Controls vs. TGOT in BAPTAstro	No	Mann-Whitney	3,55E+01	8,00E-03
						7,91E-01	2,24E-01					Basal/Wash	>0,9999					
						2,34E-01	5,60E-02					TGOT/Wash	4,00E-04					
	mESPCs frequency in CeL neurons	TGOT + BaptAstro	Yes	2,11,11	Hz	2,18E-01	1,14E-01	Friedman	6,00E+00	4,63E-02	Dunn's MC	Basal/TGOT	7,57E-02					
						3,14E-01	1,01E-01					Basal/Wash	>0,9999					
						1,50E-01	4,05E-02					TGOT/Wash	6,03E-01					
	mESPCs frequency in CeL neurons	TGOT + AP5	Yes	6,9,9	Hz	2,67E-01	6,97E-02	One-way RM ANOVA	Treatment: 5,038 Indiv: 5,583	T: 0,0310 I: 0,0014	Holm-Sidak's MC	Basal/TGOT	1,96E-01	TGOT in Controls vs. TGOT in AP5	No	Mann-Whitney	4,85E+01	1,91E-01
						4,17E-01	9,68E-02					Basal/Wash	4,16E-01					
						2,11E-01	5,82E-02					TGOT/Wash	1,13E-02					
4h	mESPCs frequency in CeL neurons	TGOT in WT	Yes	5,10,10	Hz	3,35E-01	7,23E-02	One-way RM ANOVA	Treatment: 13,06 Indiv: 1,496	T: 0,0049 I: 0,2230	Holm-Sidak's MC	Basal/TGOT	1,46E-02					
						1,16E+00	2,59E-01					Basal/Wash	1,46E-02					
						1,80E-01	4,42E-02					TGOT/Wash	9,30E-03					
	mESPCs frequency in CeL neurons	TGOT in GFAP OTR KO	Yes	1,6,8	Hz	4,69E-01	1,97E-01	Friedman	4,52E+00	0,1181	Dunn's MC	Basal/TGOT	>0,9999	TGOT in WT vs. TGOT in GFAP OTR KO	No	Mann-Whitney	1,55E+01	2,79E-02
						4,31E-01	1,54E-01					Basal/Wash	3,13E-01					
						1,88E-01	1,12E-01					TGOT/Wash	2,41E-01					
E.D.4 a	Virus efficiency	rAAV-GFAPp-C1V1(t/t)-mCherry	No	4, 24, 1090	/	6,25E+01	3,10E+00											
	Virus specificity	rAAV-GFAPp-C1V1(t/t)-mCherry	No	4, 24, 1090	/	9,88E+01	7,35E-01											

TABLE 5: Numerical values and statistical analysis of data presented in Fig.5 and Extended Data Fig.5

Fig	Statistical unit	Groups tested	Paired?	N (animals, slices, cells)	Unit	Mean	SEM	Test	Statistic	p-value	Post hoc	Comparison	p-value	Groups	Inter Group Comparison Paired	Test	Statistic	p-value
5c	APs frequency in CeL neurons	AstrOpto	Yes	2, 10, 10	Hz	2,50E-01 7,45E-01 3,00E-01	1,26E-01 3,04E-01 1,29E-01	Friedman	1,33E+01	3,00E-04	Dunn's MC	Basal/Stim Basal/Wash Stim/Wash	2,19E-02 >0,9999 7,70E-03	AstrOpto vs. AstrOpto + BAPTAstro	No	Mann-Whitney	3,45E+01	2,50E-01
	APs frequency in CeL neurons	AstrOpto + BaptAstro	Yes	2, 12, 12	Hz	5,29E-01 6,83E-01 5,13E-01	1,27E-01 3,05E-01 3,21E-01	Friedman	8,97E+00	7,30E-03	Dunn's MC	Basal/Stim Basal/Wash Stim/Wash	6,56E-01 1,56E-02 3,53E-01					
5d	APs frequency in CeL neurons	TGOT	Yes	7, 9, 9	Hz	4,33E-01 9,17E-01 3,94E-01	1,28E-01 1,73E-01 1,11E-01	One-way RM ANOVA	Treatment 21,84 Indiv: 13,11	T: 0,0004 I: <0,0001	Holm-Sidak's MC	Basal/TGOT Basal/Wash TGOT/Wash	2,00E-03 4,86E-01 3,00E-03	TGOT vs. TGOT + BAPTAstro	No	Two-tailed t-test	2,15E+00	4,97E-02
	APs frequency in CeL neurons	TGOT + BaptAstro	Yes	2, 6, 9	Hz	2,00E-01 1,17E-01 1,00E-01	8,98E-02 5,95E-02 5,07E-02	One-way RM ANOVA	Treatment: 1,179 Indiv: 19,59	T: 0,3270 I: <0,0001	Holm-Sidak's MC	Basal/TGOT Basal/Wash TGOT/Wash	5,29E-01 4,42E-01 3,62E-01					
	APs frequency in CeL neurons	TGOT + AP5	Yes	2, 7, 7	Hz	4,64E-01 4,07E-01 3,50E-01	1,08E-01 1,50E-01 1,60E-01	Friedman	3,71E+00	1,69E-01	Dunn's MC	Basal/TGOT Basal/Wash TGOT/Wash	8,67E-01 4,72E-01 >0,9999	TGOT vs. TGOT + AP5	No	Mann-Whitney	4,00E+00	5,00E-04
5f	APs frequency in CeL neurons	TGOT in WT	Yes	2, 7, 7	Hz	2,57E-01 8,21E-01 2,57E-01	1,07E-01 1,50E-01 8,69E-02	Friedman	1,11E+01	1,20E-03	Dunn's MC	Basal/TGOT Basal/Wash TGOT/Wash	4,86E-02 >0,9999 4,00E-03	WT/GFAP OTR KO	No	Mann-Whitney	1,50E+01	3,20E-02
	APs frequency in CeL neurons	TGOT in GFAP OTR KO	Yes	3, 11, 11	Hz	3,50E-01 4,00E-01 2,23E-01	6,91E-02 1,26E-01 7,02E-02	Friedman	1,17E+01	1,30E-03	Dunn's MC	Basal/TGOT Basal/Wash TGOT/Wash	>0,9999 6,00E-03 5,72E-02					
E.D. 5a	IPSCs frequency in CeM neurons	AstrOpto under DAAO	Yes	3, 7, 7	Hz	1,14E+00 1,10E+00 6,86E-01	2,86E-01 4,99E-01 3,15E-01	Friedman	3,44E+00	1,96E-01	Dunn's MC	Basal/Stim Basal/Wash Stim/Wash	8,55E-01 2,47E-01 >0,9999	TGOT + DAAO vs. TGOT + AP5	No	Mann-Whitney	1,90E+01	8,10E-01
	IPSCs frequency in CeM neurons	AstrOpto under AP5	Yes	3, 6, 6	Hz	7,75E-01 1,17E+00 8,67E-01	2,27E-01 4,38E-01 4,46E-01	Friedman	8,70E-02	>0,9999	Dunn's MC	Basal/Stim Basal/Wash Stim/Wash	>0,9999 >0,9999 >0,9999					
E.D. 5b	IPSCs frequency in CeM neuron	TGOT + DCKA	Yes	3, 15, 15	Hz	1,58E+00 1,71E+00 1,14E+00	3,25E-01 3,28E-01 2,80E-01	Friedman	3,61E+00	1,64E-01	Dunn's MC	Basal/TGOT Basal/Wash TGOT/Wash	>0,9999 7,06E-01 2,04E-01			/		
	IPSCs frequency in CeM neuron	TGOT + DNQX	Yes	4, 6, 6	Hz	1,69E+00 3,54E+00 1,82E+00	3,23E-01 7,99E-01 4,11E-01	Friedman	1,09E+01	4,20E-03	Dunn's MC	Basal/TGOT Basal/Wash TGOT/Wash	3,04E-02 >0,9999 6,10E-03					
E.D. 5c	IPSCs frequency in CeM neurons	TGOT + DAAO	Yes	3, 7, 7	Hz	8,11E-01 6,11E-01 5,67E-01	2,45E-01 1,82E-01 1,55E-01	Friedman	1,65E+00	4,79E-01	Dunn's MC	Basal/TGOT Basal/Wash TGOT/Wash	>0,9999 7,16E-01 >0,9999	TGOT + DAAO vs. TGOT + DAAO + D-Ser	No	Wilcoxon	1,50E+00	3,90E-03
	IPSCs frequency in CeM neurons	TGOT + DAAO + D-Ser			Hz	1,08E+00 2,71E+00 1,19E+00	3,58E-01 6,34E-01 2,21E-01	Friedman	1,40E+01	2,00E-04	Dunn's MC	Basal/TGOT Basal/Wash TGOT/Wash	1,20E-03 >0,9999 1,41E-02					

Panel	Measure	Treatment	Normality	n	Unit	Basal (mean)	Basal (SEM)	TGOT (mean)	TGOT (SEM)	Wash (mean)	Wash (SEM)	Test	Statistic	p-value	Post-hoc	Comparison	Post-hoc p	Normality	Test	Comparison	Stat.	p
E.D. 5d	IPSCs frequency in CeM neuron	TGOT	Yes	9, 15, 17	Hz	1,65E+00	3,91E-01	5,05E+00	6,91E-01	1,49E+00	3,10E-01	Friedman	2,55E+01	<0,0001	Dunn's MC	Basal/TGOT Basal/Wash TGOT/Wash	<0,0001 >0,9999 <0,0001	No	Mann-Whitney		3,00E+00	1,00E-04
	IPSCs frequency in CeM neuron	TGOT + dOVT	Yes	1, 6, 6	Hz	1,26E+00	1,86E-01	9,33E-01	3,07E-01	6,75E-01	2,36E-01	Friedman	9,65E+00	2,80E-03	Dunn's MC	Basal/TGOT Basal/Wash TGOT/Wash	5,82E-01 7,30E-03 2,50E-01					
E.D. 5e	IPSCs frequency in CeM neuron	TGOT1	Yes	5, 7, 7	Hz	3,69E+00	4,74E-01	8,90E+00	1,50E+00	3,32E+00	4,93E-01	One-way RM ANOVA	Treatment: 15,61 Indiv: 2,362	T: 0,0041 I: 0,0967	Holm-Sidak's MC	Basal/TGOT Basal/Wash TGOT/Wash	2,43E-02 5,93E-01 5,90E-03	No	Paired t-test	TGOT 1 vs. TGOT 2	2,41E+00	5,29E-02
	IPSCs frequency in CeM neuron	TGOT2				2,60E+00	6,93E-01	6,01E+00	1,06E+00	4,00E+00	1,42E+00	Friedman	1,23E+01	3,00E-04	Dunn's MC	Basal/TGOT Basal/Wash TGOT/Wash	1,50E-03 9,77E-02 5,45E-01					
E.D. 5f	IPSCs frequency in CeM neuron	TGOT + PPADS	Yes	3, 6, 9	Hz	1,42E+00	4,84E-01	5,41E+00	6,15E-01	2,06E+00	5,57E-01	One-way RM ANOVA	Treatment: 39,81 Indiv: 5,978	T: <0,0001 I: 0,0012	Holm-Sidak's MC	Basal/TGOT Basal/Wash TGOT/Wash	2,00E-04 1,61E-01 4,00E-04					
	IPSCs frequency in CeM neuron	TGOT + CPT	Yes	2, 11, 11	Hz	2,39E+00	6,18E-01	5,16E+00	1,23E+00	1,95E+00	4,18E-01	Friedman	1,38E+01	4,00E-04	Dunn's MC	Basal/TGOT Basal/Wash TGOT/Wash	8,60E-03 >0,9999 2,00E-03					
	IPSCs frequency in CeM neuron	TGOT + SCH	Yes	1, 6, 10	Hz	2,01E+00	5,77E-01	3,42E+00	5,15E-01	1,71E+00	4,64E-01	One-way RM ANOVA	Treatment: 5,785 Indiv: 4,715	T: 0,0115 I: 0,0025	Holm-Sidak's MC	Basal/TGOT Basal/Wash TGOT/Wash	3,38E-02 5,86E-01 1,54E-02					

TABLE 6: Numerical values and statistical analysis of data presented in Fig.6 and Extended Data Fig.6

Fig	Statistical unit	Groups tested	Paired?	N (animals, slices, cells)	Unit	Mean	SEM	Test	Statistic	p-value	Post hoc	Comparison	p-value	Inter Group Comparison: Groups	Paired	Test	Stat	p-value
6c	IPSCs frequency in CeM neurons	AstrOpto	Yes	5, 19, 19	Hz	1,96E+00 / 3,37E+00 / 2,00E+00	3,58E-01 / 6,35E-01 / 3,81E-01	Friedman	1,63E+01	3,00E-04	Dunn's MC	Basal/Stim / Basal/Wash / Stim/Wash	2,24E-02 / 6,71E-01 / 3,00E-04	AstrOpto vs. AstrOpto + BAPTAstro	No	Mann-Whitney	2,85E+01	3,70E-03
	IPSCs frequency in CeM neurons	AstrOpto + BAPTAstro	Yes	2, 9, 9	Hz	9,94E-01 / 9,22E-01 / 6,50E-01	2,22E-01 / 1,97E-01 / 1,74E-01	One-way RM ANOVA	Treatment: 1,431 Indiv: 3,145	T: 0,2692 I: 0,0244	Holm-Sidak's MC	Basal/Stim / Basal/Wash / Stim/Wash	7,73E-01 / 3,80E-01 / 3,80E-01					
6d	IPSCs frequency in CeM neurons	TGOT	Yes	9, 15, 17	Hz	1,65E+00 / 5,05E+00 / 1,49E+00 / 1,02E+00	3,91E-01 / 6,91E-01 / 3,10E-01 / 1,79E-01	Friedman	2,35E+01	<0,0001	Dunn's MC	Basal/TGOT / Basal/Wash / TGOT/Wash / Basal/TGOT	<0,0001 / >0,9999 / <0,0001 / >0,9999	TGOT vs. TGOT + BAPTAstro	No	Mann-Whitney	2,90E+01	<0,0001
	IPSCs frequency in CeM neurons	TGOT + BaptAstro	Yes	4, 17, 17	Hz	1,31E+00 / 5,47E-01 / 1,22E+00	3,51E-01 / 1,76E-01 / 5,93E-01	Friedman	1,36E+01	1,10E-03	Dunn's MC	Basal/Wash / TGOT/Wash / Basal/TGOT	1,40E-02 / 2,50E-03 / >0,9999	TGOT vs. TGOT + AP5	No	Mann-Whitney	4,00E+00	9,00E-04
	IPSCs frequency in CeM neurons	TGOT + AP5	Yes	1, 5, 5	Hz	1,13E+00 / 4,10E-01	4,22E-01 / 1,20E-01	Friedman	3,60E+00	1,82E-01	Dunn's MC	Basal/Wash / TGOT/Wash	1,74E-01 / >0,9999					
6f	IPSCs frequency in CeM neurons	TGOT in WT	Yes	4, 24, 27	Hz	1,52E+00 / 2,80E+00 / 1,49E+00	2,62E-01 / 3,88E-01 / 2,76E-01	Friedman	2,97E+01	<0,0001	Dunn's MC	Basal/TGOT / Basal/Wash / TGOT/Wash / Basal/TGOT	<0,0001 / >0,9999 / <0,0001 / >0,9999	TGOT in WT vs. TGOT in GFAP OTR KO	No	Mann-Whitney	1,33E+02	3,53E-02
	IPSCs frequency in CeM neurons	TGOT in GFAP OTR KO	Yes	3, 15, 15	Hz	1,72E+00 / 1,93E+00 / 1,53E+00	3,68E-01 / 4,37E-01 / 4,58E-01	Friedman	3,50E+00	1,74E-01	Dunn's MC	Basal/TGOT / Basal/Wash / TGOT/Wash	2,32E-01 / 4,72E-01					

Fig	Statistical unit	Groups tested	Paired?	N	Unit	Test	Statistic	p-value
6a	Mechanical pain threshold	Sham / SNI	No / No	23 / 22	g	2-way ANOVA	9,94E+03	<0,0001

Fig	Statistical unit	Groups tested	Paired?	N	Unit	Mean	SEM	Test	Statistic	p-value
E.D. 6b	Response %	TGOT+TTX / TGOT+TTX in SNI	No	12,18,136 / 6,16,74	%	6,30E-01 / 5,63E-01	5,16E-02 / 8,14E-02	2-tailed t-test	7,19E-01	4,77E-01
	AUC ratio	TGOT+TTX / TGOT+TTX in SNI	No	12,18,136 / 6,16,74	ratio	6,30E-01 / 1,28E+00	5,16E-02 / 1,63E-01	Mann-Whitney	1,06E+02	1,51E-01
	Hz ratio	TGOT+TTX / TGOT+TTX in SNI	No	12,18,136 / 6,16,74	ratio	1,62E+00 / 1,69E+00	2,22E-01 / 2,02E-01	Mann-Whitney	-2,40E-01	8,12E-01

Fig	Statistical unit	Groups tested	Paired?	N (animals, slices, cells)	Unit	Mean	SEM	Test	Statistic	p-value	Post hoc	Comparison	Comparison p-value	Groups	Inter Group Comparison Paired?	Test	Stat	p-value
E.D. 6c	IPSCs frequency in CeM neurons	TGOT in Sham	Yes	2, 9, 9	Hz	3,26E+00	6,90E-01	Friedman	1,36E+01	3,00E-04	Dunn's MC	Basal/TGOT	2,90E-03	TGOT in Sham vs. TGOT in SNI	No	Unpaired two-tailed t-test	1,04E+00	3,14E-01
						6,95E+00	1,37E+00					Basal/Wash	>0,9999					
						3,04E+00	4,37E-01					TGOT/Wash	6,60E-03					
	IPSCs frequency in CeM neurons	TGOT in SNI	Yes	2, 8, 8	Hz	1,81E+00	5,88E-01	Friedman	7,55E+00	1,86E-02	Dunn's MC	Basal/TGOT	2,61E-02					
						4,84E+00	1,49E+00					Basal/Wash	>0,9999					
						2,37E+00	7,26E-01					TGOT/Wash	1,83E-01					
E.D. 6d	IPSCs frequency in CeM neurons	TGOT + DAAO in SNI	Yes	5, 11, 11	Hz	1,21E+00	5,86E-01	Friedman	1,47E+01	1,19E-02	Dunn's MC	Basal/TGOT	>0,9999	TGOT + DAAO in SNI vs. TGOT + DAAO + D-Ser in SNI	No	Wilcoxon	5,60E+01	0,0098
						1,05E+00	3,79E-01					Basal/Wash	>0,9999					
						8,09E-01	3,09E-01					TGOT/Wash	>0,9999					
	IPSCs frequency in CeM neurons	TGOT + DAAO + D-Ser in SNI		5, 11, 11	Hz	7,27E-01	2,49E-01					Basal/TGOT	0,0176					
						2,00E+00	5,36E-01					Basal/Wash	>0,9999					
						6,32E-01	1,67E-01					TGOT/Wash	0,0661					

TABLE 7: Numerical values and statistical analysis of data presented in Fig.7 and Extended Data Fig.7

Figure	Statistical unit	Groups tested	Time	Paw	Unit	N	Mean	SEM	Test	Statistic	p-value
		SNI : Vehicle	CTRL			12	7,92E+01	1,65E+00		Time	<0,05
			0,3h			12	7,93E+01	1,88E+00		Time*Group	<0,05
			3,5h			12	7,94E+01	2,31E+00		Time*Paw	2,30E-02
			24h			9	8,03E+01	2,96E+00		Time*Group*Paw	<0,05
		SNI : TGOT	CTRL			10	7,52E+01	2,62E+00	Mixed-design ANOVA & Bonferroni		
			0,3h			10	1,23E+02	4,53E+00			
			3,5h			10	9,92E+01	3,66E+00			
			24h			9	7,70E+01	2,44E+00			
		Sham : Vehicle	CTRL			12	2,10E+02	1,91E+00			
			0,3h			12	2,06E+02	1,61E+00			
	rat threshold for pain per group at different time points before and after drug(s) injection		3,5h			12	2,06E+02	2,02E+00			
			24h			10	2,06E+02	3,00E+00			
		Sham : TGOT	CTRL			11	2,08E+02	2,19E+00			
7b			0,3h	Left	g	11	2,15E+02	1,53E+00			
			3,5h			11	2,11E+02	1,71E+00			
			24h			10	2,13E+02	4,00E+00			
		Sham : C1V1	CTRL			6	2,44E+02	1,49E+01		Time	1,00E-03
			0 min			6	2,34E+02	1,77E+01		Time*Group	7,00E-03
			15 min			6	2,21E+02	1,48E+01		Time*Paw	5,40E-02
			45 min			6	2,08E+02	1,71E+01	Mixed-design ANOVA & Bonferroni	Time*Group*Paw	8,62E-01
		SNI : C1V1	CTRL			10	7,92E+01	6,10E+00			
			0 min			10	8,23E+01	3,18E+00			
			15 min			10	7,97E+01	2,71E+00			
			45 min			10	8,00E+01	2,77E+00			
		SNI : Ctrl C1V1	CTRL			9	7,38E+01	3,52E+00			
			0 min			9	7,97E+01	3,82E+00			
			15 min			9	8,31E+01	1,44E+00			
			45 min			9	8,02E+01	2,18E+00			
		SNI : Vehicle + Ctrl C1V1				20	7,27E+01	2,72E+00		Treatment	<0,0001
		SNI : TGOT				9	5,96E+01	2,18E+00		Treatment * Surgery	4,08E-02
7c	Time spent in closed arm per rat	Sham : Vehicle + Ctrl C1V1			s	10	5,80E+01	1,58E+00	Mixed-design ANOVA & Bonferroni		
		Sham : TGOT				8	5,67E+01	2,46E+00			
		Sham : C1V1				9	5,69E+01	7,42E+00			
		SNI : C1V1				7	5,11E+01	6,59E+00			
		SNI : Vehicle + Ctrl C1V1				10	-9,55E+01	5,62E+01		Treatment	<0,0001
		SNI : TGOT				8	2,67E+02	7,49E+01		Surgery	3,16E-02
7d	Delta time spent in the paired chamber per rat	Sham : Vehicle + Ctrl C1V1			s	13	-3,56E+01	7,14E+01	Mixed-design ANOVA & Bonferroni	Treatment * Surgery	8,86E-01
		Sham : TGOT				6	4,36E+02	1,13E+02			
		Sham : C1V1				5	4,77E+02	6,98E+01			
		SNI : C1V1				8	2,59E+02	1,10E+02			
		SNI GFAP OTR KO mice -> TGOT	CTRL			13	1,92E+00	1,92E-01		Treatment	P < 0,0001
	mice pain threshold per group at different time before and after drug(s) injection		0 min			13	2,14E+00	3,02E-01		Treatment * Surgery	P < 0,0001
			15 min			13	1,65E+00	9,91E-02		Surgery	
7f			45 min	Left	g	13	2,65E+00	4,85E-01	Mixed-design ANOVA & Bonferroni		
		SNI control mice -> TGOT	CTRL			5	1,08E+00	8,00E-02			
			0 min			5	1,32E+00	8,00E-02			
			15 min			5	1,08E+00	8,00E-02			
			45 min			5	1,32E+00	8,00E-02			

Figure	Statistical unit	Groups tested	Time	Paw	Unit	N	Mean	SEM	Test used	Statistic	p-value
7f	mice pain threshold per group at different time before and after drug(s) injection	Sham GFAP OTR KO mice -> TGOT	CTRL	Left	g	8	4,50E+00	3,27E-01	Mixed-design ANOVA & Bonferroni	Time	<0,05
			0 min			8	4,50E+00	3,27E-01		Time*Group	<0,05
			15 min			8	3,80E+00	6,47E-01		Time*Paw	2,30E-02
			45 min			8	4,68E+00	5,84E-01		Time*Group*Paw	<0,05
		Sham control mice -> TGOT	CTRL			6	5,33E+00	4,22E-01			<0,0001
			0 min			6	5,33E+00	4,22E-01			
			15 min			6	5,00E+00	4,47E-01			
			45 min			6	5,00E+00	4,47E-01			
7g	Time spent in closed arm per mice	SNI GFAP OTR KO -> Vehicule				5	6,01E+01	1,10E+00	Kruskal-Wallis test with Dunn's MC		6,10E-03
		SNI GFAP OTR KO mice -> TGOT				7	5,95E+01	5,82E-01			
		SNI control mice -> Vehicule				7	6,12E+01	1,34E+00			
		SNI control mice -> TGOT			s	8	4,76E+01	1,17E+00			
		Sham GFAP OTR KO mice -> Vehicule				5	6,06E+01	1,08E+00			
		Sham GFAP OTR KO mice -> TGOT				7	5,90E+01	1,54E+00			
		Sham control mice -> Vehicule				7	4,93E+01	2,34E+00			
		Sham control mice -> TGOT				6	4,70E+01	5,20E+00			
7h	Delta time spent in the paired chamber per mice	SNI GFAP OTR KO mice -> Vehicule				4	-1,08E+02	1,26E+02	Kruskal-Wallis test with Dunn's MC		6,30E-03
		SNI GFAP OTR KO mice -> TGOT				6	-3,18E+01	2,53E+01			
		SNI control mice -> Vehicule				5	-1,04E+02	4,34E+01			
		SNI control mice -> TGOT			s	5	2,83E+02	9,52E+01			
		Sham GFAP OTR KO mice -> Vehicule				5	-4,26E+01	9,68E+01			
		Sham GFAP OTR KO mice -> TGOT				4	-1,53E+02	1,78E+02			
		Sham control mice -> Vehicule				5	-1,94E+01	3,16E+01			
		Sham control mice -> TGOT				8	3,38E+02	9,57E+01			
E.D.7b	rat threshold for pain per group at different time points before and after drug(s) injection	SNI : Vehicle	CTRL	Right	g	12	2,16E-02	1,77E+00	Mixed-design ANOVA & Bonferroni	Time	1,00E-03
			0,3h			12	2,13E-02	2,02E+00		Time*Group	7,00E-03
			3,5h			12	2,12E-02	2,28E+00		Time*Paw	5,40E-02
			24h			9	2,14E-02	2,37E+00		Time*Group*Paw	8,62E-01
		SNI : TGOT	CTRL			10	2,13E-02	2,47E+00			
			0,3h			10	2,13E-02	1,70E+00			
			3,5h			10	2,12E-02	2,23E+00			
			24h			9	2,07E-02	2,85E+00			
		Sham : Vehicle	CTRL			12	2,07E-02	1,54E+00			
			0,3h			12	2,11E-02	2,06E+00			
			3,5h			12	2,10E-02	1,97E+00			
			24h			10	2,12E-02	1,97E+00			
		Sham : TGOT	CTRL			10	2,12E-02	2,00E+00			
			0,3h			10	2,08E-02	1,57E+00			
			3,5h			10	2,10E-02	3,37E+00			
			24h			9	2,10E-02	2,67E+00			
		Sham : C1V1	CTRL			6	2,47E-02	1,35E+01			
			0 min			6	2,54E-02	1,08E+01			
			15 min			6	2,33E-02	1,05E+01			
			45 min			6	2,22E-02	4,58E+00			
		SNI : C1V1	CTRL			10	1,83E-02	1,03E+01			
			0 min			10	2,16E-02	1,10E+01			
			15 min			10	1,86E-02	1,14E+01			
			45 min			10	1,86E-02	1,13E+01			

ID	Measurement	Group	Time/Condition	Unit	n	Mean	SEM	Test	Factor	p-value
E.D.7b		SNI : Ctrl C1V1	CTRL		9	1,86E+02	1,09E+01			
			0 min		9	2,09E+02	9,75E+00			
			15 min		9	1,98E+02	9,14E+00			
			45 min		9	2,00E+02	5,71E+00			
E.D.7c	total distance per rat	SNI : Vehicle + Ctrl C1V1		m	20	9,56E+02	2,98E+02	Mixed-design ANOVA	Treatment	>0,05
		SNI : TGOT			9	1,08E+03	9,48E+01		Treatment * Surgery	>0,05
		Sham : Vehicle			10	1,15E+03	2,69E+02			
		Sham : TGOT			8	1,23E+03	1,56E+02			
		Sham : C1V1			9	1,09E+03	3,39E+02			
		SNI : C1V1			7	1,17E+03	5,67E+02			
E.D.7d	total distance per rat	SNI : Vehicle + Ctrl C1V1		m	10	1,52E+01	1,59E+00	Mixed-design ANOVA	Treatment	p=0,6272
		SNI : TGOT			8	2,77E+01	1,11E+01		Treatment * Surgery	p=0,5416
		Sham : Vehicle			13	1,96E+01	2,57E+00			
		Sham : TGOT			6	1,54E+01	3,17E+00			
		Sham : C1V1			5	1,59E+01	3,04E+00			
		SNI : C1V1			8	1,38E+01	2,05E+00			
E.D.7f	mice threshold for pain per group at different time points before and after drug(s) injection	SNI GFAP OTR KO mice -> TGOT	CTRL	g	13	4,31E+00	3,82E-01		Interaction	1,89E-01
			0 min		13	4,15E+00	1,54E-01		Neuropathy	3,36E-01
			15 min Right		13	3,54E+00	2,43E-01		Group	2,46E-02
			45 min		13	4,92E+00	2,88E-01			
		SNI control mice -> TGOT	CTRL		5	4,40E+00	4,00E-01			
			0 min		5	4,00E+00	0,00E+00			
			15 min Right		5	3,60E+00	4,00E-01			
			45 min		5	4,40E+00	4,00E-01			
		Sham GFAP OTR KO mice -> TGOT	CTRL		8	4,50E+00	3,27E-01	Mixed-design ANOVA & Bonferroni		
			0 min		8	4,00E+00	3,78E-01			
			15 min Right		8	4,50E+00	5,00E-01			
			45 min		8	4,25E+00	4,53E-01			
		Sham control mice -> TGOT	CTRL		6	5,33E+00	4,22E-01			
			0 min		6	5,33E+00	4,22E-01			
			15 min Right		6	5,00E+00	4,47E-01			
			45 min		6	4,67E+00	4,22E-01			
E.D.7g	total distance per mice	SNI GFAP OTR KO mice -> Vehicule			5	1,22E+01	3,88E-01	Kruskal-Wallis test with Dunn's MC		3,78E-02
		SNI GFAP OTR KO mice -> TGOT			7	1,27E+01	8,07E-01			
		SNI control mice -> Vehicule			7	1,21E+01	3,32E-01			
		SNI control mice -> TGOT		m	8	1,38E+01	1,14E+00			
		Sham GFAP OTR KO mice -> Vehicule			5	1,33E+01	8,25E-01			
		Sham GFAP OTR KO mice -> TGOT			7	1,07E+01	6,74E-01			
		Sham control mice -> Vehicule			7	1,16E+01	2,50E-01			
		Sham control mice -> TGOT			6	1,23E+01	1,53E+00			
E.D.7h	total distance per mice	SNI GFAP OTR KO mice -> Vehicule			4	3,24E-01	7,60E-01	Kruskal-Wallis test with Dunn's MC		3,64E-01
		SNI GFAP OTR KO mice -> TGOT			6	2,43E-01	1,38E+00			
		SNI control mice -> Vehicule			5	2,26E-01	3,95E+00			
		SNI control mice -> TGOT		m	5	3,07E+01	3,29E+00			
		Sham GFAP OTR KO mice -> Vehicule			5	2,76E-01	2,19E+00	Kruskal-Wallis test with Dunn's MC		5,50E-01
		Sham GFAP OTR KO mice -> TGOT			4	3,11E-01	5,92E+00			
		Sham control mice -> Vehicule			5	3,48E-01	5,11E+00			
		Sham control mice -> TGOT			8	2,92E-01	2,58E+00			

TABLE 8: List of reagents used in this study

Experiments	Product	Full name	Company	Company reference	Concentration Stock	Concentration final	medium
Brain Slice preparation	Kynurenic acid	4-oxo-1H-quinoline-2-carboxylic acid.	Alomone labs	K-110	see materials and methods	see materials and methods	ACSF Bath medium
	Various salts and other products for ACSFs	/	Sigma-Aldrich	see company website			ACSF Bath medium
Calcium imaging on slices	Kolliphor® EL	Polyoxyl 35 hydrogenated castor oil	Sigma-Aldrich	C5135			ACSF Bath medium
	Oregon Green BAPTA 1	/	Thermo Fisher Scientific	O6807	see materials and methods	see materials and methods	ACSF Bath medium
	Rhodamine 2	/		R1245MP			
	Pluronic F127	/		P2443			
	Sulforhodamine 101	/	Sigma-Aldrich	S7635	1 mM in H20	1 µM in ACSF	
Patch-Clamp recordings	Various salts and other products for intracellular solution	/	Sigma-Aldrich	see company website	see materials and methods	see materials and methods	ACSF Bath medium
	A438079	3-(5-(2,3-dichlorophenyl)-1H-tetrazol-1-yl)methyl pyridine hydrochloride hydrate		A9736	1 mM in H20	1 µM in ACSF	ACSF Bath medium
	1(S),9(R)-(−)-Bicuculline methiodide	(5S)-5-[(6R)-6,8-Dihydro-8-oxofuro[3,4-e]-1,3-benzodioxol-6-yl]-5,6,7,8-tetrahydro-6,6-dimethyl-1,3-dioxolo[4,5-g]isoquinolinium iodide	Sigma-Aldrich	14343	10 mM in H20	10 µM in ACSF	ACSF Bath medium
	BAPTA	1,2-Bis(2-Aminophenoxy)ethane-N,N,N′,N′-tetraacetic acid		A4926	see materials and methods	see materials and methods	see materials and methods
	DAAO	D-amino acid oxidase		A5222		0,15 U/ml, >1h30	
	D-AP5	D-(-)-2-Amino-5-phosphonopentanoic acid	Abcam	ab120003	50 mM in H20	50 µM in ACSF	ACSF Bath medium
	DCKA	5,7-Dichloro-4-hydroxyquinoline-2-carboxylic acid monohydrate	Sigma-Aldrich	D138	10 mM in DMSO	10 µM in ACSF	
	DNQX	6,7-Dinitroquinoxaline-2,3-dione	Abcam	ab120018	25 mM in DMSO	25 µM in ACSF	
Brain slice experiments and in vivo intracerebral injection	dOVT	(d(CH$_2$)$_5^1$,Tyr(Me)^2,Thr^4,Orn^8,des-Gly-NH$_2^9$)-Vasotocin trifluoroacetate salt	Bachem	H2908	1 mM in H20	1 µM in ACSF	ACSF Bath medium / Intracerebral injection (0,5 µL)
	D-Serine		Sigma-Aldrich	S4250	100 mM in H20	100 µM in ACSF	ACSF Bath medium
	Ifenprodil	erythro-4-(2-(4-Benzylpiperidin-1-yl)-1-hydroxypropyl)phenol hemitartrate	Abcam	ab120111	3 mM in H20	3 µM in ACSF	
	PPADS	4-[[4-Formyl-5-hydroxy-6-methyl-3-[(phosphonooxy)methyl]-2-pyridinyl]azo]-1,3-benzenedisulfonic acid tetrasodium salt	Sigma-Aldrich	P178	10 mM in H20	50 µM in ACSF	ACSF Bath medium
	Suramin	Suramin sodium salt	Sigma-Aldrich	S2671	10mM in H2O	75µM	
	TGOT	(Thr^4,Gly^7)-Oxytocin ; H-Cys-Tyr-Ile-Thr-Asn-Cys-Gly-Leu-Gly-NH$_2$	Bachem	H-7710	0,4 mM in H20	0,4 µM in ACSF	ACSF Bath medium / Intracerebral injection (0,5 µL)
	TTX citrate	Octahydro-12-(hydroxymethyl)-2-imino-5,9:7,10a-dimethano-10aH-[1,3]dioxocino[6,5-d] pyrimidine-4,7,10,11,12-pentol + citrate buffer	Abcam	ab120055	1 mM in H20	1 µM in ACSF	ACSF Bath medium

Category	Reagent	Supplier	Catalog No.	Stock preparation	Working concentration	Buffer
Immunohistochemistry	Anti-GFAP antibody	Abcam	ab4674	/	1:500	
	Anti-Glutamine Synthase	Merck Millipore	MAB302	/	1:500	
	Alexa 555 Goat Anti-chicken		ab150170	/	1:1000	
	Alexa 488 Goat Anti-rabbit		ab150077	/	1:1000	
	Anti-ALDH1L1 antibody	Abcam	ab87117	/	1:500	
	Alexa 680 Goat Anti-rabbit		ab175773	/	1:1000	
	Anti-NeuN antibody		ab104225	/	1:1000	
	Anti-Cre antibody	Gifted from Dr. Haikun Liu	/	/	1:1000	PBS
In situ hybridization	Denhardt's solution, lyophilised powder (50x)	Carl Roth	/	50x in H_2O	5x	50% Formamide and 5x SSC
	Yeast tRNA	Invitrogen	15401011	10 mg/ml in H_2O	0.25 mg/ml	
	Herring Sperm DNA	Promega	D1815		0.5 mg/ml	PBS
	Glycine	Sigma-Aldrich	50046		7.5 mg/ml	PK buffer
	Proteinase K	PanReas AppliChem	A3830	10 mg/ml in PK buffer	0.5 µg/ml	
	Triethanolamine	Carl Roth	6300		100 mM	H_2O
	Acetic anhydride		320102		0,25%	Acetylation buffer
	Ribonuclease A Solution	Sigma-Aldrich	R4642		20 µg/ml	RNase buffer
	2.5% Normal Goat Serum Blocking Solution	Vector Laboratories	S-1012		0.25%	Maleic acid buffer-Tween 20 (MABT)
	Blocking Reagent	Roche Diagnostics	11096176001	10% in MABT	1%	MABT
	Anti-Digoxigenin-POD	Roche Diagnostics	11207733910		1:200	0.25% NGS and 1% Blocking Reagent in MABT
	Imidazole	Merck Millipore	104716	10 mM in PBS	10 mM	PBS
	NHS-Rhodamine	Pierce Biotechnology, Thermo Fisher Scientific	46406	10 mg/ml in Dimethylformamide anhydrous	2 mg/ml	
	Tyramine hydrochloride	Sigma-Aldrich	T2879	10 mg/ml in Dimethylformamide anhydrous	0.6 mg/ml	EtOH

5.2. Article 2: Astrocytes oxytocin receptor in mice central amygdala mediates behavioral fear adaptation through $G\alpha_i$ proteins

5.2.1. Introduction

To survive, living beings have to analyze and remember their environment to react to its variations appropriately. To weigh the importance of sensorial stimuli, life developed emotions: deep and raw feelings that trigger an attraction or a repulsion toward something. These emotional values are then computed to create elaborate feelings such as fear, anger, joy, or disgust. The attribution of emotional valence takes place in a brain region buried deep in the temporal cortex named the amygdala. This structure is under the regulation of many neuromodulators among which we can find the neuropeptide oxytocin.

We showed in the first part of my Ph.D. thesis that astrocytes are involved in the neuromodulatory effect of oxytocin in the amygdala. Therefore, we decided to investigate the potential involvement of oxytocin on astrocytes in the encoding of emotional associative memory using a fear-conditioning model in mice.

5.2.2. Results

It has been shown that oxytocin regulates freezing reactions induced by fear (Knobloch et al., 2012). To investigate the role of astrocytes in this neuromodulation, we removed astrocytic OTR in the CeL/C and we measured the freezing behavior of mice during a fear conditioning protocol. Intriguingly, removing OTR from CeL/C astrocytes prevented the freezing behavior as soon as the conditioning session.

To understand the mechanism underlying the astrocyte-dependent effect of oxytocin on the establishment of freezing behavior, we assessed the morphology of astrocytes in the CeL/C. Interestingly, the fear conditioning session leads to astrocyte reactivity in the CeL/C, an effect dependent on the presence of astrocytic OTR. To assess the impact of this astrocytic reactivity on the neighboring neuronal network, we

measured the electrophysiological properties of CeL/C neurons and observed an increased excitability of those neurons, suggesting that hyperexcitability of the central amygdala may lead to an increased freezing behavior.

To unveil how oxytocin can modify the morphology of astrocytes and the activity of CeL/C neurons, we decided to investigate the intracellular pathway activated downstream of OTR and their effects. Importantly, OTR can couple two distinct intracellular pathways that depend on $G\alpha_i$ and $G\alpha_q$ proteins. Based on this information, we used biased agonists to recruit preferentially one pathway or the other. We found that the OTR-$G\alpha_q$ pathway stimulation triggers the activation of astrocytes and neurons whereas the activation of the $G\alpha_i$ pathway only leads to calcium transients in astrocytes but does not change amygdala neurons' activity.

Disconcerted, we decided to evaluate the long-term effect of these $G\alpha_i$-mediated calcium transients in amygdala astrocytes. Thus, we incubated brain slices containing the central amygdala in the biased agonists and observed that activation of the OTR-$G\alpha_i$ pathway but not the OTR-$G\alpha_q$ pathway can mimic the morpho-functional changes of the astro-neuronal network we observed after the fear conditioning session.

In addition, to show that OTR can couple the $G\alpha_i$ pathway in the brain at a cellular level, we also provided an original mechanism to explain how fear is stored in the brain and how emotional perception is modified after an episode of intense fear.

5.2.3. Personal contribution

This second project was the potting soil of my scientific blooming. I set up all experiments and performed almost all the calcium imaging and electrophysiological experiments. During the last year, I was joined by Valentin Grelot who also did electrophysiological recordings, and who will lead this project in the future. I also automatize the totality of calcium imaging, electrophysiology, and behavioral data using Python programs.

Astrocytes oxytocin receptor in mice central amygdala mediates behavioral fear adaptation through Gα$_i$ proteins

Authors

Baudon Angel, Althammer Ferdinand, Grelot Valentin, Wang Kai-Yi, Clauss--Creusot Etienne, Rouach Nathalie, Breton Rachel, Darbon Pascal, Charlet Alexandre.

Abstract

Emotions are complex feelings relying on the computation of many factors such as sensory cues and memories associated with them. The emotional value of these environmental cues is processed in the amygdala under the control of neuromodulators from other brain regions. Among them, oxytocin exerts a strong control of the neuronal network of the laterocapsular part of the central nucleus of the amygdala (CeL/C). Our previous work showed that astrocytes are an essential relay to this neuromodulation and are required for the anxiolytic effect of oxytocin. Here we investigated the involvement of oxytocin-mediated astrocyte activation in the memorization of emotionally relevant cues. Using fear conditioning and morpho-functional analysis of the CeL/C astro-neuronal network, we showed that oxytocin activates a Gαi-dependent pathway through its receptor that triggers morphological reorganization of astrocytes, resulting in the hyperexcitability of neighboring neurons. The present work identifies a central role of astrocytes in the central amygdala for behavioral fear adaptation.

Introduction

Associative learning is crucial for animals' survival, indicating when a situation requires immediate reactions and preparing the body for them. However, this mechanism can be deregulated conducting to pathological conditions, such as post-traumatic stress disorders (McDonald and Mott, 2017). To treat these pathologies, we need to understand the brain mechanisms underlying the learning, the maintenance, and the extinction of associative learning, such as fear. Despite recent advances in that field, many aspects of these mechanisms are still unknown. The learning and extinction of the fear memory rely on the collaboration of many different brain regions. Among these regions, the amygdala is crucial since lesions of this structure prevent learning and expression of fear in mammals, including rodents, monkeys, and humans (LeDoux, 2000). This structure is composed of different nuclei with distinct functions. Here we focused on the pathway that involves the basolateral complex of the amygdala (BLA) and the central nucleus of the amygdala (CeA), known to be crucial for fear learning: after its detection by sensory organs and a first integration step in the sensory cortices, the information is then transferred to the BLA. This structure computes the signal and communicates it to the CeA, which then gates the expression of fear behaviors (Duvarci and Pare, 2014). The CeA and especially its laterocapsular part (CeL/C) is under the control of endogenous neuromodulators, among which oxytocin (OT). OT elicits unfreezing in fear-conditioned rodents when released in the CeL/C, indicating an OT-related control on the expression of fear (Knobloch et al., 2012).

OT is a hypothalamic neuropeptide that can be released in various brain regions to act as a neuromodulator. This peptide can modify the excitation/inhibition balance to control the salience of emotionally important stimuli (Lefevre et al., 2021; Maldonado et al., 2021). In the CeL/C, OT can modify the activity of neuronal networks and control the integration/expression of emotions such as pain, anxiety, or fear (Baldi et al., 2021; Moscarello and Penzo, 2022; Olivera-Pasilio and Dabrowska, 2020; van den Burg and Stoop, 2019). To exert its functions, OT binds to its receptor, a GPCR named OTR (Jurek and Neumann, 2018), which has the particularity to couple both Gαq and Gαi proteins (Busnelli & Chini 2017). This receptor is transcribed in neurons but also astrocytes of the CeL/C, indicating that astrocytes can detect OT in the extracellular space (Wahis et al., 2021). While our previous work shows that astrocytic OTR is crucial for the anxiolytic effect of OT in the CeL/C, we still do not know the cellular mechanisms and interactions underlying possible neuropeptide-induced behavioral adaptation.

To elucidate this, we first knocked out the OTR of CeL/C astrocytes and observed impairment of the fear-related freezing behavior during the learning phase of the fear conditioning. To understand the involvement of astrocytic OTR in the establishment of fear-induced freezing, we evaluated

astrocytes' GFAP immunoreactivity and observed an increased astrocyte reactivity after the fear-conditioning session. Since astrocytes show important structural reorganization during intense neuronal activity (Henneberger et al., 2020) and regulate neuronal excitability by several means (Kofuji and Newman, 2004; Sibille et al., 2014), we then investigated astrocyte morphology and the excitability of neighboring neurons. These approaches allowed us to identify several associative learning induced by morpho-functional changes in the astro-neuronal network. A deeper dive into the intracellular pathways involved in these changes indicated that the OTR can bind both Gαi and Gαq proteins in astrocytes. Interestingly, only the activation of the Gαi pathway triggered changes similar to those observed after fear conditioning, indicating that an OTR-Gαi pathway may be responsible for the changes in the astro-neuronal circuit induced by associative learning. To understand the relation between astrocytes morphology and neuronal network excitability changes, we evaluated the K^+ buffering efficiency of astrocytes and observed a reduction of astrocytes' K^+ buffering in mice that have undergone fear conditioning, indicating a link between the astrocyte's morphological changes and the neuronal hyperexcitability.

Results

Deletion of astrocytic OTR in the CeL/C prevents fear-induce freezing.

Our first approach to investigate the function of astrocytic OTR in fear behaviors was to knock out these receptors in mice. To this end, we injected a recombined adeno-associated virus (rAAV) leading to the expression of the Cre recombinase under the control of the glial fibrillary-associated protein (GFAP) promoter (rAAV-GFAP-Cre) in the CeL/C of OTR floxed mice (Figure 1A), (Lee et al., 2008). This approach induces a conditional knockout of the OTR transcription in virtually all CeL/C astrocytes (GFAP OTR cKO, Wahis et al., 2021). Given that OT release in the CeA decreases the freezing behavior in rats (Knobloch et al., 2012), we expected OTR activation to mediate fear extinction. However, instead of a reduction of freezing behavior during the extinction phase, we observe an absence of freezing behavior during the conditioning phase in GFAP OTR cKO male mice ($p_{interaction} < 0.0001$, Figure 1B1). Intriguingly, this effect was not present in female mice ($p_{interaction} = 0.4660$, Figure 1B2). These first results indicate that astrocytic OTR is involved in the associative learning of fear or its expression in males but not in female mice. Since the removal of OTR from CeL/C astrocytes affects freezing behavior in male but not female mice, we then focused on the involvement of astrocytic OTR in the control of fear conditioning in male mice.
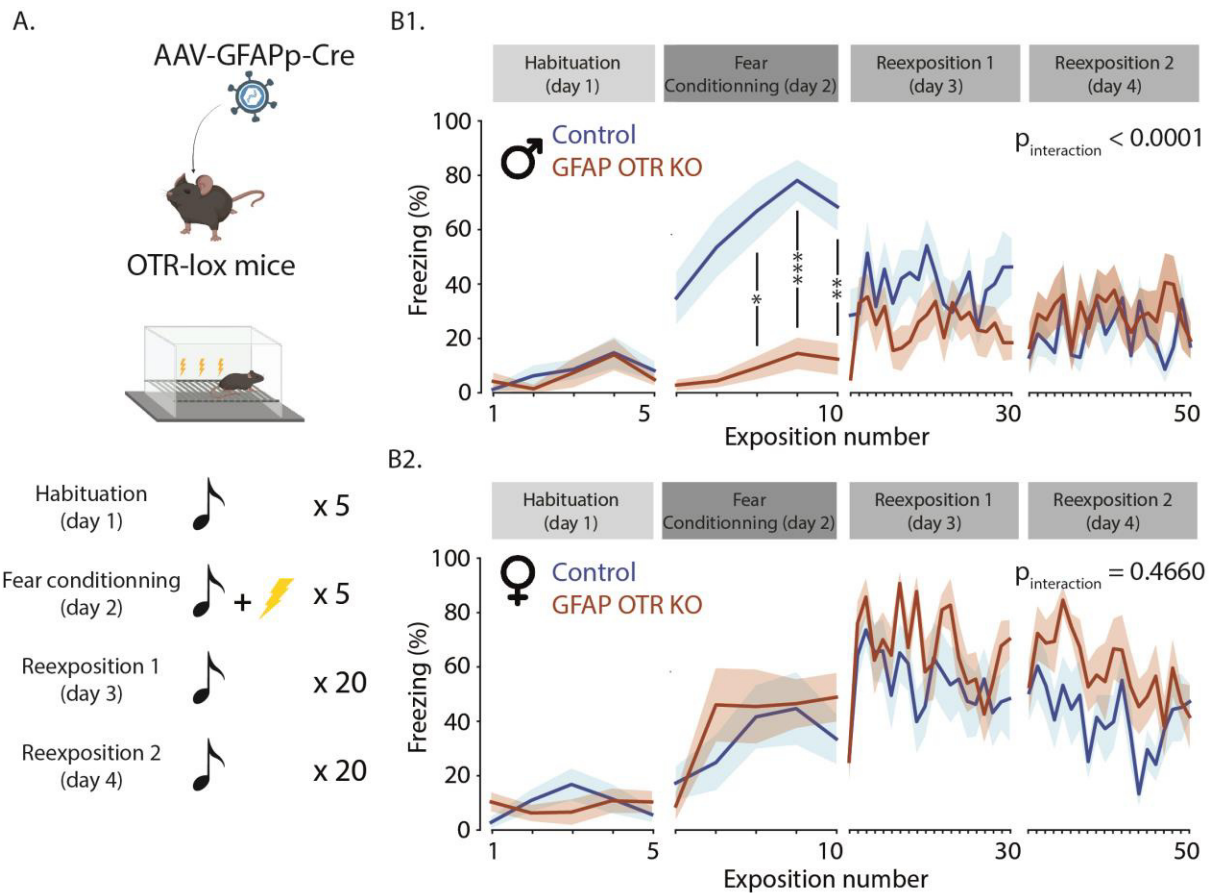
Figure 1: Impact of OTR deletion from CeL/C astrocyte on freezing behavior. A. Scheme of the experimental setup. AAV-GFAP-Cre was injected in OTR-lox mice to knock out the OTR in astrocytes 3 weeks before fear conditioning experiments. **B.** Freezing behavior was quantified in control and GFAP OTR cKO mice during the four sessions of the fear conditioning protocol. Upper panel: male mice (n_{WT} = 9 mice, $n_{GFAP\ OTR\ cKO}$ = 11 mice), Lower panel: female mice (n_{WT} = 8 mice, $n_{GFAp\ OTR\ cKO}$ = 8 mice). Data are expressed as mean across animal ± SEM. Detailed statistics can be found in *Statistic Table 1*. * p<0.05, ** p<0.01, *** P<0.001

Fear conditioning induces morpho-functional changes in the CeL/C astro-neuronal network.

Given the impaired freezing response of GFAP OTR cKO mice during fear conditioning and the plastic nature of astrocytes, we hypothesized that fear conditioning induces morphological changes in CeL/C astrocytes in an OTR-dependent manner. To test this, we injected AAV-GFAP-GFP in the CeL/C to fill astrocyte cytosol with GFP and reconstructed astrocyte morphology in naïve and fear-conditioned mice (Figure 2A). We observed a decreased complexity of astrocyte morphology after fear conditioning as measured by their peak Scholl value (naïve: 24.85±3.43, fear: 13.11±2.99, p = 0.0005). Curious to see if oxytocin was involved in this effect, we did the same experiment in GFAP OTR cKO mice, in which we found an absence of morphological changes after fear conditioning (naïve: 18.56±3.36, fear: 17.44±4.53, p = 0.9609, Figure 2B). Thus, astrocytic OTR is involved in astrocytes' morphological changes observed after fear conditioning.

In extreme situations, astrocytes can undergo physiological changes, a state known as astrocyte reactivity (Escartin et al., 2019). One common marker of this state is the upregulation of the glial fibrillary acidic protein (GFAP). Therefore, we decided to investigate whether a fear conditioning protocol can modify the amount of this protein. Interestingly, we observed an increased GFAP volume after the conditioning session of the fear protocol (naïve: 409.6±1.53μm^3, fear: 952±1.34μm^3, p < 0.001). This effect, however, was not observed in GFAP OTR cKO mice (naïve: 479±1.5μm^3, fear: 426.3±2.02μm^3, p = 0.871, Figure 2C). At this point, we supposed that GFAP expression and astrocyte morphology might be correlated. Therefore, we used AAV-GFAP-GFP injected mice to evaluate astrocyte morphology and GFAP expression of the very same cell. This analysis revealed an inverse correlation between those two parameters, with complex astrocytes expressing a small amount of GFAP (r^2 = 0.5694, p<0.0001, Figure 2D). This result indicates that astrocyte reactivity may trigger the retraction of astrocyte processes from neurons and thus, potentially make them lose their physiological functions.

Astrocytes regulate many aspects of neurons' life, especially their excitability (Kofuji and Newman, 2004). Knowing that OT can modify the neuronal electrical activity of the CeL/C by acting on astrocytes (Wahis et al., 2021), we then wondered whether this modification of astrocyte physiology affects neuronal excitability. To do so, we fear-conditioned mice and performed slice patch-clamp recordings right after the conditioning phase to evaluate different parameters of neurons' electric properties. We first evaluated the intrinsic excitability of CeL/C neurons by performing a current step protocol to measure intrinsic neuronal membrane properties but did not observe any difference between WT naïve and fear-conditioned mice ($p_{rheobase}$ = 0.496, $p_{latency\ to\ spike}$ = 0.720, $p_{number\ of\ spikes}$ = 0.970, Figure 2E and S1). To evaluate the extrinsic excitability of CeL/C neurons, we then puffed a
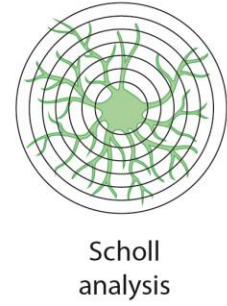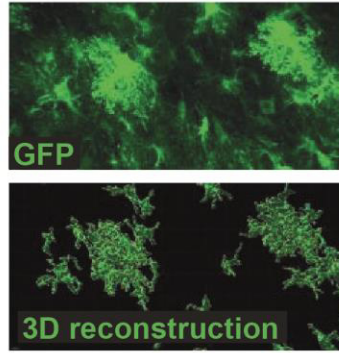
30mM K$^+$-containing solution at ~150μm of the recorded cell (Figure 2E). Interestingly, the K$^+$-induced depolarization of neurons' voltage membrane was significantly higher in fear-conditioned mice compared to their controls (naïve = 9.85±1.22, fear = 19.29±2.13, p = 0.004), but neither the kinetic nor the number of spikes triggered by this depolarization were modified (p_{rise} = 0.738, p_{decay} = 0.304, $p_{number\ of\ spikes}$ = 0.658, Figure 2E and S1). The analysis of neuronal electrophysiological properties thus indicates that fear conditioning increases the extrinsic excitability of CeL/C neurons.

To assess the involvement of astrocytic OTR in neurons' hyperexcitability, we replicated the same set of electrophysiological experiments in GFAP OTR cKO mice. We still did not observe significant differences in intrinsic membrane properties between GFAP OTR cKO mice that undergo fear conditioning and naïve controls ($p_{rheobase}$ = 0.705, $p_{latency\ to\ spike}$ > 0.999, $p_{number\ of\ spikes}$ = 0.962, Figure 2E and S1). In addition, the increased membrane voltage depolarization induced by fear conditioning in naïve mice was absent in GFAP OTR cKO mice ($p_{depolarization}$ = 0.971, p_{rise} = 0.999, p_{decay} = 0.435, $p_{number\ of\ spikes}$ > 0.999, Figure 2E and S1). This indicates that astrocytic OTR is involved in neuronal hyperexcitability induced by fear conditioning.

With this set of experiments, we demonstrated that fear conditioning induces morphological and functional changes in astrocytes and neurons of the CeL/C in an astrocytic OTR-dependent manner.
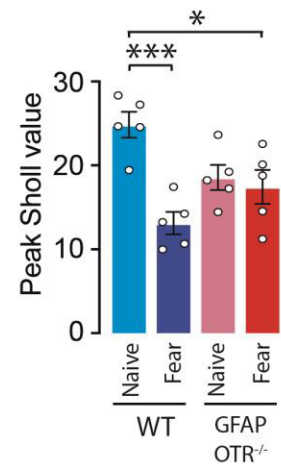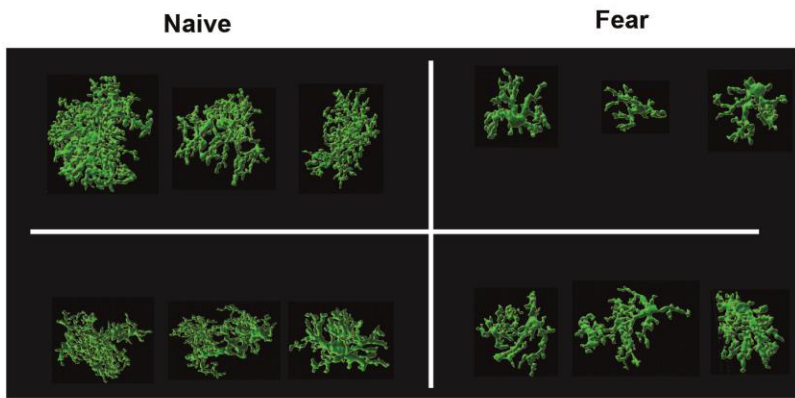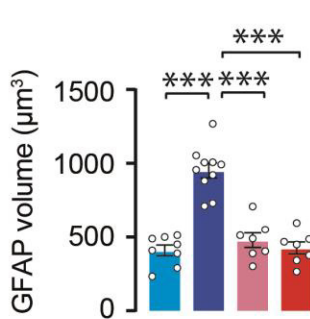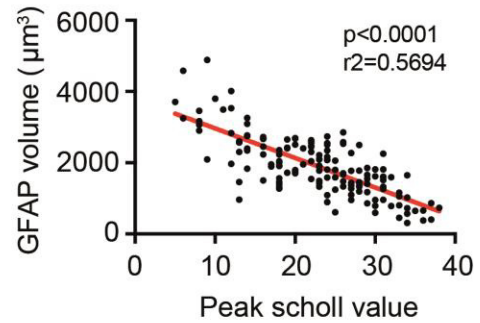
A.

AAV-GFAP-GFP

GFP

3D reconstruction

Scholl analysis

B.

Naive

Fear

WT

GFAP
OTR cKO

Peak Sholl value

***

*

Naive Fear   Naive Fear
   WT   GFAP
              OTR⁻/⁻

C.

GFAP volume (μm³)

***
*** ***

D.

GFP   GFAP   Merge

p<0.0001
r2=0.5694

GFAP volume (μm³)

Peak scholl value

E.

CeL neuron

IStep   Puff K⁺

40 mV
200 ms

40 mV
20 s

P-value vs naive

Decay
Threshold   δSpike
            α = 0.05
IStep   δVm
                              Potassium puff
nSpike
   Latency   Rise

Delta membrane voltage (mV)

**

Naive Fear   Naive Fear
   WT   GFAP
              OTR⁻/⁻
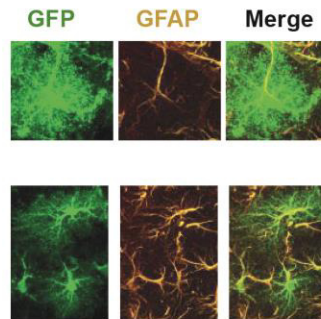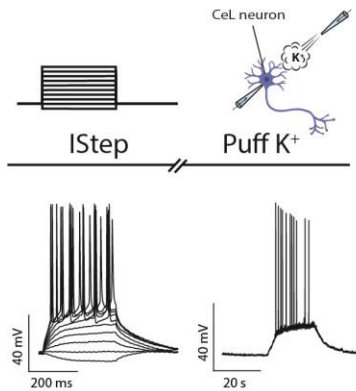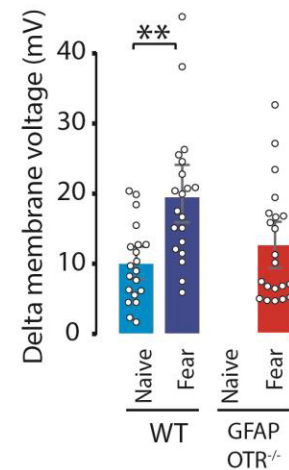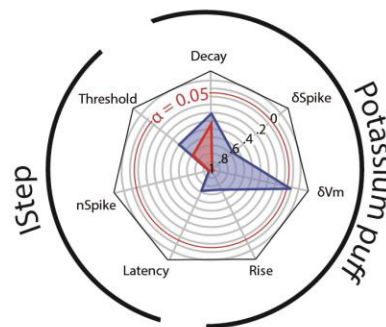
Figure 2: Morpho-functional analysis of the CeL/C astro-neuronal network after fear conditioning. A. Experimental scheme. Left: AAV-GFAP-GFP was injected in mice CeL/C to reveal astrocyte morphology. This virus was also injected with AAV-GFAP-Cre in OTR-lox mice. Three weeks after, mice were submitted to a fear conditioning protocol and fixed directly after the conditioning phase. Right: Reconstruction of CeL/C astrocytes based on their GFP expression and estimation of their ramification thanks to a Sholl analysis. n = 5 animals in each group. **B.** Quantification of astrocytes morphology by their maximum Sholl values. Examples of reconstructed astrocytes are shown in the left panel. **C.** Quantification of GFAP volume after immunostaining and 3D reconstruction. $n_{naïve}$ = 8 mice, n_{fear} = 10 mice, $n_{naïve\ GFAP\ OTR\ cKO}$ = 7 mice, $n_{fear\ GFAP\ OTR\ cKO}$ = 7 mice. **D.** Correlation plot of the relationship between astrocyte general morphology revealed by GFP and their reactivity estimated with GFAP volume. n = 153 astrocytes. **E.** Electrophysiological features of CeL/C neurons from control and fear-conditioned mice. Left: a current step and a puff of a 30mM-containing aCSF solution were applied to CeL/C neurons. Center: graphical sum up of the pvalues of the comparison of different electrophysiological features. Current steps give the spike firing threshold, the number of spikes at the second active step (nSpike), and the latency to the first spike. During the puff of potassium, we measure the difference in spike firing (δSpike), the amplitude of the depolarization (δVm), and its rise and decay constant. Right: amplitude of the membrane depolarization during the puff of a 30mM-containing aCSF. n are comprise between 18 and 25 neurons, for detail, see *Statistic Table 2*. Data are expressed as mean across animal ± SEM for panels B and C, and as mean across cell ± SEM for panel E. Detailed statistics can be found in *Statistic Table 2*. * p<0.05, ** p<0.01, *** p<0.001

OTR-Gαq activates both neurons and astrocytes but OTR-Gαi only activates astrocytes.

The activation of the OTR can trigger the activity of Gαi or Gαq proteins (Busnelli et al., 2012; Grinevich et al., 2016). Given that a growing body of evidence showed that Gαi-GPCR can trigger calcium transients in astrocytes (Durkee et al., 2019; Nagai et al., 2019), we tested whether the OTR can couple to both Gαi and Gαq in astrocytes. To do so, we evaluated the calcium activity of CeL/C astrocytes in brain slices by measuring the fluorescence of the OGB1 calcium indicator in SR101-identified astrocytes. We compared the calcium transient frequency and the area under the curve of OGB1 signals before and after a 20s application of agonists and evaluated the proportion of responding cells (Figure 3A). All three agonists increase the frequency of calcium transients in astrocytes (TGOT: p = 0.024, atosiban: p = 0.001, carbetocin: p = 0.003, Figure 3A), and the area under the curve of OGB1 fluorescence (TGOT: p = 0.002, atosiban: p < 0.001, carbetocin: p < 0.001, Figure 3A). The proportion of responding cells was also similar for all three agonists (TGOT: 54.34±6.46, atosiban: 46.93±8.09, carbetocin: 49.35±4.51, Figure S2B). To control the specificity of atosiban, we incubated brain slices in pertussis toxin (PeTX, 5µg/mL) for 5 hours to block Gαi-mediated signaling. In PeTX-incubated slices,

the application of TGOT is still able to elicit a calcium response in CeL/C astrocyte (Ca^{2+} transient frequency: $p = 0.006$, AUC: $p < 0.001$, % of response: 25.34 ± 7.83, Figure S2A). As expected, these responses were not observed after the application of the Gαi-biased agonist atosiban (Ca^{2+} transient frequency: $p = 0.316$, AUC: $p = 0.445$, % of response: 22.82 ± 5.96, Figure S2A), validating the Gαi-biased OTR activation triggered by atosiban. By measuring the calcium activity of astrocytes, we show that the activation of both Gαi and Gαq proteins downstream of the OTR triggers calcium transients in these cells (Figure 3B).

To analyze in more detail the calcium signaling induced by those agonists, we measured various features of the calcium events and observed that some parameters are differentially affected by the activation of the intracellular pathways (Figure S2B). We then compared these parameters and observed that the rise constant and the height of calcium events were lower in astrocytes stimulated with atosiban compared to those stimulated with carbetocin (Figure S2C). This last element suggests that astrocytes differentially encode the activation of the Gαi and the Gαq pathways using different shapes of calcium events.

We then assessed the ability of those G proteins activation to modulate the CeL/C neuron's activity. To this end, we injected AAV-EF1a-DIO-GFP in the CeL/C of OTR-Cre mice (Ryan et al., 2017), allowing the identification of OTR^{+} neurons based on the expression of GFP (Figure 3B). We then performed patch-clamp recordings of OTR^{+} neurons of the CeL/C and applied one of the three agonists for 20s at ~150µm of these cells using a puff pipette. The application of the full agonist TGOT tends to increase the frequency of action potential firing in OTR-expressing neurons ($p = 0.0571$), a result in accordance with previous works (Huber et al., 2005; Knobloch et al., 2012; Wahis et al., 2021). Application of atosiban neither increases nor decrease the firing rate of OTR^{+} neurons ($p_{time} = 0.8647$), indicating that activation of OTR-Gαi did not modify CeL/C OTR neurons activity. Finally, the application of carbetocin increase the firing frequency of OTR^{+} neurons ($p_{time} = 0.0487$). Note that we cannot statistically conclude on this experiment since the effectives are still small (less than 10 neurons in each conditions) but the activation of OTR-Gαq but not OTR-Gαi seems to increase neuronal activity in brain slices (Figure 3B).

Based on these results, we suggest that astrocytic OTR can couple both Gαi and Gαq proteins and that the activation of both pathways can lead to calcium transients in CeL/C astrocytes. However, only the activation of OTR-Gαq can increase the spiking frequency of OTR^{+} neurons, in line with our previous observations (Wahis et al., 2021). We were so flabbergasted by these observations that we decided to investigate what could be the function of the activation of the OTR-Gαi pathway in astrocytes.
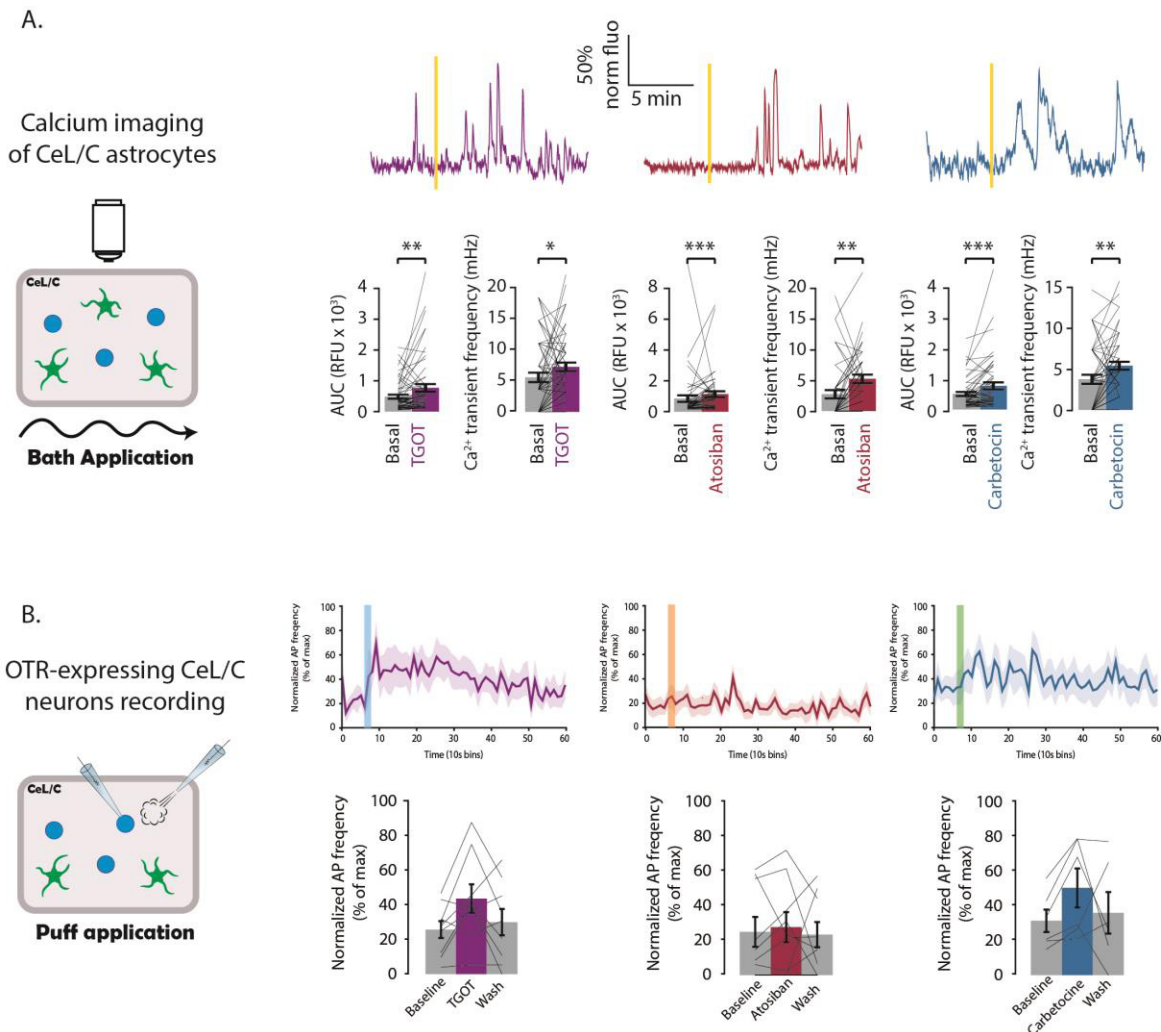
Figure 3: Analysis of the intracellular pathway activated downstream OTR. A. Calcium imaging of SR101-identified CeL/C astrocytes and bath application of the three agonists. Upper panel: example traces of astrocytic calcium response of astrocytes after application of agonists. The vertical line indicated the perfusion of the agonists in the recording bath. Lower panel: Quantification of the response. n_{TGOT} = 57 astrocytes over 13 slices, $n_{atosiban}$ = 49 astrocytes over 9 slices, $n_{carbetocin}$ = 54 astrocytes over 13 slices. **B.** Electrophysiological recording of OTR-expressing neurons in the CeL/C and the local application of the three agonists with a puff pipette. n_{TGOT} = 9 neurons, $n_{atosiban}$ = 9 neurons, $n_{carbetocin}$ = 6 neurons. Upper panel: normalized firing frequency on recorded cells. The vertical line indicates the puff application. Data are expressed as mean across cell ± SEM. Detailed statistics can be found in *Statistic Table 3*. * p<0.05, ** p<0.01, *** p<0.001.

OTR-Gαi triggers CeL/C astrocytes reactivity and control neuron excitability.

To assess what can be the function of OTR-Gαi-mediated calcium transients in CeL/C astrocytes, we decided to observe their effect in the long run. Therefore, we incubated brain slices with different agonists and evaluated astrocyte reactivity (Figure 4A). Interestingly, TGOT or atosiban incubation increased the GFAP amount in CeL/C astrocytes (p_{TGOT} = 0.007, $p_{atosiban}$ < 0.001). On the other hand, the incubation of brain slices in carbetocin did not produce such GFAP modification ($p_{carbetocin}$ = 0.055), pointing toward the involvement of Gαi and not Gαq in the modification of the GFAP cytoskeleton (Figure 4B).

Since this GFAP upregulation is similar to what we observe after fear conditioning (Figure 2), we wondered whether an incubation in an agonist could mimic the neuronal hyperexcitability observed after fear conditioning. Thus, we patch-clamped CeL/C neurons from slices incubated in one of the three agonists and puff-applied a 30mM K^+-containing solution to elicit a membrane depolarization (Figure 4C). Incubation with TGOT increased the K^+-induced depolarization of CeL/C neurons (p = 0.005), an effect prevented by the co-incubation of TGOT with the OTR antagonist dOVT (p = 0.985). Similarly, TGOT did not increase the depolarizing effect of K^+ when we specifically removed the OTR on astrocytes using the GFAP OTR cKO model (p = 0.975), indicating that astrocytic OTR is needed for the TGOT-induced hyperexcitability of CeL/C neurons. Interestingly, atosiban but not carbetocin incubation also increased the excitability of CeL/C neurons ($p_{atosiban}$ = 0.031, $p_{carbetocin}$ = 0.961). This electrophysiological study strongly suggests that activation of the Gαi protein downstream astrocytic OTR increases the excitability of CeL/C neurons in the long range.

Altogether, these data show that the activation of the OTR-Gαi pathway in CeL/C astrocytes triggers morphological modifications of astrocytes and controls the excitability of neighboring neurons. However, the precise link between astrocyte morphology and neuron activity is still missing.
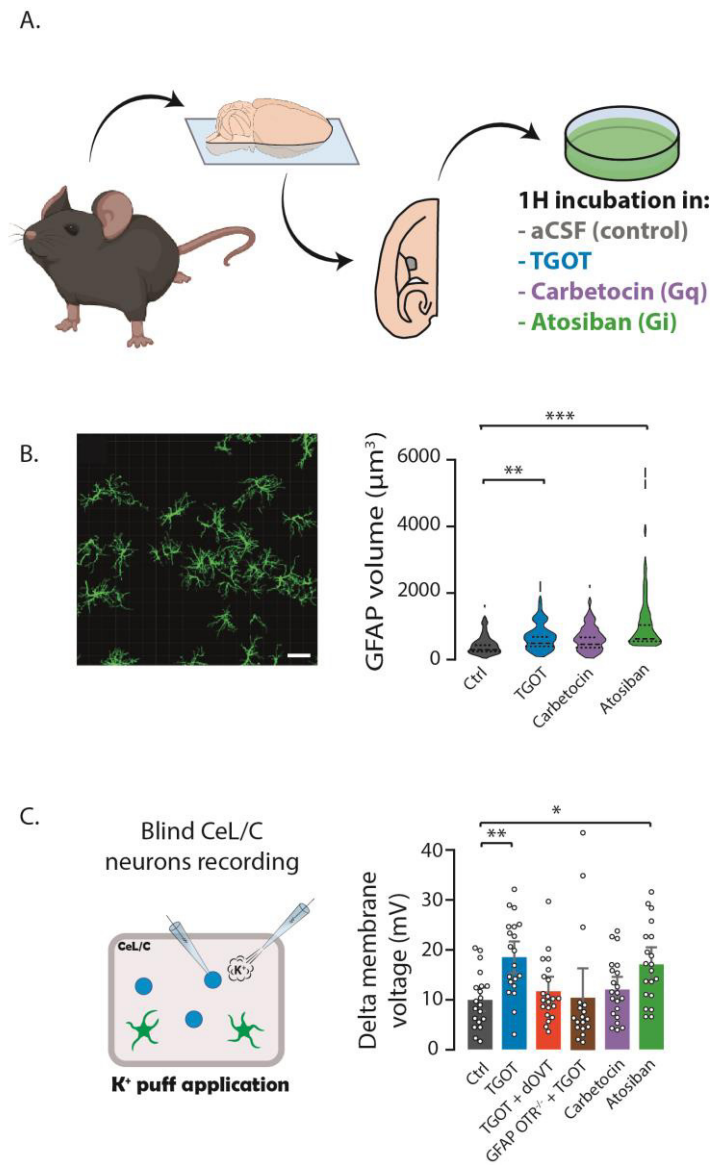
Figure 4: Effect of the different OTR intracellular coupling on the astro-neuronal network. A. Brain slices were incubated for 1 hour in the different OTR agonists before an analysis of CeL/C astrocytes reactivity (**B**) or an electrophysiological characterization of CeL/C neurons (**C**). **B.** Analysis of the GFAP expression in CeL/C astrocytes. $n_{Control}$ = 134 astrocytes, n_{TGOT} = 208 astrocytes, $n_{atosiban}$ = 271 astrocytes, $n_{carbetocin}$ = 225 astrocytes. **C.** K$^+$-induced depolarization of CeL/C neurons after incubation in various agonists. All depolarization values were compared to the control condition. n are comprised between 20 and 21 neurons. Data are expressed as mean across cell ± SEM. Detailed statistics can be found in *Statistic Table 4* and other electrophysiological parameters of CeL/C neurons can be found in *Supplementary Figure 4*. * p<0.05, ** p<0.01, *** p<0.001.

The morphological plasticity of CeL/C astrocytes regulates BLA-to-CeL/C neurotransmission by controlling K$^+$ buffering.

Astrocytes can modify neurons' activity in many ways, including neurotransmitter reuptake, energy supply, or by releasing gliotransmitters. Given that the OTR-Gαi pathway induced both a retraction of astrocyte morphology and a correlated increase in neuronal network excitability, we decided to investigate K$^+$ buffering, one of the most important astrocyte functions. Indeed, neuron activity results in an increased extracellular K$^+$ level. To prevent a rupture of K$^+$ homeostasis, astrocytes uptake the excess of extracellular K$^+$, thereby maintaining a favorable environment for neuronal activity (Kofuji and Newman, 2004; Pannasch and Rouach, 2013). This ability to buffer potassium

strongly depends on the distance between astrocyte processes and synapses. We thus hypothesize that the morphological changes induced by fear conditioning may physically modify the tripartite synapse configuration and thereby change the potassium buffering capacity of CeL/C astrocytes.

To test this hypothesis, we injected AAV-GFAP-GFP viruses in the CeL/C of mice to identify astrocyte processes and performed immunostainings against vGluT1, vGluT2, and Homer1 to reveal pre and postsynaptic elements of excitatory synapses. We then reconstructed astrocytes and synapses and observed that astrocytes from fear-conditioned mice contact significantly fewer synapses compared to astrocytes from naïve mice, suggesting that a strong emotional challenge triggers the retraction of astrocytic processes away from synapses (p = 0.0044, Figure 5A). However, this difference was not observed in GFAP OTR cKO mice, indicating that astrocytic OTR is involved in this morphological adaptation (p > 0.999, Figure 5A).

This difference of proximity between astrocyte processes and excitatory synapses makes us wonder what synaptic input might be relevant to explain the absence of freezing response observed in GFAP OTR cKO mice. Many studies point to the crucial importance of BLA-to-CeL/C projections for the learning of auditory fear conditioning (LeDoux, 2000; Li et al., 2013), so we decided to evaluate whether fear conditioning modifies the strength of BLA-to-CeL/C projections. To do so, we injected AAV-CaMKII-ChR2 viruses in the BLA of mice (Figure 5B) and two to three weeks later, we fear-conditioned them and recorded the electrophysiological response of CeL/C neurons to a 10s 20Hz photostimulation of BLA neurons. This stimulation led to a robust increase of excitatory postsynaptic currents (EPSCs) frequency and amplitude in CeL/C neurons ($p_{amplitude} < 0.001$, Figure 5B, $p_{frequency} < 0.001$, Figure S4A). According to what was observed by Li and colleagues (Li et al., 2013), we measured an increased amplitude of EPSCs triggered by BLA neurons photostimulation after fear-conditioning ($p_{interaction} = 0.001$, Figure 5B). This increased synapse strength indicates an increased weight of the BLA-to-CeL/C pathway, suggesting an encoding mechanism for emotionally relevant memories.

To investigate the potential implication of astrocytes' K^+ buffering in this increase of BLA-to-CeL/C neurotransmission, we recorded CeL/C astrocyte K^+ current triggered by the activation of BLA neurons. So, we patch-clamped SR101-label cells and verify their astrocyte identity based on the shape of their IV curve (Nishiyama et al., 2005) (Figure S4B). To isolate the portion of the current due to K^+ buffering, we performed paired recordings where we first photostimulated BLA neurons and we then replaced the recording solution with a 200µM of Ba^{2+}-containing solution to block K^+ currents. After 15 minutes, we re-photostimulated BLA neurons and we subtracted the evoked currents recorded in aCSF from the one recorded in the Ba^{2+} containing solution (Figure 5C). In naïve mice, we observed a K^+

current of -91.61±24.62 pA but in fear-conditioned animals, this amplitude is significantly decreased to –20.49±12.84 pA (p = 0.031), indicating an impairment of astrocytic K^+ buffering (Figure 5C).

Based on these results, we hypothesize that upon fear conditioning, astrocyte processes retract away from neurons and buffer less K^+ at the level of the BLA-to-CeL/C synapses, thereby increasing the strength of this connection.
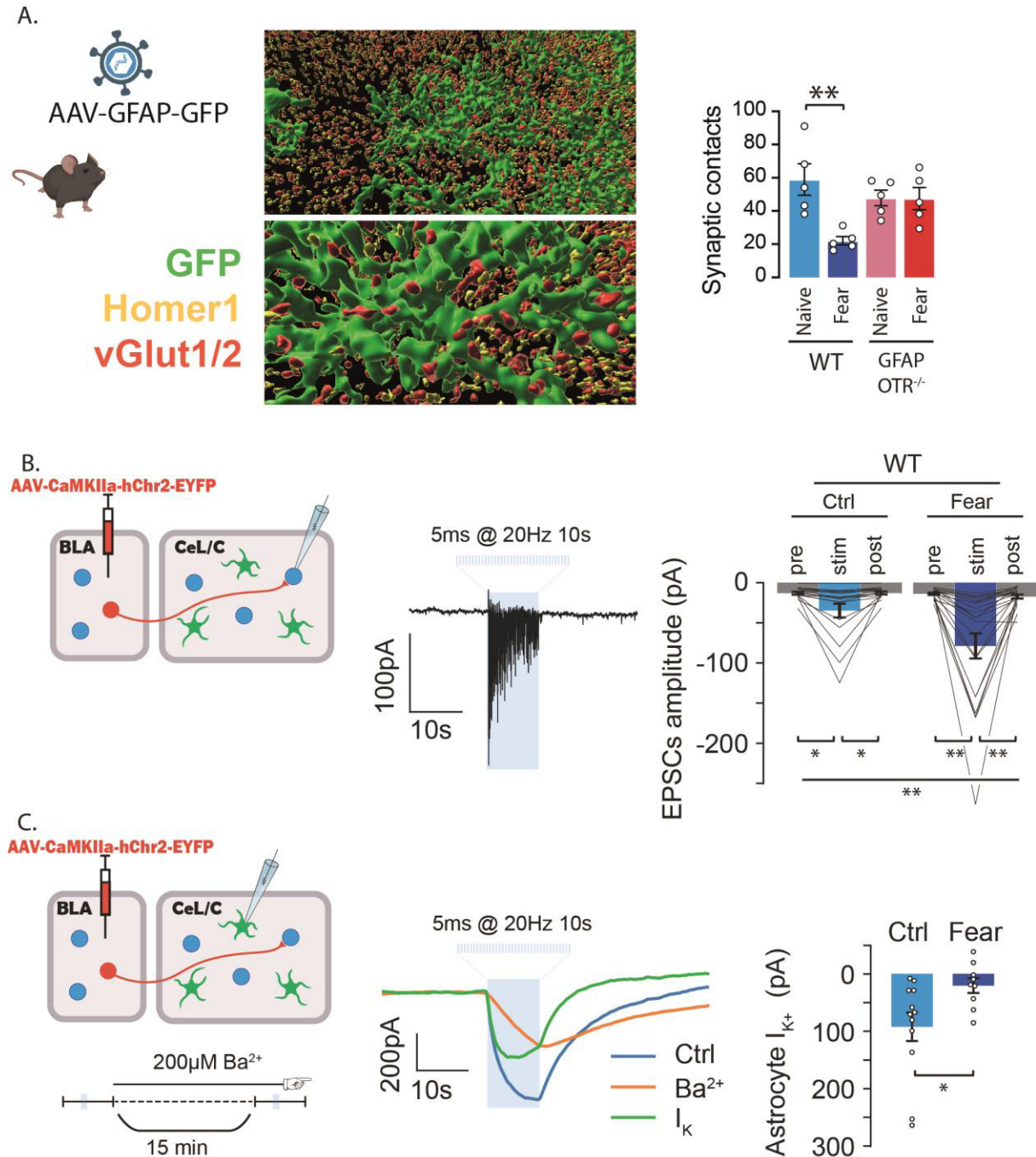

Figure 5: Involvement of astrocytic OTR on fear-conditioning induced modification of BLA-to-CeL/C excitatory synaptic transmission. A. Analysis of the distance between astrocytes processes and excitatory synapses in naïve and fear-conditioned mice. Left: mice were injected with AAV-GFAP-GFP

viruses to reveal astrocytes morphology. Middle: examples of astrocyte and synapse 3D reconstruction. Left: quantification of the distance between synapses and astrocyte processes. n = 5 animals in each group. **B**. Amplitude of BLA-to-CeL/C excitatory postsynaptic currents (EPSCs). Left: An AAV-CaMKII-ChR2 was injected in the BLA of mice and 3 weeks after, we measured the currents evoked by BLA neurons activation in CeL/C neurons. Middle: Example trace of EPSCs triggered by BLA photostimulation. Right: Mean EPSCs amplitude measured before, during, and after the photostimulation. $n_{naïve}$ = 17 neurons, n_{fear} = 21 neurons. **C.** K^+ currents recorded in CeL/C astrocytes induced by BLA-to-CeL/C synaptic transmission in naïve and fear-conditioned mice. Left: An AAV-CaMKII-ChR2 was injected in the BLA of mice and 3 weeks after, the currents evoked by BLA neuron activation were measured in CeL/C astrocytes. Middle: Example trace of the astrocytic current induced by BLA neurons stimulation before and after a 15-minute incubation in Ba^{2+} (200µM). The subtracted potassium current is shown in green. Right: Mean astrocytic potassium current amplitude measured during the photostimulation of BLA neurons. $n_{naïve}$ = 12 astrocytes, n_{fear} = 9 astrocytes. Data are expressed as mean across animal ± SEM for panel A, and as mean across cell ± SEM for panels B and C. Detailed statistics can be found in *Statistic Table 5*. * $p<0.05$, ** $p<0.01$.

Discussion

The present study shows that fear conditioning induces astrocyte plasticity in the laterocapsular nucleus of the central amygdala. This plasticity depends on astrocytic oxytocin receptors, and more precisely on an OTR-Gαi pathway. This atypical astrocyte activation results in the reduction of astrocyte K^+ buffering at the level of the BLA-to-CeL/C synapse, eventually increasing the weight of this connection. We hypothesize that this mechanism can be part of the attribution of the emotional valence triggered by fear conditioning (Figure 6).
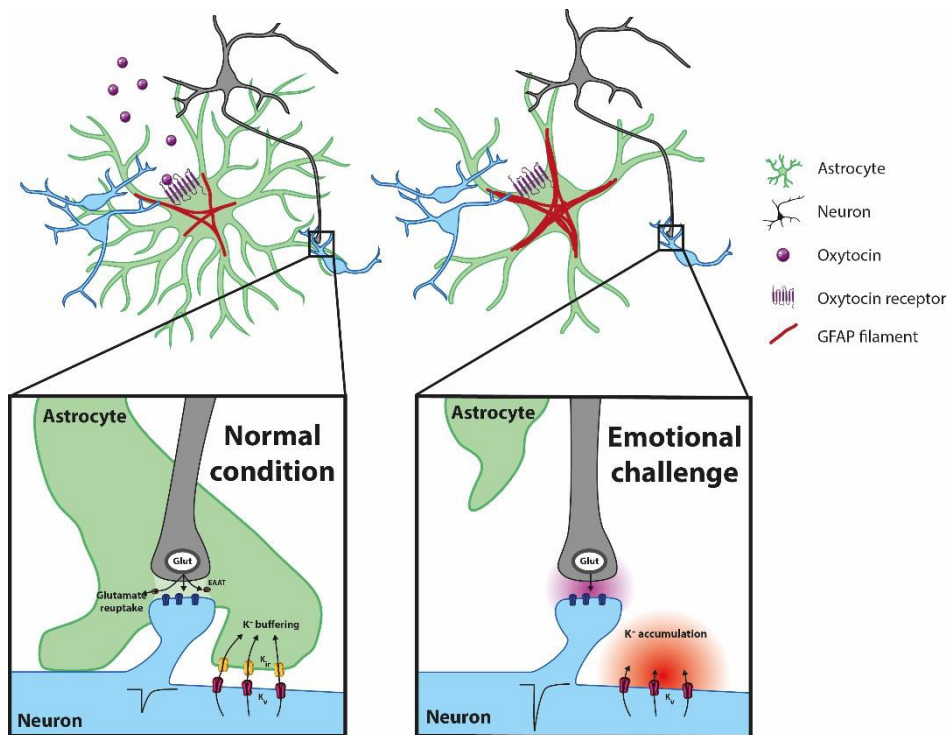
Figure 6: Hypothetical mechanism of astrocyte involvement in fear memory. In normal conditions (left) CeL/C astrocytes express few GFAP filaments and buffer potassium at the BLA-to-CeL/C synapse. After a strong emotional challenge such as fear (right), astrocyte retract their processes away from synapses, decreasing potassium buffering and ultimately increasing BLA-to-CeL/C synapses strength.

Our results showed that GFAP OTR cKO mice do not freeze during the conditioning session of the fear conditioning protocol. This observation could be explained by a lack of pain, fear, or even the behavioral impossibility to freeze. Thus, we can suggest that the mouse is afraid but does not express it with freezing. The involvement of OT has been recently highlighted in the CeA to induce a switch from passive (ie. freezing) to active response (ie. escape) to an imminent threat, thereby indicating that OT may be a regulator of fear reaction rather than of fear itself (Terburg et al., 2018). To test this

hypothesis, we could measure the plasma levels of corticosterone in mice after the conditioning phase of the fear conditioning protocol. If the same level of corticosterone is observed in control and GFAP OTR cKO mice, this could indicate that GFAP OTR cKO mice are afraid but do not express it by freezing. However, if we do not observe an increased corticosterone level in GFAP OTR cKO mice after fear conditioning, we could hypothesize a potential absence of fear in those mice. This approach, however, will not permit to discriminate between the effect of fear and pain. It seems difficult to induce acute pain without inducing fear but we can isolate fear using mice just after the retrieval of the fear memory, thereby inducing fear without pain. Still, this approach also depends on the encoding of the fear memory, introducing another parameter that can vary. An elegant approach to overcome this will be to induce an innate fear in mice, but it has been shown that innate and learned fear may be differentially regulated in the CeA (Isosaka et al., 2015). Therefore, it will be interesting to use multiple paradigms to compare their results.

We observed an increased astrocyte reactivity after the conditioning phase of the fear protocol. This modification of astrocyte physiology append relatively quickly (within 15 minutes), and co-occurs with the morphological modification of astrocyte processes. In this study, we did not investigate the molecular links between OTR-Gαi activation, astrocytes reactivity, and their morphological adaptation. Yet, Gαi pathways can activate the STAT transcription factor (Jiang and Bajpayee, 2009), which is a marker of astrocyte reactivity (Ben Haim et al., 2015). Thus, we can imagine that the first link is STAT. One step further in the mechanism, we could investigate the mechanisms linking astrocyte reactivity to their morphological changes. To our knowledge, no study has investigated the possible actors underlying this mechanism in reactive conditions but it has been shown that astrocyte can control their process morphology relatively quickly upon strong neuronal activity (Henneberger et al., 2020). A recently published study also showed a link between Gαi-GPCR activation and astrocyte morphology, indicating that the Gαi pathway may be a common mechanism for the regulation of astrocyte morphology (Cheng et al., 2023). Our approach however, identifies a small number of contact between astrocyte processes and synapses (~100), an amount excessively small compared to what has been found previously (Bushong et al., 2002). This discrepancy is explained by the stringent values we used for the identification of synapses to avoid false positives. This approach allowed us anyway to observe an increased distance between astrocytes processes and synapses after fear condition.

This retraction of astrocyte processes away from synapses decreases their ability to control the extracellular medium homeostasis. We showed that the potassium buffering ability of CeL/C astrocytes was impaired after fear conditioning but we can suggest that many other astrocyte functions can also be impacted. For instance, synaptic glutamate uptake will likely be decreased after

fear conditioning. To test this, we could block glutamate transporters using TBOA as we did for K^+ currents using Ba^{2+} (De Saint Jan and Westbrook, 2005). Therefore, if we aim to directly measure potassium levels in the extracellular space, we could use fluorescent indicators to measure either the extracellular [K+] (Sato et al., 2022) or the use of ratiometric genetically encoded K+ indicator KRIN1 expressed in astrocytes to evaluate their K+ buffering ability (Shen et al., 2019).

Methods

Animals. Animals were housed under standard conditions with food and water available *ad libitum* and maintained on a 12-h light/dark cycle. All experiments were conducted in accordance with European Union rules and approbation from the French Ministry of Research (01597.05). For *ex vivo* and *in vivo* experiments, male and female C57BL/6 mice were used. *Ex vivo* experiments used animals between 1 and 2 months old, except in experiments where rAAVs were injected, in which case animals were between 3 and 4 months old at the time of sacrifice.

Stereotaxic injections. Animals were deeply anesthetized with 4% isoflurane, and their heads were fixed in a KOPF (model 955) stereotaxic frame. Metacam (Meloxicam, 20 mg/kg) was injected in the neck to avoid inflammation and local analgesics were injected in the cutting site (Bupivacaïne, 5 mg/kg, and Lurocaïne, 2 mg/kg). The skull was then exposed, and two holes were drilled according to coordinates that were adapted from Paxinos and Watson brain Atlas. For injections in the CeL/C, we injected 200nL of rAAV1/2-gfaABC1D-GFP-IRES-Cre in the following coordinates: rostrocaudal = −1.25 mm, mediolateral = ± 3.1 mm, dorsoventral = −5.0 mm. To stimulate BLA neurons, we injected 100nL of AAV9-CaMKIIa-hChR2(H134)-EYFP in the following coordinates: rostrocaudal = −1.8 mm, mediolateral = ± 3.4 mm, dorsoventral = −5.0 mm. The wound was then sutured and the weight of the animals was followed for five days to verify the post-operatory recuperation. After ~3 weeks, mice were used for experiments.

Fear conditioning. The fear conditioning protocol was divided into four stages: habituation, conditioning, re-exposition 1, and re-exposition 2. During day 1, the habituation session of 10 minutes takes place in context A composed of a smooth white plastic floor and walls. Mice were exposed five times to a 20s-long CS tone (2kHz, 60dB) with a variable inter-tone interval (20 to 180 seconds). For the conditioning session of 10 minutes on day 2, mice were placed in context B which has a grid floor and striped walls. During this session, mice were exposed to five tones with different inter-tone time intervals but the last second of these tones coincided with a 1s-long foot shock of 0.6mA. On days 3 and 4, the re-exposition session was 12 minutes and take place in context A as the habituation session.

During these sessions, mice were exposed 20 times to the tone. Freezing behavior was quantified using the ANY-maze software as periods longer than 2 seconds where the mice did not move. Freezing measures were extracted during the 20-second sound exposition. All script used to quantify and analyses behavioral experiments are available in the following repository: https://github.com/AngelBaudon/Behavior-Analysis.

Slice preparations. Mice were anesthetized using ketamine (Ketamine 1000, 400 mg/kg) and xylazine (Paxman, 80 mg/kg) administered intraperitoneally. Intracardiac perfusion was then performed using an ice-cold NMDG-based aCSF containing (in mM): NMDG (93), KCl (2.5), NaH2PO4 (1.25), NaHCO3 (30), MgSO4 (10), CaCl2 (0.5), HEPES (20), D-glucose (25), L-ascorbic acid (5), thiourea (2), sodium pyruvate (3), N-acetyl-L-cysteine (10) and kynurenic acid (2). This solution was bubbled in 95% O_2/5% CO_2 gas all the time of the experiment and its pH was adjusted to 7.3-7.4 using HCl. After decapitation, the brain was swiftly removed in the same ice-cold dissection aCSFs and hemisectionned. 350 μm-thick horizontal slices containing the CeA were obtained using a Leica VT1000S vibratome. Slices were then put in 37 °C NMDG aCSF for 10 min before placing them in the holding chamber at room temperature containing normal aCSFs for 1 h minimum before any experiments were conducted. Normal aCSF used during all *ex vivo* experiments, is composed of (in mM): NaCl (124), KCl (2.5), NaH2PO4 (1.25), NaHCO3 (26), MgSO4 (2), CaCl2 (2), D-glucose (15), adjusted for pH values of 7.3-7.4 with HCl or NaOH and continuously bubbled in 95% O_2/5% CO_2 gas. All aCSFs' osmolality was controlled to be between 290 and 310 mOsm/L. In experiments of Fig3, the slices were then incubated in aCSF supplemented with 500nM of agonist and/or antagonist for 1 hour. For morphological analysis, slices were fixed in 4% PFA overnight and transferred in PBS-Azide. For electrophysiology and calcium imaging, slices were transferred from the holding chamber to an immersion recording chamber and superfused at a rate of 2 ml/min with normal aCSF.

Electrophysiology. Whole-cell patch-clamp recordings of CeL/C neurons and astrocytes were visually guided by infrared oblique light visualization of neurons and completed by SR101 fluorescence observation for astrocytes. Patch-clamp recordings were obtained with an Axon MultiClamp 700B Amplifier coupled to a Digidata 1440A Digitizer (Molecular Devices). Borosilicate glass electrodes (OD 1.5 mm, ID 0.86 mm; Sutter Instrument) were pulled using a horizontal flaming/brown micropipette puller (P97; Sutter Instrument) to obtain 3.5-7 MΩ recording pipettes. These pipettes were filled with an intracellular solution containing (in mM): K-Glu (125), HEPES (20), NaCl (10), and ATPNa2 (3). The pH was adjusted to 7.3-7.4 with KOH, and osmolality was checked to be between 290 and 310 mOsm/L, adjusted with water if needed. Recordings were acquired at 20 kHz using either the pClamp 10 software suite (Molecular Devices) for puff experiments or using WinWCP 4.2.2 freeware (John Dempster, SIPBS, University of Strathclyde, UK) for photostimulation experiments. Series resistance

was monitored and manually compensated (~50% typically). A current step ranging from -10 pA to 100 pA by 10 pA intervals was applied to neurons at the beginning of each recording.

For puff application of potassium, the injected current was adapted to hold the neurons at -60mV, basal activity of neurons was recorded for 20 seconds and then a 20-second long potassium puff was done at ~150μm of the recorded neuron. This protocol was repeated three times and the median value of all parameters was used for statistical analysis.

For puff application of OTR agonists, the injected current was adapted to hold the neurons at a membrane voltage where we could observe a regular spiking of the neuron (typically between -50 and -40 mV). After a one-minute recording of basal activity, we puff applied an aCSF solution containing 10 μM of the agonists (TGOT, atosiban, or carbetocin) at ~150μm of the recorded neuron and neuronal activity was monitored for an additional nine minutes. The one-minute-long quantification windows were taken at the beginning of the recording, just after the puff application, and at the end of the recording.

For optostimulation of BLA neurons, neurons were held in voltage clamp at -60mV. We then recorded 20 seconds of basal activity before stimulating with 5ms-long light stimulation at 20Hz for 10 seconds. These parameters were chosen based on the work of Servonnet *et al.*, 2020. This recording was repeated three times and the medial value of the three recordings was used for statistical analysis. The five seconds long quantification windows were taken at the beginning of the recording, just after the Optostimulation, and at the end of the recording.

For astrocytic potassium currents recordings, astrocytes were visualized using SR101 and patch-clamped at -80mV. A voltage step ranging from -100mV to 100mV by 20mV intervals was applied to astrocytes at the beginning of each recording. We then recorded 20 seconds of basal activity before stimulating with 5ms-long light stimulation at 20Hz for 10 seconds. We then change the recording medium with a recording medium containing 200μM of Ba^{2+} for 15 minutes and stimulate BLA neurons. The peak value of both currents was then subtracted to estimate the potassium component of the initial current and this value was used for further statistical analysis. All script used to quantify and analyses electrophysiological experiments are available in the following repository: https://github.com/AngelBaudon/Electrophysiology-Analysis.

Calcium imaging and identification of astrocytes. To identify astrocytes, SR101 (1 μM) was added to aCSF in a culture well, and slices were incubated for 20 min at 37 °C. The synthetic calcium indicator OGB1-AM was bulk loaded as previously described (Baudon et al., 2022), reaching final concentrations of 0.0025% (~20 μM) for calcium indicators, 0.002% for Cremophor EL, 0.01% for Pluronic F-127 and 0.5% for DMSO in aCSF and incubated for 1 hour at 37 °C. After incubation, slices were washed in aCSF

for at least 1 h before any recording was performed. Astrocytes recorded for this study were those co-labeled for SR101 and OGB1. The spinning disk confocal microscope used to perform astrocyte calcium imaging was composed of a Zeiss Axio examiner microscope with a ×40 water immersion objective (numerical aperture of 1.0), mounted with an X-Light Confocal Unit–CRESTOPT spinning disk. Images were acquired at 2 Hz with an optiMOS sCMOS camera (Qimaging). Cells within a confocal plane were illuminated for 20ms at 575nm for SR101 and 80ms at 475nm for OGB1 using a Spectra 7 LUMENCOR. The different hardware elements were synchronized through the MetaFluor 7.8.8.0 software (Molecular Devices). Because astrocytes are mechanosensitive, OTR agonists (500nM) were bath applied for 20 seconds and not puff-applied to avoid mechanical stimulation.

All analyses were conducted as in Baudon *et al.*, 2022. Astrocytic calcium levels were measured in hand-drawn regions of interest (ROIs) comprising the cell body. Further offline data analysis was performed using a custom-written Python-based script available in the following repository (https://github.com/AngelBaudon/Calcium-Imaging-Analysis). Intracellular calcium variation was estimated as changes in fluorescence signals. To take into account micro-movements of the specimen on long-duration recordings, the fluorescence values were also calculated for SR101 and subtracted from the ones of OGB1. Then, a linear regression was applied to each trace to correct the photobleaching. Calcium transients were detected using the find_peaks function of the SciPy library. More precisely, fluorescence variation was identified as a calcium peak if its prominence exceeds the 5 times the SD of the trace and if the maximum peak value surpasses 8 times the SD (for more details, see Baudon *et al.*, 2022). The number of peaks was quantified before and after the drug application. All data were normalized according to the duration of the recording, and astrocytes were labeled as 'responsive' when their AUC or their calcium transient frequency at least doubled after drug application. Because the time after stimulation is longer than the baseline (10 min versus 5 min), the probability of observing a spontaneous calcium peak is stronger after stimulation. To avoid this bias, astrocytes with only one calcium peak during the whole recording were not considered responsive. All data were expressed as a ratio (baseline/drug effect)—a ratio of one meaning neither an increase nor a decrease of the measured parameter. All calcium imaging experiments were conducted at room temperature and cells with an unstable baseline were discarded. All script used to quantify and analyses calcium imaging experiments are available in the following repository: https://github.com/AngelBaudon/Calcium-Imaging-Analysis.

Immunohistochemistry and in situ hybridization Mice were anesthetized using ketamine (Ketamin 1000, 400 mg/kg) and xylazine (Paxman, 80 mg/kg) administered intraperitoneally. Animals were then perfused transcardially with PBS, followed by 4% PFA. Brains were dissected out and post-fixed overnight in 4% PFA at 4 °C with gentle agitation. Then, 50-μm vibratome sections were cut, collected,

and stored in PBS 1X overnight at 4°C. Slices were then incubated in a PBS1X-Gelatin 0.02%-Triton 0.25% solution for permeabilization and saturation of non-specific sites during 1h at RT. Incubation of the first antibodies took place overnight at 4°C and slices were then washed and incubated with secondary antibodies overnight at 4°C. Finally, slices were mounted in an Abberior antifade medium and left for one day at 4°C in the dark for polymerization. All antibodies used and their concentrations are given in the following table:

| Antigen	Reference	Host	Dilution
GFAP	Abcam ab53554	Goat	1/200
GFP	Aves 1020	Chicken	1/200
vGlut1	Synaptic system 135511	Mouse	1/200
vGlut2	Synaptic system 135421	Mouse	1/200
Homer1	Synaptic system 160003	Rabbit	1/200
Rabbit	Interchim 715-586-152	Donkey	1/200
Mouse	Abberior STRED-1001-500UG	Goat	1/200
Chicken	Abberior STRED-1005-500UG	Goat	1/200

Assessment of astrocyte complexity and interaction analysis using Imaris. For the 3D reconstruction of astrocytes, we took Z-stack images (50-μm depth, 1-μm steps, ×40 magnification) of CeL/C using a Zeiss LSM 780 confocal microscope (1,024 × 1,024 pixels, 16-bit depth, pixel size 0.63 microns, zoom 0.7). Raw CZI files were used for further analysis using Imaris software (version 9.31, Oxford Instruments). First, Imaris was used to reconstruct the astrocyte surface using the following custom settings: surfaces Detail 0.700μm (smooth); thresholding Background subtraction (Local Contrast), the diameter of largest Sphere, which fits into the object: 2.00; Color: base, diffusion transparency: 65%. After surface reconstruction, we used the filter function to remove unspecific background signals: Filter: Volume max – 400 μm3. It is important to note that these settings have to be adjusted for every new batch/immunohistochemistry staining to guarantee a reliable reconstruction. All astrocytes with incomplete somata (cut by the x, y, or z plane) were manually removed and not included in further analysis. Fused astrocytes that were falsely recognized as one entity by the software were manually separated using the cut function or entirely removed from the sample if a separation was not feasible. The 'filter/area function' was used to remove small astrocytic segments that occurred during manual deletion. After the deletion of all background signals, the 'mask all' function was used to create the final surface reconstruction. Next, the surface reconstruction was used as the template for the filament reconstruction using the following custom settings: detect new starting points: largest Diameter 7.00μm, seed points 0.300μm; remove seed points around starting points: diameter of sphere regions:

15 µm. Seed points were corrected (either placed in or removed from the center of the somata) manually if the Imaris algorithm placed them incorrectly. All surface and filament parameters were exported into separate Excel files and used for data analysis. All images used for analysis were taken with the same confocal settings (pinhole, laser intensity, digital gain, and digital offset). Sholl analysis was performed using Imaris in the filament reconstruction mode, and individual datasets were exported into separate Excel files for further analysis (each individual sphere) per individual astrocyte. Distribution plots and correlations, as well as all statistics, were performed using GraphPad Prism version 8.0.0 (GraphPad Software).

Statistical analysis. All parametrical statistical tests were performed following correct verification of the assumptions on the distribution of data and equality of group variances, and, if not, non-parametric tests were used. Tests were performed using either GraphPad Prism software (version 8.0.0 for Windows) or the SciPy Python-based library. All values, group compositions, and statistical tests for each experiment are detailed in Supplementary Tables 1–5.

Supplementary figures

A.
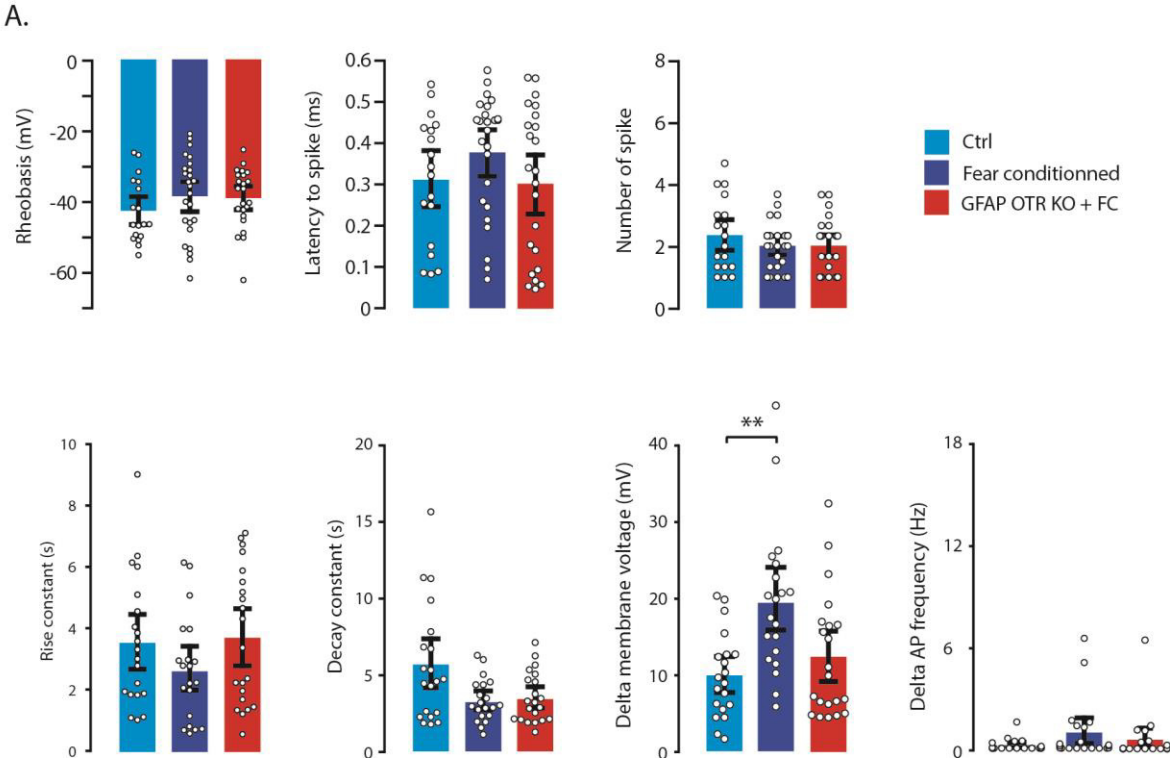
Supplementary Figure 1: Electrophysiological properties of CeL/C neurons. n are comprise between 18 and 25 neurons, for detail, see *Statistic Table 1*. Data are expressed as mean across cell ± SEM. Detailed statistics can be found in *Statistic Table 1*. ** p<0.01.
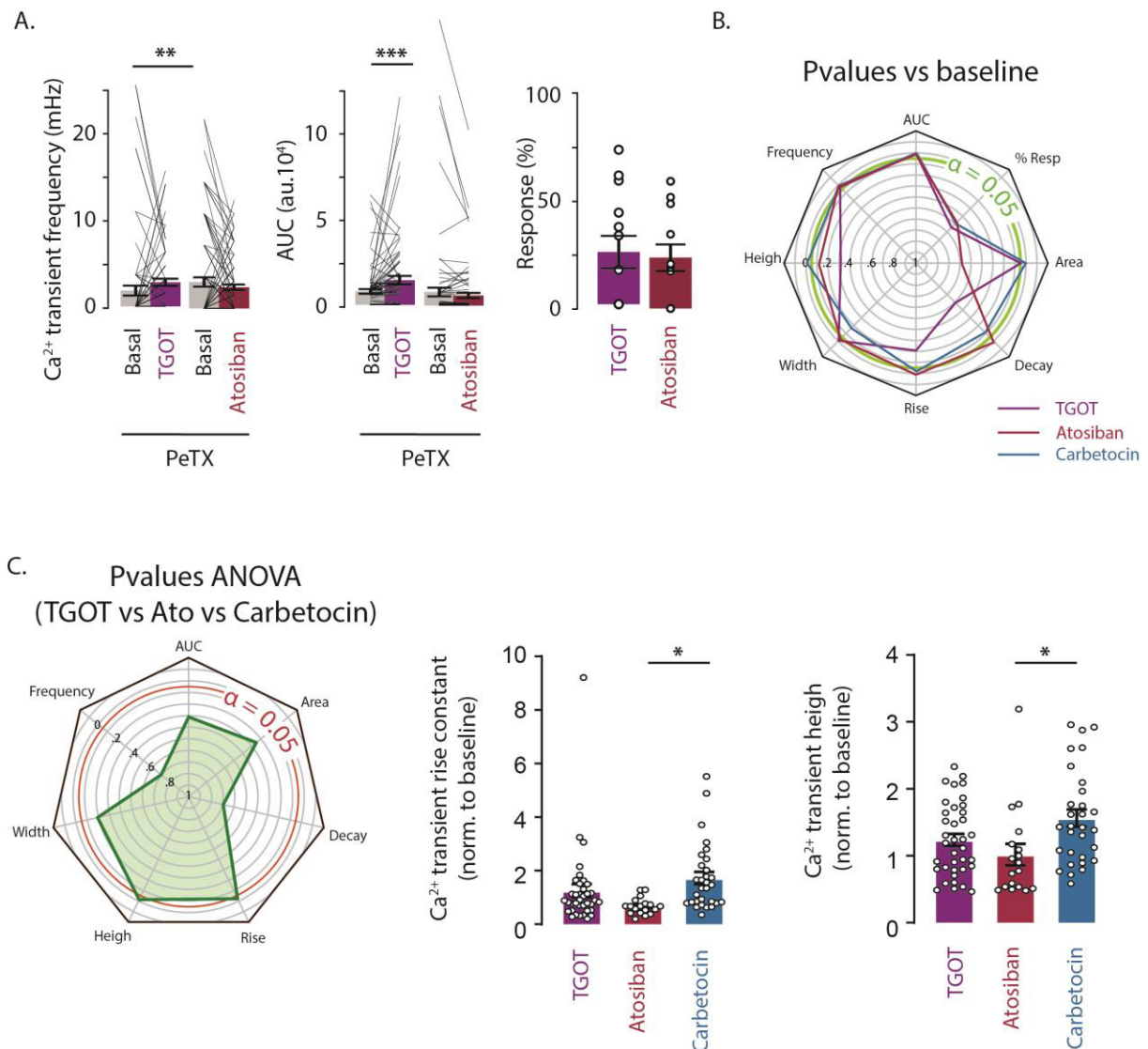
Supplementary Figure 2: Analysis of the intracellular pathway triggered by different OTR agonists. A. Effect of slice pre-incubation in pertussis toxin (PeTX) on the calcium response of CeL/C astrocyte to TGOT or atosiban. n_{TGOT} = 90 astrocytes over 13 slices, $n_{atosiban}$ = 99 astrocytes over 14 slices. **B.** Analysis of calcium events features triggered by different OTR agonists. The spider plot represents the pvalues of the comparison between spontaneous and evoked calcium signal. **C.** Comparison of calcium transient characteristics evoked by different OTR agonists. Calcium transient height and rising constant are differentially affected by carbetocin compared to the one observed after the application of atosiban. n_{TGOT} = 57 astrocytes over 13 slices, $n_{atosiban}$ = 49 astrocytes over 9 slices, $n_{carbetocin}$ = 54 astrocytes over 13 slices. Data are expressed as mean across cell ± SEM. Detailed statistics can be found in *Statistic Table 2*. * $p<0.05$, ** $p<0.01$, *** $p<0.001$.
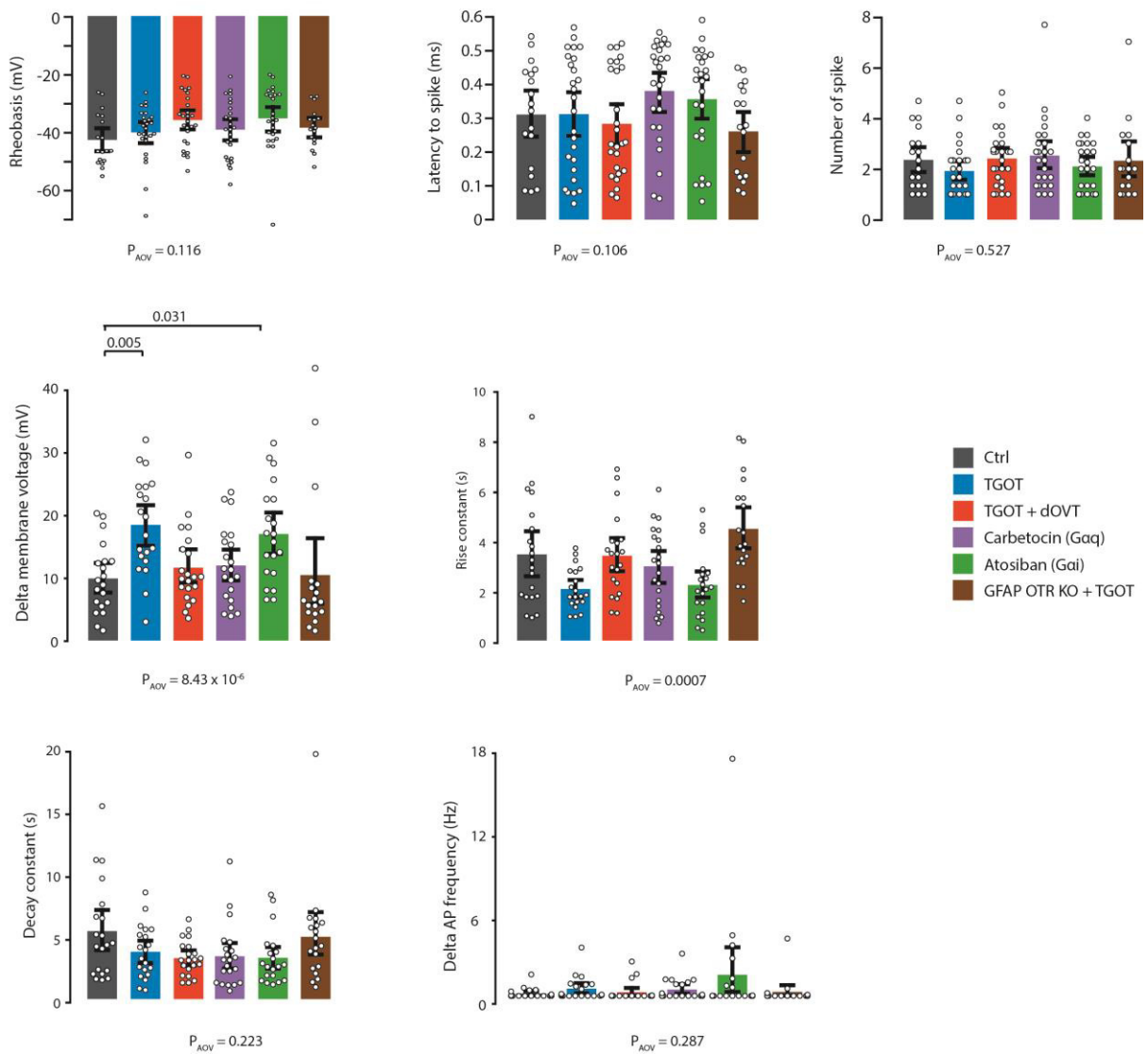
A.

Supplementary Figure 3: Electrophysiological properties of CeL/C neurons. n are comprise between 17 and 26 neurons, for detail, see *Statistic Table 3*. Data are expressed as mean across cell ± SEM. Detailed statistics can be found in *Statistic Table 3*. ** p<0.01.
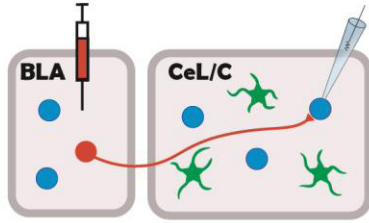
Supplementary Figure 4: Effect of BLA neuron photostimulation on CeL/C neurons and astrocytes. A. Frequency of excitatory post-synaptic currents before, during, and after the photostimulation of BLA neurons. $n_{naïve}$ = 17 neurons, n_{fear} = 21 neurons. **B.** Current-voltage relationship in CeL/C astrocytes. n = 12 astrocytes. Data are expressed as mean across cell ± SEM. Detailed statistics can be found in *Statistic Table 4*. *** p<0.001.

Bibliography

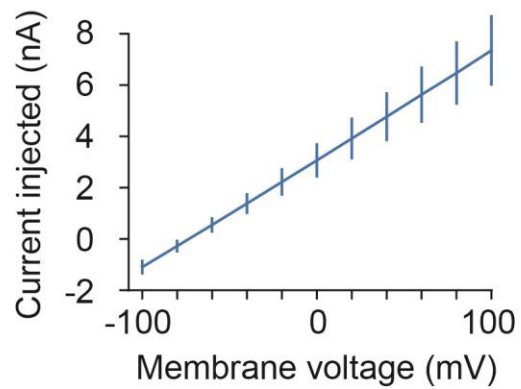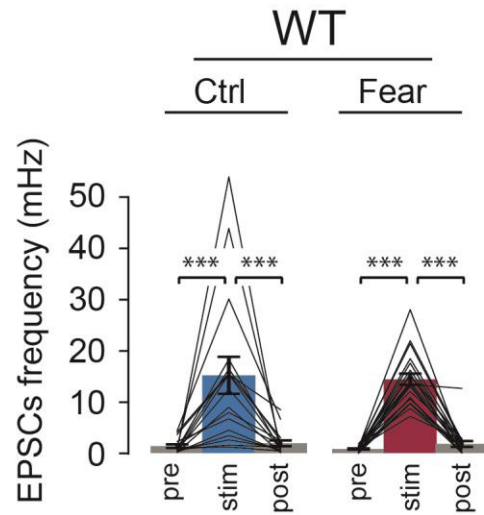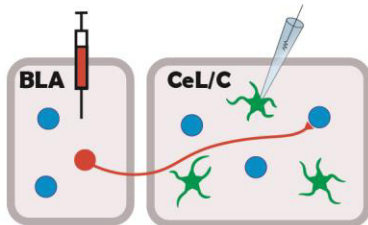Baldi, E., Costa, A., Rani, B., Passani, M.B., Blandina, P., Romano, A., Provensi, G., 2021. Oxytocin and Fear Memory Extinction: Possible Implications for the Therapy of Fear Disorders? Int. J. Mol. Sci. 22, 10000.

Baudon, A., Clauss-Creusot, E., Darbon, P., Patwell, R., Grinevich, V., Charlet, A., 2022. Calcium imaging and BAPTA loading of amygdala astrocytes in mouse brain slices. STAR Protoc. 3, 101159.

Ben Haim, L., Ceyzériat, K., Carrillo-de Sauvage, M.A., Aubry, F., Auregan, G., Guillermier, M., Ruiz, M., Petit, F., Houitte, D., Faivre, E., Vandesquille, M., Aron-Badin, R., Dhenain, M., Déglon, N., Hantraye, P., Brouillet, E., Bonvento, G., Escartin, C., 2015. The JAK/STAT3 Pathway Is a Common Inducer of Astrocyte Reactivity in Alzheimer's and Huntington's Diseases. J. Neurosci. 35, 2817–2829.

Bushong, E.A., Martone, M.E., Jones, Y.Z., Ellisman, M.H., 2002. Protoplasmic astrocytes in CA1 stratum radiatum occupy separate anatomical domains. J. Neurosci. Off. J. Soc. Neurosci. 22, 183–192.

Busnelli, M., Saulière, A., Manning, M., Bouvier, M., Galés, C., Chini, B., 2012. Functional selective oxytocin-derived agonists discriminate between individual G protein family subtypes. J. Biol. Chem. 287, 3617–3629.

Cheng, Y.-T., Luna-Figueroa, E., Woo, J., Chen, H.-C., Lee, Z.-F., Harmanci, A.S., Deneen, B., 2023. Inhibitory input directs astrocyte morphogenesis through glial GABABR. Nature.

De Saint Jan, D., Westbrook, G.L., 2005. Detecting Activity in Olfactory Bulb Glomeruli with Astrocyte Recording. J. Neurosci. 25, 2917–2924.

Durkee, C.A., Covelo, A., Lines, J., Kofuji, P., Aguilar, J., Araque, A., 2019. Gi/o protein-coupled receptors inhibit neurons but activate astrocytes and stimulate gliotransmission. Glia 67, 1076–1093.

Duvarci, S., Pare, D., 2014. Amygdala microcircuits controlling learned fear. Neuron 82, 966–980.

Escartin, C., Guillemaud, O., Carrillo-de Sauvage, M.-A., 2019. Questions and (some) answers on reactive astrocytes. Glia 67, 2221–2247.

Grinevich, V., Knobloch-Bollmann, H.S., Eliava, M., Busnelli, M., Chini, B., 2016. Assembling the Puzzle: Pathways of Oxytocin Signaling in the Brain. Biol. Psychiatry 79, 155–164.

Henneberger, C., Bard, L., Panatier, A., Reynolds, J.P., Kopach, O., Medvedev, N.I., Minge, D., Herde, M.K., Anders, S., Kraev, I., Heller, J.P., Rama, S., Zheng, K., Jensen, T.P., Sanchez-Romero, I., Jackson, C.J., Janovjak, H., Ottersen, O.P., Nagelhus, E.A., Oliet, S.H.R., Stewart, M.G., Nägerl, U.V., Rusakov, D.A., 2020. LTP Induction Boosts Glutamate Spillover by Driving Withdrawal of Perisynaptic Astroglia. Neuron 108, 919-936.e11.

Huber, D., Veinante, P., Stoop, R., 2005. Vasopressin and oxytocin excite distinct neuronal populations in the central amygdala. Science 308, 245–248.

Isosaka, T., Matsuo, T., Yamaguchi, T., Funabiki, K., Nakanishi, S., Kobayakawa, R., Kobayakawa, K., 2015. Htr2a-Expressing Cells in the Central Amygdala Control the Hierarchy between Innate and Learned Fear. Cell 163, 1153–1164.

Jiang, M., Bajpayee, N.S., 2009. Molecular mechanisms of go signaling. Neurosignals 17, 23–41.

Jurek, B., Neumann, I.D., 2018. The Oxytocin Receptor: From Intracellular Signaling to Behavior. Physiol. Rev. 98, 1805–1908.

Knobloch, H.S., Charlet, A., Hoffmann, L.C., Eliava, M., Khrulev, S., Cetin, A.H., Osten, P., Schwarz, M.K., Seeburg, P.H., Stoop, R., Grinevich, V., 2012. Evoked axonal oxytocin release in the central amygdala attenuates fear response. Neuron 73, 553–566.

Kofuji, P., Newman, E.A., 2004. Potassium buffering in the central nervous system. Neuroscience 129, 1045–1056.

LeDoux, J.E., 2000. Emotion circuits in the brain. Annu. Rev. Neurosci. 23, 155–184.

Lee, H.-J., Caldwell, H.K., Macbeth, A.H., Tolu, S.G., Young, W.S., 2008. A conditional knockout mouse line of the oxytocin receptor. Endocrinology 149, 3256–3263.

Lefevre, A., Benusiglio, D., Tang, Y., Krabichler, Q., Charlet, A., Grinevich, V., 2021. Oxytocinergic Feedback Circuitries: An Anatomical Basis for Neuromodulation of Social Behaviors. Front. Neural Circuits 15, 688234.

Li, H., Penzo, M.A., Taniguchi, H., Kopec, C.D., Huang, Z.J., Li, B., 2013. Experience-dependent modification of a central amygdala fear circuit. Nat. Neurosci. 16, 332–339.

Maldonado, P.P., Nuno-Perez, A., Kirchner, J.H., Hammock, E., Gjorgjieva, J., Lohmann, C., 2021. Oxytocin Shapes Spontaneous Activity Patterns in the Developing Visual Cortex by Activating Somatostatin Interneurons. Curr. Biol. CB 31, 322-333.e5.

McDonald, A.J., Mott, D.D., 2017. Functional neuroanatomy of amygdalohippocampal interconnections and their role in learning and memory. J. Neurosci. Res. 95, 797–820.

Moscarello, J.M., Penzo, M.A., 2022. The central nucleus of the amygdala and the construction of defensive modes across the threat-imminence continuum. Nat. Neurosci. 25, 999–1008.

Nagai, J., Rajbhandari, A.K., Gangwani, M.R., Hachisuka, A., Coppola, G., Masmanidis, S.C., Fanselow, M.S., Khakh, B.S., 2019. Hyperactivity with Disrupted Attention by Activation of an Astrocyte Synaptogenic Cue. Cell 177, 1280-1292.e20.

Nishiyama, A., Yang, Z., Butt, A., 2005. Astrocytes and NG2-glia: what's in a name? J. Anat. 207, 687–693.

Olivera-Pasilio, V., Dabrowska, J., 2020. Oxytocin Promotes Accurate Fear Discrimination and Adaptive Defensive Behaviors. Front. Neurosci. 14, 583878.

Pannasch, U., Rouach, N., 2013. Emerging role for astroglial networks in information processing: from synapse to behavior. Trends Neurosci. 36, 405–417.

Ryan, P.J., Ross, S.I., Campos, C.A., Derkach, V.A., Palmiter, R.D., 2017. Oxytocin-receptor-expressing neurons in the parabrachial nucleus regulate fluid intake. Nat. Neurosci. 20, 1722–1733.

Sato, S., Ohzawa, S., Sota, K., Sakamoto, N., Udo, A., Sueda, S., Matsuda, T., Nagai, T., Takenaka, S., 2022. Fluorescence Imaging of Extracellular Potassium Ion Using Potassium Sensing Oligonucleotide. Front. Chem. 10, 922094.

Shen, Y., Wu, S.-Y., Rancic, V., Aggarwal, A., Qian, Y., Miyashita, S.-I., Ballanyi, K., Campbell, R.E., Dong, M., 2019. Genetically encoded fluorescent indicators for imaging intracellular potassium ion concentration. Commun. Biol. 2, 18.

Sibille, J., Pannasch, U., Rouach, N., 2014. Astroglial potassium clearance contributes to short-term plasticity of synaptically evoked currents at the tripartite synapse. J. Physiol. 592, 87–102.

Terburg, D., Scheggia, D., Triana Del Rio, R., Klumpers, F., Ciobanu, A.C., Morgan, B., Montoya, E.R., Bos, P.A., Giobellina, G., van den Burg, E.H., de Gelder, B., Stein, D.J., Stoop, R., van Honk, J., 2018. The Basolateral Amygdala Is Essential for Rapid Escape: A Human and Rodent Study. Cell 175, 723-735.e16.

van den Burg, E.H., Stoop, R., 2019. Neuropeptide signalling in the central nucleus of the amygdala. Cell Tissue Res. 375, 93–101.

Wahis, J., Baudon, A., Althammer, F., Kerspern, D., Goyon, S., Hagiwara, D., Lefevre, A., Barteczko, L., Boury-Jamot, B., Bellanger, B., Abatis, M., Da Silva Gouveia, M., Benusiglio, D., Eliava, M., Rozov, A., Weinsanto, I., Knobloch-Bollmann, H.S., Kirchner, M.K., Roy, R.K., Wang, H., Pertin, M., Inquimbert, P., Pitzer, C., Siemens, J., Goumon, Y., Boutrel, B., Lamy, C.M., Decosterd, I., Chatton, J.-Y., Rouach, N., Young, W.S., Stern, J.E., Poisbeau, P., Stoop, R., Darbon, P., Grinevich, V., Charlet, A., 2021. Astrocytes mediate the effect of oxytocin in the central amygdala on neuronal activity and affective states in rodents. Nat. Neurosci. 24, 529–541.

TABLE 1: Numerical values and statistical analysis of data presented in Fig.1

Fig	Statistical unit	Groups tested	Paired ?	N	Unit	Test	Statistic	p-value
1B1	Freezing time (%)	Control	Mixed design	9	%	Mixed-Model ANOVA	Time: 3,767	0,000
		MALES					Genotype: 1,625	0,219
		GFAP OTR KO		11	%		Interaction: 4,259	<0,0001
1B2	Freezing time (%)	Control	Mixed design	8	%	Mixed-Model ANOVA	Time: 8,251	<0,0001
		FEMALES					Genotype: 4,532	0,052
		GFAP OTR KO		8	%		Interaction: 1,005	0,466

TABLE 2: Numerical values and statistical analysis of data presented in Fig.2 and Supplementary Fig.1

Fig	Statistical unit	Groups tested	Paired ?	N	Unit	Mean	SEM	Test		p-value
2B	Peak Sholl value	WT Naive	No	5	/	24,850	1,535	One-way ANOVA	WT naive vs. WT Fear	0,001
		WT Fear		5		13,110	1,339		WT naive vs. KO naive	0,063
		GFAP OTR KO Naive		5		18,560	1,502		WT naive vs. KO Fear	0,024
									WT Fear vs. KO naive	0,123
		GFAP OTR KO Fear		5		17,440	2,026		WT Fear vs. KO Fear	0,272
									KO naive vs. KO Fear	0,961
2C	GFAP volume	WT Naive	No	8	µm**3	409,600	1,535	One-way ANOVA <0,0001	WT naive vs. WT Fear	<0,0001
		WT Fear		10		952,000	1,339		WT naive vs. KO naive	0,733
		GFAP OTR KO Naive		7		479,400	1,502		WT naive vs. KO Fear	0,995
									WT Fear vs. KO naive	<0,0001
		GFAP OTR KO Fear		7		426,300	2,026		WT Fear vs. KO Fear	<0,0001
									KO naive vs. KO Fear	0,872

Fig	Statistical unit	Paired ?	N	Unit	Statistic	p-value	Test	R square
2D	Peak Sholl value GFAP	Yes	153	/ µm**3	199,700	<0,0001	Simple linear regression	0,569

Fig	Statistical unit	Groups tested	Paired ?	N	Unit	Mean	SEM	Test	p-value
2E & S1	Threshold	Ctrl	No	18	mV	-42,690	2,109	Kruskal-Wallis AOV & Dunn's MC with Sidak correction	/
		FC		25		-38,584	2,292		0,496
		FC GFAP OTR KO		25		-39,091	1,771		0,705
	Number of spike	Ctrl	No	18	/	2,352	0,275	Kruskal-Wallis AOV & Dunn's MC with Sidak correction	/
		FC		25		2,007	0,150		0,971
		FC GFAP OTR KO		25		2,014	0,187		0,962
	Latency to 1st spike	Ctrl	No	18	ms	3110,491	363,461	Kruskal-Wallis AOV & Dunn's MC with Sidak correction	/
		FC		25		3771,160	293,329		0,721
		FC GFAP OTR KO		25		3027,232	381,878		1,000
	Delta number of spike	Ctrl	No	20	/	0,181	0,086	Kruskal-Wallis AOV & Dunn's MC with Sidak correction	/
		FC		20		0,954	0,409		0,658
		FC GFAP OTR KO		20		0,527	0,310		1,000
	Rise constant	Ctrl	No	20	s	3,448	0,480	Kruskal-Wallis AOV & Dunn's MC with Sidak correction	/
		FC		20		2,546	0,386		0,738
		FC GFAP OTR KO		20		3,606	0,486		1,000
	Delta membrane voltage	Ctrl	No	20	mV	9,853	1,226	Kruskal-Wallis AOV & Dunn's MC with Sidak correction	/
		FC		20		19,290	2,139		0,004
		FC GFAP OTR KO		20		12,399	1,765		0,972
	Decay constant	Ctrl	No	20	s	5,437	0,863	Kruskal-Wallis AOV & Dunn's MC with Sidak correction	/
		FC		20		3,079	0,315		0,305
		FC GFAP OTR KO		20		3,274	0,359		0,436

TABLE 3: Numerical values and statistical analysis of data presented in Fig,3 and Supplementary Fig,2

Fig	Statistical unit	Groups tested	Time	Paired ?	N	Unit	Mean	SEM	Test	p-value
3A	Calcium transient frequency	TGOT	Baseline		57 cells over 13 slices	mHz	5,588	0,771	Wilcoxon	0,025
			TGOT				7,302	0,700		
		Atosiban	Baseline	Yes	49 cells over 9 slices		2,721	0,664	Wilcoxon	0,001
			Atosiban				5,187	0,671		
		Carbetocin	Baseline		54 cells over 13 slices		3,772	0,558	Wilcoxon	0,004
			Carbetocin				5,442	0,498		
	AUC	TGOT	Baseline		57 cells over 13 slices	AUC	477,244	64,233	Wilcoxon	0,002
			TGOT				760,365	124,716		
		Atosiban	Baseline	Yes	49 cells over 9 slices		836,754	210,418	Wilcoxon	0,001
			Atosiban				1119,905	190,862		
		Carbetocin	Baseline		54 cells over 13 slices		381,056	49,530	Wilcoxon	0,001
			Carbetocin				577,164	86,612		
3B	Action potential frequency	TGOT	Baseline	Yes	9	Hz	0,288	0,060	One way RM aov & Tukey HSD 0,0503	A vs B: 0,0571 A vs C: 0,787 B vs C: 0,2328
			TGOT				0,525	0,123		
			Wash				0,335	0,094		
		Atosiban	Baseline	Yes	9		0,250	0,086	One way RM aov & Tukey HSD 0,0503	A vs B: 0,8647 A vs C: 0,9888 B vs C: 0,9085
			Atosiban				0,278	0,087		
			Wash				0,234	0,073		
		Carbetocin	Baseline	Yes	6		0,314	0,065	One way RM aov & Tukey HSD 0,3067	A vs B: 0,0487 B vs C: 0,9407 B vs C: 0,6294
			Carbetocin				0,505	0,113		
			Wash				0,360	0,120		
S2A	Calcium transient frequency	TGOT + PeTX	Baseline	Yes	90 cells over 13 slices	mHz	1,852	0,571	Wilcoxon	0,007
			TGOT				2,824	0,412		
		Atosiban + PeTX	Baseline		99 cells over 14 slices		3,105	0,549	Wilcoxon	0,316
			Atosiban				2,487	0,329		
	AUC	TGOT + PeTX	Baseline	Yes	90 cells over 13 slices	AUC	7905,722	1334,185	Wilcoxon	0,001
			TGOT				14466,208	2514,151		
		Atosiban + PeTX	Baseline		99 cells over 14 slices		8217,201	2629,234	Wilcoxon	0,445
			Atosiban				6113,855	1560,095		
	Proportion of responsive cells	TGOT + PeTX		Yes	90 cells over 13 slices	%	25,342	7,825	/	/

		responsive cells	Atosiban + PeTX		99 cells over 14 slices		22,823	5,963	Wilcoxon	0,025
S2B	Calcium transient frequency	TGOT	Baseline		57 cells over 13 slices	mHz	5,588	0,771	Wilcoxon	0,001
			TGOT				7,302	0,700		
		Atosiban	Baseline	Yes	49 cells over 9 slices		2,721	0,664	Wilcoxon	0,004
			Atosiban				5,187	0,671		
		Carbetocin	Baseline		54 cells over 13 slices		3,772	0,558	Wilcoxon	0,002
			Carbetocin				5,442	0,498		
	AUC	TGOT	Baseline		57 cells over 13 slices	AUC	477,244	64,233	Wilcoxon	0,001
			TGOT				760,365	124,716		
		Atosiban	Baseline	Yes	49 cells over 9 slices		836,754	210,418	Wilcoxon	0,001
			Atosiban				1119,905	190,862		
		Carbetocin	Baseline		54 cells over 13 slices		381,056	49,530	Wilcoxon	0,316
			Carbetocin				577,164	86,612		
	Height	TGOT	Baseline		57 cells over 13 slices	RFU	7,098	0,711	Wilcoxon	0,119
			TGOT				7,844	0,816		
		Atosiban	Baseline	Yes	49 cells over 9 slices		19,414	3,748	Wilcoxon	0,005
			Atosiban				15,217	2,401		
		Carbetocin	Baseline		54 cells over 13 slices		6,396	1,097	Wilcoxon	0,007
			Carbetocin				8,763	1,082		
	Width	TGOT	Baseline		57 cells over 13 slices	seconds	11,714	1,267	Wilcoxon	0,034
			TGOT				13,639	1,143		
		Atosiban	Baseline	Yes	49 cells over 9 slices		11,887	1,903	Wilcoxon	0,164
			Atosiban				17,635	2,539		
		Carbetocin	Baseline		54 cells over 13 slices		10,576	0,926	Wilcoxon	0,208
			Carbetocin				13,074	1,282		
	Rise	TGOT	Baseline		57 cells over 13 slices	/	0,577	0,072	Wilcoxon	0,000
			TGOT				0,482	0,052		
		Atosiban	Baseline	Yes	49 cells over 9 slices		1,681	0,410	Wilcoxon	0,019
			Atosiban				0,850	0,118		
		Carbetocin	Baseline		54 cells over 13 slices		0,455	0,065	Wilcoxon	0,492
			Carbetocin				0,645	0,082		
	Decay	TGOT	Baseline		57 cells over 13 slices	/	-0,420	0,053	Wilcoxon	0,001
			TGOT				-0,353	0,037		
		Atosiban	Baseline	Yes	49 cells over 9 slices		-1,103	0,296	Wilcoxon	
			Atosiban				-0,602	0,071		

Measurement	Treatment	Condition	Yes/No	Cells	Unit	Value 1	Value 2	Test	p	Comparison	p
Area	Carbetocin	Baseline Carbetocin		54 cells over 13 slices		-0,341 / -0,403	0,076 / 0,052	Wilcoxon	0,114		
	TGOT	Baseline TGOT		57 cells over 13 slices		149,021 / 222,578	15,694 / 35,415	Wilcoxon	0,047		
	Atosiban	Baseline Atosiban	Yes	49 cells over 9 slices	RF**2	518,809 / 601,526	139,609 / 159,146	Wilcoxon	0,580		
	Carbetocin	Baseline Carbetocin		54 cells over 13 slices		150,234 / 262,714	25,877 / 45,522	Wilcoxon	0,007		
% of responsive cell per recording	TGOT		Yes	57 cells over 13 slices		0,543	0,065				
	Atosiban			49 cells over 9 slices		0,469	0,081				
	Carbetocin			54 cells over 13 slices		0,494	0,045				
Calcium transient frequency	TGOT		Yes	57 cells over 13 slices	mHz	2,512	2,659	One way RM AOV & Tukey's MC	0,696	TGOT vs, Atosiban	0,736
	Atosiban			49 cells over 9 slices		2,937	3,562			TGOT vs, Carbetocin	>0,9999
	Carbetocin			54 cells over 13 slices		2,508	2,517			Atosiban vs, Carbetocin	0,738
AUC	TGOT		No	57 cells over 13 slices	AUC	1,840	1,400	One way RM aov & Tukey HSD	0,312	TGOT vs, Atosiban	0,693
	Atosiban			49 cells over 9 slices		2,078	1,964			TGOT vs, Carbetocin	0,731
	Carbetocin			54 cells over 13 slices		1,626	1,024			Atosiban vs, Carbetocin	0,279
Height	TGOT		Yes	57 cells over 13 slices	RFU	1,239	0,545	One way RM AOV & Tukey's MC	0,013	TGOT vs, Atosiban	0,447
	Atosiban			49 cells over 9 slices		1,018	0,680			TGOT vs, Carbetocin	0,099
	Carbetocin			54 cells over 13 slices		1,564	0,702			Atosiban vs, Carbetocin	0,014
Width	TGOT		No	57 cells over 13 slices	/	1,390	0,715	One way RM aov & Tukey HSD	0,192	TGOT vs, Atosiban	0,168
	Atosiban			49 cells over 9 slices		1,922	1,278			TGOT vs, Carbetocin	0,857
	Carbetocin			54 cells over 13 slices		1,522	1,145			Atosiban vs, Carbetocin	0,387
Rise	TGOT		Yes	57 cells over 13 slices	/	1,256	1,512	One way RM AOV & Tukey's MC	0,022	TGOT vs, Atosiban	0,244
	Atosiban			49 cells over 9 slices		0,672	0,305			TGOT vs, Carbetocin	0,287
	Carbetocin			54 cells over 13 slices		1,725	1,254			Atosiban vs, Carbetocin	0,017
Decay	TGOT		No	57 cells over 13 slices	/	0,417	4,155	One way RM aov & Tukey HSD	0,693	TGOT vs, Atosiban	0,992
	Atosiban			49 cells over 9 slices		0,752	0,436			TGOT vs, Carbetocin	0,741
	Carbetocin			54 cells over 13 slices		-1,342	15,600			Atosiban vs, Carbetocin	0,749
Area	TGOT		No	57 cells over 13 slices	/	1,754	1,195	One way RM aov & Tukey HSD	0,251	TGOT vs, Atosiban	0,349
	Atosiban			49 cells over 9 slices		2,942	4,806			TGOT vs, Carbetocin	0,347
	Carbetocin			54 cells over 13 slices		2,773	3,097			Atosiban vs, Carbetocin	0,980

S2C

TABLE 4: Numerical values and statistical analysis of data presented in Fig,4 and Supplementary Fig,3

Fig	Statistical unit	Groups tested	Paired ?	N	Unit	Mean	SEM	Test	p-value vs Ctrl	
4B	GFAP volume	Control	No	134	µm **3	493,000	25,240	One-way ANOVA & Tukey's MC <0,0001	Control vs. TGOT	0,007
		TGOT		208		741,000	28,580		Control vs. Carbetocin	0,055
		Carbetocin		225		689,300	25,340		Control vs. Atosiban	<0,0001
		Atosiban		271		1203,000	57,510		TGOT vs. Carbetocin	0,929
									TGOT vs. Atosiban	<0,0001
									Carbetocin vs. Atosiban	<0,0001
	Threshold	Ctrl	No	18	mV	-42,690	2,109	Kruskal-Wallis AOV & Dunn's MC with Sidak correction	/	
		TGOT		26		-40,098	1,815		0,850	
		dOVT		26		-35,823	1,758		0,102	
		Atosiban		25		-35,257	2,164		0,042	
		Carbetocin		25		-39,130	1,965		0,801	
		GFAP OTR KO + TGOT		17		-38,458	1,670		0,800	
	Number of spike	Ctrl	No	18	/	2,352	0,275	Kruskal-Wallis AOV & Dunn's MC with Sidak correction	/	
		TGOT		26		1,910	0,197		0,669	
		dOVT		26		2,397	0,210		1,000	
		Atosiban		25		2,090	0,188		0,993	
		Carbetocin		25		2,520	0,289		1,000	
		GFAP OTR KO + TGOT		17		2,314	0,369		0,998	
	Latency to 1st spike	Ctrl	No	18	ms	3110,491	363,461	Kruskal-Wallis AOV & Dunn's MC with Sidak correction	/	
		TGOT		26		3118,397	340,438		1,000	
		dOVT		26		2834,686	307,556		1,000	
		Atosiban		25		3560,413	314,987		0,957	
		Carbetocin		25		3805,920	296,240		0,608	
		GFAP OTR KO + TGOT		17		2607,608	320,824		0,940	
4C & S3A	Delta number of spike	Ctrl	No	20	/	0,181	0,086	Kruskal-Wallis AOV & Dunn's MC with Sidak correction	/	
		TGOT		20		0,540	0,197		0,879	
		dOVT		21		0,271	0,151		1,000	
		Atosiban		20		1,579	0,902		0,999	
		Carbetocin		21		0,468	0,171		1,000	
		GFAP OTR KO + TGOT		19		0,281	0,225		0,938	

Parameter		Group	n	Unit	Value	SEM	Test	p-value
Rise constant	No	Ctrl	20	s	3,448	0,480		/
		TGOT	20		2,063	0,185	Kruskal-Wallis	0,179
		dOVT	21		3,392	0,353		1,000
		Atosiban	20		2,224	0,294	AOV & Dunn's MC with Sidak correction	0,334
		Carbetocin	21		2,970	0,338		1,000
		GFAP OTR KO + TGOT	19		4,471	0,440		0,375
Delta membrane voltage	No	Ctrl	20	mV	9,853	1,226		/
		TGOT	20		18,361	1,712	Kruskal-Wallis	0,005
		dOVT	21		11,573	1,335		0,986
		Atosiban	20		16,913	1,709	AOV & Dunn's MC with Sidak correction	0,032
		Carbetocin	21		11,906	1,321		0,962
		GFAP OTR KO + TGOT	19		10,144	2,597		0,975
Decay constant	No	Ctrl	20	s	5,437	0,863		/
		TGOT	20		3,784	0,475	Kruskal-Wallis	0,896
		dOVT	21		3,270	0,309		0,534
		Atosiban	20		3,292	0,476	AOV & Dunn's MC with Sidak correction	0,262
		Carbetocin	21		3,414	0,547		0,250
		GFAP OTR KO + TGOT	19		4,973	0,925		1,000

TABLE 5: Numerical values and statistical analysis of data presented in Fig,5 and Supplementary Fig,4

Fig	Statistical unit	Groups tested	Time	Paired ?	N	Unit	Mean	SEM	Test	Statistic	p-value	post-hoc
5A	Number of contacts between astrocyte processes and excitatory synapses	WT Naive		No	5	/	58,960	21,300	One-way ANOVA & Tukey's MC	WT naive vs. WT Fear	0,006	0,004
		WT Fear			5		22,080	5,744		WT naive vs. KO naive		0,618
		GFAP OTR KO Naive			5		47,830	10,550		WT naive vs. KO Fear		0,594
										WT Fear vs. KO naive		0,052
		GFAP OTR KO Fear			5		47,450	14,890		WT Fear vs. KO Fear		0,056
										KO naive vs. KO Fear		>0,9999
5B	CPSE amplitude	Naive	Pre-stim	Yes	17	pA	-13,170	1,732	Mixed model ANOVA and Tukey's MC	Stim: 21,75	<0,0001	0,026
			Stim				-34,698	8,568				0,819
			Post-stim				-12,880	1,745		Group: 4,913	0,033	0,029
		Fear conditionned	Pre-stim	Yes	21		-13,875	1,399				0,002
			Stim				-78,860	15,585		Interaction: 5,232	0,008	0,215
			Post-stim				-17,304	2,466				0,001
S4A	CPSE freqency	Naive	Pre-stim	Yes	17	Hz	0,001	0,000	Mixed model ANOVA and Tukey's MC	Stim: 47,86	<0,0001	<0,0001
			Stim				0,015	0,004				0,992
			Post-stim				0,002	0,001		Group: 0,132	0,033	<0,0001
		Fear conditionned	Pre-stim	Yes	21		0,001	0,000				<0,0001
			Stim				0,014	0,001		Interaction: 0,029	0,008	0,934
			Post-stim				0,002	0,001				<0,0001
5C	Potassium current amplitude	Naive		No	12	pA	91,610	24,620	Unpaired T-test	2,320	0,031	
		Fear conditionned			9		20,490	12,840				

6. Methodological considerations

6.1. On the models

Rodents. Even if their evolutionary lineage diverged ~75 million years ago (Zhao et al., 2004), humans and rodents still share anatomical, physiological, and genetic similarities, making them ideally suited for biological research (Bryda, 2013). However, many behavioral, anatomical, and mechanistic features differ between rodents and humans. For instance, rodents are lissencephalic whereas humans are gyrencephalic, indicating a radical difference in cortex size and organization (Sun and Hevner, 2014). Moreover, human astrocytes are different from rodents astrocytes in terms of size, morphology, and diversity (Perez-Catalan et al., 2021; Verkhratsky and Nedergaard, 2018). Functional differences have also been detected since Ca^{2+} waves travel faster in humans than in rodent tissue (Augusto-Oliveira et al., 2020). Thus, although rodents are very suited to study biology and especially behavior, we must carefully consider the relevance of the tests used and their transposability to humans.

I began my Ph.D. work with rats, but at some point, we had to switch to mice to benefit from genetic models such as the GFAP OTR-flox line. From this point, I only used mice because of the availability of many transgenic mice lines, a personal unease to work with rats and to favor the comparability of our work with the literature.

Males and Females. Another caveat in the transposability of data is the impact of sex differences on obtained data. In the first part of my thesis, I conducted experiments in both male and female mice (Wahis et al., 2021). The use of both sexes introduces a potential bias due to different concentrations of OT in a basal state. For instance, OT and OTR expressions are usually higher in females than in males (Carter, 2007). Moreover, the level of OT varies during the estrous cycle, with a peak during ovulation (Froemke and Carcea, 2017). Thus, in my second project, I tested the involvement of astrocytic OTR in both sexes and observed that freezing reactions were affected by astrocytic OTR removal in male but not in female mice. This observation is intriguing since no sexual dimorphism of OT fibers innervation (Otero-García et al., 2016) and of OTR expression (Uhl-Bronner et al., 2005) have been found in the CeA. In the future, it will be interesting to investigate the involvement of astrocytic OTR in different stages of the estrous cycle.

6.2. On the technics

mRNA are not proteins. To reveal the presence of the OTR on CeL/C astrocytes, we used *in situ* hybridization, thereby labeling the mRNA of the OTR and not the receptor itself. This choice was motivated by the relative unfiability of available antibodies against the OTR (Unpublished observations from *F. Althammer*). Thus, we used *in situ* hybridization to indicate whether astrocytes can transcript the *Oxtr* gene. Nevertheless, even if the mRNA expression is a good hint of OTR expression, it may not be correlated with the presence of the receptor since many mechanisms can control the translation of mRNA into protein (Jiménez et al., 2022). To overcome this issue, we showed that the OTR agonist TGOT could directly activate astrocytes, thereby pointing toward an expression of a functional OTR in CeL/C astrocytes.

On the use of TGOT instead of OT. In addition to its action of OTR, OT can activate AVP receptors and especially the V1a receptor ($EC_{50} = 120nM$) (Chini et al., 2017). There is an anatomical distinction between the expression of OTR and V1a in the CeA, with OTR being expressed in the CeL/C whereas V1a is present in the CeM (Figure 37, Huber et al., 2005). Moreover, OT fibers seem to form more varicosities in the CeL/C than in the CeM, suggesting it is more released in the former and less in the latter (Figure 37, Knobloch et al., 2012). These two elements indicate that OT may activate CeL/C OTR without affecting V1a activity in the CeM. In our experiments, however, we bath-applied OTR agonists, flooding the slice without any spatial selectivity. To overcome this issue we used the selective OTR agonist TGOT but we cannot exclude that in the brain, OT may diffuse and reach the CeM and in this case, our study will omit a part of OT signaling mediated by V1a receptors. For this reason among others, we intend to reproduce the results obtained using TGOT with the endogenous release of OT mediated by optostimulation of OT neurons.
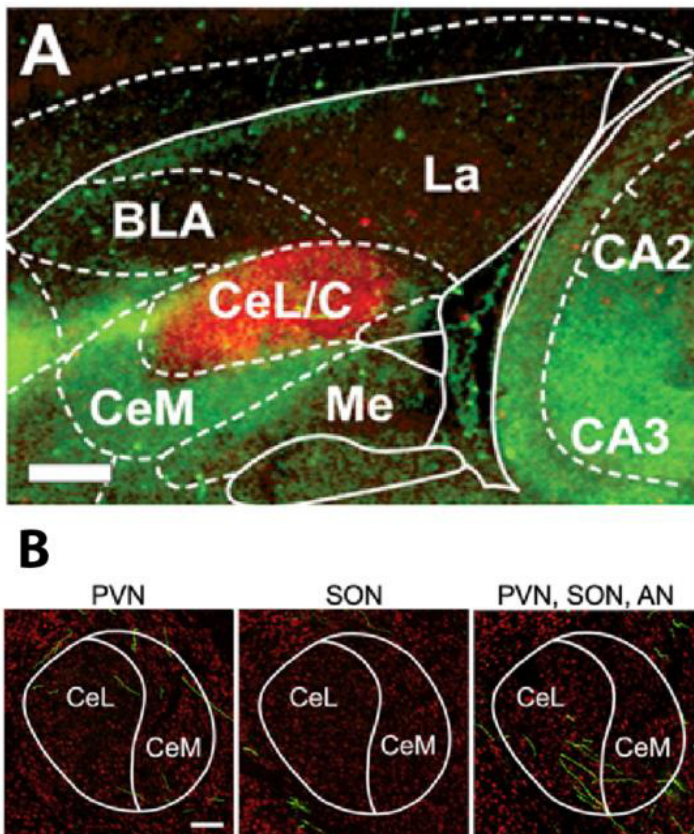
Figure 37: The oxytocin system in the central amygdala. A. Histoautoradiography of oxytocin (red) and vasopressin (green) binding site in the amygdala. From Huber et al., 2005. Scale bar = 400 μm. B. Venus-expressing oxytocin fibers in the central amygdala. The three panels show the oxytocin fibers that arise from the paraventricular nucleus (PVN), the supraoptic nucleus (SON), or all the hypothalamic oxytocinergic nuclei. From Knobloch et al., 2012. Scale bar = 100 μm. AN: accessory nuclei, La: lateral amygdala, BLA: basal amygdala, CeL/C: laterocapsular subdivision of the central amygdala, CeM: medial subdivision of the central amygdala, Me: medial amygdala, CA2 & 3: Cornu Ammonis 2 and 3.

On the dyes and calcium indicators. To identify astrocytes, we incubated slices in sulforhodamine 101 (SR101), an anionic dye that stains astrocytes (Verkhratsky and Nedergaard, 2018). However, it has been shown that SR101 at high concentrations can be cytotoxic and induce seizure-like activity in cortical neurons (Rasmussen et al., 2016). Authors have reported such an effect at doses exceeding 100μM, suggesting that the dose we used (1μM) should not induce such disturbance of the neuronal network activity. When using the Rhodamine 2 calcium indicator (Rhod2), however, I observed a high proportion of cell death but no report on this effect has been published, suggesting that my loading protocol was not optimal. I changed many parameters on this protocol but never managed to have slices as well conserved as when I used Oregon BAPTA green 1 (OGB1). As an alternative, one can suggest the use of genetically encoded calcium indicators (GECI). The advantage of GECI also

resides in the possibility to image not only the soma of astrocytes but also the gliopil of these cells. This aspect is really important since somatic calcium events represent only ~3% of all astrocytic calcium activity (Bindocci et al., 2017). However, calcium events triggered by GPCR activation seem to encompass the soma (Shigetomi et al., 2010), suggesting that even if calcium imaging at the level of astrocyte soma is not the best approach to visualize the entire calcium activity, it stays a good indicator of the GPCR-triggered calcium transients.

Another problem of *ex vivo* calcium imaging is also the cell death due to the slicing procedure since cellular integrity is disrupted at the top of the slice. To overcome this problem, we could use *in vivo* calcium imaging. This approach also allows the observation of the temporal dynamics of neuronal and astrocytic calcium activities during fear conditioning. However, since this procedure requires to perform heavy surgeries in adult animals and cannot easily be used in combination with local application of agonists, we mostly used *ex vivo* calcium imaging to decipher the effect of OTR activation on astrocytes.

Calcium experiments have no wash. When evaluating the transient activity of cells, we usually compare a basal activity with an induced activity, and then this modification of activity must return to baseline levels. This control shows that the cell is not dying and that the effect is transitory and physiological. However, in calcium imaging experiments, I could not observe such a return to baseline levels since the application of OTR agonists triggered a long-lasting (>15 min) modification of calcium activity in astrocytes. One solution should have been to increase the recording time to evaluate the total calcium activity time of astrocytes but this was not possible since microscopes (at least our) tend to drift during long recordings. To overcome this issue, one can replace the focus manually but it would have introduced a strong bias. Thus, we choose to control this potential effect of cell death by performing calcium imaging in a recording medium supplemented with antagonists. These experiments showed us that calcium transients were indeed elicited by OTR activation. This long-lasting calcium activity of astrocytes was one of the reasons why we investigated the effects of OTR activation in the long term.

Channelrhodopsins are not suited to trigger astrocyte activity. To exogenously trigger calcium transients in astrocytes, we used a red-shifted channelrhodopsin named C1V1. Using calcium imaging, I controlled the efficiency of C1V1 to trigger calcium signaling in astrocytes and observed robust activation of CeL/C astrocytes after the photostimulation of this channel. However, the opening of such cation aspecific channel at the astrocytic plasma membrane triggers the massive release of K^+, increasing the concentration of this ion in the extracellular fluid and thereby increasing neuronal excitability (Octeau et al., 2019). Thus, channelrhodopsin is not the ideal tool to activate astrocyte calcium signaling. Alternatively, we could have used exogenous receptors that activate the $G\alpha_q$ pathway such as hM3Dq or photoactivatable $G\alpha_q$-GPCRs. To this end, I have tested the photoactivatable α_1 adrenergic receptor (Opto-α_1AR or OptoGq) (Adamsky et al., 2018; Airan et al., 2009) and obtained a robust increase in calcium signaling after photostimulating this receptor. The use of this more physiological way to stimulate astrocytes must be used in the future to assess more precisely the effect of the $G\alpha_q$-induced activation of astrocytes. This approach implies the genetic targeting of astrocytes to make them express the photoactivable receptor, for instance with GFAP promoter.

On the use of the GFAP promoter. All viral constructs used to target astrocytes have been built using the GFAP *GfaABC1D* promoter. However, only a part of astrocytes expresses the GFAP in the brain (Augusto-Oliveira et al., 2020; Khakh, 2019). It seems that this proportion varies across brain regions but no data exist to my knowledge on the proportion of GFAP$^+$ astrocytes in the CeL/C. Given the striatum-like nature of the CeL/C, the proportion of GFAP-expressing astrocytes may be similar between the CeL/C and the striatum. Sadly, it has been shown that GFAP is a bad astrocyte marker in the striatum (Khakh, 2019). However, our data show that the use of the GFAP promoter to knock out the oxytocin receptor in astrocytes efficiently abolishes the presence of the receptor in CeL/C astrocytes identified with glutamine synthase, a much more trustworthy marker of astrocytes. Three reasons may explain this result: 1) GFAP may be expressed (or at least transcribed) in all CeL/C astrocytes, 2) all OTR-expressing astrocytes in the CeL/C may also express GFAP, or 3) the stereotaxic injection of the AAV induce transient gliosis that triggers GFAP expression in astrocytes. In the first hypothesis, virtually all astrocytes must transcribe the *Gfap* gene. This is unlikely since as shown in striatal astrocytes from the caudate nucleus,

the GFAP mRNA is found in only ~70% of vimentin-expressing astrocytes (O'Leary et al., 2020). Fortunately, this potential targeting of an astrocyte population did not change our conclusion since it did not affect the knockout of the OTR.

On the slice incubation in agonists. To identify the intracellular pathway involved in the morpho-functional changes of the CeL/C astro-neuronal network, we incubated brain slices in different biased agonists to stimulate either the OTR-$G\alpha_q$ or the OTR-$G\alpha_i$ pathway. This approach was simple to set but it implies several caveats.

First, $G\alpha_i$ and $G\alpha_q$ biased agonists (carbetocin and atosiban) have different effects on OTR desensitization: carbetocin triggers OTR internalization whereas atosiban did not induce such desensitization (Jurek and Neumann, 2018; Passoni et al., 2016). This implies that slices incubated with carbetocin were probably less stimulated than the ones incubated in atosiban due to OTR internalization.

At the intracellular level, carbetocin leads to an interaction between OTR and β-arrestin but atosiban leads to a sustained ERK1/2 phosphorylation (Jurek and Neumann, 2018). Since β-arrestin can trigger various downstream effects (Jean-Charles et al., 2017), the loss of this interaction could modify many aspects of OTR signaling. However, we can suggest that this biased mechanism may exist in the physiological signaling of OTR.

To trigger morpho-functional changes in the CeL/C astro-neuronal network, we used two approaches: the first one was to induce fear conditioning in mice and the second one was to incubate brain slices in OTR agonists. The slice incubation lasts for one hour but the fear conditioning session was only ten minutes. The discrepancy found its origin in the fact that we began those experiments by incubating slices in agonists as done by Wang and colleagues which observed a difference in GFAP immunoreactivity after 30 minutes (Wang and Hatton, 2009). We then wanted to test whether the observations we made *ex vivo* stays true after a "physiological" stimulation such as fear conditioning. To avoid too much animal suffering and to allow comparison with the literature, we did not perform a one-hour fear conditioning session but we did a "normal" fear-conditioning paradigm with a conditioning session of 10 minutes. Interestingly, agonist incubation and fear conditioning have produced the same modification of astrocyte morphology and neuronal excitability, suggesting that ten minutes should be sufficient to modify the astro-neuronal network in the CeL/C.

On the puff of K⁺ to stimulate neurons. To evaluate the excitability of CeL/C neurons, I puffed a high K⁺ containing aCSF (30mM). The elevated amount of this ion in the extracellular fluid results in the reduction of its relative importance in the setting of the membrane voltage of cells, thereby depolarizing them. This approach produces robust and reproducible data. However, such stimulation is not physiological since in normal conditions, the level of extracellular potassium ([K⁺]EC) does not vary that much in such a big area (Kofuji and Newman, 2004). Indeed, I puffed a 30mM K⁺ containing aCSF at a distance of ~150µm of the recorded neuron. The physiological [K⁺]EC is around 3mM and high neuronal activity can elevate it to a ceiling level of 12mM, a level that can be exceeded only in pathological conditions (Kofuji and Newman, 2004). However, since I have puffed this K⁺ solution relatively far from the recorded neurons to avoid mechanical stimulation, the concentration of K⁺ that reached the recorded cell was much lower than 30mM. The precise amount of K⁺ around the recorded neuron is difficult to evaluate since it depends on the diffusion properties of the K⁺ (size, charge, anisotropy, *etc.*), the properties of the tissue (tortuosity, ECS volume, uptake by glial cells, *etc.*) and the potential involvement of neighboring neurons that can release K⁺ during the stimulation. However, I tried to evaluate this quantity according to the depolarization it produces. Indeed, if we assume that the only difference before and during the K⁺ puff is the [K⁺]EC, then the variation of the membrane voltage of neurons must reflect this increase in [K⁺]EC. The membrane voltage of a neuron is given by the Goldman-Hodgkin-Katz voltage equation (GHK, Tamagawa, 2019):

$$Vm = \frac{RT}{F} ln \left(\frac{P_{Na} [Na^+]_{out} + P_K [K^+]_{out} + P_{Cl} [Cl^-]_{in}}{P_{Na} [Na^+]_{in} + P_K [K^+]_{in} + P_{Cl} [Cl^-]_{out}} \right)$$

Where Vm is the membrane voltage, R is the ideal gas constant, T is the temperature, F is Faraday's constant, P_{ion} is the permeability of the membrane for an ion, and [ion]out/in is the concentration of an ion outside/inside the cell, respectively. Given the amount of Na⁺, K⁺, and Cl⁻ in the aCSF and the intracellular solution I have used for patch clamp experiments and generic values for the permeability, we can do the following resolution:

$$Vm = \frac{8.314 * 300}{96485} ln \left(\frac{0.05 * 151.25 + 1 * 2.5 + 0.45 * 10}{0.05 * 16 + 1 * 125 + 0.45 * 130.5} \right) = -65.64 \, mV$$

In the measure I made, the average membrane voltage was -62.27 ± 1.28 mV. The 3.5 mV difference observed is probably because this equation does not take into account minority ions such as Mg^{2+}, Ca^{2+}, SO_4^{2-} and HCO_3^- in the extracellular medium and ATP in the intracellular solution. These two values are anyway really close, indicating that the generic values I used are in the good range and thus, the GHK equation correctly estimates the membrane voltage of CeL/C neurons. Once this is verified, I have used the GHK equation to estimate the $[K^+]_{EC}$. Given that the K^+ puff induces a 9.85 ± 2 mV depolarization, I reuse the GHK equation isolating the $[K^+]_{EC}$ and give a theoretical membrane voltage of -65.64 + 9.85 = -55.79 mV.

$$Vm = \frac{RT}{F} \ln\left(\frac{P_{Na}\,[Na^+]_{out} + P_K\,[K^+]_{out} + P_{Cl}\,[Cl^-]_{in}}{P_{Na}\,[Na^+]_{in} + P_{Na}\,[K^+]_{in} + P_{Cl}\,[Cl^-]_{out}}\right)$$

$$\Leftrightarrow \quad [K^+]_{out} = \frac{e^{\frac{Vm*F}{RT}}*(P_{Na}\,[Na^+]_{in} + P_{Na}\,[K^+]_{in} + P_{Cl}\,[Cl^-]_{out}) - P_{Na}\,[Na^+]_{out} - P_{Cl}\,[Cl^-]_{in}}{P_K}$$

Resolution:

$$[K^+]_{out} = \frac{e^{\frac{-0.05579 * 96485}{8.314 * 300}}*(0.05 * 16 + 1 * 125 + 0.45 * 130.5) - 0.05 * 151.25 - 0.45 * 10}{1} = 9.26\,mM$$

Thus, if all the depolarization we observed is due to an increase in $[K^+]_{EC}$, the final concentration reaching the neuron is ~9mM, indicating a dilution/buffering of 70% of the puffed potassium. As mentioned above, this 9mM value is in the physiological $[K^+]_{EC}$ range and can be reached during episodes of high neuronal activity. In fear-conditioned mice, however, the mean observed depolarization is 19.29mV, indicating that the potassium level can reach 18.65mM, suggesting a dysregulation of the $[K^+]_{EC}$ homeostatic control in those individuals.

To predict future results I programmed a model to evaluate the theoretical concentration of potassium reaching the neuron after the K^+ puff. To this end, I used the below formula developed to estimate the observed concentration of a molecule at a given distance of a pressure ejection site (Syková, 2004):

$$C_{f(r,t)} = \frac{UC_i}{\alpha} \frac{\lambda^x \lambda^y \lambda^z}{(4Dt\pi)^{3/2}} e^{-\frac{r^2}{4Dt} - k't}$$

$$C_{f(r,t)} = \frac{10^{-8} * 3 * 10^{-2}}{0.21} \frac{0.1 * 1.56 * 1.56}{(4 * 11.1 * 10^{-6} * t * \pi)^{3/2}} e^{-\frac{10^{-2^2}}{4 * 11.1 * 10^{-6} * t} - 0.1 * t}$$

Where C_f = Concentration of potassium reaching the neuron (M), t = time (s), r = distance between puff site and recorded neuron (cm), U = volume ejected (L), C_i = initial concentration of potassium at puffing site (M), α = volume fraction of the tissue, λ = tortuosity of the x, y, and z-axis, D = free diffusion coefficient, k' = first order kinetic constant. I estimated the ejected volume to be ~100nL and took other values from Syková, 2004. α and λ were measured in the striatum of adult rats. The first-order kinetic constant k' is a value that includes several mechanisms difficult to evaluate, such as entry of the molecule into cells and loss across the blood-brain barrier.

I looped this equation 20 times to mimic the 20-second-long K^+ puff I did and summed the 20 sweeps obtained. This approach allows me to obtain a K^+ kinetics similar to the one observed experimentally although smaller. Indeed, The maximum $[K^+]_{EC}$ obtained with the model is 5.3mM (Figure 38) although the $[K^+]_{EC}$ inferred based on the amplitude of neurons depolarization was ~9mM. This difference could be due to the absence of consideration of the basal $[K^+]_{EC}$ in the extracellular fluid which is ~3mM (Kofuji and Newman, 2004). Moreover, I puffed the K^+-containing aCSF toward the recorded neuron; thus, this solution diffused preferentially in this direction. Since their no directionality in this model, I modified the tortuosity of the medium in the x-axis to mimic an anisotropy that favors K^+ diffusion toward the recorded neuron. This trick is not theoretically exact and it would be more accurate to apply a force vector to this equation to better mimic K^+ diffusion in this experimental setup.

Then, I changed the first-order kinetic constant to mimic a decrease in K^+ buffering and I observed a two-fold increase of $[K^+]_{EC}$ after K^+ puffing compared to the previous simulation ($[K^+]_{EC}$ max = 10.13mM compared to 5.3mM, Figure 38). Interestingly, this two-fold increase of potassium is also what I inferred based on $[K^+]_{EC}$ approximation based on neurons' depolarization (from 9 to 18mM).

Albeit not accurate, this model succeeds to mimic the variation of $[K^+]_{EC}$ after the local puff of K^+. The modification of K^+ buffering also mimics the variation of $[K^+]_{EC}$ observed after fear-conditioning, suggesting the involvement of astrocytes in this effect.

The script producing this model is available in the following repository: https://github.com/AngelBaudon/K-modelisation.
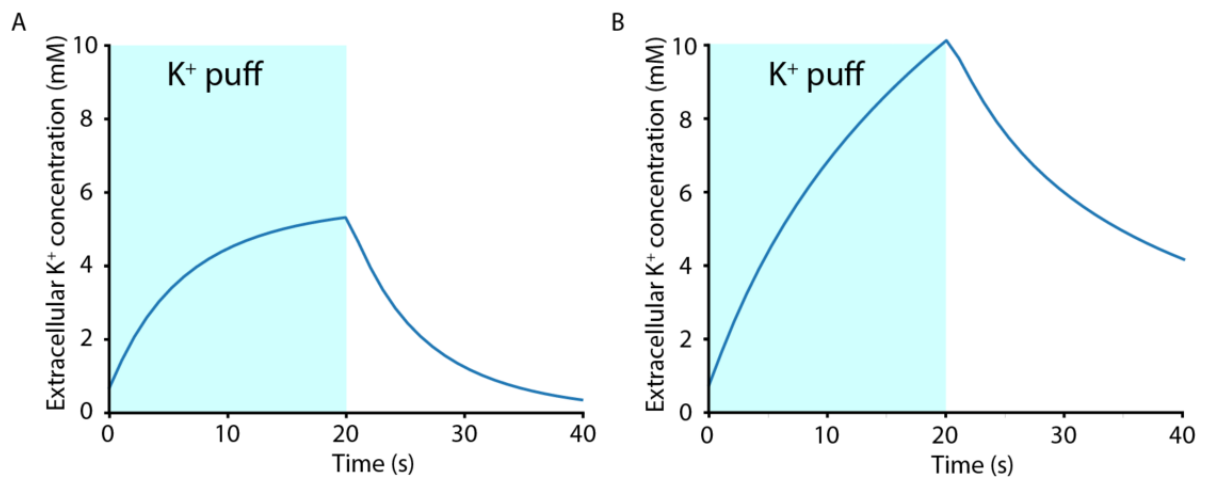
Figure 38: Model of extracellular potassium concentration ($[K^+]_{EC}$) at 100µm of the pressure ejection site during and after a 20s-long puff of a 30mM-containing K^+ solution. A. $[K^+]_{EC}$ modeled with a first-order kinetic constant of 0.1. B. $[K^+]_{EC}$ modeled with a first-order kinetic constant of 0.01. The light blue rectangle shows the duration of the potassium puff.

6.3. On the analysis

On the quantification windows of electrophysiology analysis. In the first publication I contributed to (Wahis et al., 2021), electrophysiology data were acquired in 20 minutes-long recordings with the OTR agonist bath applied in the perfusion system of the electrophysiology recording chamber. Using this approach, it is really difficult to estimate the entering time of the peptide since it dilutes in the aCSF and forms a concentration gradient during the tubing time. Moreover, the arrival of the agonist on the recorded cell can vary a lot depending on the position of the slice in the chamber and the depth of the recorded cell in the slice. In addition, the OTR is a GPCR and thus its activation does not produce a clear, massive effect on the neuron's membrane voltage that we can detect instantly but the observed effects rise slowly and last for variable times. Finally, we described a mechanism that involved glial cells before reaching neurons, adding a delay to the observed effect. For all those reasons, the quantification window of electrophysiological events has been determined for each neuron by selecting the 20-second frame with the maximum activity in the 10 minutes following the application of the agonist. This analysis method has caveats:

1) random spontaneous activity will be selected and identified as an effect of the agonist, and 2) selected windows within 10 minutes are compared to fixed windows before agonists application (to estimate basal activity) and at the end of the recording (to evaluate the wash). Since some quantifications were fixed and others were chosen, this introduced a strong bias and pushed the quantification toward an increased activity. Even if this bias was controlled by the use of antagonists, we decided to change this analysis method during the second part of my Ph.D. To this end, I developed experiments that avoid this bias using direct application of the agonist by a puff pipette or by performing photostimulation of neurons, allowing the quantification of events in fixed windows.

On the use of a homemade Dunnett's p-value correction module. In some experiments I have conducted, I have decided *a priori* to compare all conditions to a single control instead of comparing each condition to all the others (Chen and Kianifard, 1997). The rationale behind this decision is to test only the relevant comparisons and thus reduce the number of tests to decrease the family-wise error rate. Since this error rate is $FWER \leq 1 - (1 - \alpha)^C$ (where α is the significance level and C is the number of comparisons), the more comparisons made, the more errors will occur. To overcome this, the alpha correction procedure reduces the alpha level and adjusts the family-wise error rate to a final alpha of the chosen value (eg. 0.05). Since I have performed all my analyses in Python to make them open access, I intended to run Dunnett's alpha correction procedure with Python but this statistical test was not implemented. Thus, I programmed a way to evaluate the exact corrected p-value of the multiple comparisons using the following approach:

1) Find the correct Dunnett distribution using the degrees of freedom of the data.
2) Find the standard deviation of this distribution by dividing the p-value at α = 0.05 by 1.96 since in normal distributions, the interval μ ± 1.96*σ (where μ is the mean and σ is the standard deviation) contains 95% of the values.
3) Calculate a z-score of the between-group difference weighted by the standard deviation of the Dunnett distribution.
4) Find the exact p-value by transposing the z-score on a standard normal distribution and calculate the survival function of this point. This value indicates the area under the curve after a border, thereby giving the proportion of variables that lies after this border (*ie.* the p-value).

Although I have to verify with professional statisticians if this approach is correct, this script has been tested with many random data and it always produces results coherent with Dunnett's tables. It can be found on the following repository (https://github.com/AngelBaudon/Calcium-Imaging-Analysis/tree/main/ToolKit) and I will submit it to scipy.stat which is an endeavor of independent programmers to offer open-source statistical tests.

On the nature of miniature excitatory postsynaptic events (mEPSCs). In the first project I contributed to, we tried to evaluate whether astrocytes were directly responsible for EPSCs recorded in CeL/C neurons. To do so, we recorded those neurons in an aCSF that prevents neuronal activity (tetrodotoxin), blocks inhibitory neurotransmission (bicuculline), and increases NMDA receptor opening probability (0 Mg^{2+}). The use of such an external medium has been shown to reveal high-amplitude slow inward currents (SIC) triggered by astrocytic release of glutamate and activation of NR2B-containing NMDA receptors at extrasynaptic sites (Angulo et al., 2004; Fellin et al., 2004; Jourdain et al., 2007; Kovács and Pál, 2017; Parri et al., 2001; Pasti et al., 2001; Xu et al., 2007). However, the presence of such events has been contested and some thought that it might not occur during physiological conditions but only during astrocyte swelling upon hypo-osmolar conditions (Agulhon et al., 2008; Walch and Fiacco, 2022). In our case, we do observe such events although very rarely, suggesting that it may not be the principal way astrocytes increase neuronal excitation.

7. Scientific discussion

7.1. What is the function of neuronal OTR?

After the removal of OTR from CeL astrocytes, we observed a complete loss of OT neuromodulatory effect. This was quite astonishing given that we found the OTR mRNA in only 20% of astrocytes and 70% of neurons. The first explanation can be an amplification of the OT signal in the astrocyte network, extending the neuroactive effect of OT both spatially and temporally. However, it looks unlikely that OT has no direct effect on CeL neurons, thus we can hypothesize that OT may act in concert with neurons and astrocytes to produce a synergistic effect. For instance, this can be achieved by increasing the membrane voltage of neurons and simultaneously triggering gliotransmitter release from astrocytes.

Moreover, our estimation of the proportion of OTR-expressing neurons in the CeL can also be overestimated. Our results show that 70% of CeL neurons transcribe the OTR mRNA, however, the OTR mRNA has been previously observed in 65% of PKCδ^{+} neurons which represent ~50% of the CeL (Haubensak et al., 2010). This suggests that the proportion of OTR mRNA-positive CeL neurons can be much lower than what we found. This discrepancy is probably due to an OTR mRNA probe or an analysis difference, for instance in the choice of the fluorescence threshold to classify a neuron as expressing the OTR mRNA. Nevertheless, even if the proportion of OTR-expressing neurons is overestimated in our study, it is the same for astrocytes and thus, the question remains the same. A possible part of the response can rely on the ability of the astrocyte to form functional syncitia and thus potentially amplify the OT neuromodulatory signal within a functionally defined population of astrocytes.

In any case, it will be interesting to knock out neuronal OTR and investigate the direct effect of OT on neurons in amygdala-related behaviors.

7.2. Why are there astrocyte subpopulations?

Around 20% of CeL astrocytes express the OTR mRNA and half of recorded astrocytes respond to an OTR agonist application. This indicates that some CeL astrocytes communicate and form a functional syncytium that does not include all CeL astrocytes, thereby forming two functional populations of astrocytes. The formation of such a subnetwork can be observed through the scope of the contextual guidance theory (Murphy-Royal et al., n.d.). According to this theory, astrocytes may sense contextual triggers (in our case, oxytocin) that convey information about the physiological and emotional state of the animal. Once detected by astrocytes, these signals trigger a variety of consequences on astrocyte physiology including secretion of gliotransmitters, morphological rearrangement, etc. All these contextualizers modify neurons' activity and wiring to tune the system toward one state or another. Interestingly, a corollary of this theory is the presence of different, non-overlapping, subpopulations of astrocytes that have a defined set of contextualizing rules. Thus, the 50% proportion of CeL astrocytes that are sensitive to OT may be put in parallel with the fact that CeL neurons can be broadly divided into two subpopulations: SOM and PKCδ expressing neurons (Kim et al., 2017). If OT-sensitive astrocytes truly form a subnetwork with their own contextualizing rules, we can imagine that this network may exert a contextual tuning of one population of neurons, thereby controlling their activity. This hypothesis can be tested using optogenetics to trigger the release of endogenous OT, and the use of the CaMPARI system (Serra et al., 2022) to identify OT-sensitive astrocytes. This approach can be completed with staining of SOM and PKCδ neurons to test whether the territory of OT-sensitive astrocytes contains a defined population of neurons. In a third time, we can patch-clamp SOM or PKC neurons, depending on the population present in OT-sensitive astrocyte territory, and monitor the astro-neuronal communication. However, to measure this gliotransmission, we must know the agonist and receptor involved.
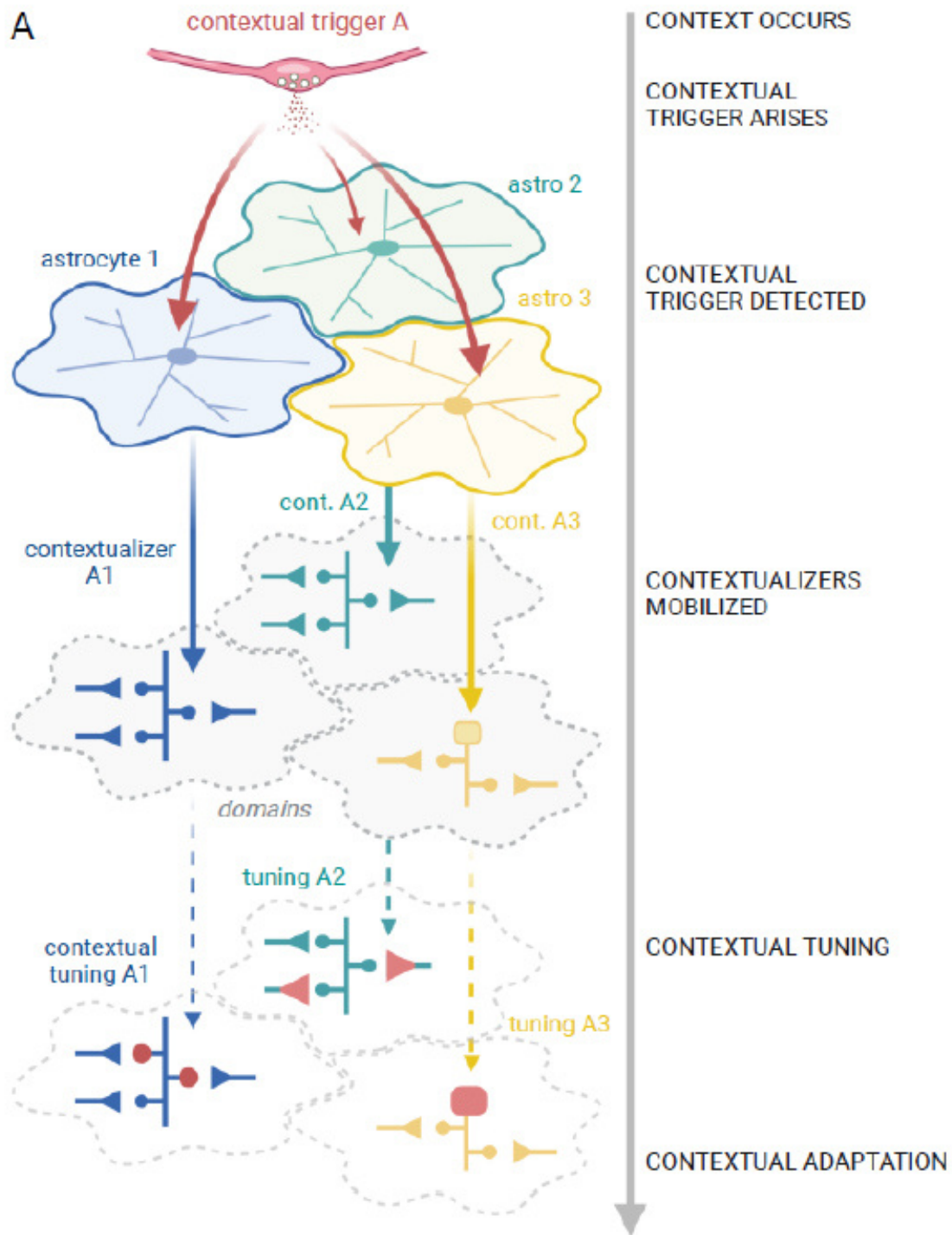
Figure 39: Astrocytes may form functional compartments. Upon stimulation, a contextual trigger can activate different astrocytes. These astrocytes may react differentially to this new context and tune the neural system according to their contextualizing rules. These circuit-specific modifications may allow the different neuronal networks to adapt to the new context. From Murphy-Royal et al., n.d.

7.3. Which gliotransmitter astrocytes release?

We have shown that after OTR activation, astrocytes excite CeL neurons through the activation of NMDA receptors. We observe a loss of this effect when the NMDAr co-agonist binding site is blocked or when the extracellular d-serine is removed (Wahis et al., 2021) (Fig 5b & c). This means that 1) d-serine is the endogenous agonist of NMDAr in the CeL, as shown in the hippocampus and the cerebellum (Mothet et al., 2000), and 2) that the astro-neuronal communication relies on the activation of NMDAr. Thus, the gliotransmitter involved in this communication can be either the d-serine or the glutamate. In an additional experiment, we supplemented the extracellular medium with d-serine and this does not change the basal frequency of IPSCs in CeM neurons, suggesting no change in CeL neurons activity. Moreover, the subsequent activation of OTR triggers an increase in these IPSCs frequency, indicating that the phenomenon is not occluded. Together, these two observations designate glutamate as the gliotransmitter involved. It should have been interesting to perform the reverse experiment: blocking all glutamatergic signalization (AMPA and mGluR) except NMDAr, removing extracellular glutamate using L-glutamate oxidase (Hazim Abdul Hameed and Hussein Ali, 2021), and applying an OTR agonist. Thus, if we observe an increase in CeL neurons activity this could indicate that astrocytes release glutamate that activates NMDAr. Interestingly, I have found no study that has used this enzyme to remove extracellular glutamate in brain slices. This is probably because we often assume that glutamate is present at low levels in ECS whereas serine is present at higher levels (~10 folds) (Lerma et al., 1986), thus probably exerting a tonic activation of NMDAr. However, the concentrations of glutamate and d-serine measured in the ECS are very variable from one study to another, ranging between 25nM and 30µM for the glutamate (Herman et al., 2011). Moreover, even if L-serine is present in the ECS at high levels, this may not be the case for D-serine, which is ~10 times less concentrated in hippocampal ECS (Horio et al., 2011). All these discrepancies can be attributed to differences in measurement techniques and to the region and physiological variation, such as wakefulness and circadian rhythm (Papouin et al., 2012).

7.4. How can Gα$_i$ trigger calcium transients?

Since the last decade, a growing number of studies have shown that the activation of Gα$_i$-GPCRs triggers calcium transients in astrocytes (Durkee et al., 2019; Gaidin et al., 2020; Nagai et al., 2021, 2019; Shigetomi and Koizumi, 2023). This is quite strange given that the canonical Gα$_i$ pathway does not lead to an increase in intracellular Ca^{2+} but to a decrease in cAMP. For the oxytocin receptors, some studies conducted in Chinese hamster ovary cells and myometrial cells have revealed that the activation of the Gα$_i$-OTR pathway leads to calcium transients in a PLC- and IP$_3$-dependent manner (Hoare et al., 1999; Phaneuf et al., 1993; Willets et al., 2009). Moreover, this activation involved the activity of the Gβγ complex of the Gα$_i$ protein (Hoare et al., 1999). These observations can be interpreted in light of a recent study that has demonstrated the ability of Gβγ complexes from Gα$_i$ proteins to empower the Gα$_q$ signalization (Pfeil et al., 2020). Importantly, the mechanism they propose involves that Gβγ complexes relieve PLC autoinhibition but are not sufficient to completely overcome PLC autoinhibition, and thus, the activation of a Gα$_q$ protein is needed to trigger the Calcium transient. In astrocytes, the involvement of βγ complexes have also been described as necessary to trigger calcium transients after Gα$_i$-GPCR activation (Durkee et al., 2019), thus we can imagine that Gα$_i$-GPCR put astrocyte in an "ON" mode that makes them respond to every little variation of their environment.

7.5. Astrocyte reactivity

On many aspects, we can consider this "ON" mode of astrocytes as a reactive mode. The major landmark of astrocyte reactivity is the upregulation of intermediate filaments such as GFAP. We observed this upregulation as soon as 15 to 20 minutes after the beginning of the conditioning session (10 minutes of conditioning and 5 to 10 minutes to anesthetize and perfuse the mice). This delay is short compared to the timing usually observed for GFAP upregulation, which ranges from hours to days (Escartin et al., 2019; Liu et al., 2012; O'Callaghan et al., 2014; Takano et al., 2014). To explain this discrepancy, we can imagine that globular GFAP monomers can polymerize during the fear conditioning protocol, thereby bypassing the transcription of the *Gfap* gene and the translation of the mRNA into protein. Thus, GFAP may not be detectable as a globular cytosolic protein but can be immunostained after its

polymerization. To test this hypothesis, we could do punches of the CeL/C and quantify the amount of GFAP proteins. If this amount of GFAP monomers is the same in naïve and fear-conditioned animals, this could indicate that fear conditioning increases GFAP polymerization rather than its transcription/translation. We could also investigate whether a rapid translation of pre-existing *Gfap* mRNA occurred after fear conditioning by comparing GFAP protein level and mRNA level measures by qRT-PCR.

Reactive astrocytes are also characterized by the activation of intracellular pathways such as JAK/STAT3 (Ben Haim et al., 2015; Escartin et al., 2021; Priego et al., 2018). Interestingly, the activation of Gi/o proteins can lead to the activation of this pathway (Jiang and Bajpayee, 2009), indicating how the activation of the OTR-Gα_i pathway can trigger astrocyte reactivity. It could be interesting to evaluate STAT3 phosphorylation in future experiments to evaluate the activation of this protein. If this pathway is indeed involved in CeL/C astrocyte reactivity after fear conditioning, we can imagine blocking it using STAT inhibitors or reversing astrocytes reactivity by stimulating intracellular pathways that deactivate astrocytes (Escartin et al., 2019). If the blockade/reversal of astrocyte reactivity can prevent CeL/C neurons' excitability, this can indicate a potential target for future therapies for post-traumatic stress disorders.

7.6. Unveiling the region-specific effect of OT

The vast majority of studies investigating the effect of OT on astrocytes have been done in the hypothalamus (Di Scala-Guenot et al., 1994; Di Scala-Guenot and Strosser, 1992; Wang et al., 2017; Wang and Hatton, 2009, 2007a, 2007b reviewed in Baudon et al., 2022). So when we conceptualized the second project of my thesis, we based our hypothesis on the results observed in this structure and suggested that OT may reduce GFAP immunoreactivity in CeA astrocytes. However, when we observed that TGOT strongly increases GFAP staining in the CeA, we were flabbergasted. We thus searched for other reports of an increase in GFAP staining after OTR activation and found no published reports of similar observations. However, we found a thesis manuscript that described an increased GFAP quantity in the amygdala 20 minutes after intracerebroventricular infusion OT. In this study, they observed a rapid elongation of astrocyte processes after a 10 min incubation in 500nM

OT. Even if these results have to be carefully considered since they did not pass through the process of peer reviewing, it seems to indicate that OT may have different effects depending on the brain region.

7.7. Reconcile love and fear

Since the beginning of the 20th century, a growing number of studies investigates the involvement of OT in emotions. In many aspects, OT has been associated with positive emotions and for that reason, this neuropeptide is considered a hormone that promotes well-being, reduces stress and anxiety, and favors interindividual bonding (Lee et al., 2009; Lefevre et al., 2021). However, many reports (including the present manuscript) are difficult to reconcile with this vision and tend to indicate that OT functions may be different depending on the physiological state of the animal or the brain region where OT is released (Quintana and Guastella, 2020). For instance, OT is known to decrease anxiety and fear behaviors but stressful events have been reported to increase OT quantity in the blood and the CeA (Ebner et al., 2005; Lee et al., 2009). On social behaviors, albeit hypothalamic OT neurons were shown to increase social interactions and recognition (Maroun and Wagner, 2016; Resendez et al., 2020; Tan et al., 2019; Tang et al., 2020), OT neurons in the bed nucleus of the stria terminalis were recently reported to increase social avoidance and social anxiety (Duque-Wilckens et al., 2020). Similarly, OT increases aggressive behaviors in squirrel monkeys and post-partum aggressiveness in female rodents (Lee et al., 2009). In our data, we observed that activation of astrocytic OTRs in the CeA has a rewarding effect *per se* (Figure 7h in Wahis et al., 2021) but also that its activation during the conditioning phase of a fear conditioning protocol is necessary to observe the establishment of the freezing response (Baudon et al., *in preparation*, Figure 1). Thus, it seems that the brush of scientific literature can paint no unifying portrait of OT functions for now, but we can try to understand the region-specific effects of OT depending on the organization and function of this structure.

8. Conclusion

Overall, this Ph.D. work has highlighted the role of astrocytes in the neuromodulatory effect of oxytocin in the central amygdala. In the first part of this work, we focused on the rapid neuromodulatory effect of oxytocin and we unveil the direct action of this peptide on a subpopulation of amygdala astrocytes. Once activated, these cells secrete gliotransmitters that activate neighboring neurons, eventually modifying amygdala-related behaviors (Wahis et al., 2021). In a second time, we evaluate the long-term effect of oxytocin on the amygdala astro-neuronal network and we observed that oxytocin leads to astrocyte reactivity by activating an OTR-Gα_i pathway. This modification of astrocyte physiology controls neuronal excitability and may be involved in the establishment of fear-related behavior (Baudon et al., *in preparation*).

The endeavor of deciphering the way astrocytes and neurons communicates is in line with a global effort of these last years to understand how astrocytes are involved in the computational power of the brain (Bazargani and Attwell, 2016; Savtchouk and Volterra, 2018; Volterra and Meldolesi, 2005). For too long, we tried to understand the brain's inner workings only through the prism of a digital code carried by neurons but this simplified vision has to evolve and take into account the involvement of glial cells and even of the extracellular matrix (Syková, 2004). The inner clockworks of the brain are infinitely complex but make it the most intriguing and beautiful machine of the human-known universe.

9. Annexes

9.1. Liste des publications

Baudon, A., Charlet, A., 2020. Un engramme ocytocinergique pour apprendre et contrôler sa peur. médecine/sciences 36, 9–11. doi:10.1051/medsci/2019252

Baudon, A., Charlet, A., 2022. Les sentiments naissent sous de bonnes étoiles, ou comment les astrocytes contrôlent nos émotions. médecine/sciences 38, 138–140. doi:10.1051/medsci/2021255

Baudon, A., Clauss–Creusot, E., Althammer, F., Schaaf, C.P., Charlet, A., 2022. Emerging role of astrocytes in oxytocin-mediated control of neural circuits and brain functions. Progress in Neurobiology 217, 102328. doi:10.1016/j.pneurobio.2022.102328

Baudon, A., Clauss Creusot, E., Charlet, A., 2022. Rôle émergent des astrocytes dans le Contrôle des circuits neuronaux et des fonctions cérébrales modulés par l'ocytocine. Biologie Aujourd'hui 216, 155–165. doi:10.1051/jbio/2022022

Baudon, A., Clauss-Creusot, E., Darbon, P., Patwell, R., Grinevich, V., Charlet, A., 2022. Calcium imaging and BAPTA loading of amygdala astrocytes in mouse brain slices. STAR Protocols 3, 101159. doi:10.1016/j.xpro.2022.101159

Tang, Y., Benusiglio, D., Lefevre, A., Hilfiger, L., Althammer, F., Bludau, A., Hagiwara, D., **Baudon, A.**, Darbon, P., Schimmer, J., Kirchner, M.K., Roy, R.K., Wang, S., Eliava, M., Wagner, S., Oberhuber, M., Conzelmann, K.K., Schwarz, M., Stern, J.E., Leng, G., Neumann, I.D., Charlet, A., Grinevich, V., 2020. Social Touch promotes interfemale communication via activation of parvocellular oxytocin neurons. Nature Neuroscience 23, 1125–1137. doi:10.1038/s41593-020-0674-y

Wahis, J., **Baudon, A.**, Althammer, F., Kerspern, D., Goyon, S., Hagiwara, D., Lefevre, A., Barteczko, L., Boury-Jamot, B., Bellanger, B., Abatis, M., Da Silva Gouveia, M., Benusiglio, D., Eliava, M., Rozov, A., Weinsanto, I., Knobloch-Bollmann, H.S., Kirchner, M.K., Roy, R.K., Wang, H., Pertin, M., Inquimbert, P., Pitzer, C., Siemens, J., Goumon, Y., Boutrel, B., Lamy, C.M., Decosterd, I., Chatton, J.-Y., Rouach, N., Young, W.S., Stern, J.E., Poisbeau, P., Stoop, R., Darbon, P., Grinevich, V., Charlet, A., 2021. Astrocytes mediate the effect of oxytocin in the central amygdala on neuronal activity and affective states in rodents. Nature Neuroscience 24, 529–541. doi:10.1038/s41593-021-00800-0

Baudon, A., Grelot, V., Althammer, F., Clauss--Creusot, E., Krabichler, Q., Grelot, V., Grinevich, V., Charlet, A. Central amygdala astrocytes oxytocin receptor Gαi pathway mediates behavioral adaptation in mice. *In preparation*.

9.2. Liste des communications

Présentations

L'ocytocine au cœur de nos émotions, A. Baudon, P. Darbon.
Conférence grand publique du Jardin des sciences, 10 mars 2022, Strasbourg.

Oxytocin Acts on Astrocytes in the Central Amygdala to Promote a Positive Emotional State. A. Baudon. NeuroStra scientific day, 17 mai 2022, Strasbourg.

Central amygdala astrocytes are gatekeepers of oxytocin-induced behavioral adaptation to fear. A. Baudon, X-Mas Symposium of Oxytocin Friends, 5 décembre 2022, Mannheim.

Poster

Astrocytes mediate the effect of oxytocin on the local amygdala circuitry that underlie emotional behaviour, J. Wahis, A. Baudon, D. Kerspern, F. Althammer, V. Grinevich, A. Charlet. Federation of European Neuroscience Societies, 11-15 juillet 2020, forum dématérialisé.

Deciphering the central amygdala oxytocin-induced astrocytic and neuronal intracellular activity, A. Baudon, J. Burger, E. Clauss--Creusot, D. Kerspern, A. Charlet. NeuroFrance, 19-21 mai 2021, forum dématérialisé.

Deciphering the central amygdala oxytocin-induced astrocytic and neuronal intracellular activity, A. Baudon, J. Burger, E. Clauss--Creusot, D. Kerspern, A. Charlet. XV European Glial Meeting 5-9 juillet 2021, forum dématérialisé.

Astrocytes mediate the effect of oxytocin on the local amygdala circuitry that underlie emotional behaviour, J. Wahis, A. Baudon, D. Kerspern, F. Althammer, V. Grinevich, A. Charlet. Meeting of the French Glial Cells Club, 18-22 octobre 2021, forum dématérialisé.

Astrocytes mediate the effect of oxytocin on the local amygdala circuitry that underlie emotional behaviour, J. Wahis, A. Baudon, D. Kerspern, F. Althammer, V. Grinevich, A. Charlet. Federation of European Neuroscience Societies, 9-13 juillet 2022, Paris, France.

Oxytocin-induced astrocyte remodelling promote neuronal activity in the central amygdala. A. Baudon, Q. Krabichler, F. Althammer, E. Clauss--Creusot, V. Grinevich, A. Charlet. Meeting of the French Glial Cells Club, 12-14 octobre 2022, Sète, France.

Central amygdala astrocytes oxytocin receptor Gαi pathway mediates behavioral adaptation in mice. A. Baudo, F. Althammer2, E. Clauss--Creusot1, Q. Krabichler, V. Grelot, V. Grinevich, A. Charlet. International Astrocyte School, 26 avril au 1 avril 2023, Bertinoro, Italy.

Central amygdala astrocytes oxytocin receptor Gαi pathway mediates behavioral adaptation in mice. A. Baudon, F. Althammer, E. Clauss--Creusot, Q. Krabichler, V. Grelot, V. Grinevich, A. Charlet. Meeting of the French Glial Cells Club, 23 mai 2023, Lyon, France.

Central amygdala astrocytes oxytocin receptor Gαi pathway mediates behavioral adaptation in mice. A. Baudon, F. Althammer, E. Clauss--Creusot, Q. Krabichler, V. Grelot, V. Grinevich, A. Charlet. NeuroFrance, 24-26 mai 2023, Lyon, France.

9.3. Calcium imaging and BAPTA loading of amygdala astrocytes in mouse brain slices.

Baudon, A., Clauss-Creusot, E., Darbon, P., Patwell, R., Grinevich, V., Charlet, A.

STAR Protocols

Protocol

Calcium imaging and BAPTA loading of amygdala astrocytes in mouse brain slices

Angel Baudon,
Etienne Clauss-
Creusot, Pascal
Darbon, Ryan
Patwell, Valery
Grinevich,
Alexandre Charlet

acharlet@unistra.fr

Highlights

Protocol describes
calcium imaging and
BAPTA loading on
astrocytes in mouse
brain slices

Calcium imaging is a
simple yet reliable
tool to study
astrocyte activity

Patch-clamp-
mediated loading of
BAPTA allows the
disruption of
astrocytic activity

Calcium imaging can
assess BAPTA
diffusion within the
astrocytic network

Astrocytes are glial cells that exhibit calcium signaling-mediated activity. Here, we present a protocol to monitor and manipulate astrocyte calcium activity from mouse amygdala slices. In the first part of this protocol, we describe the procedure of astrocyte calcium imaging. In the second part, we detail how to disrupt astrocyte calcium activity by patch-clamp-mediated loading of BAPTA. These two approaches are presented separately but they can also be used simultaneously to monitor the effects of disruption on an astrocyte network.

STAR Protocols

Protocol

Calcium imaging and BAPTA loading of amygdala astrocytes in mouse brain slices

Angel Baudon,[1,3] Etienne Clauss-Creusot,[1,3] Pascal Darbon,[1] Ryan Patwell,[2] Valery Grinevich,[2]
Q1 and Alexandre Charlet[1,4,5,*]

Q6 [1]Centre National de la Recherche Scientifique and University of Strasbourg, Institute of Cellular and Integrative Neuroscience, INCI CNRS UPR3212, 8, Allée du Général Rouvillois, Strasbourg, 67000 France

[2]Department of Neuropeptide Research in Psychiatry, Central Institute of Mental Health, University of Heidelberg, Mannheim, 68159 Germany

[3]These authors contributed equally

Q7 [4]Technical contact

[5]Lead contact

*Correspondence: acharlet@unistra.fr
https://doi.org/10.1016/j.xpro.2022.101159

SUMMARY

Astrocytes are glial cells that exhibit calcium signaling-mediated activity. Here, we present a protocol to monitor and manipulate astrocyte calcium activity from mouse amygdala slices. In the first part of this protocol, we describe the procedure of astrocyte calcium imaging. In the second part, we detail how to disrupt astrocyte calcium activity by patch-clamp-mediated loading of BAPTA. These two approaches are presented separately but they can also be used simultaneously to monitor the effects of disruption on an astrocyte network.

For complete details on the use and execution of this protocol, please refer to Wahis et al. (2021).

Q4 Q3 Q2 **BEFORE YOU BEGIN**
Q5

Calcium imaging requires a confocal fluorescence microscope and an illumination system capable of achieving a high temporal resolution (sampling frequency > 1 Hz). For the calcium indicator, we use Oregon Green BAPTA 1 coupled to an AcetoxyMethyl ester group (OGB1-AM) because it preferentially stains astrocytes, but this protocol can be used with other AM-coupled calcium indicators as well. For example, Rhod2-AM can be used as a red wavelength alternative. However, in our hands, we observe more cell death with Rhod2-AM than with OGB1-AM. One can also use ratiometric calcium indicators such as Fura 2, Fluo-4 or Indo-1. However, while this approach allows for an accurate estimation of the intracellular calcium concentration, it also has the drawback of requiring three wavelengths of light, thereby restricting the use of other fluorescent labeling approaches. The Kd value should also be considered when choosing a calcium indicator. For example, if the goal of the experiment is to monitor small events, then an indicator with a high Kd (e.g., Fluo-4FF) would be ideal, whereas a dye with a lower Kd (e.g., OGB1) would be preferable for monitoring bigger calcium events due to a lower degree of saturation (Delvendahl et al., 2015). Yet another approach that may be used in conjunction with this protocol would be the use of genetically encoded calcium indicators such as GCaMP, or the newly developed Salsa6f ratiometric analogs (for use in astrocytes, see Wakida et al., 2020).

For required tools, please see key resources table and materials and equipment for references.

In the present paper, the two protocols were performed in mouse horizontal slices, containing the central nucleus of the amygdala.

XPRO 101159
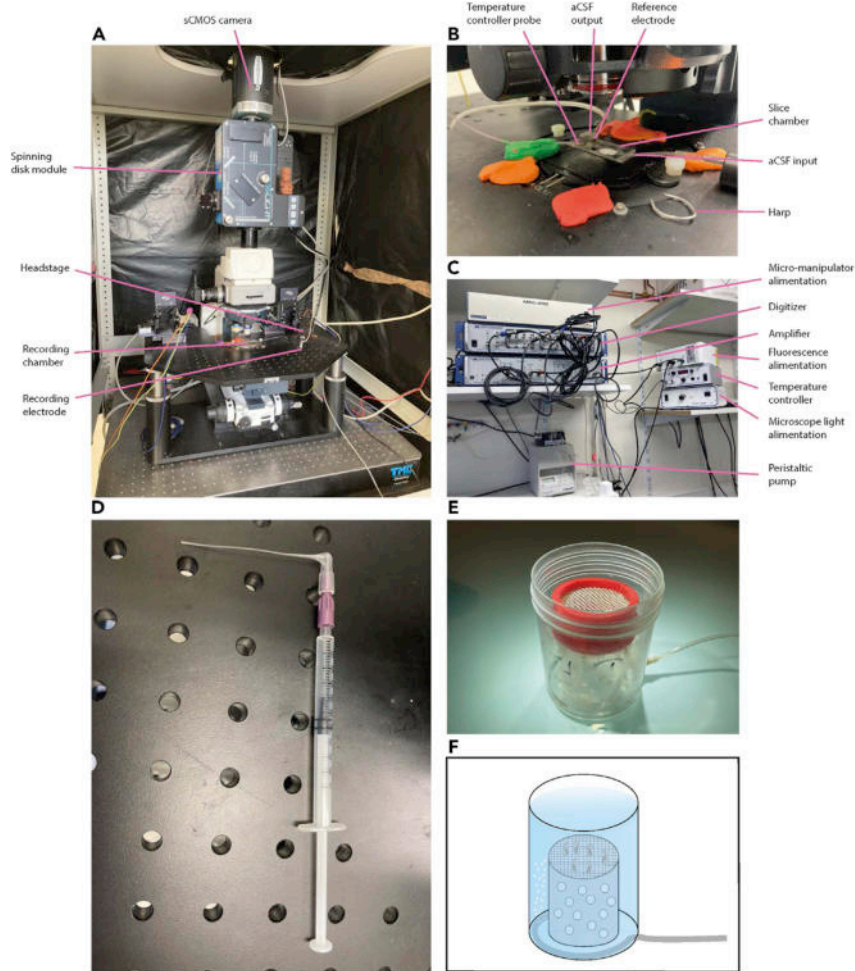
Figure 1. Material for calcium imaging and patching of astrocytes

(A) Microscope equipped with a spinning disk module and a sCMOS camera for calcium imaging. This microscope is placed on a Gibraltar table along with the recording chamber, the headstage and the recording electrode. The assembled instruments are placed on an anti-vibration table.

(B) Magnified photo of a recording chamber divided into 3 parts: one space for the slice and aCSF input, one for the aCSF output and one for the reference electrode. The harp is placed on the slice to avoid any movement during recordings.

(C) All the equipment needed for patch clamp (for more details, see key resources table).

(D) Example of a manually pulled tip used to fill the pipette in patch-clamp. The tip is mounted on a filter placed on a 1 mL syringe to avoid clogging the tip.

(E) Photo of a recovery chamber.

(F) Scheme of the recovery chamber, a pierced tube is fixed at the bottom of the chamber to bring carbogen in the aCSF of the chamber.

The calcium imaging setup is composed of a Zeiss Axio examiner microscope equipped with a 40× water immersion objective and a mounted X-Light Confocal unit – CRESTOPT spinning disk (Figure 1A). We use a LED light source for excitation and emission data are acquired at 2 Hz with an optiMOS sCMOS camera (Figure 1A). All of these hardware elements are interfaced with a computer running MetaFluor (ver. 7.8.8.0) software.

The patch-clamp setup is composed of an Axon MultiClamp 700B amplifier coupled to an ADC Digidata 1440A Digitizer (Figure 1C). Data are acquired at a sampling rate of 20 kHz and stored on a computer using the pClamp (ver. 10) software suite.

STAR Protocols
Protocol

If needed, prepare aCSF, the perfusion solution and the internal solution in advance (see materials and equipment).

Experiments have to be performed in accordance with ethical rules and approbation from your local institutions.

Slice preparation

⏱ Timing: 2 h

1. Anesthetize the mouse with an *i.p.* injection of ketamine and paxman at 400 mg/kg and 80 mg/kg respectively.

   Note: one can also use isoflurane inhalation followed by quick decapitation.

2. Access the heart by performing a laparotomy and a thoracotomy, being careful not to damage the internal organs (Figures 2A and 2B). Use a 50 mL syringe filled with cold (4°C) perfusion solution (see materials and equipment), insert the needle into the left ventricle and cut the right atrium. Exsanguinate the animal until there is no more blood flowing from the heart (typically, 10 mL is enough).

   Note: Heart perfusion is not essential for young animals (<P30-40) to obtain proper slices.

   Note: To perform the exsanguination, you can also use a peristaltic pump to have better control over the flow of the perfusion solution.

   Note: Observe the liver during the perfusion. If the perfusion procedure is done properly, its color should change from red to almost white.

3. Once perfusion has finished, decapitate the animal using scissors. Place the head in a Petri dish containing cold oxygenated perfusion solution. Open the scalp using the scalpel and remove the part of the skull covering the brain using scissors and forceps (Figure 2C). Extract the brain from the skull and place it in another Petri dish filled with clean cold oxygenated perfusion solution.

   Note: If you are fast enough (< 3 min), this step can be done outside the perfusion solution to save both time and solution. For the sake of reproducibility, we highly recommend that the first few attempts be done as described here until you get used to it.

   ⚠ CRITICAL: It is important to transfer the brain into a clean Petri dish immediately after extraction as the first Petri dish will contain blood and parts of the skull that might damage the brain tissue.

4. Using a scalpel, remove the cerebellum and the olfactory bulbs. Separate the two hemispheres by cutting along the sagittal axis (Figure 2D). Then, slice off a portion of the cortex to flatten the dorsal part of the brain (Figure 2E).

   ⚠ CRITICAL: It is important to cut the dorsal part of the brain as flat as possible to fix the brain correctly and have identical slices throughout the days.

5. Put some glue on the vibratome sample holder. Reassemble the brain (Figure 2F), fix it on its dorsal surface by sliding it from the spoon onto the sample holder, and slice it using a vibratome to obtain 350 μm thick slices. This will allow the slicing of both hemispheres together with the same accuracy (Figure 2G).
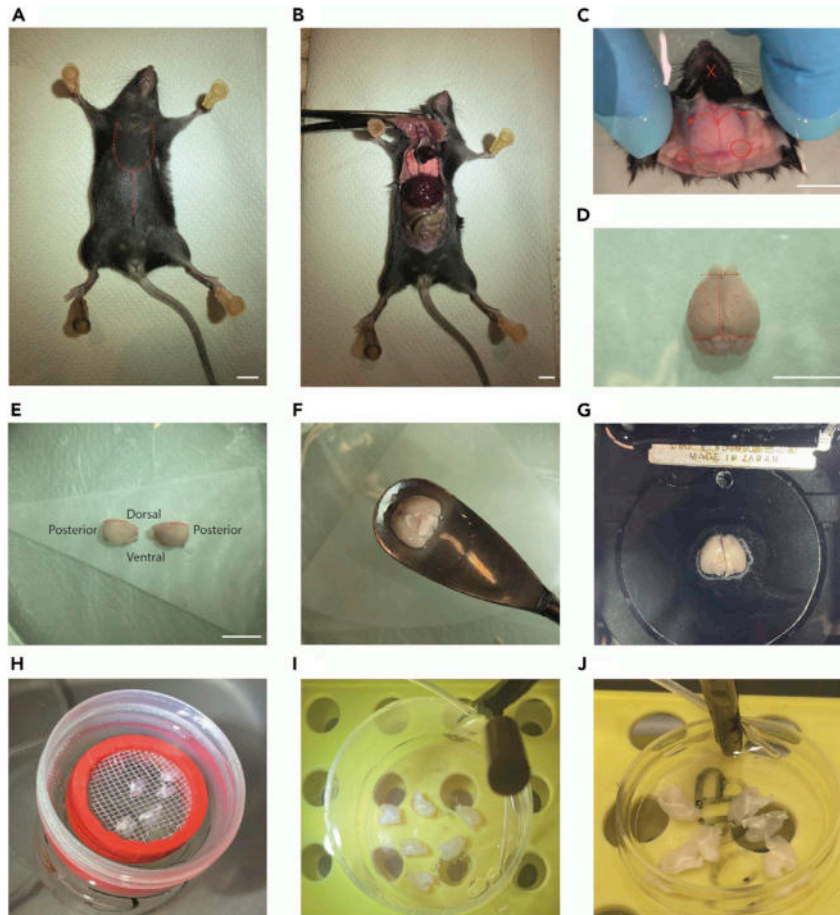
Figure 2. Slice preparation and dye loading

(A) The mouse is fixed by the paws using syringe needles. The red dotted lines show where to cut for clear access to the heart.

(B) Photo of the mouse after performing the laparotomy and thoracotomy.

(C) After opening the scalp, cut the skull following the dotted red line. Then remove the two parts of the skull as indicated by the red arrows. The two red circles show important bones to remove to avoid damaging the brain during the extraction. Stick the tips of closed scissors in the red cross and open them to remove the lateral part of the skull. This last step is optional but facilitates brain extraction.

(D) Brain after extraction. The red dotted lines show where to cut to remove the cerebellum, olfactory bulbs and hemisect the brain.

(E) After hemisecting the brain, cut the two parts following the red dotted lines to flatten the dorsal part of the brain. Scale bar A–E = 1 cm.

(F) Use a spoon-shaped tool to retrieve the brain after re-assembling it. Dry the remaining liquid and fix it on its dorsal surface.

(G) Fixed brain before slicing.

(H) Photo of the slices placed in the recovery chamber.

(I) Photo of the slices placed in the culture well for SR101 staining.

(J) Photo of the slices placed in the culture well for OGB1-AM loading.

> **Note:** Use a spoon-shaped tool to put the brain on the vibratome sample holder. The glue we use sets when in contact with a liquid. Thus, dry the spoon and the dorsal surface of the brain as much as possible.

> **Note:** We use a Leica VT1000S vibratome with the following parameters: (1) 0° blade angle; (2) 7.5 (75 Hz) vibration frequency; (3) 1 (0.05 mm/s) progression speed.

STAR Protocols
Protocol

CellPress
OPEN ACCESS

> ⚠ CRITICAL: during the slicing, it is essential to keep the solution containing the brain as cold as possible by adding ice around the slicing tank (you can also pour ethanol into the ice to keep it cooler). Failing to keep the solution cold enough will cause the brain to soften, which may cause it to be crushed by the razor blade. Furthermore, keeping the brain cold will reduce both the activity of degradation enzymes and the metabolic activity within the cells.

6. Transfer the slices into a recovery chamber containing aCSF (see materials and equipment), oxygenated with carbogen for 1 h at 25°C (Figure 2H, for recovery chamber details, see Figures 1E and 1F).

> ⚠ CRITICAL: Starting from this point, all manipulations have to be performed in the dark.

Slice incubations for SR101 dye loading

> ⏱ Timing: 30 min

7. While waiting for the slices to recover in the chamber, pour 10 mL of aCSF into a culture well and add 10 μL of SR101 (1 mM) so the final concentration of SR101 will be 1 μM. Connect a carbogen line to the well to make it bubble at a modest rate (∼2–3 bubbles/second). Carefully position the bubbling culture well into the heating bath at 37°C (Figure 2I).

> *Note:* You can make a platform with a test tube rack so the well will heat properly and not sink.

8. After 1-h recovery (step 6), transfer the slices from the recovery chamber into the culture well containing SR101 using either a brush or a Pasteur pipette and let them incubate for 20–30 min (Figure 2I).

> *Note:* Make sure that the slices do not overlap with each other and that the carbogen bubbling does not move them around.

Slice incubations for calcium dye loading

> ⏱ Timing: 1 h

9. The following step is only applicable for calcium imaging.
   a. During the incubation period of step 8, prepare the OGB1-AM solution. Add 2 μL of PF-127 (20% in DMSO) and 8 μL of Cremophor EL (0.5% in DMSO) in the OGB1-AM vial. Vortex 1 min. Wrap the vial in aluminum foil to avoid photodamage and ultrasonicate it for 10–20 min.

> *Note:* If you do not have a sonication bath, you can use a thermomixer at max speed, 40°C for 10 min.

   b. Centrifuge the aliquot for 5 s to get all the droplets to the bottom of the vial. Carefully add 20 μL of aCSF to the vial and homogenize the solution by gently pipetting up and down without making bubbles.
   c. At the end of the SR101 incubation time, transfer the slices into a small culture well containing 3 mL aCSF. Put a carbogen line in the well and adjust the carbogen flow to produce 1 bubble every 2 s. Carefully position the bubbling culture well into the heating bath at 37°C (Figure 2J).

> *Note:* Maintain the orientation of the slices such that the same side is loaded with both SR101 and OGB1-AM.

Note: Surfactants tend to produce foam that will desiccate the slices. Try to adjust the carbogen flow in such a way as to keep the bubbles along the well wall and not floating above the slices.

Note: You can also put the carbogen line just above the level of the aCSF such that it oxygenates the solution without producing foam. To do so, pipet 3 mL into the well and make a hand-made hole just above the level of the aCSF.

d. Slowly and carefully, deposit 6–10μL of OGB1-AM solubilized into Cremophor and PF-127 directly onto your region of interest to ensure that it will receive exposure to a high concentration of dye. Repeat the operation for all other slices. Incubate for 45 min to 1 h in the dark.

⚠ CRITICAL: Cover the incubation well with a lid to avoid evaporation and dehydration of the slices. Leave a tiny space between the lid and the well to allow carbogen to escape from the well.

Recovery

⏱ Timing: 1 h

10. After the incubation period, transfer the slices to a recovery chamber filled with aCSF oxygenated with carbogen. Incubate at 25°C for at least 1 h before starting experiments (Figure 2H).

Note: At this point, you can take a break to eat.

KEY RESOURCES TABLE

REAGENT or RESOURCE	SOURCE	IDENTIFIER
Chemicals, peptides, and recombinant proteins		
Oregon Green 488 BAPTA-1, AM, cell permeant – Special Packaging	Thermo Fisher Scientific	Cat#O6807
Sulforhodamine 101 (SR101)	Merck	Cat#S7635
NaCl	Sigma-Aldrich	793566
KCl	Carlo Erba	471177
NaH_2PO_4	Sigma-Aldrich	S9638
$NaHCO_3$	Sigma-Aldrich	S5761
D-Glucose	Sigma-Aldrich	G8270
$MgSO_4$	Merck	63139
$CaCl_2$	Carlo Erba	433381
NMDG	Sigma-Aldrich	M2004
HEPES	Sigma-Aldrich	H4034
L-Ascorbic Acid	Sigma-Aldrich	95209
Thiourea	Sigma-Aldrich	T8656
Sodium Pyruvate	Sigma-Aldrich	P2256
N-Acetyl-L-Cysteine	Sigma-Aldrich	A7250
Kynurenic acid	Alomone labs	K-110
BAPTA	Thermo Fisher Scientific	B1204
Na_2ATP	Sigma-Aldrich	A2383
Na_2GTP	Sigma-Aldrich	51120
$MgCl_2$	Sigma-Aldrich	208337
PF-127	Sigma-Aldrich	P2443

(*Continued on next page*)

STAR Protocols
Protocol

CellPress
OPEN ACCESS

Continued

REAGENT or RESOURCE	SOURCE	IDENTIFIER
Cremophor EL	Sigma-Aldrich	238470-1 SET
DMSO	Sigma-Aldrich	D8418
Experimental models: Organisms/strains		
1–2 months old C57BL6/J male or female mice	Chronobiotron UMS3415	n/a
Software and algorithms		
MetaFluor 7.8.8.0	Molecular Devices	n/a
pClamp 10	Molecular Devices	n/a
uEye Cockpit	iDS software suite	n/a
MultiClamp 700b commander	Molecular Devices	n/a
Fiji	Schindelin et al. (2012)	https://imagej.net/software/fiji/downloads
Deposited data		
Example code	Alexandre Charlet's lab	https://github.com/AngelBaudon/Canal.git
Other		
Vibratome	Leica Biosystems	VT1000S
pH meter	Hanna instruments	HI 2210
Micro-osmometer	Löser	Type 6
Ultrasonic cleaner	Branson	5510-MT
Amplifier	Axon Instruments	Digitizer
Digitizer	Axon Instruments	MultiClamp 700B
Microscope	Zeiss	Examiner A1
Manipulators	Sutter Instrument	MPC-325
Light source (patch)	Lumen Dynamics	XT640-W
LED light source	Lumencor	7-CLX-NA
Peristaltic pump	Gilson	Minipuls 3
Anti-vibration table	Photon Lines	63-7590M
Recording chamber	Multichannel systems	RC-26G
Spinning disk	CrEST	X-LIGHT
sCMOS camera	QImaging	optiMOS
uEye camera	iDS	UI-1240LE-NIR-GL
Electrode holder + Ag wire	Warner instruments	QSW-T15P
Flaming/Brown micropipette puller	Sutter Instrument	P-97
Borosilicate glass	Sutter instrument	BF150-86-7.5HP
Nalgene 4-mm syringe filters purple	Thermo Fisher Scientific	176-0020
26G needle	Agani	SAN2613R1
Syringe 1 mL	Sigma-Aldrich	Z683531
Syringe 20 mL	Sigma-Aldrich	Z116882
Syringe 50 mL	Sigma-Aldrich	Z118400
Ketamine	Virbac France	211101
Paxman	Virbac France	221631
Qualitative filter paper 413	VWR	516-0817
Scalpel	Fine Science Tools	10004-13
Scalpel blades	Fine Science Tools	10021-00
Dumont forceps	Fine Science Tools	11254-20
Bonn scissors	Fine Science Tools	14184-09
Fine scissors – Sharp-blunt	Fine Science Tools	14028-10
Paintbrush	Princeton	Round – natural red sable
Loctite Superglue-3	Dutscher	999227

Note: The resources listed here are what we use at the time of writing this protocol. There are currently many different alternatives and new versions of some products may become available in the future.

MATERIALS AND EQUIPMENT

- aCSF

Reagent	Final concentration (mM)	Amount
H$_2$O	n/a	1 L
NaCl	124	7.2416 g
KCl	2.5	0.1864 g
NaH$_2$PO$_4$	1.25	0.1725 g
NaHCO$_3$	26	2.1843 g
D-Glucose	15	2.7030 g
MgSO$_4$	2	0.493 g
CaCl$_2$	2	0.294 g

Should be stored at 4°C. Maximum storage time ~2 weeks.

- Perfusion solution

Reagent	Final concentration (mM)	Amount
H$_2$O	n/a	5 L
NMDG	93	90.7773 g
KCl	2.5	0.9319 g
NaH$_2$PO$_4$	1.25	0.8625 g
NaHCO$_3$	30	12.6015 g
HEPES	20	23.8310 g
D-Glucose	25	22.5250 g
L-Ascorbic Acid	5	4.4030 g
Thiourea	2	0.7612 g
Sodium Pyruvate	3	1.6506 g
N-Acetyl-L-Cysteine	10	8.1595 g
Kynurenic acid	2.5	2.3646 g
MgSO$_4$	10	12.324 g
CaCl$_2$	0.5	0.3675 g

Should be stored and used at 4°C. Maximum storage time ~2 weeks. If you prepare large volumes, you can freeze it at −20°C and keep it for up to 1 year.

Note: You will have to use a lot of HCl while adjusting the pH.

Alternatives: You can also use sucrose instead of NMDG. We use it at a concentration of 180 mM and adjust the N-acetyl-L-Cysteine to 5 mM instead of 10 mM.

- Internal solution for astrocyte patch-clamp

Reagent	Final concentration (mM)	Amount
H$_2$O	n/a	50 mL
KMeSO$_4$	125	838.75 mg
HEPES	10	119.15 mg
BAPTA	10	314.4 mg
Na$_2$ATP	4	110.228 mg
Na$_2$GTP	0.4	10.4636 mg
MgCl$_2$	4	19.042 mg

Should be stored at −20°C and used at 4°C. Maximum storage time ~1 year.

STAR Protocols
Protocol

CellPress
OPEN ACCESS

Note: This last solution should be prepared and used on ice as ATP/GTP is unstable at room temperature. We recommend weighing and adding these two components last. As soon as ATP/GTP is added, keep the solution at 4°C.

Note: For the aCSF and perfusion solutions- after adding all powders to the water, bubble the solution with carbogen for about 15–20 minutes to activate the bicarbonate pH buffer. For all solutions, titrate the pH to 7.3–7.4 at room temperature (RT; 20°C–25°C) (except the internal solution at 4°C to avoid ATP/GTP degradation), as needed, using HCl or NaOH to acidify or alkalinize the solution, respectively. Because $CaCl_2$ equilibrates slowly, we add it after pH titration.

If needed, adjust the osmolality to 300 $\pm$ 10 mOsm/kg by adding water or NMDG/glucose/sucrose to decrease or increase the osmolality, respectively.

Note: It is not recommended to adjust the osmolality as it will change ions concentrations. It is preferable to optimize the protocol beforehand to have the correct osmolality every time.

- Required tools

Equipment	Surgical instruments	Consumable
• Carbogen gas supplier (95% O_2, 5% CO_2)	• Scalpel	• Ketamine (400 mg/kg)
• Vibratome Leica VT1000S	• Forceps	• Paxman (80 mg/kg)
• Heating bath	• Scissors	• 1 mL/20 mL/50 mL syringe
• Fluorescence microscope	• Paintbrush	• 26G needle
• Recording chamber (Figure 1B)	• Superglue	• Blotting paper
• Peristaltic pump		• aCSF
• For calcium imaging: spinning disk (Figures 1A–1C)		• Perfusion solution
• For BAPTA loading: Patch-clamp set-up (Figures 1A–1C)		• OGB1-AM
• Recovery chamber (Figures 1E and 1F)		• SR101
• pH meter		• PF-127 (20% in DMSO)
• Osmometer		• Cremophor EL (0.5% in DMSO)

STEP-BY-STEP METHOD DETAILS
Calcium imaging of astrocytes

⊙ Timing: 3–7 h

Astrocytes, as with any glial cell, do not fire action potentials. However, they do exhibit calcium-based excitability in certain contexts (Charles et al., 1991). For instance, the cytosolic calcium concentration of astrocytes increases in response to many types of stimuli such as neurotransmitter signaling, mechanical stimulation and variations in pH (Khakh and Benjamin, 2019). The following protocol describes a method to monitor these calcium fluctuations in astrocytes.

Follow the initial steps (1–10) for slice preparation, as described in the preparation section above.

1. Transfer the slices into an aCSF filled recording chamber (see key resources table) connected to a peristaltic pump that provides a continuous flow of oxygenated aCSF (∼2 mL/min) at room temperature (or any temperature as needed by the experiment).
2. Place a holding harp on top of the slice to prevent movement.

Note: make sure that the strings of the harp are not too close to the recording site. Otherwise, it will bend your slice and thereby prevent consistent focus with the microscope.

3. Use an Axio examiner Zeiss microscope (or Olympus BX51WI Japan for example) with a 4× objective to identify your region of interest. Set the microscope to infrared differential interference contrast (IR-DIC, ʎ = 750–790nm) and visualize the image with the uEye cockpit software (or Andor iQ 3.2 for example).

   Note: Use an appropriate atlas to identify landmarks that will help you locate your structure of interest.

4. Switch to a 40× water-immersion objective and find the surface of the slice.
5. Open the MetaFluor software and click the "Configure" menu to set the following parameters:
   a. Spinning disk pinhole diameter: 70 µm.
   b. Spinning disk rotation speed: 15.000 rpm.
   c. Wavelength: 575 nm for SR101, 475 nm for OGB.
   d. Exposure time: 20 ms for SR101, 80 ms for OGB.
   e. Illumination intensity: 220 µW for SR101, 580 µW for OGB.
   f. Exposure time: 20 ms for SR101, 80 ms for OGB.
   g. Sampling frequency: 2 Hz (500 ms interval between acquisitions).

   ⚠ CRITICAL: Before switching on the fluorescent light, do not forget to put your microscope in confocal mode. The high intensity of the wide-field mode will bleach the calcium indicator.

   ⚠ CRITICAL: Finely tune your illumination time and intensity to avoid fluorescence bleaching. To do so, we recommend starting at an illumination intensity of 0 µW and an illumination time of 20 ms then progressively increase both values. In our hands, we typically set the illumination intensity between 580 µW and 1040 µW and find that good OGB1 loading can be seen at an illumination time of 20 ms. We never illuminate more than 100 ms.

6. Cells labeled with SR101 are astroxcytes.
   a. Find a focal plane that includes several of them (Figure 3A & Method video S1).

   b. Check the shape of the cells: a healthy cell must have a ramified morphology with observable proximal processes (Figures 3A and 3B). If the cells exhibit a round, swelled shape, it may indicate that these cells are dead or dying. If so, refer to Troubleshooting.
   c. You can observe 3 kinds of cells: (1) the ones that are labeled with both markers (SR101 and OGB, yellow merge in Figure 3A), indicating that astrocytes are well loaded with both indicators; (2) the cells SR101 negative, that are probably neurons; and (3) cells labeled with SR101 but that are OGB1 negative.

   Note: In this last configuration, try to run the experiment anyway, the labeling is maybe too weak to be seen at resting state but can be enough to detect calcium transients. If you did not see any variation of the OGB1 fluorescence, refer to Troubleshooting.

   Note: To guarantee a good signal/noise ratio, you must adjust the focal plane in such a way as to both see the cell and distinguish the proximal processes.

7. Click on "Save pictures" and choose an appropriate folder. Click on "Zero clock" and then "Start". Your data must be saved as independent pictures in the selected folder. At the end of a 10-min recording, you should have 2400 pictures (1200 for the SR101 channel and 1200 for the OGB1 channel).

   Note: Because the files produced are very large, be sure that you correctly set the sampling frequency regarding the event you want to observe. The sampling frequency should be at
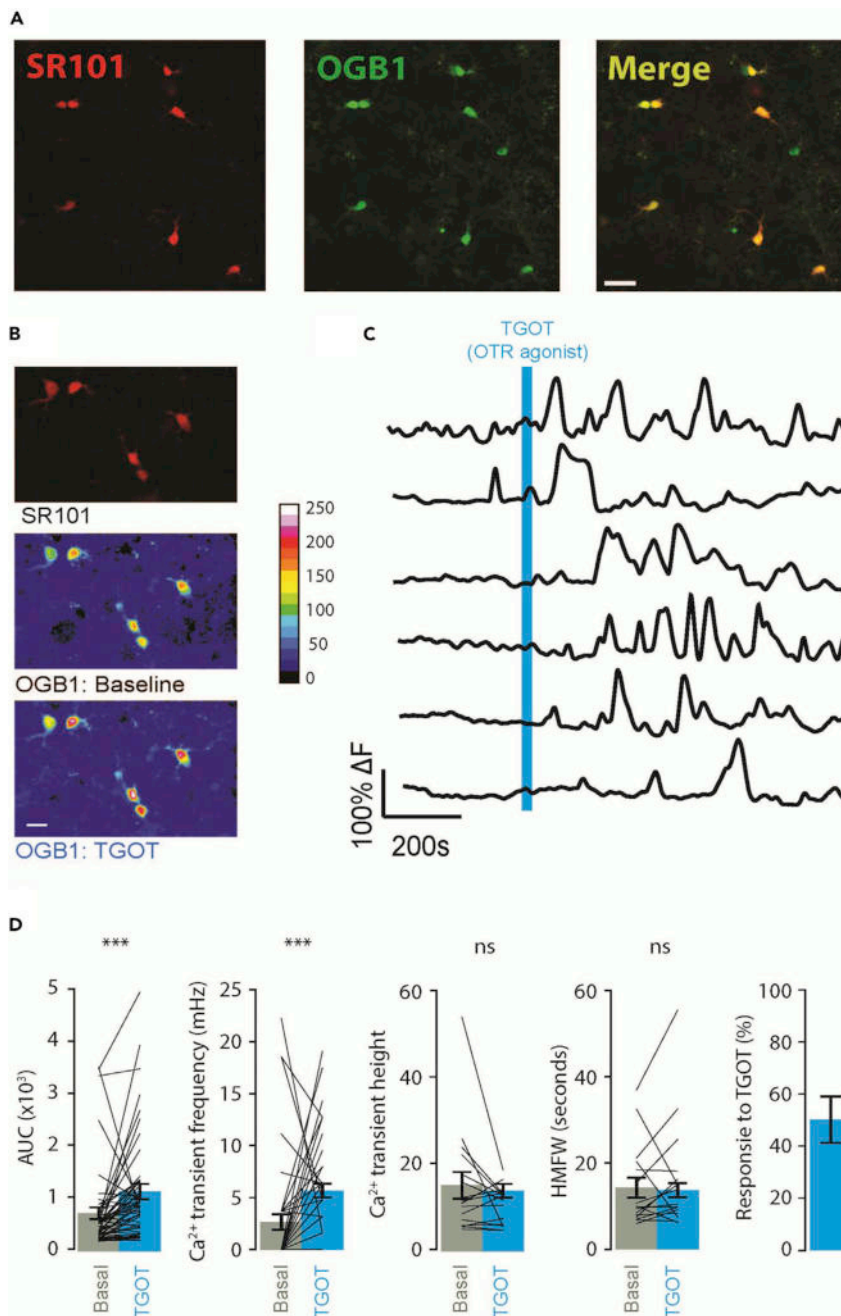
Figure 3. Expected results from a calcium imaging experiment
(A) Stacked picture of SR101 staining (left), OGB1 staining (middle) and the merge of both labels (right). Scale bar = 50 μm.
(B) Pseudo-colorized images showing the increase of fluorescence after application of an OTR agonist (TGOT 1 nM 10 s duration) on OGB1-loaded astrocytes. Upper panel: SR101 staining; middle panel: basal OGB1 fluorescence; lower panel: OGB1 intensity after application of an OTR agonist (TGOT 1 nM, 10-s duration). Scale bar = 50 μm.
(C) Traces of OGB1 fluorescence over time. The blue bar represents the application of TGOT 1 nM 10-s duration.
(D) Quantification of the effect of TGOT 1 nM on astrocytic activity. From left to right: variation of AUC, frequency, calcium transient height, half-max full width (FWHM), and proportion of responsive cells after TGOT application. The gray histograms represent baseline values and the blue histograms represent the quantification of the TGOT effect. Data are represented as mean $\pm$ SEM. ***$p < 0.001$, Paired t test.

least twice as high as the maximal frequency of the events recorded (see Nyquist-Shannon theorem). For somatic global calcium transients that last for more than 2 seconds, a 2 Hz sampling frequency is sufficient. In our hands, a 10-minute recording at 2 Hz results in an individual picture size of ∼1 MB (∼2.4 GB of pictures in total).

8. At the desired time, apply a drug or any kind of stimulation to see if it changes astrocyte calcium activity. We apply an oxytocin receptor agonist, the TGOT at [1 nM] for 10 s through the perfusion system (Figures 3B–3D).

> *Note:* If your perfusion aCSF is in a close loop, be sure to discard the solution for ∼5 minutes to avoid contamination of your clean aCSF stock.

Patch-clamp-mediated BAPTA loading of astrocytes

⊙ Timing: 3–7 h

Astrocyte communication is largely based on intracellular calcium signaling (Khakh and Benjamin, 2019). Thus, blocking these transients using calcium chelators will inhibit astrocytic activity. As astrocytes create a large network interconnected *via* gap junctions, loading a chelator in just a few astrocytes is sufficient to block calcium transients across a local network. Thus, this approach can be used to observe the effects of blocking calcium-dependent astrocyte communication on the activity of a nearby neuronal network. In this section, we describe the detailed steps needed to perform patch clamp on an astrocyte and the protocol used to load BAPTA into the astrocytic network. This experiment can also be performed with other calcium chelators such as EGTA, but we choose to use BAPTA because its binding kinetics is ∼40 times faster than EGTA, allowing for the blockade of local and rapid calcium transients (Naraghi and Neher, 1997).

> *Optional:* this protocol can be used in combination with the calcium imaging of astrocytes. If you intend to do so, please follow the 'optional' steps such as this one that indicates what steps are required from both protocols.

Follow the initial steps (1–10, except step 9) for slice preparation, as described in the preparation section above.

> *Optional:* If you intend to perform BAPTA loading together with calcium imaging, follow the initial steps (1–10, including step 9) for slice preparation, as described in the preparation section above.

9. Transfer the slices into an aCSF filled recording chamber connected to a peristaltic pump that provides a continuous flow of oxygenated aCSF (∼2 mL/min) at room temperature (or any temperature as needed by the experiment).
10. Use an Axio examiner Zeiss microscope (or Olympus BX51WI Japan for example) with a 4× objective to identify your region of interest. Set the microscope to infrared differential interference contrast (IR-DIC, ʌ = 750–790 nm) and visualize the image with the uEye cockpit software (or Andor iQ 3.2 for example).
11. Switch to a 40× water-immersion objective and find the surface of the slice.

> *Note:* At this point, you should visualize the cells with infrared illumination to verify that the slice is 'healthy'. Check that there are no or only a few dead cells, which can be discriminated by their round shape and absence of clear edges.

12. Visualize SR101 labeled astrocytes by illuminating the slice with yellow ∼575 nm light. Once you identify your shining star (i.e., the cell you want to patch), do not adjust the microscopic stage position (in neither the x nor y-axes) or you may lose track of it (Figure 4A).

CellPress
OPEN ACCESS

Note: One should keep several considerations in mind when choosing a cell to patch: (1) Deep cells are harder to visualize and are more easily disrupted by the pipette-induced movement of the tissue above. (2) A healthy cell is not round. (3) Bigger cells are easier to patch.

Optional: If you intend to perform BAPTA loading together with calcium imaging, also refer to step 5 and 6 and try to find several healthy astrocytes in the same stage position.

Note: In uEye Cockpit, press 'Ctrl + right click' to place a marker on the screen. This will help you return to the cell more easily. Alternatively, place a small chunk of putty (e.g. Play Dough) on the screen for each target cell.

13. To get a pipette above the slice:
    a. Raise the objective far away from the slice, while still keeping the lens submerged in the solution.
    b. Take a pulled pipette (borosilicate glass; outer $\varnothing$: 1.5 mm; inner $\varnothing$: 0.86 mm; length: 7.5 cm, see key resources table) previously filled with the internal solution.

Note: To create a pipette filler: place a pipetman tip on a 1 mL syringe. Use a flame to heat the tip and pull it until it is thin enough to enter the pipette, blow air into it with the syringe while doing this to avoid clogging. Use a razor blade to cut the end of the pulled tip and then verify that it is not blocked by pushing water through it. If the water does not flow through the tip, replace it and start over. It may take several attempts to obtain a working tip (see Figure 1D for an example of how it should look).

    c. Insert the pipette onto the AgCl electrode.
    d. Put positive pressure (about 1 mL of air with a syringe). This will help avoid clogging your pipette while moving through the tissue. Position the pipette in the bath using the manipulator.
    e. If you are using pClamp, use the membrane test to determine the resistance of the pipette (if the signal is drifting, see troubleshooting). Otherwise, in voltage-clamp, apply a voltage step of 5–10mV and measure the current transients to calculate the pipette's resistance using Ohm's law. It must be ~6 ± 2 MΩ (see troubleshooting for more details). A lower value means the tip is too large (or broken) and a higher value means the tip is too thin. In either case, it will be difficult to patch a cell.

Note: The instruction manual of your pipette puller contains helpful instructions on how to pull the pipette to achieve the desired resistance.

    f. Under infrared light, bring the pipette tip under the objective using the micromanipulator. Move the pipette along the x and y axes until you see a shadow moving on the screen of the computer and then adjust the objective to focus on it. Then, move the pipette until the tip is in focus.

Note: While positioning the pipette tip, it is important to continuously monitor both the computer screen and the actual pipette to ensure the tip does not hit any obstacles (e.g. the objective).

⚠ CRITICAL: Once the pipette is in the bath, extreme caution must be used when moving it along the z-axis. Uncontrolled movement of the pipette can result in damage to both the tissue and the recording chamber.

    g. The next goal is to safely lower the pipette just above the slice.
        i. First, lower the objective.

XPRO 101159
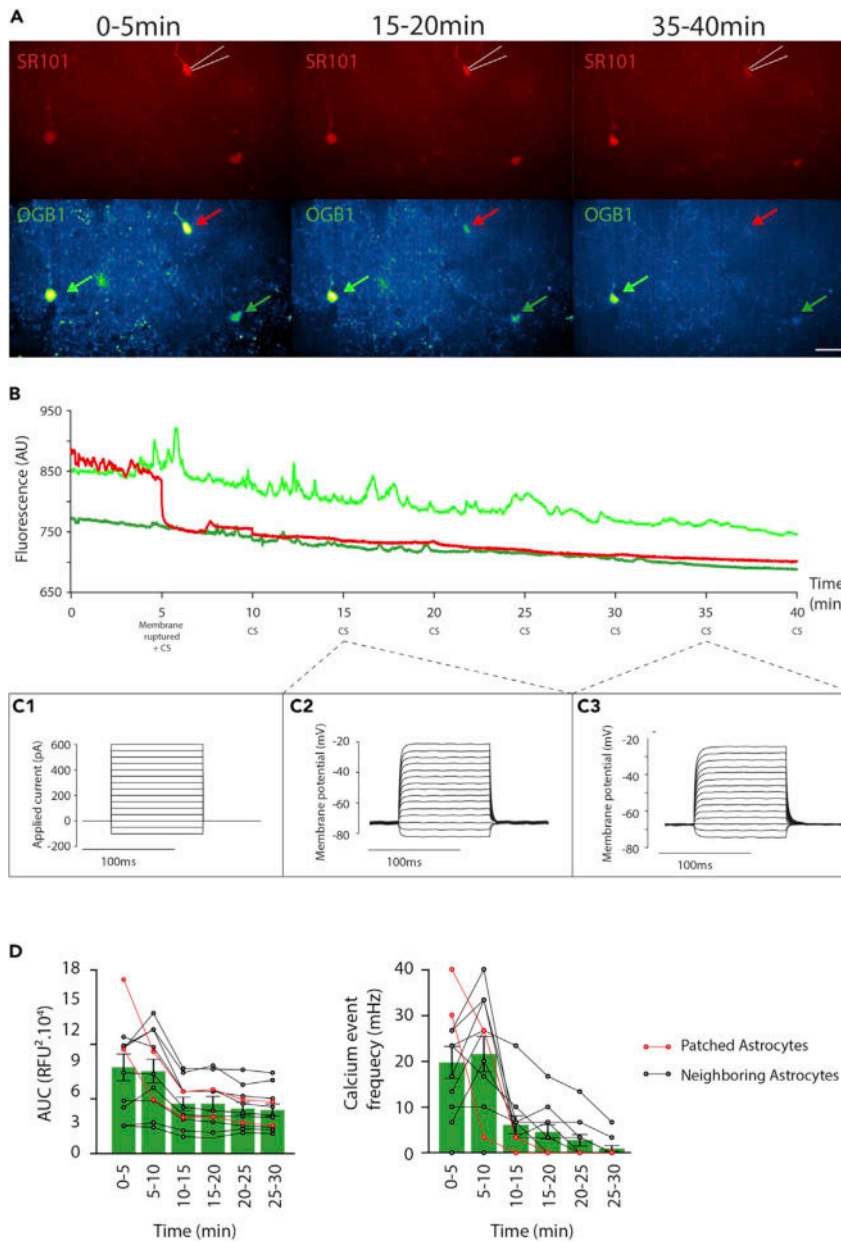
Figure 4. Patch-clamp mediated BAPTA loading in astrocytes

(A) Pseudo-colorized images showing SR101 (top) and OGB1 (bottom) at the beginning of the recording (left), after 15 min (middle) and 35 min (right) of recording. The white lines represent the pipette. The three arrows indicate the signals of the cells shown in (B). Scale bar = 50 μm.

(B) Raw signals showing the evolution of OGB1 fluorescence from the same three cells shown in A that were recorded for 40 min. At 5 min, the patched cell membrane is ruptured (orange).

(C) Example of current step (CS) realized during the recording in (B). Left: command step of the CS: 15 steps of 100 ms starting at −100 pA and incremented by 50 pA. Right: membrane potential of the astrocyte recorded in response to the CS.

(D) Quantification of the effect of BAPTA loading in astrocytes. Left: Quantification of the area under the curve (AUC) of calcium measurement in astrocytes. This value is expressed in relative fluorescence unit^2 (RFU^2). Right: Quantification of calcium transients in astrocytes. The astrocyte membrane is ruptured at 5 min. The red points indicate the values for patched astrocytes and the black ones for neighboring cells.

STAR Protocols
Protocol

CellPress
OPEN ACCESS

    ii. Then lower the pipette until you can see it again.
    iii. Repeat this sequence until you are just above the slice.

Note: you cannot go all the way down with the objective because you will bend/break the pipette and you cannot go down only with the pipette because you will not know when you will be near the tissue.

14. Once you are just above the tissue.
    a. Position the pipette tip above the targeted cell, slightly to its side.
    b. Switch the microscope channel to see the fluorescent labeling of astrocytes.
    c. Lower the pipette down into the tissue until you are on the same level as the top of the target cell.
    d. Move the pipette toward the cell (see Method video S1).

Note: To make positioning of the pipette easier, you can move the objective up and down to help identify your current location within the tissue.

Note: Usually, it is easier to approach the cell diagonally.

15. Two indicators can be used to confirm you are on the target cell.
    a. The first is visual: the positive pressure within the pipette creates a visible deflection (dimple) on the membrane.
    b. The second indicator is the pipette resistance: when you get close enough to the cell, the tip of the pipette becomes enclosed by a pocket of membrane and thus increases the resistance. You can expect an increase of about 0.2 MΩ–1 MΩ (see Method video S1).
16. Release the positive pressure (this increases the resistance as more membrane enters the pipette).

Note: When releasing the positive pressure, the resistance should increase up to at least 15–20 MΩ. The better the pipette is positioned on the cell, the higher the resistance will go (sometimes even directly up to gigaseal).

17. Gently apply negative pressure by mouth until you achieve a gigaseal (i.e., a pipette resistance of several GΩ).

Note: After reaching 100 MΩ, start holding the potential at the desired membrane potential value (−80 mV), this will help reach the gigaseal.

Note: Astrocytic membranes are much more fragile than neuronal membranes. If you are accustomed to patching neurons, then be extra gentle during seal formation and membrane opening.

Optional: To confirm that calcium has been correctly chelated by the BAPTA in the patched cell, start the calcium imaging (see step 7) once the giga seal is reached. Wait 5 min before opening the cell.

18. When the gigaseal is reached, apply negative pressure in the pipette by repetitive suctions until the membrane opens.
19. If the astrocyte opens correctly, you will see capacitive transients and the resistance will drop by several tens of MΩ. You can also look at the calculated membrane resistance by clicking the "Cell" button on pClamp. This resistance must be ∼20 MΩ for astrocytes and ∼200 MΩ for neurons in the central amygdala.

Optional: If you are performing calcium imaging at the same time, you should see a drop in the fluorescence of the patched cell (Figure 4B & Method video S1).

20. Switch to current-clamp mode to check the resting membrane potential, which should be around −80/−90 mV.
    a. Apply current steps of 15 steps starting at −100 pA incremented by 50 pA and lasting 100 ms each. This is to verify that the patched cell is truly an astrocyte.
    b. Thus, the membrane potential should have increased to at least −30 mV and you should not have seen any action potentials (Figure 4C).

    Note: If the patched cell is a neuron or even if you just patched a presynaptic terminal, you should see action potentials (Bischofberger et al., 2006).

21. Wait 20 min (Wallraff et al., 2006) to let the BAPTA diffuse in the astrocyte network. Monitor the access resistance regularly to make sure the membrane of the astrocyte is still open and that the astrocyte is still alive.

    Optional: If you are performing calcium imaging and patch-mediated BAPTA loading simultaneously, you will observe an immediate fluorescence quenching in the patched cell and a progressive loss of fluorescence in the neighboring astrocytes after 10–20 min. For more details, see expected outcomes and Figure 4.

22. Remove the pipette very slowly and carefully along the x-axis, as this is the best direction for avoiding damage to the cell. It is extremely important to avoid any damage to the cell during this step, as the goal is to reseal the membrane.

    Note: When the membrane is resealed, you should see the pipette resistance reach the GΩ range again as you will inevitably tear off a part of the membrane during removal.

23. Repeat all the steps from 13 to 21 on another astrocyte located approximately one screen (200 μm) apart to ensure the efficient diffusion of BAPTA within the local network.

EXPECTED OUTCOMES

Here, we share a protocol to investigate the involvement of astrocytes and their networks in brain function. We present *ex vivo* approaches to both monitor astrocytic calcium activity (Figure 3) and interfere with their activity at the microcircuit scale (Figure 4).

While one can also investigate astrocytic membrane potential changes using patch clamp in a current clamp mode, tracking of fluorescence variations using a calcium sensor, such as OGB1, in the cytosol further allows one to test whether astrocytes respond to a given stimulus using calcium-associated mechanisms. To distinguish astrocytes from other cells, we use SR101 because it allows a relatively simple way to label astrocytes in wild-type mice. Thus, by selecting cells labeled with both SR101 and OGB1 (Figure 3A), we can restrict our measurements of calcium-mediated OGB1 fluorescence variations to putative astrocytes only (Figures 3B and 3C). Alternatively, one can use genetically labeled astrocytes (e.g., GFAP-GFP mice, Zhuo et al., 1997).

The protocol described here can achieve a variety of experimental goals. One classical experiment is the application of a given drug to quantify its effects on astrocytic calcium signaling. For example, we applied the oxytocin receptor agonist, TGOT [1 nM], for 10 s via the peristaltic perfusion system used to supply aCSF to the recording chamber. One of the outputs of this experiment was a video recording that allowed us to assess visually the effects of an applied pharmacological agent to astrocytic calcium activity. The output data can further be used to quantify several effects of interest

STAR Protocols
Protocol

CellPress
OPEN ACCESS

through calculations such as the global area under the curve (AUC), the frequency of calcium transients, the duration of calcium transients, *etc.* (Figure 3D). You can find an example of these calculations in the following section, quantification and statistical analysis.

A fine analysis of the calcium signals may answer numerous critical questions regarding the upstream mechanisms that trigger calcium transients in astrocytes. However, this technique alone does not provide information about the downstream effects of calcium signaling in astrocytes. Therefore, we also present here a protocol to load the calcium chelator, BAPTA, specifically into a local astrocyte network to disrupt calcium-dependent cellular mechanisms (Figure 4). This approach does not alone produce results *per se* but it may be coupled to other recording techniques. For example, one method to validate BAPTA diffusion in the astrocytic network is to incorporate the use of calcium imaging. To do so, we load astrocytes with SR101 and OGB1 (See Calcium imaging of astrocytes) and then patch SR101 positive cells (See patch-clamp-mediated BAPTA loading of astrocytes). The output recording allows us to observe a rapid reduction of OGB1 fluorescence in the patched cell followed by a slower reduction of fluorescence in other cells within the same field of view (Figures 4A, 4B, and 4D; Method video S1). Another application of this method is to load BAPTA into astrocytes and then record the neuronal activity from a nearby network. For example, our group has previously used this method to uncover the critical role of astrocyte-mediated neuromodulation on oxytocin signaling mechanisms in amygdala neuronal networks (Wahis et al., 2021).

QUANTIFICATION AND STATISTICAL ANALYSIS

In this section, we provide some examples of how to analyze the calcium imaging data. Note that the following examples are by no means an exhaustive list of possible analyses, which should always be chosen within the context of the scientific question being addressed.

1. Launch the open-source FIJI software (Schindelin et al., 2012, available here) and import your recordings.
2. Adjust the brightness and contrast to visualize the cells (Image → Adjust → Brightness/Contrast) and check the quality of your recording. If you see motion artifacts, correct them with a motion correction macro (see Nicholas Schneider's macro available here, instructions here). In our case, we perform recordings in a single plane, therefore all recordings that drift along the z-axis cannot be corrected and must be removed.
3. Run the Bleach correction module (Image → Adjust → Bleach Correction, documentation here). We use the "Simple ratio" method as we have found that it produces adequate correction with minimal distortion of the data.
4. Select the "Oval" tool on the FIJI toolbar and manually draw the Region of Interest (ROI) on the SR101 video, then add it to the ROI manager by pressing the [t] shortcut. Click "Show all" to see which ROIs you have already drawn.
5. Extract the fluorescence signal from each ROI by clicking "More → Multi Measure" in the ROI manager panel. A window containing a table of the results will pop up when it is complete. You can save the table directly or copy the results into a spreadsheet.
6. Open the saved results in the analysis software of your choice. Below, we describe an analysis pipeline that uses a python-based routine (available in the resource availability section), but the analysis can be applied to any programming language.
7. Preprocessing:
   a. Read-in the ROI data extracted from Fiji and plot the SR101 data to check if the curve is stable. The intensity of the dye should be constant over time, so if the SR101 curve is not straight then consider rechecking the raw recording for motion or drift in the z-axis. If a motion correction routine is not enough to correct SR101 intensity changes, then exclude the recording from further analysis.
   b. Correct potential micromovements by subtracting the OGB1 signal from the SR101 signal. Note that a simple subtraction method would introduce noise from the SR101 signal into

the OGB1 signal. For that reason, we perform a polynomial regression on the SR101 curve using the Savitzky-Golay filter of the scipy.signal library (window = 51, order = 1) to estimate the trend of the SR101 curve. Doing so, we can subtract the trend of the SR101 trace without introducing noise into the OGB1 signal.

c. Smoothen the resulting curve without modifying the calcium transient dynamics by applying another, less-stringent polynomial filter (savgol_filter, windows = 11, order = 3).

d. Define two analysis windows: one for the quantification of the baseline activity and another for the quantification of the effect of stimulation. In our recordings, we stimulate astrocytes by applying the oxytocinergic agonist TGOT [1nM] for 10 s, 5 min after the recording begins. Therefore, the windows we select are: (1) 0–5 min for baseline, and (2) 5–10 min for the TGOT effect.

e. If the windows you choose have different sizes, calculate a ratio to normalize the data according to the duration of each window. For example, if the first window (baseline) is 5 min and the second is 10 min, you must normalize the analyzed parameters (number of calcium transients, area under the curve…) according to the relative duration of each window. To do so, calculate a ratio based on the duration of each window with the following formula:

$$r = \frac{\text{duration of window 1}}{\text{duration of window 2}}$$

8. Processing:

a. Find the area under the curve (AUC) for each cell using a trapezoid method. Ensure that the function you choose to apply does not evaluate the negative AUC, otherwise it will bias your results by summing the upward and downward deflections. In our case, we remove all negative values before using the "trapz" function of the "NumPy" package. Split the resulting AUC values according to your analysis windows then sum the data and normalize it with the previously calculated ratio.

b. Find calcium transients in your curve using the "find_peak" function of the "scipy.signal" library. The parameter of the detection depends on the events you want to identify. An important consideration here is the detection threshold, which must be proportional to the standard deviation (SD) of the curve. One issue with this method is that highly active cells have higher SDs, which results in fewer detectable peaks. To avoid this issue, we perform a non-stringent polynomial regression (savgol_filter(windows = 31, order = 3)) and subtract it from the curve to obtain the residuals (i.e., the noise without the peaks). We then calculate the SD of these residuals and use it as the threshold for peak detection. In our case, we use a minimal height of 8×SD, a prominence of 5×SD and a minimal inter-peak distance of 10 points (corresponding to 5 s in our recordings with a 2 Hz sampling frequency). The height is the minimum height in absolute value and the prominence is the relative height compared to neighboring peaks. This last parameter avoids multiple detections of the same peak that satisfy the "height" parameter. Once you have the index of each peak, compute their frequency within each of the chosen analysis windows.

c. For each calcium transient index, find the amplitude of each peak. Then, calculate the half-maximum amplitude to measure the Full Width at Half Maximum (FWHM) to evaluate the duration of each peak. We choose to compute the FWHM because it is more reliable than the total duration, wherein you have to find the precise foot peak, which can be especially difficult in calcium imaging due to the potential for slow rise/decay.

d. Evaluate the responsiveness of each cell to the stimulation. To do so, compare the calcium transient frequency and the AUC during the baseline and drug exposure. We base the response criteria on both calcium transient frequency and AUC to cover the diverse variety of responses observed (e.g., numerous calcium transients and/or single important transient). The baseline activity of astrocytes is heterogeneous due to the stochastic occurrence of

STAR Protocols
Protocol

calcium transients. Therefore, we do not evaluate the response based on the SD of the baseline, but rather as a percentage of calcium transient frequency and/or the AUC increase before versus after drug exposure. We classify an astrocyte as responsive if the frequency of calcium spike or AUC increases by 20% after drug exposure.

9. Run paired statistical tests to evaluate if the applied stimulus modified astrocyte activity. If you have two quantification windows, evaluate the normality of your data using a Shapiro-Wilk test and, depending on the result, run either a parametric paired t test or a non-parametric Wilcoxon test. If you have three or more quantification windows, check the normality of the data and their homoscedasticity with a Levene's test. If data follow a normal distribution and their variances are equal, run a One-Way repeated measure ANOVA followed by a pairwise Tukey HSD post-hoc. Otherwise, run a Friedmann test followed by a Conover post-hoc test and a Bonferroni correction of the p value.

LIMITATIONS

The present protocol provides a relatively easy method to selectively label, monitor and disrupt the activity of astrocytes. However, there are several technical limitations to consider.

First, the loading of the AM coupled calcium indicator involves the use of a detergent, which affects the viability of the cells. Indeed, if the slices spend too much time in the AM dye mix, you will likely see several dead cells under the microscope (i.e., swollen and circular).

Another potential problem of this dye loading method is the intracellular distribution of the indicator. While AM loading of calcium indicators is an easy way to infuse the dye in the cytosol of cells, it only provides calcium signals from the soma and the proximal processes. This is of particular importance for astrocytes because they have a huge surface/volume ratio, where the processes represent ~95% of the cell surface (Khakh and Benjamin, 2019) and therefore the inability of the dyes to reach the distal processes may have a significant impact on the resulting observations. To overcome this limitation, Khakh's laboratory has developed membrane-tethered variants of the GCaMP3 and GCaMP6f genetically encoded calcium indicators (reviewed in Shigetomi et al., 2016). Another potential approach is to patch astrocytes with a version of OGB1 that cannot cross the membrane. In this way, high concentrations of OGB1 can be achieved in the cytosol, which would cause the dye to diffuse further into the processes and thereby allow for better visualization. However, this latter approach involves a disruption of the astrocytic membrane and a dilution of the cytosolic content by the intra-pipette solution, which can severely affect astrocytic integrity.

Another limitation to consider is that calcium indicators tend to bleach easily. While this is not a problem for short recordings (<30 min), the change in gain can be substantial across longer recordings. Additionally, in this protocol, we load a non-ratiometric calcium indicator (Maravall et al., 2000). This can be a limitation if you want to compare the AUC across different astrocytes because it is impossible to load each cell identically and thus the gain will vary from cell to cell. However, this issue can be overcome by normalizing the data for each cell with its baseline values.

Since calcium indicators are derived from chelators (e.g., OGB comes from BAPTA), indicator loading in the cell perturbs the endogenous calcium toolbox. Indeed, it has been shown that the loading of such indicators changes the diffusion dynamics of calcium into the cell, shortening its reach and decreasing the concentration of free calcium ions in the cytosol (Semyanov et al., 2020). For these reasons, it is not recommended to couple that type of loading with the measurement of the downstream effects of calcium signaling.

We base our identification of astrocytes on SR101 staining. This method is widely used because it is quite simple to implement either *in vivo* or *ex vivo*. SR101 is taken up into the cytosol of astrocytes through the thyroid hormone transporter OATP1C1 (Schnell et al., 2015). However, the specificity of such labeling is controversial and quite heterogeneous among brain regions (Hülsmann et al., 2017).

In our case, all SR101-positive patched cells did not fire action potentials and had a low membrane resistance, strongly suggesting an astrocytic identity. Moreover, it has been shown that SR101 can be cytotoxic at high concentrations and produce seizure-like local field potential activity *in vivo* (Rasmussen and Nedergaard, 2016). In our hands, we did not observe excessive cell death during the experiments.

The size of the astrocytic network within the structure being studied introduces another limitation concerning the loading of BAPTA. Simply put, the more astrocytes within a given network, the harder it will be to disrupt the activity of the whole astrocytic network. This limitation could technically be overcome by patching more astrocytes; however, this would result in very long protocols. An alternative approach could be to disrupt astrocytic network function using genetic models. For instance, the exogenous expression of Calcium Exchanger (CalEx) in astrocytes can decrease calcium signaling in these cells by extruding cytosolic calcium (Nagai et al., 2021).

Finally, the present protocol describes how to monitor/disrupt astrocyte activity in brain slices. However, this approach introduces bias in that the slicing procedure considerably changes cell activity and connectivity. To overcome this issue, one can perform *in vivo* calcium imaging using genetically Q8 encoded calcium indicators, such as GCaMP (for a complete protocol, see Tang et al., 2021).

TROUBLESHOOTING
Problem 1
The slices roll when the razor blade cuts the brain (step 5 of "Slice preparation").

Potential solution
Try to reduce the speed of the Vibratome or increase the vibration frequency of the blade. If this is not enough to produce good slices, be sure that your slicing milieu is cold enough (4°C) by adding some ice and/or some ethanol around the tank.

Problem 2
There are many dead cells in the slice (step 6 of "calcium Imaging of astrocytes").

Q9 #### Potential solution
A high occurrence of cell death can be explained by several factors:

The brain extraction was too slow and/or it was damaged during the process.

The perfusion solution is not cold enough during the slicing procedure. To prevent this, you can put a thermometer in the slicing tank. If the temperature is above 4°C, add some ice until it reaches the very top of the slicing tank. You also can add some ethanol on the ice.

The incubation time of AM dye is too long. Consider reducing it. For some potentially cytotoxic indicators (Rhod2-AM), loading at room temperature instead of 37°C can increase cell viability.

The slices were agitated too much. Be careful that the bubbles present during the recovery period do not agitate your slices. Also, take extra care when transferring them to different locations. One alternative to consider is using the back of a Pasteur pipette instead of a brush.

Avoid using old solutions (aCSF, perfusion solution) and always ensure that there is no bacterial growth before using them. It is ideal to use fresh solutions for each recording day.

Always verify the pH and osmolality when preparing the solutions.

Regularly check that your slices are properly oxygenated.

STAR Protocols
Protocol

CellPress
OPEN ACCESS

Problem 3

It is hard to focus on the entire field of view when performing calcium imaging (step 6 of "calcium imaging of astrocytes").

Potential solution

This problem can occur when the strings of the harp that hold the slice are to close too each other. In this case, the slice surface becomes bent and is no longer parallel to the optic plane of the microscope. To solve this, you can cut out a string from the middle of the harp and then position the harp on the slice such that your recording area lies in the gap you just created. If this does not solve the issue, then double-check that your recording chamber and microscope are perfectly horizontal and not tilted in any direction.

Problem 4

The slice moves during the calcium imaging (step 6 of "calcium imaging of astrocytes").

Potential solution

The solution depends on the axis of the movement:

If the slice moves in the x/y axes, verify that your harp is correctly positioned at the bottom of the recording chamber. Use harps that fit perfectly in the chamber (as is the case with those provided by Harvard Apparatus). Alternatively, your harp may not be heavy enough to counterbalance the flow produced by the peristaltic pump. To correct this you can:

Build a heavier harp.

Build/buy an arena where the harp fits the chamber better.

Check that there is no air entering the tubing, as this can introduce air bubbles into the circuit, which then make the recording milieu vibrate as they pass through the recording chamber.

The flow of the peristaltic pump may be too high and should be reduced as needed.

If the slice moves in the z-axis, it is probably because the strings of your harp are spaced too far apart. Either move the slice to a narrower gap of the harp or try using a different harp.

Problem 5

The calcium indicators bleach too much (step 6 of "Calcium Imaging of astrocytes").

Potential solution

If the calcium indicator bleaching is so strong that it will change the interpretation of your data, you have to adjust the duration and intensity parameters of the illumination. In our case, we never illuminate for more than 100 ms. For the illumination intensity, we find the best values are between 580 μW and 1040 μW. However, since all setups are different, we strongly recommend you try several intensity values within your setup.

Problem 6

OGB1 signal is absent/weak (step 6 of "calcium imaging of astrocytes").

Potential solution

If you cannot see any signal in the green channel (OGB1), there is probably an issue with OGB1-AM solubilization in the Cremophor EL + PF-127 mix. This can be due to the degradation of the PF-127, which must be kept in an air-proof vial. We usually keep aliquots of PF-127 in 1mL tubes, covered with Parafilm. Issues in dye solubilisation can also be due to the sonication step. Consider increasing

the time/intensity of the sonication. You can also try to incubate the mix in a heating bath at 40°C for 20 min; however, in our hands, this produces less solubilisation of the mix.

Problem 7
Opening the cell is difficult (step 17 of "patch-clamp-mediated BAPTA loading of astrocytes").

Potential solution
Patching small cells is more challenging than bigger ones. Consider some of the following steps to make it easier:

Try using a small pipette tip (around 6–8 MΩ) for smaller cells, but do not exceed 9 MΩ as this would make it even harder.

If after several trials you still struggle to achieve a gigaseal and/or cannot open the cell, it may be because you are not actually on the cell but rather only nearby. Try to get on the cell as you would normally and then move either slightly closer or away from it to understand how to get on a cell correctly. Practice makes perfect in this case.

Problem 8
During the membrane test, the signal is constantly drifting, even after doing the pipette offset (step 13 of "patch-clamp-mediated BAPTA loading of astrocytes").

Potential solution
The recording electrode is probably no longer adequately chlorinated. To chlorinate it, run an electrolysis reaction in 3 M KCl. Connect the electrode to the positive pole of a battery and a cable to the negative one. Dip both in the KCl solution and let them sit for 15s. You should see the solution bubble.

Problem 9
The pipette is clogged (step 13 of "patch-clamp-mediated BAPTA loading of astrocytes").

Potential solution
Try to remove the clog by applying a strong pressure (with the syringe for example). If the clog is still there, change the pipette.

RESOURCE AVAILABILITY
Lead contact
Further information and requests for resources and reagents should be directed to and will be fulfilled by the lead contact, Alexandre CHARLET acharlet@unistra.fr.

Materials availability
This study did not generate new unique reagents.

Data and code availability
This protocol did not include a particular code. However, to see an example of the code that can be used, feel free to check our public repository where our routines are available at https://github.com/AngelBaudon/Canal.git.

SUPPLEMENTAL INFORMATION
Supplemental information can be found online at https://doi.org/10.1016/j.xpro.2022.101159.

STAR Protocols
Protocol

CellPress
OPEN ACCESS

AUTHOR CONTRIBUTIONS

Patch loading of astrocytes, E.C.C.; Calcium imaging, A.B.; Supervision, A.C. All authors wrote and edited the manuscript.

DECLARATION OF INTERESTS

The authors declare no competing interests.

REFERENCES

Bischofberger, J., Engel, D., Li, L., Geiger, J.R., and Jonas, P. (2006). Patch-clamp recording from mossy fiber terminals in hippocampal slices. Nat. Protoc. 1, 2075–2081.

Charles, A.C., Merrill, J.E., Dirksen, E.R., and Sanderson, M.J. (1991). Intercellular signaling in glial cells: calcium waves and oscillations in response to mechanical stimulation and glutamate. Neuron 6, 983–992.

Delvendahl, I., Jablonski, L., Baade, C., Matveev, V., Neher, E., and Hallermann, S. (2015). Reduced endogenous Ca^{2+} buffering speeds active zone Ca^{2+} signaling. Proc. Natl. Acad. Sci. 112, E3075–E3084.

Hülsmann, S., Hagos, L., Heuer, H., and Schnell, C. (2017). Limitations of sulforhodamine 101 for brain imaging. Front. Cell Neurosci. 11, 44.

Khakh, B.S., and Benjamin, D. (2019). The emerging nature of astrocyte diversity. Annu. Rev. Neurosci. 42, 187–207.

Maravall, M., Mainen, Z.F., Sabatini, B.L., and Svoboda, K. (2000). Estimating intracellular calcium concentrations and buffering without wavelength ratioing. Biophys. J. 78, 2655–2667.

Nagai, J., Bellafard, A., Qu, Z., Yu, X., Ollivier, M., Gangwani, M.R., Diaz-Castro, B., Coppola, G., Schumacher, S.M., Golshani, P., et al. (2021). Specific and behaviorally consequential astrocyte Gq GPCR signaling attenuation in vivo with IβARK. Neuron 109, 2256–2274.e9.

Naraghi, M., and Neher, E. (1997). Linearized buffered Ca^{2+} diffusion in microdomains and its implications for calculation of [Ca^{2+}] at the mouth of a calcium channel. J. Neurosci. 17, 6961–6973.

Rasmussen, R., and Nedergaard, M.; Nicolas Caesar Petersen (2016). Sulforhodamine 101, a widely used astrocyte marker, can induce cortical seizure-like activity at concentrations commonly used. Sci. Rep. 6, 30433.

Schindelin, J., Arganda-Carreras, I., Frise, E., Kaynig, V., Longair, M., Pietzsch, T., Preibisch, S., Rueden, C., Saalfeld, S., Schmid, B., et al. (2012). Fiji: an open-source platform for biological-image analysis. Nat. Methods 9, 676–682.

Schnell, C., Shahmoradi, A., Wichert, S.P., Mayerl, S., Hagos, Y., Heuer, H., Rossner, M.J., and Hülsmann, S. (2015). The multispecific thyroid hormone transporter OATP1C1 mediates cell-specific sulforhodamine 101-labeling of hippocampal astrocytes. Brain Struct. Funct. 220, 193–203.

Semyanov, A., Henneberger, C., and Agarwal, A. (2020). Making sense of astrocytic calcium signals - from acquisition to interpretation. Nat. Rev. Neurosci. 21, 551–564.

Shigetomi, E., Patel, S., and Khakh, B.S. (2016). Probing the complexities of astrocyte calcium signaling. Trends Cell Biol. 26, 300–312.

Wahis, J., Baudon, A., Althammer, F., Kerspern, D., Goyon, S., Hagiwara, D., Lefevre, A., Barteczko, L., Boury-Jamot, B., Bellanger, B., et al. (2021). Astrocytes mediate the effect of oxytocin in the central amygdala on neuronal activity and affective states in rodents. Nat. Neurosci. 24, 529–541.

Wakida, N.M., Gomez-Godinez, V., Li, H., Nguyen, J., Kim, E.K., Dynes, J.L., Othy, S., Lau, A.L., Ding, P., Shi, L., et al. (2020). Calcium dynamics in astrocytes during cell injury. Front. Bioeng. Biotechnol. 8, 912.

Wallraff, A., Köhling, R., Heinemann, U., Theis, M., Willecke, K., and Steinhäuser, C. (2006). The impact of astrocytic gap junctional coupling on potassium buffering in the hippocampus. J. Neurosci. 26, 5438–5447.

Zhuo, L., Sun, B., Zhang, C.L., Fine, A., Chiu, S.Y., and Messing, A. (1997). Live astrocytes visualized by green fluorescent protein in transgenic mice. Dev. Biol. 187, 36–42.

XPRO 101159

9.4. Emerging role of astrocytes in oxytocin-mediated control of neural circuits and brain functions.

Baudon, A., Clauss–Creusot, E., Althammer, F., Schaaf, C.P., Charlet, A.
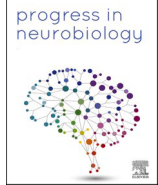
Review article

Emerging role of astrocytes in oxytocin-mediated control of neural circuits and brain functions

Angel Baudon [a],[1], Etienne Clauss Creusot [a],[1], Ferdinand Althammer [b], Christian P. Schaaf [b], Alexandre Charlet [a],[*]

[a] Centre National de la Recherche Scientifique and University of Strasbourg, Institute of Cellular and Integrative Neuroscience, Strasbourg 67000 France
[b] Institute of Human Genetics, Heidelberg University, Heidelberg, Germany

ARTICLE INFO

ABSTRACT

The neuropeptide oxytocin has been in the focus of scientists for decades due to its profound and pleiotropic effects on physiology, activity of neuronal circuits and behaviors, among which sociality. Until recently, it was believed that oxytocinergic action exclusively occurs through direct activation of neuronal oxytocin receptors. However, several studies demonstrated the existence and functional relevance of astroglial oxytocin receptors in various brain regions in the mouse and rat brain. Astrocytic signaling and activity is critical for many important physiological processes including metabolism, neurotransmitter clearance from the synaptic cleft and integrated brain functions. While it can be speculated that oxytocinergic action on astrocytes predominantly facilitates neuromodulation via the release of specific gliotransmitters, the precise role of astrocytic oxytocin receptors remains elusive. In this review, we discuss the latest studies on the interaction between the oxytocinergic system and astrocytes, including detailed information about intracellular cascades, and speculate about future research directions on astrocytic oxytocin signaling.

1. Introduction

The hypothalamic neuropeptide oxytocin (OT) has been in the focus of researchers for several decades, ever since it was first described by Sir Henry H. Dale (Dale, 1906). Due to its prosocial and trust-enhancing effects, the popular press even coined the term *love hormone*. In fact, OT is involved in a plethora of social interactions and emotional processes and is pivotal for pair bonding (Young and Wang, 2004) and attachment (Insel and Young, 2001). Current data suggest that OT first emerged around 600 million years ago (Gwee et al., 2009) and evolved with its sister peptide arginine-vasopressin (AVP) from a common ancestor peptide, namely vasotocin (Gwee et al., 2009; Theofanopoulou et al., 2021). Its function is the regulation of osmolarity, one of the crucial homeostasis parameters. It is assumed that over time, the vasotocin gene duplicated and gave rise to two distinct neuropeptides with different properties and physiological functions. While the first evolutionary lineage leads to AVP, which can be found in all vertebrates and is still critical for osmoregulation and control of blood pressure, the alternate path is at the origin of oxytocin-like peptides whose structures

are dependent on the species: Isotocin can be found in fish, mesotocin is present in amphibia and reptiles, and OT is synthesized in all mammals (Gimpl and Fahrenholz, 2001; Jurek and Neumann, 2018; Theofanopoulou et al., 2021). It has been recently proposed to standardize the nomenclature of these two peptides across species to OT for all oxytocin-like peptides and VT for all AVP-like ones (Theofanopoulou et al., 2021).

In mammals, the gene encoding OT (*Oxt*) is transcribed in the hypothalamus, and its mRNA is one of the most prevalent hypothalamic-specific mRNAs (Gautvik et al., 1996; Gimpl and Fahrenholz, 2001). Like many other peptides, OT mRNA is translated into an inactive precursor, which is then cleaved into smaller fragments, ultimately resulting in the active oxytocin peptide. Following synthesis, OT is stored in large dense-core vesicles (Leng and Ludwig, 2008), released via calcium-dependent exocytosis (Leng and Ludwig, 2008; Ludwig and Stern, 2015; Maicas-Royo et al., 2018; Tobin et al., 2012) and acts on the membrane-bound, G-protein-coupled oxytocin receptor (OTR) (Jurek and Neumann, 2018). To date, two distinct intracellular signaling cascades have been identified following OTR activation: $G\alpha_{i/o}$- and

Gα$_q$-dependent pathways (Jurek and Neumann, 2018).

Different modes of OT release in the central nervous system have been described including axonal release (Grinevich et al., 2016; Knobloch et al., 2012), somato-dendritic release (Ludwig and Leng, 2006) and en passant release (Bakos et al., 2018; Fuxe et al., 2012; Ludwig and Leng, 2006). OT is also released into the portal circulation through the neurohypophysis in the posterior pituitary and reaches a variety of peripheral targets via the blood stream. Targeted, local release of OT within different brain regions that express OTR allows the peptide to act both as a neurotransmitter (Althammer et al., 2021; Buijs, 1983; Landgraf and Neumann, 2004; Leng and Ludwig, 2008; Stoop, 2012) and a neuromodulator (Mitre et al., 2018; Owen et al., 2013; Stoop, 2012; Tirko et al., 2018), thus affecting a wide range of behaviors (Froemke and Young, 2021; Grinevich and Neumann, 2020). Past research on OT was solely focused on its direct effects on neural circuits. As a result, the prevailing hypothesis was that OTergic actions are exclusively mediated by neurons and this view has not been challenged until recently (Wahis et al., 2021). Moreover, a growing body of evidence suggests that oxytocin also acts directly on non-neuronal cells (Havranek et al., 2017; Mairesse et al., 2019; Tasker et al., 2012; Wang and Hatton, 2009).

Recent studies suggest that neuronal and glial cells in the brain exist in a 1:1 ratio in the human brain, albeit the individual proportions strongly depend on brain regions and species (von Bartheld et al., 2016). Glial cells are composed of several types including astrocytes, microglia or oligodendrocytes. Per definition, they are non-electrically excitable. Thus, for a long time it was believed that they are merely passive cells and do not actively participate in sensory processing and signal transduction. While, to our knowledge, there is currently no evidence suggesting OTergic action on oligodendrocytes, it has been shown that oxytocin influences microglia activity (Inoue et al., 2019; Panaro et al., 2020), neural progenitor differentiation (Palanisamy et al., 2018) and pituicyte stellation (Rosso et al., 2002). Importantly, evidence has been accumulating to demonstrate an action of oxytocin on astrocytes (Di Scala-Guenot et al., 1994; Panatier et al., 2006; Wahis et al., 2021).

Astrocytes are paramount for brain homeostasis, nutrient supply and metabolism. They account for ~20–40 % of all glial cells, depending on the species and brain region (Augusto-Oliveira et al., 2020). Within the last two decades astrocytes emerged as key players involved in neuromodulation and neuroinflammation both in the healthy and diseased brain. It is particularly intriguing how astrocytes mediate the function of local neurocircuits. Neurons and astrocytes are fundamentally different in their morphology and activity kinetics: neurons have characteristic dendrites and axons allowing the formation of long-range projections, while astrocytes possess a myriad of tiny filaments to infiltrate the local environment and can respond to many signaling cues; neurons have a millisecond-range electrical activity, whereas the duration of astrocytic calcium transients can range from minutes to hours (Bazargani and Attwell, 2016). This drastic temporal dynamic difference between the two cell types could affect the way that different neuromodulators operate within these microcircuits. Thus, it is imperative to understand the interplay of neurons and glial cells in response to neuromodulators to fully decipher their respective role in brain function. In this review, we explore the current literature on the action of OT on astrocytes, and we propose new models that could explain several observed phenomena.

2. Oxytocin effects on astrocytes

2.1. The oxytocin receptor is expressed in astrocytes

In the brain, OT is mainly synthesized in three distinct hypothalamic nuclear formations: the paraventricular nucleus, supraoptic nucleus and scattered accessory nuclei. A feature of OTergic neurons is the somato-dendritic release, which prompted researchers to explore the role of OT in the hypothalamus. In the mid-80 s, it was shown that following high secretion/infusion of OT in this structure, active changes in the morphology of astrocytes occur in vivo (Salm et al., 1985; Theodosis

et al., 1986a; Theodosis et al., 1986b). Thus, Di Scala-Guenot and Strosser performed binding studies to investigate whether cultured astrocytes from the hypothalamus express the OTR. Using autoradiography of radioactive ligands, they found that the OTR is distributed all over the soma and processes of cells morphologically similar to those expressing the glial fibrillary acidic protein (GFAP), suggesting their astrocytic identity (Di Scala-Guenot and Strosser, 1992). In addition, using the same methods, OTR have been found in GFAP-expressing cells in primary cultures of spinal astrocytes (Evrard et al., 1997). With the help of in situ hybridization or immunolabeling, recent studies detected OTR expression in rodent astrocytes in the supraoptic nucleus of the hypothalamus (Wang and Hatton, 2006), the auditory cortex (Mitre et al., 2016), the central amygdala (Wahis et al., 2021), the ventral striatum (Amato et al., 2022), the hippocampus (Althammer et al., 2022b) and even in the frontal cortex of humans (McKay et al., 2019) (Fig. 1A). Moreover, OTR can be co-immunoprecipitated with GFAP in supraoptic nucleus (SON) lysates, indicating that the receptor is bound to the astrocytic cytoskeleton (Wang et al., 2017). While each of these results suffer from inherent technical limitation, inviting to prudence when interpreting the presented data, OTR seems widely expressed in astrocytes of several brain structures.

In all cases, this evidence does not provide proof of the receptor functionality. It must be noted here that albeit OTR expression in neurons is observed in a myriad of species and brain regions (Gould and Zingg, 2003; Mitre et al., 2016; Newmaster et al., 2020; Young and Song, 2020), these studies did not investigate actual OTR expression levels in neurons on a quantitative, single cell basis. To the best of our knowledge, no studies have been published yet that directly assessed and compared neuronal and astrocytic OTR expression levels. However, a reanalysis of published in situ hybridization data for OTR mRNA suggest that astrocytic OTR levels could be 2–3-fold lower in the amygdala (Althammer et al., 2022a; Wahis et al., 2021) and dorsal CA2 region (Althammer et al., 2022b) (Fig. 1B). This constitutes an experimental challenge for scientists willing to study the cell-type specific OTR. Thus, a combination of single cell RNA sequencing or cell-type specific western blots together with precise pharmacological experiments would be needed to unequivocally demonstrate the presence and function of astrocytic OTR. In addition, a new generation novel genetic models could help to provide a deeper insight into cell-type specific OTR expression and function.

2.2. Astrocytic oxytocin receptors are functional

The first indication of a direct action of OT on glial cells dates back to the mid-90 s, when Di Scala-Guenot and colleagues performed calcium imaging on cultured hypothalamic astrocytes. They observed that OT or [Thr^{4}Gly^7]-oxytocin (TGOT, a selective OTR agonist) application triggers monophasic calcium responses in the majority of recorded astrocytes, but also calcium oscillation in ~15 % of them (Di Scala-Guenot et al., 1994). Such observation done in pure astrocytic culture suggests that astrocyte directly react to oxytocin. However, cultured astrocytes are known to be really different from those found in situ, both in term of morphology, protein expression and calcium signaling (Foo et al., 2011; Shigetomi et al., 2010a, 2010b).

More recently, it has been showed that optogenetic photostimulation and subsequent release of OT from axonal terminals within the central amygdala triggers calcium transients in local astrocytes ex vivo (Wahis et al., 2021). This strongly suggests that endogenous OT release is sufficient to induce astrocyte calcium signaling. Yet, this effect could result indirectly from the activation of OTR on neighboring neuron terminals/fibers. Using a Cre/Lox approach, we knock out the OTR in GFAP expressing cells and observed a decrease of OTR-induced calcium responses in astrocytes. Despite the potential issue regarding a putative Cre leakage from GFAP positive cells (Hu et al., 2020b; Stifter and Greter, 2020) this experiment corroborates the hypothesis that OT-mediated astrocyte activity might be dependent on astrocytic OTR
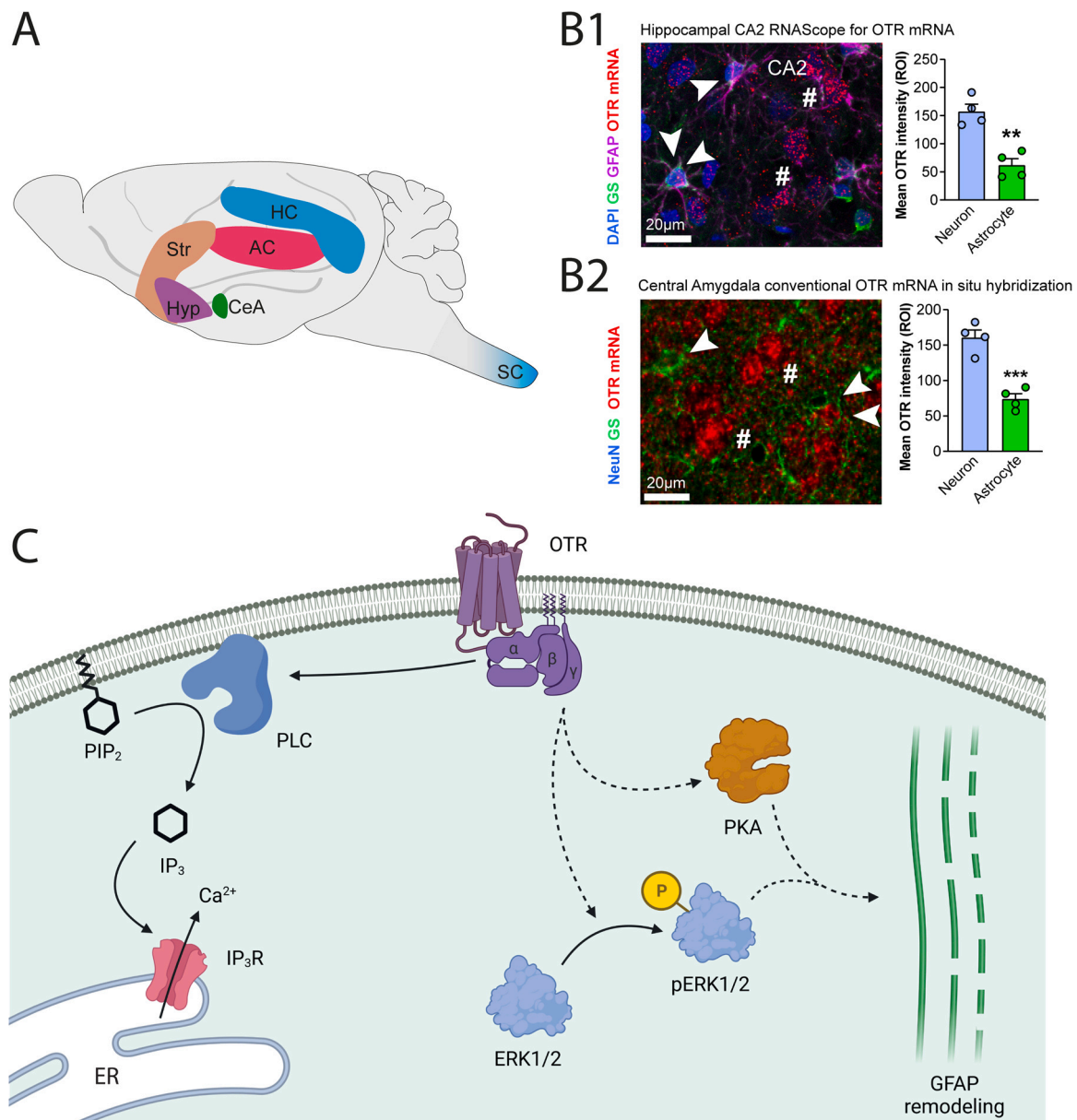
Fig. 1. Astrocytic oxytocin receptor distribution in the brain. A. Known localization of astrocytic oxytocin receptor (OTR) in the rodent brain. Described in situ: Striatum (Str), Hypothalamus (Hyp), Central Amygdala (CeA), Auditory Cortex (AC). Described in culture: Spinal Cord (SC). B1. Combined RNAScope for OTR mRNA and immunohistochemical staining against glutamine synthetase and GFAP in dorsal CA2 of a wistar rat. Single white arrowhead highlights OTR-negative astrocyte, double arrowhead highlights OTR-positive astrocyte and hashtags highlight OTR-positive, GS-negative neurons. Bar graph shows that respective OTR mRNA transcript levels in astrocytes are significantly lower than neuronal OTR mRNA levels (n = 4 rats per group, 70–120 cells analyzed per animal, **p < 0.01). Recreated from Wahis et al., 2021. B2. Combined approach of conventional in situ hybridization for OTR mRNA and immunohistochemical staining against glutamine synthetase in the central amygdala of a wistar rat. Single white arrowhead highlights OTR-negative astrocyte, double arrowhead highlights OTR-positive astrocyte and hashtags highlight OTR-positive, GS-negative neurons. Bar graph shows that respective OTR mRNA transcript levels in astrocytes are significantly lower than neuronal OTR mRNA levels (n = 4 rats per group, 70–120 cells analyzed per animal, ***p < 0.001). Recreated from Althammer et al. (2022b). C. Intracellular pathways triggered by the activation of astrocytic OTR. Left: activation of the $G\alpha_q$ protein triggers the activation of the PLC-IP$_3$ pathway that results in a calcium release from the endoplasmic reticulum (ER). Right: dissociation of the $\beta\gamma$ complex is suggested to mediate the sequential activation of ERK1/2 and PKA that ultimately results in a reorganization of the GFAP cytoskeleton.

(Wahis et al., 2021). However, even if this GFAP OTR KO model highlights the involvement of OTR in astrocyte activity, it does not rule out a potential participation of a neurotransmitter co-released together with OT from OTergic axon terminals.

Based on these observations, it seems plausible that functional OTR could be expressed in astrocytes in several regions of the central nervous system. To fully understand the precise effect of OT on astrocytes, it is important to have a close look at the intracellular pathway triggered by binding of OT to astrocytic OTR.

2.3. Oxytocin receptor-dependent signaling in astrocytes

The oxytocin receptor (OTR) is a member of the class A G-protein coupled receptors (GPCR) family, composed of seven transmembrane domains. In mammals, the OTR is encoded by a single gene, however, its intracellular coupling is complex. The intracellular loops and the intracellular C-terminal domain link heterotrimeric G protein complexes. Each of them is composed of three subunits: G_α, G_β, G_γ. Upon binding of their ligands, conformational changes of the receptor lead to

the replacement of the guanine diphosphate bound to the G_α by a guanine triphosphate. G_α then dissociate from the $G_{\beta\gamma}$ complex and act on various enzymes that produce second messengers. Interestingly, the OTR is functionally coupled to G_q and/or $G_{i/o}$ proteins and its activation can produce a calcium surge from intracellular calcium stores (Busnelli and Chini, 2018; Gimpl and Fahrenholz, 2001; Jurek and Neumann, 2018; Phaneuf et al., 1993). Apart from its effect on calcium signaling, the activation of OTR can activate various intracellular pathways second messengers, including cAMP, phospholipase C (PLC) and protein kinase C (PKC) (Chatterjee et al., 2016) (Fig. 1C).

In astrocytes, OT-induced intracellular pathways are currently unclear, with yet few studies raising different hypothesis. Indeed, application of OT or an OTR agonist on astrocyte cell cultures seems to trigger calcium transients via a mechanism that is independent of extracellular calcium influx but depends on endoplasmic reticulum stores (Di Scala-Guenot et al., 1994). These seminal data suggest are in accordance with the recruitment of the classical PLC-dependent G_q pathway in cultured hypothalamic astrocytes.

In addition, OT application on SON slices increased the quantity of phosphorylated extracellular signal-regulated kinase 1/2 (ERK 1/2), strengthening the hypothesis that OTR activation in astrocytes affects the MAPK pathway in astrocytes (Wang and Hatton, 2007). Wang and colleagues further showed that OT decreases the expression of GFAP in SON astrocytes (Wang et al., 2017). This effect seems to be mediated by the $G_{\beta\gamma}$ subunits of the G protein coupled to the OTR, which triggers the sequential activation of ERK1/2 and protein kinase A (PKA) (Wang et al., 2017). It is noteworthy that activation of ERK1/2 and PKA seems to have antagonistic effects on GFAP stability and that the consecutive action of ERK and PKA is needed: PKA initially provokes the breakdown of GFAP filament and then ERK1/2 stabilizes newly synthesized filaments (Wang et al., 2017). Recently, a study in astrocyte-like cells from astrocytoma showed that knockdown of OTR prevented OT-induced phosphorylation of ERK and interfered with the proliferation and antioxidant effects of OTR activation (Alanazi et al., 2020), thereby strengthening the idea of an OTR-mediated regulation of the MAPK pathway (Fig. 1C).

As previously mentioned, OTR can also couple $G_{i/o}$ proteins (Busnelli and Chini, 2018; Busnelli et al., 2012; Hoare et al., 1999; Phaneuf et al., 1993; Strakova et al., 1998) but to our knowledge, no evidence has shown that stimulation of astrocytic OTR can trigger the activity of $G_{i/o}$ proteins in astrocytes. It is also possible that the OTR couples different G-protein in the same cell type as shown in neuron-like cells (Gravati et al., 2010). This coupling might also depend on OTR localization in different microdomains of the plasma membrane (Rimoldi et al., 2003).

3. Oxytocin-induced modulation of astrocyte morphology and functions

Knowing that functional OTR are expressed in astrocytes, one can investigate the effect of OTR activation in those cells. Several studies indicate that binding of OT to astrocytic OTR triggers astrocyte calcium transients (Kuo et al., 2009; Wahis et al., 2021; Zatkova et al., 2018). However, the downstream targets and ultimate consequences of astrocytic OTR signaling remain somewhat elusive. In this chapter we summarize the consequences of OTR activation on astrocyte morphology and neuronal network activity.

3.1. Morphological consequences of astrocytic oxytocin receptor activation

Hypothalamic OT neurons release the peptide locally, a phenomenon known as somato-dendritic release (Ludwig and Leng, 2006). This form of peptide release is thought to facilitate a local feedback mechanism, as well as to prime the neuroendocrine cells during challenging physiological situations such as parturition, lactation or other homeostatic challenges (Brown et al., 2013, 2020).

Already in the mid 80′s it was reported that these conditions induce a strong OT release and lead to an important decrease in GFAP staining density within SON (Salm et al., 1985; Wang and Hatton, 2009). Furthermore, OT infusion in the SON resulted in an increase of neuronal somata contacts (Langle et al., 2003; Theodosis et al., 1986a, 1986b). This strongly suggests that OT can modify astrocyte morphology. This hypothesis was further confirmed in hypothalamic SON slices. Indeed, under normal conditions, there is almost no neuronal juxtaposition, as astrocytic processes separate them, but OT application triggers the retraction of astrocytic processes, leaving OTergic neurons in close contact. This modification of the astrocytic cytoarchitecture appears to be calcium-dependent (Langle et al., 2003). While authors did not provide an explanation for this interesting observation, it can be speculated that activation of astrocytic OTR alters the astrocytic cytoskeleton by interfering with microtubule/actin dynamics. Indeed, it has been shown that calcium transients in astrocytes can regulate actin-remodeling proteins, such as cofilin. This has been demonstrated in the hippocampus where long term potentiation triggers withdrawal of peridendritic astrocyte processes from potentiated synapses (Henneberger et al., 2020). Interestingly, such OT-mediated reorganization of the actin cytoskeleton has been observed in SON neurons, and probably in nearby astrocytes following OT application (Wang and Hatton, 2007) (Fig. 2).

These morphological changes of hypothalamic astrocytes could potentially have many drastic and long-lasting consequences on the overall network activity. First, astrocytes maintain homeostasis for ions like potassium, which is known to be strongly implicated in neuronal excitability (Verkhratsky and Nedergaard, 2018). Thus, a reduction in astrocytic coverage could lead to important changes of the membrane potential of neighboring neurons. Second, astrocytes are important mediators of neurotransmitter clearance from the synaptic cleft. For example, GLT-1 and GAT transporters are present on the astrocytic processes and facilitate clearing of extracellular glutamate and GABA, respectively. Thus, a reduction in the clearance rate inevitably results in an increased extracellular concentration of neurotransmitters, which ultimately results in an amplification of post-synaptic currents. Moreover, the neurotransmitters can spill over the synaptic cleft and activate presynaptic (e.g. mGluRs) or extrasynaptic (e.g. NMDA) receptors to promote a feedback regulatory effect or to modulate the efficiency/potency of neighboring synapses (Oliet et al., 2008). Third, the retraction of astrocytic processes may declutter the extracellular space, allowing the formation of new synapses, as suggested for the hypothalamus (Hatton et al., 1984) (For a more general review on the effects of astrocytes morphological modification, see Lawal et al., 2022).

In addition, astrocytes are known to release neuroactive molecules described as gliotransmitters. By retracting astrocytic processes, it is plausible that less gliotransmitters reach their receptors expressed by the surrounding neurons, leading to a change in the transmission of information.

3.2. Astrocytic oxytocin receptor functions in gliotransmission

The concept of communication from astrocytes to neurons by the release of gliotransmitters was first introduced in the 90′s (Grandes et al., 1991) but the first demonstration of a direct communication between astrocytes and neurons was done by Parpura and colleagues, when they observed that glutamate released from astrocytes caused an increase in calcium activity of nearby neurons (Parpura et al., 1994). Later, adenosine triphosphate (ATP) was also shown to act on neuronal P2X receptors after being released by astrocytes (Zhang et al., 2003). It is important to note, however, that the mechanism underlying gliotransmission is still somewhat controversial (Fiacco and McCarthy, 2018; Sloan and Barres, 2014), albeit the majority of researchers in the field seem to acknowledge its existence (Araque et al., 2014; Savtchouk and Volterra, 2018).

In the SON, Panatier and colleagues showed that astrocytes express the serine racemase, an enzyme that converts L-serine to D-serine and
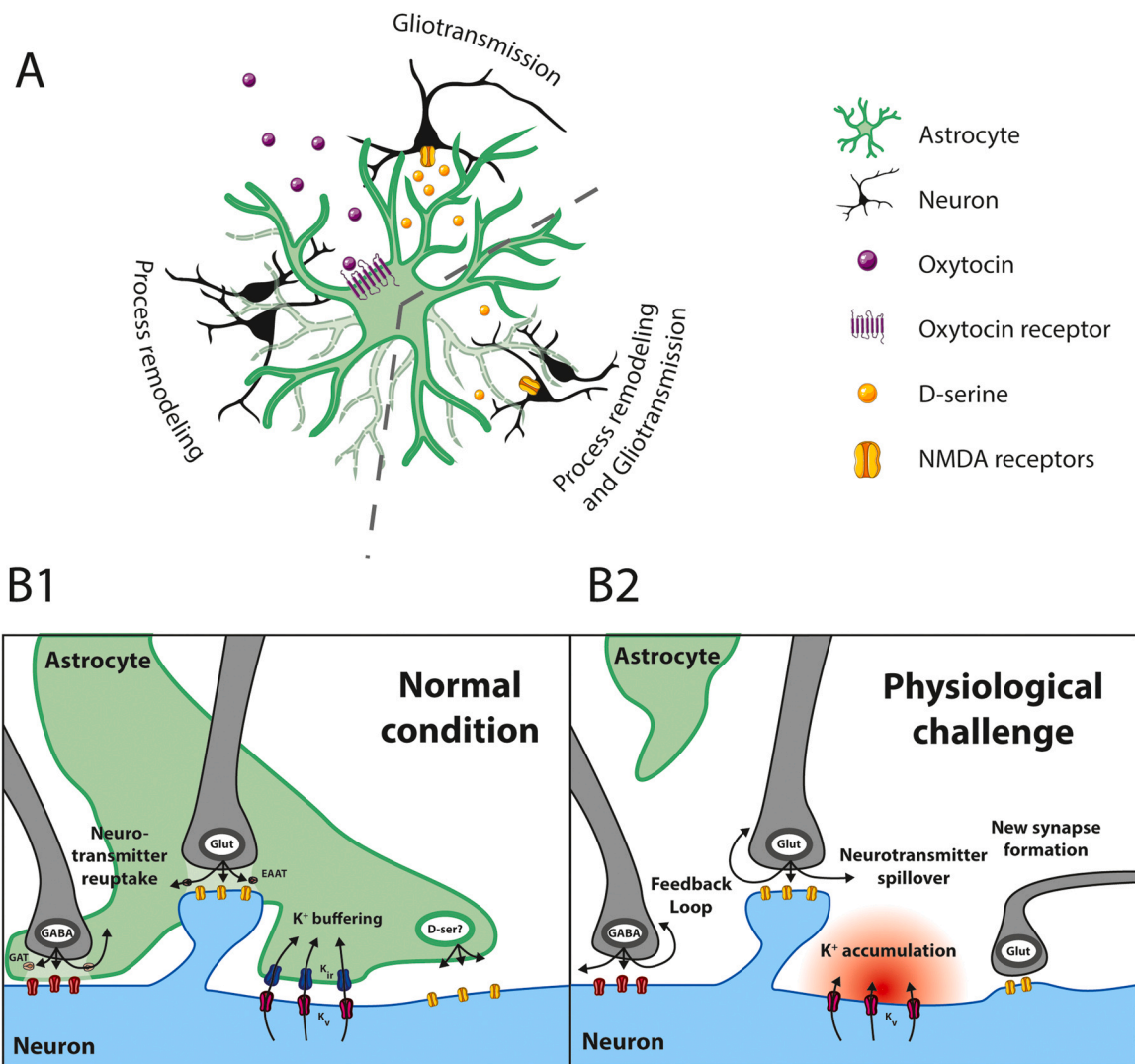
Fig. 2. Effects of OTR activation on astrocytes. A. *Top:* OTR activation modulate astroneuronal communication. This gliotransmission has been seen in the hypothalamus where OT stimulation decreases the amount of available D-serine, and in the central amygdala where the opposite action has been observed. *Bottom left:* astrocytic OTR activation triggers the remodeling of astrocytic processes, as seen by their retraction in the hypothalamus and their length increased in cultured astrocytes. *Bottom right:* suggested hypothesis in which both mechanisms could occur at the same time. For instance, a retraction astrocytic processes could explain the decrease in D-serine availability observed in the hypothalamus. B. Proposed astrocyte-neuron interactions under normal conditions (astrocyte process extension, B1) and during physiological challenge (astrocyte process retraction, B2) based on our own experimental data.

that this D-serine is the endogenous ligand of the glycine site on NMDAR in the SON (Panatier et al., 2006). Furthermore, they demonstrated that NMDA currents are strongly impaired in D-amino acid oxidase (DAAO) -treated SON slices, an enzyme that breaks down extracellular D-serine. This impairment is rescued by the acute application of exogenous D-serine. These results suggest that astrocytes synthesize and release D-serine to induce an NMDA-dependent signal. Panatier and colleagues also performed *ex vivo* recordings of NMDA currents in SON neurons from virgin or lactating rats. They showed that in lactating rats, the AMPA/NMDA ratio was similar compared to virgin animal slices treated with DAAO and could also be rescued when applying D-serine. Given that NMDAR activation appeared to be essential for the establishment of long-term potentiation (LTP), they investigated the involvement of this receptor using several LTP protocols in neurons of the SON of virgin or lactating animals. In virgin animals, they observed a normal establishment of LTP compared to lactating rats in which no LTP occurred unless they supplied the slice with D-serine. Hence, it seems that D-serine supply from astrocytes is essential for neuronal plasticity in the SON (Panatier et al., 2006). However, it is noteworthy that the astrocytic

origin of D-serine is still under debate (Coyle et al., 2020; Ivanov and Mothet, 2019; Papouin et al., 2017).

More recently, we studied the implication of astrocytes in the lateral part of the central amygdala (CeL) in the regulation of neuronal activity in response to OT. In this structure, a population of CeL astrocytes seems to express the OTR and its activation triggers an increase in their calcium activity (Wahis et al., 2021). Furthermore, these changes in calcium activity seem to be linked to an increase in the electrical activity of neighboring CeL neurons. This increase is dependent on NMDAR and sensitive to the D-serine degrading enzyme DAAO, suggesting that astrocytes modulate the activity of CeL neurons by releasing D-serine (Fig. 2). At a behavioral level, this neuronal network modulation seems to reduce negative emotional values such as anxiety. This demonstrates that CeA astrocytes are actively involved in the OT-induced modulation of a neuronal network (Wahis et al., 2021).

Another circuit where astrocytes have been involved in the regulation of neuronal circuits can be found in the medial basal hypothalamus (Parent et al., 2008). In this structure, authors found no OTR in vivo on GnRH neurons, but on neighboring cells thought to be astrocytes, as

suggested by OTR expression in astrocytes in vitro (Parent et al., 2008). Interestingly, intraperitoneal injection of OT reduced the GnRH interpulse interval known to be involved in sexual maturation. Suggesting that only astrocytes express the OTR in this structure, one can wonder how OT modulates GnRH release in the blood (ie. GnRH neuron activity). Given that OT induce the Prostaglandin E$_2$ (PGE$_2$) release (Strakova et al., 1998), they hypothesized that it might mediate the communication between astrocytes and GnRH neurons. Indeed, they found that PGE$_2$ mimicked the OT effect by decreasing the GnRH interpulse interval. This study suggests that OT acts directly on astrocytes of the medial basal hypothalamus to trigger PGE$_2$ release, which then acts on GnRH neurons to modulate the pulsatile neuronal secretion of GnRH and, ultimately, the sexual maturation.

Based on these observations, OT-activated astrocytes could communicate with neighboring neurons by releasing several gliotransmitters, such as D-serine or PGE$_2$.

4. Oxytocin and astrocytes: a glimpse into future research directions

Within the last years, OTergic signaling in astrocytes emerged as an important mechanism involved in the regulation of astrocyte morphology, calcium signaling and even affects physiological regulation and emotional processing. However, several key questions about OTR-expressing astrocytes and their interaction with nearby neural cells remain.

4.1. Can an astrocytic relay explain the pleiotropic effects of oxytocin?

One of the biggest enigmas in OTergic research is that one neuropeptide seems to facilitate a seemingly endless list of behaviors (Froemke and Young, 2021; Jurek and Neumann, 2018; Mitre et al., 2018). To exert these functions, OTergic fibers and OTR are found in various brain regions such as the cortices, amygdala, hippocampus, hypothalamic nuclei, septum and thalamus (Knobloch et al., 2012; Mitre et al., 2016; Zhang et al., 2020). However, astrocytic OTR have been identified in only a few of them (see section *The oxytocin receptor is expressed in astrocytes*). In addition, their functions are even less studied, with evidences of functional OTR existing only in the hypothalamic astrocyte cultures (Di Scuala Guenot et al., 1994) and in the amygdala (Wahis et al., 2021) (see section *Astrocytic oxytocin receptors are functional*).

Intriguingly, OT occasionally seems to elicit opposing behaviors depending on the involved brain regions or social context (De Dreu et al., 2011; Jurek and Meyer, 2020; Ma et al., 2015; Neumann and Slattery, 2016). Thus, it is important to note that astrocytes are known to be more than simple relays to neurotransmitters, even reversing the excitation/inhibition polarity of an input. This mechanism, called "incongruent", has been demonstrated in several models such as the CA3-CA1 synapse where a GABA input is transformed into glutamate release (Caudal et al., 2020). However, if and how astrocytes are involved in the contradictory effects of OT on neural circuits and behavior, is currently unclear.

Furthermore, neuropeptidergic cells co-express and co-release various neurotransmitters (Nusbaum et al., 2001; Svensson et al., 2018; van den Pol, 2012). In hypothalamic OT neurons, several studies showed co-release of both glutamate and OT (Althammer et al., 2021; Eliava et al., 2016; Grinevich and Ludwig, 2021; Hasan et al., 2019; Hrabovszky and Liposits, 2008; van den Pol, 2012). There are several potential cross-talks between the glutamatergic and the oxytocinergic system, which could explain some of the pleiotropic context-, experience- and brain region-dependent effects of OT release (Froemke and Young, 2021; Grinevich and Stoop, 2018; Jurek and Neumann, 2018; Lee et al., 2009; Mitre et al., 2018). For instance, varying degrees of OT and glutamate could be released from the same axonal terminal, and potentially act on different postsynaptic elements, thus providing

fine-tuning of neural circuits. Moreover, OT-induced calcium transients can be blocked with an mGluR1a antagonist and promoted by an agonist (Kuo et al., 2009). This suggests that mGluR1a can form functional heteromers with OTR, thus adding a new level of complexity to the OTR intracellular pathways. However, no physical interaction has been demonstrated to date.

Since OT has been shown by suggested modulate the activity of TRPV1 channel (Nersesyan et al., 2017), and given that astrocytes also express these channels in various species and brain regions (reviewed in (Kong et al., 2017) it is also possible that some OT actions on astrocytes may be mediated through these channels. Aside, there is currently no evidence that OT can directly activate TRPV1 channels in astrocytes (Gonzalez-hernandez and Charlet, 2018). Finally, it has recently been shown that OTR can physically heteromerize with the A2A adenosine receptor in the striatum. The functional effect of this association has been tested in striatal gliosomes and it was observed that OT prevents evoked glutamate release only if the A2A is not activated (Amato et al., 2022). In future studies, it will be interesting to evaluate the effect of the concomitant activation of these receptors in a basal condition. Moreover, it has been shown that OTR can heteromerize with D2R in the striatum (Romero-Fernandez 2013). Given the intricate cooperation of the oxytocin and the dopamine systems in social behaviors such as partner preference (Young and Wang, 2004), it can be interesting to assess the presence of such heteromers in astrocytes.

Therefore, the study of astrocytes involvement in OT-induced modulation of brain functions, in all its complexity, might be the key to unravel how OT exert its pleiotropic functions through modulation of numerous brain regions. However, this should be completed by considering the whole brain environment, from physiology to pathology.

4.2. Do astrocytes-mediated oxytocinergic functions vary in a brain region or pathophysiological state manner?

To date, the functions of putatively OT-activated astrocytic have only been studied in exceptional physiological conditions such as lactation and parturition in the SON (Panatier et al., 2006), sexual maturation in the medial basal hypothalamus (Parent et al., 2008) and chronic pain in the CeA (Wahis et al., 2021). However, the default role of OT-activated astrocytic subpopulation also remains unclear. This can be explained by a cofounding factor inherent of biological studies. Indeed, it is easier to study mechanisms that involve strong changes in physiological processes rather than small, everyday challenges that slightly modify the activity of neuronal circuits. There might be physiological processes during which OTergic activation of OT-sensitive astrocytes is not critical and where activation of OTR-expressing neurons is sufficient.

One can also imagine that OT can trigger different effects according to the targeted region. For instance, it has been shown in the hypothalamus that OT triggers retraction of astrocytic processes during high-demanding OT situations, which is linked to a reduction in D-serine release by the astrocytes (Panatier et al., 2006). Conversely, OTR activation in the CeL seems to trigger the release of D-serine by the astrocytes (Wahis et al., 2021), suggesting morphological effect different than the retraction observed in the SON. This hypothesis is supported by in vitro assessment of OT action on glial morphology that reveal an unforeseen OT-mediated increase in astrocytes-like U-87 MG cells processes length (Zatkova et al., 2018). Thus, OT effects on astrocyte morphology and functions could be region-dependent.

Therefore, it will not be surprising to discover that OT effects on astrocyte morphology is region- and function-specific, paving the way to a better understanding of the plural OT functions in pathophysiological conditions.

4.3. What are the relative contributions of astrocytes and neurons to OT functions?

Given that OTR has been shown to be expressed in both astrocytes and neurons, it is coherent to interrogate their respective contribution to OT functions. At first sight, one may suggest that OT acts on neuronal OTR to trigger a rapid, short lasting neuromodulation. On the other side, OT action on astrocytes may result in slower and longer mechanisms such as the metabolic regulation, release of lactate or gene regulation.

However, CeA ablation of astrocytic OTR impaired the OT-induced neuromodulation of the local microcircuit (Wahis et al., 2021). This absence of OT-evoked neuromodulation despite the presence of neuronal OTR raises two hypotheses: i) OT only needs to act on astrocytes to exert its neuromodulatory effect, ii) OT needs to activate simultaneously astrocytic and neuronal OTR. In the first scenario, OT initially acts on astrocytes to trigger the release of gliotransmitters which, in turn, increases neuronal excitability. However, this seems less probable since a higher portion of CeA neurons express OTR compared to astrocytes. The alternative scenario involves the concomitant activation of both cell types: OT could act on OTR-expressing neurons to increase membrane potential, thus priming CeA neurons and enabling an astrocyte-driven long-lasting, sustained activation of the neural network. In fact, besides its intracellular calcium releasing action by the G_q-PLC-IP$_3$R pathway, OT was shown to inhibit Na$^+$-activated K$^+$ leak channels in the myometrium (Ferreira et al., 2019) and spinal cord (Breton et al., 2009). These mechanisms can keep neurons closer to their firing threshold potential, thus making them more likely to respond to incoming stimuli. At the same time, OT can bind to astrocytic OTR to triggers calcium transients and ultimately, the release of gliotransmitters such as D-serine. Knowing the role of OT signaling in synaptic plasticity (Rajamani et al., 2018) and LTP formation (Lin et al., 2012), it seems plausible that coordinated dual activation of both NMDA and OTR could result in a potentiated neural response.

In addition, OT can act directly on OTR-expressing neurons and indirectly on other neurons. For instance, CeA neurons can be broadly divided into SOM-expressing and PKCδ-expressing neurons (Haubensak et al., 2010; Hunt et al., 2017), which are thought to have antagonistic functions, at least in fear, anxiety (Janak and Tye, 2015) and pain expression (Wilson and Murphy, 2009). Haubensak and colleagues have shown that OTR expressing cells are more likely to be PKCδ, congruently with the fear-OFF function of those cells (Haubensak et al., 2010). In this context, one can imagine that OT directly activates PKCδ-positive neurons and indirectly inhibits PKCδ negative neurons, thus favoring a disinhibition of PKCδ-expressing neurons.

To decide between those hypotheses, it will be interesting to specifically ablate neuronal, but not astrocytic, OTR and to evaluate the effect of OT on those cells.

4.4. Are intracellular pathways recruited downstream of the OTR different between astrocytes and neurons?

As mentioned before, the OTR has the surprising feature to couple both the $G_{i/o}$ and the G_q pathways (Busnelli and Chini, 2018). This point is of crucial importance given that activation of G_q and $G_{i/o}$ proteins have opposite functions on neuronal excitability, with the former favoring neuronal spiking and the latter preventing it. To our knowledge, all published studies investigating the effect of OT on neuronal firing found an activity increase, suggesting no $G_{i/o}$ coupling in neurons (Alberi et al., 1997; Barrett et al., 2021; Crane et al., 2020; Eliava et al., 2016; Hu et al., 2020a; Knobloch et al., 2012; Ryan et al., 2017; Wang and Hatton, 2004, 2007). However, since the recruitment of both pathways in astrocytes was shown, independently of OTR, to trigger calcium transients (Durkee et al., 2019; Mehina et al., 2017), differentiating the pathway recruited cannot be done based on their calcium activity. To overcome this issue, biased agonists have been developed to trigger preferentially the recruitment of $G_{i/o}$ proteins (*e.g.* Atosiban) or

G_q proteins (*e.g.* Carbetocin) (Busnelli et al., 2012). It will be interesting for the next studies to investigate the recruitment of one pathway or the other in astrocytes and neurons.

5. Conclusions

Research in the last two decades has shown that astrocytes are much more than passive cells needed for neuronal support. It has become evident that astrocytes play a major role in metabolism, homeostasis, sensory information processing and cognitive functions. Many neuromodulators that influence these functions also modulate astrocytic calcium activity, suggesting that astrocytes may be involved in the regulation of neuronal circuit activity. Among these neuromodulators, OT has been shown to trigger calcium transients in astrocytes, highlighting a way of integrating OTergic information in the central nervous system. The difference in the temporal dynamic between astrocytes and neurons allows for an intricate interplay between the two cell types and could drastically influence the function of neuromodulators.

The finding that OT induces morphological changes in hypothalamic astrocytes and thus directly affects neuronal transmission gives rise to a series of interesting hypotheses. OT could potentially gate a precise and temporally restricted enhancement of neurotransmission in local microcircuits during important physiological situations. Retraction of astrocytic processes does not only make room for more extracellular signaling, but also impedes astrocytic clearing of transmitters via specific transporters. Thus, OTergic priming of astrocytes could potentially have long-lasting effects on neural network activity. This would be in line with the idea that astrocytes can integrate, process and transmit information as part of an astro-neuronal network. Future studies are needed to precisely assess the role of neuronal OTR in these astrocyte-neuron networks. It seems plausible that activation of astrocytes by OT precedes OTR-mediated activation of neurons and that OTergic signaling in neurons enables sustained activity of the astrocyte-neuronal networks. Finally, it remains unknown how OTergic signaling in astrocytes affects various behavioral paradigms and diseases, in which a compromised OT has been identified as an underlying cause such as autism spectrum disorder (Anagnostou et al., 2014; Domes et al., 2013; Ford and Young, 2021; Gordon et al., 2013; Guastella et al., 2010), Prader-Willi syndrome (Swaab, 1997; Swaab et al., 1995; Tauber et al., 2017, 2011) or PTSD (Anagnostou et al., 2014; Domes et al., 2013; Ford and Young, 2021; Frijling, 2017; Frijling et al., 2014; Gordon et al., 2013; Guastella et al., 2010; Meyer-Lindenberg et al., 2011; Olff et al., 2010; Swaab, 1997; Swaab et al., 1995; Tauber et al., 2017).

Author contributions

All authors discussed and elaborated the ideas, wrote the first draft and corrected it until the final version was obtained. All authors contributed to the article and approved the submitted version.

References

Alanazi, M.M., Havranek, T., Bakos, J., Cubeddu, L.X., Castejon, A.M., 2020. Cell proliferation and anti-oxidant effects of oxytocin and oxytocin receptors: role of extracellular signal-regulating kinase in astrocyte-like cells. Endocr. Regul. 54, 172–182.

Alberi, S., Dreifuss, J.J., Raggenbass, M., 1997. The oxytocin-induced inward current in vagal neurons of the rat is mediated by G protein activation but not by an increase in the intracellular calcium concentration. Eur. J. Neurosci. 9, 2605–2612.

Althammer, F., Eliava, M., Grinevich, V., 2021. Central and peripheral release of oxytocin: relevance of neuroendocrine and neurotransmitter actions for physiology and behavior. Handb. Clin. Neurol. 180, 25–44.

Althammer, F., Krause, E.G., de Kloet, A.D., Smith, J., Grinevich, V., Charlet, A., Stern, J. E., 2022a. Identification and three-dimensional reconstruction of oxytocin receptor expressing astrocytes in the rat and mouse brain. STAR Protoc. 3, 101160.

Althammer, F., Roy, R.K., Lefevre, A., Najjar, R.S., Schoenig, K., Bartsch, D., Eliava, M., Feresin, R., Hammock, E.A.D., Murphy, A.Z., Charlet, A., Grinevich, V., Stern, J.E., 2022b. Altered PVN-to-CA2 hippocampal oxytocin pathway and reduced number of oxytocin-receptor expressing astrocytes in heart failure rats. J. Neuroendocr.

Amato, S., Averna, M., Guidolin, D., Pedrazzi, M., Pelassa, S., Capraro, M., Passalacqua, M., Bozzo, M., Gatta, E., Anderlini, D., Maura, G., Agnati, L.F., Cervetto, C., Marcoli, M., 2022. Heterodimer of A2A and oxytocin receptors regulating glutamate release in adult striatal astrocytes. Int J. Mol. Sci. 23.

Anagnostou, E., Soorya, L., Brian, J., Dupuis, A., Mankad, D., Smile, S., Jacob, S., 2014. Intranasal oxytocin in the treatment of autism spectrum disorders: a review of literature and early safety and efficacy data in youth. Brain Res. 1580, 188–198.

Araque, A., Carmignoto, G., Haydon, P.G., Oliet, S.H., Robitaille, R., Volterra, A., 2014. Gliotransmitters travel in time and space. Neuron 81, 728–739.

Augusto-Oliveira, M., Arrifano, G.P., Takeda, P.Y., Lopes-Araujo, A., Santos-Sacramento, L., Anthony, D.C., Verkhratsky, A., Crespo-Lopez, M.E., 2020. Astroglia-specific contributions to the regulation of synapses, cognition and behaviour. Neurosci. Biobehav Rev. 118, 331–357.

Bakos, J., Srancikova, A., Havranek, T., Bacova, Z., 2018. Molecular mechanisms of oxytocin signaling at the synaptic connection. Neural Plast. 2018, 4864107.

Barrett, L.R., Nunez, J., Zhang, X., 2021. Oxytocin activation of paraventricular thalamic neurons promotes feeding motivation to attenuate stress-induced hypophagia. Neuropsychopharmacology 46, 1045–1056.

Bazargani, N., Attwell, D., 2016. Astrocyte calcium signaling: the third wave. Nat. Neurosci. 19, 182–189.

Breton, J.D., Poisbeau, P., Darbon, P., 2009. Antinociceptive action of oxytocin involves inhibition of potassium channel currents in lamina II neurons of the rat spinal cord. Mol. Pain. 5, 63.

Brown, C.H., Bains, J.S., Ludwig, M., Stern, J.E., 2013. Physiological regulation of magnocellular neurosecretory cell activity: integration of intrinsic, local and afferent mechanisms. J. Neuroendocr. 25, 678–710.

Brown, C.H., Ludwig, M., Tasker, J.G., Stern, J.E., 2020. Somato-dendritic vasopressin and oxytocin secretion in endocrine and autonomic regulation. J. Neuroendocr. 32, e12856.

Buijs, R.M., 1983. Vasopressin and oxytocin–their role in neurotransmission. Pharm. Ther. 22, 127–141.

Busnelli, M., Chini, B., 2018. Molecular basis of oxytocin receptor signalling in the brain: what we know and what we need to know. Curr. Top. Behav. Neurosci. 35, 3–29.

Busnelli, M., Sauliere, A., Manning, M., Bouvier, M., Gales, C., Chini, B., 2012. Functional selective oxytocin-derived agonists discriminate between individual G protein family subtypes. J. Biol. Chem. 287, 3617–3629.

Caudal, L.C., Gobbo, D., Scheller, A., Kirchhoff, F., 2020. The paradox of astroglial Ca(2 +) signals at the interface of excitation and inhibition. Front Cell Neurosci. 14, 609947.

Chatterjee, O., Patil, K., Sahu, A., Gopalakrishnan, L., Mol, P., Advani, J., Mukherjee, S., Christopher, R., Prasad, T.S., 2016. An overview of the oxytocin-oxytocin receptor signaling network. J. Cell Commun. Signal 10, 355–360.

Coyle, J.T., Balu, D., Wolosker, H., 2020. D-Serine, the shape-shifting NMDA receptor Co-agonist. Neurochem Res 45, 1344–1353.

Crane, J.W., Holmes, N.M., Fam, J., Westbrook, R.F., Delaney, A.J., 2020. Oxytocin increases inhibitory synaptic transmission and blocks development of long-term potentiation in the lateral amygdala. J. Neurophysiol. 123, 587–599.

Dale, H.H., 1906. On some physiological actions of ergot. J. Physiol. 34, 163–206.

De Dreu, C.K., Greer, L.L., Van Kleef, G.A., Shalvi, S., Handgraaf, M.J., 2011. Oxytocin promotes human ethnocentrism. Proc. Natl. Acad. Sci. USA 108, 1262–1266.

van den Pol, A.N., 2012. Neuropeptide transmission in brain circuits. Neuron 76, 98–115.

Di Scala-Guenot, D., Strosser, M.T., 1992. Oxytocin receptors on cultured astroglial cells. Kinetic and pharmacological characterization of oxytocin-binding sites on intact hypothalamic and hippocampic cells from foetal rat brain. Biochem J. 284 (Pt 2), 491–497.

Di Scala-Guenot, D., Mouginot, D., Strosser, M.T., 1994. Increase of intracellular calcium induced by oxytocin in hypothalamic cultured astrocytes. Glia 11 (3), 269–276. https://doi.org/10.1002/glia.440110308, 7960031.

Domes, G., Heinrichs, M., Kumbier, E., Grossmann, A., Hauenstein, K., Herpertz, S.C., 2013. Effects of intranasal oxytocin on the neural basis of face processing in autism spectrum disorder. Biol. Psychiatry 74, 164–171.

Durkee, C.A., Covelo, A., Lines, J., Kofuji, P., Aguilar, J., Araque, A., 2019. Gi/o protein-coupled receptors inhibit neurons but activate astrocytes and stimulate gliotransmission. Glia 67, 1076–1093.

Eliava, M., Melchior, M., Knobloch-Bollmann, H.S., Wahis, J., da Silva Gouveia, M., Tang, Y., Ciobanu, A.C., Triana del Rio, R., Roth, L.C., Althammer, F., Chavant, V., Goumon, Y., Gruber, T., Petit-Demouliere, N., Busnelli, M., Chini, B., Tan, L.L., Mitre, M., Froemke, R.C., Chao, M.V., Giese, G., Sprengel, R., Kuner, R., Poisbeau, P., Seeburg, P.H., Stoop, R., Charlet, A., Grinevich, V., 2016. A new population of parvocellular oxytocin neurons controlling magnocellular neuron activity and inflammatory pain processing. Neuron 89, 1291–1304.

Evrard, M.E., Strosser, M.T., Di Scala-Guenot, D., 1997. Pharmacological characterization of oxytocin-binding sites in rat spinal cord membranes: comparison with embryonic cultured spinal cord neurones and astrocytes. J. Neuroendocr. 9, 553–560.

Ferreira, J.J., Butler, A., Stewart, R., Gonzalez-Cota, A.L., Lybaert, P., Amazu, C., Reinl, E.L., Wakle-Prabagaran, M., Salkoff, L., England, S.K., Santi, C.M., 2019. Oxytocin can regulate myometrial smooth muscle excitability by inhibiting the Na(+) -activated K(+) channel, Slo2.1. J. Physiol. 597, 137–149.

Fiacco, T.A., McCarthy, K.D., 2018. Multiple lines of evidence indicate that gliotransmission does not occur under physiological conditions. J. Neurosci. 38, 3–13.

Foo, L.C., Allen, N.J., Bushong, E.A., Ventura, P.B., Chung, W.S., Zhou, L., Cahoy, J.D., Daneman, R., Zong, H., Ellisman, M.H., Barres, B.A., 2011. Development of a method for the purification and culture of rodent astrocytes. Neuron 71, 799–811.

Ford, C.L., Young, L.J., 2021. Refining oxytocin therapy for autism: context is key. Nat. Rev. Neurol.

Frijling, J.L., 2017. Preventing PTSD with oxytocin: effects of oxytocin administration on fear neurocircuitry and PTSD symptom development in recently trauma-exposed individuals. Eur. J. Psychotraumatol 8, 1302652.

Frijling, J.L., van Zuiden, M., Koch, S.B., Nawijn, L., Goslings, J.C., Luitse, J.S., Biesheuvel, T.H., Honig, A., Bakker, F.C., Denys, D., Veltman, D.J., Olff, M., 2014. Efficacy of oxytocin administration early after psychotrauma in preventing the development of PTSD: study protocol of a randomized controlled trial. BMC Psychiatry 14, 92.

Froemke, R.C., Young, L.J., 2021. Oxytocin, neural plasticity, and social behavior. Annu Rev. Neurosci. 44, 359–381.

Fuxe, K., Borroto-Escuela, D.O., Romero-Fernandez, W., Ciruela, F., Manger, P., Leo, G., Diaz-Cabiale, Z., Agnati, L.F., 2012. On the role of volume transmission and receptor-receptor interactions in social behaviour: focus on central catecholamine and oxytocin neurons. Brain Res 1476, 119–131.

Gautvik, K.M., de Lecea, L., Gautvik, V.T., Danielson, P.E., Tranque, P., Dopazo, A., Bloom, F.E., Sutcliffe, J.G., 1996. Overview of the most prevalent hypothalamus-specific mRNAs, as identified by directional tag PCR subtraction. Proc. Natl. Acad. Sci. USA 93, 8733–8738.

Gimpl, G., Fahrenholz, F., 2001. The oxytocin receptor system: structure, function, and regulation. Physiol. Rev. 81, 629–683.

Gonzalez-Hernandez, A, Charlet, A, 2018. Oxytocin, GABA, and TRPV1, the Analgesic Triad? Front Mol Neurosci 11 (398), 00398. https://doi.org/10.3389/fnmol.2018.00398.

Gordon, I., Vander Wyk, B.C., Bennett, R.H., Cordeaux, C., Lucas, M.V., Eilbott, J.A., Zagoory-Sharon, O., Leckman, J.F., Feldman, R., Pelphrey, K.A., 2013. Oxytocin enhances brain function in children with autism. Proc. Natl. Acad. Sci. USA 110, 20953–20958.

Gould, B.R., Zingg, H.H., 2003. Mapping oxytocin receptor gene expression in the mouse brain and mammary gland using an oxytocin receptor-LacZ reporter mouse. Neuroscience 122, 155–167.

Grandes, P., Kq, K.Q.D., Morino, P., Cuenod, M., Streit, P., 1991. Homocysteate, an excitatory transmitter candidate localized in glia. Eur. J. Neurosci. 3, 1370–1373.

Gravati, M., Busnelli, M., Bulgheroni, E., Reversi, A., Spaiardi, P., Parenti, M., Toselli, M., Chini, B., 2010. Dual modulation of inward rectifier potassium currents in olfactory neuronal cells by promiscuous G protein coupling of the oxytocin receptor. J. Neurochem 114, 1424–1435.

Grinevich, V., Stoop, R., 2018. Interplay between oxytocin and sensory systems in the orchestration of socio-emotional behaviors. Neuron 99, 887–904.

Grinevich, V., Neumann, I.D., 2020. Brain oxytocin: how puzzle stones from animal studies translate into psychiatry. Mol. Psychiatry.

Grinevich, V., Ludwig, M., 2021. The multiple faces of the oxytocin and vasopressin systems in the brain. J. Neuroendocr. 33, e13004.

Grinevich, V., Knobloch-Bollmann, H.S., Eliava, M., Busnelli, M., Chini, B., 2016. Assembling the puzzle: pathways of oxytocin signaling in the brain. Biol. Psychiatry 79, 155–164.

Guastella, A.J., Einfeld, S.L., Gray, K.M., Rinehart, N.J., Tonge, B.J., Lambert, T.J., Hickie, I.B., 2010. Intranasal oxytocin improves emotion recognition for youth with autism spectrum disorders. Biol. Psychiatry 67, 692–694.

Gwee, P.C., Tay, B.H., Brenner, S., Venkatesh, B., 2009. Characterization of the neurohypophysial hormone gene loci in elephant shark and the Japanese lamprey: origin of the vertebrate neurohypophysial hormone genes. BMC Evol. Biol. 9, 47.

Hasan, M.T., Althammer, F., Silva da Gouveia, M., Goyon, S., Eliava, M., Lefevre, A., Kerspern, D., Schimmer, J., Raftogianni, A., Wahis, J., Knobloch-Bollmann, H.S., Tang, Y., Liu, X., Jain, A., Chavant, V., Goumon, Y., Weislogel, J.M., Hurlemann, R., Herpertz, S.C., Pitzer, C., Darbon, P., Dogbevia, G.K., Bertocchi, I., Larkum, M.E., Sprengel, R., Bading, H., Charlet, A., Grinevich, V., 2019. A fear memory engram and its plasticity in the hypothalamic oxytocin system. Neuron 103 (133–146), e138.

Hatton, G.I., Perlmutter, L.S., Salm, A.K., Tweedle, C.D., 1984. Dynamic neuronal-glial interactions in hypothalamus and pituitary: implications for control of hormone synthesis and release. Peptides 5 (Suppl 1), 121–138.

Haubensak, W., Kunwar, P.S., Cai, H., Ciocchi, S., Wall, N.R., Ponnusamy, R., Biag, J., Dong, H.W., Deisseroth, K., Callaway, E.M., Fanselow, M.S., Luthi, A., Anderson, D. J., 2010. Genetic dissection of an amygdala microcircuit that gates conditioned fear. Nature 468, 270–276.

Havranek, T., Lestanova, Z., Mravec, B., Strbak, V., Bakos, J., Bacova, Z., 2017. Oxytocin modulates expression of neuron and glial markers in the rat hippocampus. Folia Biol. (Praha) 63, 91–97.

Henneberger, C., Bard, L., Panatier, A., Reynolds, J.P., Kopach, O., Medvedev, N.I., Minge, D., Herde, M.K., Anders, S., Kraev, I., Heller, J.P., Rama, S., Zheng, K., Jensen, T.P., Sanchez-Romero, I., Jackson, C.J., Janovjak, H., Ottersen, O.P.,

Nagelhus, E.A., Oliet, S.H.R., Stewart, M.G., Nagerl, U.V., Rusakov, D.A., 2020. LTP induction boosts glutamate spillover by driving withdrawal of perisynaptic astroglia. Neuron 108 (919–936), e911.

Hoare, S., Copland, J.A., Strakova, Z., Ives, K., Jeng, Y.J., Hellmich, M.R., Soloff, M.S., 1999. The proximal portion of the COOH terminus of the oxytocin receptor is required for coupling to g(q), but not g(i). Independent mechanisms for elevating intracellular calcium concentrations from intracellular stores. J. Biol. Chem. 274, 28682–28689.

Hrabovszky, E., Liposits, Z., 2008. Novel aspects of glutamatergic signalling in the neuroendocrine system. J. Neuroendocr. 20, 743–751.

Hu, B., Boyle, C.A., Lei, S., 2020a. Oxytocin receptors excite lateral nucleus of central amygdala by phospholipase Cbeta- and protein kinase C-dependent depression of inwardly rectifying K(+) channels. J. Physiol. 598, 3501–3520.

Hu, N.Y., Chen, Y.T., Wang, Q., Jie, W., Liu, Y.S., You, Q.L., Li, Z.L., Li, X.W., Reibel, S., Pfrieger, F.W., Yang, J.M., Gao, T.M., 2020b. Expression patterns of inducible cre recombinase driven by differential astrocyte-specific promoters in transgenic mouse lines. Neurosci. Bull. 36, 530–544.

Hunt, S., Sun, Y., Kucukdereli, H., Klein, R., Sah, P., 2017. Intrinsic circuits in the lateral central amygdala. eNeuro 4.

Inoue, T., Yamakage, H., Tanaka, M., Kusakabe, T., Shimatsu, A., Satoh-Asahara, N., 2019. Oxytocin Suppresses inflammatory responses induced by lipopolysaccharide through inhibition of the eIF-2-ATF4 pathway in mouse microglia. Cells 8.

Insel, T.R., Young, L.J., 2001. The neurobiology of attachment. Nat. Rev. Neurosci. 2, 129–136.

Ivanov, A.D., Mothet, J.P., 2019. The plastic d-serine signaling pathway: sliding from neurons to glia and vice-versa. Neurosci. Lett. 689, 21–25.

Janak, P.H., Tye, K.M., 2015. From circuits to behaviour in the amygdala. Nature 517, 284–292.

Jurek, B., Neumann, I.D., 2018. The oxytocin receptor: from intracellular signaling to behavior. Physiol. Rev. 98, 1805–1908.

Jurek, B., Meyer, M., 2020. Anxiolytic and anxiogenic? how the transcription factor MEF2 might explain the manifold behavioral effects of oxytocin. Front Endocrinol. (Lausanne) 11, 186.

Knobloch, H.S., Charlet, A., Hoffmann, L.C., Eliava, M., Khrulev, S., Cetin, A.H., Osten, P., Schwarz, M.K., Seeburg, P.H., Stoop, R., Grinevich, V., 2012. Evoked axonal oxytocin release in the central amygdala attenuates fear response. Neuron 73, 553–566.

Kong, W.L., Peng, Y.Y., Peng, B.W., 2017. Modulation of neuroinflammation: Role and therapeutic potential of TRPV1 in the neuro-immune axis. Brain Behav. Immun. 64, 354–366.

Kuo, J., Hariri, O.R., Micevych, P., 2009. An interaction of oxytocin receptors with metabotropic glutamate receptors in hypothalamic astrocytes. J. Neuroendocr. 21, 1001–1006.

Landgraf, R., Neumann, I.D., 2004. Vasopressin and oxytocin release within the brain: a dynamic concept of multiple and variable modes of neuropeptide communication. Front Neuroendocr. 25, 150–176.

Langle, S.L., Poulain, D.A., Theodosis, D.T., 2003. Induction of rapid, activity-dependent neuronal-glial remodelling in the adult rat hypothalamus in vitro. Eur. J. Neurosci. 18, 206–214.

Lawal, O, Ulloa Severino, F.P., Eroglu, C, 2022. The role of astrocyte structural plasticity in regulating neural circuit function and behavior. Glia 70 (8), 1467–1483. https://doi.org/10.1002/glia.24191.

Lee, H.J., Macbeth, A.H., Pagani, J.H., Young 3rd, W.S., 2009. Oxytocin: the great facilitator of life. Prog. Neurobiol. 88, 127–151.

Leng, G., Ludwig, M., 2008. Neurotransmitters and peptides: whispered secrets and public announcements. J. Physiol. 586, 5625–5632.

Lin, Y.T., Huang, C.C., Hsu, K.S., 2012. Oxytocin promotes long-term potentiation by enhancing epidermal growth factor receptor-mediated local translation of protein kinase Mzeta. J. Neurosci. 32, 15476–15488.

Ludwig, M., Leng, G., 2006. Dendritic peptide release and peptide-dependent behaviours. Nat. Rev. Neurosci. 7, 126–136.

Ludwig, M., Stern, J., 2015. Multiple signalling modalities mediated by dendritic exocytosis of oxytocin and vasopressin. Philos. Trans. R. Soc. Lond. B Biol. Sci. 370.

Ma, Y., Liu, Y., Rand, D.G., Heatherton, T.F., Han, S., 2015. Opposing oxytocin effects on intergroup cooperative behavior in intuitive and reflective minds. Neuropsychopharmacology 40, 2379–2387.

Maicas-Royo, J., Leng, G., MacGregor, D.J., 2018. A predictive, quantitative model of spiking activity and stimulus-secretion coupling in oxytocin neurons. Endocrinology.

Mairesse, J., Zinni, M., Pansiot, J., Hassan-Abdi, R., Demene, C., Colella, M., Charriaut-Marlangue, C., Rideau Batista Novais, A., Tanter, M., Maccari, S., Gressens, P., Vaiman, D., Soussi-Yanicostas, N., Baud, O., 2019. Oxytocin receptor agonist reduces perinatal brain damage by targeting microglia. Glia 67, 345–359.

McKay, E.C., Beck, J.S., Khoo, S.K., Dykema, K.J., Cottingham, S.L., Winn, M.E., Paulson, H.L., Lieberman, A.P., Counts, S.E., 2019. Peri-infarct upregulation of the oxytocin receptor in vascular dementia. J. Neuropathol. Exp. Neurol. 78, 436–452.

Mehina, E.M.F., Murphy-Royal, C., Gordon, G.R., 2017. Steady-State Free Ca(2+) in astrocytes is decreased by experience and impacts arteriole tone. J. Neurosci. 37, 8150–8165.

Meyer-Lindenberg, A., Domes, G., Kirsch, P., Heinrichs, M., 2011. Oxytocin and vasopressin in the human brain: social neuropeptides for translational medicine. Nat. Rev. Neurosci. 12, 524–538.

Mitre, M., Minder, J., Morina, E.X., Chao, M.V., Froemke, R.C., 2018. Oxytocin modulation of neural circuits. Curr. Top. Behav. Neurosci. 35, 31–53.

Mitre, M., Marlin, B.J., Schiavo, J.K., Morina, E., Norden, S.E., Hackett, T.A., Aoki, C.J., Chao, M.V., Froemke, R.C., 2016. A distributed network for social cognition enriched for oxytocin receptors. J. Neurosci. 36, 2517–2535.

Nersesyan, Y., Demirkhanyan, L., Cabezas-Bratesco, D., Oakes, V., Kusuda, R., Dawson, T., Sun, X., Cao, C., Cohen, A.M., Chelluboina, B., Veeravalli, K.K., Zimmermann, K., Domene, C., Brauchi, S., Zakharian, E., 2017. Oxytocin modulates nociception as an agonist of pain-sensing TRPV1. Cell Rep. 21, 1681–1691.

Neumann, I.D., Slattery, D.A., 2016. Oxytocin in general anxiety and social fear: a translational approach. Biol. Psychiatry 79, 213–221.

Newmaster, K.T., Nolan, Z.T., Chon, U., Vanselow, D.J., Weit, A.R., Tabbaa, M., Hidema, S., Nishimori, K., Hammock, E.A.D., Kim, Y., 2020. Quantitative cellular-resolution map of the oxytocin receptor in postnatally developing mouse brains. Nat. Commun. 11, 1885.

Nusbaum, M.P., Blitz, D.M., Swensen, A.M., Wood, D., Marder, E., 2001. The roles of co-transmission in neural network modulation. Trends Neurosci. 24, 146–154.

Olff, M., Langeland, W., Witteveen, A., Denys, D., 2010. A psychobiological rationale for oxytocin in the treatment of posttraumatic stress disorder. CNS Spectr. 15, 522–530.

Oliet, S.H., Panatier, A., Piet, R., Mothet, J.P., Poulain, D.A., Theodosis, D.T., 2008. Neuron-glia interactions in the rat supraoptic nucleus. Prog. Brain Res 170, 109–117.

Owen, S.F., Tuncdemir, S.N., Bader, P.L., Tirko, N.N., Fishell, G., Tsien, R.W., 2013. Oxytocin enhances hippocampal spike transmission by modulating fast-spiking interneurons. Nature 500, 458–462.

Palanisamy, A., Kannappan, R., Xu, Z., Martino, A., Friese, M.B., Boyd, J.D., Crosby, G., Culley, D.J., 2018. Oxytocin alters cell fate selection of rat neural progenitor cells in vitro. PLoS One 13, e0191160.

Panaro, M.A., Benameur, T., Porro, C., 2020. Hypothalamic neuropeptide brain protection: focus on oxytocin. J. Clin. Med 9.

Panatier, A., Gentles, S.J., Bourque, C.W., Oliet, S.H., 2006. Activity-dependent synaptic plasticity in the supraoptic nucleus of the rat hypothalamus. J. Physiol. 573, 711–721.

Papouin, T., Henneberger, C., Rusakov, D.A., Oliet, S.H.R., 2017. Astroglial versus neuronal D-serine: fact checking. Trends Neurosci. 40, 517–520.

Parent, A.S., Rasier, G., Matagne, V., Lomniczi, A., Lebrethon, M.C., Gerard, A., Ojeda, S. R., Bourguignon, J.P., 2008. Oxytocin facilitates female sexual maturation through a glia-to-neuron signaling pathway. Endocrinology 149, 1358–1365.

Parpura, V., Basarsky, T.A., Liu, F., Jeftinija, K., Jeftinija, S., Haydon, P.G., 1994. Glutamate-mediated astrocyte-neuron signalling. Nature 369, 744–747.

Phaneuf, S., Europe-Finner, G.N., Varney, M., MacKenzie, I.Z., Watson, S.P., Lopez Bernal, A., 1993. Oxytocin-stimulated phosphoinositide hydrolysis in human myometrial cells: involvement of pertussis toxin-sensitive and -insensitive G-proteins. J. Endocrinol. 136, 497–509.

Rajamani, K.T., Wagner, S., Grinevich, V., Harony-Nicolas, H., 2018. Oxytocin as a modulator of synaptic plasticity: implications for neurodevelopmental disorders. Front Synaptic Neurosci. 10, 17.

Rimoldi, V., Reversi, A., Taverna, E., Rosa, P., Francolini, M., Cassoni, P., Parenti, M., Chini, B., 2003. Oxytocin receptor elicits different EGFR/MAPK activation patterns depending on its localization in caveolin-1 enriched domains. Oncogene 22, 6054–6060.

Romero-Fernandez, W, Borroto-Escuela, D.O., Agnati, L.F., Fuxe, K, 2013. Evidence for the existence of dopamine D2-oxytocin receptor heteromers in the ventral and dorsal striatum with facilitatory receptor-receptor interactions. Mol Psychiatry 18 (8), 849–850. https://doi.org/10.1038/mp.2012.103.

Rosso, L., Peteri-Brunback, B., Vouret-Craviari, V., Deroanne, C., Van Obberghen-Schilling, E., Mienville, J.M., 2002. Vasopressin and oxytocin reverse adenosine-induced pituicyte stellation via calcium-dependent activation of Cdc42. Eur. J. Neurosci. 16, 2324–2332.

Ryan, P.J., Ross, S.I., Campos, C.A., Derkach, V.A., Palmiter, R.D., 2017. Oxytocin-receptor-expressing neurons in the parabrachial nucleus regulate fluid intake. Nat. Neurosci. 20, 1722–1733.

Salm, A.K., Smithson, K.G., Hatton, G.I., 1985. Lactation-associated redistribution of the glial fibrillary acidic protein within the supraoptic nucleus. immunocytochemical Study Cell Tissue Res. 242, 9–15.

Savtchouk, I., Volterra, A., 2018. Gliotransmission: beyond black-and-white. J. Neurosci. 38, 14–25.

Shigetomi, E., Kracun, S., Khakh, B.S., 2010a. Monitoring astrocyte calcium microdomains with improved membrane targeted GCaMP reporters. Neuron Glia Biol. 6, 183–191.

Shigetomi, E., Kracun, S., Sofroniew, M.V., Khakh, B.S., 2010b. A genetically targeted optical sensor to monitor calcium signals in astrocyte processes. Nat. Neurosci. 13, 759–766.

Sloan, S.A., Barres, B.A., 2014. Looks can be deceiving: reconsidering the evidence for gliotransmission. Neuron 84, 1112–1115.

Stifter, S.A., Greter, M., 2020. STOP floxing around: specificity and leakiness of inducible Cre/loxP systems. Eur. J. Immunol. 50, 338–341.

Stoop, R., 2012. Neuromodulation by oxytocin and vasopressin. Neuron 76, 142–159.

Strakova, Z., Copland, J.A., Lolait, S.J., Soloff, M.S., 1998. ERK2 mediates oxytocin-stimulated PGE2 synthesis. Am. J. Physiol. 274, E634–E641.

Svensson, E., Apergis-Schoute, J., Burnstock, G., Nusbaum, M.P., Parker, D., Schioth, H. B., 2018. General principles of neuronal co-transmission: insights from multiple model systems. Front Neural Circuits 12, 117.

Swaab, D.F., 1997. Prader-Willi syndrome and the hypothalamus. Acta Paediatr. Suppl. 423, 50–54.

Swaab, D.F., Purba, J.S., Hofman, M.A., 1995. Alterations in the hypothalamic paraventricular nucleus and its oxytocin neurons (putative satiety cells) in Prader-Willi syndrome: a study of five cases. J. Clin. Endocrinol. Metab. 80, 573–579.

Tasker, J.G., Oliet, S.H., Bains, J.S., Brown, C.H., Stern, J.E., 2012. Glial regulation of neuronal function: from synapse to systems physiology. J. Neuroendocr. 24, 566–576.

Tauber, M., Mantoulan, C., Copet, P., Jauregui, J., Demeer, G., Diene, G., Roge, B., Laurier, V., Ehlinger, V., Arnaud, C., Molinas, C., Thuilleaux, D., 2011. Oxytocin may be useful to increase trust in others and decrease disruptive behaviours in patients with Prader-Willi syndrome: a randomised placebo-controlled trial in 24 patients. Orphanet J. Rare Dis. 6, 47.

Tauber, M., Boulanouar, K., Diene, G., Cabal-Berthoumieu, S., Ehlinger, V., Fichaux-Bourin, P., Molinas, C., Faye, S., Valette, M., Pourrinet, J., Cessans, C., Viaux-Sauvelon, S., Bascoul, C., Guedeney, A., Delhanty, P., Geenen, V., Martens, H., Muscatelli, F., Cohen, D., Consoli, A., Payoux, P., Arnaud, C., Salles, J.P., 2017. The use of oxytocin to improve feeding and social skills in infants with prader-willi syndrome. Pediatrics 139.

Theodosis, D.T., Chapman, D.B., Montagnese, C., Poulain, D.A., Morris, J.F., 1986a. Structural plasticity in the hypothalamic supraoptic nucleus at lactation affects oxytocin-, but not vasopressin-secreting neurones. Neuroscience 17, 661–678.

Theodosis, D.T., Montagnese, C., Rodriguez, F., Vincent, J.D., Poulain, D.A., 1986b. Oxytocin induces morphological plasticity in the adult hypothalamo-neurohypophysial system. Nature 322, 738–740.

Theofanopoulou, C., Gedman, G., Cahill, J.A., Boeckx, C., Jarvis, E.D., 2021. Universal nomenclature for oxytocin-vasotocin ligand and receptor families. Nature 592, 747–755.

Tirko, N.N., Eyring, K.W., Carcea, I., Mitre, M., Chao, M.V., Froemke, R.C., Tsien, R.W., 2018. Oxytocin transforms firing mode of CA2 hippocampal. Neurons Neuron 100 (593–608), e593.

Tobin, V., Leng, G., Ludwig, M., 2012. The involvement of actin, calcium channels and exocytosis proteins in somato-dendritic oxytocin and vasopressin release. Front Physiol. 3, 261.

Verkhratsky, A., Nedergaard, M., 2018. Physiology of astroglia. Physiol. Rev. 98, 239–389.

von Bartheld, C.S., Bahney, J., Herculano-Houzel, S., 2016. The search for true numbers of neurons and glial cells in the human brain: A review of 150 years of cell counting. J. Comp. Neurol. 524, 3865–3895.

Wahis, J., Baudon, A., Althammer, F., Kerspern, D., Goyon, S., Hagiwara, D., Lefevre, A., Barteczko, L., Boury-Jamot, B., Bellanger, B., Abatis, M., Da Silva Gouveia, M., Benusiglio, D., Eliava, M., Rozov, A., Weinsanto, I., Knobloch-Bollmann, H.S., Kirchner, M.K., Roy, R.K., Wang, H., Pertin, M., Inquimbert, P., Pitzer, C., Siemens, J., Goumon, Y., Boutrel, B., Lamy, C.M., Decosterd, I., Chatton, J.Y.,

Rouach, N., Young, W.S., Stern, J.E., Poisbeau, P., Stoop, R., Darbon, P., Grinevich, V., Charlet, A., 2021. Astrocytes mediate the effect of oxytocin in the central amygdala on neuronal activity and affective states in rodents. Nat. Neurosci.

Wang, P., Qin, D., Wang, Y.F., 2017. Oxytocin rapidly changes astrocytic GFAP plasticity by differentially modulating the expressions of pERK 1/2 and protein kinase A. Front Mol. Neurosci. 10, 262.

Wang, Y.F., Hatton, G.I., 2004. Milk ejection burst-like electrical activity evoked in supraoptic oxytocin neurons in slices from lactating rats. J. Neurophysiol. 91, 2312–2321.

Wang, Y.F., Hatton, G.I., 2006. Mechanisms underlying oxytocin-induced excitation of supraoptic neurons: prostaglandin mediation of actin polymerization. J. Neurophysiol. 95, 3933–3947.

Wang, Y.F., Hatton, G.I., 2007. Interaction of extracellular signal-regulated protein kinase 1/2 with actin cytoskeleton in supraoptic oxytocin neurons and astrocytes: role in burst firing. J. Neurosci. 27, 13822–13834.

Wang, Y.F., Hatton, G.I., 2009. Astrocytic plasticity and patterned oxytocin neuronal activity: dynamic interactions. J. Neurosci. 29, 1743–1754.

Wilson, Y.M., Murphy, M., 2009. A discrete population of neurons in the lateral amygdala is specifically activated by contextual fear conditioning. Learn Mem. 16, 357–361.

Young, L.J., Wang, Z., 2004. The neurobiology of pair bonding. Nat. Neurosci. 7, 1048–1054.

Young, W.S., Song, J., 2020. Characterization of oxytocin receptor expression within various neuronal populations of the mouse dorsal hippocampus. Front Mol. Neurosci. 13, 40.

Zatkova, M., Bacova, Z., Puerta, F., Lestanova, Z., Alanazi, M., Kiss, A., Reichova, A., Castejon, A.M., Ostatnikova, D., Bakos, J., 2018. Projection length stimulated by oxytocin is modulated by the inhibition of calcium signaling in U-87MG cells. J. Neural Transm. (Vienna) 125, 1847–1856.

Zhang, B., Qiu, L., Xiao, W., Ni, H., Chen, L., Wang, F., Mai, W., Wu, J., Bao, A., Hu, H., Gong, H., Duan, S., Li, A., Gao, Z., 2020. Reconstruction of the hypothalamo-neurohypophysial system and functional dissection of magnocellular oxytocin neurons in the brain. Neuron.

Zhang, J.M., Wang, H.K., Ye, C.Q., Ge, W., Chen, Y., Jiang, Z.L., Wu, C.P., Poo, M.M., Duan, S., 2003. ATP released by astrocytes mediates glutamatergic activity-dependent heterosynaptic suppression. Neuron 40, 971–982.

9.5. Un engramme ocytocinergique pour apprendre et contrôler sa peur.

Baudon, A., Charlet, A.

Un engramme ocytocinergique pour apprendre et contrôler sa peur

Angel Baudon, Alexandre Charlet

CNRS et université de Strasbourg, institut des neurosciences cellulaires et intégratives (INCI, UPR3212),
8 allée du Général Rouvillois, 67000 Strasbourg, France.
acharlet@unistra.fr

Mémoire et engramme

La mémoire est un processus permettant aux êtres vivants de stocker des informations afin de mieux s'adapter à leur environnement. L'idée d'une représentation physique de la mémoire remonte à plus de 2 000 ans. En 350 avant J.-C., Aristote théorisait que « *le processus de stimulation sensorielle marque une sorte d'impression du percept, juste comme un sceau laisse son empreinte dans une cire chaude* » [1]. Cette idée a progressivement conduit à l'hypothèse selon laquelle des ensembles de cellules, organisés et sélectivement activés, forment les blocs de base de la trace mnésique, l'engramme. Cette hypothèse constitue aujourd'hui un champ majeur d'investigations, guidant l'étude des mécanismes cellulaires et moléculaires sousjacents à l'encodage et la préservation de la mémoire, qui restent pourtant encore mal connus. Ainsi, les informations seraient encodées par l'activité de micro-circuits précis au sein d'un réseau de neurones, de la même manière qu'une constellation peut se dessiner dans la voûte céleste. Une équipe internationale animée et coordonnée par Alexandre Charlet (France) et Valery Grinevich (Allemagne) a récemment montré que des engrammes sont susceptibles de se former dans certaines régions du cerveau comme l'hypothalamus.

Ocytocine et amygdale cérébrale

Afin de mettre en évidence un tel engramme, Hasan *et al.* [2] se sont intéressés à la création d'un souvenir de peur associée au contexte chez le rat. Chez cette espèce, la peur peut se manifester par une réaction comportementale d'immobilité appelée pétrification. Cette prétrification est sous le contrôle de nombreuses structures, ou régions, du cerveau, dont l'amygdale, une structure sous-corticale au cœur de la modulation des émotions, et l'hypothalamus, une région apparue très tôt au cours de l'évolution, impliquée dans l'homéostasie et la modulation de l'équilibre émotionnel. L'activité électrique des neurones de l'amygdale est modulée par l'activité de nombreux neurotransmetteurs ou neuromodulateurs, dont le glutamate, l'acide γ-amino-butyrique (GABA), la vasopressine, et l'ocytocine [3]. L'ocytocine, découverte en 1906 par Sir Henry Dales [4], est un petit peptide de neuf acides aminés synthétisé presque exclusivement dans l'hypothalamus, plus particulièrement dans le noyau paraventriculaire. Ce neuropeptide est produit par de grands neurones dits magnocellulaires, capables de sécréter l'ocytocine dans le sang, et par de petits neurones dits parvocellulaires, ne libérant l'ocytocine que dans le système nerveux central [5]. L'ocytocine joue un rôle majeur dans le comportement prosocial en favorisant les interactions sociales, la confiance, l'empathie, le comportement parental ou, plus généralement, les interactions sociales [5]. Outre ces effets désormais bien décrits et très médiatisés, on lui reconnaît aujourd'hui d'importantes fonctions comme molécule analgésique [6], anti-stress et anxiolytique, impliquant notamment sa libération axonale dans l'amygdale [2,7]. Ainsi, la libération d'ocytocine endogène dans l'amygdale *(Figure 1A)* induit une forte diminution de la réaction de peur conditionnée (pétrification) chez le rat, suggérant que le dialogue entre l'hypothalamus et l'amygdale pourrait être fortement impliqué dans le contrôle des comportements de peur.

Pourtant, comment expliquer qu'un neuropeptide synthétisé dans un seul noyau cérébral puisse posséder autant de fonctions complémentaires ? Est-il possible d'isoler et de définir des sous-populations fonctionnelles de neurones ocytocinergiques ? C'est ce questionnement qui a poussé les chercheurs à s'intéresser à ces ensembles de cellules hypothalamiques potentiellement impliqués.

Un engramme ocytocinergique contrôlant la peur

En utilisant une combinaison de vecteurs viraux permettant l'identification des neurones activés durant une courte fenêtre temporelle, les chercheurs ont montré que seule une sous-population de neurones ocytocinergiques hypothalamiques (~ 13 %) est active durant l'exposition à un stimulus induisant une réaction de peur chez le rat *(Figure 1B)*. Grâce au système viral utilisé, ils ont pu faire exprimer des récepteurs exogènes uniquement par ces neurones activés lors d'une peur, ce qui leur a permis de manipuler leur activité. L'utilisation d'outils optogénétiques et chimiogénétiques leur
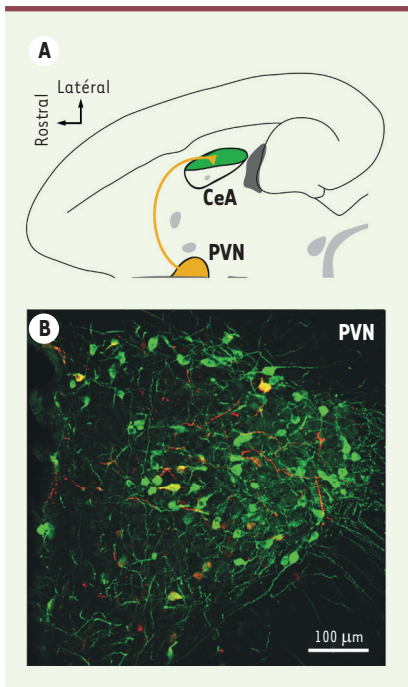
Figure 1. *Identification des neurones activés lors d'une peur chez le rat. A.* Les neurones ocytocinergiques du noyau paraventriculaire de l'hypothalamus (PVN ; en orange) projettent leurs axones vers l'amygdale centrale (CeA ; en vert). *B.* Seuls ~ 13 % des neurones ocytocinergiques sont activés par une expérience de peur. En vert : immunomarquage de l'ocytocine révélant tous les neurones produisant ce neuropeptide. En rouge : expression de la molécule fluorescente mCherry par les seuls neurones activés.

Figure 2. *Schéma récapitulatif des expériences présentées. 1.* Une expérience de peur chez le rat induit une plasticité neuronale qui se traduit notamment par un *switch* fonctionnel de neurotransmetteur entre ocytocine (OT) et glutamate (Glu). *2.* La propriété de dépendance du contexte de la population des neurones activés atteste de l'existence d'un engramme ocytocinergique. parvOT : neurones parvocellulaires produisant l'ocytocine ; magnOT, neurones magnocellulaires produisant l'ocytocine ; AMPA-R : récepteur AMPA du glutamate.

a ainsi permis de montrer que l'excitation spécifique de ce groupe de neurones écourte la durée de la pétrification, et qu'à l'inverse, leur inhibition augmente cette durée. Ainsi, ces quelques neurones ocytocinergiques sont à la fois nécessaires et suffisants pour contrôler la réaction de peur chez le rat *(Figure 2)* [2].

Cependant, les critères de nécessité et de suffisance dans la modulation d'une émotion par un groupe de neurones ne permettent pas d'établir l'existence d'un engramme. Il est également important de montrer que ce groupe de neurones est recruté spécifiquement lors d'une émotion donnée. Aussi, les chercheurs ont comparé les populations neuronales activées lors de réactions de peur obtenues par l'exposition des rats à différents contextes. Par cette approche, ils ont montré que les assemblées de neurones activés sont spécifiquement associées à un contexte donné. Ainsi, il existe dans l'hypothalamus un engramme constitué de neurones ocytocinergiques permettant d'associer un contexte précis à une émotion de peur *(Figure 2)*.

Un engramme pourvu de plasticité

On sait que les souvenirs se modifient au fil des expériences vécues. Les chercheurs ont donc voulu savoir si l'engramme ocytocinergique découvert est, à l'image de la mémoire, capable de plasticité. À cette fin, ils ont enregistré l'activité électrophysiologique de neurones de l'amygdale. Les données électrophysiologiques et transcriptomiques obtenues ont permis de montrer que les neurones hypothalamiques libèrent majoritairement de l'ocytocine dans l'amygdale chez les rats « naïfs », c'est-à-dire non exposés au conditionnement de peur *(Figure 1-2)*. Étonnamment, après que l'animal a vécu une première expérience de peur les neurones hypothalamiques libèrent préférentiellement du glutamate *(Figure 2)*. Une telle variation du type de neurotransmetteur libéré permet d'expliquer que la maîtrise de la peur *via* l'hypothalamus est plus rapide et

plus importante face à un stimulus déjà rencontré. Cet important changement de neurotransmetteur libéré, ce « *switch* fonctionnel » de l'ocytocine vers le glutamate, démontre ainsi l'existence d'une véritable plasticité fonctionnelle de cet engramme [2]. Finalement, une peur donnée induit le recrutement d'un groupe de neurones ocytocinergiques de l'hypothalamus permettant le contrôle de cette peur. Par ailleurs, une expérience de peur modifie le fonctionnement de cet engramme en provoquant un changement du neurotransmetteur libéré, de l'ocytocine vers le glutamate. Une telle conversion de la molécule sécrétée est en accord avec la vision selon laquelle les processus cognitifs et émotionnels seraient modulés par un équilibre entre les neuropeptides, dont l'activité neuromodulatrice est lente, et les neurotransmetteurs « classiques » (*e.g.* glutamate, GABA, acétylcholine), qui ont une activité bien plus brève [8]. Dans ce contexte, l'ocytocine laisse place au glutamate après le conditionnement de peur associée au contexte chez le rat, modifiant ainsi la rapidité de réaction face à un stimulus effrayant et donc potentiellement dangereux, afin de permettre une meilleure adaptation homéostatique (fréquence cardiaque, activité métabolique, etc.) [2].

Cibler cet engramme pour agir sur la peur pathologique

Hasan et collaborateurs ont donc découvert que des engrammes répondant à tous les critères de la théorie synaptique de la mémoire [9] peuvent se former dans l'hypothalamus. Ils ont ainsi montré pour la première fois que les souvenirs ne sont pas uniquement stockés dans les structures cérébrales dites supérieures (cortex, hippocampe) [10], mais aussi dans des régions apparues beaucoup plus tôt au cours de l'évolution, telles que l'hypothalamus. Cette découverte majeure incite à rechercher l'existence des engrammes dans les différentes régions cérébrales et à en explorer l'intégration. Comprendre les circuits anatomiques et fonctionnels impliqués dans une mémoire émotionnelle telle que celle de la peur pourrait permettre l'émergence de nouvelles stratégies thérapeutiques, notamment quand la peur devient pathologique, comme dans le cas de l'anxiété chronique ou du stress post-traumatique. ◊

An oxytocinergic engram to learn and control our fear

RÉFÉRENCES

1. On memory and reminiscence; written 350 B.C.E by Aristote, translated by J.I. Beare. http://classics.mit.edu/Aristotle/memory.html
2. Hasan M, Althammer F, Silva da Gouveia M, *et al*. A fear memory engram and its plasticity in the hypothalamic oxytocin system. *Neuron* 2019 ; 103 : 133-46.
3. Viviani D, Charlet A, van den Burg E, *et al*. Oxytocin selectively gates fear responses through distinct outputs from the central amygdala. *Science* 2011 ; 333 : 104-7.
4. Dale H. On some physiological actions of ergot. *J Physiol* 1906 ; 34 : 163-206.
5. Lee H, Macbeth A, Pagani J, Young W. Oxytocin: the great facilitator of life. *Prog Neurobiol* 2009 ; 88 : 127-51
6. Eliava M, Melchior M, Knobloch-Bollmann H, *et al*. A new population of parvocellular oxytocin neurons controlling magnocellular neuron activity and inflammatory pain processing. *Neuron* 2016 ; 89 : 1291-304.
7. Knobloch H, Charlet A, Hoffmann L, *et al*. Evoked axonal oxytocin release in the central amygdala attenuates fear response. *Neuron* 2012 ; 73 : 553-66.
8. Merighi A, Salio C, Ferrini F, Lossi L. Neuromodulatory function of neuropeptides in the normal CNS. *J Chem Neuroanat* 2011 ; 42 : 276-87.
9. Martin S, Grimwood P, Morris R. Synaptic plasticity and memory: an evaluation of the hypothesis. *Annu Rev Neurosci* 2000 ; 23 : 649-711.
10. Kitamura T, Ogawa S, Roy D, *et al*. Engrams and circuits crucial for systems consolidation of a memory. *Science* 2017 ; 356 : 73-8.

MAGAZINE

NOUVELLES

9.6. Les sentiments naissent sous de bonnes étoiles, ou comment les astrocytes contrôlent nos émotions.

Baudon, A., Charlet, A.

Les sentiments naissent sous des bonnes étoiles, ou comment les astrocytes contrôlent nos émotions

Angel Baudon, Alexandre Charlet

CNRS et Université de Strasbourg,
Institut des neurosciences cellulaires et intégratives (INCI, UPR3212), 8 allée du Général Rouvillois,
67000 Strasbourg, France.
acharlet@unistra.fr

Le cerveau : des neurones…

Le cerveau est le siège de la pensée, des émotions, et de la gestion de nos réactions, normales ou pathologiques, en réponse à notre environnement. Cet organe est composé de plusieurs centaines de milliards de cellules. Parmi elles, les neurones ont particulièrement attiré le regard de la recherche et de la médecine en raison de leur activité électrique. Cette activité est à l'origine d'un codage binaire, en apparence assez simple, qui a donné beaucoup d'espoirs aux neuroscientifiques cherchant à décrypter le code neuronal dans le but de comprendre nos comportements les plus complexes, une approche qui a d'ailleurs connu quelques succès spectaculaires au cours des dernières décennies.

… et des cellules gliales, parmi lesquelles les astrocytes

Cependant, le cerveau possède presqu'autant de cellules gliales que de neurones [1], ainsi nommées car elles ont d'abord été considérées comme de la glu sans autre rôle que celui de soutien pour les neurones. Mais les vingt dernières années ont vu s'accumuler de nombreuses preuves que les cellules gliales sont aussi des acteurs du traitement de l'information dans le cerveau. Parmi ces cellules, les astrocytes, en particulier, collaborent étroitement avec les neurones, dont ils modifient directement l'activité [2]. Des substances neuroactives détectées par les astrocytes recrutent ainsi des voies de signalisation qui entraînent des variations de la concentration intracellulaire des ions calcium, permettant à ces cellules de moduler l'activité du réseau neuronal environnant. S'il est désormais établi que les neurotransmetteurs classiques, tels que le glutamate ou l'adrénaline, peuvent déclencher une signalisation calcique dans les astrocytes [2], les effets potentiels des neurohormones sur ces cellules restent, quant à eux, mal connus.

Nous avons étudié les effets de l'ocytocine sur les astrocytes chez deux rongeurs [3] : la souris (*Mus musculus*) et le rat (*Rattus norvegicus*), génétiquement plus proche de nous que ne l'est la souris [4].
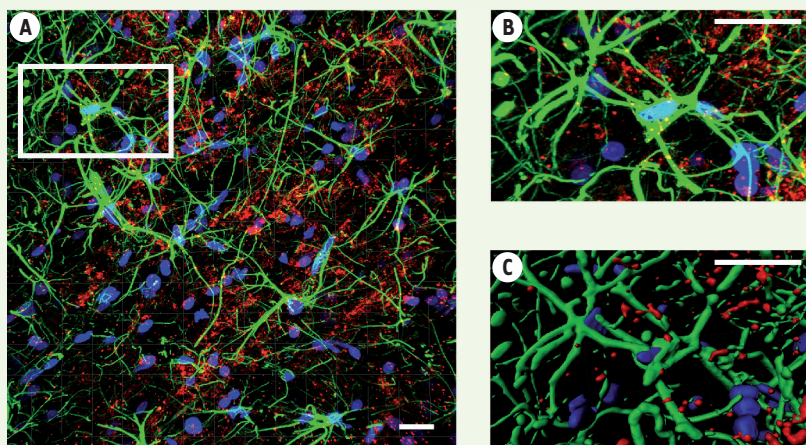
Figure 1. *Les astrocytes de l'amygdale expriment le récepteur de l'ocytocine.* (A, B) Images de microscopie confocale en plan large (*A*) et détail d'un astrocyte (*B*). Les astrocytes sont révélés par marquage de la glutamine synthase (en vert), et l'ARN messager codant le récepteur de l'ocytocine par une fluorescence rouge. Les noyaux cellulaires sont révélés par une fluorescence bleue (DAPI). (*C*) Reconstruction tridimensionnelle permettant une quantification spatiale de la structure cellulaire et des marqueurs utilisés. Barre d'échelle : 10 μm.

L'ocytocine module l'activité des astrocytes

L'ocytocine, un neuropeptide de 9 acides aminés, est connu pour son rôle dans le contrôle des émotions (douleur, anxiété) et dans les interactions sociales, et plus généralement comme promoteur du bien-être [5-7]. On pensait jusqu'alors que les effets de l'ocytocine impliquaient uniquement son action directe sur les neurones. Or, nous avons montré que certains astrocytes de l'amygdale, une structure cérébrale impliquée dans le contrôle des émotions, expriment le récepteur de l'ocytocine (*Figure 1*). Ces astrocytes présentent des caractéristiques distinctes : ils sont plus grands que leurs voisins, possèdent plus de ramifications, et sont en contact avec de nombreux astrocytes dépourvus de ce récepteur. L'imagerie dynamique du calcium intracellulaire a confirmé que l'ocytocine active directement de très nombreux astrocytes de l'amygdale, et que ces derniers peuvent transmettre l'information aux astrocytes voisins grâce à leurs jonctions communicantes (*gap junctions*) (*Figure 2*).

Du circuit neuronal au comportement : les astrocytes relaient le message ocytocinergique

L'analyse électrophysiologique du réseau neuronal de l'amygdale a indiqué que les astrocytes de l'amygdale activés par l'ocytocine pourraient sécréter un neuromodulateur, la D-sérine, qui favoriserait la neurotransmission glutamatergique *via* les récepteurs NMDA (N-méthyl-D-aspartate) du glutamate, et ainsi augmenter l'activité des neurones environnants (*Figure 2*). Les astrocytes joueraient donc un rôle actif dans la modulation de l'activité du réseau neuronal de l'amygdale [2]. Cette modulation a été observée dans l'amygdale centrale, où l'effet anxiolytique de l'ocytocine avait précédemment été en partie élucidé [6] (➡).

Nous avons étudié l'implication comportementale de l'activation du réseau astro-neuronal de l'amygdale en modifiant son activité par différentes techniques. Chez certains animaux, les astrocytes de l'amygdale ont été activés par une technique optogénétique, tandis que chez d'autres, le récepteur de l'ocy-

tocine a été supprimé dans les astrocytes, empêchant ainsi leur activation directe par l'ocytocine. Les animaux ont ensuite été soumis à des tests comportementaux de nociception (perception sensorielle de la douleur), d'évaluation de l'anxiété, ou de valence émotionnelle, souvent associée à l'aspect émotionnel de la douleur [8, 9]. Il apparaît que si la nociception semble peu impactée par l'activation du réseau astroneuronal de l'amygdale par l'ocytocine, cette dernière induit en revanche une forte diminution de l'anxiété et une nette préférence de place[1], témoin d'une modification de la valeur émotionnelle accordée à l'environnement (*Figure 2*). Ainsi, une situation stressante semblera moins anxiogène, une douleur paraîtra moins importante, et la sensation de bien-être sera renforcée.

Perspectives

Nous avons donc montré, dans deux espèces de rongeurs, que la libération d'ocytocine au sein de l'amygdale agit directement sur les astrocytes, dont l'activation provoque à son tour une augmentation de l'activité neuronale se traduisant par une diminution des comportements anxieux. Cette découverte étaye la théorie selon laquelle les neurones et les astrocytes constitueraient des canaux de communication ayant des cinétiques différentes : les influx électriques portés par les neurones sont brefs et rapides (de la milliseconde à la seconde), tandis que les signaux calciques produits par les astrocytes sont longs et lents (de la seconde à plusieurs dizaines de minutes). Ainsi, le sentiment diffus et prolongé de bien-être suivant la libération d'ocytocine peut être expliqué par le recrutement d'un réseau astrocytaire au sein de l'amygdale.

---

[1] Le test de « préférence de place » (*conditioned place preference*, CPP) permet de tester la valence émotionnelle d'un stimulus. Le dispositif expérimental comporte une arène contenant deux chambres. L'animal reçoit une stimulation (injection d'un agent pharmacologique, stimulation optique, etc.) dans un des deux compartiments puis, lors de la phase de test, on observe si l'animal préfère passer du temps dans le compartiment où il a reçu le stimulus, ou dans l'autre (où il a par exemple reçu un placebo dans le cas de l'injection d'une solution).
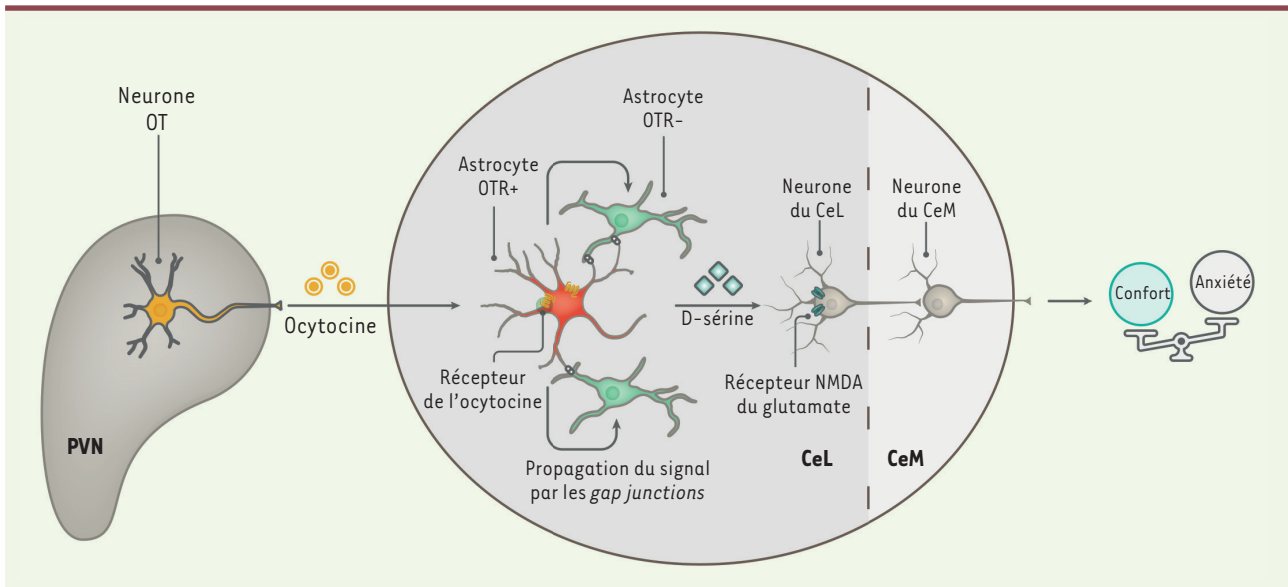
Figure 2. *Schéma récapitulatif des effets de l'ocytocine sur le réseau astro-neuronal de l'amygdale centrale.* L'ocytocine (OT) synthétisée par certains neurones du noyau paraventriculaire de l'hypothalamus (PVN) est sécrétée au sein de l'amygdale centrale latérale (CeL). Là, elle se lie à son récepteur (OTR) présent notamment sur les astrocytes (en rouge), ce qui provoque une augmentation de la concentration intracellulaire des ions calcium. Ce signal est transmis aux astrocytes voisins (en vert) à travers les jonctions communicantes (*gap junctions*) entre ces cellules. Cette activation du réseau astrocytaire libère la D-sérine, qui agit sur les récepteurs NMDA du glutamate neuronaux, facilitant l'activation des neurones du CeL, et aboutissant à l'inhibition des neurones de l'amygdale centrale médiane (CeM). La modulation de ce réseau astro-neuronal par l'OT diminue l'anxiété et induit une sensation de confort.

On sait que l'anxiété généralisée et la dépression accompagnent fréquemment les douleurs chroniques, qui touchent aujourd'hui près de 20 % de la population [10]. Or, nos résultats montrent que l'activation d'une population astrocytaire spécifique par l'ocytocine affecte l'un des aspects les plus délétères de la douleur chronique : son impact sur la sphère émotionnelle. En ce sens, ces résultats sont prometteurs, car ils permettent d'imaginer de nouveaux traitements de la douleur chronique, ciblant les cellules gliales et, potentiellement, sans effet indésirable. ◊

Reaching for the stars: How astrocytes regulate positive emotions via oxytocin

RÉFÉRENCES

1. Herculano-Houzel S. The glia/neuron ratio: how it varies uniformly across brain structures and species and what that means for brain physiology and evolution. *Glia* 2014 ; 62 : 1377-91.
2. Khakh BS, Sofroniew MV. Diversity of astrocyte functions and phenotypes in neural circuits. *Nat Neurosci* 2015 ; 18 : 942-52.
3. Wahis J, Baudon A, Althammer F, *et al.* Astrocytes mediate the effect of oxytocin in the central amygdala on neuronal activity and affective states in rodents. *Nat Neurosci* 2021 ; 24 : 529-41.
4. Rat Genome Sequencing Project Consortium. Genome sequence of the Brown Norway rat yields insights into mammalian evolution. *Nature* 2004 ; 428 : 493-521.
5. Eliava M, Melchior M, Knobloch-Bollmann HS, *et al.* A new population of parvocellular oxytocin neurons controlling magnocellular neuron activity and inflammatory pain processing. *Neuron* 2016 ; 89 : 1291-304.
6. Baudon A, Charlet A. Un engramme ocytocinergique pour apprendre et contrôler sa peur. *Med Sci (Paris)* 2020 ; 36 : 9-11.
7. Tang Y, Benusiglio D, Lefevre A, *et al.* Social touch promotes interfemale communication via activation of parvocellular oxytocin neurons. *Nat Neurosci* 2020 ; 23 : 1125-37.
8. Veinante P, Yalcin I, Barrot M. The amygdala between sensation and affect: a role in pain. *J Mol Psychiatry* 2013 ; 1 : 1-9.
9. King T, Vera-Portocarrero L, Gutierrez T, *et al.* Unmasking the tonic-aversive state in neuropathic pain. *Nat Neurosci* 2009 ; 12 : 1364-6.
10. Woo AK. Depression and anxiety in pain. *Reviews in Pain* 2010 ; 4 : 8-12.

9.7. Social Touch promotes interfemale communication via activation of parvocellular oxytocin neurons.

Tang, Y., Benusiglio, D., Lefevre, A., Hilfiger, L., Althammer, F., Bludau, A., Hagiwara, D., **Baudon, A.**, Darbon, P., Schimmer, J., Kirchner, M.K., Roy, R.K., Wang, S., Eliava, M., Wagner, S., Oberhuber, M., Conzelmann, K.K., Schwarz, M., Stern, J.E., Leng, G., Neumann, I.D., Charlet, A., Grinevich, V.

Social touch promotes interfemale communication via activation of parvocellular oxytocin neurons

Yan Tang[1,9,10], Diego Benusiglio[1,10], Arthur Lefevre[1,2,10], Louis Hilfiger[2,10], Ferdinand Althammer[1,3], Anna Bludau[4], Daisuke Hagiwara[1], Angel Baudon[2], Pascal Darbon[2], Jonas Schimmer[1], Matthew K. Kirchner[3], Ranjan K. Roy[3], Shiyi Wang[1], Marina Eliava[1], Shlomo Wagner[5], Martina Oberhuber[6], Karl K. Conzelmann[6], Martin Schwarz[7], Javier E. Stern[3], Gareth Leng[8], Inga D. Neumann[4,11], Alexandre Charlet[2,11 ✉] and Valery Grinevich[1,3,11 ✉]

Oxytocin (OT) is a great facilitator of social life but, although its effects on socially relevant brain regions have been extensively studied, OT neuron activity during actual social interactions remains unexplored. Most OT neurons are magnocellular neurons, which simultaneously project to the pituitary and forebrain regions involved in social behaviors. In the present study, we show that a much smaller population of OT neurons, parvocellular neurons that do not project to the pituitary but synapse onto magnocellular neurons, is preferentially activated by somatosensory stimuli. This activation is transmitted to the larger population of magnocellular neurons, which consequently show coordinated increases in their activity during social interactions between virgin female rats. Selectively activating these parvocellular neurons promotes social motivation, whereas inhibiting them reduces social interactions. Thus, parvocellular OT neurons receive particular inputs to control social behavior by coordinating the responses of the much larger population of magnocellular OT neurons.

The hypothalamic neuropeptide OT promotes various types of social behavior[1–3]. OT is mainly synthesized in neurons of the paraventricular nuclei (PVN) and supraoptic nuclei (SON) of the hypothalamus. The vast majority of these neurons project to the posterior pituitary, where OT is secreted into the blood for essential physiological effects, such as suckling-induced milk letdown and regulation of uterine contractions during birth[4]. In parallel, these neurons project axonal collaterals to forebrain regions[5] that express OT receptors (OTRs), including the central nucleus of the amygdala, nucleus accumbens, lateral septum, hippocampus and medial prefrontal cortex[6,7]. Studies employing microdialysis to measure OT concentrations within socially relevant brain regions revealed that OT is released in the bed nucleus of the stria terminalis, lateral septum and central nucleus of the amygdala during social investigation of a conspecific[2,8,9]. However, to date, no direct measurement of OT neuron activity during actual social interaction of freely moving conspecifics has been performed, although it was recently reported that social approach triggers calcium release in PVN OT neurons in immobilized, head-fixed male mice[10].

Several studies suggest that female–female interactions are predominantly mediated via somatosensory inputs[11,12], whereas other interactions such as male–male, male–female or parental contact may rely on other sensory modalities. However, whether these sensory stimulations can activate OT neurons is unknown because, to date, there has been no direct recording of activity from identified

OT neurons during actual social behavior. In an attempt to address these points, in the present study, we performed ex vivo and in vivo manipulation of OT neuron activity primarily in the PVN—the main source of OT in the brain[5]—to decipher their involvement in the modulation of social interaction in freely moving female rats.

Results

PVN OT neurons are activated on social interaction. To identify OT neurons electrophysiologically, we injected a recombinant adeno-associated virus (rAAV-OTp-ChR2-mCherry) bilaterally into the PVN to induce expression of the light-sensitive ion channel Channelrhodopsin-2 (ChR2) under the control of the OT promoter[5,13]. This resulted in 90.4% of ChR2-expressing neurons being OT positive, showing the high specificity of the infection in the PVN (Extended Data Fig. 1a). We then recorded individual neurons in the PVN using implanted tetrodes combined with an optic fiber to identify the OT neurons by their electrophysiological response to blue-laser pulses, similar to methods described previously[14].

In total, we recorded 90 neurons in 10 adult female rats at the diestrus phase of the ovarian cycle, while monitoring the behavior of the rats and their ultrasonic vocalizations during both open field (OF) exploration and free social interactions (FSIs) (Fig. 1a,b). Of these neurons, 15 (in 5 animals) were stringently identified as single OT neurons (Extended Data Fig. 1e). In the OF arena, the patterns of spiking activity of these neurons (Fig. 1d and Extended

Data Fig. 2d) were indistinguishable from those of OT neurons observed under basal conditions in anesthetized rats, because these neurons displayed typical OT neuron characteristics[15]. Specifically, they all display a low rate of tonic firing (~1 Hz) with a low index of dispersion of spikes (<1), and a distribution of interspike intervals consistent with random spike generation subject to a prolonged relative refractory period. In contrast, during episodes of FSI with an unfamiliar conspecific, the same neurons fired at a higher rate (mean increase 1.5 ± 0.4 spikes s^{-1}, $P = 0.001$, $n = 15$; Fig. 1c,d) and more irregularly; the second-by-second firing rates showed a high index of dispersion, reflecting the prominent occurrence of clusters of spikes (Fig. 1d and Extended Data Fig. 1n).

As revealed by cross-correlation analysis, OT neurons also displayed increased synchronicity during FSI (mean pairwise correlation: OF, 0.10 ± 0.04; FSI, 0.40 ± 0.08, $P = 0.001$; Extended Data Fig. 1k–l). In anesthetized rats, adjacent OT neurons showed no such cross-correlated activity. We also recorded local field potentials in the PVN and found a substantial increase of oscillatory power in the theta (5–10 Hz) frequency band during FSI (Extended Data Fig. 1f–h). The spike activity of OT neurons tended to be phase-locked with theta oscillations during FSI, but not in the OF arena (Extended Data Fig. 1i,j). In contrast to OT neurons, non-OT PVN neurons did not show an increase in spiking activity when comparing exploratory behavior and social interaction (Extended Data Fig. 2e–g).

Thus, during FSI with actual physical contact, OT neurons in the PVN were more active and exhibited frequent clusters of spikes, and this activity was correlated among the OT neurons.

Social physical contact increases PVN OT neuron activity. To examine which component of social interaction activates these neurons, we first recorded their neuronal activity during a chambered social interaction (CSI)[16]. In this setup, experimental and stimulus rats were separated by a transparent wall with small holes (7.5 mm), allowing rats to see, sniff and hear, but not touch, each other (Fig. 1e).

OT neurons showed little change in spiking activity between CSI and baseline recordings in an OF (CSI: 1.4 ± 0.4 spikes s^{-1}; OF: 1.0 ± 0.2 spikes s^{-1}, $P = 0.14$; Fig. 1f). When the wall was removed to allow FSI, the same OT neurons displayed a significant increase in activity (FSI: 3.0 ± 0.4 spikes s^{-1}, $P < 0.001$; Fig. 1f), accompanied by an increase in index of dispersion (FSI 3.2 ± 0.4, CSI 1.3 ± 0.3, $P = 0.006$ versus FSI; OF 0.9 ± 0.2, $P = 0.004$ versus FSI). To estimate the amount of OT axonal release due to the increase in firing rate, together with the altered firing pattern, we employed an activity (spike)-dependent model of OT secretion[17] (Extended Data Fig. 2h–j) that quantitatively captures the features of stimulus secretion coupling at the nerve terminals.

To dissect which sensory modalities activate OT neurons during FSI, we categorized rat social behaviors into 'sniffing', 'head-to-head'

and 'crawled on top' or 'being crawled' events and constructed peristimulus time histograms (PSTHs) of spiking activity before, during and after the onset of each sequence (Fig. 1g,h). 'Crawled on top' and 'being crawled' induced the greatest increases in firing rates ($P = 0.036$ and 0.024, respectively; Supplementary Video 1), whereas 'sniffing', 'chasing' and 'head-to-head' events induced lesser, non-significant changes (Fig. 1h and Extended Data Fig. 2a–c). In addition, ultrasonic vocalizations during FSI revealed the appearance of bands between 40 and 90 kHz known to be related to social communication in rats[18] (Extended Data Fig. 3a,b), but we found no time-locked (in ranges up to ± 5 s) correlation between OT neuron activity and ultrasonic vocalizations (Extended Data Fig. 3c–e). Although we could not discriminate individual ultrasonic vocalizations between the two conspecifics, we hypothesized that OT neurons were activated mainly by physical contacts and investigated this further by modeling gentle, non-nociceptive mechanical stimuli.

Gentle non-nociceptive mechanical stimuli trigger OT neuron activation. To test whether somatosensory stimulation itself is sufficient to increase OT cell activity, we performed controlled tactile stimulations using compressed air delivery (airpuffs) in isoflurane-anesthetized rats as described previously[19] (Fig. 2a). Stimulation of the skin on the dorsal body region by airpuffs (at three sites) reproducibly activated 19 of 23 (83%) recorded PVN OT neurons (mean increase 1.3 ± 0.5 spikes s^{-1}, mean $P = 0.021$; Fig. 2a,b and Extended Data Fig. 4a,b).

Airpuffs applied to the abdominal skin produced few or no changes in their activity (mean change 0.5 ± 0.3 spikes s^{-1}, $P = 0.33$), and there were no detected effects after stimulation of the anogenital area or the whiskers pad (Extended Data Fig. 4c). For potential involvement of the olfactory system in PVN OT neuron activation during social interaction, we exposed female rats to either a neutral odor (clean bedding) or a socially relevant odor (urinated-on female bedding). We found that the exposure to odorants did not elicit significant changes in either firing rate or spike distribution ($P = 0.34$ or 0.48, respectively; Extended Data Fig. 4d–f) in any of the recorded OT neurons. There was also no difference on presentation of neutral odor. Hence, we concluded that somatosensory inputs are the dominant signals that activate PVN OT neurons during social interactions.

ParvOT neurons respond to gentle non-nociceptive mechanical stimuli. Although the overwhelming majority of OT neurons in the PVN (97%) are magnocellular OT (magnOT) neurons, there is also a population of parvocellular OT (parvOT) neurons (~3%) that do not project to the pituitary[20], but that are crucial for the transmission of nociceptive signals to the magnOT cells[13].

Fig. 1 | In vivo recording of individual OT neurons in the PVN. a, Setup for recordings of behavior, ultrasonic vocalizations and neural activity. **b,** Video-tracking and electrophysiological recording from a rat alone in the OF arena (top) and during FSI (bottom): animal movement path (blue line), location of prominent OT cell activity (colored dots), heatmap of time spent by the rat in different locations. **c,** Example firing rate of four identified OT neurons recorded simultaneously during FSI. Red bars indicate periods of social interaction. **d,** Average firing rate of 15 OT neurons from 5 rats: OF baseline 1.1 ± 0.4 Hz, not socially interacting (not-SI) 1.6 ± 0.3 Hz and SI 2.6 ± 0.2 Hz (OF not-SI, $P = 0.07$; OF SI, $P = 0.001$; not-SI SI, $P = 0.03$; one-way ANOVA). Average index of dispersion on 1-s time bins of 15 OT neurons: OF 0.9 ± 0.2, not-SI 1.4 ± 0.3, SI 3.4 ± 0.4 (OF not-SI, $P = 0.16$; OF SI, $P = 0.0004$; not-SI SI, $P = 0.001$; one-way ANOVA). Average pairwise Pearson's correlation of spiking activity (1-s time bins) of 17 OT neuron pairs recorded in OF and SI ($P = 0.005$, unpaired, two-sided Student's t-test). **e,** Frames of recorded videos (top) of experimental rats that were placed either alone (OF), or with a mesh between rats (CSI) or for FSI with a stimulus rat; representative spike raster plots of an OT cell in each condition (bottom). **f,** Average firing rate of 15 OT neurons while rats underwent OF, CSI and FSI tests (OF CSI $P = 0.14$; OF FSI, $P = 0.004$; CSI FSI, $P = 0.006$; $n = 15$ cells; one-way ANOVA). Average index of dispersion on 1-s time bins (OF CSI, $P = 0.21$; OF FSI, $P = 0.001$; CSI FSI, $P = 0.003$; $n = 15$ cells; one-way ANOVA). Average pairwise Pearson's correlation of spiking activity (1-s time bins) of 17 OT neuron pairs (OF CSI, $P = 0.39$; OF FSI, $P = 0.002$; CSI FSI, $P = 0.003$; one-way ANOVA). **g,** Normalized firing rates of OT neurons during each behavior; 'crawling on top' and 'being crawled' elicited the strongest responses (*$P = 0.036$, **$P = 0.024$; $n = 8$ cells, one-way ANOVA, followed by Tukey's post hoc test). **h,** Representative spike raster plots, averaged response and PSTHs of OT cell activity during 'crawling on top' (increased response, $P = 0.036$, $n = 6$ cells, Wilcoxon's test) and 'being crawled' (increased response, $P = 0.024$, $n = 6$ cells; Wilcoxon's test) behaviors. Data represented as mean $\pm$ s.e.m.

To study whether parvOT neurons are also activated by non-nociceptive stimuli, we applied airpuffs to conscious rats trained and adapted for short-term immobilization. For this purpose, we first used rats that had been injected systemically with the retrograde tracer Fluorogold to label all neurons in the brain that project outside the blood–brain barrier, including in particular magnOT,
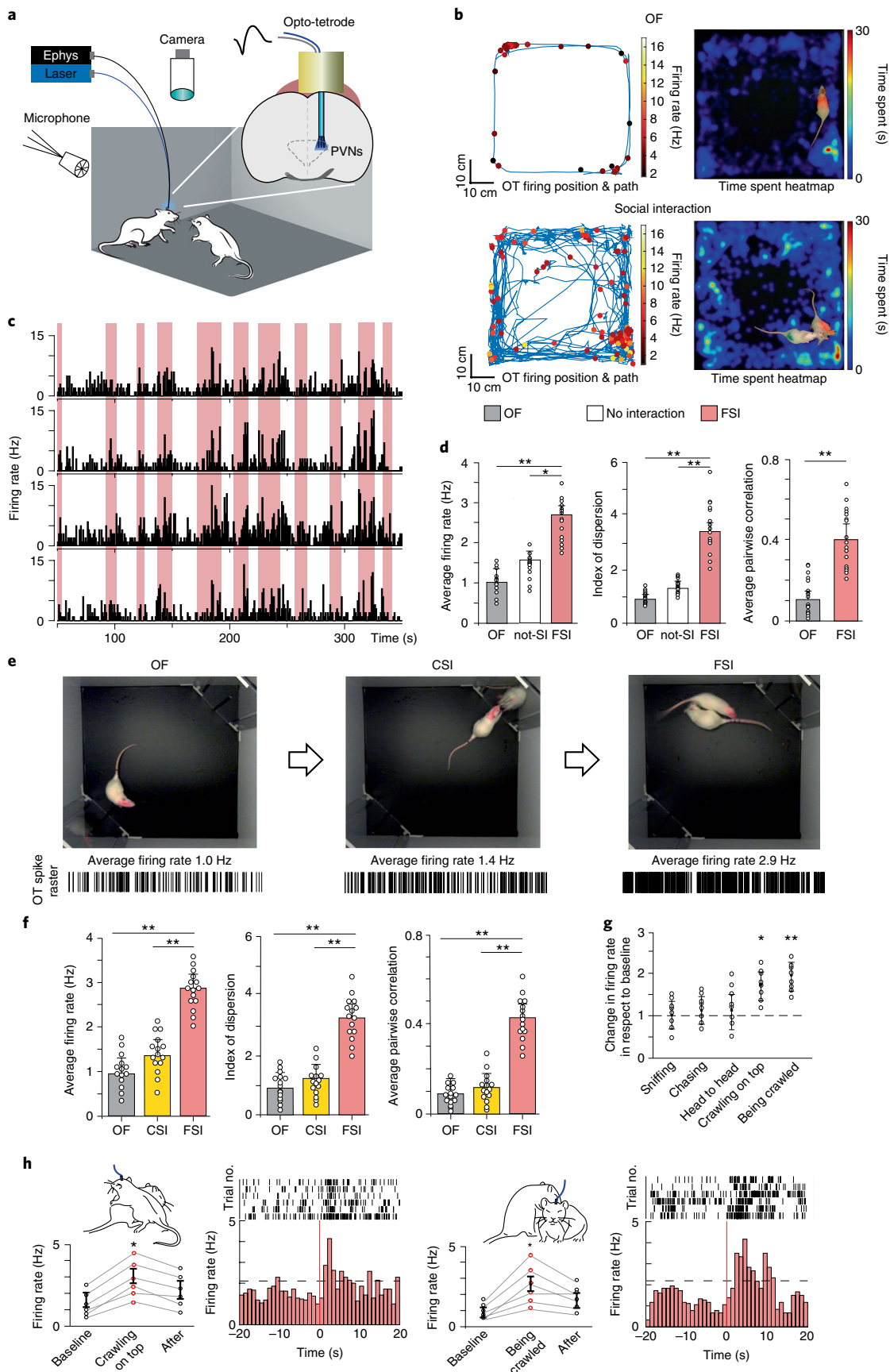
but not parvOT, neurons. To identify neurons strongly activated by airpuffs, we used the expression of *c-fos* as an indicator of activated OT neurons. Previous studies have found that *c-fos* expression is activated in a non-identified OT neuron cell type after social interaction in voles[21], mice[22] and rats[23]. Immunocytochemistry revealed the presence of *c-fos* in 30% of parvOT neurons in the PVN of stimulated rats (average 12.4 ± 3 neurons per PVN per hemisphere, $n = 4$; Fig. 2c and Supplementary Table 1a), but not in magnOT neurons or in any OT neurons in nonstimulated control rats, indicating that airpuffs specifically applied to the dorsal body region seem to predominantly activate parvOT neurons. In a second step, we labeled parvOT neurons retrogradely by injecting the canine adenovirus serotype 2 (CAV2-Cre)[24] into the SON, and concomitantly injected the Cre-responder rAAV-expressing mCherry under the control of the OT promoter into the PVNs. In line with our previous results, airpuffs induced *c-fos* expression exclusively in retrogradely labeled mCherry-positive OT neurons (average 47.6%, 7.5 ± 3 neurons per PVN per hemisphere, $n = 4$; Fig. 2d and Supplementary Table 1b).

To explore the role of parvOT neurons in social interaction and their response to gentle non-nociceptive mechanical stimuli (airpuffs), we chose to manipulate their activity via virally expressed, designer receptors exclusively activated by designer drugs (DREADDs). To this end, we used a similar Cre-dependent viral-based strategy employing OTp-DIO-hM4D(Gi)-mCherry and OTp-DIO-hM3D(Gq)-mCherry rAAVs (Fig. 2e,f). As a first step, we verified the efficiency of DREADDs in modulating of parvOT neuron activity ex vivo, showing that hM3D(Gq)-CNO-induced parvOT activation significantly increased the spontaneous action potential (AP) frequency (baseline 0.85 ± 0.39 Hz versus clozapine *N*-oxide (CNO) 1.31 ± 0.51 Hz, $n = 9$; $P = 0.0039$; Extended Data Fig. 5a–c) and the number of evoked APs (16.18 ± 3.89 APs versus CNO 22.55 ± 5.66 APs, $n = 11$; $P = 0.0314$; Extended Data Fig. 5d–f). Consistent with this, hM4D(Gi)-CNO-induced inhibition ($10 \mu M$, 6 min) significantly decreased both the spontaneous AP frequency (baseline 1.38 ± 0.38 Hz versus CNO 0.36 ± 0.18 Hz, $n = 7$; $P = 0.0469$; Extended Data Fig. 5g–i) and the number of evoked APs (baseline 13 ± 2.02 APs versus CNO 7.75 ± 2.03 APs, $n = 11$; $P = 0.0007$; Extended Data Fig. 5j–l).

After the ex vivo results, we next performed in vivo recording in anesthetized animals to better understand the airpuff-induced activation of parvOT. For this purpose, PVN parvOT activity was imaged using the GCaMP6s reporter and fiber photometry[25] (Fig. 2e–h). Then, rats were injected with the DREADD ligand CNO ($3 mg kg^{-1}$ intraperitoneally) and OT neuron Ca^{2+} transients were analyzed. Chemogenetic activation of the parvOT neurons

enhanced the Ca^{2+} response to airpuffs ($45 \pm 9\%$ increase of area under the curve (AUC; $P = 0.03$; Fig. 2i). Conversely, chemogenetic inhibition of the parvOT neurons reduced the response to airpuffs ($65 \pm 5\%$ decrease of AUC; $P = 0.009$ compared with control; Fig. 2j).

Thus, we concluded that gentle non-nociceptive mechanical stimulation of the dorsal region activates parvOT neurons, which we hypothesized may drive the activity of the larger population of magnOT neurons.

Intra-PVN connectivity of parvOT and magnOT neurons. To validate this hypothesis, we first looked for direct synaptic contact of parvOT neurons on to magnOT somata and/or dendrites via injection of OTp-DIO-GFP rAAV into the PVN and Cav2-Cre into the SON to specifically label parvOT neurons (Extended Data Fig. 6a,b) in analogy to a previous study[13]. For three-dimensional (3D) reconstruction of interposition between axons of parvOT neurons and somatodendritic domains of magnOT neurons, we employed the IMARIS technique[26,27]. This approach allows precise identification of the location of synaptic contact by quantifying overlap with SYN-immunoreactive puncta. By performing IMARIS-assisted Sholl analysis, we found synaptic-like contacts of parvOT neurons with magnOT somata and dendrites (Fig. 3a and Extended Data Fig. 6; 6 dendritic contacts, 124 somatic contacts, $n = 354$) as well as an average chance of innervation of 34.9% (Fig. 3b), indicating that approximately a third of PVN magnOT neurons receive parvOT input. Based on these anatomical observations, we performed patch-clamp recording for functional validation of parvOT–magnOT neuron connection via rAAV-OTp-DIO-ChR2-mCherry (to label specifically parvOT) and rAAV-OTp-Venus (to label all OT neurons) injected into the PVN and Cav2-Cre injected into the SON (Fig. 3g). First, we confirmed the magnOT nature of recorded neurons through the presence of a hyperpolarizing transient outward rectification, as well as a weak low-threshold depolarization (Fig. 3h), by comparison to the electrophysiological properties of identified parvOT neurons (Fig. 3c–f). We observed that stimulation of parvOT neurons evoked responses in 45% of recorded magnOT neurons (9 of 20; Fig. 3i) with a significant increase in postsynaptic current (PSC) frequencies (baseline 0.158 ± 0.055 Hz versus ChR2 0.346 ± 0.15 Hz, $n = 9$; $P < 0.01$; Fig. 3i). Next, we aimed to visualize Ca^{2+} variations in magnOT neurons on DREADD-mediated activation of parvOT neurons via rAAV-OTp-DIO-hM3D(Gq)-mCherry and rAAV-OTp-GCaMP6s injected into the PVN and Cav2-Cre into the SON (Fig. 4a–d). After application of CNO ($10 \mu M$, 1 min), we observed that $40 \pm 8\%$ of recorded magnOT neurons responded to parvOT hM3D(Gq) stimulation, again confirming described

---

Fig. 2 | Gentle non-nociceptive mechanical stimuli trigger OT neuron activation. a, Head-fixed rats injected with rAAV-pOT-ChR2-mCherry were stimulated with airpuffs at anterior, central and posterior portions of the dorsal body region, whereas OT neurons were recorded with an opto-electrode. Top: PSTH example of OT neuron responses to airpuffs. Bottom: normalized PSTHs of 10 (of 23) recorded OT neuron responses to airpuffs in three dorsal body regions ((i) anterior; (ii) central; (iii) posterior); red indicates high spiking activity. ITR, inverted terminal repeat; NS, not significant. **b,** Top: statistics of average firing rate of OT neuron responses to airpuff stimulations (peak versus baseline, *$P = 0.017$, **$P = 0.025$, ***$P = 0.021$; $n = 23$ cells from 8 rats; one-way ANOVA followed by Bonferroni's post hoc comparison) indicates a significant increase above basal rate (dashed line). Bottom: latency of OT neuron responses to airpuffs. All data shown as average $\pm$ s.e.m. **c,** Fluorogold-injected rats received continuous airpuffs for 10 min and were killed and perfusion-fixed 90 min later. PVN slices were triple stained with antibodies against OT (blue), Fluorogold (red) and *c-fos* (green). The confocal image shows a Fluorogold-negative parvocellular OT neuron expressing *c-fos* (1 of 99 such double-labeled neurons observed in 4 rats). Scale bars, 100 and 10 μm (inset). **d,** Rats injected bilaterally with CAV2-Cre into the SON and rAAV-OTp-DIO-mCherry into the PVN were exposed to airpuffs for 10 min and killed 90 min later. The confocal image shows *c-fos* expression in a parvOT neuron (mCherry-positive, labeled via the retrograde CAV2-Cre, and is 1 of 60 such triple-labeled neurons observed in 4 rats). Scale bars, 100 and 10 μm (inset). **e,f,** Viral vectors for recording Ca^{2+} signals in GCaMP6s-expressing OT neurons during chemogenetic activation (**e**) or silencing (**f**) of parvocellular OT neurons. **g,h,** Examples of fiber photometry-based Ca^{2+} signals of PVN OT neuron population during airpuff stimulation (orange bars). Top: response to airpuffs 30–60 min after saline injection (control); bottom: response to airpuffs 30–60 min after CNO-induced activation (**g**) or silencing (**h**) of parvOT neurons. **i,** Average traces of Ca^{2+} responses to airpuffs 30–60 min after injection of either CNO to activate (Gq) parvOT neurons or saline (control). Each graphic is the average of 33 airpuff responses (11 airpuffs per animal, $n = 3$; AUC 0–30 s after airpuffs, relative to control; *$P = 0.03$, paired, two-sided Student's *t*-test). **j,** Average traces of Ca^{2+} responses to airpuffs 30–60 min after injection of either CNO to silence (Gi) parvOT neurons or saline (control). Each graphic is the average of 33 airpuff responses (11 airpuffs per animal, $n = 3$; AUC 0–30 s after airpuffs, relative to control; **$P = 0.007$, paired, two-sided Student's *t*-test). All data show average $\pm$ s.e.m.

anatomical connectivity (Figs. 3b,i and 4d). In responsive neurons, the number of Ca²⁺ transients was significantly increased, a result mirrored by the increase of AUCs (Fig. 4d). However, the width of these Ca²⁺ transients did not show any significant change, indicating that parvOT-induced magnOT activity does not trigger long-lasting Ca²⁺ transients, but several bursts of sharp Ca²⁺ peaks, as observed
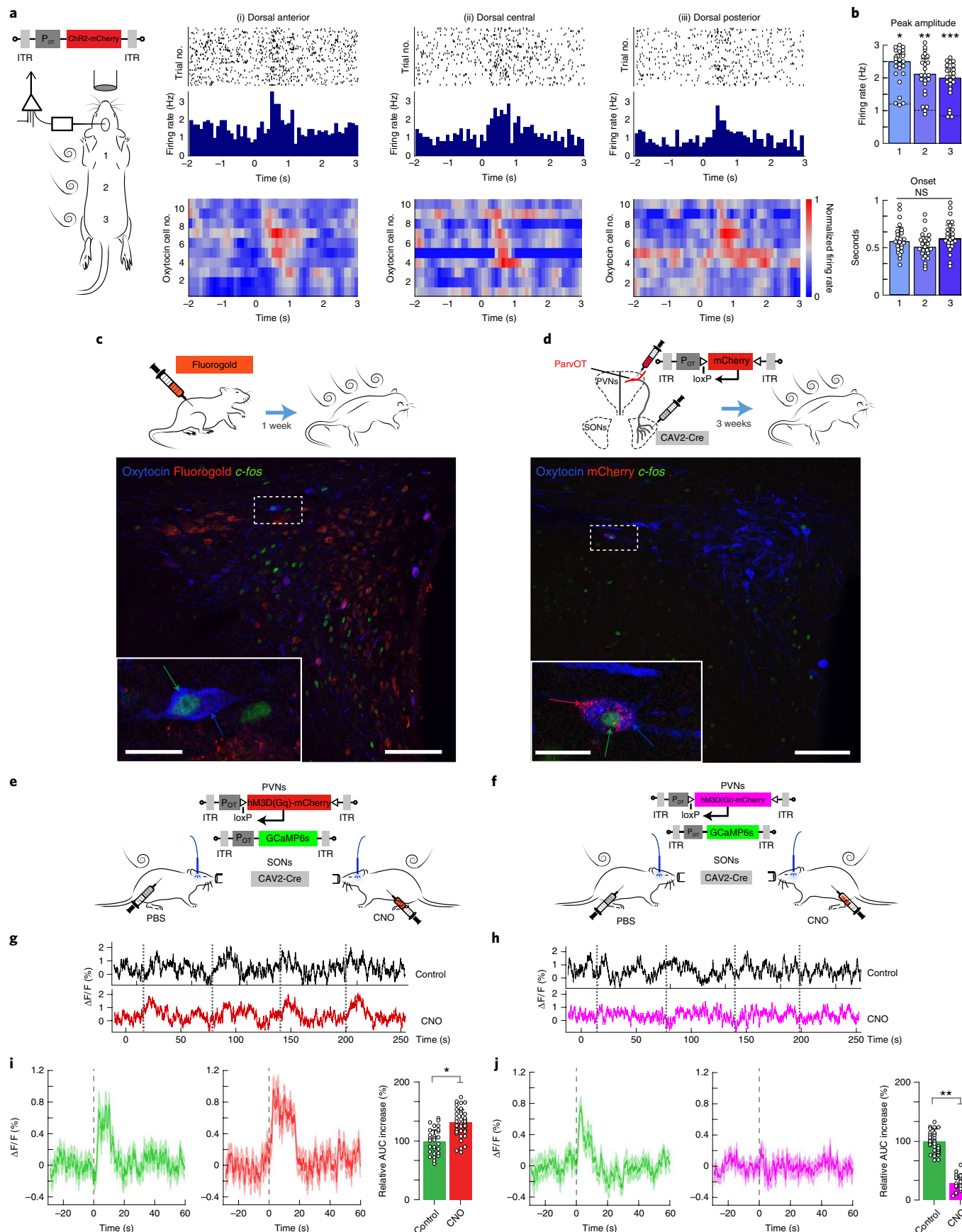
in the example traces (Fig. 4b). This feature was further confirmed by plotting the time course of Ca²⁺ event probability, showing that the probability of observing magnOT Ca²⁺ transients is increased over the 4 min after the ex vivo CNO treatment (Fig. 4c). These data indicate that parvOT neurons synapse on magnOT neurons within the PVN to drive their activity, as similarly reported for SON magnOT neurons in vivo[13].

Magnocellular neurons and their release of OT into blood, controlled by parvOT neurons. Using similar viral strategies, we expressed DREADDs—hM3D(Gq) or hM4D(Gi)—specifically in parvOT neurons and injected rAAV-OTp-GCaMP6s into the PVNs to express the Ca²⁺ indicator GCaMP6s in all PVN OT neurons (1,193 of 1,371 OT neurons expressed GCaMP6s, 87 ± 4%, $n = 4$; Fig. 4p). This allowed us to monitor the global activity of PVN OT neurons via fiber photometry in isoflurane-anesthetized rats on activation/inhibition of parvOT neurons. Activation of parvOT cells induced an increase in Ca²⁺ fluorescent signal of the PVN OT neuron population approximately 30 min after CNO injection (intraperitoneal 3 mg kg⁻¹) and lasting for >2 h (Fig. 4e–h). Conversely, inhibition of parvOT neurons decreased Ca²⁺ fluorescent signals of the general population 30 min after CNO injection and the effect lasted for more than 2 h (Fig. 4i–l). Administration of CNO did not have any effect on the Ca²⁺ signal in control animals lacking the

DREADD receptors (Fig. 4m–o). Considering that the contribution of parvOT neurons to the OT population Ca²⁺ signal is negligible (Extended Data Fig. 7a–e), those results suggest that changes in parvOT neuron activity directly influence the firing pattern of large populations of PVN magnOT neurons. The similar kinetics of Ca²⁺ signal fluctuations after CNO activation of parvOT PVN neurons, together with airpuff application, were detected during recording of magnOT neurons in the SON, which do not contain parvOT neurons (Extended Data Fig. 7f–o).

To investigate whether parvOT-induced magnOT activity is followed by actual OT release, we analyzed neurohypophyseal OT release after chemogenetic activation of parvOT neurons. We performed blood sampling from the jugular vein before and after CNO injection (3 mg kg⁻¹; Fig. 4q) and found a significant increase in plasma OT 45 min ($P = 0.00093$ versus basal; $P = 0.0036$ versus OTp-mCherry control) and 90 min ($P = 0.002$ versus basal; $P = 0.0017$ versus OTp-mCherry control; Fig. 4r) after intraperitoneal CNO injections.

Fig. 3 | Intra-PVN connectivity of parvOT and magnOT neurons. a, Images show the 3D surface reconstruction of OT, GFP and SYN. Circles with dashed lines indicate the overlap of OT, GFP and SYN. Scale bar, 10 μm. **b**, Confocal image shows a single magnOT neuron (purple) innervated by a parvOT fiber (green). Scale bar, 10 μm. Dot–plot graph shows that the chance of innervation by parvOT neurons depends on the anatomical location of magnOT neurons within the PVN. Bar graph shows the average chance for magnOT PVN neurons to be innervated by parvOT axons ($n = 214$ cells from 3 rats). **c**, Schema of the viral injection into the SON and PVN plus the electrophysiological recording in the PVN (with pipette) for the recording of parvOT neurons (expressing mCherry + GFP) and magnOT neurons (expressing mCherry). **d**, Comparison of average and individual points of voltage amplitude between parvOT neurons ($n = 17$ cells from 4 rats) and magnOT neurons ($n = 7$ cells from 4 rats) for different electrophysiological parameters (AP; parvOT 70.12 ± 2.87 mV versus magnOT 71.65 ± 7.414 mV; $P = 0.82$, unpaired, two-sided Student's t-test; transient outward rectification (TOR): magnOT = 4.39 ± 0.79 mV; low threshold depolarization (LTD): parvOT 14.88 ± 0.81 mV versus magnOT 5.93 ± 1.98 mV; **$P = 0.0019$, two-sided Mann–Whitney U-test). **e**, Example responses of three parvOT neurons to a hyperpolarizing current at −100 pA followed by four current injections starting from 0 to 60 pA. **f**, Example responses of three magnOT neurons to a hyperpolarizing current at −100 pA followed by four current injections starting from 0 pA to 60 pA. **g**, Left: schematic representation of viral vectors injected in the PVN (OTp-DIO-ChR2-mCherry and OTp-Venus) and the SON (CAV2-Cre) to transduce the expression of ChR2-mCherry in parvOT neurons and of Venus in PVN OT neurons. Right: image showing viral expression in the PVN in one of four rats. Scale bar, 100 μm. **h**, Average and individual points of voltage amplitude of magnOT neurons ($n = 8$ cells from 4 rats) for different electrophysiological parameters: AP, TOR and LTD. **i**, Average percentage (45%) of responding magnOT neurons ($n = 9$ cells) in all the magnOT neurons that have been recorded ($n = 20$ cells from 4 rats). MagnOT PSC frequency reversibly increases after parvOT ChR2 photostimulation ($n = 9$ cells). Example responses of three magnOT neurons in voltage clamp configuration at −70 mV before and after the ChR2 optogenetic stimulation of parvOT neurons. Baseline versus BL: **$P < 0.001$; baseline versus wash: **$P < 0.001$, Friedman's test followed by Dunn's post hoc test. BL, blue light. All data are represented as mean + s.e.m.
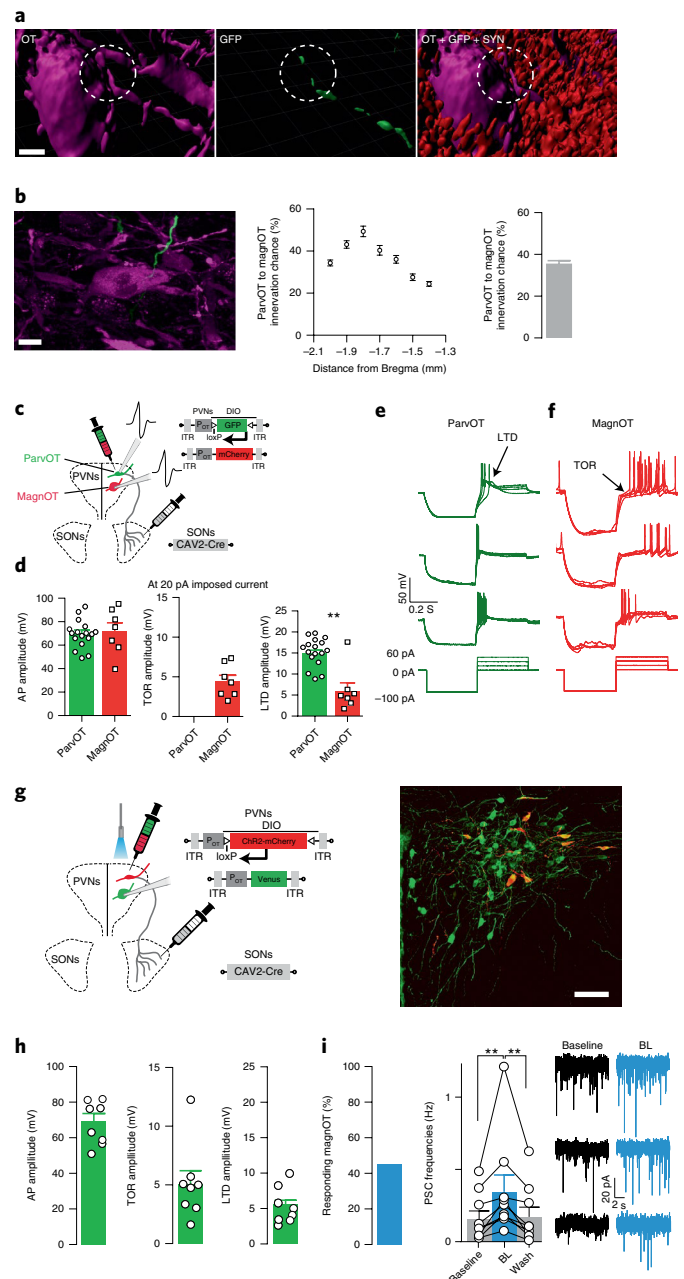
Taken collectively, these results indicate that parvOT neurons tightly control magnOT neuron activity in vivo to regulate peripheral OT release.

Differential neural inputs to parvOT and PVN magnOT neurons. These findings suggest that parvOT neurons act as 'first responders to somatosensory input', conveying information to the rest of the PVN OT neuronal population (that is, magnOT neurons). Hence, we asked whether parvOT neurons receive more synaptic inputs than magnOT ones in the PVN. In an attempt to assess potential differences of synaptic inputs to parvOT and magnOT neurons, we used IMARIS to quantify the total amount of SYN fluorescence at somata and dendrites. To perform an unbiased analysis, we created spheres that precisely engulfed magnOT and parvOT somata and accounted for individual variances in cell roundness and surface area (Methods). We found statistically significant differences at both the soma (Fig. 5a) and dendritic locations (Fig. 5b, at two different locations, 5 and 20 μm from the soma) and analyzed a total of 104 neurons (parvOT = 56, magnOT = 48), suggesting that parvOT neurons might receive more overall synaptic input.

Next, to uncover the origin of synaptic inputs to parvOT and magnOT neurons, we employed the retrograde trans-synaptic, EnvA-pseudotyped, G-deletion-mutant rabies virus (Rb-GFP[28]). To specifically distinguish inputs to parvOT and magnOT neurons, we used a double-conditional approach, which allows retrotracing of inputs to OT neurons that project to an area of choice (SON for parvOT and posterior pituitary for magnOT) (Methods; Fig. 5c,e).

In both groups of rats, we found green fluorescent protein (GFP)-expressing neurons in numerous brain regions, including the septum, medial preoptic area and amygdala (Fig. 5d,f and Extended Data Fig. 8h), demonstrating that parvOT and magnOT

neurons receive a large number of common inputs (Supplementary Table 2). However, we detected the presence of GFP neurons in the paraventricular nucleus of thalamus, insula and habenula only after infection of parvOT neurons (Extended Data Fig. 8i), whereas GFP neurons in the substantia nigra were found only after primary infection of magnOT neurons (Extended Data Fig. 8j). In line with the IMARIS analysis, the total number of neurons projecting to parvOT and magnOT neurons was 1,963.6 ± 710 and 694.8 ± 121 neurons, respectively (P = 0.02; Fig. 5g). Although we did not find between-group differences in the proportion of inputs coming from hypothalamic and extrahypothalamic areas (Fig. 5h), the periqueductal gray and subfornical organ showed preferential innervation of parvOT and magnOT neurons, respectively (Fig. 5i). This indicates that parvOT neurons receive at least partially distinct, and more pronounced neuronal inputs than magnOT neurons.

ParvOT neurons modulate social behavior. To test whether this small population of parvOT neurons can modulate social behavior by their effects on the activity of the much more abundant magnOT neurons, we used the previously described chemogenetic approach to silence or activate them during behavioral tests (Fig. 6a). Then 3 weeks after viral injection, rats were injected intraperitoneally with either CNO (3 mg kg⁻¹) or saline 60 min before social interaction tests (Fig. 6b). Selective inhibition of the parvOT neurons resulted in less social interaction: in the FSI test, the time spent with a conspecific was reduced by 37 ± 6 s (over 5-min sessions, P < 0.001; Supplementary Video 2). By contrast, in the CSI test, where no physical contact is allowed, the time spent by the experimental rat approaching the stimulus rat was unchanged (Fig. 6c–e; n = 15 rats). Conversely, CNO-induced activation of parvOT neurons led to more social interaction: in the FSI test, the time spent with a conspecific increased

Fig. 4 | Magnocellular neurons and their release of OT into blood are controlled by parvOT neurons. a, To allow the expression of hM3D(Gq) on parvOT PVN to SON projecting neurons, rats' SON are infected with a CAV2-Cre rAAV and the PVN are infected with an AAV, allowing the Cre-dependent expression of hM3D(Gq) under the control of the OT promoter. We also make PVN OT neurons express the calcium indicator GCaMP6s to monitor calcium transients in parvOT neurons. **b**, Example traces of the effect of CNO (10 μM, 6 min) on PVN oxytocinergic neuron calcium activity. **c**, CNO application increases the number of calcium transients by 5-fold ± 1-fold (solid line: average, shaded area: s.e.m., P = 0.0019, Wilcoxon's test) and the AUC by 15- ± 9-fold (P = 0.0043, Wilcoxon's test) in 40 ± 8% of recorded magnOT neurons (n = 20 slices from 7 rats, 70 cells). **d**, Calcium event probability, fraction of responses, number of peaks, AUC and peak duration of calcium events in PVN OT neurons. After CNO application, the probability of observing a calcium peak is increased over ~4 min, but the duration of those peaks remains unchanged (ratio = 2 ± 0.7, P = 0.46, paired, two-sided Student's t-test). Bar plots show mean ± s.e.m. **e–h**, Schema of viral vectors injected and implanted optic fiber-for-fiber photometry recording (**e**) of PVN OT neurons with concomitant DREADD-Gq activation of parvOT neurons. Example traces (**f**) of recorded GCaMP6s signal from PVN OT neurons before and after CNO-induced activation of parvOT neurons. Normalized AUC of GCaMP6s signal (**g**, solid line: average, shaded area: s.e.m., 1-min bin size) of PVN OT neurons showing increase of cellular activity after parvOT activation mediated by CNO intraperitoneal injection (indicated by arrow). The 30-min averaged AUC (**h**) showing a gradual increase of cellular activity (baseline AUC versus 0–30 min, P = 0.0606, versus 30–60 min, *P = 0.0403) that lasts at least 120 min (baseline AUC versus 60–90 min, *P = 0.028; versus 90–120 min, *P = 0.0325, n = 6 rats, two-way ANOVA and Tukey's corrected post hoc comparison). **i–l**, Schema of viral vectors injected and implanted optic fiber for fiber photometry recording (**i**) of PVN OT neurons with concomitant DREADD-Gi inhibition of parvOT neurons. Example traces (**j**) of recorded GCaMP6s signal from PVN OT neurons before and after CNO-induced inhibition of parvOT neurons. Normalized AUC of GCaMP6s signal (**k**, solid line: average, shaded area: s.e.m., 1-min bin size) of PVN OT neurons showing decrease of cellular activity after parvOT inhibition mediated by intraperitoneal CNO injection (indicated by arrow). The 30-min averaged AUC (**l**) showing a gradual decrease of cellular activity (baseline AUC versus 0–30 min, P = 0.058, versus 30–60 min, ***P = 0.00013) that lasts at least 120 min (baseline AUC versus 60–90 min, 90–120 min, ***P = 0.00019, n = 3 rats, two-way ANOVA and Tukey's corrected post hoc comparison). **m–o**, Schema of viral vectors injected and implanted optic fiber-for-fiber photometry recording (**m**) of PVN OT neurons in control animals (DREADD free) expressing GFP in parvOT neurons. Normalized AUC of GCaMP6s signal (**n**, solid line: average, shaded area: s.e.m., 1-min bin size) of PVN OT neurons showing no significant changes in Ca²⁺ signal on CNO injection. No significant changes are detected in 30-min averaged AUC (**o**) up to 120 min (P = 0.109, n = 2 rats, two-way ANOVA and Tukey's corrected post hoc comparison). **p**, Panels of immunostained section of the PVN showing post hoc verification of implanted optic fiber above the PVN and co-localization of immunoreactive GCaMP6s (green, top left), DIO-hM3D(Gq)-mCherry (red, bottom left) and OT (blue, right) in one of six rats. Arrows indicate mCherry-positive parvOT neurons. Scale bars, 100 μm and 10 μm (inset). **q**, Schema of viral vectors injected for DREADD-Gq activation of parvOT neurons and blood sampling from the jugular vein. **r**, Chemogenetic activation of parvOT neurons evokes peripheral OT release. Plasma OT (pg ml⁻¹) taken under basal conditions and 45 and 90 min after intraperitoneal CNO (3 mg kg⁻¹; depicted by arrow; n = 8 rats parvOT Gq group, n = 6 rats control group). At 45 min, ++P = 0.00093 versus basal (−45 min), **P = 0.0036 versus control (OTp-mCherry) and, at 90 min, ++P = 0.002 versus basal, **P = 0.0017 versus control. Two-way repeated-measures ANOVA with Bonferroni post hoc correction. Data are presented as mean ± s.e.m.

by 10 ± 6 s ($P = 0.04$). In the CSI test, no significant difference in approaching time was measured between saline- and CNO-injected rats (Fig. 6f–h; $n = 9$ rats).

Inhibition and activation of parvOT neurons also had opposite effects on crawling behavior (Fig. 6e,h). Moreover, after inhibiting parvocellular OT neurons, rats often actively avoided
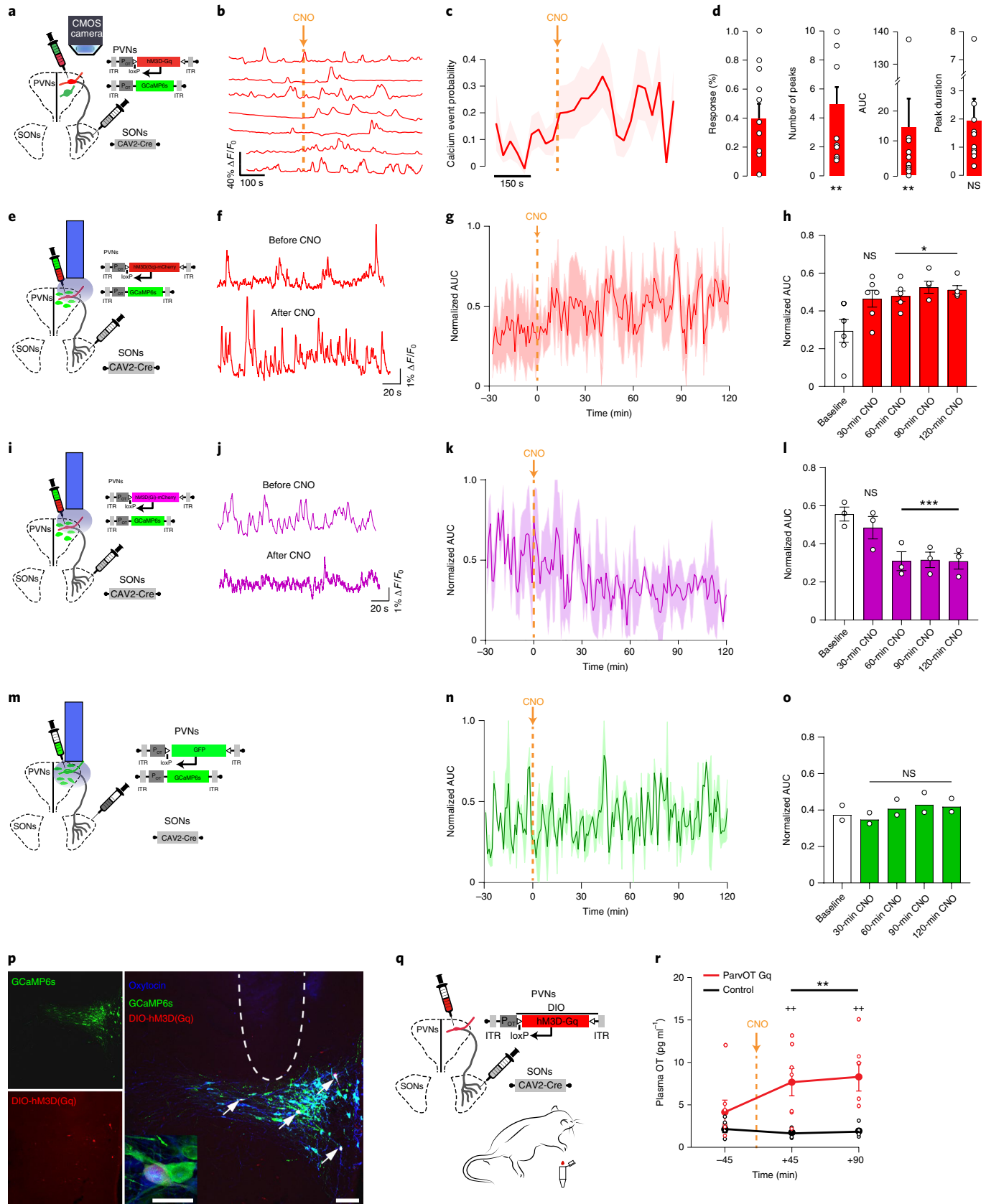
the stimulus rat, a behavior never observed in the control group (Extended Data Fig. 9c). Control rats injected with control virus rAAV-OTp-DIO-GFP receiving saline or CNO showed no behavioral differences (Extended Data Fig. 9a).

To show that alterations of social behaviors induced by DREADD-based manipulation of parvOT neuron activity were indeed an effect mediated by central OT release, the parvOT activation (Gq) experiment was repeated while applying an OTR antagonist[29] by intracerebroventricular infusion (0.75 µg per 5 µl)[30]. Compared with saline-infused control animals, OTR antagonist-infused animals showed a strong reduction in social interactions (37 ± 18% reduction, $P = 0.007$, $n = 12$ rats), regardless of CNO administration, whereas, without OTR antagonist, CNO application caused increased social interactions (16 ± 3% increase, $P = 0.04$, $n = 12$; Fig. 6i and Extended Data Fig. 9h). We did not observe a CNO- or OTR antagonist-induced effect on locomotor activity (Extended Data Fig. 9b,d–e). This result confirms that the downstream effect on CNO-induced activation of parvOT neurons of social behavior is indeed mediated by OT and its receptors. In a second group of rats ($n = 10$) expressing GFP in parvOT neurons, administration of an OTR antagonist also had a comparable effect in reducing social behavior; as expected, CNO itself did not have any effect on social interaction of animals (Fig. 6j and Extended Data Fig. 9i).

Discussion

In the present study, we provide evidence that somatosensory stimulation in female rats activates parvOT neurons, which subsequently drive the activation of the much larger population of magnOT neurons. Using ex vivo and in vivo approaches, we demonstrated that parvOT neurons synapse on magnOT neurons to elicit a central effect of OT to promote interfemale communication.

Social touch evokes OT neuronal activity. The use of single-unit in vivo recording precludes discrimination between parvOT and magnOT neurons. However, considering the limited number of parvOT neurons (~30 parvOT cells[13] versus ~1,200 magnOT cells[31] in the PVN of each hemisphere), it is highly likely that we exclusively recorded from magnOT cells. In support, we found that nonaggressive social interactions of female rats and, in particular, physical contacts elicited a coordinated, clustered spiking activity of PVN OT neurons—a pattern that strongly facilitates activity-dependent secretion of OT from nerve terminals of magnOT cells in the pituitary[17] (Extended Data Fig. 2h–j). This activity is almost synchronous across recorded OT neurons, and is highly correlated with theta rhythmicity of PVN local field potentials. These coordinated changes in OT neuronal electrical activity occurred only during FSI, allowing physical contacts between conspecifics, but not during CSI, where physical touch between animals was prevented by a barrier. Moreover, detailed analysis of PVN OT neuron activity during social behaviors revealed that the highest increase in neuronal firing occurred immediately after (0–10 s) crawling on top

or being crawled behaviors (Fig. 1), that is, social contacts involving activation of cutaneous sensory nerves.

To test whether non-noxious repetitive somatosensory stimulations directly influence PVN OT neuron activity, even in the absence of other stimuli, we applied airpuff stimulations to the skin of the dorsal area of the rat, in lightly anesthetized conditions, while measuring action potentials of PVN neurons. Notably, airpuffs induced a significant increase in spiking activity of most (83%) recorded putative magnOT neurons, but had little or no effect on the activity of non-OT PVN neurons, reinforcing the idea that somatosensory inputs selectively activate magnOT neurons. This finding is in line with previous studies[32] that reported increased OT plasma levels in rats after 10 min of massage-like stroking. Furthermore, the stimulation of low-threshold mechanoreceptors, particularly the touch-sensitive nerve fiber C-tactile afferents is known to trigger OT release, and has been associated with increased social motivation in rodents and humans[33].

ParvOT neurons control PVN magnOT neuron activity. To shed light on the causal link between somatosensory stimulation and social behavior, we focused our research on a specific subtype of 'parvocellular' OT neurons. These neurons communicate with various autonomic centers in the brain stem and spinal cord[20], and are involved in analgesia during acute pain[13].

When we applied low-intensity, non-noxious cutaneous stimulation (airpuff) in awake rats, we observed a sustained increase of c-fos expression in parvOT neurons in the PVN (Fig. 2). Of note, we found that airpuffs induced c-fos expression in parvOT, but not in magnOT, neurons. However, the absence of c-fos expression in magnOT cells does not necessarily indicate the absence of their increasing activity[34–36]. Indeed, only dramatic physiological challenges such as hemorrhage, salt loading or fear evoke c-fos expression in magnOT neurons[34,37]. Importantly, during lactation magnOT neurons release a large amount of OT into the peripheral circulation although an increase in c-fos expression was never found. In analogy, our findings demonstrate increased OT plasma concentrations after chemogenetic activation of parvOT neurons (Fig. 4) via a demonstrated parvOT → magnOT connectivity, although without detectable c-fos immunosignal in magnOT neurons releasing the neuropeptide into the blood.

Furthermore, chemogenetic activation or inhibition of parvOT neurons via DREADDs resulted, respectively, in an increase or decrease in OT neuron activity in response to the airpuff stimulation (Fig. 2). This suggests that parvOT neurons can be activated by both nociceptive[13] and non-nociceptive stimuli (in the present study) and subsequently promote analgesia as well as social behavior. Such pleotropic effects of OT originating from the same parvOT neurons require further investigation.

To provide additional evidence that parvOT neurons modulate magnOT neuron activity within the PVN, we employed a

Fig. 5 | ParvOT neurons receive more inputs than magnOT neurons. a, Three-dimensional reconstruction of parvOT and magnOT neurons and the quantification of SYN fluorescence. Asterisks (white) indicate the placement of the spheres (yellow) used to quantify the total amount of SYN fluorescence (red). Top: the placement of a sphere around a magnOT neuron soma; bottom: the placement of a sphere on to a parvOT neuron dendrite. Scale bars, 5 µm. **b**, Quantification of SYN fluorescence in close proximity to parvOT ($n = 56$ cells from 3 rats) and magnOT ($n = 48$ cells from 3 rats) neurons at somatic (top) and dendritic locations (bottom) considering differences in cellular roundness and surface area (adjusted) (unpaired, two-sided Student's t-test, ***$P < 0.0001$). **c,e**, Virus injection strategy to retrotrace inputs from parvOT (**c**) and magnOT (**e**) neurons, respectively. **d,f**, Schema representing the proportion of inputs (number of inputs from one brain area/total number of inputs) from each brain area to parvOT (**d**) and magnOT (**f**) neurons, respectively. Brain areas projecting only to parvOT or magnOT neurons are circled in green or purple, respectively. See Supplementary Table 2 for a full list of abbreviations for structures in **d** and **f**. **g**, Quantification of the total number of inputs to parvOT and magnOT neurons (two-sided Student's t-test, *$P = 0.0223$, $n = 5$ rats per group). **h**, Proportion of inputs to parvOT and magnOT neurons located in or outside the hypothalamus. Numbers indicate average number of neurons. **i**, Bar graphs showing the proportion of inputs coming from brain areas that show preferential innervation of parvOT or magnOT neurons. Two-sided Student's t-test; asterisks indicate significant difference: *$P = 0.0315$, **$P = 0.0153$, ***$P = 0.0264$, ****$P = 0.0299$, *****$P = 0.0453$ and ******$P = 0.0011$; $n = 5$ rats per group. Data represented as mean ± s.e.m.

combination of immunohistochemistry and 3D anatomical reconstruction. We found 1.5- to 4-fold more synaptic-like contacts on parvOT somata and dendrites compared with the respective compartments of magnOT neurons (Fig. 5). This finding is supported by retrograde tracing data, which demonstrate substantially more inputs to parvOT neurons than to magnOT neurons (Fig. 5).

Do parvOT neurons control social behavior?. To investigate how parvOT neurons modulate social behavior, we performed chemogenetic manipulation of parvOT neurons by viral means. We found that targeted activation or inhibition of parvOT neurons increased or decreased the total time of social interaction with a conspecific, respectively. Furthermore, the intracerebroventricular
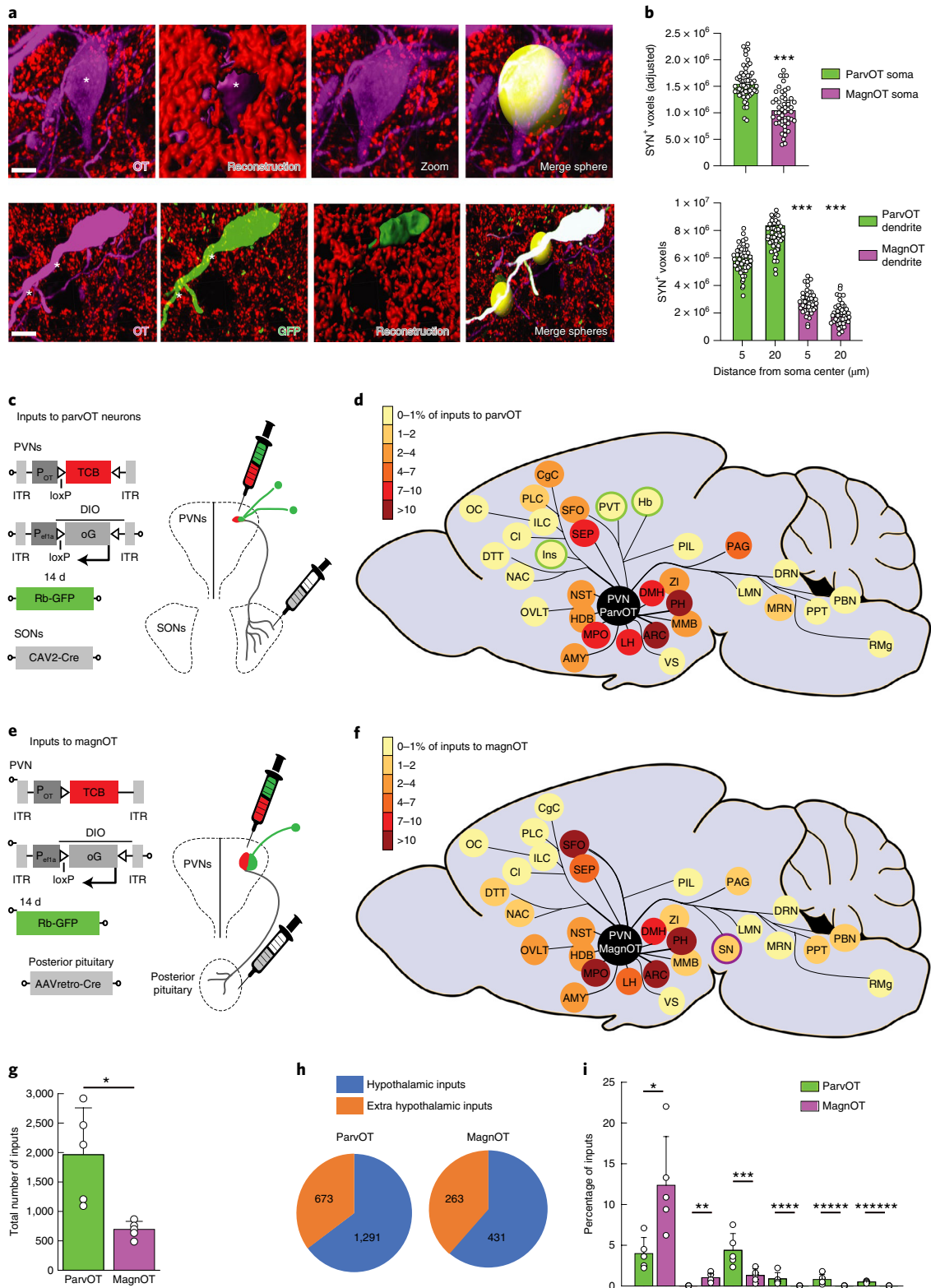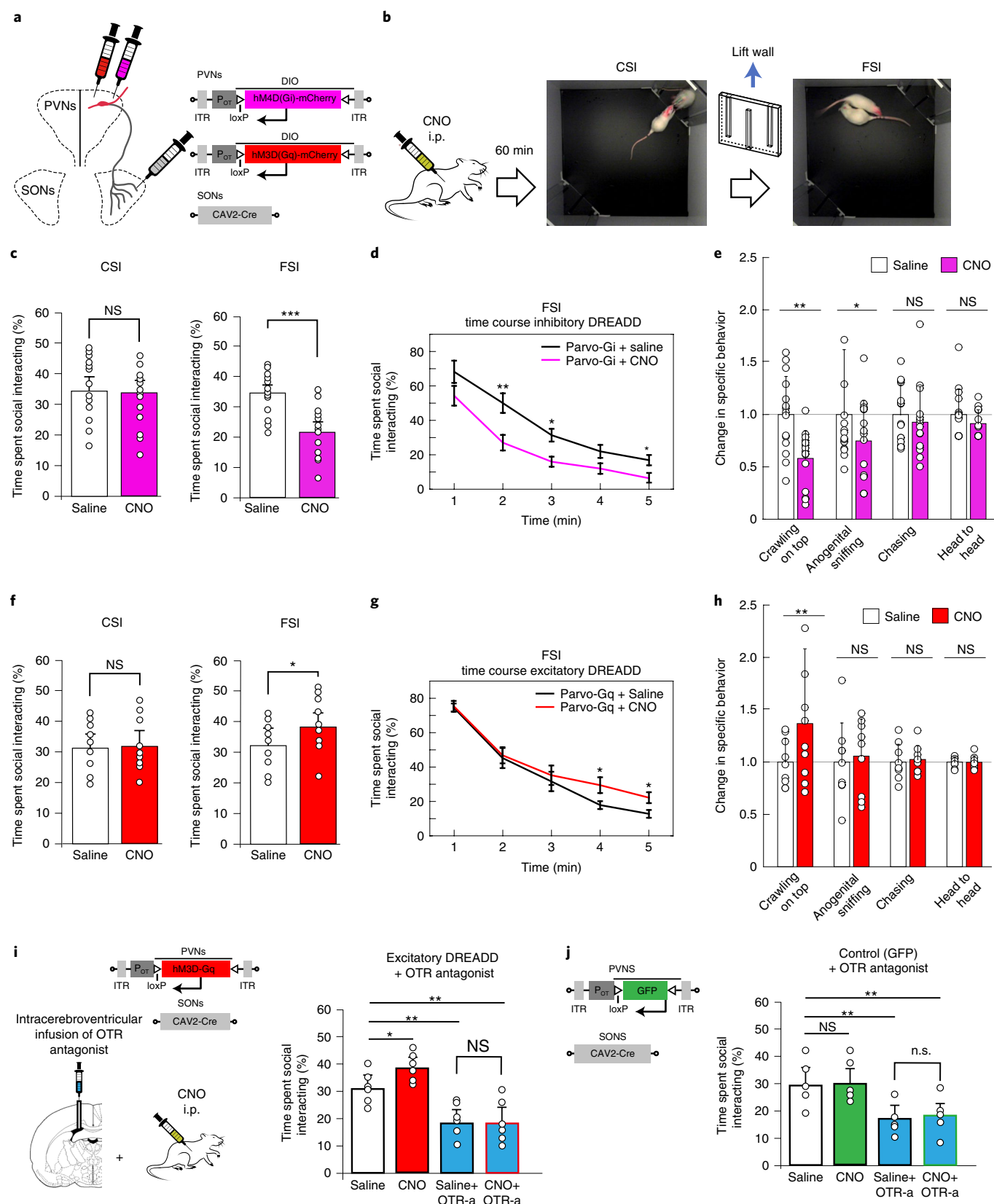
application of an OTR antagonist prevented CNO-induced social interaction after chemogenetic activation of parvOT neurons (Fig. 6). This suggests that the excitation of parvOT neurons is transmitted to magnOT cells, which, in turn, project axonal collaterals to numerous forebrain regions[5,7]. Given that parvOT neurons

exclusively project to the brain stem and spinal cord[38], our results allow the hypothesis that the OTR antagonist blocks the action of OT released from magnOT axons in socially relevant brain regions, resulting in the attenuation of social communication between female conspecifics.

Fig. 6 | Modulation of parvocellular OT neurons alters social behavior. a, Viral vectors used to express genes of interest (hM4D(Gi)-mCherry or hM3D(Gq)-mCherry) in parvOT neurons. **b**, CNO or saline was injected intraperitoneally (i.p.) 60 min before the behavioral tests. **c**, Silencing parvOT neurons (Parvo-Gi group): percentage of time spent by an experimental rat injected with saline or CNO socially interacting with a conspecific in CSI ($P = 0.41$) and FSI ($n = 15$ rats, ***$P = 0.0001$, paired, two-sided Student's t-test), calculated over the 5-min session. **d**, Temporal dynamics of time spent in social interaction in 1-min bins (second minute, **$P = 0.01$; third minute *$P = 0.03$; fifth minute *$P = 0.04$; $n = 15$ rats, two-way ANOVA time × treatment). **e**, Parvo-Gi group: time spent in different social behaviors in rats injected with saline or CNO: crawling on top (**$P = 0.008$), sniffing (*$P = 0.012$), chasing ($P = 0.13$), head to head ($P = 0.31$) ($n = 15$ rats, one-way ANOVA, Tukey's corrected post hoc comparison). **f**, Activation of parvOT neurons (Parvo-Gq group): average time spent in social interaction with conspecific stimulus in CSI ($P = 0.32$) and FSI ($n = 9$ rats, *$P = 0.04$, paired, two-sided Student's t-test) after CNO or saline injection. **g**, Temporal dynamics of time spent in social interaction in 1-min bins for rats injected with CNO or saline (fourth minute, $P = 0.03$; fifth minute, $n = 9$ rats, $P = 0.05$, two-way ANOVA time × treatment). **h**, Parvo-Gq group: time spent in different social behaviors in rats injected with saline or CNO: mounting (**$P = 0.006$), sniffing ($P = 0.44$), chasing ($P = 0.27$), head to head ($P = 0.11$) ($n = 9$ rats, one-way ANOVA, Tukey's corrected post hoc comparison). **i**, OTR antagonist intracerebroventricular infusion decreases social interaction even in the presence of pharmacological activation (hM3D-Gq) of parvOT neurons. Percentage of social interaction time is shown in different conditions: saline (control), CNO, OTR antagonist (OTR-a) or CNO + OTR antagonist administration. Time spent social interacting over 5-min sessions. Saline intraperitoneally and intracerebroventricularly: 90 ± 19 s; CNO intraperitoneally and saline intracerebroventricularly: 105 ± 15 s, *$P = 0.04$, $n = 6$ rats; saline intraperitoneally and OTR antagonist intracerebroventricularly: 54 ± 17 s, **$P = 0.007$; CNO intraperitoneally and OTR antagonist intracerebroventricularly: 56 ± 16 s, **$P = 0.009$, $n = 6$ rats (one-way ANOVA and Tukey's corrected post hoc comparison). **j**, Control group in which parvOT neurons express GFP. Saline intraperitoneally and intracerebroventricularly: 88 ± 18 s; CNO intraperitoneally and saline intracerebroventricularly: 89 ± 14 s, $n = 5$ rats; saline intraperitoneally and OTR antagonist intracerebroventricularly: 53 ± 14 s, **$P = 0.008$; CNO intraperitoneally and OTR antagonist intracerebroventricularly: 57 ± 15 s, **$P = 0.001$, $n = 5$ rats (one-way ANOVA and Tukey's corrected post hoc comparison). All data are represented as mean ± s.e.m.

A stable OT-mediated social interaction throughout female life?. Although we exclusively used virgin females in our present study, it will be important to investigate how pregnancy and lactation change the OT-dependent response to somatosensory stimulation. Given the drastic activation of the OT system and close physical contact with the offspring peripartum[39–41], it is plausible that the reward of tactile stimulation changes as well. Moreover, due to the interaction of OT and prolactin during the milk letdown reflex[42,43], the nipples might become more sensitive to the suckling of pups, which could translate into a more rewarding experience for mothers. Further studies are needed to assess the intricate interrelationship of social touch, social behavior and social motivation, which requires concomitant actions of OT, serotonin and dopamine within the nucleus accumbens and ventral tegmental area[22,44], in females as well as males. Accordingly, we found that parvOT, but not magnOT, neurons are innervated by neurons of the insular cortex, which is a critical region processing social touch[45], and could thus be potentially involved in the recruitment of the oxytocinergic system during social tactile stimulation.

Taken together, our data extend the current knowledge of the interrelationship of intracerebral OT release, social touch and its behavioral correlates. Our results suggest that parvOT neurons translate mechanosensory information from the periphery into social behavior (Extended Data Fig. 10), but the precise ascending pathways from cutaneous nerves—via the parvOT → magnOT circuit—to forebrain regions controlling social behaviors await further investigation.

Although intranasal OT application has improved clinical outcomes of schizophrenia, post-traumatic stress disorders and autism spectrum disorders, there is still an ongoing debate about the validity of these findings[46], suggesting that evoking endogenous OT release might be a more reliable way to exploit the benefits of this neuropeptide. Thus, a combination of gentle touch, social interaction and/or intranasal OT application might be a powerful tool to treat human mental diseases, in which the OT system is compromised[47,48].

Online content

Any methods, additional references, Nature Research reporting summaries, extended data, supplementary information, acknowledgements, peer review information; details of author contributions and competing interests; and statements of data and code availability are available at https://doi.org/10.1038/s41593-020-0674-y.

References

1. Lee, H.-J., Macbeth, A. H., Pagani, J. & Scott Young, W. 3rd. Oxytocin: the great facilitator of life. *Prog. Neurobiol.* **88**, 127–151 (2010).
2. Jurek, B. & Neumann, I. D. The oxytocin receptor: from intracellular signaling to behavior. *Physiol. Rev.* **98**, 1805–1908 (2018).
3. Walum, H. & Young, L. J. The neural mechanisms and circuitry of the pair bond. *Nat. Rev. Neurosci.* **19**, 643–654 (2018).
4. Russell, J. A., Leng, G. & Douglas, A. J. The magnocellular oxytocin system, the fount of maternity: adaptations in pregnancy. *Front. Neuroendocrinol.* **24**, 27–61 (2003).
5. Knobloch, H. S. et al. Evoked axonal oxytocin release in the central amygdala attenuates fear response. *Neuron* **73**, 553–566 (2012).
6. Marlin, B. J. & Froemke, R. C. Oxytocin modulation of neural circuits for social behavior. *Dev. Neurobiol.* **77**, 169–189 (2017).
7. Grinevich, V. & Stoop, R. Interplay between oxytocin and sensory systems in the orchestration of socio-emotional behaviors. *Neuron* **99**, 887–904 (2018).
8. Dumais, K. M., Alonso, A. G., Immormino, M. A., Bredewold, R. & Veenema, A. H. Involvement of the oxytocin system in the bed nucleus of the stria terminalis in the sex-specific regulation of social recognition. *Psychoneuroendocrinology* **64**, 79–88 (2016).
9. Dumais, K. M., Alonso, A. G., Bredewold, R. & Veenema, A. H. Role of the oxytocin system in amygdala subregions in the regulation of social interest in male and female rats. *Neuroscience* **330**, 138–149 (2016).
10. Resendez, S. L. et al. Social stimuli induce activation of oxytocin neurons within the paraventricular nucleus of the hypothalamus to promote social behavior in male mice. *J. Neurosci.* **40**, 2282–2295 (2020).
11. Bobrov, E., Wolfe, J., Rao, R. P. & Brecht, M. The representation of social facial touch in rat barrel cortex. *Curr. Biol.* **24**, 109–115 (2014).
12. Chen, P. & Hong, W. Neural circuit mechanisms of social behavior. *Neuron* **98**, 16–30 (2018).
13. Eliava, M. et al. A new population of parvocellular oxytocin neurons controlling magnocellular neuron activity and inflammatory pain processing. *Neuron* **89**, 1291–1304 (2016).
14. Lima, S. Q., Hromádka, T., Znamenskiy, P. & Zador, A. M. PINP: a new method of tagging neuronal populations for identification during in vivo electrophysiological recording. *PLoS ONE* **4**, e6099 (2009).
15. Leng, T., Leng, G. & MacGregor, D. J. Spike patterning in oxytocin neurons: capturing physiological behaviour with Hodgkin–Huxley and integrate-and-fire models. *PLoS ONE* **12**, e0180368 (2017).
16. Netser, S., Haskal, S., Magalnik, H. & Wagner, S. A novel system for tracking social preference dynamics in mice reveals sex- and strain-specific characteristics. *Mol. Autism* **8**, 53 (2017).
17. Maícas-Royo, J., Leng, G. & MacGregor, D. J. A predictive, quantitative model of spiking activity and stimulus-secretion coupling in oxytocin neurons. *Endocrinology* **159**, 1433–1452 (2018).
18. Portfors, C. V. Types and functions of ultrasonic vocalizations in laboratory rats and mice. *J. Am. Assoc. Lab. Anim. Sci.* **46**, 28–34 (2007).

19. Lenschow, C. et al. Sexually monomorphic maps and dimorphic responses in rat genital cortex. *Curr. Biol.* **26**, 106–113 (2016).
20. Althammer, F. & Grinevich, V. Diversity of oxytocin neurones: beyond magno- and parvocellular cell types? *J. Neuroendocrinol.* **30**, e12549 (2018).
21. Johnson, Z. V. et al. Central oxytocin receptors mediate mating-induced partner preferences and enhance correlated activation across forebrain nuclei in male prairie voles. *Horm. Behav.* **79**, 8–17 (2016).
22. Hung, L. W. et al. Gating of social reward by oxytocin in the ventral tegmental area. *Science* **357**, 1406–1411 (2017).
23. Okabe, S., Yoshida, M., Takayanagi, Y. & Onaka, T. Activation of hypothalamic oxytocin neurons following tactile stimuli in rats. *Neurosci. Lett.* **600**, 22–27 (2015).
24. Bru, T., Salinas, S. & Kremer, E. J. An update on canine adenovirus type 2 and its vectors. *Viruses* **2**, 2134–2153 (2010).
25. Gunaydin, L. A. et al. Natural neural projection dynamics underlying social behavior. *Cell* **157**, 1535–1551 (2014).
26. VanRyzin, J. W. et al. Microglial phagocytosis of newborn cells is induced by endocannabinoids and sculpts sex differences in juvenile rat social play. *Neuron* **102**, 435–449.e6 (2019).
27. Erny, D. et al. Host microbiota constantly control maturation and function of microglia in the CNS. *Nat. Neurosci.* **18**, 965–977 (2015).
28. Wickersham, I. R. et al. Monosynaptic restriction of transsynaptic tracing from single, genetically targeted neurons. *Neuron* **53**, 639–647 (2007).
29. Manning, M., Stoev, S., Cheng, L. L., Ching Wo, N. & Chan, W. Y. Design of oxytocin antagonists, which are more selective than atosiban. *J. Pept. Sci.* **7**, 449–465 (2001).
30. Grund, T. et al. Neuropeptide S activates paraventricular oxytocin neurons to induce anxiolysis. *J. Neurosci.* **37**, 12214–12225 (2017).
31. Rhodes, C. H., Morriell, J. I. & Pfaff, D. W. Immunohistochemical analysis of magnocellular elements in rat hypothalamus: Distribution and numbers of cells containing neurophysin, oxytocin, and vasopressin. *J. Comp. Neurol.* **198**, 45–64 (1981).
32. Uvnäs-Moberg, K., Handlin, L. & Petersson, M. Self-soothing behaviors with particular reference to oxytocin release induced by non-noxious sensory stimulation. *Front. Psychol.* **5**, 1529 (2015).
33. Walker, S. C., Trotter, P. D., Swaney, W. T., Marshall, A. & Mcglone, F. P. C-tactile afferents: Cutaneous mediators of oxytocin release during affiliative tactile interactions? *Neuropeptides* **64**, 27–38 (2017).
34. Brown, C. H., Bains, J. S., Ludwig, M. & Stern, J. E. Physiological regulation of magnocellular neurosecretory cell activity: integration of intrinsic, local and afferent mechanisms. *J. Neuroendocrinol.* **25**, 678–710 (2013).
35. Hoffman, G. E. & Lyo, D. Anatomical markers of activity in neuroendocrine systems: are we all 'Fos-ed out'? *J. Neuroendocrinol.* **14**, 259–268 (2002).
36. Hoffman, G. E., Smith, M. S. & Verbalis, J. G. c-Fos and related immediate early gene products as markers of activity in neuroendocrine systems. *Front. Neuroendocrinol.* **14**, 173–213 (1993).
37. Hasan, M. T. et al. A fear memory engram and its plasticity in the hypothalamic oxytocin system. *Neuron* **103**, 133–146.e8 (2019).
38. Stern, J. E. Electrophysiological and morphological properties of pre-autonomic neurones in the rat hypothalamic paraventricular nucleus. *J. Physiol.* **537**, 161–177 (2001).
39. Bosch, O. J. Brain oxytocin correlates with maternal aggression: link to anxiety. *J. Neurosci.* **25**, 6807–6815 (2005).
40. Fenelon, V. S., Poulain, D. A. & Theodosis, D. T. Fos synthesis and neuronal activation: analysis of Fos immunoreactivity in identified magnocellular neurons during lactation. *Ann. N.Y. Acad. Sci.* **689**, 508–511 (1993).
41. Neumann, I., Douglas, A. J., Pittman, Q. J., Russell, J. A. & Landgraf, R. Oxytocin released within the supraoptic nucleus of the rat brain by positive feedback action is involved in parturition-related events. *J. Neuroendocrinol.* **8**, 227–233 (1996).
42. Augustine, R. A. et al. Prolactin regulation of oxytocin neurone activity in pregnancy and lactation. *J. Physiol.* **595**, 3591–3605 (2017).
43. Kennett, J. E. & McKee, D. T. Oxytocin: an emerging regulator of prolactin secretion in the female rat. *J. Neuroendocrinol.* **24**, 403–412 (2012).
44. Dölen, G., Darvishzadeh, A., Huang, K. W. & Malenka, R. C. Social reward requires coordinated activity of nucleus accumbens oxytocin and serotonin. *Nature* **501**, 179–184 (2013).
45. McGlone, F., Wessberg, J. & Olausson, H. Discriminative and affective touch: sensing and feeling. *Neuron* **82**, 737–755 (2014).
46. Leng, G. & Ludwig, M. Reply to: Improving research standards to restore trust in intranasal oxytocin. *Biol. Psychiatry* **79**, e55–e56 (2016).
47. Meyer-Lindenberg, A., Domes, G., Kirsch, P. & Heinrichs, M. Oxytocin and vasopressin in the human brain: social neuropeptides for translational medicine. *Nat. Rev. Neurosci.* **12**, 524–538 (2011).
48. Grinevich, V. & Neumann, I. D. How puzzle stones from animal studies translate into psychiatry. *Mol. Psychiatry* https://doi.org/10.1038/s41380-020-0802-9 (2020).

Methods

Animals. Female Wistar rats aged 4–8 weeks were purchased from Janvier and housed under standard laboratory conditions (12-h light:dark cycle, lights on at 07:00, 22–24 °C, 50 ± 5% humidity, free access to food and water). All experiments were conducted under license G-102/17 (authorized by the German Animal Ethics Committee of the Baden Württemberg, Regierungspräsidium Karlsruhe) and in accordance with German law, under license 3668-2016011815445431 from the French Ministry and EU regulations. In total, 194 rats were used, of which 15 were excluded due to mistargeting or insufficient expression of viral vectors (Supplementary Table 3).

Viruses. The rAAVs (serotype 1/2) used in the present study (carrying the conserved region of the OT promoter and genes of interest in direct or 'floxed' orientations) were cloned and produced as reported previously[5,13,30,49]. HEK293T cells (Addgene, catalog no. 240073) were used for the virus production. The rAAVs produced included: rAAV-OTp-mCherry/ Venus, rAAV-OTp-ChR2-mCherry, rAAV-OTp-DIO-ChR2-mCherry, rAAV-OTp-DIO-hM3D(Gq)-mCherry, rAAV-OTp-DIO-hM4D(Gi)-mCherry, rAAV-OTp-DIO-GFP, rAAV-OTp-DIO-ChR2-EYFP, rAAV-OTp-GCaMP6s, rAAV-OTp-TCB (TVA fused mCherry) and rAAV-Ef1A-DIO-oG. The CAV2-CMV-Cre was purchased from the Institute of Molecular Genetics[24]. The rAAVretro-Ef1A-Cre was purchased from the Salk Institute Viral Vector Core. Modified rabies virus was produced at the Gene Center Rabies laboratory, Ludwig Maximilian University.

Stereotactic injections of viral vectors. For stereotactic injections of viruses, rats were anesthetized with a mixture of ketamine (65 mg per kg body weight) and xylazine (14 mg per kg birth weight). The rAAV genomic titers were determined using QuickTiter AAV Quantitation Kit (Cell Biolabs, Inc.) and reverse transcription PCR using the ABI 7700 cycler (Applied Biosystems). The rAAV titers were between 10^9 and 10^{10} genomic copies $μl^{-1}$. We injected 300 nl per PVN. CAV2-Cre was purchased from the Institute of Molecular Genetics (diluted to 10^9 genomic copies $μl^{-1}$, 300 nl per SON). Viruses were injected via a glass pipette into the target regions at 150 nl min^{-1} using a syringe pump as previously described[50]. Coordinates were chosen in accordance with a rat brain atlas[51] for PVN (anteroposterior (A/P): −1.8 mm; mediolateral (M/L): ±0.3 mm; dorsoventral (D/V): −8 mm), SON (A/P: −1.8 mm, M/L: ±1.2 mm, D/V: −9.25 mm) and posterior pituitary (A/P: −5.6 mm, M/L: ±0.1 mm, D/V: −10.5 mm). Verification of injection and implantation sites and expression of genes of interest was confirmed in all rats post hoc in 50-μm sections containing the PVN and SON (Histology).

Ex vivo experiments. *Slice preparation.* Some 4–8 weeks after injection of the viruses into the PVN and SON of 5-week-old virgin female rats, animals were anesthetized using ketamine (Imalgene 90 mg kg^{-1}) and xylazine (Rompun, 10 mg kg^{-1}) administered intraperitoneally. Then, intracardiac perfusion was performed with an ice-cold, N-methyl-D-glucamine (NMDG)-based artificial cerebrospinal fluid (aCSF), which contained (in mM): NMDG (93), KCl (2.5), NaH$_2$PO$_4$ (1.25), NaHCO$_3$ (30), MgSO$_4$ (10), CaCl$_2$ (0.5), 4-(2-hydroxyethyl)-1-piperazine-ethanesulfonic acid (Hepes) (20), D-glucose (25), L-ascorbic acid (5), thiourea (2), sodium pyruvate (3), N-acetyl-L-cysteine (10) and kynurenic acid (2). The pH was adjusted to 7.4 using either NaOH or HCl, after bubbling in 95% O$_2$/5% CO$_2$ gas. Rats were then decapitated, the brains removed and 350-μm-thick coronal slices containing the hypothalamus were obtained using a Leica VT1000s vibratome. Slices were warmed for 10 min in 35 °C NMDG aCSF and placed for a minimum of 1 h in a holding chamber at room temperature, containing normal aCSF. Normal aCSF, also used during all ex vivo experiments, is composed of (in mM): NaCl (124), KCl (2.5), NaH$_2$PO$_4$ (1.25), NaHCO$_3$ (26), MgSO$_4$ (2), CaCl$_2$ (2) and D-glucose (15), adjusted to a pH value of 7.4 with HCl or NaOH, and continuously bubbled with 95% O$_2$/5% CO$_2$ gas. All aCSF was checked for osmolality and kept to a value of between 305 and 310 mosmol. In electrophysiology or calcium-imaging experiments, slices were transferred from the holding chamber to an immersion recording chamber and superfused at a rate of 2 ml min^{-1}. CNO-containing solution (10 μM) was applied in a bath through a 6-min-long pumping episode, corresponding to several times the volume of the recording chamber (two applications per slice maximum). All ex vivo experiments were conducted at room temperature.

Patch-clamp recording. Whole-cell patch-clamp recordings were visually guided by infrared oblique light videomicroscopy (DM-LFS; Leica), using 4- to 9-MΩ borosilicate pipettes filled with a KMeSO$_4$-based intrapipette solution composed of (in mM): KMeSO$_4$ (135), NaCl (8), Hepes (10), ATPNa$_2$ (2) and GTPNa (0.3). The pH was adjusted to 7.3 with KOH and osmolality checked to be 300 mosmol l^{-1}, and adjusted with sucrose if needed. Data were acquired with an Axopatch 200B (Axon Instruments) amplifier and digitized with a Digidata 1440A (Molecular Devices). Series capacitances and resistances were compensated electronically. Data were sampled at 20 kHz and low-pass filtered at 5 kHz using the pClamp10 software (Axon Instruments). Further analysis was performed using Clampfit 10.7 (Molecular Devices) and Mini analysis v.6 software (Synaptosoft) in a semi-automated fashion (automatic detection of events with chosen parameters followed by a visual validation).

Evoked activity. To test the effects of CNO on neuronal excitability ex vivo, we used a current step method. For this purpose, we make PVN → SON projecting neurons express the DREADD receptors by injecting rats' SON with a CAV2-Cre virus (rAAV-CAV-Cre) and PVN with an OT-specific Cre-inducible DREADD construct (rAAV-OTp-DIO-hM4D(Gi)-mCherry or OTp-DIO-hM3D(Gq)-mCherry). Then, 6–8 weeks after infection, coronal slices were prepared and fluorescent neurons (indicative of the viral expression) were selected for whole-cell patch-clamp recordings. After establishing the clamp, neurons were recorded in current clamp mode with 0 pA injected. To test the effects of DREADD activation—hM4D(Gi) or hM3D(Gq)—neurons were subjected to the following current steps: for hM4D(Gi), neurons received an injection of an −100 pA negative current to hyperpolarize the neuron membrane (reaching −100 mV) before each step. These steps start at −80 pA and increase by 20 pA, reaching +120 pA. For hM3D(Gq), steps start at −20 pA and increase by 10 pA, reaching 80 pA. To quantify the effects of DREADD activation, the number of APs triggered by these steps was evaluated.

Spontaneous activity. To evaluate the effect of DREADD activation on neuronal activity, neurons were also recorded 2 min before and after CNO exposure in voltage or current clamp mode. In these cases, the frequency of the PSCs or APs was quantified.

Identification of parvOT and magnOT. The identity of PVN OT neurons was verified through a current step protocol[52]; this method has been used in several other studies to allow discrimination between parvocellular and magnocellular neurons[13,53–56]. Neurons received an injection of an −100 pA current to hyperpolarize the neuron membrane (reaching −100 mV) before each step. These steps start at 0 pA and increase by 20 A, reaching +60 pA. To discriminate between parvOT and magnOT, we have measured the hyperpolarizing notch and the T-outward rectification.

ChR2 stimulation of SON's parvOT neurons. To decipher the connection between SON parvOT neurons and PVN magnOT neurons, we used an optogenetic strategy. First, we identified PVN OT neurons by injecting rats' PVN with an rAAV containing the coding sequence of the fluorescent marker Venus, under the control of the OT promoter (OTp-Venus). Then, we aimed to specifically activate SON → PVN projection by using a combination of two rAAVs: the first was injected in the SON and induces the expression of the Cre recombinase in SON-targeting neurons, and the second was injected into the PVN to allow the expression of the ChR2 in OT neurons after a Cre-dependent recombination (OTp-DIO-ChR2-mCherry). Then, 6–8 weeks after infection, coronal slices containing the PVN were prepared and the Venus$^+$/mCherry$^-$ neurons were selected for whole-cell patch-clamp recordings. This combination of fluorescent markers allows us to select PVN OT neurons that are not directly targeting the SON.

Neurons were recorded for 2 min in the voltage clamp to establish the baseline frequency of PSCs and, then, we performed an optogenetic stimulation of ChR2-expressing oxytocinergic neurons by applying light pulses (10 ms at 30 Hz for 20 s) using light source X-Cite 110LED from Excelitas Technologies, through a GFP filter, controlled by a Clampex-driven TTL. Neurons were also recorded during the ChR2 stimulation to observe that the neurons were not expressing ChR2 itself. Finally, we continued to recorded 10 min after the stimulation to observe the effect of the SON parvOT neuron stimulation on the PSC frequency of the recorded neurons. PSCs were detected using Mini analysis v.6 software (Synaptosoft).

Calcium imaging. To test whether the chemogenetic activation of PVN → SON projecting oxytocinergic neurons can modify the intra-PVN microcircuit activity, we used an ex vivo calcium-imaging approach. To this end, rats' SON were infected with CAV2-Cre and the PVN with a virus allowing the expression of hM3D(Gq) under the control of OT promoter after a Cre-dependent recombination (OTp-DIO-hM3D(Gq)-mCherry). We also made PVN OT neurons express the calcium indicator GCaMP6s using a third viral vector (rAAV-OTp-GCaMP6s). Then, 6–8 weeks after infection, coronal slices containing the PVN were prepared and neurons that were positive for GCaMP, but negative for mCherry, were recorded. To perform this fluorescence microscopy, we used a Zeiss Axio examiner microscope with a ×40 water immersion objective (numerical aperture of 1.0), mounted with an X-Light Confocal unit—CRESTOPT spinning disk. Images were acquired at 5 Hz with an optiMOS sCMOS camera (Qimaging). Neurons within a confocal plane were illuminated for 100 ms at wavelength $λ = 475$ nm using a Spectra 7 LUMENCOR. The different hardware elements were synchronized through the MetaFluor software (Molecular Devices, LLC). Neuron calcium levels were measured in a hand-drawn region of interest (ROI). In all recordings, the Fiji rolling ball algorithm was used to increase the signal:noise ratio. Recordings in which movements/drifts were visible were discarded.

Offline data analysis was performed using a customized python-based script.

First, a linear regression and a median filter were applied to each trace. Peaks were then detected using the 'find_peaks' function of the SciPy library.

More precisely, fluorescence variation was identified as a calcium peak if its prominence exceeded twice the s.d. and if the maximum peak value surpasses three fluorescence units. The ROIs with zero calcium variations were excluded from the analysis. The remaining ROIs were considered as living neurons and the number of peaks quantified before and after the drug application. The AUC was estimated as the sum of the local area of each peak to avoid a biased AUC estimation due to baseline drift. All these data were normalized according to the duration of the recording and neurons were labeled as 'responsive' when their AUC or number of peaks was increased by at least 20% after drug application. As the time post-stimulation is longer than the baseline, the probability of observing a spontaneous calcium peak is stronger post-stimulation. To avoid this bias, neurons with only one calcium peak during the whole recording were removed from responsive neurons. The response probability was calculated as the number of responsive neurons with at least 1 calcium event per time bin (30 s) divided by the number of responsive neurons in each recording. Finally, all data were normalized per slice and this result was used as the statistical unit. All data were compared using paired statistical analysis (before versus after drug application) and the results are expressed as a ratio (baseline:drug effect), with a ratio of 1 meaning neither an increase nor a decrease in the measured parameter.

In vivo opto-electrode recordings. *Implantation of opto-electrodes.* Silicon probes (A1x32-Poly3-10mm, NeuroNexus) containing a 32-channel single shank combined with an optic fiber (diameter: 100 μm, Thorlabs) (opto-electrodes) were used in acute (anesthetized and head-fixed) recordings. For freely moving recordings, 32-channel chronic opto-electrodes were hand made, consisting of 8 tetrodes and 1 specially designed microdrive. The microdrives and tetrodes were manually assembled as described previously[57]. The tetrodes were made with 0.0005-inch tungsten wires (Stablohm 675, California Fine Wire Company). Eight tetrodes and an optic fiber (200 μm, Thorlabs) were loaded into the microdrive via a guiding tube and were arranged in parallel order. Assembled opto-electrodes were gold plated and the impedance of each channel was measured between 250 and 350 kΩ. For implantation, rats were anesthetized with 2% isoflurane and placed in a stereotaxic frame. Bregma position and horizontal level were aligned during the implantation. Opto-electrode tips were implanted into the target location and the microdrive was fixed on the skull by six microscrews (Knupfer) and dental cement (Paladur, Heraeus Kulzer).

Optogenetic identification of OT neurons. Electrophysiological signals were acquired by an Open-Ephys acquisition board and sampled at 30 kHz. To identify ChR2+ OT neurons in the PVN, pulses of blue light ($\lambda = 473$ nm, DreamLasers) were delivered by the optic fiber while recording extracellular electrical activity of the neurons. The pulse train was controlled by a pulse generator (Master9, A.M.P.I.), and pulses had a duration of 10 ms and were applied at stimulation frequencies of 1, 5 and 10 Hz. In each session, the laser output at the optic fiber terminal was measured as 20 mW mm^{-2}. Neurons with a clear time-locked response to light pulses (spikes within 2–8 ms from onset of pulses) were classified as OT neurons (Extended Data Fig. 1e).

Analysis of spike waveforms. Spike sorting was done manually in Plexon Offline Sorter v.4.0 (Plexon, Inc.), with tetrode mode. The raw data were filtered at 250 Hz with a Butterworth high-pass filter, and waveform detection thresholds were placed at −0.5 to +0.8% of the analog-to-digital converter range (or −0.32 or ~−0.51 mV), depending on the signal:noise ratio. Magnocellular neurons have spikes with a width at half-amplitude of about 0.5 ms, an absolute refractory period of about 2.5 ms and a long relative refractory period, reflecting a prominent hyperpolarizing afterpotential[17]. Therefore, the sample length in waveform detection was set to 1.4 ms (400 μs pre-threshold period; at the 30-kHz sampling rate, a single waveform consists of 42 data points and, in the tetrode waveform, each unit detected 168 data points), and dead time was set to 1.2 ms. Next, the detected waveforms were aligned at the valley point, when the neurons were depolarized at their maximum, and principal component analysis and slice features of waveform were plotted and projected into 3D space for visual separation of clusters into presumptive single units. The timestamp feature was used to exclude mechanical noise recorded at the same time across four channels among the tetrodes. In different recording sessions (for example, OF and social interaction), we analyzed whether the features of spike waveforms remain consistent with the 3D plot results. After clustering, units with a minimum interevent interval exceeding 2,500 μs were accepted as single hypothalamic neurons. Units displaying minimum interevent intervals between 1,200 and 2,500 μs were recognized as arising from multiple neurons and excluded from the statistics of the study.

Statistical analyses of spike patterning. From segments of stationary activity recorded in OF conditions, interspike interval distributions were constructed to verify that these were consistent with distributions characteristic of OT neurons under basal conditions recorded in anesthetized rats[58]. To quantify the regularity of spike firing, we calculated the index of dispersion (IoD) of firing rate in 1-s bins as the ratio of the variance to the mean. For events that arise as a result of a random process that is invariant in time, the IoD will be equal to 1, independent of the

mean rate and the binwidth. If events arise more regularly than chance, the IoD will be <1, and if they are more variable than expected by chance—as when spikes occur in clusters or bursts—the IoD will be >1.

In OT neurons, spikes cannot arise purely randomly because of the refractory period, and the IoD reduces slightly with increasing firing rate because, at higher rates, the relative refractory period is larger as a proportion of the mean interspike interval. The IoD also reduces with increasing binwidth because OT neurons also display a prolonged activity-dependent afterhyperpolarization that acts to stabilize mean firing rates over a timescale of seconds. Collectively the known intrinsic membrane properties of rat OT neurons, as tested through computational models, imply that, if spikes arise as a result of a purely random and time-invariant process, then the IoD of the firing rate in 1-s bins will be in the range 0.3–1.0 for neurons firing at up to 6 spikes s^{-1}, depending on firing rate and individual variability in membrane properties[17,58].

LFPs in the PVN. Local field potentials (LFPs) were sampled at 1 kHz with a low-pass filter. Subsequent analysis was done using customized MATLAB (MathWorks) scripts. We estimated the power spectrum density of the LFP signal using a multi-tapper approach, based on Thomson's method ('pmtm' function). Spectrograms were computed for each recording using a standard 'spectrogram' function. The power of theta oscillations was calculated as an average of power spectrum densities in the range 5–10 Hz. Phase-lock analysis was performed to investigate the relationship between theta oscillations in the PVN and the timing of spikes in OT neurons. The phase of the oscillatory activity was extracted with Hilbert's transformation ('Hilbert's' function) and converted into angle degrees. Then, we used Rayleigh's tests for circular uniformity, which indicate whether there is a significant correlation between the timing of spikes and a specific phase of the theta cycle (Extended Data Fig. 1h–j).

In vivo fiber photometry. *Optic-guided implantation of optic fibers.* We injected a modified adenovirus (AAV-OTp-GCaMP6s) bilaterally into the PVN or SON to transduce expression of the Ca^{2+} indicator GCaMP6s in OT neurons, and verified that this was expressed cell specifically (87 ± 4% of OT neurons, $n = 1,371$ neurons, $n = 4$ rats, Fig. 4p). Optic fibers (M127L01 diameter 400 μm, numerical aperture 0.50, length 10 mm, Thorlabs) were implanted ~100 μm above the dorsal border of the PVN (A/P: −1.8 mm; M/L: 0.35 mm; D/V: −7.85 mm) or SON (A/P: −1.25 mm; M/L: 1.90 mm; D/V: −9.0 mm) under 1.5% isoflurane anesthesia. Four 1-mm screws (Knupfer) and a metal implant guide (OGL, Thorlabs) were attached to the skull with OptiBond FL (Kerr) and fixed using dental cement (Paladur, Heraeus Kulzer).

During implantation, the implantable cannula was fixed in an adaptor (ADAL3, Thorlabs) attached to a stereotactic holder, whereas the other end of the cannula was connected through a pre-bleached Patch cord (Thorlabs, FP400URT) to the photodetector and light-emitting diode (LED) of the fiber photometry system (FOM, NPI Electronic). The digitized photometry signal was monitored and recorded via a digital input/output board (Open-Ephys) to the DAQ system (Open Ephys) with 0.1- to 20-Hz bandpass filter and 20-s timescale set in to visualize the Ca^{2+} signal online, while the cannula tip was gradually lowered into the PVN at 1 mm min^{-1}. When the optic fiber tip was close to the PVN where GCaMP6s was expressed, a slight increase in the signal baseline and a minor spontaneous fluctuation could be visually detected. During implantation, rats were under 1.5% isoflurane anesthesia and the body temperature was kept stable at 37 °C by a heating plate (Temperature controller 69001, RWD Life Science). The LED power in the fiber photometry system was set at a constant value between 5 and 10 mW mm^{-2}. The fiber photometry recordings were conducted after 1 week of recovery from the implantation. Fiber photometry raw data were sampled at 30 kHz in Open-Ephys GUI and analyzed with customized MATLAB scripts.

Fiber photometry data analysis. Digitized optical signal acquired from the fiber photometry system was first downsampled at 3,000 Hz and then low-pass filtered (MATLAB 'butterworth' function) at 10 Hz to exclude noise at higher frequency. Second, to correct the baseline drifting due to photo-bleaching of fluorophores, we fitted the signal with a polynomial curve (MATLAB 'polyfit' function) and subtracted it from the signal. Next, we smoothed the signal with a Savitzky–Golay filter (MATLAB 'smooth' function, option 'sgolay'). For each experiment, the signal F was converted to $\Delta F/F_0$ by:

$$\Delta F/F(t) = \frac{F(t) - F_0}{F_0}$$

where t is time and F_0 was calculated as the average value of F of a 600-s recording at the start of the experiment. The data were subdivided into 1-min bins and the mean $\Delta F/F_0$ was calculated for each bin. We detected calcium transients similar to those reported in our previous study[59]. Finally, we calculated the AUC of the Ca^{2+} signal (MATLAB 'trapz' function) to estimate the cumulative fluorescence for each bin and normalized the AUC to values from 0 to 1. Values of normalized AUC were displayed in a 1-min bin and averaged in 30-min bins. The ratios of AUCs between experimental and control conditions were used for quantitative analysis and called 'relative AUC increase'.

Application of airpuffs and OT neuron response. Airpuffs from a pressurized air can (Toolcraft, 20793T, 400 ml) were applied through a stiff micropipette tip with a 2-mm opening positioned 10–15 mm above the skin in an area of ~2 cm². A plastic cover with 2-cm holes was placed above the rat's body to restrict the area of stimulation. The controlled air pressure was 1.139 g cm⁻³. During in vivo electrophysiology recordings, in each stimulation point, five airpuffs (duration 0.2 s, interval between puffs 1 s) were delivered in sequence with intervals of 1 min between sequences (Fig. 2a and Extended Data Fig. 4). During fiber photometry recordings, one airpuff (duration 1 s) was applied every 1 min (Fig. 2e–j).

OT neuron response to airpuff stimulations. We applied airpuffs to the skin of three regions of the rat's dorsal body area (anterior, central and posterior parts), two regions of the rat's ventral area (abdomen and anogenital area) and the whiskers on both sides. We considered a recorded neuron as responsive to airpuff stimulations if the average firing rate after (from 0 s to 2 s) stimulus onset increased by at least twice the s.d. of the baseline activity (2 s before stimulus onset). Onset of the response was calculated as the time at which the firing rate of a responsive neuron increased by 1× the s.d. of the baseline activity. We recorded the activity of $n = 23$ OT neurons in response to airpuffs applied to the rat's dorsal body area, which showed variable response latencies of up to 30 s (Extended Data Fig. 4a,b); 10 of those neurons exhibited a response within 1 s after stimulus onset and are shown in Fig. 2a,b.

Blood sampling and plasma OT measurements. To monitor neurohypophyseal OT release after chemogenetic activation of hypothalamic parvOT neurons, we performed blood sampling from the jugular vein in urethane-anesthetized rats. After surgery, rats were placed on a heating pad for the rest of the experiment to maintain constant body temperature. The jugular vein catheter was connected to a 1-ml syringe containing sterile heparinized saline (30 U ml⁻¹); 45 min before, and 45 min as well as 90 min after, intraperitoneal CNO, 500 μl blood was drawn (Fig. 4q,r), which was replaced by 500 μl sterile saline. After each sample, the catheter was filled with heparinized saline to avoid blood clotting. Blood samples were collected in ethylenediaminetetraacetic acid (EDTA) tubes (Bayer) on ice, centrifuged (5,000g, for 10 min at 4 °C), and 200-μl plasma samples were stored at −80 °C before extraction and OT quantification by radioimmunoassay. The OT content in extracted plasma was analyzed by a highly sensitive radioimmunoassay with a detection limit of 0.1 pg and cross-reactivity <0.7% (RIAgnosis)[60,61].

Behavior. Starting from 14 d before behavioral tests, vaginal smears were collected to monitor ovarian cycle. Rats in the metestrus, proestrus and estrus phases were excluded from the experiments and reintroduced once they reached diestrus.

Behavioral tests were conducted in an arena (material nonabsorbent to odors) with dimensions 60 × 60 × 60 cm³ under dim light conditions (<20 lux; lux-meter SO 200K, Sauter). On the day before the test, the experimental rat was exposed to the arena for 15 min for habituation. The arena was cleaned with 70% ethanol after each session to eliminate residual odors. Experimental and stimulus rats were housed in separate cages and had not previous encountered each other before the social interaction tests. The same rat was exposed to social interaction tests twice on separate days, each time with a different social stimulus rat so that the experimental paradigm always represented interaction with a novel, unfamiliar conspecific.

OF test. The experimental rat was placed in a corner of the arena and was allowed to freely explore the environment. These tests served as a 'baseline' for social interaction tests.

FSI test. The experimental and the stimulus rats were placed in opposite corners of the arena at the same time and were allowed to freely interact with each other and/or explore the environment.

CSI test. For this test, two Plexiglas transparent meshes (dimensions 20 × 30 × 1 cm³) provided with three openings/holes (dimensions 15 × 0.75 cm²) were placed in two opposite corners of the arena. The mesh separated a little triangular area (14 × 14 × 20 cm³, corresponding to ~3% of the total area of the arena) from the rest of the arena (central compartment). The experimental rat was placed in the central compartment whereas the stimulus rat was placed in one of the two little compartments. The two rats were able to see, hear and smell each other through the openings, but they were not able to touch each other.

Chemogenetic inhibition or activation of parvocellular OT neurons by DREADD. To selectively activate or inhibit parvocellular OT neurons, rats were injected with rAAV-OTp-DIO-hM3D(Gq)-mCherry (Parvo-Gq group), rAAV-OTp-DIO-hM4D(Gi)-mCherry (Parvo-Gi group) or rAAV-OTp-DIO-GFP (Parvo-GFP control group) into the PVN and CAV2-Cre into the SON, as previously described[13].

All groups (Parvo-Gq, Parvo-Gi and Parvo-GFP) were subjected to the same protocol. On day 1 experimental rats were exposed to the OF arena for 15 min for habituation. On day 2, the experimental rat was injected intraperitoneally

with either CNO or saline solution 60 min before starting the tests, and was then subjected to one CSI and one FSI session for 5 min each.

Intracerebroventricular administration of OTR antagonist. Guide cannulas were implanted above the lateral ventricle for intracerebroventricular infusion of the OTR antagonist *des*-Gly-NH₂,d(CH₂)₅(Tyr(Me)²,Thr⁴)OVT[29]. OTR antagonist 0.75 μg per 5 μl (ref. [30,62]) was infused 15 min before the behavioral tests. Four groups of rats were studied, which received intraperitoneal injection and intracerebroventricular infusion of saline/saline, CNO/saline, saline/OTR antagonist or CNO/OTR antagonist, respectively.

Video and audio analyses of behavior. The videos were recorded using a GigE color HD camera (Basler AG). The tracks of the experimental and stimulus rats were extracted from videos using two software packages: Ethovision XT v.11.5 (Noldus) and MATLAB Toolbox idTracker (MathWorks). The results of the two software packages were compared and crossvalidated. The distance moved by each rat, the velocity, time spent in different areas of the arena, and distance between rats and time spent in close proximity were calculated automatically. Social interactions were also analyzed manually to classify social behaviors into different categories: 'sniffing', 'chasing', 'crawling on top', 'being crawled' and 'head-to-head' approaching; the time spent by the experimental rat for each behavioral category was used for all analyses. Manual scoring of social behavior scoring was done by a researcher (different from the person who performed the experiment) who was blind to treatment conditions.

Ultrasonic vocalizations were recorded with an ultrasound microphone (Avisoft-Bioacustic) and analyzed using Avisoft-SASlab Pro v.5.2 software. After calculation of a sound spectrogram, the vocalization time, duration and frequency were extracted. Each 'call' was classified into a non-social (peak frequency ~22 kHz) or an appetitive/social (peak frequency ~50 kHz) call. Social vocalizations were further classified into trills (<10 ms), single component calls (>10 ms, not modulated) and complex vocalizations (>10 ms, frequency modulated or combined)[63].

Freely moving single unit recordings: experimental groups. Open field and FSI groups: experimental rats implanted with opto-electrodes for single-unit recordings in the PVN were subjected to one OF session and one FSI session for 10 min each. Between the two sessions the rat was placed in the home cage (single housed) for 15 min.

Open field, CSI and FSI groups: experimental rats implanted with opto-electrodes for single-unit recordings in the PVN were subjected to one OF, one CSI and one FSI session for 10 min each, without pauses in between. Stimulus rats were placed in one of the little chambers separated by a Plexiglas mesh at the start of the CSI session; the wall was then lifted up (Fig. 6b) at the start of the FSI session, allowing the stimulus rat to join the experimental rat in the central compartment.

Histology. Anesthetized rats were transcardially perfused with phosphate-buffered saline (PBS) followed by 4% paraformaldehyde (PFA). Brains were dissected out and post-fixed overnight in 4% PFA at 4 °C with gentle agitation. Then, 50-μm vibratome coronal sections containing the PVN and the SON were cut and collected. Immunohistochemistry was performed on free-floating sections using the following antibodies: anti-OT (PS38, 1:2,000; mouse; kindly provided by H. Gainer), anti-OT (T-5021, 1:50,000, Peninsula, guinea-pig), anti-SYN (Abcam, anti-rabbit, ab32127, 1:1,000), anti-Ds-Red (Clontech, catalog no. 632397, 1:1,000; rabbit), anti-GFP (Abcam, ab13970, 1:1,000, chicken), anti-c-fos (Cell Signaling, catalog no. 9F6, 1:500, rabbit), anti-Fluorogold (Protos Biotech. catalog no. NM-101, 1:1,000, guinea-pig) and anti-Cre (Novagen, catalog no. 69050, 1:2,000, mouse). Further information on validation of primary antibodies can be found in the Nature Research Reporting Summary. The signals were visualized with the following secondary antibodies: CysTyr3 conjugate (711-165-152) or CysTyr5 conjugate (Jackson Immuno-Research Laboratories, 115-175-146) or Alexa 488 (Invitrogen, A11039) and Alexa 594 (Invitrogen, A11012) and Alexa-594 (Jackson Immuno-Research Laboratories, 715-585-151) and Alexa-647 (Jackson Immuno-Research Laboratories, 713-645-147). All secondary antibodies were diluted 1:500.

Fluorogold treatment and visualization. To discriminate between magnOT and parvOT neurons, rats received a single injection of Fluorogold (Santa Cruz Biotechnology, 15 mg per kg birth weight intraperitoneally) 7 d before the perfusion. Brain sections were stained with a primary antibody for Fluorogold (guinea-pig anti-FG, dilution 1:1,000, Protos Biotech Corp) and Fluorogold immunosignal was visualized by secondary antibodies conjugated with CysTyr3 (Jackson Immuno-Research Laboratories, goat anti-rabbit, dilution 1:500). The co-localization of Fluorogold, OT and c-fos signals was manually quantified in the PVN ($n = 4$ rats, 6 sections per brain).

Images of immunostained tissue sections. All images were acquired on a Leica TCS SP5 (DKFZ Light Microscopy Facility), confocal laser-scanning microscope. Digitized images were analyzed using Fiji (National Institute of Mental Health) and Adobe Photoshop CS5 (Adobe).

Confocal microscopy and 3D IMARIS analysis. For the 3D reconstruction of OT neurons, we took z-stack images (50 μm depth, 1-μm steps, ×40 magnification) of PVN and SON using a Zeiss LSM 780 confocal microscope (1,024 × 1,024 pixels, 16-bit depth, pixel size 0.63 μm, zoom 0.7). Raw czi files were used for further analysis with IMARIS[26,27,64] software (v.9.31, Oxford Instruments: https://imaris.oxinst.com). First, IMARIS was used to reconstruct the cellular surface using the following customized settings: surface detail 0.700 μm (smooth); thresholding background subtraction (local contrast), diameter of largest sphere, which fits into the object: 2.00; color: base; diffusion transparency: 65%. After surface reconstruction, we used the filter function to remove unspecific background signals: filter: volume maximum 400 μm³. After deletion of all background signals the 'mask all' function was used to create the final surface reconstruction. Next, the surface reconstruction was used as the template for the filament reconstruction using the following customized settings: detect new starting points: largest diameter 7.00 μm, seed points 0.300 μm; remove seed points around starting points: diameter of sphere regions: 15 μm. Seed points were corrected for (either placed in or removed from the center of the somata) manually if the IMARIS algorithm placed them incorrectly. All surface and filament parameters were exported into separate Excel files and used for data analysis. For all quantifications, we used 6–8 ×40 z-stacks per animal (2 z-stacks per brain hemisphere). We used a computer suited for IMARIS analysis (Intel Core i7 8700 @ 3.2 GHz, 64 GB RAM, x-64-bit, Windows 10 Enterprise). All images used for analysis were taken with the same confocal settings (pinhole, laser intensity, digital gain and digital offset). Sholl analysis was performed using IMARIS in the filament reconstruction mode and individual datasets were exported into separate Excel files for further analysis. To assess the number of SYN⁺/GFP⁺ axons, we used a simplified version of the Sholl analysis, where we included only the first two to eight spheres (starting in the soma center) until either we could detect SYN⁺/GFP intersections or they were >2 μm apart from the border of the respective soma. The total amount of immunofluorescence (SYN) was calculated using the extract intensity/number of spots function. First, we created spheres that precisely engulfed the respective somata (parvOT and magnOT neurons) so that both ends of the cell soma (maximum diameter) touched the border of the respective sphere. To account for individual variability in roundness and surface area, we calculated the surface area for each individual OT cell using the surface reconstruction mode. Given that cells with a larger surface area occupy more 3D space within the artificially constructed sphere, which could confound precise quantification of SYN fluorescence, we adjusted each calculated value (SYN⁺ voxels per sphere) based on the surface area. Assuming an inverse almost-linear relationship between cell volume and the total amount of SYN fluorescence within a sphere, we calculated the degree of occupancy (that is, percentage) for each soma within the respective sphere. Finally, we calculated the final SYN⁺ voxels using the following equation: (Number of SYN⁺ voxels) × (Degree of occupancy). For the quantification along the dendrites we used spheres with a 10-μm radius along the dendrite for both parvOT and magnOT neurons.

Projection-specific, trans-synaptic retrograde tracing. Input tracing experiments were performed in female Wistar rats (aged 10–12 weeks). We used Rb-GFP[28] to monosynaptically retrogradely trace neurons projecting to parvOT and magnOT neurons. Rb-GFP selectively enters neurons expressing the avian sarcoma and leukosis virus receptor (TVA), and can spread presynaptically only from neurons expressing the rabies virus glycoprotein (we used the optimized glycoprotein, oG, used previously[65]). We injected a 300 nl mixture of 1:1 rAAV-OTp-TCB:rAAV-Ef1A-DIO-oG into the right PVN of female rats. Then, to specifically trace inputs to parvOT neurons, we injected rats (n = 5) with CAV2-CMV-Cre into the right SON (Extended Data Fig. 8a). In another group of rats (n = 5), we employed a similar strategy to express oG only in magnOT neurons: we injected an AAV retrograde-expressing Cre (rAAVretro-Ef1A-Cre) into the posterior pituitary (Extended Data Fig. 8c, based on previous work[66]). This strategy makes Rb-GFP selectively enter all OT neurons, but specifically spread retrogradely from neurons expressing oG (that is, parvOT or magnOT neurons). After 2 weeks, we injected 300 nl EnvA ΔG-EGFP into the right PVN, and, 7 d later, animals were perfused with 4% PFA. The number of projecting neurons was quantified from brain sections as follows: every third 50-μm section was imaged and neurons were counted, and then multiplied by three, to estimate the real number of inputs. GFP⁺ neurons on the injected hemisphere were counted and assigned to brain areas based on classifications of the Paxinos Mouse Brain Atlas[37], using anatomical landmarks in the sections visualized by tissue autofluorescence. Very few contralateral inputs were noticed and we therefore decided to neglect them. Although we had good infection at injection sites for both parvOT and magnOT groups (Extended Data Fig. 8g), starter neurons could not be reliably counted, because rabies virus toxicity prevented us correctly visualizing mCherry in the PVN. Thus, the analysis presented here does not take into account inputs to OT neurons from within the PVN. The percentage of inputs from each region was obtained by dividing the number of inputs from one region by the total number of inputs. Input regions that were detected in a subset of animals only were discarded from the analysis. We used unpaired, two-sided Student's t-tests to compare the total number of inputs with parvOT and magnOT neurons and χ² tests to compare proportions of inputs between regions.

We controlled TVA being selectively expressed in OT neurons by injecting control rats (n = 2) with rAAV-OTp-TCB in the PVN, and staining for OT. This revealed that most OT neurons expressed mCherry and no non-OT neurons expressed mCherry (Extended Data Fig. 8e). Furthermore, we verified that Rb-GFP was selectively entering OT neurons by injecting control rats (n = 2) with rAAV-OTp-TCB, and Rb-GFP 2 weeks later. This resulted in specific expression of GFP in PVN OT neurons (Extended Data Fig. 8f).

In each rat, we confirmed the SON injection site by staining for Cre for the parvOT neurons tracing (Extended Data Fig. 8a,b) and injecting a virus Cre-dependently expressing mCherry in the SON of magnOT neuron tracing, which led to expression of mCherry in SON magnocellular neurons (Extended Data Fig. 8c,d).

OT secretion model. The OT secretion model[17] simulates stimulus-secretion coupling in OT neurons. The model is a continuous approximation of the stochastic release process from all neuronal compartments. It is based on extensive studies on activity-dependent hormone secretion from magnocellular neurosecretory neurons[58] and it matches experimental data closely. In the model, when spikes invade the secretory terminals, exocytosis occurs in response to fast rising Ca^{2+} concentrations (e). At higher frequencies, the spikes broaden, producing a larger increase in e. The rate of secretion is modeled as the product of: e raised to the power of φ (which accounts for the cooperativeness of the Ca^{2+} activation), of the pool of releasable OT p, and a secretion-scaling factor α, and is calculated as:

$$s = e^{\varphi} \times \alpha \times p$$

where $\varphi = 2$ and $\alpha = 0.003$ pg s⁻¹.

The nonlinear dependence of the secretion rate gives high secretion probability on short spike intervals. To infer OT secretion arising from the spike trains observed in the present study, the recorded event timings were used to drive the secretion model described fully elsewhere[17]. The published model is scaled to quantitatively match secretion from the pituitary nerve terminals of a single OT neuron. The scaling factor α cannot be used for absolute quantitative estimates of release within the brain, but the relative efficacy of two firing patterns can be compared using the model, because α is eliminated in the ratio.

Statistics. Statistical analyses were performed using SigmaPlot v.11 (Systat) and GraphPad Prism v.7.05 (GraphPad Software). The two-sided, Wilcoxon's signed-rank W-test was used to compare the variation of spike frequencies measured for the same neuron in different conditions. The two-sided Mann–Whitney U-test was used to compare low threshold depolarization in different cells. Two-sided Student's t-tests were used to compare average values in two conditions when the data satisfied assumptions of normality. Pearson's correlation coefficient was used to measure the linear correlation between firing rate and animals' distance. One-way analysis of variance (ANOVA), followed by a multiple comparison post hoc test, was used to compare averages in three or more conditions. Two-way ANOVA, followed by a multiple comparison post hoc test, was used to analyze electrophysiological or behavioral data with repeated measures and CNO/saline/OTR antagonist treatment (time × treatment). No statistical methods were used to predetermine sample size, but our sample sizes are similar to those reported in previous publications[5,13,30].

Differences were considered significant for $P < 0.05$. Asterisks were used to indicate the significance level: *$0.01 \leq P < 0.05$, **$0.001 \leq P < 0.01$, ***$P < 0.001$. Statistical analyses of neuronal spike trains and local field potentials, such as PSTHs, auto- and cross-correlation, spike burst analysis, power spectrum density and phase locking were performed using NeuroExplorer 3 (Nex Technologies) and customized MATLAB scripts.

Randomization and blinding. Randomization was used to assign brain samples and animals to experimental groups whenever possible, with the constraint that, in social behavior experiments, interacting rats had to be unfamiliar conspecifics, as described under Methods.

Most of the measurements were made using a machine, and are not subject to operator bias, with the exception of manual scoring of social behaviors from videos; in this case, all scorings were done by a researcher (different from the one who performed the experiment) who was blind to treatment conditions.

Reporting Summary. Further information on research design is available in the Nature Research Reporting Summary linked to this article.

Data and code availability

Python code (used for ex vivo calcium-imaging data analysis in Fig. 4a–d) and MATLAB code (used for in vivo fiber photometry data analysis in Fig. 4e–o and Extended Data Fig. 7a–n) can be found in Supplementary Software. All data that support the findings of the present study, as well as MATLAB codes for the analysis of extracellular recording data, are available from the corresponding author upon reasonable request.

References

49. Menon, R. et al. Oxytocin signaling in the lateral septum prevents social fear during lactation. *Curr. Biol.* **28**, 1066–1078.e6 (2018).
50. Grinevich, V. et al. Somatic transgenesis. *Viral Vectors* **3**, 243–274 (2016).
51. Paxinos, G. & Watson, C. *The Rat Brain in Stereotaxic Coordinates*, 7th edn (Elsevier Acad. Press, 2014).
52. Tasker, J. G. & Dudek, F. E. Electrophysiological properties of neurones in the region of the paraventricular nucleus in slices of rat hypothalamus. *J. Physiol.* **434**, 271–293 (1991).
53. Chu, C.-P. et al. Effects of stresscopin on rat hypothalamic paraventricular nucleus neurons in vitro. *PLoS ONE* **8**, e53863 (2013).
54. Luther, J. A. & Tasker, J. G. Voltage-gated currents distinguish parvocellular from magnocellular neurones in the rat hypothalamic paraventricular nucleus. *J. Physiol.* **523**, 193–209 (2000).
55. Luther, J. A. et al. Neurosecretory and non-neurosecretory parvocellular neurones of the hypothalamic paraventricular nucleus express distinct electrophysiological properties. *J. Neuroendocrinol.* **14**, 929–932 (2002).
56. Yuill, E. A., Hoyda, T. D., Ferri, C. C., Zhou, Q.-Y. & Ferguson, A. V. Prokineticin 2 depolarizes paraventricular nucleus magnocellular and parvocellular neurons. *Eur. J. Neurosci.* **25**, 425–434 (2007).
57. Tang, Y., Benusiglio, D., Grinevich, V. & Lin, L. Distinct types of feeding related neurons in mouse hypothalamus. *Front. Behav. Neurosci.* **10**, 91 (2016).
58. Maícas Royo, J., Brown, C. H., Leng, G. & MacGregor, D. J. Oxytocin neurones: intrinsic mechanisms governing the regularity of spiking activity. *J. Neuroendocrinol.* **28**, 28 (2016).
59. Grund, T. et al. Chemogenetic activation of oxytocin neurons: temporal dynamics, hormonal release, and behavioral consequences. *Psychoneuroendocrinology* **106**, 77–84 (2019).
60. de Jong, T. R. et al. Salivary oxytocin concentrations in response to running, sexual self-stimulation, breastfeeding and the TSST: the Regensburg Oxytocin Challenge (ROC) study. *Psychoneuroendocrinology* **62**, 381–388 (2015).
61. Landgraf, R., Neumann, I., Holsboer, F. & Pittman, Q. J. Interleukin-1β stimulates both central and peripheral release of vasopressin and oxytocin in the rat. *Eur. J. Neurosci.* **7**, 592–598 (1995).
62. Neumann, I. D., Maloumby, R., Beiderbeck, D. I., Lukas, M. & Landgraf, R. Increased brain and plasma oxytocin after nasal and peripheral administration in rats and mice. *Psychoneuroendocrinology* **38**, 1985–1993 (2013).
63. Ishiyama, S. & Brecht, M. Neural correlates of ticklishness in the rat somatosensory cortex. *Science* **354**, 757–760 (2016).
64. Althammer, F., Ferreira-Neto, H. C., Rubaharan, M., Roy, K. R. & Stern, J. E. Three-dimensional morphometric analysis reveals time-dependent structural changes in microglia and astrocytes in the central amygdala and hypothalamic paraventricular nucleus of heart failure rats. *Res. Sq.* https://doi.org/10.21203/rs.3.rs-22630/v1 (2020).
65. Kim, E. J., Jacobs, M. W., Ito-Cole, T. & Callaway, E. M. Improved monosynaptic neural circuit tracing using engineered rabies virus glycoproteins. *Cell Rep.* **15**, 692–699 (2016).
66. Zhang, B. et al. Reconstruction of the hypothalamo-neurohypophysial system and functional dissection of magnocellular oxytocin neurons in the brain. Preprint at *bioRxiv* https://doi.org/10.1101/2020.03.26.007070 (2020).

Author contributions

Y.T., D.B., A.L., A.C. and V.G. designed and conceived the project. L.H. and P.D. performed the ex vivo electrophysiology. L.H. and A. Baudon did the ex vivo calcium imaging. Y.T., D.B. and S.W. performed the in vivo electrophysiology. Y.T. and A.L. did the fiber photometry. Y.T., D.B. and S.W. performed the behavioral experiments and analyses. D.B., M.E., D.H. and F.A. did the immunohistochemistry and confocal microscopy. A.L. and J.S. performed the trans-synaptic labeling of OT neuron inputs. M.S., M.O. and K.K.C. assisted with virus design for trans-synaptic labeling. F.A., M.K.K., R.K.R. and J.E.S. did the 3D reconstruction and analysis. A. Bludau and I.D.N. calculated the plasma OT dosages. G.L. did the modeling. Y.T., D.B., A.L., L.H., F.A., I.D.N., A.C. and V.G. prepared the manuscript. I.D.N., A.C. and V.G. supervised and administered the project, and acquired the funding.

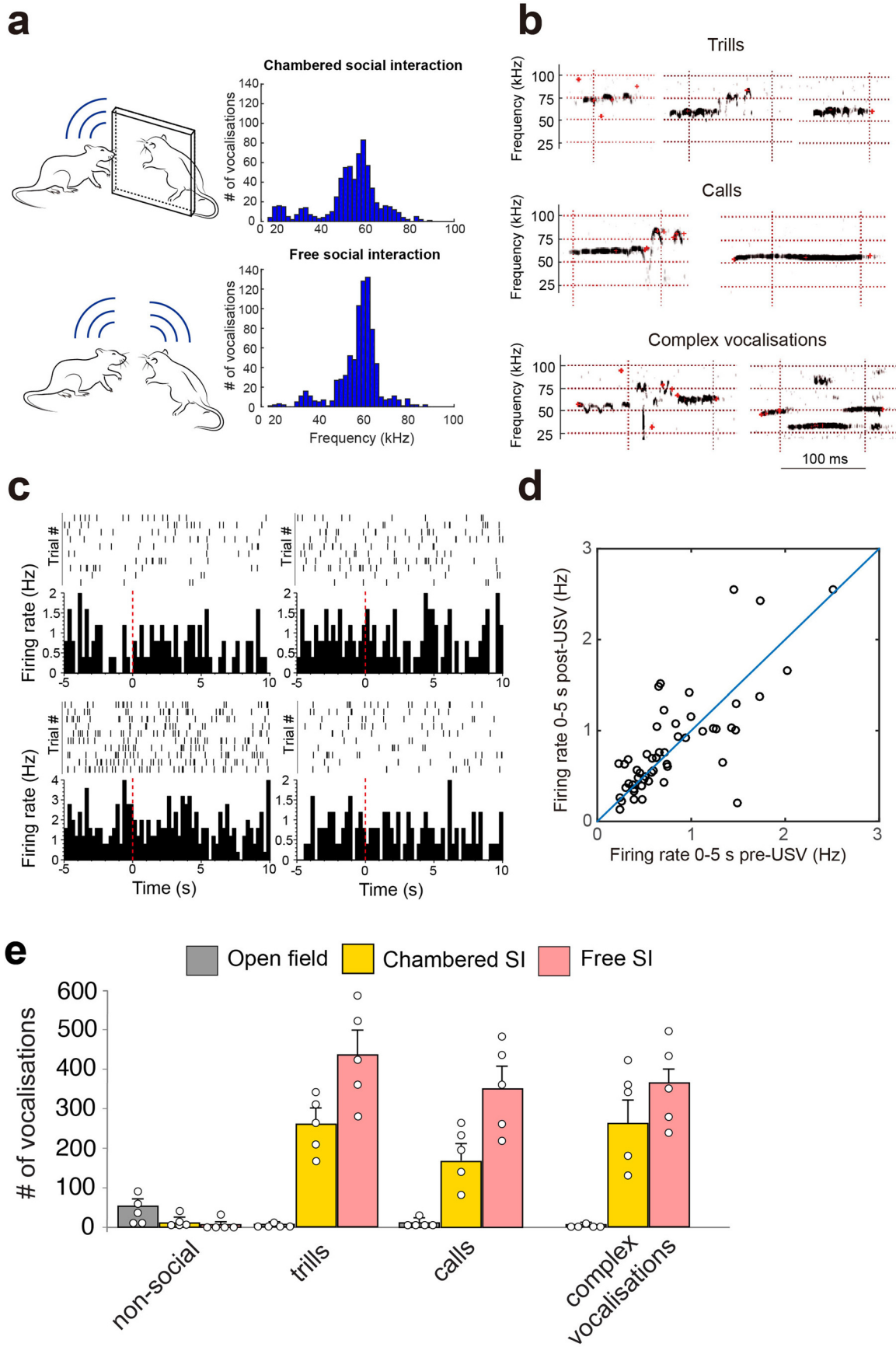**Extended Data Fig. 1 | See next page for caption.**

Extended Data Fig. 1 | Recording of optogenetically identified oxytocin neurons, local field potential, phase locking, synchronization and spike distribution. a, The cell type specificity of rAAV-OTp-ChR2-mCherry expression in OT cells. OT-immunosignal (green) colocalizes with ChR2-mCherry (red) signal; the overlay appears in yellow. Scale bar = 100 μm. Bottom, right: quantification of the colocalization mCherry/ChR2 (red bar, 90.8 ± 3.9 %) and mCherry/OT immnoreactive cells (green bar, 82.6 ± 7.7 %). Bar plots show mean ± SEM. **b**, Post-hoc verification of implanted optoprobe location in the PVN in a representative animal (one of five rats). Scale bar = 100 μm. **c**, Sorted extracellular spike waveforms (n = 175 action potentials) of a representative single unit optically-identified as OT neurons. **d**, Silicon probe (NeuroNexus) with 32-channel single shank were used in acute (anesthetized) single units recording. Sorted units and their location in the channels map were visualized with Phy-GUI (klusta, Python). Spike sorting was manually done in Plexon Offline Sorter 4.0 (Plexon, Inc.). **e**, PSTHs illustrating two optogenetically-identified oxytocin neurons by their response to blue light pulses (1 Hz, 5 Hz and 10 Hz laser stimulation, 10 ms, λ=473 nm, 10 mW/mm^2). In both neurons, low frequency stimulation evoked spikes with a relatively constant short latency of 2-10 ms. **f**, Power spectrogram of the local field potential (LFP) in the PVN recorded before (open field, OF), during and after (OF) a free social interaction (FSI) session. **g**, Average theta (5-10 Hz) power recorded during and FSI session is significantly higher than before FSI session (p = 0.03, n = 5 rats, paired two-sided t test). All data represented as mean + SEM. **h**, P value distribution of phase-locking between theta (5-10 Hz) oscillations and OT cells spikes during exploratory (OF) or social (FSI) behavior (** p = 0.0089, n = 15 cells from 5 rats, paired two-sided t test; box plot shows median 10th, 25th, 75th, and 90th percentiles; min/max: OF, 0.07/0.99; SI, 0.002/0.08). **i, j**, Example traces (black) of LFP in the PVN and band-pass (5-10 Hz) filtered theta oscillations (red) during exploratory (OF) or social (FSI) behavior. Examples of distribution of four OT neurons firing in relation to LFP theta oscillations; OT neurons spikes are phase-locked with theta oscillations (** P = 0.0014, n = 15 cells) during social interaction (FSI, **j**), but not during exploratory behavior (**i**). Circular representation of OT neurons firing in relation to theta oscillation phase shows phase locking during social behavior (**l**) exclusively. No significant difference of spike-phase coupling between social behavior subtypes (P = 0.28). Significance of phase locking are determined by Rayleigh test for circular uniformity. **k, l**, Cross-correlation of pairs of oxytocin neurons recorded simultaneously. During open field (**k**) test there is no detectable correlation between oxytocin neurons spiking activity, but during social interaction (**l**) there is a significant increase (P = 0.0038, n = 12 cell pairs) of temporally correlated spikes within a time window of τ = 1.2 ± 0.5 s (mean correlation half-time). **m, n**, Examples of interspike interval (ISI, time bins = 10 ms) histograms of four OT neurons recorded during exploratory behavior (OF, **m**) and during social interaction (FSI, **n**). During FSI there is a prominent increase of spikes with short intervals due to increased spike clustering.
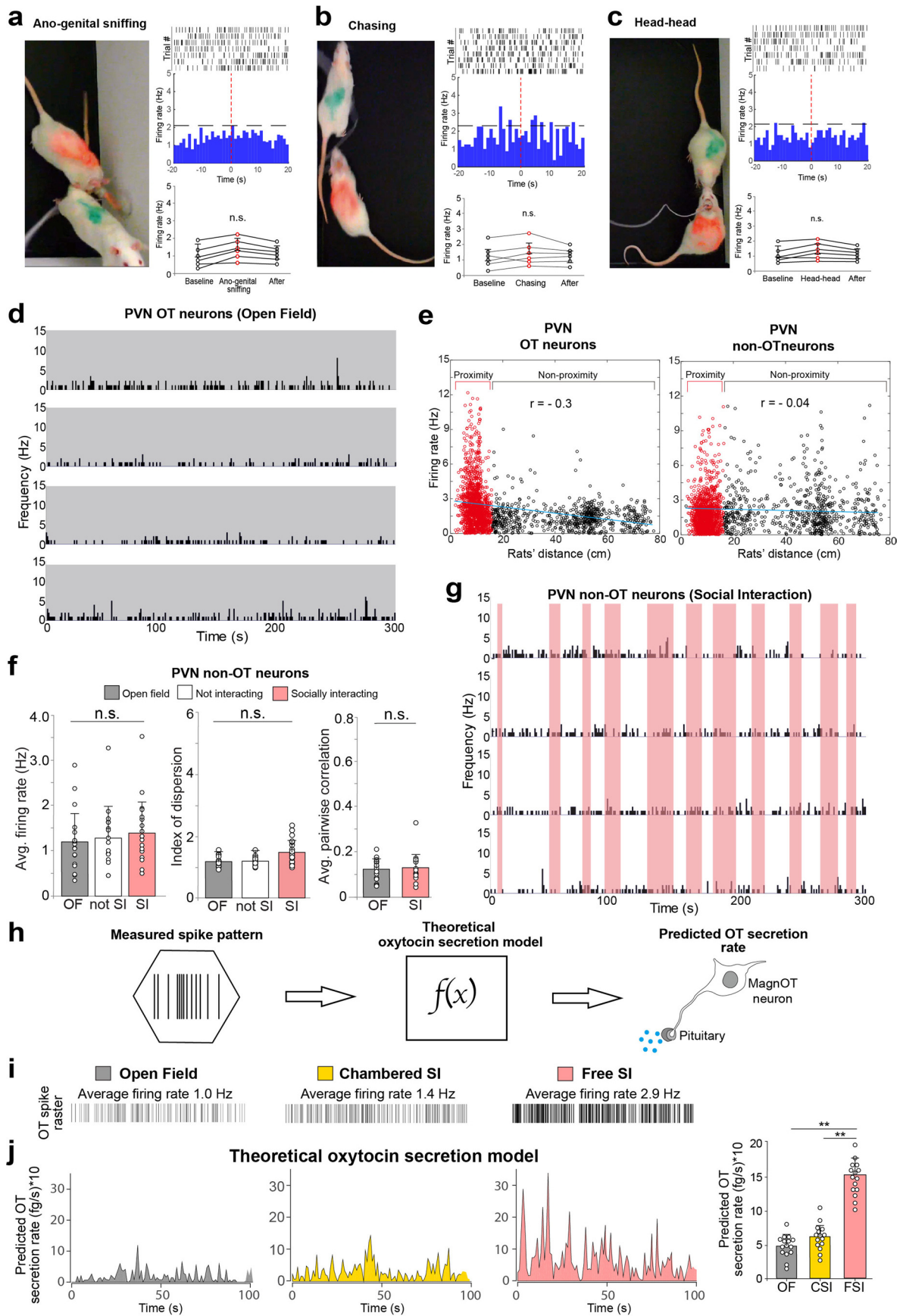
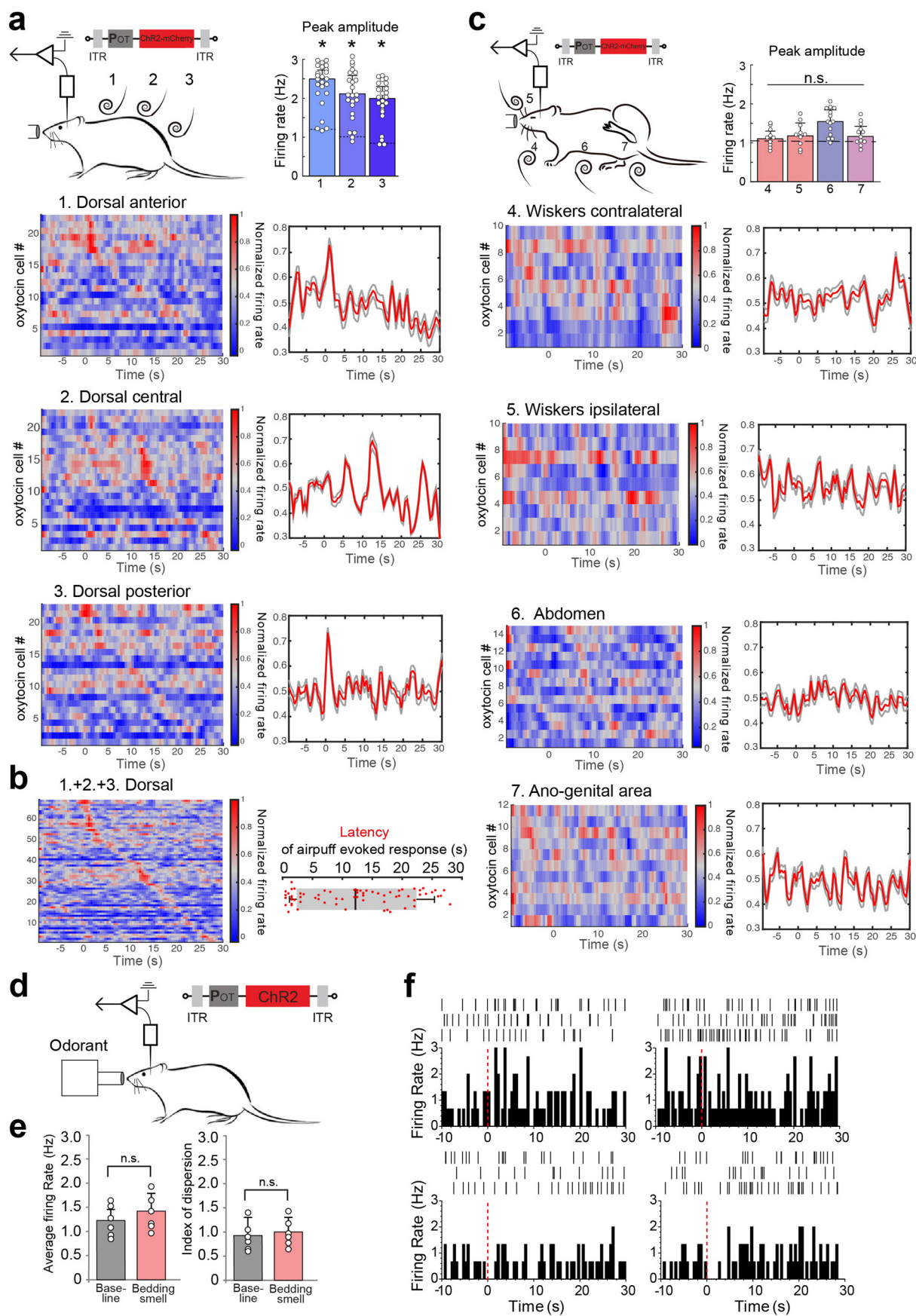**Extended Data Fig. 2 | See next page for caption.**

Extended Data Fig. 2 | Analysis of social interactions, the firing rate of oxytocin and non-oxytocin PVN neurons, and activity-dependent model of oxytocin secretion. a-c, Examples of manually classified social interaction behaviors: *ano-genital sniffing*, *chasing*, *head-to-head* events. PSTHs of a single unit identified as oxytocin neurons aligned to the onset of the specific behavior. Averaged (10 s time bin) PSTHs responses before, during, and after each behavior (0 to +10 s vs. basal $P = 0.12$, $P = 0.45$, $P = 0.88$, respectively, n = 6 cells per behavior, two-sided Wilcoxon test). **d**, Example firing rate of four PVN OT neurons recorded during exploratory (OF) behavior. **e**, Linear regression of PVN OT and non-OT neuronal firing rate in relation to rat's distance in the area during FSI. OT neuronal activity shows a moderate negative correlation with distance ($r = -0.3$, $p = 0.0092$), while non-OT neurons do not show any significant correlation ($r = -0.04$, $P = 0.11$). **f**, Example firing rate of four PVN non-OT neurons recorded during social interaction. **g**, Average firing rate of 21 non-OT neurons from five rats (OF baseline 1.2 ± 0.2 Hz, not socially interacting (not SI) firing rate 1.2 ± 0.2 Hz, and social interacting (SI) firing rate 1.4 ± 0.2 Hz; $P = 0.83$, $P = 0.23$, $P = 0.34$, one-way ANOVA). Average index of dispersion on 1-s time bins of 21 non-OT cells (OF 1.1 ± 0.2, not SI 1.1 ± 0.2, SI 1.4 ± 0.3, $P = 0.78$, $P = 0.07$, $P = 0.11$, one-way ANOVA). Average pairwise Pearson correlation of spiking activity (1-s time bins) of 21 non-OT neurons' pairs recorded in OF and FSI ($P = 0.98$, paired two-sided t test). All data show average + SEM. **h**, Schematic illustration of the theoretical model used to estimate the amount of secreted oxytocin from axonal terminals given the measured neuronal spike pattern. **i**, Average firing rate of OT cells from rats that underwent open field (OF), CSI, and FSI tests. **j**, Predicted OT secretion rate for a representative OT cell in each condition (left). Average OT predicted secretion rate (right) in each condition (OF-CSI, $P = 0.11$, OF-FSI, ** $P = 0.005$, OF-CSI, ** $P = 0.007$, spike pattern data used for prediction are from n = 15 cells from 5 rats, one-way ANOVA followed by Tukey's post hoc test). Data represented as mean + SEM.
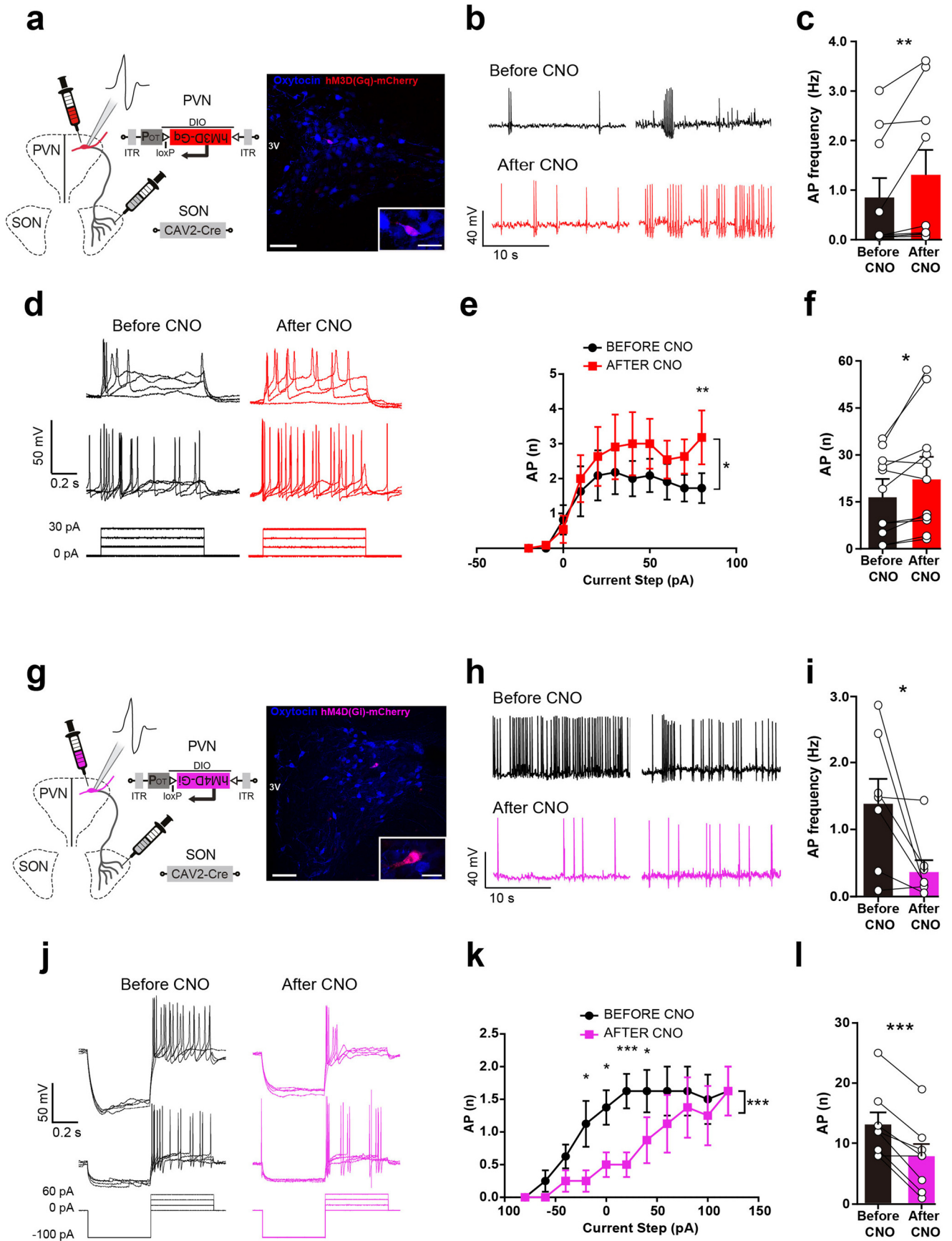
Extended Data Fig. 3 | See next page for caption.

Extended Data Fig. 3 | Ultra Sound Vocalizations (USVs) and OT neuronal activity. a, Histograms of USVs peak frequency distribution during CSI (top) and FSI (bottom). **b**, Examples of sound spectrograms showing USVs events classified as whistles, calls, or complex vocalizations. **c**, PSTHs of oxytocin neurons spiking activity aligned to USVs onset (red dashed line) show no significant time-locked correlation between them. **d**, Firing rate of oxytocin neurons 0-5 s before USV events versus 0-5 s after USV events showing no significant correlation ($P = 0.24$, n = 53 vocalisations, two-sided Wilcoxon test). **e**, Total number of USVs registered in 5 pairs (experimental and stimulus animal) of rats during OF, CSI, and FSI tests divided - according to their frequency and duration – in non-social (< 25 kHz), trills (< 10 ms), calls (> 10 ms, not modulated), and complex vocalizations (> 10 ms, frequency modulated or mixed). All data represented as mean + SEM.

Extended Data Fig. 4 | See next page for caption.

Extended Data Fig. 4 | Oxytocin neurons response to airpuffs and to socially-related olfactory stimuli. a, Illustration of single-unit recordings of oxytocin neurons during airpuffs applied to 1. anterior, 2. central, 3. posterior (n = 23 cells from 8 rats) part of the dorsal body region. Average increase response of oxytocin neurons compared to baseline for different stimulations regions (*P = 0.017, *P = 0.025, *P = 0.021 respectively, n = 23 cells from 8 rats, one-way ANOVA followed by Bonferroni post hoc comparison). PSTHs showing single oxytocin neurons (left) and averaged (right) and response to repeated airpuffs in all stimulation sites. **b**, Combined PSTHs of 1., 2., 3., showing different response latency of oxytocin neuron to airpuff stimulations on the dorsal body area. **c**, Single-unit recordings of oxytocin neurons during airpuff stimulations on: whiskers (n = 10 cells), abdomen (n = 14 cells), and anogenital area (n = 12 cells). Average increase response of oxytocin neurons compared to baseline for different stimulation regions. PSTHs showing single oxytocin neurons (left) and averaged (right) and response to repetitive airpuff stimulations in all stimulation sites. All data represented as mean + SEM. **d**, Illustration of the experimental setup for recording oxytocin neurons activity (opto-electrodes) during presentation of olfactory stimuli. **e**, Average firing rate and index of dispersion of six oxytocin neurons 10 s before presentation of the olfactory stimuli vs 10 s after; no significant changes are detected (P = 0.34, P = 0.48, n = 6 cells from 3 rats, paired two-sided t test). Data represented as average + SEM. **f**, PSTHs of 4 (out of 6 recorded) oxytocin neurons spiking activity aligned to onset of olfactory cues (red dashed line) - urinated bedding smell; no significant changes in firing rate are detected.

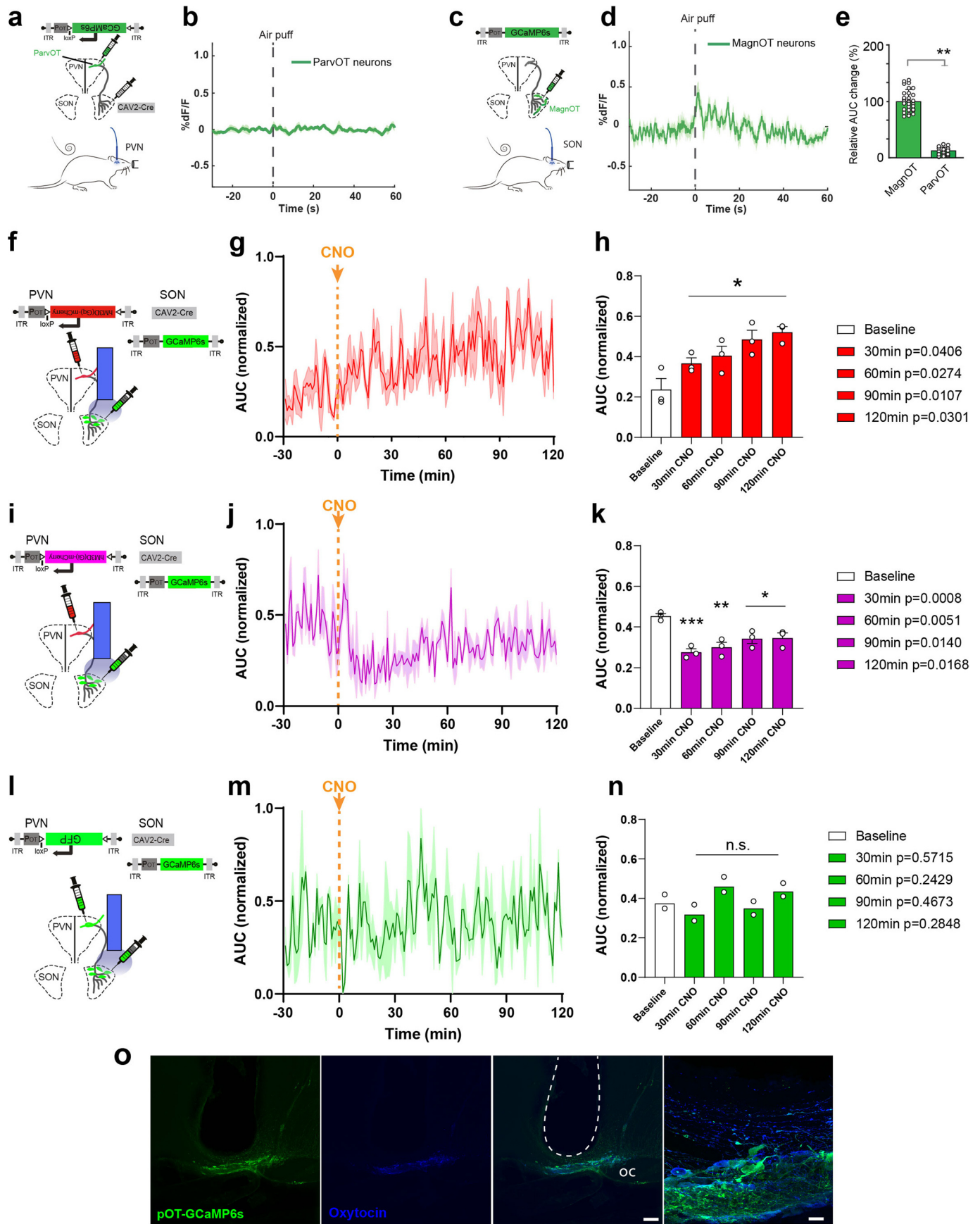**Extended Data Fig. 5 | See next page for caption.**

Extended Data Fig. 5 | *Ex vivo* **effects of excitatory hM3D(Gq) and inhibitory hM4D(Gi) DREADD in parvOT neurons. a**, Schema of viral vectors injected for *ex vivo* recording of parvOT neurons with concomitant DREADD-Gq activation. The picture shows hM3D(Gq) (purple) and OT (blue) immunoreactivities in the PVN of one out five rats. Scale bar = 100 μm and (inset) 10 μm. **b-c**, Spontaneous response from parvOT neurons expressing hM3D(Gq) in before and after the CNO bath application; b example traces, c quantification (baseline 0.85 ± 0.39 Hz vs CNO 1.31 ± 0.51 Hz, n = 9 cells from 5 rats; *P* = 0.0039). **d-f**, Evoked responses from parvOT neurons expressing hM3D(Gq) to current injections before and after the CNO bath application; (**d**) example traces, (**e**) quantification per step (before CNO current step 80 pA 1.727 ± 0.428 nAP vs after CNO current step 80 pA 3.182 ± 0.772 nAP, n = 11; **$P < 0.01$); (**f**) quantification of the average response (16.18 ± 3.89 AP vs CNO 22.55 ± 5.66 AP, n = 11 cells from 5 rats; *P* = 0.0314). **g**, Schema of viral vectors injected for *ex-vivo* recording of parvOT neurons with concomitant DREADD-Gi excitation. The picture shows hM4D(Gi) (purple) and OT (blue) immunoreactivities in the PVN of one out seven rats. Scale bar = 100 μm and (inset) 10 μm. **h-i**, Spontaneous response from parvOT neurons expressing hM4D(Gi) in before and after the CNO bath application; b example traces, c quantification (baseline 1.38 ± 0.38 Hz vs CNO 0.36 ± 0.18 Hz, n = 7 cells from 7 rats; *P* = 0.0469). **j-l**, Evoked responses from parvOT neurons expressing hM4D(Gi) to current injections before and after the CNO bath application; (**j**) example traces, (**k**) quantification per step (before CNO current step 20 pA 1.625 ± 0.263 nAP vs after CNO current step 20 pA 0.5 ± 0.189 nAP, n = 8; ***$P < 0.001$); **l**, quantification of the average response (baseline 13 ± 2.02 AP vs CNO 7.75 ± 2.03 AP, n = 8 cells from 7 rats; p = 0.0007). All results are expressed as average ± SEM. The statistical significances: * $P < 0.05$; ** $P < 0.01$; *** $P < 0.001$ (two-sided Wilcoxon test: c and i; Two-way ANOVA followed by a Holm-Sidak post hoc test: e and k; Paired two-sided t test: f and l). Open circles indicate individual cells.
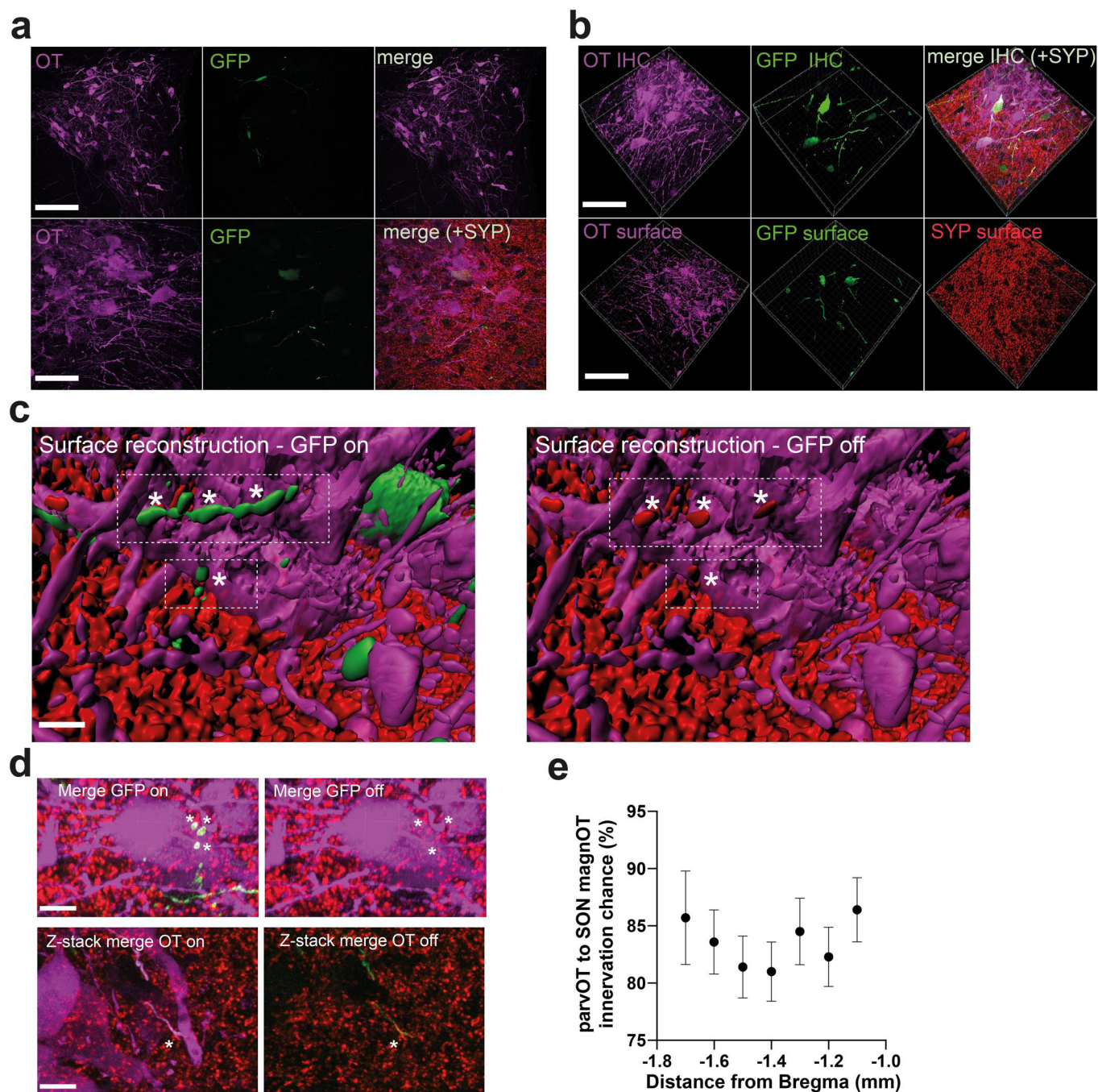
Extended Data Fig. 6 | Three-dimensional reconstruction and assessment of parvOT-magnOT connectivity. a, Confocal images show specific labeling of parvOT neurons using CAV2-Cre in combination with OTp-DIO-GFP. Top panel shows a representative PVN (one out of three independent experiments, n = 3 rats) image with 2 labeled parvOT neurons. Bottom panel shows an image with higher magnification and overlay with synaptophysin (SYN). OT = purple, GFP = green, SYN = red. Scale bars = 200 μm (top panel) and 50 μm (bottom panel). **b**, Images show raw fluorescent confocal z-stacks and surface reconstruction of individual fluorescent channels (one out of three independent experiments, n = 3 rats). The top panel shows fluorescent signals of OT, GFP and merge (+SYN). The bottom panel shows the same channels with applied surface reconstruction. Bottom images have been vertically flipped to enhance visualization of the reconstructed channels. Scale bars = 75 μm. **c**, Images show the IMARIS three-dimensional surface reconstruction of OT, GFP and SYN. Boxes with dashed lines and asterisks indicate the overlap of GFP and SYN. In the right panel the overlap between OT (purple) and GFP (green) has been manually removed to visualize the GFP/SYN (green/red) overlap (n = 169 cells from 3 rats). Scale bar = 10 μm. **d**, Confocal images show synaptic contact of parvOT neurons with magnOT somata and dendrites. Top panel shows axo-somatic contact. Bottom panel shows axo-dendritic contact using a high magnification confocal z-stack. Asterisks indicate synaptic contact. Scale bars = 10 μm. **e**, Quantification of SON OT neuron chance to receive innervation by parvOT neurons in respect to their rostro-caudal location (n = 169 cells from 3 rats). All data are presented as mean ± SEM.

Extended Data Fig. 7 | See next page for caption.

Extended Data Fig. 7 | Fiber photometry recording of PVN parvOT neurons and SON magnOT neurons with chemogenetic manipulation of parvOT neurons. a-b, Schema of viral vectors injected (CAV2-Cre in the SON and OTp-DIO-GCaMP6s in the PVN) and implanted optic fiber for fiber photometry recording of PVN parvOT neurons (a). No Ca^{2+} transient nor changes in Ca^{2+} signal upon 'airpuff' stimulation were detected when recording parvOT neurons exclusively (b, solid line: average, shaded area: SEM, n = 3 rats). **c-d**, Schema of viral vectors injected and implanted optic fiber for fiber photometry recording of SON magnOT neurons (c). Examples of fiber photometry-based Ca^{2+} signals of SON magnOT population during airpuff stimulation (d); the graphic is an average of 33 airpuff responses (11 airpuffs per animal, n = 3 rats). **e**, Relative change in the area under the curve (AUC) 0-30 s after airpuffs with respect to 30 s before the stimuli, of SON magnOT vs. parvOT neurons (solid line: average, shaded area: SEM, n = 33 airpuffs from 3 rats, ** $P = 0.008$, unpaired two-sided t test). Data show mean + SEM. **f-g-h**, Schema of viral vectors injected and implanted optic fiber for fiber photometry recording (f) of SON OT neurons with concomitant DREADD-Gq activation of parvOT neurons. Normalized area under the curve (AUC) of GCaMP6s signal (g, solid line: average, shaded area: SEM, 1 min bin size) of SON OT neurons showing increase of cells activities after parvOT activation mediated by CNO i.p. injection (indicated by arrow). 30-min averaged AUC (h) showing a gradual increase in cellular activity and lasting at least 120 min (* $P = 0.0406$, * $P = 0.0274$, * $P = 0.0107$, * $P = 0.0301$, n = 3 rats, two-way ANOVA Tukey's corrected post-hoc comparison). Data show mean + SEM. **i-j-k**, Schema of viral vectors injected and implanted optic fiber for fiber photometry recording (i) of SON OT neurons with concomitant DREADD-Gi inhibition of parvOT neurons. Normalized area under the curve (AUC) of GCaMP6s signal (j, solid line: average, shaded area: SEM, 1 min bin size) of PVN OT neurons showing a decrease of cellular activity after parvOT inhibition mediated by i.p. CNO injection (indicated by arrow). 30-min averaged AUC (k) shows a sharp decrease in cellular activity that lasts at least 60 min and then gradually recovers (*** $P = 0.0008$, ** $P = 0.0051$, * $P = 0.0140$, * $P = 0.0168$, n = 3 rats, two-way ANOVA Tukey's corrected post-hoc comparison). Data show mean + SEM. **l-m-n**, Schema of viral vectors injected and implanted optic fiber for fiber photometry recording (l) of SON OT neurons in control animals (DREADD-free) expressing GFP in parvOT neurons. Normalized area under the curve (AUC) of GCaMP6s signal (m, solid line: average, shaded area: SEM, 1 min bin size) of PVN OT neurons showing no significant changes in Ca^{2+} signal upon CNO injection. No significant changes are detected in 30-min averaged AUC (n) up to 120 min ($P = 0.5715$, $P = 0.2429$, $P = 0.4673$, $P = 0.2848$, n = 2 rats, two-way ANOVA Tukey's corrected post-hoc comparison). Data show mean values. **o**, Panels of an immunostained section of the SON (one of out of eight independent experiments) showing post-hoc verification of implanted optic fiber above the SON and co-localization of immunoreactive, GCaMP6s (green), oxytocin (blue), and merged channels. Scale bar 100 μm and 10 μm (inset).
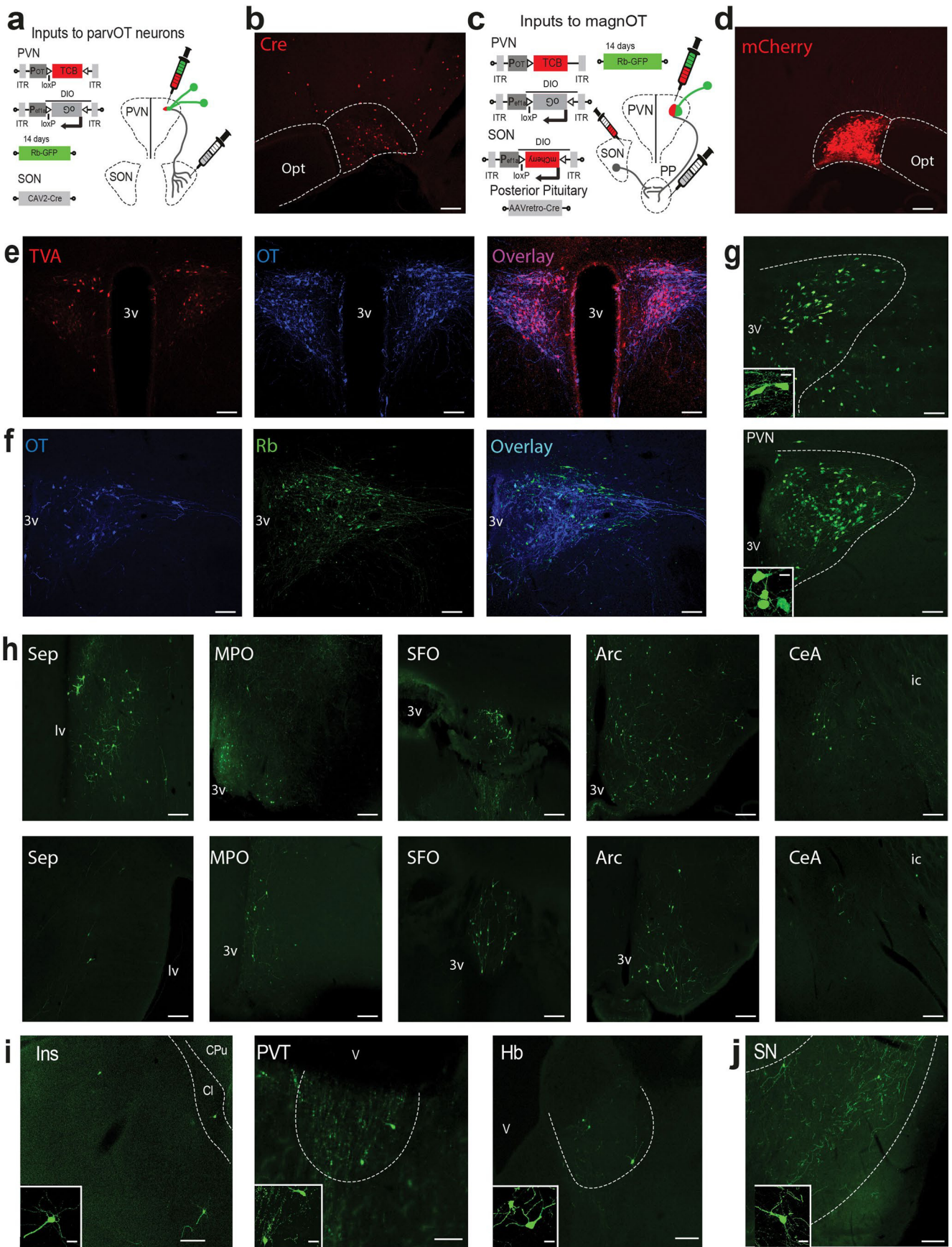
Extended Data Fig. 8 | See next page for caption.

Extended Data Fig. 8 | Inputs to parvOT and magnOT neurons. a, c, Virus injection strategy to retrotrace inputs from parvOT and magnOT neurons, respectively and to control injection sites of Cre (n = 5 rats). **b, d**, Injection site of CAV2-Cre in SON and of AAVretro-Cre in PP were confirmed by staining for Cre or mCherry in SON (n = 5 rats). **e**, Immunofluorescence for mCherry (red, fused to TVA), OT (blue) and overlay of the PVN from a rat injected with rAAV-OTp-TCB (n = 2 rats). **f**, Immunofluorescence for OT (blue), GFP (Green) and overlay of the PVN from a rat injected with rAAV-OTp-TCB, and Rb-GFP two weeks later (n = 2 rats). **g**, Injection site of rabies in parvOT (Top) and magnOT (bottom) groups (n = 5 rats). **h**, Epifluorescence microscope images showing neurons monosynaptically retrolabelled by Rabies-GFP in various brain areas projecting to both parvOT and magnOT neurons. Top line: neurons projecting to parvOT neurons; Bottom line: neurons projecting to magnOT neurons (n = 5 rats). **i, j**, Epifluorescence microscope images showing neurons monosynaptically retrolabelled by Rabies-GFP in brain areas projecting specifically to parvOT (i) or magnOT neurons (j) (n = 5 rats). All scale bars = 100 μm. All scale bars in insert = 10 μm. Brain areas legend: Amygdala: AMY, Arcuate hypothalamic nucleus: Arc, Bed nucleus of stria terminalis: NST, Cingulate cortex: CgC, Claustrum: Cl, Dorsal raphe nucleus: DRN, Dorsal tenia tecta: DTT, Dorsomedial hypothalamic area: DMH, Habenular nucleus: Hb, Horizontal limb of diagonal band nucleus: HDB, Infralimbic cortex: ILC, Insular cortex: Ins, Lateral hypothalamic area: LH, Lateral lemniscus nucleus: LMN, Lateral septal nucleus: SEP, Mammillary body: MMB, Medial preoptic area: MPO, Median raphe nucleus: MRN, Nucleus accumbens: NAC, Orbital cortex: OC, Parabrachial nucleus: PBN, Paraventricular thalamus: PVT, Pedunculopontine tegmental nucleus: PPT, Periaqueductal gray area: PAG, Posterior hypothalamic nucleus: PH, Posterior intralaminar thalamus: PIL, Prelimbic cortex: PLC, Raphe magnus nucleus: RMg, Subfornical organ:SFO, Substancia nigra: SN, Vascular organ of lamina terminalis: OVLT, Ventral Subiculum: VS, Zona incerta: ZI.
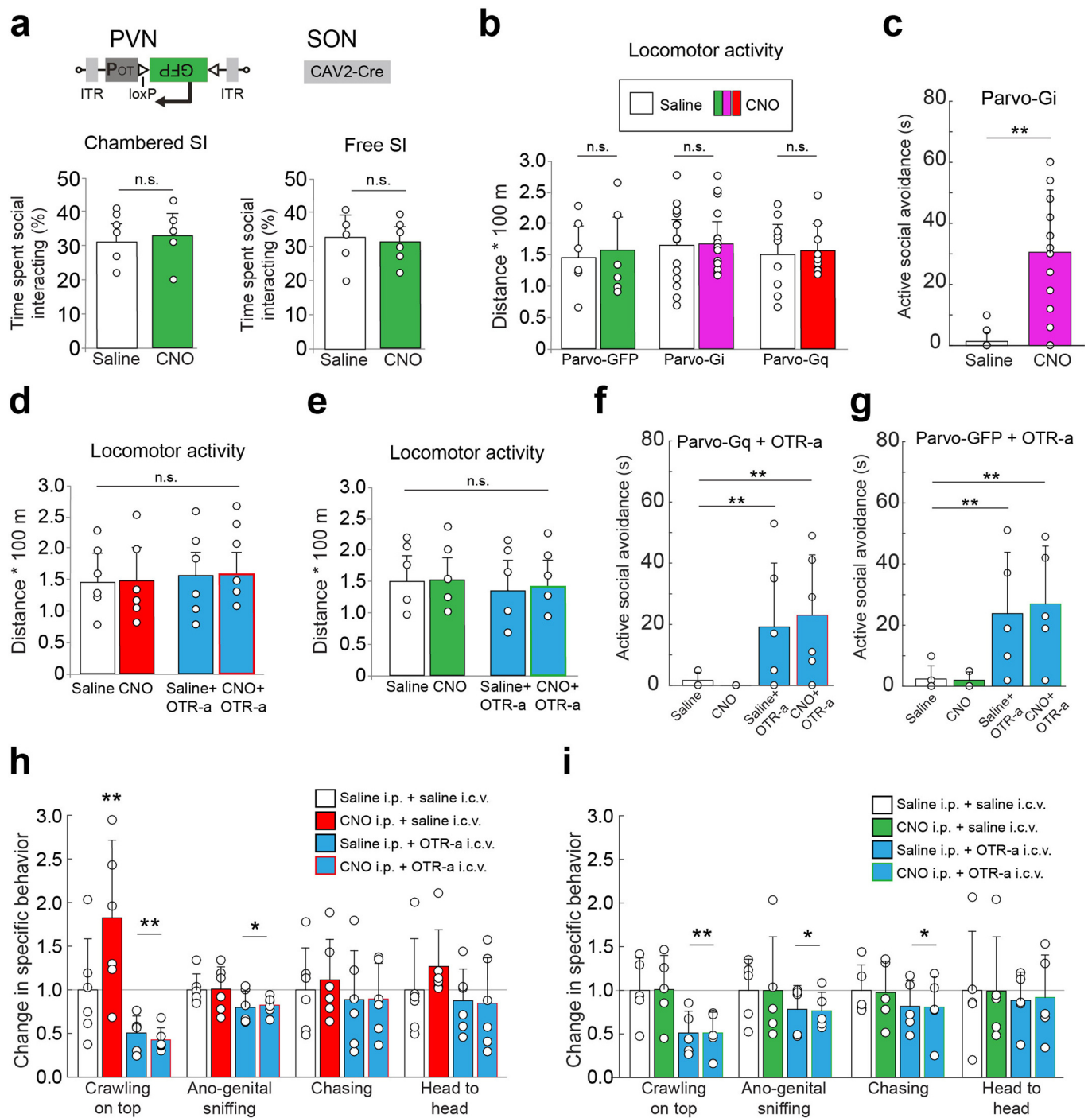
Extended Data Fig. 9 | Effects of DREADD activation of parvocellular oxytocin neurons on social behaviors. a, Parvocellular oxytocin-GFP control group: time spent by rats injected with saline or CNO socially interacting with conspecific stimulus in CSI ($P=0.34$) and FSI session ($P=0.29$, n=6 rats, paired two-sided t test). **b**, CNO does not affect locomotor activity: average distance run by experimental rats (n=6 rats GFP group, n=15 rats Parvo-Gi group, n=9 rats Parvo-Gq group) injected with saline or CNO during an open field (OF) test. No significant changes were detected, one-way ANOVA Tukey's corrected post-hoc comparison. **c**, Quantification of 'active social avoidance' behavior of experimental rat (actively escaping from stimulus rat, which is trying to interact) expressing inhibitory DREADD hM4D(Gi) in parvOT neurons and injected either with saline (control) or CNO. The total time of free social interaction session is 5 minutes. ** $P=0.0096$, n=15 rats, paired two-sided t test). **d-e**, OT receptor antagonist (OTR-a), CNO, or both do not affect locomotor activity: average distance run by experimental rats (d: $P=0.79$, n=6 rats saline/CNO/saline, $P=0.92$ n=6 rats saline/CNO/OTR-a; e: $P=0.73$, n=5 rats saline/CNO/saline, p=0.64, n=5 rats saline/CNO/OTR-a) injected with saline/CNO/OTR-a during an open field (OF) test. One-way ANOVA Tukey's corrected post-hoc comparison. **f-g**, Quantification of 'active social avoidance' behavior of experimental rat after administration of saline/CNO/OTR-a. Infusion of OTR-a induced an increase of avoidance behavior (Parvo-Gq: ** $P=0.0027$, ** $P=0.0018$, n=6 rats per group, Parvo-GFP: **$P=0.0042$, **$P=0.0013$, n=5 rats per group, one-way ANOVA Tukey's corrected post-hoc comparison). **h-i**, Time spent in different subtype of social behavior of experimental rat expressing excitatory DREADD hM3D(Gq) (h) or GFP (i) in parvOT neurons after administration of saline/CNO/OTR-a. Crawling on top behavior was the subtype most affected by parvOT neurons chemogenetic activation and by infusion of OTR-a (Parvo-Gq: ** $P=0.01$, **$P=0.004$, *$P=0.023$, n=6 rats per group, Parvo-GFP: **$P=0.006$, *$P=0.035$, *$P=0.047$, one-way ANOVA Tukey's corrected post-hoc comparison). All data represented as mean + SEM.
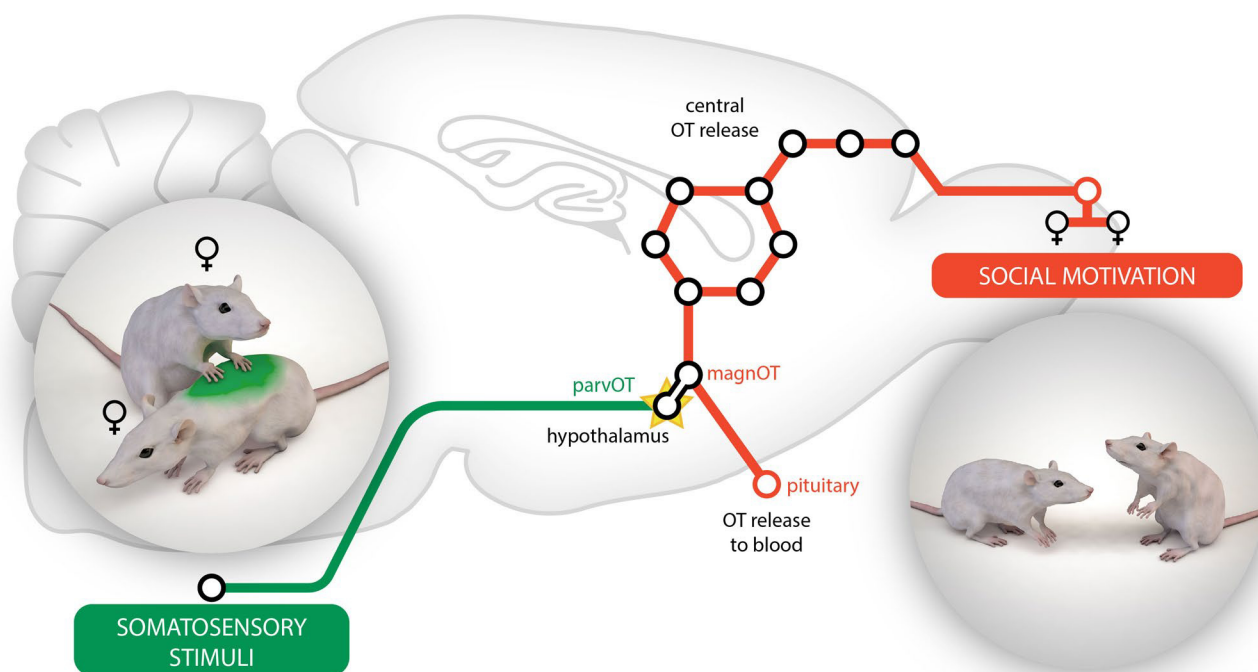
Extended Data Fig. 10 | Working hypothesis. Non-nociceptive signals ('social touch') arising from stimulation of dorsal body parts of interacting virgin female rats converge onto hypothalamic parvocellular oxytocin neurons via ascending pathways. As a consequence, the somatosensory-driven activation of parvocellular oxytocin neurons is transmitted to magnocellular oxytocin neurons inducing central oxytocin release in the social-relevant forebrain areas (as schematically depicted by circles representing nine amino acids in the oxytocin molecule), to support motivated social communication between female conspecifics.

natureresearch

Corresponding author(s): Valery Grinevich

Last updated by author(s): Jun 7, 2020

Reporting Summary

Nature Research wishes to improve the reproducibility of the work that we publish. This form provides structure for consistency and transparency in reporting. For further information on Nature Research policies, see Authors & Referees and the Editorial Policy Checklist.

Statistics

For all statistical analyses, confirm that the following items are present in the figure legend, table legend, main text, or Methods section.

n/a	Confirmed	
☐	☒	The exact sample size (*n*) for each experimental group/condition, given as a discrete number and unit of measurement
☐	☒	A statement on whether measurements were taken from distinct samples or whether the same sample was measured repeatedly
☐	☒	The statistical test(s) used AND whether they are one- or two-sided *Only common tests should be described solely by name; describe more complex techniques in the Methods section.*
☐	☒	A description of all covariates tested
☐	☒	A description of any assumptions or corrections, such as tests of normality and adjustment for multiple comparisons
☐	☒	A full description of the statistical parameters including central tendency (e.g. means) or other basic estimates (e.g. regression coefficient) AND variation (e.g. standard deviation) or associated estimates of uncertainty (e.g. confidence intervals)
☐	☒	For null hypothesis testing, the test statistic (e.g. *F*, *t*, *r*) with confidence intervals, effect sizes, degrees of freedom and *P* value noted *Give P values as exact values whenever suitable.*
☒	☐	For Bayesian analysis, information on the choice of priors and Markov chain Monte Carlo settings
☒	☐	For hierarchical and complex designs, identification of the appropriate level for tests and full reporting of outcomes
☐	☒	Estimates of effect sizes (e.g. Cohen's *d*, Pearson's *r*), indicating how they were calculated

Our web collection on statistics for biologists contains articles on many of the points above.

Software and code

Policy information about availability of computer code

Data collection	Ex-vivo electrophysiological data were collected using pClamp 10 (Axon Instrument). In-vivo electrophysiological data were collected using Open-Ephys GUI (v0.4), software that is public available (http://www.open-ephys.org/gui). Behavioral experiments were recorded using Ethovision XT 11.5 (Noldus).
Data analysis	Data analysis was performed using Clampfit 10.7 (Molecular Devices, USA), Mini analysis 6 (Synaptosoft, USA), Avisoft-SASlab Pro 5.0 (Avisoft Bioacustic, Germany), Offline Sorter (Plexon, USA), and Neuroexplorer 3 (Nex Technologies, USA). Statistical analysis was performed using SigmaPlot 11 (Systat, USA), GraphPad Prism 7.05 (GraphPad Software, San Diego, California, USA), and custom scripts written in MATLAB R2015a (MathWorks, USA). All codes and algorithms used in the analysis are available from the corresponding author upon reasonable request.

For manuscripts utilizing custom algorithms or software that are central to the research but not yet described in published literature, software must be made available to editors/reviewers. We strongly encourage code deposition in a community repository (e.g. GitHub). See the Nature Research guidelines for submitting code & software for further information.

Data

Policy information about availability of data

All manuscripts must include a data availability statement. This statement should provide the following information, where applicable:

- Accession codes, unique identifiers, or web links for publicly available datasets
- A list of figures that have associated raw data
- A description of any restrictions on data availability

The data that support the findings of this study are available from the corresponding author upon reasonable request.

Field-specific reporting

Please select the one below that is the best fit for your research. If you are not sure, read the appropriate sections before making your selection.

☒ Life sciences ☐ Behavioural & social sciences ☐ Ecological, evolutionary & environmental sciences

For a reference copy of the document with all sections, see nature.com/documents/nr-reporting-summary-flat.pdf

Life sciences study design

All studies must disclose on these points even when the disclosure is negative.

Sample size	Sample size was determined to be adequate based on the magnitude and consistency of measurable differences between groups and/or experimental conditions.
Data exclusions	Data obtained from 15 rats were excluded from the analysis due to mistargeting or insufficient expression of viral vectors.
Replication	Experiments were repeated so that our data are based on at least three independent experiments with similar results. All attempts at replication were successful. The precise number of repeats are given in the text or in figure legends.
Randomization	Randomization was used to assign brain samples and animals to experimental groups whenever possible, with the constraint that in social behavior experiments rats had to be between unknown conspecifics, as described in Method section on page 44.
Blinding	Most of the measurements are made using a machine, and are not subject to operator bias, with the exception of manual scoring of social behaviors from videos; in this case, all scoring were done by a researcher (different from the one who performed the experiment) that was blind to treatment conditions.

Reporting for specific materials, systems and methods

We require information from authors about some types of materials, experimental systems and methods used in many studies. Here, indicate whether each material, system or method listed is relevant to your study. If you are not sure if a list item applies to your research, read the appropriate section before selecting a response.

Materials & experimental systems

n/a	Involved in the study
☐	☒ Antibodies
☐	☒ Eukaryotic cell lines
☒	☐ Palaeontology
☐	☒ Animals and other organisms
☒	☐ Human research participants
☒	☐ Clinical data

Methods

n/a	Involved in the study
☒	☐ ChIP-seq
☒	☐ Flow cytometry
☒	☐ MRI-based neuroimaging

Antibodies

Antibodies used	Primary antibodies: anti-oxytocin (PS38, mouse, kindly provided by Dr. Harold Gainer, NIH, Bethesda, USA), anti-oxytocin (T-5021, guinea pig, 1:50,000; Peninsula) anti-synaptophysin (ab32127, rabbit, 1:1,000, Abcam), anti-Ds-Red (#632397, rabbit, 1:1000, Clontech), anti-GFP (ab13970, chicken, 1:1000, Abcam), anti c-Fos (#9F6, rabbit, 1:500, Cell Signaling), anti-Fluorogold (NM-101, guinea pig, 1:1000, Protos Biotech), anti-Cre (#69050, mouse, 1:2000, Novagen). Secondary antibodies: CY3-conjugated (711-165-152, 1:500, Jackson Immuno-Reseach), CY5-conjugated (115-175-146, 1:500, Jackson Immuno-Research), Alexa 488 (A11039, 1:500, Invitrogen), Alexa 594 (A11012, 1:500, Invitrogen), Alexa 594 (715-585-151, 1:500, Jackson Immuno-Research), Alexa 647 (713-645-147, 1:500, Jackson Immuno-Research).
Validation	Validation of anti-oxytocin (PS38) immunohistochemistry in rat was first reported in (Ben-Barak et al., J. of Neurosci., 1985). Validation of anti-oxytocin (T-5021), anti-Ds-Red (#632397), anti-GFP (ab13970), anti c-Fos (#9F6), anti-Fluorogold (NM-101), immunohistochemistry in rat was reported in (Hasan et al., Neuron, 2019). Validation of anti-synaptophysin (ab32127) immunohistochemistry in rat was reported in (Lecanu et al., Neuroscience, 2010). Validation of anti-Cre (#69050) immunohistochemistry in mouse was reported in (Rajji et al., J. of Neurosci., 2006).

Eukaryotic cell lines

Policy information about cell lines

Cell line source(s)	Human embryonic kidney (HEK) 293T cell line was originally purchased from Addgene, USA (catalog number #240073).

Authentication	Cells authentication was done by microscopic inspection.
Mycoplasma contamination	All cell lines were tested negative for mycoplasma contamination.
Commonly misidentified lines (See ICLAC register)	No commonly misindentified cell lines were used in this study.

Animals and other organisms

Policy information about studies involving animals; ARRIVE guidelines recommended for reporting animal research

Laboratory animals	Four to eight-week old female Wistar rats purchased from Janvier, France and were housed under standard laboratory conditions: 12-h light/dark cycle, lights on at 07:00, 22-24 °C, 50 +/- 5% humidity, free access to food and water.
Wild animals	The study did not involve wild animals.
Field-collected samples	The study did not involve samples collected from the field.
Ethics oversight	All experiments were conducted under animal lisence G-102/17 authorized by the German Animal Ethics Committee of the Baden Württemberg (Regierungspräsidium Karlsruhe, Germany) and in accordance with the German low, under license 3668-2016011815445431 from the French Ministry, and under EU regulations.

Note that full information on the approval of the study protocol must also be provided in the manuscript.

L'ocytocine est un neuropeptide hypothalamique doté d'un large éventail de fonctions. De son rôle crucial dans l'accouchement à son implication dans le comportement maternel, ses fonctions ont été largement étudiées depuis des décennies. De nombreux travaux ont récemment mis en évidence son implication dans des comportements complexes, tels que la reconnaissance sociale et l'attachement inter-individuel, le contrôle de la douleur ou la modulation de l'anxiété. Ainsi, outre son action physiologique directe sur la contractilité de l'utérus et des glandes mammaires, l'ocytocine s'est taillé petit à petit une place en tant que neuromodulateur contrôlant les aspects émotionnels de nos vies. La manière dont le cerveau génère ces émotions est capitale dans la survie des êtres vivants, leur indiquant quand la prudence est de mise ou à l'inverse, quand l'organisme peut prendre du repos et régénérer son stock énergétique.

Au sein du cerveau, il existe une structure particulièrement impliquée dans la reconnaissance et l'attribution de la valeur émotionnelle des éléments de l'environnement : l'amygdale. L'évolution a donné à cette petite région située à la base du cerveau le dur labeur d'analyser les stimuli environnementaux et d'y associer une valeur émotionnelle, allant du vif désagrément causé par une expérience de douleur au doux plaisir d'un bon repas. Cette fonction est réalisée par un circuit de cellules électriquement activables : les neurones. Ainsi, l'amygdale est composée de plusieurs types de neurones dont l'activité vas assigner une valeur positive ou négative à une émotion. Qui plus est, l'activité de ces réseaux de neurones est sous l'influence de nombreux neuromodulateurs, molécules ayant le pouvoir de contrôler la manière dont les neurones interagissent, dressant le contexte dans lequel les neurones vont dialoguer. Ainsi, certains neuromodulateurs vont favoriser l'activité des neurones générant des émotions négatives alors que d'autres vont stimuler les neurones ayant un effet opposé.

Au sein de l'amygdale, et plus particulièrement de la partie centro-latérale de celle-ci, l'ocytocine possède un puissant effet neuromodulateur pouvant diminuer les émotions négatives telles que la peur et l'anxiété. Curieusement, l'effet de ce neuropeptide est relativement lent à se mettre en place, suggérant une action indirecte sur les neurones de l'amygdale. Bien que le dogme actuel est que l'ocytocine agisse exclusivement via des récepteurs neuronaux dans le système nerveux central, des études conduites dans une autre zone du cerveau au début des années 90 ont démontré que le récepteur de l'ocytocine était présent à la surface des cellules gliales, et plus particulièrement des astrocytes. Ces cellules étoilées aux fonctions multiples ne sont pas électriquement excitables, et sont donc considérées comme n'étant pas impliquées dans le traitement et l'analyse de l'information au

sein du cerveau. Faisant fi de ces considérations désuètes, nous nous sommes donc intéressés au rôle de l'ocytocine sur les astrocytes et de l'impact de ces cellules sur l'activité du réseau neuronal de l'amygdale centro-latérale.

Si des influx électriques bref comme ceux présents dans les neurones ne sont pas détectés dans les astrocytes, il est cependant possible d'y observer de nombreuses variations du niveau de calcium intracellulaire. Cette activité calcique peut avoir de nombreux effets cellulaires et c'est pourquoi elle est considérée comme un marqueur d'activité des astrocytes. Ainsi, nous avons enregistré les variations de concentration du calcium intracellulaire dans les astrocytes de l'amygdale centro-latérale. Nous avons pu observer que l'application de ce neuromodulateur induit des augmentations transitoires de la concentration de calcium intracellulaire et ce, même en présence de bloqueurs de l'activité neuronale. Nous avons ensuite réitéré l'expérience chez des souris dont les astrocytes n'expriment pas le récepteur de l'ocytocine et n'avons pas pu obtenir de réponse calcique suite à l'application du neuropeptide, indiquant une action directe de l'ocytocine sur son récepteur exprimé à la surface des astrocytes.

Forts de ces premiers résultats, nous nous sommes ensuite interrogés sur l'implication de ces variations calciques astrocytaires sur la fonction neuromodulatrice de l'ocytocine au sein de l'amygdale centro-latérale. Pour ce faire, nous avons enregistré l'activité électrique des neurones de cette structure. Nous avons observé que l'activation du récepteur ocytocinergique augmente la fréquence de potentiel d'action dans ces neurones, indiquant une augmentation de l'activité de ces derniers. Nous avons ensuite reproduit cette expérience en utilisant des souris n'exprimant pas le récepteur ocytocinergique astrocytaire où l'application d'un agoniste ocytocinergique n'était plus à même de faire varier l'activité du circuit neuronal, indiquant ainsi que l'action de l'ocytocine sur les astrocytes est nécessaire à son effet neuromodulateur sur les neurones de l'amygdale centro-latérale.

Dans le souci d'évaluer la pertinence de ces résultats à l'échelle comportementale, nous avons ensuite réalisé divers tests comportementaux visant à évaluer l'anxiété, la douleur et la valeur émotionnelle de celle-ci sur des modèles de souris et de rats ayant des douleurs neuropathiques ainsi que leur contrôle. De façon surprenante, l'activation du récepteur de l'ocytocine ne semble moduler que peu le seuil de sensibilité mécanique mais son action est beaucoup plus marquée sur les conséquences émotionnelles de la douleur. En effet, l'infusion

d'un agoniste ocytocinergique est à même de diminuer l'anxiété chez les souris neuropathiques et de diminuer la valeur émotionnelle négative liée à celle-ci.

Ainsi, ce premier volet de ma thèse a permis de mettre en évidence que l'ocytocine peut directement activer les astrocytes de l'amygdale centro-latérale qui relaient à leur tour le message aux neurones en augmentant leur excitabilité. Les résultats de ce circuit peuvent *in fine* se lire au niveau comportemental par une diminution de comportement de type anxieux et une réduction de la valeur émotionnelle de la douleur.

Dans un second temps, nous nous sommes intéressés à l'effet à long terme de l'ocytocine sur les astrocytes et les neurones de l'amygdale centro-latérale. Pour ce faire, nous avons tout d'abord choisi un comportement connu pour être particulièrement modulé par l'ocytocine : la réaction de peur. Nous avons tout d'abord estimé l'activité des neurones ocytocinergiques de l'hypothalamus au cours de l'apprentissage de cette peur et de son rappel et observé une augmentation de l'activité de ces neurones lors de l'apprentissage de la peur. Curieux de ce résultat, nous nous sommes ensuite penché sur l'action que pouvait avoir la libération d'ocytocine dans l'amygdale centro-latérale dans la mise en place du souvenir de peur. Pour ce faire, nous avons exposé des souris à un protocole de peur conditionnée et observé que contrairement aux souris contrôles, l'apprentissage de la peur est altéré chez les souris dont les astrocytes n'expriment pas le récepteur ocytocinergique astrocytaire.

Afin de comprendre pourquoi ces souris semblent insensibles au conditionnement de peur, nous nous sommes intéressées aux adaptations fonctionnelles de l'amygdale induites par la peur. Dans un premier temps, nous avons évalué l'excitabilité extrinsèque et intrinsèque des neurones de l'amygdale centro-latérale et nous avons observé que le conditionnement de peur induit une hyperexcitabilité des neurones de cette structure. Dans la mesure où l'effet de la peur sur l'hyperexcitabilité des neurones est dépendant du récepteur ocytocinergique astrocytaire, nous nous sommes ensuite dirigés vers l'implication de ces cellules gliales dans la modification fonctionnelle du circuit amygdalien.

Des études conduites dans l'hypothalamus ont mis en évidence que lors d'un évènement physiologique fort, la morphologie astrocytaire est modifiée sous l'action de l'ocytocine, favorisant ainsi l'activité neuronale. Nous avons donc voulu évaluer la morphologie des astrocytes de l'amygdale centro-latérale avant et après le protocole de peur conditionnée. Nous avons observé que ces cellules subissent une réorganisation

morphologique conséquente sous l'effet de la peur. Dans l'espoir de comprendre le lien entre cette réorganisation morphologique des astrocytes et l'hyperexcitabilité neuronale, nous nous sommes penchés sur un des aspects les plus capitaux de la physiologie astrocytaire : le tamponnage du potassium extracellulaire. Au cours de l'activité neuronale, ces cellules relâchent du potassium dans le milieu extracellulaire, augmentant ainsi la concentration de cet ion à proximité de la membrane neuronale et provoquant une dépolarisation de la membrane plasmique neuronale. Dans ce procédé, les astrocytes recapturent rapidement le potassium extracellulaire afin d'éviter l'hyperexcitabilité du circuit neuronal. Ainsi, nous avons décidé de tester si la modification morphologique des astrocytes s'accompagne d'une modification du tamponnage du potassium suite à l'activité neuronale. Cette expérience n'est à ce jour pas encore terminée mais si l'univers y est favorable, les résultats de cette dernière vous seront communiqués au cours de la soutenance de la présente thèse.

Ainsi, le travail que j'ai effectué au cours de cette thèse a permis de mettre en lumière l'implication des astrocytes de l'amygdale dans l'effet neuromodulateur de l'ocytocine aussi bien à court qu'à long terme. En plus de démontrer pour la première fois l'effet direct de l'ocytocine sur les astrocytes, mes travaux ont permis d'identifier ces cellules gliales comme acteur incontournable de la plasticité émotionnelle au sein de l'amygdale. Ce nouveau niveau de compréhension des mécanismes sous-tendant les émotions met en avant un nouveau type d'action de l'ocytocine jusqu'alors inexploré et pave le chemin à de nouvelles approches pour traiter les troubles émotionnels en modulant pharmacologiquement l'activité du système ocytocinergique.

10. Bibliography

Acevedo-Rodriguez, A., Mani, S.K., Handa, R.J., 2015. Oxytocin and Estrogen Receptor β in the Brain: An Overview. Front. Endocrinol. 6, 160.

Adamsky, A., Kol, A., Kreisel, T., Doron, A., Ozeri-Engelhard, N., Melcer, T., Refaeli, R., Horn, H., Regev, L., Groysman, M., London, M., Goshen, I., 2018. Astrocytic Activation Generates De Novo Neuronal Potentiation and Memory Enhancement. Cell 174, 59-71.e14.

Adke, A.P., Khan, A., Ahn, H.-S., Becker, J.J., Wilson, T.D., Valdivia, S., Sugimura, Y.K., Martinez Gonzalez, S., Carrasquillo, Y., 2021. Cell-Type Specificity of Neuronal Excitability and Morphology in the Central Amygdala. eNeuro 8, ENEURO.0402-20.2020.

Adolphs, R., Tranel, D., Damasio, H., Damasio, A., 1994. Impaired recognition of emotion in facial expressions following bilateral damage to the human amygdala. Nature 372, 669–672.

Agarwal, A., Wu, P.-H., Hughes, E.G., Fukaya, M., Tischfield, M.A., Langseth, A.J., Wirtz, D., Bergles, D.E., 2017. Transient Opening of the Mitochondrial Permeability Transition Pore Induces Microdomain Calcium Transients in Astrocyte Processes. Neuron 93, 587-605.e7.

Agulhon, C., Petravicz, J., McMullen, A.B., Sweger, E.J., Minton, S.K., Taves, S.R., Casper, K.B., Fiacco, T.A., McCarthy, K.D., 2008. What is the role of astrocyte calcium in neurophysiology? Neuron 59, 932–946.

Ahrens, S., Wu, M.V., Furlan, A., Hwang, G.-R., Paik, R., Li, H., Penzo, M.A., Tollkuhn, J., Li, B., 2018. A Central Extended Amygdala Circuit That Modulates Anxiety. J. Neurosci. Off. J. Soc. Neurosci. 38, 5567–5583.

Airan, R.D., Thompson, K.R., Fenno, L.E., Bernstein, H., Deisseroth, K., 2009. Temporally precise in vivo control of intracellular signalling. Nature 458, 1025–1029.

Alberi, S., Dreifuss, J.J., Raggenbass, M., 1997. The oxytocin-induced inward current in vagal neurons of the rat is mediated by G protein activation but not by an increase in the intracellular calcium concentration. Eur. J. Neurosci. 9, 2605–2612.

Amico, J.A., Mantella, R.C., Vollmer, R.R., Li, X., 2004. Anxiety and stress responses in female oxytocin deficient mice. J. Neuroendocrinol. 16, 319–324.

Andersen, J.V., Christensen, S.K., Westi, E.W., Diaz-delCastillo, M., Tanila, H., Schousboe, A., Aldana, B.I., Waagepetersen, H.S., 2021. Deficient astrocyte metabolism impairs glutamine synthesis and neurotransmitter homeostasis in a mouse model of Alzheimer's disease. Neurobiol. Dis. 148, 105198.

Angulo, M.C., Kozlov, A.S., Charpak, S., Audinat, E., 2004. Glutamate released from glial cells synchronizes neuronal activity in the hippocampus. J. Neurosci. Off. J. Soc. Neurosci. 24, 6920–6927.

Araque, A., Carmignoto, G., Haydon, P.G., Oliet, S.H.R., Robitaille, R., Volterra, A., 2014. Gliotransmitters travel in time and space. Neuron 81, 728–739.

Araque, A., Parpura, V., Sanzgiri, R.P., Haydon, P.G., 1998. Glutamate-dependent astrocyte modulation of synaptic transmission between cultured hippocampal neurons. Eur. J. Neurosci. 10, 2129–2142.

Araque, A., Parpura, V., Sanzgiri, R.P., Haydon, P.G., 1999. Tripartite synapses: glia, the unacknowledged partner. Trends Neurosci. 22, 208–215.

Arizono, M., Inavalli, V.V.G.K., Panatier, A., Pfeiffer, T., Angibaud, J., Levet, F., Ter Veer, M.J.T., Stobart, J., Bellocchio, L., Mikoshiba, K., Marsicano, G., Weber, B., Oliet, S.H.R., Nägerl, U.V., 2020. Structural basis of astrocytic Ca2+ signals at tripartite synapses. Nat. Commun. 11, 1906.

Ashwell, K.W.S., Lajevardi, S.-E., Cheng, G., Paxinos, G., 2006. The hypothalamic supraoptic and paraventricular nuclei of the echidna and platypus. Brain. Behav. Evol. 68, 197–217.

Aten, S., Kiyoshi, C.M., Arzola, E.P., Patterson, J.A., Taylor, A.T., Du, Y., Guiher, A.M., Philip, M., Camacho, E.G., Mediratta, D., Collins, K., Boni, K., Garcia, S.A., Kumar, R., Drake, A.N., Hegazi, A., Trank, L., Benson, E., Kidd, G., Terman, D., Zhou, M., 2022. Ultrastructural view of astrocyte arborization, astrocyte-astrocyte and astrocyte-synapse contacts, intracellular vesicle-like structures, and mitochondrial network. Prog. Neurobiol. 213, 102264.

Augusto-Oliveira, M., Arrifano, G.P., Takeda, P.Y., Lopes-Araújo, A., Santos-Sacramento, L., Anthony, D.C., Verkhratsky, A., Crespo-Lopez, M.E., 2020. Astroglia-specific contributions to the regulation of synapses, cognition and behaviour. Neurosci. Biobehav. Rev. 118, 331–357.

Bakos, J., Srancikova, A., Havranek, T., Bacova, Z., 2018. Molecular Mechanisms of Oxytocin Signaling at the Synaptic Connection. Neural Plast. 2018, 4864107.

Baldi, E., Costa, A., Rani, B., Passani, M.B., Blandina, P., Romano, A., Provensi, G., 2021. Oxytocin and Fear Memory Extinction: Possible Implications for the Therapy of Fear Disorders? Int. J. Mol. Sci. 22, 10000.

Bale, T.L., Davis, A.M., Auger, A.P., Dorsa, D.M., McCarthy, M.M., 2001. CNS region-specific oxytocin receptor expression: importance in regulation of anxiety and sex behavior. J. Neurosci. Off. J. Soc. Neurosci. 21, 2546–2552.

Barnett, M.W., Larkman, P.M., 2007. The action potential. Pract. Neurol. 7, 192–197.

Barrett, L.R., Nunez, J., Zhang, X., 2021. Oxytocin activation of paraventricular thalamic neurons promotes feeding motivation to attenuate stress-induced hypophagia. Neuropsychopharmacol. Off. Publ. Am. Coll. Neuropsychopharmacol. 46, 1045–1056.

Baudon, A., Clauss Creusot, E., Althammer, F., Schaaf, C.P., Charlet, A., 2022. Emerging role of astrocytes in oxytocin-mediated control of neural circuits and brain functions. Prog. Neurobiol. 217, 102328.

Bazargani, N., Attwell, D., 2016. Astrocyte calcium signaling: the third wave. Nat. Neurosci. 19, 182–189.

Bazaz, A., Ghanbari, A., Vafaei, A.A., Khaleghian, A., Rashidy-Pour, A., 2022. Oxytocin in dorsal hippocampus facilitates auditory fear memory extinction in rats. Neuropharmacology 202, 108844.

Beierlein, M., Regehr, W.G., 2006. Brief bursts of parallel fiber activity trigger calcium signals in bergmann glia. J. Neurosci. Off. J. Soc. Neurosci. 26, 6958–6967.

Ben Haim, L., Ceyzériat, K., Carrillo-de Sauvage, M.A., Aubry, F., Auregan, G., Guillermier, M., Ruiz, M., Petit, F., Houitte, D., Faivre, E., Vandesquille, M., Aron-Badin, R., Dhenain, M., Déglon, N., Hantraye, P., Brouillet, E., Bonvento, G., Escartin, C., 2015. The JAK/STAT3 Pathway Is a Common Inducer of Astrocyte Reactivity in Alzheimer's and Huntington's Diseases. J. Neurosci. 35, 2817–2829.

Berlin, S., Artzy, E., Handklo-Jamal, R., Kahanovitch, U., Parnas, H., Dascal, N., Yakubovich, D., 2020. A Collision Coupling Model Governs the Activation of Neuronal GIRK1/2 Channels by Muscarinic-2 Receptors. Front. Pharmacol. 11.

Berridge, M.J., Bootman, M.D., Lipp, P., 1998. Calcium--a life and death signal. Nature 395, 645–648.

Berridge, M.J., Bootman, M.D., Roderick, H.L., 2003. Calcium signalling: dynamics, homeostasis and remodelling. Nat. Rev. Mol. Cell Biol. 4, 517–529.

Berridge, M.J., Lipp, P., Bootman, M.D., 2000. The versatility and universality of calcium signalling. Nat. Rev. Mol. Cell Biol. 1, 11–21.

Beyeler, A., Dabrowska, J., 2020. Neuronal diversity of the amygdala and the bed nucleus of the stria terminalis. Handb. Behav. Neurosci. 26, 63–100.

Bezzi, P., Gundersen, V., Galbete, J.L., Seifert, G., Steinhäuser, C., Pilati, E., Volterra, A., 2004. Astrocytes contain a vesicular compartment that is competent for regulated exocytosis of glutamate. Nat. Neurosci. 7, 613–620.

Bindocci, E., Savtchouk, I., Liaudet, N., Becker, D., Carriero, G., Volterra, A., 2017. Three-dimensional Ca2+ imaging advances understanding of astrocyte biology. Science 356, eaai8185.

Bologna, M., Paparella, G., Fasano, A., Hallett, M., Berardelli, A., 2020. Evolving concepts on bradykinesia. Brain J. Neurol. 143, 727–750.

Breton, J.-D., Veinante, P., Uhl-Bronner, S., Vergnano, A.M., Freund-Mercier, M.J., Schlichter, R., Poisbeau, P., 2008. Oxytocin-induced antinociception in the spinal cord is mediated by a subpopulation of glutamatergic neurons in lamina I-II which amplify GABAergic inhibition. Mol. Pain 4, 19.

Bryda, E.C., 2013. The Mighty Mouse: The Impact of Rodents on Advances in Biomedical Research. Mo. Med. 110, 207–211.

Bushong, E.A., Martone, M.E., Jones, Y.Z., Ellisman, M.H., 2002. Protoplasmic astrocytes in CA1 stratum radiatum occupy separate anatomical domains. J. Neurosci. Off. J. Soc. Neurosci. 22, 183–192.

Busnelli, M., Chini, B., 2018. Molecular Basis of Oxytocin Receptor Signalling in the Brain: What We Know and What We Need to Know. Curr. Top. Behav. Neurosci. 35, 3–29.

Busnelli, M., Saulière, A., Manning, M., Bouvier, M., Galés, C., Chini, B., 2012. Functional selective oxytocin-derived agonists discriminate between individual G protein family subtypes. J. Biol. Chem. 287, 3617–3629.

Campbell-Smith, E.J., Holmes, N.M., Lingawi, N.W., Panayi, M.C., Westbrook, R.F., 2015. Oxytocin signaling in basolateral and central amygdala nuclei differentially regulates the acquisition,

expression, and extinction of context-conditioned fear in rats. Learn. Mem. Cold Spring Harb. N 22, 247–257.

Carter, C.S., 2007. Sex differences in oxytocin and vasopressin: implications for autism spectrum disorders? Behav. Brain Res. 176, 170–186.

Chai, H., Diaz-Castro, B., Shigetomi, E., Monte, E., Octeau, J.C., Yu, X., Cohn, W., Rajendran, P.S., Vondriska, T.M., Whitelegge, J.P., Coppola, G., Khakh, B.S., 2017. Neural Circuit-Specialized Astrocytes: Transcriptomic, Proteomic, Morphological, and Functional Evidence. Neuron 95, 531-549.e9.

Charles, A.C., Merrill, J.E., Dirksen, E.R., Sanderson, M.J., 1991. Intercellular signaling in glial cells: calcium waves and oscillations in response to mechanical stimulation and glutamate. Neuron 6, 983–992.

Chatterjee, O., Patil, K., Sahu, A., Gopalakrishnan, L., Mol, P., Advani, J., Mukherjee, S., Christopher, R., Prasad, T.S.K., 2016. An overview of the oxytocin-oxytocin receptor signaling network. J. Cell Commun. Signal. 10, 355–360.

Chen, M., Kianifard, F., 1997. A multiple comparison procedure to control the strong stagewise family error rate in comparing test treatments and a control. J. Biopharm. Stat. 7, 355–367.

Chen, W.-H., Lien, C.-C., Chen, C.-C., 2022. Neuronal basis for pain-like and anxiety-like behaviors in the central nucleus of the amygdala. Pain 163, e463–e475.

Chieng, B.C.H., Christie, M.J., Osborne, P.B., 2006. Characterization of neurons in the rat central nucleus of the amygdala: cellular physiology, morphology, and opioid sensitivity. J. Comp. Neurol. 497, 910–927.

Chini, B., Verhage, M., Grinevich, V., 2017. The Action Radius of Oxytocin Release in the Mammalian CNS: From Single Vesicles to Behavior. Trends Pharmacol. Sci. 38, 982–991.

Clapham, D.E., Neer, E.J., 1997. G protein beta gamma subunits. Annu. Rev. Pharmacol. Toxicol. 37, 167–203.

Conti, F., Sertic, S., Reversi, A., Chini, B., 2009. Intracellular trafficking of the human oxytocin receptor: evidence of receptor recycling via a Rab4/Rab5 "short cycle." Am. J. Physiol. Endocrinol. Metab. 296, E532-542.

Corkrum, M., Covelo, A., Lines, J., Bellocchio, L., Pisansky, M., Loke, K., Quintana, R., Rothwell, P.E., Lujan, R., Marsicano, G., Martin, E.D., Thomas, M.J., Kofuji, P., Araque, A., 2020. Dopamine-Evoked Synaptic Regulation in the Nucleus Accumbens Requires Astrocyte Activity. Neuron 105, 1036-1047.e5.

Cottet, M., Albizu, L., Perkovska, S., Jean-Alphonse, F., Rahmeh, R., Orcel, H., Méjean, C., Granier, S., Mendre, C., Mouillac, B., Durroux, T., 2010. Past, present and future of vasopressin and oxytocin receptor oligomers, prototypical GPCR models to study dimerization processes. Curr. Opin. Pharmacol. 10, 59–66.

Cragg, B., Ji, G., Neugebauer, V., 2016. Differential contributions of vasopressin V1A and oxytocin receptors in the amygdala to pain-related behaviors in rats. Mol. Pain 12, 1744806916676491.

Crane, J.W., Holmes, N.M., Fam, J., Westbrook, R.F., Delaney, A.J., 2020. Oxytocin increases inhibitory synaptic transmission and blocks development of long-term potentiation in the lateral amygdala. J. Neurophysiol. 123, 587–599.

Croft, W., Reusch, K., Tilunaite, A., Russell, N.A., Thul, R., Bellamy, T.C., 2016. Probabilistic encoding of stimulus strength in astrocyte global calcium signals. Glia 64, 537–552.

Dale, H.H., 1906. On some physiological actions of ergot. J. Physiol. 34, 163–206.

de la Mora, M.P., Pérez-Carrera, D., Crespo-Ramírez, M., Tarakanov, A., Fuxe, K., Borroto-Escuela, D.O., 2016. Signaling in dopamine D2 receptor-oxytocin receptor heterocomplexes and its relevance for the anxiolytic effects of dopamine and oxytocin interactions in the amygdala of the rat. Biochim. Biophys. Acta 1862, 2075–2085.

Del-Bel, E., De-Miguel, F.F., 2018. Extrasynaptic Neurotransmission Mediated by Exocytosis and Diffusive Release of Transmitter Substances. Front. Synaptic Neurosci. 10, 13.

Devost, D., Zingg, H.H., 2003. Identification of dimeric and oligomeric complexes of the human oxytocin receptor by co-immunoprecipitation and bioluminescence resonance energy transfer. J. Mol. Endocrinol. 31, 461–471.

Di Castro, M.A., Chuquet, J., Liaudet, N., Bhaukaurally, K., Santello, M., Bouvier, D., Tiret, P., Volterra, A., 2011. Local Ca2+ detection and modulation of synaptic release by astrocytes. Nat. Neurosci. 14, 1276–1284.

Di Scala-Guenot, D., Mouginot, D., Strosser, M.T., 1994. Increase of intracellular calcium induced by oxytocin in hypothalamic cultured astrocytes. Glia 11, 269–276.

Di Scala-Guenot, D., Strosser, M.T., 1992. Oxytocin receptors on cultured astroglial cells. Kinetic and pharmacological characterization of oxytocin-binding sites on intact hypothalamic and hippocampic cells from foetal rat brain. Biochem. J. 284 (Pt 2), 491–497.

Dölen, G., Darvishzadeh, A., Huang, K.W., Malenka, R.C., 2013. Social reward requires coordinated activity of nucleus accumbens oxytocin and serotonin. Nature 501, 179–184.

Dumont, E.C., Martina, M., Samson, R.D., Drolet, G., Paré, D., 2002. Physiological properties of central amygdala neurons: species differences. Eur. J. Neurosci. 15, 545–552.

Duque-Wilckens, N., Torres, L.Y., Yokoyama, S., Minie, V.A., Tran, A.M., Petkova, S.P., Hao, R., Ramos-Maciel, S., Rios, R.A., Jackson, K., Flores-Ramirez, F.J., Garcia-Carachure, I., Pesavento, P.A., Iñiguez, S.D., Grinevich, V., Trainor, B.C., 2020. Extrahypothalamic oxytocin neurons drive stress-induced social vigilance and avoidance. Proc. Natl. Acad. Sci. U. S. A. 117, 26406–26413.

Durkee, C.A., Covelo, A., Lines, J., Kofuji, P., Aguilar, J., Araque, A., 2019. Gi/o protein-coupled receptors inhibit neurons but activate astrocytes and stimulate gliotransmission. Glia 67, 1076–1093.

Duvarci, S., Pare, D., 2014. Amygdala microcircuits controlling learned fear. Neuron 82, 966–980.

Ebner, K., Bosch, O.J., Krömer, S.A., Singewald, N., Neumann, I.D., 2005. Release of oxytocin in the rat central amygdala modulates stress-coping behavior and the release of excitatory amino acids. Neuropsychopharmacol. Off. Publ. Am. Coll. Neuropsychopharmacol. 30, 223–230.

Ehrlich, I., Humeau, Y., Grenier, F., Ciocchi, S., Herry, C., Lüthi, A., 2009. Amygdala inhibitory circuits and the control of fear memory. Neuron 62, 757–771.

Eliava, M., Melchior, M., Knobloch-Bollmann, H.S., Wahis, J., da Silva Gouveia, M., Tang, Y., Ciobanu, A.C., Triana Del Rio, R., Roth, L.C., Althammer, F., Chavant, V., Goumon, Y., Gruber, T., Petit-Demoulière, N., Busnelli, M., Chini, B., Tan, L.L., Mitre, M., Froemke, R.C., Chao, M.V., Giese, G., Sprengel, R., Kuner, R., Poisbeau, P., Seeburg, P.H., Stoop, R., Charlet, A., Grinevich, V., 2016. A New Population of Parvocellular Oxytocin Neurons Controlling Magnocellular Neuron Activity and Inflammatory Pain Processing. Neuron 89, 1291–1304.

Endo, F., Kasai, A., Soto, J.S., Yu, X., Qu, Z., Hashimoto, H., Gradinaru, V., Kawaguchi, R., Khakh, B.S., 2022. Molecular basis of astrocyte diversity and morphology across the CNS in health and disease. Science 378, eadc9020.

Escartin, C., Galea, E., Lakatos, A., O'Callaghan, J.P., Petzold, G.C., Serrano-Pozo, A., Steinhäuser, C., Volterra, A., Carmignoto, G., Agarwal, A., Allen, N.J., Araque, A., Barbeito, L., Barzilai, A., Bergles, D.E., Bonvento, G., Butt, A.M., Chen, W.-T., Cohen-Salmon, M., Cunningham, C., Deneen, B., De Strooper, B., Díaz-Castro, B., Farina, C., Freeman, M., Gallo, V., Goldman, J.E., Goldman, S.A., Götz, M., Gutiérrez, A., Haydon, P.G., Heiland, D.H., Hol, E.M., Holt, M.G., Iino, M., Kastanenka, K.V., Kettenmann, H., Khakh, B.S., Koizumi, S., Lee, C.J., Liddelow, S.A., MacVicar, B.A., Magistretti, P., Messing, A., Mishra, A., Molofsky, A.V., Murai, K.K., Norris, C.M., Okada, S., Oliet, S.H.R., Oliveira, J.F., Panatier, A., Parpura, V., Pekna, M., Pekny, M., Pellerin, L., Perea, G., Pérez-Nievas, B.G., Pfrieger, F.W., Poskanzer, K.E., Quintana, F.J., Ransohoff, R.M., Riquelme-Perez, M., Robel, S., Rose, C.R., Rothstein, J.D., Rouach, N., Rowitch, D.H., Semyanov, A., Sirko, S., Sontheimer, H., Swanson, R.A., Vitorica, J., Wanner, I.-B., Wood, L.B., Wu, J., Zheng, B., Zimmer, E.R., Zorec, R., Sofroniew, M.V., Verkhratsky, A., 2021. Reactive astrocyte nomenclature, definitions, and future directions. Nat. Neurosci. 24, 312–325.

Escartin, C., Guillemaud, O., Carrillo-de Sauvage, M.-A., 2019. Questions and (some) answers on reactive astrocytes. Glia 67, 2221–2247.

Espinosa de Los Monteros-Zúñiga, A., Martínez-Lorenzana, G., Condés-Lara, M., González-Hernández, A., 2021. In Vivo Dissection of Two Intracellular Pathways Involved in the Spinal Oxytocin-Induced Antinociception in the Rat. ACS Chem. Neurosci. 12, 3140–3147.

Fadok, J.P., Krabbe, S., Markovic, M., Courtin, J., Xu, C., Massi, L., Botta, P., Bylund, K., Müller, C., Kovacevic, A., Tovote, P., Lüthi, A., 2017. A competitive inhibitory circuit for selection of active and passive fear responses. Nature 542, 96–100.

Fellin, T., 2009. Communication between neurons and astrocytes: relevance to the modulation of synaptic and network activity. J. Neurochem. 108, 533–544.

Fellin, T., Pascual, O., Gobbo, S., Pozzan, T., Haydon, P.G., Carmignoto, G., 2004. Neuronal synchrony mediated by astrocytic glutamate through activation of extrasynaptic NMDA receptors. Neuron 43, 729–743.

Fernando, R.N., Larm, J., Albiston, A.L., Chai, S.Y., 2005. Distribution and cellular localization of insulin-regulated aminopeptidase in the rat central nervous system. J. Comp. Neurol. 487, 372–390.

Ferretti, V., Maltese, F., Contarini, G., Nigro, M., Bonavia, A., Huang, H., Gigliucci, V., Morelli, G., Scheggia, D., Managò, F., Castellani, G., Lefevre, A., Cancedda, L., Chini, B., Grinevich, V., Papaleo, F., 2019. Oxytocin Signaling in the Central Amygdala Modulates Emotion Discrimination in Mice. Curr. Biol. CB 29, 1938-1953.e6.

Fiacco, T.A., Agulhon, C., Taves, S.R., Petravicz, J., Casper, K.B., Dong, X., Chen, J., McCarthy, K.D., 2007. Selective stimulation of astrocyte calcium in situ does not affect neuronal excitatory synaptic activity. Neuron 54, 611–626.

Froemke, R.C., Carcea, I., 2017. Chapter 13 - Oxytocin and Brain Plasticity. In: Legato, M.J. (Ed.), Principles of Gender-Specific Medicine (Third Edition). Academic Press, San Diego, pp. 161–182.

Fu, J.-Y., Yu, X.-D., Zhu, Y., Xie, S.-Z., Tang, M.-Y., Yu, B., Li, X.-M., 2020. Whole-Brain Map of Long-Range Monosynaptic Inputs to Different Cell Types in the Amygdala of the Mouse. Neurosci. Bull. 36, 1381–1394.

Gaidin, S.G., Zinchenko, V.P., Sergeev, A.I., Teplov, I.Y., Mal'tseva, V.N., Kosenkov, A.M., 2020. Activation of alpha-2 adrenergic receptors stimulates GABA release by astrocytes. Glia 68, 1114–1130.

Gimpl, G., Fahrenholz, F., 2001. The oxytocin receptor system: structure, function, and regulation. Physiol. Rev. 81, 629–683.

Gravati, M., Busnelli, M., Bulgheroni, E., Reversi, A., Spaiardi, P., Parenti, M., Toselli, M., Chini, B., 2010. Dual modulation of inward rectifier potassium currents in olfactory neuronal cells by promiscuous G protein coupling of the oxytocin receptor. J. Neurochem. 114, 1424–1435.

Grinevich, V., Knobloch-Bollmann, H.S., Eliava, M., Busnelli, M., Chini, B., 2016. Assembling the Puzzle: Pathways of Oxytocin Signaling in the Brain. Biol. Psychiatry 79, 155–164.

Grinevich, V., Ludwig, M., 2021. The multiple faces of the oxytocin and vasopressin systems in the brain. J. Neuroendocrinol. 33, e13004.

Grosche, J., Matyash, V., Möller, T., Verkhratsky, A., Reichenbach, A., Kettenmann, H., 1999. Microdomains for neuron-glia interaction: parallel fiber signaling to Bergmann glial cells. Nat. Neurosci. 2, 139–143.

Gunduz-Cinar, O., Brockway, E.T., Castillo, L.I., Pollack, G.A., Erguven, T., Holmes, A., 2020. Selective sub-nucleus effects of intra-amygdala oxytocin on fear extinction. Behav. Brain Res. 393, 112798.

Guzzi, F., Zanchetta, D., Cassoni, P., Guzzi, V., Francolini, M., Parenti, M., Chini, B., 2002. Localization of the human oxytocin receptor in caveolin-1 enriched domains turns the receptor-mediated inhibition of cell growth into a proliferative response. Oncogene 21, 1658–1667.

Gwee, P.-C., Tay, B.-H., Brenner, S., Venkatesh, B., 2009. Characterization of the neurohypophysial hormone gene loci in elephant shark and the Japanese lamprey: origin of the vertebrate neurohypophysial hormone genes. BMC Evol. Biol. 9, 47.

Haber, M., Zhou, L., Murai, K.K., 2006. Cooperative astrocyte and dendritic spine dynamics at hippocampal excitatory synapses. J. Neurosci. Off. J. Soc. Neurosci. 26, 8881–8891.

Han, Y., Yu, L.-C., 2009. Involvement of oxytocin and its receptor in nociceptive modulation in the central nucleus of amygdala of rats. Neurosci. Lett. 454, 101–104.

Harper, K.M., Knapp, D.J., Butler, R.K., Cook, C.A., Criswell, H.E., Stuber, G.D., Breese, G.R., 2019. Amygdala Arginine Vasopressin Modulates Chronic Ethanol Withdrawal Anxiety-Like Behavior in the Social Interaction Task. Alcohol. Clin. Exp. Res. 43, 2134–2143.

Hartley, N.D., Gaulden, A.D., Báldi, R., Winters, N.D., Salimando, G.J., Rosas-Vidal, L.E., Jameson, A., Winder, D.G., Patel, S., 2019. Dynamic remodeling of a basolateral-to-central amygdala glutamatergic circuit across fear states. Nat. Neurosci. 22, 2000–2012.

Hasan, M.T., Althammer, F., Silva da Gouveia, M., Goyon, S., Eliava, M., Lefevre, A., Kerspern, D., Schimmer, J., Raftogianni, A., Wahis, J., Knobloch-Bollmann, H.S., Tang, Y., Liu, X., Jain, A., Chavant, V., Goumon, Y., Weislogel, J.-M., Hurlemann, R., Herpertz, S.C., Pitzer, C., Darbon, P., Dogbevia, G.K., Bertocchi, I., Larkum, M.E., Sprengel, R., Bading, H., Charlet, A., Grinevich, V., 2019. A Fear Memory Engram and Its Plasticity in the Hypothalamic Oxytocin System. Neuron 103, 133-146.e8.

Hasbi, A., Devost, D., Laporte, S.A., Zingg, H.H., 2004. Real-time detection of interactions between the human oxytocin receptor and G protein-coupled receptor kinase-2. Mol. Endocrinol. Baltim. Md 18, 1277–1286.

Haubensak, W., Kunwar, P.S., Cai, H., Ciocchi, S., Wall, N.R., Ponnusamy, R., Biag, J., Dong, H.-W., Deisseroth, K., Callaway, E.M., Fanselow, M.S., Lüthi, A., Anderson, D.J., 2010. Genetic dissection of an amygdala microcircuit that gates conditioned fear. Nature 468, 270–276.

Hazim Abdul Hameed, D., Hussein Ali, E., 2021. Extraction and Purification of Extracellular L-Glutamate Oxidase from Streptomyces. Arch. Razi Inst. 76, 769–779.

Henneberger, C., Bard, L., Panatier, A., Reynolds, J.P., Kopach, O., Medvedev, N.I., Minge, D., Herde, M.K., Anders, S., Kraev, I., Heller, J.P., Rama, S., Zheng, K., Jensen, T.P., Sanchez-Romero, I., Jackson, C.J., Janovjak, H., Ottersen, O.P., Nagelhus, E.A., Oliet, S.H.R., Stewart, M.G., Nägerl, U.V., Rusakov, D.A., 2020. LTP Induction Boosts Glutamate Spillover by Driving Withdrawal of Perisynaptic Astroglia. Neuron 108, 919-936.e11.

Herget, U., Wolf, A., Wullimann, M.F., Ryu, S., 2014. Molecular neuroanatomy and chemoarchitecture of the neurosecretory preoptic-hypothalamic area in zebrafish larvae. J. Comp. Neurol. 522, 1542–1564.

Herman, M.A., Nahir, B., Jahr, C.E., 2011. Distribution of extracellular glutamate in the neuropil of hippocampus. PloS One 6, e26501.

Hoare, S., Copland, J.A., Strakova, Z., Ives, K., Jeng, Y.J., Hellmich, M.R., Soloff, M.S., 1999. The proximal portion of the COOH terminus of the oxytocin receptor is required for coupling to g(q), but not g(i). Independent mechanisms for elevating intracellular calcium concentrations from intracellular stores. J. Biol. Chem. 274, 28682–28689.

Horio, M., Kohno, M., Fujita, Y., Ishima, T., Inoue, R., Mori, H., Hashimoto, K., 2011. Levels of D-serine in the brain and peripheral organs of serine racemase (Srr) knock-out mice. Neurochem. Int. 59, 853–859.

Hu, B., Boyle, C.A., Lei, S., 2021. Activation of Oxytocin Receptors Excites Subicular Neurons by Multiple Signaling and Ionic Mechanisms. Cereb. Cortex N. Y. N 1991 31, 2402–2415.

Huber, D., Veinante, P., Stoop, R., 2005. Vasopressin and oxytocin excite distinct neuronal populations in the central amygdala. Science 308, 245–248.

Hunt, S., Sun, Y., Kucukdereli, H., Klein, R., Sah, P., 2017. Intrinsic Circuits in the Lateral Central Amygdala. eNeuro 4, ENEURO.0367-16.2017.

Inoue, T., Kimura, T., Azuma, C., Inazawa, J., Takemura, M., Kikuchi, T., Kubota, Y., Ogita, K., Saji, F., 1994. Structural organization of the human oxytocin receptor gene. J. Biol. Chem. 269, 32451–32456.

Iwasaki, M., Lefevre, A., Althammer, F., Clauss Creusot, E., Łąpieś, O., Petitjean, H., Hilfiger, L., Kerspern, D., Melchior, M., Küppers, S., Krabichler, Q., Patwell, R., Kania, A., Gruber, T., Kirchner, M.K., Wimmer, M., Fröhlich, H., Dötsch, L., Schimmer, J., Herpertz, S.C., Ditzen, B., Schaaf, C.P., Schönig, K., Bartsch, D., Gugula, A., Trenk, A., Blasiak, A., Stern, J.E., Darbon, P., Grinevich, V., Charlet, A., 2023. An analgesic pathway from parvocellular oxytocin neurons to the periaqueductal gray in rats. Nat. Commun. 14, 1066.

Jean-Charles, P.-Y., Kaur, S., Shenoy, S.K., 2017. G Protein-Coupled Receptor Signaling Through β-Arrestin-Dependent Mechanisms. J. Cardiovasc. Pharmacol. 70, 142–158.

Jiang, M., Bajpayee, N.S., 2009. Molecular mechanisms of go signaling. Neurosignals 17, 23–41.

Jiménez, A., Lu, D., Kalocsay, M., Berberich, M.J., Balbi, P., Jambhekar, A., Lahav, G., 2022. Time-series transcriptomics and proteomics reveal alternative modes to decode p53 oscillations. Mol. Syst. Biol. 18, e10588.

Jourdain, P., Bergersen, L.H., Bhaukaurally, K., Bezzi, P., Santello, M., Domercq, M., Matute, C., Tonello, F., Gundersen, V., Volterra, A., 2007. Glutamate exocytosis from astrocytes controls synaptic strength. Nat. Neurosci. 10, 331–339.

Juif, P.-E., Poisbeau, P., 2013. Neurohormonal effects of oxytocin and vasopressin receptor agonists on spinal pain processing in male rats. Pain 154, 1449–1456.

Jurek, B., Neumann, I.D., 2018. The Oxytocin Receptor: From Intracellular Signaling to Behavior. Physiol. Rev. 98, 1805–1908.

Karagiannis, A., Gallopin, T., Lacroix, A., Plaisier, F., Piquet, J., Geoffroy, H., Hepp, R., Naudé, J., Le Gac, B., Egger, R., Lambolez, B., Li, D., Rossier, J., Staiger, J.F., Imamura, H., Seino, S., Roeper, J., Cauli, B., 2021. Lactate is an energy substrate for rodent cortical neurons and enhances their firing activity. eLife 10, e71424.

Keshavarzi, S., Sullivan, R.K.P., Ianno, D.J., Sah, P., 2014. Functional properties and projections of neurons in the medial amygdala. J. Neurosci. Off. J. Soc. Neurosci. 34, 8699–8715.

Khakh, B.S., 2019. Astrocyte-Neuron Interactions in the Striatum: Insights on Identity, Form, and Function. Trends Neurosci. 42, 617–630.

Khakh, B.S., Deneen, B., 2019. The Emerging Nature of Astrocyte Diversity. Annu. Rev. Neurosci. 42, 187–207.

Khakh, B.S., Sofroniew, M.V., 2015. Diversity of astrocyte functions and phenotypes in neural circuits. Nat. Neurosci. 18, 942–952.

Kim, J., Zhang, X., Muralidhar, S., LeBlanc, S.A., Tonegawa, S., 2017. Basolateral to Central Amygdala Neural Circuits for Appetitive Behaviors. Neuron 93, 1464-1479.e5.

Kim, J.H., Lee, J.-E., Kim, T., Yeom, M.H., Park, J.S., di Luccio, E., Chen, H., Dong, Z., Lee, K.W., Kang, N.J., 2020. 7,3',4'-Trihydroxyisoflavone, a Metabolite of the Soy Isoflavone Daidzein, Suppresses α-Melanocyte-Stimulating Hormone-Induced Melanogenesis by Targeting Melanocortin 1 Receptor. Front. Mol. Biosci. 7, 577284.

Knobloch, H.S., Charlet, A., Hoffmann, L.C., Eliava, M., Khrulev, S., Cetin, A.H., Osten, P., Schwarz, M.K., Seeburg, P.H., Stoop, R., Grinevich, V., 2012. Evoked axonal oxytocin release in the central amygdala attenuates fear response. Neuron 73, 553–566.

Knobloch, H.S., Grinevich, V., 2014. Evolution of oxytocin pathways in the brain of vertebrates. Front. Behav. Neurosci. 8, 31.

Kofuji, P., Araque, A., 2021. G-Protein-Coupled Receptors in Astrocyte-Neuron Communication. Neuroscience 456, 71–84.

Kofuji, P., Newman, E.A., 2004. Potassium buffering in the central nervous system. Neuroscience 129, 1045–1056.

Kovács, A., Pál, B., 2017. Astrocyte-Dependent Slow Inward Currents (SICs) Participate in Neuromodulatory Mechanisms in the Pedunculopontine Nucleus (PPN). Front. Cell. Neurosci. 11, 16.

Kritman, M., Lahoud, N., Maroun, M., 2017. Oxytocin in the amygdala and not the prefrontal cortex enhances fear and impairs extinction in the juvenile rat. Neurobiol. Learn. Mem. 141, 179–188.

Lahoud, N., Maroun, M., 2013. Oxytocinergic manipulations in corticolimbic circuit differentially affect fear acquisition and extinction. Psychoneuroendocrinology 38, 2184–2195.

Lanska, D.J., 2018. The Klüver-Bucy Syndrome. Front. Neurol. Neurosci. 41, 77–89.

László, K., Péczely, L., Géczi, F., Kovács, A., Zagoracz, O., Ollmann, T., Kertes, E., Kállai, V., László, B., Berta, B., Karádi, Z., Lénárd, L., 2020. The role of D2 dopamine receptors in oxytocin induced place preference and anxiolytic effect. Horm. Behav. 124, 104777.

Lawal, O., Ulloa Severino, F.P., Eroglu, C., 2022. The role of astrocyte structural plasticity in regulating neural circuit function and behavior. Glia 70, 1467–1483.

LeDoux, J.E., 2000. Emotion circuits in the brain. Annu. Rev. Neurosci. 23, 155–184.

Lee, H.-J., Macbeth, A.H., Pagani, J.H., Young, W.S., 2009. Oxytocin: the great facilitator of life. Prog. Neurobiol. 88, 127–151.

Lefevre, A., Benusiglio, D., Tang, Y., Krabichler, Q., Charlet, A., Grinevich, V., 2021. Oxytocinergic Feedback Circuitries: An Anatomical Basis for Neuromodulation of Social Behaviors. Front. Neural Circuits 15, 688234.

Leng, G., Ludwig, M., 2008. Neurotransmitters and peptides: whispered secrets and public announcements. J. Physiol. 586, 5625–5632.

Lentz, T., 2023. Nervous system | Definition, Function, Structure, & Facts | Britannica [WWW Document]. URL https://www.britannica.com/science/nervous-system (accessed 4.12.23).

Lerma, J., Herranz, A.S., Herreras, O., Abraira, V., Martín del Río, R., 1986. In vivo determination of extracellular concentration of amino acids in the rat hippocampus. A method based on brain dialysis and computerized analysis. Brain Res. 384, 145–155.

Li, H., Penzo, M.A., Taniguchi, H., Kopec, C.D., Huang, Z.J., Li, B., 2013. Experience-dependent modification of a central amygdala fear circuit. Nat. Neurosci. 16, 332–339.

Lim, D., Semyanov, A., Genazzani, A., Verkhratsky, A., 2021. Calcium signaling in neuroglia. Int. Rev. Cell Mol. Biol. 362, 1–53.

Lin, Y.-L., Yang, Z.-S., Wong, W.-Y., Lin, S.-C., Wang, S.-J., Chen, S.-P., Cheng, J.-K., Lu, H., Lien, C.-C., 2022. Cellular mechanisms underlying central sensitization in a mouse model of chronic muscle pain. eLife 11, e78610.

Liu, C., Li, Y., Lein, P.J., Ford, B.D., 2012. Spatiotemporal patterns of GFAP upregulation in rat brain following acute intoxication with diisopropylfluorophosphate (DFP). Curr. Neurobiol. 3, 90–97.

Lopez de Armentia, M., Sah, P., 2004. Firing properties and connectivity of neurons in the rat lateral central nucleus of the amygdala. J. Neurophysiol. 92, 1285–1294.

Luo, P.X., Zakharenkov, H.C., Torres, L.Y., Rios, R.A., Gegenhuber, B., Black, A.M., Xu, C.K., Minie, V.A., Tran, A.M., Tollkuhn, J., Trainor, B.C., 2022. Oxytocin receptor behavioral effects and cell types in the bed nucleus of the stria terminalis. Horm. Behav. 143, 105203.

Malik, M., Ward, M.D., Fang, Y., Porter, J.R., Zimmerman, M.I., Koelblen, T., Roh, M., Frolova, A.I., Burris, T.P., Bowman, G.R., Imoukhuede, P.I., England, S.K., 2021. Naturally Occurring

Genetic Variants in the Oxytocin Receptor Alter Receptor Signaling Profiles. ACS Pharmacol. Transl. Sci. 4, 1543–1555.

Maroun, M., Wagner, S., 2016. Oxytocin and Memory of Emotional Stimuli: Some Dance to Remember, Some Dance to Forget. Biol. Psychiatry 79, 203–212.

Martina, M., Royer, S., Paré, D., 1999. Physiological properties of central medial and central lateral amygdala neurons. J. Neurophysiol. 82, 1843–1854.

McCarthy, M.M., McDonald, C.H., Brooks, P.J., Goldman, D., 1996. An anxiolytic action of oxytocin is enhanced by estrogen in the mouse. Physiol. Behav. 60, 1209–1215.

McCullough, K.M., Morrison, F.G., Hartmann, J., Carlezon, W.A., Ressler, K.J., 2018. Quantified Coexpression Analysis of Central Amygdala Subpopulations. eNeuro 5, ENEURO.0010-18.2018.

McKay, E.C., Counts, S.E., 2020. Oxytocin Receptor Signaling in Vascular Function and Stroke. Front. Neurosci. 14, 574499.

McNeill, J., Rudyk, C., Hildebrand, M.E., Salmaso, N., 2021. Ion Channels and Electrophysiological Properties of Astrocytes: Implications for Emergent Stimulation Technologies. Front. Cell. Neurosci. 15, 644126.

Mederos, S., Sánchez-Puelles, C., Esparza, J., Valero, M., Ponomarenko, A., Perea, G., 2021. GABAergic signaling to astrocytes in the prefrontal cortex sustains goal-directed behaviors. Nat. Neurosci. 24, 82–92.

Meguro, Y., Miyano, K., Hirayama, S., Yoshida, Y., Ishibashi, N., Ogino, T., Fujii, Y., Manabe, S., Eto, M., Nonaka, M., Fujii, H., Ueta, Y., Narita, M., Sata, N., Yada, T., Uezono, Y., 2018. Neuropeptide oxytocin enhances μ opioid receptor signaling as a positive allosteric modulator. J. Pharmacol. Sci. 137, 67–75.

Mens, W.B., Witter, A., van Wimersma Greidanus, T.B., 1983. Penetration of neurohypophyseal hormones from plasma into cerebrospinal fluid (CSF): half-times of disappearance of these neuropeptides from CSF. Brain Res. 262, 143–149.

Mergenthaler, P., Lindauer, U., Dienel, G.A., Meisel, A., 2013. Sugar for the brain: the role of glucose in physiological and pathological brain function. Trends Neurosci. 36, 587–597.

Meunier, C., Wang, N., Yi, C., Dallerac, G., Ezan, P., Koulakoff, A., Leybaert, L., Giaume, C., 2017. Contribution of Astroglial Cx43 Hemichannels to the Modulation of Glutamatergic Currents by D-Serine in the Mouse Prefrontal Cortex. J. Neurosci. Off. J. Soc. Neurosci. 37, 9064–9075.

Mitre, M., Marlin, B.J., Schiavo, J.K., Morina, E., Norden, S.E., Hackett, T.A., Aoki, C.J., Chao, M.V., Froemke, R.C., 2016. A Distributed Network for Social Cognition Enriched for Oxytocin Receptors. J. Neurosci. Off. J. Soc. Neurosci. 36, 2517–2535.

Miyano, K., Yoshida, Y., Hirayama, S., Takahashi, H., Ono, H., Meguro, Y., Manabe, S., Komatsu, A., Nonaka, M., Mizuguchi, T., Fujii, H., Higami, Y., Narita, M., Uezono, Y., 2021. Oxytocin Is a Positive Allosteric Modulator of κ-Opioid Receptors but Not δ-Opioid Receptors in the G Protein Signaling Pathway. Cells 10, 2651.

Moscarello, J.M., Penzo, M.A., 2022. The central nucleus of the amygdala and the construction of defensive modes across the threat-imminence continuum. Nat. Neurosci. 25, 999–1008.

Mothet, J.P., Parent, A.T., Wolosker, H., Brady, R.O., Linden, D.J., Ferris, C.D., Rogawski, M.A., Snyder, S.H., 2000. D-serine is an endogenous ligand for the glycine site of the N-methyl-D-aspartate receptor. Proc. Natl. Acad. Sci. U. S. A. 97, 4926–4931.

Murphy-Royal, C., Ching, S., Papouin, T., n.d. Contextual guidance: An integrated theory for astrocytes function in brain circuits and behavior [WWW Document]. URL https://www.x-mol.net/paper/article/1594744529616343040 (accessed 4.13.23).

Nagai, J., Rajbhandari, A.K., Gangwani, M.R., Hachisuka, A., Coppola, G., Masmanidis, S.C., Fanselow, M.S., Khakh, B.S., 2019. Hyperactivity with Disrupted Attention by Activation of an Astrocyte Synaptogenic Cue. Cell 177, 1280-1292.e20.

Nagai, J., Yu, X., Papouin, T., Cheong, E., Freeman, M.R., Monk, K.R., Hastings, M.H., Haydon, P.G., Rowitch, D., Shaham, S., Khakh, B.S., 2021. Behaviorally consequential astrocytic regulation of neural circuits. Neuron 109, 576–596.

Navarro, G., Cordomí, A., Casadó-Anguera, V., Moreno, E., Cai, N.-S., Cortés, A., Canela, E.I., Dessauer, C.W., Casadó, V., Pardo, L., Lluís, C., Ferré, S., 2018. Evidence for functional pre-coupled complexes of receptor heteromers and adenylyl cyclase. Nat. Commun. 9, 1242.

Nersesyan, Y., Demirkhanyan, L., Cabezas-Bratesco, D., Oakes, V., Kusuda, R., Dawson, T., Sun, X., Cao, C., Cohen, A.M., Chelluboina, B., Veeravalli, K.K., Zimmermann, K., Domene, C., Brauchi, S., Zakharian, E., 2017. Oxytocin Modulates Nociception as an Agonist of Pain-Sensing TRPV1. Cell Rep. 21, 1681–1691.

Nett, W.J., Oloff, S.H., McCarthy, K.D., 2002. Hippocampal astrocytes in situ exhibit calcium oscillations that occur independent of neuronal activity. J. Neurophysiol. 87, 528–537.

Neugebauer, V., Mazzitelli, M., Cragg, B., Ji, G., Navratilova, E., Porreca, F., 2020. Amygdala, neuropeptides, and chronic pain-related affective behaviors. Neuropharmacology 170, 108052.

Neumann, I.D., Krömer, S.A., Toschi, N., Ebner, K., 2000. Brain oxytocin inhibits the (re)activity of the hypothalamo-pituitary-adrenal axis in male rats: involvement of hypothalamic and limbic brain regions. Regul. Pept. 96, 31–38.

Newmaster, K.T., Nolan, Z.T., Chon, U., Vanselow, D.J., Weit, A.R., Tabbaa, M., Hidema, S., Nishimori, K., Hammock, E.A.D., Kim, Y., 2020. Quantitative cellular-resolution map of the oxytocin receptor in postnatally developing mouse brains. Nat. Commun. 11, 1885.

O'Callaghan, J.P., Kelly, K.A., VanGilder, R.L., Sofroniew, M.V., Miller, D.B., 2014. Early activation of STAT3 regulates reactive astrogliosis induced by diverse forms of neurotoxicity. PloS One 9, e102003.

Octeau, J.C., Gangwani, M.R., Allam, S.L., Tran, D., Huang, S., Hoang-Trong, T.M., Golshani, P., Rumbell, T.H., Kozloski, J.R., Khakh, B.S., 2019. Transient, Consequential Increases in Extracellular Potassium Ions Accompany Channelrhodopsin2 Excitation. Cell Rep. 27, 2249-2261.e7.

Oettl, L.-L., Ravi, N., Schneider, M., Scheller, M.F., Schneider, P., Mitre, M., da Silva Gouveia, M., Froemke, R.C., Chao, M.V., Young, W.S., Meyer-Lindenberg, A., Grinevich, V., Shusterman, R., Kelsch, W., 2016. Oxytocin Enhances Social Recognition by Modulating Cortical Control of Early Olfactory Processing. Neuron 90, 609–621.

Okubo, Y., 2020. Astrocytic Ca2+ signaling mediated by the endoplasmic reticulum in health and disease. J. Pharmacol. Sci. 144, 83–88.

O'Leary, L.A., Davoli, M.A., Belliveau, C., Tanti, A., Ma, J.C., Farmer, W.T., Turecki, G., Murai, K.K., Mechawar, N., 2020. Characterization of Vimentin-Immunoreactive Astrocytes in the Human Brain. Front. Neuroanat. 14, 31.

Oliet, S.H.R., Mothet, J.-P., 2009. Regulation of N-methyl-D-aspartate receptors by astrocytic D-serine. Neuroscience 158, 275–283.

Oliveira, V.E. de M., de Jong, T.R., Neumann, I.D., 2022. Synthetic Oxytocin and Vasopressin Act Within the Central Amygdala to Exacerbate Aggression in Female Wistar Rats. Front. Neurosci. 16, 906617.

Olivera-Pasilio, V., Dabrowska, J., 2020. Oxytocin Promotes Accurate Fear Discrimination and Adaptive Defensive Behaviors. Front. Neurosci. 14, 583878.

Ostroff, L.E., Manzur, M.K., Cain, C.K., Ledoux, J.E., 2014. Synapses lacking astrocyte appear in the amygdala during consolidation of Pavlovian threat conditioning. J. Comp. Neurol. 522, 2152–2163.

Otero-García, M., Agustín-Pavón, C., Lanuza, E., Martínez-García, F., 2016. Distribution of oxytocin and co-localization with arginine vasopressin in the brain of mice. Brain Struct. Funct. 221, 3445–3473.

Oti, T., Satoh, K., Uta, D., Nagafuchi, J., Tateishi, S., Ueda, R., Takanami, K., Young, L.J., Galione, A., Morris, J.F., Sakamoto, T., Sakamoto, H., 2021. Oxytocin Influences Male Sexual Activity via Non-synaptic Axonal Release in the Spinal Cord. Curr. Biol. CB 31, 103-114.e5.

Panatier, A., Vallée, J., Haber, M., Murai, K.K., Lacaille, J.-C., Robitaille, R., 2011. Astrocytes are endogenous regulators of basal transmission at central synapses. Cell 146, 785–798.

Pangršič, T., Potokar, M., Stenovec, M., Kreft, M., Fabbretti, E., Nistri, A., Pryazhnikov, E., Khiroug, L., Giniatullin, R., Zorec, R., 2007. Exocytotic release of ATP from cultured astrocytes. J. Biol. Chem. 282, 28749–28758.

Pannasch, U., Rouach, N., 2013. Emerging role for astroglial networks in information processing: from synapse to behavior. Trends Neurosci. 36, 405–417.

Papouin, T., Dunphy, J.M., Tolman, M., Dineley, K.T., Haydon, P.G., 2017. Septal Cholinergic Neuromodulation Tunes the Astrocyte-Dependent Gating of Hippocampal NMDA Receptors to Wakefulness. Neuron 94, 840-854.e7.

Papouin, T., Ladépêche, L., Ruel, J., Sacchi, S., Labasque, M., Hanini, M., Groc, L., Pollegioni, L., Mothet, J.-P., Oliet, S.H.R., 2012. Synaptic and extrasynaptic NMDA receptors are gated by different endogenous coagonists. Cell 150, 633–646.

Parekh, A.B., 2011. Decoding cytosolic Ca2+ oscillations. Trends Biochem. Sci. 36, 78–87.

Parpura, V., Basarsky, T.A., Liu, F., Jeftinija, K., Jeftinija, S., Haydon, P.G., 1994. Glutamate-mediated astrocyte-neuron signalling. Nature 369, 744–747.

Parpura, V., Grubišić, V., Verkhratsky, A., 2011. Ca(2+) sources for the exocytotic release of glutamate from astrocytes. Biochim. Biophys. Acta 1813, 984–991.

Parri, H.R., Gould, T.M., Crunelli, V., 2001. Spontaneous astrocytic Ca2+ oscillations in situ drive NMDAR-mediated neuronal excitation. Nat. Neurosci. 4, 803–812.

Passoni, I., Leonzino, M., Gigliucci, V., Chini, B., Busnelli, M., 2016. Carbetocin is a Functional Selective Gq Agonist That Does Not Promote Oxytocin Receptor Recycling After Inducing β-Arrestin-Independent Internalisation. J. Neuroendocrinol. 28, n/a.

Pasti, L., Zonta, M., Pozzan, T., Vicini, S., Carmignoto, G., 2001. Cytosolic calcium oscillations in astrocytes may regulate exocytotic release of glutamate. J. Neurosci. Off. J. Soc. Neurosci. 21, 477–484.

Perea, G., Araque, A., 2005. Properties of synaptically evoked astrocyte calcium signal reveal synaptic information processing by astrocytes. J. Neurosci. Off. J. Soc. Neurosci. 25, 2192–2203.

Perea, G., Araque, A., 2007. Astrocytes potentiate transmitter release at single hippocampal synapses. Science 317, 1083–1086.

Perea, G., Navarrete, M., Araque, A., 2009. Tripartite synapses: astrocytes process and control synaptic information. Trends Neurosci. 32, 421–431.

Perez-Alvarez, A., Navarrete, M., Covelo, A., Martin, E.D., Araque, A., 2014. Structural and functional plasticity of astrocyte processes and dendritic spine interactions. J. Neurosci. Off. J. Soc. Neurosci. 34, 12738–12744.

Perez-Catalan, N.A., Doe, C.Q., Ackerman, S.D., 2021. The role of astrocyte-mediated plasticity in neural circuit development and function. Neural Develop. 16, 1.

Petravicz, J., Fiacco, T.A., McCarthy, K.D., 2008. Loss of IP3 receptor-dependent Ca2+ increases in hippocampal astrocytes does not affect baseline CA1 pyramidal neuron synaptic activity. J. Neurosci. Off. J. Soc. Neurosci. 28, 4967–4973.

Pfeil, E.M., Brands, J., Merten, N., Vögtle, T., Vescovo, M., Rick, U., Albrecht, I.-M., Heycke, N., Kawakami, K., Ono, Y., Ngako Kadji, F.M., Hiratsuka, S., Aoki, J., Häberlein, F., Matthey, M., Garg, J., Hennen, S., Jobin, M.-L., Seier, K., Calebiro, D., Pfeifer, A., Heinemann, A., Wenzel, D., König, G.M., Nieswandt, B., Fleischmann, B.K., Inoue, A., Simon, K., Kostenis, E., 2020. Heterotrimeric G Protein Subunit Gαq Is a Master Switch for Gβγ-Mediated Calcium Mobilization by Gi-Coupled GPCRs. Mol. Cell 80, 940-954.e6.

Phaneuf, S., Europe-Finner, G.N., Varney, M., MacKenzie, I.Z., Watson, S.P., López Bernal, A., 1993. Oxytocin-stimulated phosphoinositide hydrolysis in human myometrial cells: involvement of pertussis toxin-sensitive and -insensitive G-proteins. J. Endocrinol. 136, 497–509.

Pomrenze, M.B., Tovar-Diaz, J., Blasio, A., Maiya, R., Giovanetti, S.M., Lei, K., Morikawa, H., Hopf, F.W., Messing, R.O., 2019. A Corticotropin Releasing Factor Network in the Extended Amygdala for Anxiety. J. Neurosci. Off. J. Soc. Neurosci. 39, 1030–1043.

Priego, N., Zhu, L., Monteiro, C., Mulders, M., Wasilewski, D., Bindeman, W., Doglio, L., Martínez, Liliana, Martínez-Saez, E., Ramón Y Cajal, S., Megías, D., Hernández-Encinas, E., Blanco-Aparicio, C., Martínez, Lola, Zarzuela, E., Muñoz, J., Fustero-Torre, C., Piñeiro-Yáñez, E., Hernández-Laín, A., Bertero, L., Poli, V., Sanchez-Martinez, M., Menendez, J.A., Soffietti, R., Bosch-Barrera, J., Valiente, M., 2018. STAT3 labels a subpopulation of reactive astrocytes required for brain metastasis. Nat. Med. 24, 1024–1035.

Quintana, D.S., Guastella, A.J., 2020. An Allostatic Theory of Oxytocin. Trends Cogn. Sci. 24, 515–528.

Rasmussen, R., Nedergaard, M., Petersen, N.C., 2016. Sulforhodamine 101, a widely used astrocyte marker, can induce cortical seizure-like activity at concentrations commonly used. Sci. Rep. 6, 30433.

Resendez, S.L., Namboodiri, V.M.K., Otis, J.M., Eckman, L.E.H., Rodriguez-Romaguera, J., Ung, R.L., Basiri, M.L., Kosyk, O., Rossi, M.A., Dichter, G.S., Stuber, G.D., 2020. Social Stimuli Induce Activation of Oxytocin Neurons Within the Paraventricular Nucleus of the Hypothalamus to Promote Social Behavior in Male Mice. J. Neurosci. Off. J. Soc. Neurosci. 40, 2282–2295.

Rettori, V., Canteros, G., Renoso, R., Gimeno, M., McCann, S.M., 1997. Oxytocin stimulates the release of luteinizing hormone-releasing hormone from medial basal hypothalamic explants by releasing nitric oxide. Proc. Natl. Acad. Sci. U. S. A. 94, 2741–2744.

Rickenbacher, E., Perry, R.E., Sullivan, R.M., Moita, M.A., 2017. Freezing suppression by oxytocin in central amygdala allows alternate defensive behaviours and mother-pup interactions. eLife 6, e24080.

Rimoldi, V., Reversi, A., Taverna, E., Rosa, P., Francolini, M., Cassoni, P., Parenti, M., Chini, B., 2003. Oxytocin receptor elicits different EGFR/MAPK activation patterns depending on its localization in caveolin-1 enriched domains. Oncogene 22, 6054–6060.

Romero-Fernandez, W., Borroto-Escuela, D.O., Agnati, L.F., Fuxe, K., 2013. Evidence for the existence of dopamine D2-oxytocin receptor heteromers in the ventral and dorsal striatum with facilitatory receptor-receptor interactions. Mol. Psychiatry 18, 849–850.

Root, C.M., Denny, C.A., Hen, R., Axel, R., 2014. The participation of cortical amygdala in innate, odour-driven behaviour. Nature 515, 269–273.

Roozendaal, B., Koolhaas, J.M., Bohus, B., 1992. Central amygdaloid involvement in neuroendocrine correlates of conditioned stress responses. J. Neuroendocrinol. 4, 483–489.

Roy, R.K., Augustine, R.A., Brown, C.H., Schwenke, D.O., 2018. Activation of oxytocin neurons in the paraventricular nucleus drives cardiac sympathetic nerve activation following myocardial infarction in rats. Commun. Biol. 1, 160.

Ryan, P.J., Ross, S.I., Campos, C.A., Derkach, V.A., Palmiter, R.D., 2017. Oxytocin-receptor-expressing neurons in the parabrachial nucleus regulate fluid intake. Nat. Neurosci. 20, 1722–1733.

Sahlender, D.A., Savtchouk, I., Volterra, A., 2014. What do we know about gliotransmitter release from astrocytes? Philos. Trans. R. Soc. Lond. B. Biol. Sci. 369, 20130592.

Sandhu, M., Cho, A., Ma, N., Mukhaleva, E., Namkung, Y., Lee, S., Ghosh, S., Lee, J.H., Gloriam, D.E., Laporte, S.A., Babu, M.M., Vaidehi, N., 2022. Dynamic spatiotemporal determinants modulate GPCR:G protein coupling selectivity and promiscuity. Nat. Commun. 13, 7428.

Santello, M., Bezzi, P., Volterra, A., 2011. TNFα controls glutamatergic gliotransmission in the hippocampal dentate gyrus. Neuron 69, 988–1001.

Santello, M., Toni, N., Volterra, A., 2019. Astrocyte function from information processing to cognition and cognitive impairment. Nat. Neurosci. 22, 154–166.

Savtchouk, I., Volterra, A., 2018. Gliotransmission: Beyond Black-and-White. J. Neurosci. Off. J. Soc. Neurosci. 38, 14–25.

Schousboe, A., Scafidi, S., Bak, L.K., Waagepetersen, H.S., McKenna, M.C., 2014. Glutamate metabolism in the brain focusing on astrocytes. Adv. Neurobiol. 11, 13–30.

Semyanov, A., Henneberger, C., Agarwal, A., 2020. Making sense of astrocytic calcium signals - from acquisition to interpretation. Nat. Rev. Neurosci. 21, 551–564.

Serra, I., Esparza, J., Delgado, L., Martín-Monteagudo, C., Puigròs, M., Podlesniy, P., Trullás, R., Navarrete, M., 2022. Ca2+-modulated photoactivatable imaging reveals neuron-astrocyte glutamatergic circuitries within the nucleus accumbens. Nat. Commun. 13, 5272.

Sheldrick, E.L., Flint, A.P., 1985. Endocrine control of uterine oxytocin receptors in the ewe. J. Endocrinol. 106, 249–258.

Shepherd, G.M.G., Raastad, M., 2003. Axonal varicosity distributions along parallel fibers: a new angle on a cerebellar circuit. Cerebellum Lond. Engl. 2, 110–113.

Shigetomi, E., Koizumi, S., 2023. The role of astrocytes in behaviors related to emotion and motivation. Neurosci. Res. 187, 21–39.

Shigetomi, E., Kracun, S., Sofroniew, M.V., Khakh, B.S., 2010. A genetically targeted optical sensor to monitor calcium signals in astrocyte processes. Nat. Neurosci. 13, 759–766.

Shigetomi, E., Patel, S., Khakh, B.S., 2016. Probing the Complexities of Astrocyte Calcium Signaling. Trends Cell Biol. 26, 300–312.

Shigetomi, E., Saito, K., Sano, F., Koizumi, S., 2019. Aberrant Calcium Signals in Reactive Astrocytes: A Key Process in Neurological Disorders. Int. J. Mol. Sci. 20, 996.

Sibille, J., Pannasch, U., Rouach, N., 2014. Astroglial potassium clearance contributes to short-term plasticity of synaptically evoked currents at the tripartite synapse. J. Physiol. 592, 87–102.

Sladek, C.D., Song, Z., 2012. Diverse Roles of G-Protein Coupled Receptors in Regulation of Neurohypophyseal Hormone Secretion. J. Neuroendocrinol. 24, 554–565.

Smith, M.P., Ayad, V.J., Mundell, S.J., McArdle, C.A., Kelly, E., López Bernal, A., 2006. Internalization and desensitization of the oxytocin receptor is inhibited by Dynamin and clathrin mutants in human embryonic kidney 293 cells. Mol. Endocrinol. Baltim. Md 20, 379–388.

Srinivasan, R., Huang, B.S., Venugopal, S., Johnston, A.D., Chai, H., Zeng, H., Golshani, P., Khakh, B.S., 2015. Ca(2+) signaling in astrocytes from Ip3r2(-/-) mice in brain slices and during startle responses in vivo. Nat. Neurosci. 18, 708–717.

Steimer, T., 2002. The biology of fear- and anxiety-related behaviors. Dialogues Clin. Neurosci. 4, 231–249.

Stephan, J., Eitelmann, S., Zhou, M., 2021. Approaches to Study Gap Junctional Coupling. Front. Cell. Neurosci. 15, 640406.

Stoop, R., 2012. Neuromodulation by oxytocin and vasopressin. Neuron 76, 142–159.

Strakova, Z., Soloff, M.S., 1997. Coupling of oxytocin receptor to G proteins in rat myometrium during labor: Gi receptor interaction. Am. J. Physiol. 272, E870-876.

Sun, T., Hevner, R.F., 2014. Growth and folding of the mammalian cerebral cortex: from molecules to malformations. Nat. Rev. Neurosci. 15, 217–232.

Sun, Y., Qian, L., Xu, L., Hunt, S., Sah, P., 2020. Somatostatin neurons in the central amygdala mediate anxiety by disinhibition of the central sublenticular extended amygdala. Mol. Psychiatry.

Sutkeviciute, I., Vilardaga, J.-P., 2020. Structural insights into emergent signaling modes of G protein-coupled receptors. J. Biol. Chem. 295, 11626–11642.

á, E., 2004. Extrasynaptic volume transmission and diffusion parameters of the extracellular space. Neuroscience 129, 861–876.

Taché, Y., Bonaz, B., 2007. Corticotropin-releasing factor receptors and stress-related alterations of gut motor function. J. Clin. Invest. 117, 33–40.

Takano, T., He, W., Han, X., Wang, F., Xu, Q., Wang, X., Oberheim Bush, N.A., Cruz, N., Dienel, G.A., Nedergaard, M., 2014. Rapid manifestation of reactive astrogliosis in acute hippocampal brain slices. Glia 62, 78–95.

Tamagawa, H., 2019. Mathematical expression of membrane potential based on Ling's adsorption theory is approximately the same as the Goldman–Hodgkin–Katz equation. J. Biol. Phys. 45, 13–30.

Tan, Y., Singhal, S.M., Harden, S.W., Cahill, K.M., Nguyen, D.-T.M., Colon-Perez, L.M., Sahagian, T.J., Thinschmidt, J.S., de Kloet, A.D., Febo, M., Frazier, C.J., Krause, E.G., 2019. Oxytocin Receptors Are Expressed by Glutamatergic Prefrontal Cortical Neurons That Selectively Modulate Social Recognition. J. Neurosci. Off. J. Soc. Neurosci. 39, 3249–3263.

Tang, Y., Benusiglio, D., Lefevre, A., Hilfiger, L., Althammer, F., Bludau, A., Hagiwara, D., Baudon, A., Darbon, P., Schimmer, J., Kirchner, M.K., Roy, R.K., Wang, S., Eliava, M., Wagner, S., Oberhuber, M., Conzelmann, K.K., Schwarz, M., Stern, J.E., Leng, G., Neumann, I.D., Charlet, A., Grinevich, V., 2020. Social touch promotes interfemale communication via activation of parvocellular oxytocin neurons. Nat. Neurosci. 23, 1125–1137.

Tang, Y., Chen, Z., Tao, H., Li, C., Zhang, X., Tang, A., Liu, Y., 2014. Oxytocin activation of neurons in ventral tegmental area and interfascicular nucleus of mouse midbrain. Neuropharmacology 77, 277–284.

Terburg, D., Scheggia, D., Triana Del Rio, R., Klumpers, F., Ciobanu, A.C., Morgan, B., Montoya, E.R., Bos, P.A., Giobellina, G., van den Burg, E.H., de Gelder, B., Stein, D.J., Stoop, R., van Honk, J., 2018. The Basolateral Amygdala Is Essential for Rapid Escape: A Human and Rodent Study. Cell 175, 723-735.e16.

Terenzi, M.G., Ingram, C.D., 2005. Oxytocin-induced excitation of neurones in the rat central and medial amygdaloid nuclei. Neuroscience 134, 345–354.

Terrillon, S., Durroux, T., Mouillac, B., Breit, A., Ayoub, M.A., Taulan, M., Jockers, R., Barberis, C., Bouvier, M., 2003. Oxytocin and vasopressin V1a and V2 receptors form constitutive homo- and heterodimers during biosynthesis. Mol. Endocrinol. Baltim. Md 17, 677–691.

Theodosis, D.T., Poulain, D.A., Oliet, S.H.R., 2008. Activity-dependent structural and functional plasticity of astrocyte-neuron interactions. Physiol. Rev. 88, 983–1008.

Theparambil, S.M., Hosford, P.S., Ruminot, I., Kopach, O., Reynolds, J.R., Sandoval, P.Y., Rusakov, D.A., Barros, L.F., Gourine, A.V., 2020. Astrocytes regulate brain extracellular pH via a neuronal activity-dependent bicarbonate shuttle. Nat. Commun. 11, 5073.

Thompson, J.M., Neugebauer, V., 2017. Amygdala Plasticity and Pain. Pain Res. Manag. 2017, 8296501.

Thurley, K., Tovey, S.C., Moenke, G., Prince, V.L., Meena, A., Thomas, A.P., Skupin, A., Taylor, C.W., Falcke, M., 2014. Reliable encoding of stimulus intensities within random sequences of intracellular Ca2+ spikes. Sci. Signal. 7, ra59.

Tirko, N.N., Eyring, K.W., Carcea, I., Mitre, M., Chao, M.V., Froemke, R.C., Tsien, R.W., 2018. Oxytocin Transforms Firing Mode of CA2 Hippocampal Neurons. Neuron 100, 593-608.e3.

Tobin, V.A., Arechaga, G., Brunton, P.J., Russell, J.A., Leng, G., Ludwig, M., Douglas, A.J., 2014. Oxytocinase in the female rat hypothalamus: a novel mechanism controlling oxytocin neurones during lactation. J. Neuroendocrinol. 26, 205–216.

Todd, K.J., Darabid, H., Robitaille, R., 2010. Perisynaptic glia discriminate patterns of motor nerve activity and influence plasticity at the neuromuscular junction. J. Neurosci. Off. J. Soc. Neurosci. 30, 11870–11882.

Tsujimoto, M., Hattori, A., 2005. The oxytocinase subfamily of M1 aminopeptidases. Biochim. Biophys. Acta 1751, 9–18.

Tunstall, B.J., Kirson, D., Zallar, L.J., McConnell, S.A., Vendruscolo, J.C.M., Ho, C.P., Oleata, C.S., Khom, S., Manning, M., Lee, M.R., Leggio, L., Koob, G.F., Roberto, M., Vendruscolo, L.F., 2019. Oxytocin blocks enhanced motivation for alcohol in alcohol dependence and blocks alcohol effects on GABAergic transmission in the central amygdala. PLoS Biol. 17, e2006421.

Uhl-Bronner, S., Waltisperger, E., Martínez-Lorenzana, G., Condes Lara, M., Freund-Mercier, M.J., 2005. Sexually dimorphic expression of oxytocin binding sites in forebrain and spinal cord of the rat. Neuroscience 135, 147–154.

Veinante, P., Freund-Mercier, M.J., 1997. Distribution of oxytocin- and vasopressin-binding sites in the rat extended amygdala: a histoautoradiographic study. J. Comp. Neurol. 383, 305–325.

Veinante, P., Yalcin, I., Barrot, M., 2013. The amygdala between sensation and affect: a role in pain. J. Mol. Psychiatry 1, 9.

Verhoog, Q.P., Holtman, L., Aronica, E., van Vliet, E.A., 2020. Astrocytes as Guardians of Neuronal Excitability: Mechanisms Underlying Epileptogenesis. Front. Neurol. 11, 591690.

Verkhratsky, A., Nedergaard, M., 2018. Physiology of Astroglia. Physiol. Rev. 98, 239–389.

Verkhratsky, A., Untiet, V., Rose, C.R., 2020. Ionic signalling in astroglia beyond calcium. J. Physiol. 598, 1655–1670.

Vilardaga, J.-P., Bünemann, M., Feinstein, T.N., Lambert, N., Nikolaev, V.O., Engelhardt, S., Lohse, M.J., Hoffmann, C., 2009. GPCR and G proteins: drug efficacy and activation in live cells. Mol. Endocrinol. Baltim. Md 23, 590–599.

Viviani, D., Charlet, A., van den Burg, E., Robinet, C., Hurni, N., Abatis, M., Magara, F., Stoop, R., 2011. Oxytocin selectively gates fear responses through distinct outputs from the central amygdala. Science 333, 104–107.

Volterra, A., Liaudet, N., Savtchouk, I., 2014. Astrocyte Ca^{2+} signalling: an unexpected complexity. Nat. Rev. Neurosci. 15, 327–335.

Volterra, A., Meldolesi, J., 2005. Astrocytes, from brain glue to communication elements: the revolution continues. Nat. Rev. Neurosci. 6, 626–640.

Wahis, J., Baudon, A., Althammer, F., Kerspern, D., Goyon, S., Hagiwara, D., Lefevre, A., Barteczko, L., Boury-Jamot, B., Bellanger, B., Abatis, M., Da Silva Gouveia, M., Benusiglio, D., Eliava, M., Rozov, A., Weinsanto, I., Knobloch-Bollmann, H.S., Kirchner, M.K., Roy, R.K., Wang, H., Pertin, M., Inquimbert, P., Pitzer, C., Siemens, J., Goumon, Y., Boutrel, B., Lamy, C.M., Decosterd, I., Chatton, J.-Y., Rouach, N., Young, W.S., Stern, J.E., Poisbeau, P., Stoop, R., Darbon, P., Grinevich, V., Charlet, A., 2021. Astrocytes mediate the effect of oxytocin in the central amygdala on neuronal activity and affective states in rodents. Nat. Neurosci. 24, 529–541.

Walch, E., Fiacco, T.A., 2022. Honey, I shrunk the extracellular space: Measurements and mechanisms of astrocyte swelling. Glia 70, 2013–2031.

Wang, H., Song, G., Chuang, H., Chiu, C., Abdelmaksoud, A., Ye, Y., Zhao, L., 2018. Portrait of glial scar in neurological diseases. Int. J. Immunopathol. Pharmacol. 31, 2058738418801406.

Wang, P., Qin, D., Wang, Y.-F., 2017. Oxytocin Rapidly Changes Astrocytic GFAP Plasticity by Differentially Modulating the Expressions of pERK 1/2 and Protein Kinase A. Front. Mol. Neurosci. 10, 262.

Wang, T., Zhou, C., Tang, A., Wang, S., Chai, Z., 2006. Cellular mechanism for spontaneous calcium oscillations in astrocytes. Acta Pharmacol. Sin. 27, 861–868.

Wang, Y.-F., Hatton, G.I., 2007a. Dominant role of betagamma subunits of G-proteins in oxytocin-evoked burst firing. J. Neurosci. Off. J. Soc. Neurosci. 27, 1902–1912.

Wang, Y.-F., Hatton, G.I., 2007b. Interaction of extracellular signal-regulated protein kinase 1/2 with actin cytoskeleton in supraoptic oxytocin neurons and astrocytes: role in burst firing. J. Neurosci. Off. J. Soc. Neurosci. 27, 13822–13834.

Wang, Y.-F., Hatton, G.I., 2009. Astrocytic plasticity and patterned oxytocin neuronal activity: dynamic interactions. J. Neurosci. Off. J. Soc. Neurosci. 29, 1743–1754.

Wilhelmsson, U., Bushong, E.A., Price, D.L., Smarr, B.L., Phung, V., Terada, M., Ellisman, M.H., Pekny, M., 2006. Redefining the concept of reactive astrocytes as cells that remain within their unique domains upon reaction to injury. Proc. Natl. Acad. Sci. U. S. A. 103, 17513–17518.

Willets, J.M., Brighton, P.J., Mistry, R., Morris, G.E., Konje, J.C., Challiss, R.A.J., 2009. Regulation of oxytocin receptor responsiveness by G protein-coupled receptor kinase 6 in human myometrial smooth muscle. Mol. Endocrinol. Baltim. Md 23, 1272–1280.

Wilson, B.C., Terenzi, M.G., Ingram, C.D., 2005. Differential excitatory responses to oxytocin in sub-divisions of the bed nuclei of the stria terminalis. Neuropeptides 39, 403–407.

Wilson, T.D., Valdivia, S., Khan, A., Ahn, H.-S., Adke, A.P., Martinez Gonzalez, S., Sugimura, Y.K., Carrasquillo, Y., 2019. Dual and Opposing Functions of the Central Amygdala in the Modulation of Pain. Cell Rep. 29, 332-346.e5.

Windle, R.J., Shanks, N., Lightman, S.L., Ingram, C.D., 1997. Central oxytocin administration reduces stress-induced corticosterone release and anxiety behavior in rats. Endocrinology 138, 2829–2834.

Xiao, L., Priest, M.F., Nasenbeny, J., Lu, T., Kozorovitskiy, Y., 2017. Biased Oxytocinergic Modulation of Midbrain Dopamine Systems. Neuron 95, 368-384.e5.

Xu, J., Peng, H., Kang, N., Zhao, Z., Lin, J.H.-C., Stanton, P.K., Kang, J., 2007. Glutamate-induced exocytosis of glutamate from astrocytes. J. Biol. Chem. 282, 24185–24197.

Ye, J., Veinante, P., 2019. Cell-type specific parallel circuits in the bed nucleus of the stria terminalis and the central nucleus of the amygdala of the mouse. Brain Struct. Funct. 224, 1067–1095.

Young, W.S., Gainer, H., 2003. Transgenesis and the study of expression, cellular targeting and function of oxytocin, vasopressin and their receptors. Neuroendocrinology 78, 185–203.

Yu, K., Garcia da Silva, P., Albeanu, D.F., Li, B., 2016. Central Amygdala Somatostatin Neurons Gate Passive and Active Defensive Behaviors. J. Neurosci. Off. J. Soc. Neurosci. 36, 6488–6496.

Zahm, D.S., 2006. The evolving theory of basal forebrain functional-anatomical "macrosystems." Neurosci. Biobehav. Rev. 30, 148–172.

Zhang, B., Qiu, L., Xiao, W., Ni, H., Chen, L., Wang, F., Mai, W., Wu, J., Bao, A., Hu, H., Gong, H., Duan, S., Li, A., Gao, Z., 2021. Reconstruction of the Hypothalamo-Neurohypophysial System and Functional Dissection of Magnocellular Oxytocin Neurons in the Brain. Neuron 109, 331-346.e7.

Zhao, S., Shetty, J., Hou, L., Delcher, A., Zhu, B., Osoegawa, K., de Jong, P., Nierman, W.C., Strausberg, R.L., Fraser, C.M., 2004. Human, Mouse, and Rat Genome Large-Scale Rearrangements: Stability Versus Speciation. Genome Res. 14, 1851–1860.

Zoellner, L.A., Rothbaum, B.O., Feeny, N.C., 2011. PTSD not an anxiety disorder? DSM committee proposal turns back the hands of time. Depress. Anxiety 28, 853–856.

Zorec, R., Araque, A., Carmignoto, G., Haydon, P.G., Verkhratsky, A., Parpura, V., 2012. Astroglial excitability and gliotransmission: an appraisal of Ca2+ as a signalling route. ASN Neuro 4, e00080.

Angel BAUDON

Étude de l'effet de l'ocytocine sur le circuit astro-neuronal de l'amygdale centrale

Study of the oxytocin effect on the central amygdala astro-neuronal network

Résumé

L'ocytocine est un neuropeptide hypothalamique ipmliqué dans le contrôle des émotions. Pour cette raison, je me suis intéressé à l'effet de ce peptide sur l'activité des astrocytes et des neurones de l'amygdale, une structure impliquée dans l'attribution de la valeur émotionnelle. Dans un premier temps, j'ai évalué l'effet à court terme de l'ocytocine sur les astrocytes et sur les neurones. Cette première approche nous a permis de démontrer que l'ocytocine pouvait directement activer les astrocytes de l'amygdale. Ces derniers peuvent ensuite augmenter l'activité des neurones qui les entourent en libérant des molécules neuroactives. Dans un second temps, je me suis intéressé à l'effet de l'ocytocine sur les astrocytes sur le long terme. En évaluant la morphologie et la fonction de ces derniers, nous avons pu mettre en évidence que l'ocytocine provoque une plasticité morpho-fonctionnelle des astrocytes de l'amygdale, ainsi contrôlant l'excitabilité des neurones sur le long terme.

Dans l'ensemble, mon travail de thèse a permis de mettre en évidence l'implication des astrocytes dans l'effet neuromodulateur de l'ocytocine.

Mots clefs : Astrocyte, Ocytocine, Amygdale

Résumé en anglais

Oxytocin is a hypothalamic neuropeptide involved in the control of emotions. For this reason, I studied the effect of this peptide on the activity of astrocytes and neurons of the amygdala, a structure involved in the attribution of the emotional value of things. In the first step, I evaluated the short-term effect of oxytocin on astrocytes and neurons. This first approach allowed us to demonstrate that oxytocin could directly activate astrocytes in the amygdala. These astrocytes can then increase the activity of the surrounding neurons by releasing neuroactive molecules. In the second step, I focused on the effect of oxytocin on astrocytes in the long term. By evaluating the morphology and function of these cells, we showed that oxytocin induces a morpho-functional plasticity of astrocytes in the amygdala, thus controlling the excitability of neurons in the long term.

Overall, my thesis work has demonstrated the involvement of astrocytes in the neuromodulatory effect of oxytocin.

Keywords: Astrocytes, Oxytocin, Amygdala.